



THÈSE

En vue de l'obtention du

DOCTORAT DE L'UNIVERSITÉ DE TOULOUSE

Délivré par : *l'Institut Supérieur de l'Aéronautique et de l'Espace (ISAE)*

Présentée et soutenue le 07/05/2019 par :
MAXIME FIORE

Influence of cavity flow on turbine aerodynamics

JURY

PAUL TUCKER	Cambridge	Rapporteur
VITTORIO MICHELASSI	Baker Hughes (GE)	Rapporteur
ISABELLE TREBINJAC	Ecole Centrale Lyon	Examineur
J.-F. BOUSSUGE	CERFACS	Examineur
ERIC LIPPINOIS	Safran Aircraft Engines	Examineur
NICOLAS GOURDAIN	ISAE	Directeur
PIERRE GINIBRE	Safran Aircraft Engines	Invité

École doctorale et spécialité :

MEGEP : Dynamique des fluides

Unité de Recherche :

CERFACS-CFD (UMR 5318) et ISAE-DAEP

Remerciements

Je remercie les membres du jury d'avoir gentiment accepté d'évaluer mes travaux de thèse: Madame la présidente du jury, professeur Isabelle Trébinjac pour sa grande expertise concernant les turbomachines et son extrême gentillesse. Un grand merci aux deux rapporteurs professeur Paul G. Tucker et professeur Vittorio Michelassi pour avoir lu mon travail en détails. C'est une des principales raisons qui m'a poussé à rédiger le manuscrit en anglais, la possibilité d'être lu par ces références dans le domaine des turbomachines.

Mes premiers remerciements relatifs à mes connaissances vont à mes encadrants qui m'ont fait confiance, suivi et ont permis que cette thèse se passe dans les meilleures conditions possibles. Jean-François, merci pour ton aide, tu as toujours été de bon conseil pour les présentations et les rendre un peu moins pénibles à suivre que les premières versions réalisées. Nicolas, ta compétence technique dans les turbomachines et les simulations numériques n'ont jamais cessé de m'impressionner. Je suis extrêmement reconnaissant pour toute l'aide que tu m'as apporté, toujours avec gentillesse et humilité. Tout ceci sans oublier les petits mots de soutien qui sont très importants dans les moments un peu plus difficiles d'une thèse. Eric, je te remercie pour l'accueil et l'accompagnement au début de la thèse à Safran Aircraft Engine et plus généralement tout du long de la thèse. Autant sur le plan personnel que technique, je suis très admiratif de ta personne. Merci Pierre, les quelques connaissances que je peux avoir des turbines, c'est une petite partie de toutes tes connaissances.

Ces trois années de thèse au Cerfacs n'auraient pas été si agréables sans la présence de stagiaires, doctorants, post-doc, permanents, personnel administratif (Chantal la joie communicative), secrétariat (Nicole et Marie) et équipe informatique. Un grand merci à l'équipe "elsA": Majd, mon premier co-bureau, pour toute ta gentillesse, ta bienveillance (je pense aux vacances), et ton aide durant la thèse. Mathieu, un grand merci pour toutes ces discussions agréables, ton aide (et ce jusqu'à la soutenance), je me demande vraiment ce qu'attend Ferrari pour te recruter ! Romain (Biolchi), transmets moi un peu de ta tranquillité. Marc, merci pour toute ton aide sur elsA, Antares et plus généralement pour ton extrême humilité et simplicité, pensée pour Frédéric, Alexia et Adèle également. Je remercie Félix (la classe), Valou (notre goal), Jarjar (pour la gentille relecture de thèse), Kelu (le mec cool), Omar (la sérénité incarnée), Quentin (monsieur vélo), Julien (l'agenda de ministre), Christopher (le goal de haut niveau), Luis (le vrai expert en turbomachines), Nico (le buteur), Greg (l'homme qui attendait le train sur un terrain de foot), Mélissa, Dario (il est enfin possible d'associer vos deux prénoms dans des remerciements de thèse) Pierre et Laure (j'essaierai d'être plus assidu sur les pots de départs / arrivés), pour ces quelques pauses partagées ensemble. Je ne saurais également oublier la team "LBM": Gauthier, Thomas (Tastoul), Florian, Christophe, Johan, Danny et Bastien (je te mets dans cette case car même si tu fais de la combustion, un jour la LBM fera de la combustion). Je remercie l'équipe de foot du Cerfacs, l'En Avant Cerfacs, pour ces trois années passées. Je profite de ces remerciements pour m'excuser de ne pas avoir envoyé certaines feuilles de match, il est possible que cela

nous ait coûté quelques points (et une place en poule 4). J'en remercie les joueurs: Nico (tes talents de dissimulation ne sont plus à démontrer), Camille (le président en poste), Ekhi (comment fais-tu pour courir autant ?), Victor (les gourdes sont dans ta voiture !), Crespo, Romain (Bizzari).

Je pense à l'ONERA au sein duquel j'ai fait mon stage de fin d'études. Merci à Maxime Bouyges, je n'aurais pu espérer meilleur co-bureau, la stabilité des écoulements, le foot, nos prénoms, cela faisait beaucoup trop de points en commun pour ne pas s'entendre. Merci à Pierre, expérimentateur dans l'âme, grand joueur de foot, le tout dans une modestie et simplicité légendaire. Merci à mes encadrants: Maxime, je ne pensais pas qu'il était possible d'avoir un encadrant avec qui je jouerais au foot et qui aurait toujours cet esprit d'un jeune étudiant insouciant. Olivier, merci pour ta gentillesse et toute l'attention que tu portes pour m'aider. Grégoire, je suis très admiratif de votre compétence scientifique (ce qui rend toujours difficile pour moi le tutoiement), le tout dans une très grande gentillesse et simplicité. Un grand merci à vous trois car vous m'avez beaucoup aidé à la suite du stage ainsi que pour pouvoir réaliser cette thèse, je vous en suis très reconnaissant.

Je remercie mes amis du foot de Montech, c'est toujours un plaisir de vous retrouver: Benoit (nous étions amis avant de naître je pense), José (le vrai buteur espagnol), Gaby (le goal au dégagement redoutable), Pierre (petit machoc), Thibault (ton entrain m'impressionnera toujours), Yécin (le vrai joueur pro), Julien Gayet (la cisaille), Julien Ambal (le grand gaillard), Morad, Christopher, Romain (dans un 777).

Je remercie mes amis du lycée (communément appelé le groupe "ninooon" en référence à cette expression émise par Kelyann lorsque quelque chose ne se passait pas comme prévu). Merci à Kelyann (mon binôme de SVT), Pierre (à nos premiers ramassages de balles au tennis), Charlie (c'est un monde parallèle...), Etienne (un jour on aura la Ligue des Champions avec le PSG), Anto (avait-on vu quelqu'un travailler si peu en math et avoir d'aussi bonnes notes ?), Florian (je suis sûr qu'au moment auquel j'écris, tu es en train de courir), Vince (je serai toujours là pour te rappeler les fins de soirées difficiles), Victor (si un jour nous sommes ennuyés avec la justice, toi seul pourra nous sauver), Anastasia (la première docteur, tu peux être fière de ton parcours), Eloa (tu es la prochaine sur la liste des docteurs, ça va bien se passer), Maud (le temps semble glisser sur toi, tu me donneras la recette j'espère un jour !), Nora (je ne peux m'empêcher d'avoir ta voix dans ma tête lorsque cette phrase apparaît: "mais d'accord"), Chachou (notre artiste du groupe), Emilie (pas trop de folies). Merci à Matthieu et César pour les quelques fois où l'on peut se voir dans l'année et bonne chance à toi César pour la dernière ligne droite dans ta thèse. Merci à Stella, tu me fais penser que l'on ne saurait se restreindre à la science, la littérature compte aussi ! Une petite pensée pour Juliette ma voisine et amie de longue date, bonne chance pour tes derniers examens de notaire. Julie-Marie, merci pour ton amitié.

Je remercie ma famille: mes grands-parents, oncles, tantes et cousins, mon frère et mes parents pour tout ce qu'ils m'ont apporté, je leur dois beaucoup.

Résumé

Les turbomachines sont largement utilisées pour la production d'électricité et pour la propulsion aérienne. Une augmentation, même minime, du rendement de ces machines peut avoir un effet important sur la consommation et les émissions polluantes à l'échelle mondiale. Concernant la propulsion aérienne, les architectures à fort taux de dilution ont permis d'augmenter le rendement propulsif (la conversion des gaz éjectés en sortie de la turbomachine en poussée pour l'avion par principe d'action/réaction). Le rendement thermique a également été amélioré en augmentant le taux de compression entre l'entrée de la turbomachine et la chambre de combustion. L'augmentation du rendement thermique étant devenu de plus en plus difficile à obtenir, un intérêt croissant est porté aux prélèvements d'air dans une turbomachine. Ces prélèvements alimentent le système d'air secondaire pour la pressurisation cabine, les étanchéités des paliers des arbres haute et basse pression, etc. Une partie de cet air sert également à refroidir les composants en aval de la chambre de combustion fonctionnant dans un environnement de plus en plus chaud. Cet air sert à alimenter les cavités en pied de turbine sous la plateforme pour refroidir les disques rotor. Cependant, une partie de cet air s'échappe dans la veine principale ce qui occasionne des pertes supplémentaires pour la turbine par des phénomènes de mélange. Cette thèse a pour objectif de mieux comprendre ces phénomènes d'interaction entre l'air de cavité et de veine principale afin d'en réduire les pertes associées. Cette problématique est étudiée par l'intermédiaire de simulations numériques sur deux configurations testées expérimentalement et l'utilisation d'une approche basée sur des bilans d'énergie connue sous le nom d'exergie. Différentes modélisations de l'écoulement et de la turbulence ont été employées au cours de cette thèse avec des simulations RANS, LES et LES-LBM basées sur différents codes CFD: elsA, AVBP et Pro-LB. Les simulations numériques ont d'abord été menées sur une cascade d'aubes linéaire basse vitesse en amont de laquelle se trouvait une cavité avec entrefer. Cela a permis d'étudier le phénomène d'interaction entre l'air de veine et de cavité pour différentes géométries d'entrefer et débits de cavité. L'étude de cette configuration a permis de montrer l'influence de l'écoulement de cavité sur les écoulements secondaires se développant dans l'espace inter-aube et la couche de mélange à l'interface cavité/veine principale sur les instationnarités observées dans la veine principale. La seconde configuration d'étude est une turbine bi-étage avec cavités et différents débits de cavité en pied, plus proche d'une configuration industrielle. L'effet de rotation du disque par rapport à la configuration en grille d'aube linéaire a permis de montrer que l'injection de l'air de cavité dans la veine principale est réalisée selon un mécanisme complexe avec l'influence des sillages amont, de l'effet potentiel aval et de l'entraînement dans la cavité avec un processus d'alimentation des structures secondaires (structures normales à la direction de l'écoulement) de façon similaire à la cascade d'aubes linéaire.

Mots-clés: aérodynamique turbine, écoulements de purge en pied d'aube, espace inter-disque, entrefer, processus de mélange, pertes, simulations numériques.

Abstract

Turbomachinery is widely used for electrical power generation mechanical drive and aviation industries. Any efficiency improvement can have a significant impact on overall fuel consumption and global emission. The continuous effort to improve efficiency by higher pressure ratio, temperature and aerodynamic improvement in the main annulus passage of the gas turbine made possible to reach a high degree of efficiency. Since the current benefit for increased pressure, temperature and main annulus aerodynamic improvement have become more and more difficult to achieve, a further insight has been given to the flow in mixing and cooling areas. These topics are inherent in gas turbines due to hot gas flows in the main annulus downstream of the combustion chamber. Some relatively cold air is collected at the compressor to achieve various tasks through the secondary air system as bearing pressurization or turbine disc cooling in order to ensure a safe operation. However, the cooling comes as a cost since it is compressed at an appropriate pressure but does not contribute to the cycle output and the net contribution is negative. In addition, the cooling that blows in the cavities of the turbine reduces the output power due to losses associated with the main annulus mixing processes. This thesis aims at understanding the loss generation processes that occur in the main annulus due to the additional purge flow blowing. This phenomenon is tackled using numerical simulation of two configurations with experimental data available and the use of a method to track loss generation based on an exergy formulation (energy balance in the purpose to generate work). This formulation enables a local and directional evaluation of losses. RANS, LES and LES-LBM simulation have been performed with the different solvers available during this thesis: elsA, AVBP and Pro-LB. First, the simulations were led on a low speed linear five nozzle guide vane cascade with an upstream cavity to primarily study the interaction process between the cavity and the mainstream flow over different rim seal geometries and purge flow rates. This configuration made possible to highlight the influence of the purge flow on secondary flows developing in the passage as well as the influence of the mixing layer at the rim-seal interface on pressure fluctuations and passage vortex unsteadiness. The second configuration is a two-stage low-speed low pressure turbine more realistic and closer to an industrial configuration. Different purge flow rates could be supplied in the cavity. The additional rotating effect induced by the rotor disc as well as rotor/stator interaction provided additional phenomena compared to the linear cascade configuration: a complex blowing of the cavity flow in the mainstream due to the cavity entrainment effect, wakes and potential effect, an interaction of upstream wakes and secondary vortices on downstream rows while the feeding process of secondary structures by the cavity flow showed similar behavior than the linear cascade.

Keywords : axial turbine aerodynamic, cavity purge flow, wheel-space, rim seal, mixing processes, loss accounting, exergy analysis, numerical simulation.

Contents

	Page
Contents	iv
Nomenclature	viii
Introduction	xiii
General context	xiii
Gas turbine principles	xv
Turbine component	xvii
Overview of the thesis	xxii
 1 Ingestion and blowing processes	
at rim seal interface	1
1.1 Characterization of the turbine cavity flow	2
1.1.1 Modeling the laminar disc flow	2
1.1.2 Enclosed annular rotor/stator cavity flow	4
1.1.3 Ingestion process without external flow	7
1.2 The superimposed mainstream flow	10
1.2.1 Quasi-symmetric axial flow in the main annulus	10
1.2.2 Swirling flow without blades	11
1.2.3 Non-axisymmetric pressure distribution	11
1.3 Local effects at the rim seal interface	14
1.3.1 Shear layer	14
1.3.2 Turbulent mass transport	14
1.4 Large scale flow structures in the cavity	15
1.4.1 The main features of the large scale flow structures	15
1.4.2 The different likely initial mechanisms	16
 2 Analyzing losses in the flow field	19
2.1 Loss accounting and tracking using an exergy formulation	20
2.1.1 The general thermodynamic laws	21
2.1.2 Exergy: a link between loss and gas turbine efficiency	24
2.1.3 Balance equations for exergy and useful work	31
2.1.4 The application of exergy to numerical simulation	40
2.2 Losses in a turbine	49

2.2.1	Unsteadiness in gas turbine flows	49
2.2.2	The flow in near-wall region	52
2.2.3	Blade losses	59
2.2.4	Endwall losses	64
2.2.5	Tip clearance leakage flow	70
2.2.6	Transport of upstream non-uniform flow structures in a down- stream cascade	72
2.3	Influence of purge flow blowing in the mainstream	75
2.3.1	Viscous shear layer	75
2.3.2	Losses due to change of reaction	76
2.3.3	Influence on turbine secondary flow	77
3	Linear cascade configuration	81
3.1	Experimental setup	82
3.1.1	Inlet parameters	83
3.1.2	Experimental data	84
3.2	Numerical setup and convergence	86
3.2.1	Numerical setup	86
3.2.2	Convergence	94
3.3	Experimental/numerical comparison	99
3.3.1	Flow around the blade	100
3.3.2	Pressure loss coefficient downstream blade	104
3.4	Main flow feature	106
3.4.1	Incoming boundary layer at shroud	106
3.4.2	Incoming boundary layer at hub	109
3.4.3	Blade flow feature	112
3.4.4	Flow downstream of the blade	113
3.5	Unsteady phenomena within the cascade	115
3.5.1	Horse shoe vortex process at shroud	115
3.5.2	Horse shoe vortex and Kelvin-Helmholtz process at hub	116
3.6	The influence of turbulence	118
3.6.1	Turbulence modeling	118
3.6.2	Turbulence injection in LES simulation using AVBP	125
3.7	Application of exergy formulation to track losses	129
3.7.1	Exergy analysis in the simulation domain	130
3.7.2	Influence of purge flow rate	151
3.7.3	Influence of rim seal geometry	156
3.7.4	Entropy generation from LES simulation	159
4	Two-stage annular configuration	165
4.1	Experimental setup	166
4.1.1	Inlet parameters	168
4.1.2	Experimental data	168
4.2	Numerical setup and convergence	170
4.2.1	Numerical setup	170
4.2.2	Numerical parameters	173
4.2.3	Convergence	175

4.3	Experimental/numerical comparison	175
4.3.1	Flow around the blade	175
4.3.2	Pressure loss coefficient downstream of the blade	176
4.4	Phase-averaged flow field	177
4.4.1	Cavity flow field	178
4.4.2	Main annulus flow field	184
4.4.3	The flow at the interface between the cavity and the main annulus	190
4.5	Application of exergy formulation to track losses	194
4.5.1	The work extracted by rotor rows	195
4.5.2	Viscous and thermal anergy production along the domain . . .	196
4.5.3	Evolution of exergy in the simulation domain	202
Conclusions and perspectives		209
	Recalling the objectives	209
	Conclusion from a methodological point of view	210
	Conclusion from a physical point of view	211
	Future works	212
A Numerical methods		215
A.1	Equations in fluid dynamics	216
A.1.1	Early development of fluid dynamics	216
A.1.2	Navier-Stokes equations	219
A.1.3	Lattice-Boltzmann Method	222
A.2	Turbulence modeling	231
A.2.1	Direct numerical simulation	233
A.2.2	(U)RANS simulation	234
A.2.3	Large Eddy Simulation (LES)	237
A.3	Discretization of the equations	240
A.3.1	Boundary conditions	240
A.3.2	Meshing strategy	245
A.3.3	Numerical parameters and flow solvers	247
A.4	Numerical convergence	249
A.4.1	RANS	249
A.4.2	LES	249
A.5	Reducing information by averaging	250
A.5.1	Statistical convergence	251
A.5.2	Temporal averaging: the comparison against experiment . . .	253
A.5.3	Quantities to be temporally and spatially averaged	254
A.5.4	Performance quantities	255
B Derivation of energy-related transport equations		261
B.1	Energy-related transport equations	262
B.1.1	Transport equation for internal, kinetic and total energy . . .	262
B.1.2	Transport equation for total enthalpy	263
B.2	Exergy and useful work	264
B.2.1	Transport equation for exergy and useful work	264

B.2.2	Control volume analysis for exergy and useful work transport equations	265
B.3	The evaluation of viscosity in numerical simulation	271
B.3.1	The influence of turbulence modelling on actual viscosity . . .	271
B.3.2	The influence of spatio-temporal discretization on actual viscosity	271
C	Boundary layer thickness	277
C.1	Methods for boundary layer thickness estimation	277
C.2	Implementation in the boundary layer module	280
C.3	Comparison of boundary layer thickness against elsA solver output .	281
	List of Figures	282
	List of Tables	293
	Bibliography	297

Nomenclature

Latin letters

(E_{tot}, E_k, E_p, e)	Total, kinetic, potential and internal energy	$[kg.m^2.s^{-2}]$
\dot{Q}	Heat source	$[kg.m^{-1}.s^{-2}]$
ζ	Pressure loss coefficient downstream blade	$[-]$
A	Area	$[m^2]$
C_d	Loss coefficient	$[-]$
C_p	Pressure coefficient around blade	$[-]$
c_p	Constant pressure heat capacity	$[kg.m^2.s^{-2}.K^{-1}]$
c_v	Constant volume heat capacity	$[kg.m^2.s^{-2}.K^{-1}]$
D	Dimension of space	$[-]$
f	Velocity distribution function	$[-]$
G	Cavity aspect ratio	$[-]$
h	Enthalpy	$[kg.m^2.s^{-2}]$
H_f	Shape factor	$[-]$
J	Low-pass filter function kernel	$[-]$
K_n	Knudsen number	$[-]$
Pr	Prandtl number	$[-]$
R	Universal gas constant	$[kg.m^2.s^{-2}.K^{-1}.mol^{-1}]$
r	Specific mixture gas constant	$[m^2.s^{-2}.K^{-1}]$
$Re_e, Re_\delta, Re_\theta$	Reynolds number based on characteristic, displacement and momentum thickness	$[-]$

t	Time	[s]
t_{relax}	Relaxation time	[s]
T_u	Turbulence intensity	[-]
u_i	Velocity field (u_1, u_2, u_3)	[m.s ⁻¹]
V	Volume	[m ³]
x_i	Coordinate system (x_1, x_2, x_3)	[m]
y^+	Non dimensional wall distance	[-]
(s^+ , n^+ , r^+)	Streamwise, normal and radial non-dimensional wall distance	[-]
B	Availability function	[kg.m ⁻² .s ⁻²]
F	Body forces	[m ⁻² .s ⁻²]
I	Integral length scale	[m]
k	Turbulent kinetic energy	[m ² .s ⁻²]
L	Characteristic length	[m]
M	Particle position at (x,y,z)	[-]
Ma	Mach number	[-]
p	Pressure	[kg.m ⁻¹ .s ⁻²]
Q	Heat transfer	[kg.m ⁻² .s ⁻²]
Ro	Rossby number	[-]
s	Entropy	[kg.m ⁻¹ .s ⁻²]
W	Work	[kg.m ⁻² .s ⁻²]
Y	Loss coefficient in terms of enthalpy	[-]

Greek letters

(δ, θ)	Boundary layer displacement and momentum thickness	[m]
α	Particle velocity lattice	[-]
β	Reduced frequency	[-]
χ	Exergy	[kg.m ⁻² .s ⁻²]
Δ	Characteristic length of the mesh	[m]
ϵ	Turbulent dissipation	[kg.m ⁻² .s ⁻²]

η	Efficiency	$[-]$
γ	Ratio of specific heat capacity	$[-]$
κ	Wavenumber	$[m]$
λ	Thermal conductivity	$[kg.m.s^{-3}.K^{-1}]$
μ	Dynamic viscosity	$[kg.m^2.s^{-1}]$
μ'	Coefficient of bulk viscosity	$[kg.m^2.s^{-1}]$
ν	Kinematic viscosity	$[m^2.s^{-1}]$
ω	Pulsation or angular velocity	$[s^{-1}]$
Ω	Collision operator	$[-]$
ϕ	Instantaneous flow field variable	
ρ	Density field	$[kg.m^{-3}]$
τ	Viscous stress tensor	$[kg.m^2.s^{-2}]$
τ_r	Reynolds stress tensor	$[kg.m^2.s^{-2}]$
ν	Kolmogorov length scale	$[m]$
Ξ	Useful work	$[kg.m^{-2}.s^{-2}]$
ξ	Particle speed	$[m.s^{-1}]$

Subscripts and superscripts

$."$	Fluctuating quantity from Favre averaging
$'$	Fluctuating quantity from Reynolds averaging
$."$	Normalized value at the wall or in time
$\bar{\cdot}$	Reynolds averaging operator
$\tilde{\cdot}$	Favre averaging operator
c	Critical
$edge$	Edge of the boundary layer
ref	Reference state
tot	Total quantity
$turb$	Turbulent quantity
eq	Equilibrium

rev Reversible process

Abbreviations

SGS Subgrid Scale Model

BGK Bhatnagar-Gross-Krook

CFD Computational Fluid Dynamics

DMD Dynamical Mode Decomposition

DNS Direct Numerical Simulation

LES Large-Eddy Simulation

NSCBC Navier-Stokes Characteristics Boundary Conditions

RANS Reynolds Averaged Navier-Stokes

RSM Reynolds Stress Models

SFC Specific Fuel Consumption

TCF/TVF Turbine Center Frame/Turbine Vane Frame

URANS Unsteady Reynolds Averaged Navier-Stokes

Introduction

Context

The Twentieth century have shown the development of heavier-than-air flying machines. The Wright brothers demonstrated that the basic technical problems had been overcome at the start of the century by succeeding the first controlled powered fly on December 17, 1903 near Kitty Hawk, N.C. Flight capabilities made quickly possible to flight over longer distance with Louis Bleriot that was able to flight from Calais, France to Dover, England on July 25, 1909 in a monoplane with a 25-horsepower engine. The first and second World War induced the strong development of aviation especially for military purposes with the development of the Fokker Eindecker fighter (1915). Most of the developments in the aeronautical industry prior and during World War II happened in the military sphere with a main breakthrough being the development and first operations of reaction engines. The theory on jet engine was first introduced in England by Frank Whittle in 1928. Hans von Ohain (engineer at Heinkel company) began jet engine developments in 1935 in Germany and demonstrated the feasibility of jet engine propulsion in early 1937 and first flight of an aircraft equipped with a jet engine in 1939 with the Heinkel He 176. Based on these works, the Junkers aviation firm produced the first jet engines (Junkers Jumo 004) for the military aircraft, the Messerschmitt Me 262 in 1940. Concerning commercial air passenger service, it began in the United States as soon as 1914 but knew strong development during the interwar period with the Boeing's 247 introduced in 1933 and the DC-3 from the Douglas Aircraft Company. From technological breakthrough during Second World War, the first commercial aircraft equipped with reaction engines was the Comet developed by De Havilland company in United-Kingdom with first flight in 1949. Growing demand for passenger airline services soon pushed the commercial aviation industry to even further advancements in passenger capacity and comfort, new elevation capabilities, and speed. This growth still continues in the 21st century: the number of people transported has increased by 60% since 2003 and may double in the next 20 years. Meanwhile, pollution, noise, cost and safety issues are becoming increasingly critical, with ever more restrictive standards. Jet engines were the most able to tackle these different issues due to high power generation, low emission, possibility of heat generation while having a relative compactness and reliability. This explains why this technology have become the most popular type of engine to equip commercial

aircraft over the past decades.

To reach the standards promoted by the International Civil Aviation Organization (ICAO), the efficiency of the engine (i.e. its fuel consumption) has to be improved. Indeed, for an A320 aircraft, a reduction by 15% of the fuel consumption would represents a saving of 1.4 millions litres of fuel (~ 1000 cars emissions) and 3600 tons of CO_2 ($\sim 240\,000$ trees absorption) per aircraft by year 2020. With almost 20 000 existing aircraft in the world, it thus represents an important economic and environmental issue. With rising of oil prices, fuel consumption has become the dominant cost factor in all airlines. This enforces airline companies to invest in new fuel saving approaches. In the context of global warming and global energy consumption increase, the reduction of aeronautical transport footprint is also a common expectation. One of the main potential fuel reduction lies in the engines themselves by increasing their efficiency. Before World War Two, turbomachine designs improvements largely proceeded on a trial and error basis. The explosion of research on aircraft engines in the 1940's and 50's led to a better understanding in the flow mechanisms that were still improved until nowadays making possible to reach high degrees of efficiency.

The increase in energy conversion has been mainly accomplished through three paths. The use of bypassing flow engines such as turbofan architectures where more flow is accelerated in the bypass annulus compared to the primary one that contributes to a better propulsive efficiency. The increase of pressure ratio and combustion chamber temperature that improve the thermal efficiency. Some current engines can operate up to 50 atmospheres (the pressure ratio between combustion chamber inlet and engine inlet) and 2000 K. Aerodynamic designs improvement of the mainstream components like compressor, combustion chamber or turbine enabled a more efficient transfer of work between the shaft and the mainstream air. An alternative measure of engine efficiency is the Specific Fuel Consumption (SFC) which is the input fuel mass flow required by the engine to get a unit of thrust. Wisler [1] showed that a 1% increase in the aerodynamic efficiency of low pressure turbine could improve in the same magnitude the engine specific fuel consumption for a modern commercial turbofan engine. Main annulus designs improvement contributing to the thermal (cycle) efficiency. The increase of thermal efficiency by an increased pressure and temperature ratio led to an increase of thermal stresses for the turbine component requiring additional cooling system to ensure a safe operation of the gas turbine. The secondary air system consists in air bleeding at the compressor to be supplied in the different parts of the turbine like the blades or inter-disc cavities to cool down the environment. An optimal efficiency being found between the potential thermal efficiency gain due to pressure/temperature increase and loss associated to the secondary air system. As material limitations and ever more complex aerodynamic solutions in the turbine main annulus have made more and more difficult to improve its efficiency, new ways have been investigated. This is especially true for the study of secondary air interaction with the main annulus flow. Since temperature has constantly increased in the gas turbine main flow path, the need for cooling system has been increased to maintain a safe operation for the gas turbine. Additional losses related to theses secondary air systems have also increased. Therefore, a promising way to reduce losses in the turbine has emerged by

optimizing the bleed air system, this being possible under a better understanding of the interaction processes between the secondary and mainstream flow. The study of this interaction is mainly possible in three ways: analytical, experimental and numerical approaches.

Numerical simulation tools have start to developed since 1970's. These tools make possible to develop new technical solutions, reduce the conception time as well as the number of configurations to be tested experimentally. With the increase of the computational power, Computational Fluid Dynamics (CFD) has appeared to be an interesting way to study the flows that can be difficult to access with experimental means. Over the years, the increasing computer capabilities made possible to use numerical methods providing more insight in the flow behavior in gas turbine: two-dimensional Euler computation (inviscid flow), 2.5-dimensional Euler computation (two-dimensional computations over several blade span), three dimensional Euler computation. Current methods used in the industry deal with viscous and turbulent flows by performing Reynolds Averaged Navier-Stokes (RANS) and unsteady computations with Unsteady-RANS (URANS) simulations. These simulations take into account the periodic unsteadiness arising for instance, from the relative motion of the blades and for low frequency instabilities but fully model the turbulence. To overcome this limitation, a solution is the use of Large-Eddy Simulations (LES), which is an unsteady approach that solves the large eddies of turbulence and models only the smallest ones with a more universal behavior. However, the LES of a full stage of turbomachinery is about 100 to 10000 times more expensive than a URANS simulation depending on the Reynolds number ($Re^{1.8}$ [2]) which ranges between 10^4 and 10^7 in turbomachinery for aeronautical applications. This approach is currently mainly used for research purposes. This thesis aims at studying the impact of a particular part of the secondary air system related to the inter-disc cavity cooling by assessing the influence of the cavity flow on the turbine main annulus flow. This study is led using numerical simulations. This section will be devoted to give more details about the notion of efficiency in a gas turbine and secondary air system briefly introduced previously.

Gas turbine principles

A gas turbine is based on the Joule-Brayton cycle (1872) which describes the workings of a constant-pressure steady heat engine exchanging work and heat with a flow crossing the engine. The ideal cycle is first introduced as a reference to be then compared against a real cycle. The notion of isentropic process that will be used for some processes of the cycle refers to a process composed of a succession of states that can be reversely recovered without heat transfer and primarily seen as a process with no loss generation. The departure from the isentropic process corresponding to loss generation measured by a quantity called entropy (see Fig. 1). The fluid that is generally ambient air is collected at the inlet of the gas turbine (1) and drawn into a compressor where the flow is compressed, under an isentropic process (1-2). The compressed air then runs in a combustion chamber where fuel is added under a constant pressure (isobaric) process. The pressurized air and fuel mixture is then ignited releasing energy that mimic an external heat release Q_b in the Brayton cycle

and causing the fluid temperature and combustion products to increase (2-3). The fluid is then expanded in a turbine under an isentropic process (3-4). Part of the extracted work is given back to the compressor and the propulsion fan in an aircraft engine, the remaining useful work (W) is then either used to accelerate the flow in a nozzle providing a propulsive jet to generate thrust or expanded in an additional turbine to generate power on the shaft. This last configuration can be used for electrical power generation, induce the rotation of the main rotor of a helicopter or the propeller of an aircraft for instance. The flow is finally released into the atmosphere considered as a constant pressure environment (4-1). Usually, a gas turbine operates in an open circuit since the exiting fluid is not driven back as an intake to the gas turbine. The open circuit gas turbine cannot be said to operate on a thermodynamic cycle, however, its performance is often assessed by treating it as equivalent to a closed cycle. For a cyclic gas turbine in which the fluid is circulated continu-

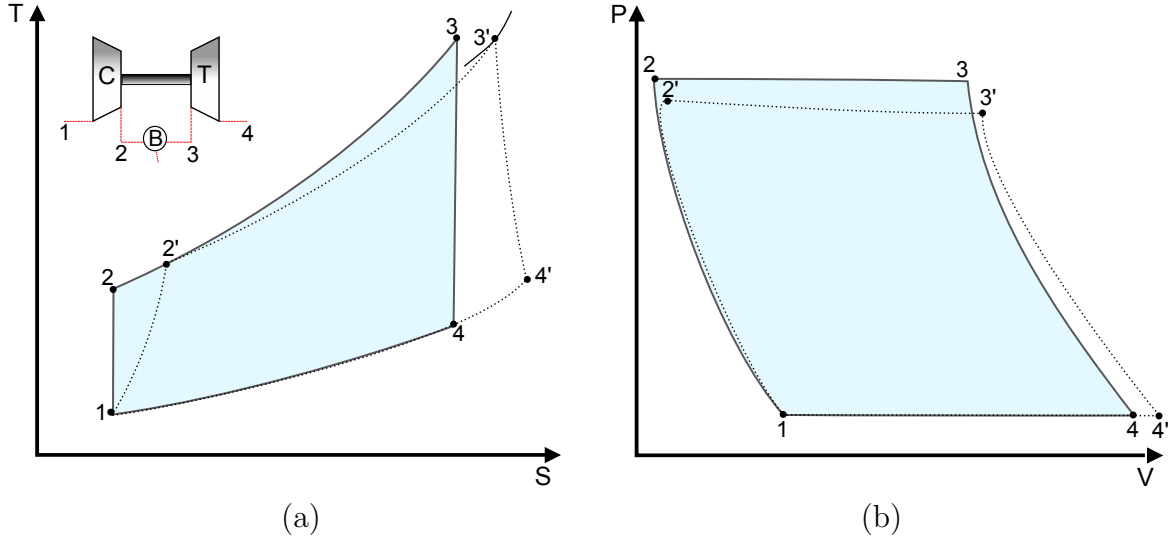


Figure 1: Ideal and real (denoted ') Brayton cycle in T-S (a) and P-V diagrams (b)

ously, one criterion of performance is the thermal or cycle efficiency $\eta = W/Q_b$ with W the net work output and Q_b the heat supplied emanating from the combustion process of the fuel with air. The cyclic heat engine achieves maximum efficiency by operating on a reversible cycle called the Carnot cycle. For a given (maximum) temperature of supply $T_{max} = T_2$ at which all heat generated by the combustion process is received and a given minimum temperature of heat rejection $T_{min} = T_1$, the thermal efficiency is $\eta_{Carnot} = (T_{max} - T_{min})/T_{max} = 1 - (p_1/p_2)^{\gamma-1/\gamma}$. The Carnot engine is a useful hypothetical device in the study of the real gas turbine thermodynamic cycle since it provides a measure of the best performance that can be achieved under the given boundary conditions of temperature or pressure indifferently. In a real engine, losses are generated during the different processes of the Joule-Brayton cycle. Compression and expansion are generally not isentropic. Adiabatic nature of the processes is generally an acceptable assumption in compressors and turbines since the thermal transfer at the walls are generally low compared to the work transfer but losses are generated during the various processes. For the compressor (see Fig. 1), the pressure increase is lower (1,2') with respect to the isentropic process

(1,2) while for the turbine, the pressure decrease is lower (3',4'). The output power is decreased compared to the isentropic process and lead to an additional specific fuel consumption to achieve the same power output as the isentropic process. In addition, all the heat is generally not supplied at the maximum (specified) temperature and is not rejected at the lowest (specified) temperature since the flow exiting the nozzle has generally a higher temperature compared to the ambient one. The efficiency of the real Joule-Brayton cycle is a function of temperature, pressure ratio and components efficiency (see Fig. 2a).

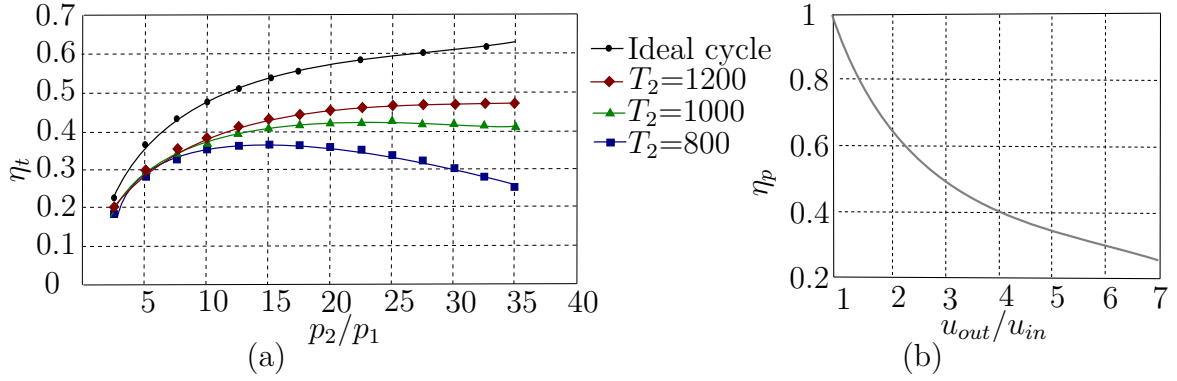


Figure 2: Thermal efficiency for the ideal and real processes at different inlet combustion chamber temperature for compressor and turbine efficiency set to 0.9 (a) and propulsive efficiency for the jet engine based on the ratio between outlet and inlet velocity (b)

Turbine component

The work extracted by the turbine is partially used to drive the compressor by a shaft linking compressor and turbine components. This architecture is known as jet engine and is the simplest configuration encountered in gas turbine (see Fig. 3a). Modern gas turbines are often composed of two or three steps of compression and expansion processes. The flow at the inlet is compressed in the low, intermediate and high pressure compressor stages and is expanded in high, intermediate and low pressure turbine stages. Each stage level being linked by coaxial shafts. Under a nominal and stabilized regime, the power extracted by high and intermediate turbine stages equilibrate the power given to the intermediate and high pressure compressor stages. The low pressure turbine is linked to the low pressure compressor. The low pressure compressor is generally composed of the fan module and additional stages known as booster. The fan module accelerates air at the inlet and partially redirects the flow in the intermediate or high pressure stages to follow the Joule-Brayton cycle, while the remaining flow is driven outward to generate thrust by accelerating the flow and is referred as turbofan architecture (see Fig. 3b). In commercial aircraft engines where the purpose is to accelerate the flow, turbofan and propeller architectures are more usual since they provide a better propulsive efficiency (η_p) than jet engines. The

overall efficiency of the turbomachine being the product of thermal and propulsive efficiency. By accelerating the flow, the gas turbine induces thrust under the action reaction principle. The propulsive efficiency quantifies the conversion of the fluid acceleration by the gas turbine to the net thrust for the gas turbine. From simple approach, the propulsive efficiency can be approached by $\eta_p = 1/(1+(u_{out}/u_{in}))$ where u_{in} and u_{out} are velocity at the inlet and outlet of the gas turbine. This equality states that it is more energy efficient to accelerate a large amount of air by a small amount, than it is to accelerate a small amount of air by a large amount, even though the thrust is the same¹ (see Fig. 2b). This is why turbofan engines and propellers are commonly used since more mass flow experiences lower acceleration by fan or propeller over a large area compared to highly accelerated flow at outlet for jet engines. Propeller architectures are generally used for low to medium speed ranges while turbofan architectures are generally used for high subsonic flows since propeller architectures suffer from shocks issues at such velocity speed, strongly decreasing their efficiency. The analysis of the Joule-Brayton cycle shows that the engine

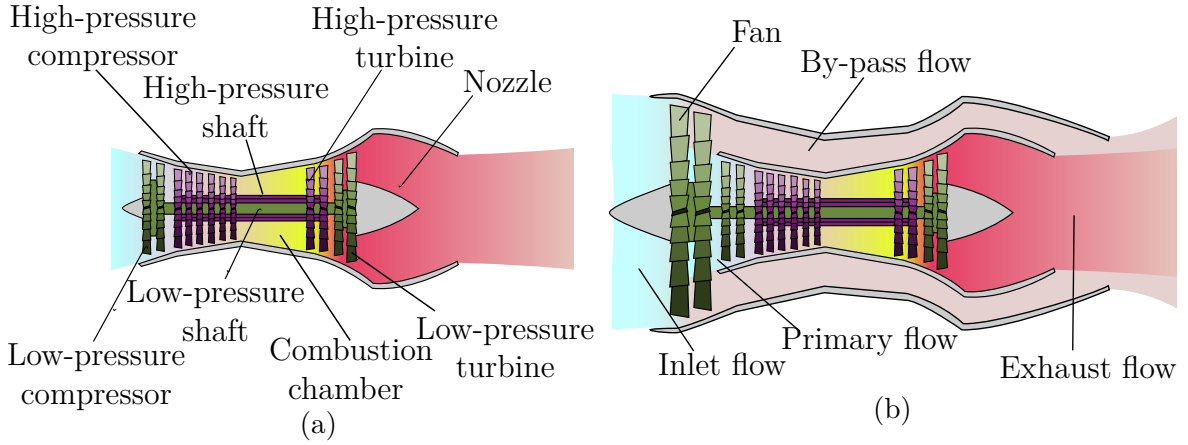


Figure 3: Jet engine (a) and turbofan (b) architectures Adapted from *Wikipedia: The jet engine*

efficiency is increased with the turbine inlet temperature and pressure ratio increase. Pressure ratio increase for compressors leads to a reduction of flow path section that increase relative tip gap and induce more losses. Temperature increase requires the use of additional devices to cool down combustion chamber and turbine due to limit of metallurgical components. This leads to more complexity that generate more losses. Performance enhancement for gas turbine application is generally a trade-off between the potential increase in the cycle efficiency and the undesired side effects of this potential energy conversion increase. The focus will be given to low pressure turbines in this thesis. Burnt gases from the combustion chamber are expanded in the high pressure turbine, then travel in the Turbine Vane Frame (TVF) / Turbine Center Frame (TCF)² to be finally expanded in the low pressure turbine. The mechanical constraints for rotor cascade are high due to high rotation velocity.

¹for propulsion efficiency close to one, there is virtually no thrust

²Refers to the structural frame that separate the high pressure turbine and the low pressure one. Some frame can be used as nozzle guide vane and are referred to turbine vane frame

In current aircraft engines, the rotation velocity of low pressure turbine is mainly limited by the velocity at the tip of the fan blade (when losses related to shocks become important) since they are coupled by the shaft. In upcoming and future commercial aircraft engines, inertial constraints for low pressure turbine could be increased since the low pressure turbine and fan will be coupled by a gearbox which will make possible to increase the rotational velocity of the low pressure turbine inducing higher stress for this component. The incoming turbine temperature went from 1050 K of the Whittle W1 engine (1940) to values currently observed around 1800 K for high pressure turbines that is well above the melting point of the turbine components. The thermal stress is also important in the low pressure turbine since the temperature at the inlet has kept increasing during these past few decades to achieve higher efficiency of the thermodynamic cycle. Thermal and mechanical constraints are high for the turbine components and can reduce the operating life or even induce damages. Additional systems must be provided to ensure a safe and efficient operation of the engine. This is made possible by the use of the secondary air system.

Secondary air system

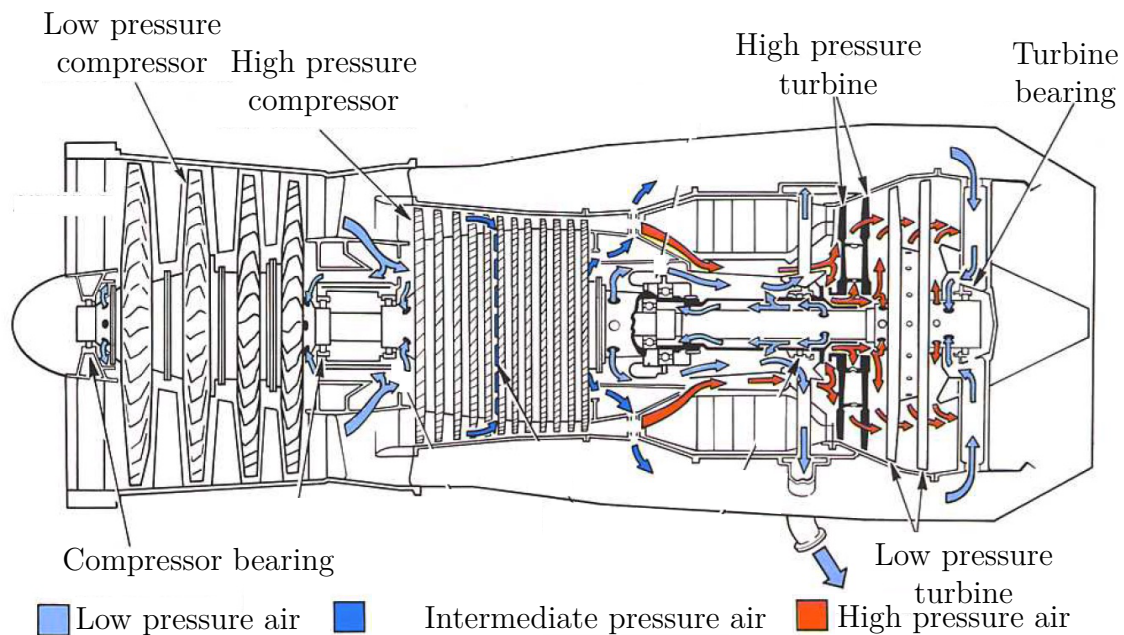


Figure 4: Sketch of a gas turbine secondary air system. Courtesy of Rolls-Royce, *The Jet Engine* [3]

The engine internal air system is defined as those airflows which do not directly contribute to the engine thrust since not participating in the combustion process. Some relatively cold air called secondary air is bled at the tip and hub of the compressor to be expelled overboard in a system of external pipes to the gas turbine or underneath the main gas path (see Fig. 4). Up to one fifth of the total engine core mass airflow may be used in the secondary air system. An increasing amount of

work is transferred to the air as it progresses in the compressor to raise its pressure and temperature. Therefore, to reduce engine performance losses, the air is taken as early as possible from the compressor, taking into account pressure and mass flow rates requirements of each particular function/component³. Secondary air can be used for different purposes:

- feed the ventilation systems of flight station compartment;
- cool down engine accessories where a considerable amount of heat can be produced of which the electrical generator;
- pressurize bearings on which the various shaft rotate and equilibrate the axial efforts of the rotor discs (axial loads);
- cool down the cavities at shroud especially where vanes are held and at the tip of rotor blades in order to control the turbine blade tip clearances;
- cool down the vanes and blades since the mainstream temperature is often well above the melting points of alloys used for the blades and platform. Secondary air can be used in different technological solutions. Cold air can travel through ribbed channels in the inner vane/blade part to increase turbulence and heat transfer. Impinging jet technologies can promote heat transfer with inner blade skin. Film cooling on blade and platform where cold air blows promotes a thin layer of cold air to protect the component.

Under the mainstream passage, cavities are induced by the necessary gaps between the static and rotating rows. Specific platform shapes are generally designed at the interface between two adjacent rows referred as rim seal in order to prevent the hot main annulus gas ingestion (see Fig. 5b). However, these architectures are generally not sufficient to prevent overheating and potential damages for rotor discs. Part of the mainstream flow could enter in these cavities and impinge rotor discs. Since the rotor discs are mechanically loaded, the additional thermal stress could decrease strongly the operating life of this component or even lead to mechanical failure. Part of the secondary air is therefore supplied to cool down the cavities underneath the mainstream passage. Secondary air, commonly called purge flow when dealing with cavity air supply, is injected either axially with swirl or radially in holes circumferentially spread and makes possible to cool down the air in the cavities. The temperature ratio between the secondary and mainstream flow is typically in the order of 0.6 for the first low pressure turbine stage and tends to increase in downstream stages. In addition, a sealing effect is promoted at the rim seal interface since the pressurized cooling air prevents ingestion of the hot main annulus flow. A schematic view of a secondary air system in the turbine is proposed in Fig. 5.

³Due to the use of passive devices for the secondary air system, the pressure at the station where the air is collected must be higher than the pressure where air is supplied

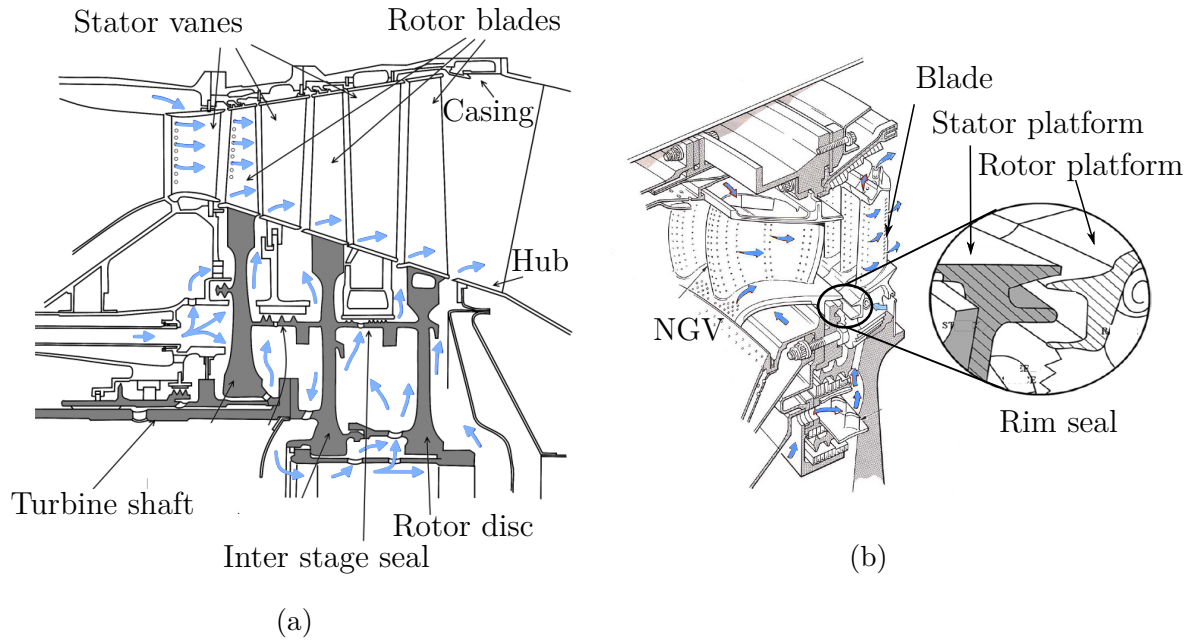


Figure 5: Secondary air system in a turbine component (a) and at the rim seal interface (b). Courtesy of Rolls-Royce, *The Jet Engine* [3]

Main context ideas and purpose of this thesis

The overall efficiency of a gas turbine can be split in two contributions that are propulsive and thermal (cycle) efficiency. The first contribution is mainly induced by the gas turbine architecture and the ability to accelerate slowly a great amount of flow. The thermal efficiency depends on pressure, temperature ratio (between the incoming flow and the inlet of the combustion chamber) and the efficiency of the different components in the gas turbine (compressor, combustion chamber, turbine, nozzle). Higher thermal efficiency have been reached by increasing pressure and temperature ratio, leading to stronger thermal stresses for the turbine. The temperature increase enforced the use of additional cooling system known as secondary air systems where some relatively cold air is collected at the compressor. For the turbine cavities underneath the platform, this system cools down rotor discs but induces additional losses for the turbine by blowing of the cavity purge flow in the main annulus. From an efficiency point of view, the challenge in designing this system is twofold:

- the ability to improve the thermal transfer in the cavity to reduce the amount of purge flow taken at the compressor. From an engine designer's point of view, minimizing purge flow for engine efficiency must be balanced against the probability of unexpected thermal degradation and seal life;
- the interaction process between the purge and mainstream flow that induces losses and reduce the efficiency of the turbine.

This thesis aims at providing a general framework to evaluate the potential benefit of an increased temperature to the thermal efficiency versus the potential side effects

due to more flow extracted at the compressor to cool down the turbine and the additional flow blowing in the turbine main annulus. As it will be seen, the thermal efficiency benefit and bleed air negative effect on the gas turbine efficiency can be approached by general thermodynamic analysis. The current thesis focuses on the last contribution that requires a more local analysis. The goal is to better understand the interaction process between the purge and mainstream flow, the underlying mechanisms of loss in order to reduce their contribution and increase the turbine efficiency that contributes to the thermal cycle efficiency.

Overview of the thesis

To understand the temporal and spatial evolution of the purge flow blowing in the mainstream and inducing losses, the underlying phenomena related to non-uniform time-varying ingress-egress at the rim seal interface need to be described.

This description is proposed in Chap. 1 introducing the processes occurring in the turbine cavity, main annulus and rim seal leading to the ingestion and blowing phenomena taking place at the rim seal interface. The description of the fluid motion in the turbine cavity is first introduced by considering simplified cavity to reach more complex and realistic configuration. The related disc pumping effect on the ingestion process is discussed. Then, the influence of the main annulus flow as well as local processes at the rim seal interface on ingestion are presented. These phenomena are responsible for the unsteady non-uniform flow at the rim seal interface that can leak in the mainstream and induce additional losses compared to a smooth configuration (i.e. without technological effects).

Loss generation of the blowing flow in the mainstream requires a quantification of loss. In this study an exergy formulation has been used and will be presented in Chap. 2. This notion of exergy, not commonly used in gas turbine, consists in performing energy balances in the purpose to generate work. The use of this approach in current study aims at setting under a same basis the different benefits (if one can increase the temperature in the combustion chamber) and drawbacks associated to purge flow taking place at the different scales (whole gas turbine, turbine component and locally in the turbine). The use of this approach in the numerical simulations performed in this study requires several prerequisite steps. This concerns the simulation convergence, temporal and spatial averaging procedure that will be detailed in this chapter to be compliant with the exergy formulation. The study of loss incurred by purge flow requires the knowledge of the existing literature about the mechanisms of loss without and with purge flow blowing at the hub of the turbine. So, this chapter will be devoted to introduce the mechanisms of loss known at current stage of knowledge.

The study of loss generation in the mainstream due to purge flows has been led mainly by two configurations for which experimental data were available. Chapter 3 is devoted to the study of the first configuration which is a static linear cascade with an upstream cavity including various rim seal geometries and purge flow rates. Different numerical approaches (RANS, LES and LES-LBM) are used in this chapter to analyse the effect of turbulence modelling and turbulence injection at the inlet of the domain. A description of the main annulus flow field, the flow at rim seal inter-

face and unsteady phenomena is proposed. The influence of the rim seal geometry and purge flow rate is studied in conjunction with the exergy analysis to describe the different mechanisms taking place in the turbine component and the underlying mechanisms of loss.

Chapter 4 introduces the second configuration studied numerically with a LES solver that is a two-stage rotating turbine configuration. The main purpose of this configuration is to study the influence of multi-rows interactions and rotating cavities under the hub platform known to strongly influence the ingestion and blowing process at the rim seal interface. The same strategy based on exergy balance is used to characterize the mechanisms of loss and the influence of purge flow.

Appendix A is devoted to describe the numerical basis used in this study. Therein, a brief historical review leading to the well-known Navier-Stokes equations and the corresponding system of equations for modelling fluid dynamics is introduced. An alternative approach to model fluid dynamics is also introduced based on the Boltzmann equation. Turbulence modelling issues contained in all previous set of equations are introduced and potential modeling approaches are detailed. Spatial, temporal discretization of the equations and numerical parameters are also described. This chapter makes possible to evaluate the degree of uncertainty related to the numerical simulation as well as some numerical assumptions on which special care is required to properly analyse the result of the numerical simulations. Details for temporal and spatial averaging procedure concerning numerical simulation data is also proposed.

Appendix B introduces and details the energy-related equation used to draw the exergy analysis proposed in Chap. 2. The boundary layer thickness estimation used in the study to split the whole domain in boundary layer contributions and a remaining domain is introduced in App. C.

At the begin of each chapter, an abstract/introduction is proposed in blue box. Similarly, each chapter is concluded by a summary and discussion of the major results in same blue boxes. When important partial results are described in a section, a summary of the section is proposed in green boxes.

Theory is when you know everything but nothing works. Practice is when everything works but no one knows why. In our lab, theory and practice are combined: nothing works and no one knows why.

— Albert Einstein

1

Ingestion and blowing processes at rim seal interface

This chapter describes the physical phenomena leading to ingestion and blowing at rim seal interface. The underlying phenomena were depicted by Johnson et al. [4] with several main mechanisms: the three-dimensional and time-dependent vane/blade pressure field in main annulus, the disc pumping effect in the cavity and localized effects in the rim seal. These local effects are related to three dimensionality of the rim seal region and geometry, the turbulent transport and flow entrainment in the overlap region. The first two mechanisms tend to impose a time-dependent pressure field slightly above (mainstream field) and below the rim seal interface (cavity field), while the third mechanism tends to modify the permeability function or discharge coefficient of rim seal. For a local pressure drop imposed by the mainstream and the cavity across the rim seal, the local mass flow rate of ingress or egress is driven by geometry and phenomena occurring at the rim seal interface. In the cavity, the main characteristics of the flow field will be introduced by presenting simpler configurations flow field to illustrate some features of the flow for more complex geometries encountered in low pressure turbines and further explain the disc pumping effect. In the main annulus, sources for pressure asymmetry and unsteadiness will be discussed to explain the time-dependent vane/blade pressure field. The main mechanisms at the rim seal interface impacting the discharge coefficient will also be depicted. Large scale flow structures have been identified more recently to be a potential source of ingress for cavity in low pressure turbines and will be discussed in last part of this chapter.

1.1	Characterization of the turbine cavity flow	2
1.1.1	Modeling the laminar disc flow	2
1.1.2	Enclosed annular rotor/stator cavity flow	4
1.1.3	Ingestion process without external flow	7
1.2	The superimposed mainstream flow	10
1.2.1	Quasi-symmetric axial flow in the main annulus	10
1.2.2	Swirling flow without blades	11
1.2.3	Non-axisymmetric pressure distribution	11
1.3	Local effects at the rim seal interface	14
1.3.1	Shear layer	14
1.3.2	Turbulent mass transport	14
1.4	Large scale flow structures in the cavity	15
1.4.1	The main features of the large scale flow structures	15
1.4.2	The different likely initial mechanisms	16

1.1 Characterization of the turbine cavity flow

The purpose of this section is to describe the main flow features related to enclosed rotor/stator cavity encountered in turbines. The description is structured by going from simple to more complex physics/flow features and follows overall the chronological understanding on this topic. A turbine cavity can be primarily seen as a two facing disc configuration, one rotating being the rotor disc and a stationary disc being confined between an inner shaft and the hub platform of main annulus at the circumference (see Fig. 1.1). The laminar flow encountered in one and two-discs configurations with possible rotation is first introduced since analytical models have been derived to describe the corresponding flow behavior. The influence of the inner and outer shaft as well as turbulence influence on the cavity flow is more complex and cannot be properly handled analytically. Thus it will be discussed based on experimental data and numerical simulations.

1.1.1 Modeling the laminar disc flow

1.1.1.1 Flow initially at rest over an infinite rotating disc

Ekman [5] (1905) was among the first to explore the flow behavior of a fluid initially at rest over an infinite rotating disc assuming a bulk rotation of the fluid far from the disc known as "free disc" configuration. Later on, Von Kármán [6] studied analytically the same configuration assuming that the flow far from the disc is at rest. He derived a self-similar profile, solving exactly the axisymmetric stationary Navier-Stokes equations in cylindrical coordinates. Using a matched asymptotic expansion, Cochran [7] obtained a more accurate solution to the problem and pointed out that the mean axial velocity far from the disc converged to a constant negative value that is now referred to the "Von Kármán viscous pump" phenomenon. When describing the main feature of the flow in this kind of configuration, the fluid is coupled to the disc motion in a non-slipping velocity condition which leads to a fluid velocity

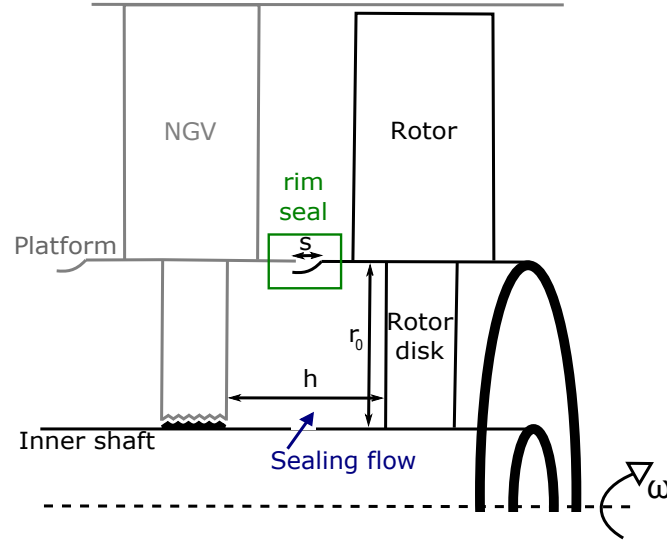


Figure 1.1: Sketch of a one stage turbine including the cavity between the nozzle guide vane and the rotor

tangential to the wall and equal to the local disc velocity. When moving away from the disc normal to its surface, a thin layer of fluid is put in rotation due to viscous effects and radially ejected due to the centrifugal and Coriolis forces. This effect is larger at the disc periphery because it features the highest local rotational velocity. Because there is a net radial outflow close to the disc surface, this flow must be compensated to satisfy the conservation of mass resulting in an inflow in the axial direction toward the disc (see Fig. 1.2a). In addition, outside of the boundary layer developing in the vicinity of the rotating disc, the flow was shown to be rotating with an inviscid core flow manner. In rotor/stator disc configurations encountered in turbine cavity, the rotation of the disc can induce a rotating core flow that extends to the stationary disc. This observation motivated the study of a rotating core flow on a stationary disc as described in the next subsection.

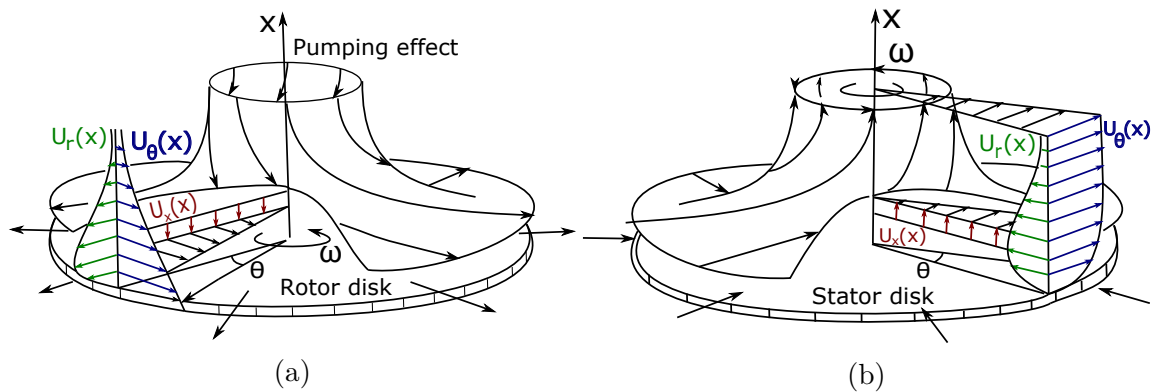


Figure 1.2: Flow behaviour of a fluid initially at rest put in motion by a rotating disc (a) and a rotating fluid over a stationary disc (b). From Schlichting [8]

1.1.1.2 Rotating flow over an infinite stationary disc

The rotating fluid over an infinite stationary disc was first studied by Bödewadt[9], applying the same strategy as Cochran to derive a self-similar solution. The flow analysis showed that far from the disc centrifugal and Coriolis forces are exactly balanced by the radial pressure gradient. Closer to the disc, since the circumferential velocity has to decrease to vanish at the disc, the centrifugal forces diminish and the pressure gradient leads to a radially inward flow that is balanced by an axial flow in the opposite direction to the disc. Batchelor [10] showed that the ratio of fluid and disc rotation velocities were sufficient to characterize the steady laminar flow over an infinite disc.

1.1.1.3 The flow between two facing discs

In the same work, the author extended the analysis to two infinite parallel discs by obtaining the differential equations of the motion and gave a description of the nature of the flow for various ratio of angular velocity between the two discs. Faller [11] was able to unify the three fundamental flows: rotating disc over a flow at rest, rotation flow over a static disc and the mixed conditions of rotation under one parametrized set of equations. The disc and fluid are considered to be rotating around the same axis x with angular velocities ω_d and ω_f respectively. Two key parameters are the inter-disc Reynolds number $Re_h = h^2 \omega / \nu$ (with h the inter disc distance and ω the system angular velocity, see Fig. 1.1 for characteristic length) and the Rossby number Ro that describes the angular velocity difference between the fluid (f) and the discs (d)

$$Ro = \frac{\Delta\Omega}{\Omega} \quad \text{with} \quad \Omega = \frac{\Omega_f}{2 - Ro} + \frac{\Omega_d}{2 + Ro}. \quad (1.1)$$

In the expression eq.(1.1), it is possible to retrieve the Bödewadt layer for $Ro = 1$ and $\Omega = \Omega_f$, Ekman layer for $Ro = 0$ and $\Omega = \Omega_d$, the Von-Kármán layer for $Ro = -1$ and $\Omega = \Omega_d$. Figure 1.3 shows non dimensional axial velocity u_x , azimuthal velocity u_θ and radial velocity components u_r evolution against axial coordinate for three inter disc Reynolds numbers $Re_h \in \{10^2, 10^3, 10^4\}$ where velocity components are defined as:

$$u_x(x) = \frac{u_x^*(x)}{r\omega}, \quad u_\theta(x) = \frac{u_\theta^*(x)}{r\omega}, \quad u_r(x) = \frac{u_r^*(x)}{\sqrt{\nu\omega}}, \quad (1.2)$$

where * superscript indicates dimensional quantities and r a reference radius. The description of these unenclosed rotating disc configurations can illustrate some of the main characteristics of enclosed cavity flow that will be then discussed and can be used as initial design criteria for the kind of complex geometry encountered in low pressure turbine cavities.

1.1.2 Enclosed annular rotor/stator cavity flow

In turbine cavities, rotating and stationary discs are in alternating sequence with stationary disc on the upstream part and the rotating disc on the downstream part

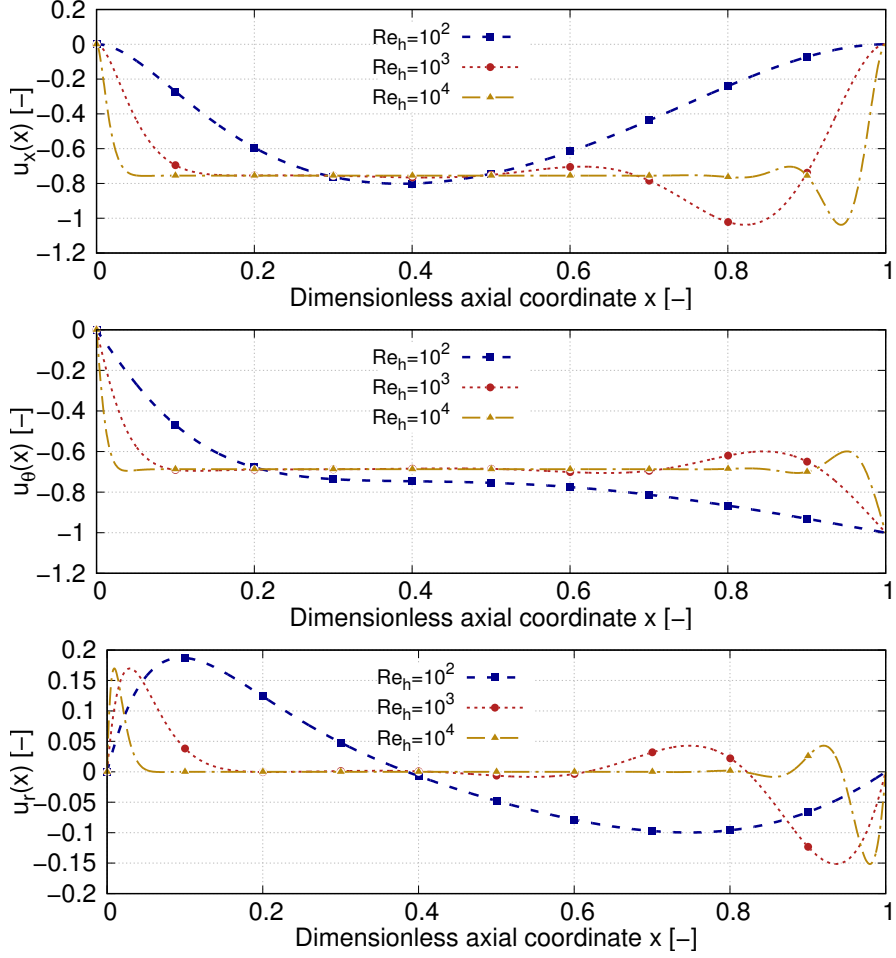


Figure 1.3: Auto-similar velocity profiles of the laminar flow between a rotor and a stator for different inter-disc Reynolds numbers Re_h . Top: axial velocity, middle: azimuthal velocity, bottom: radial velocity. The analytical derivation and computation of the velocity profiles is proposed in Bridel-Bertomeu [12]

when considering the cavity between a stator rotor stage and conversely for the cavity between an upstream rotor row and a downstream nozzle guide vane row. Because of the enclosed environment, the first complication is the coaxial inner annulus being the shaft that can strongly modify the idealized picture of a flow over an infinite disc. Batchelor [10] and Stewartson [13] have considered the flow theoretically in this situation, with diverging predictions on the flow behaviour. Nevertheless, experimental works have shown that time-variant phenomena of considerable complexity can be observed under certain geometrical conditions as stated by Maroti et al. [14]. Further complications emerge by considering the presence of the main annulus hub platform in the outer part. This configuration of enclosed cavity facing rotor/stator discs strongly differs from a free disc configuration and analytical description of the flow cannot be derived from the Navier-Stokes equations. Before considering any possible turbulent flow in the cavity, Roger and Lance [15] and Sirivat [16] showed respectively numerically and experimentally that the laminar flow regime in an enclosed or partially enclosed rotor/stator cavity in these two studies can be classified

depending on the axial gap h . If h is large enough, the Bödewadt (stator) and Ekman (rotor) layers are separated. However, for small values of h , the boundary layers merge and the flow behaves like a "torsional Couette flow". For turbulent flows, Daily and Nece [17] have conducted an extensive experimental study and concluded on the existence of four main flow regimes depending on two dimensionless parameters, the disc Reynolds number $Re_\theta = r_0^2 \omega / \nu$ and the aspect ratio of the cavity $G = h/r_0$ where r_0 is the outer radius of the discs and ν the kinematic viscosity of the fluid. Owen and Rogers [18] used boundary layer equations to determine the transition line equations between the four regimes in the (Re_θ, G) diagram:

- the two laminar regimes (category I for merged boundary layers, II for separated) are separated by a line $Re_\theta G^{11/5} \simeq 2.9$;
- the transition to turbulence for flows with separated boundary layers (regime II to IV) occurs at $Re_\theta \simeq 1.58 \times 10^5$;
- the common boundary to the two turbulent regimes (category III for merged boundary layers, IV for separated) is defined by $Re_\theta G^{16/3} \simeq 7.8 \times 10^{-3}$;
- the line between regimes I and III is such that $Re_\theta G^{10/9} \simeq 366$;
- the common boundary to regimes II and III satisfies the equation $Re_\theta G^{16/15} \simeq 4.6 \times 10^6$.

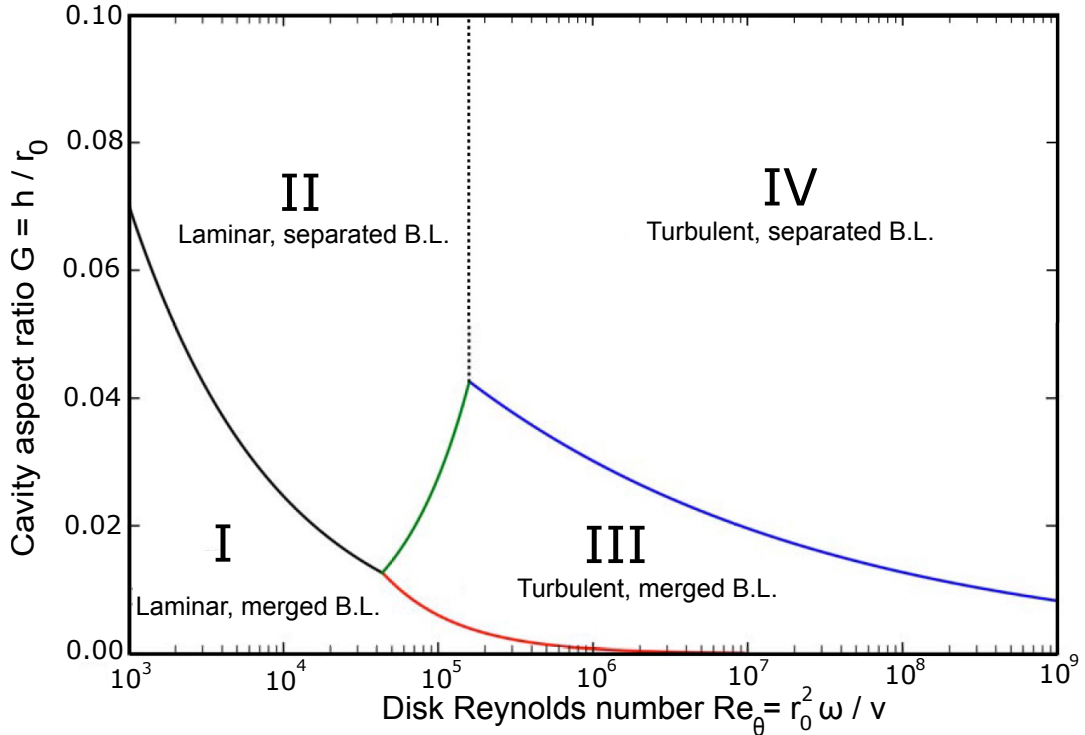


Figure 1.4: Categories of flow encountered in enclosed rotor-stator cavity. Adapted from Owen and Rogers [18]

Figure 1.4 shows a diagram first introduced by Owen and Rogers [18], that summarizes these results and gives a visual representation of the domains of definition of

all four regimes in the (Re_θ, G) plane. Depending on the distance between the two discs, the rotating speed and fluid viscosity, the flow structure has been characterized using experiments and numerical simulations. If the two discs are comparatively far from each other, an inviscid rotating fluid core develops in the axial center of the cavity rotating in a rigid body manner. On both discs, a thin boundary layer is developed. The core is dominated by an axial flow toward the rotating disc, while in the outer region, the flow is directed towards the stator disc leading to fluid movement in the meridional plane. If the discs are close to each other, the mentioned boundary layer merges conversely and the inviscid core disappears.

1.1.3 Ingestion process without external flow

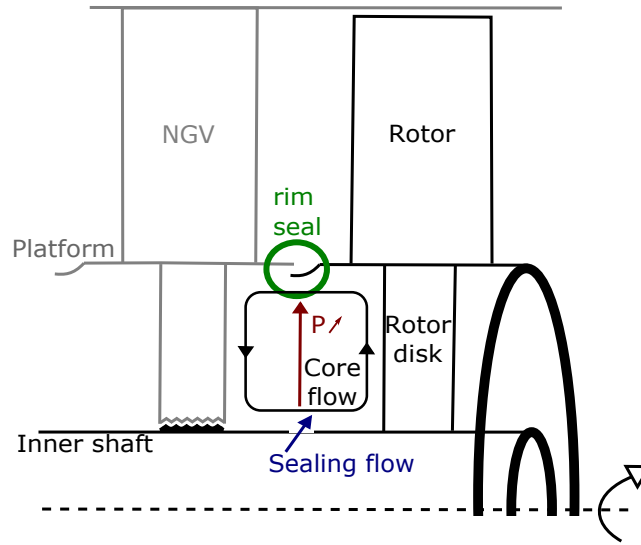


Figure 1.5: Sketch of turbine cavity and main annulus with main central core and pressure increase with radius

The Reynolds number and cavity aspect ratio encountered in low pressure turbine cavity are generally high enough to be within the domain of turbulent and separated boundary layers between the stator and rotor side. This boundary layer flow is fed by the purge flow and recirculation within the cavity which may include some ingested flow (see Fig 1.5). Despite the complicated flow in these cavities, the rigid body rotation observed for laminar infinite discs stands as a good approximation of the central flow (see non-zero azimuthal velocity of central Fig. 1.3). Based on an inviscid version of the Navier-Stokes equations (Euler) expressed in cylindrical coordinates, one can derive a relation between the radial pressure evolution and the azimuthal velocity by

$$\frac{dp}{dr} = \frac{\rho u_\theta^2}{r}. \quad (1.3)$$

The rigid body rotation of the central core induces an increase of tangential velocity component with radius resulting in a pressure increase with radius. Furthermore, increasing the disc rotation speed leads to a tangential velocity increase in the core

flow and thus higher pressure in the outer part of the core flow slightly below the rim seal. If the pressure exceeds the pressure level of the main stream, this can lead to flow from the cavity blowing into the main annulus. This process is known as the disc pumping effect. Without any external flow, the pressure field can exhibit slight azimuthal non-uniformities in the cavity and in the mainstream close to the rim seal. The potential purge flow blowing into the main annulus is therefore generally not homogeneous azimuthally. To satisfy mass conservation in the cavity, this outflow has to be compensated by an equivalent inflow. Even without any purge flow, the mainstream flow is ingested in the cavity due to radial pressure gradients. These

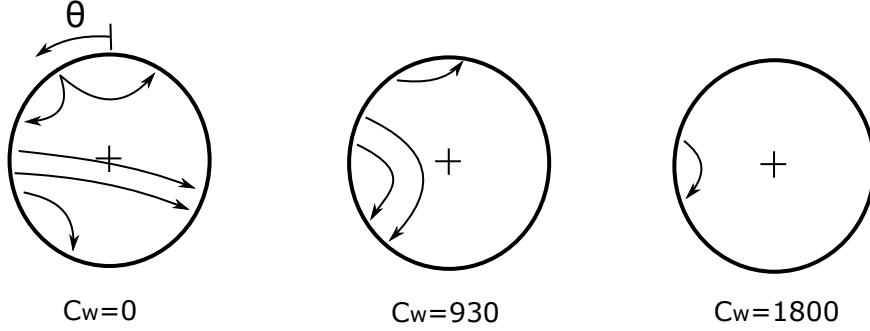


Figure 1.6: Observed flow patterns in the wheel space for simple rim seal at various non-dimensionalized purge flow rate C_w supplied in the cavity. From Phadke and Owen [19]

azimuthally non-uniform patterns of flow transfer between the cavity and the main annulus have been especially observed by Phadke and Owen [19] and are generally to be avoided when the mainflow is at high temperature. The second possibility that can be made in conjunction with the former mechanism is the supply of purge flow, which can partially compensate the cavity flow blowing into the mainstream due to disc pumping effect. This ingestion process is referred to rotationally induced ingress in the literature.

Among the first experiments of rotor/stator cavity with rim seal without external flow, Bailey and Owen [20, 21] conducted experiments aiming at determining the minimum amount of purge flow \dot{m} (non dimensionalized by $C_w = \dot{m}/(\mu r_0)$) to be internally supplied to prevent ingestion. This coolant flow was compensating the fluid blowing from the cavity due to the disc pumping effect and was shown to increase linearly (with a coefficient α depending on rim seal geometry) with the rotation velocity. This velocity, non dimensionalized by the rotating Reynolds number Re_θ and the gap between static and rotating arm s ($G_c = s/r_0$) provides the following equality for simple rim seals:

$$C_{w,min} = \alpha G_c Re_\theta. \quad (1.4)$$

This study was supplemented for more complex rim seal geometries including axial overlapping (see for example geometry 5 in Fig. 3.2) at same gap size by Phadke and Owen [19] (see Fig. 1.7). They observed similar linear relationship between the minimum sealing flow required to seal the cavity $C_{w,min}$ and rotating Reynolds number Re_θ . Reducing the gap size was shown to decrease the required purge flow rate

supply especially when approaching the boundary layer thickness over the free disc. At the time, geometries with small radial clearance in axial overlapping geometries were shown to be more favourable since they minimize the coolant flow requirements regarding simple axial geometry (see rim seal designs 5 and 6 in Fig. 1.7). Also, decreasing the radial clearance was shown to have more effect than increasing the axial overlap.

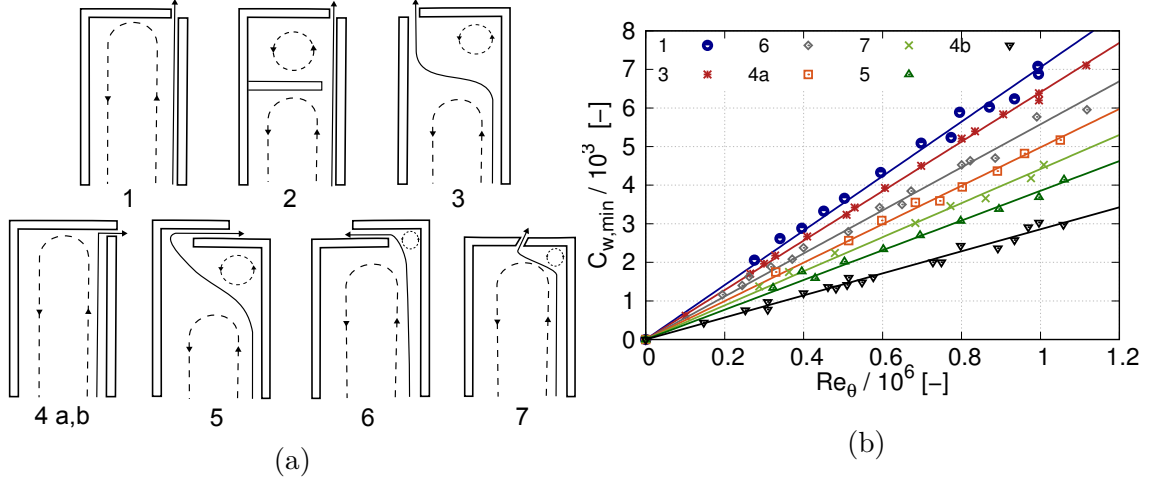


Figure 1.7: The different rim seal geometries (a) and the corresponding variation of $C_{w,min}$ with Re_{θ} with $G_c = 0.01$. Adapted from Phadke and Owen [19]

From simplified approach, the turbine cavity can be seen as a two facing disc configuration. Analytical developments on infinite disc configuration have been able to derive the flow motion in the cavity due to the rotating rotor disc. For Reynolds numbers observed in gas turbine cavity, the flow is characterized by two thin boundary layers developing on the rotor and stator disc separated by a core flow. In real configuration where the inner shaft and enclosed cavity contribution are to be taken into account, experimental studies have shown the turbulent nature of the flow and confirmed distinct boundary layers developing on rotor and stator side. One of the main flow feature is that the central inviscid core rotates and induces a pressure increase with radius. This pressure increase causes the cavity flow to egress and the mainstream flow to be ingested in the cavity. The increasing need of sealing flow with increasing disc rotation speed was confirmed in rotor/stator experiments showing linear trend between sealing supply and disc rotation for a wide range of rim seal geometries.

1.2 The superimposed mainstream flow

1.2.1 Quasi-symmetric axial flow in the main annulus

Without external flow, the ingestion process was shown to be induced by the disc pumping effect promoted by the rotation of rotor disc. The minimum sealing flow rate $C_{w,min}$ was shown to be increasing with the rotation Reynolds number Re_θ of the rotor disc. In real gas turbine application, an external flow is added to the rotating cavity corresponding to the main annulus flow. Phadke and Owen [22] conducted experiments of rotating cavity including quasi-symmetric mainstream flow. When the mainstream Reynolds number $Re_u = ur_0/\nu$ was sufficiently high regarding the rotation Reynolds number, the minimum sealing flow rate $C_{w,min}$ was no longer depending on the rotation Reynolds number Re_θ but only on the Reynolds number of mainstream flow (see Fig. 1.8). When dealing with configuration taking

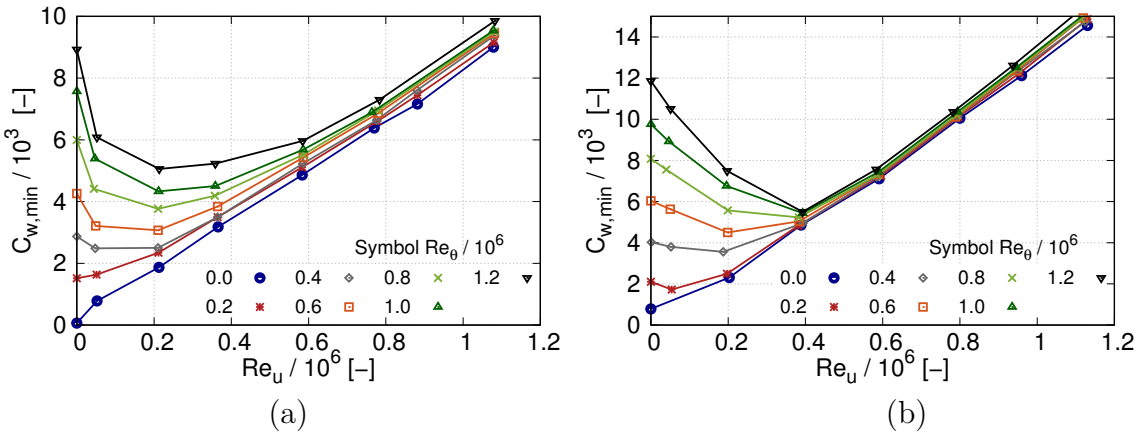


Figure 1.8: The effect of Re_θ on the variation of $C_{w,min}$ with mainflow Reynolds Re_u for axial rim seal at two gap ratio $Gc = 0.01$ (a) and $Gc = 0.02$ (b). Adapted from Phadke and Owen [22]

into account both the cavity and main flow, two effects drive the ingestion process according to the authors: the rotationally induced ingress strongly related to the rotation Reynolds number and the externally induced ingress. Depending on the characteristic Reynolds numbers of these two phenomena, the minimum sealing flow necessary can either be rotationally, externally dominated or a combination of the two, known as combined ingress. The externally induced effect is strongly related to the flow field imposed in the main annulus by the Reynolds number in the main field Re_u . For small values of Re_u/Re_θ , the rotation effect dominates and sealing flow rate evolves according to Re_θ . For large values of Re_u/Re_θ , there is an external-flow dominated regime in which the ingestion process is virtually independent of Re_θ . In modern gas turbine, the ratio is generally high enough to consider the main annulus influence as the dominant contribution to the ingress process compared to the disc pumping effect. The purpose of this subsection is to highlight the main contributors for understanding the influence of main flow on ingress process.

1.2.2 Swirling flow without blades

The effect of the main flow swirling without blades on the ingestion process of a rotor/stator cavity with rim seal and purge flow was originally investigated by Daniels et al. [23]. The experiments were conducted at a rotating Reynolds number $Re_\theta = 5.1 \times 10^6$, on simple and axial overlapping rim seals (rim seal geometry 3 and 6 in Fig. 1.7) with two gap width between the static and rotating arms $s/r_0 = 0.0024$ and $s/r_0 = 0.0048$. The swirling fraction of the mainstream flow was set to a fraction of the tangential velocity at the tip of the rotating disc, respectively 0.6, 1 and 2 times the tangential velocity. CO₂ gas was used as purge flow. Sealing effectiveness was assessed by measuring the CO₂ concentration C regarding CO₂ concentration of the purge gas C_p and in the simulated gas path C_o through the sealing effectiveness parameter ϕ :

$$\phi = \frac{C - C_o}{C_p - C_o}. \quad (1.5)$$

For simple and axial overlapping with the two gaps width tested, the tangential

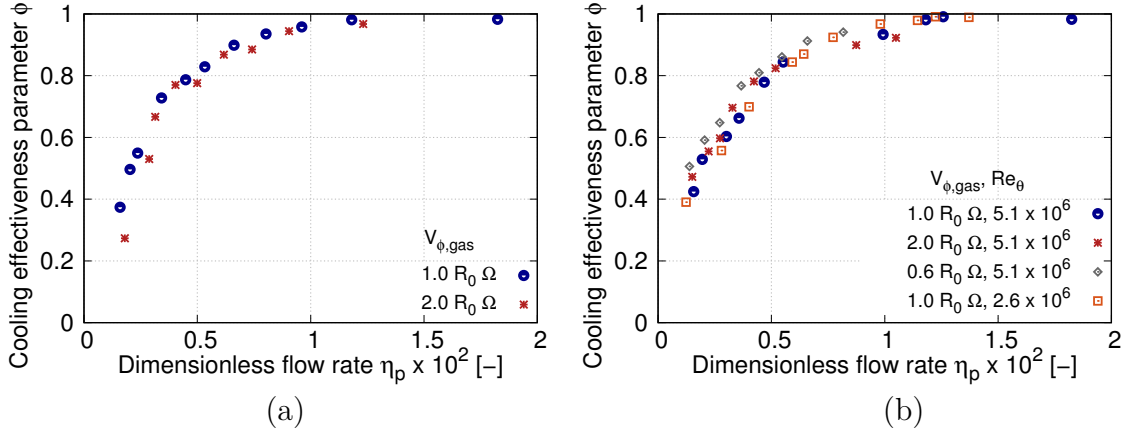


Figure 1.9: Sealing effectiveness for simple (a) and axial overlapping (b) rim seal $s/r_0 = 0.0048$, at various mainstream swirl flow fraction. Adapted from Phadke and Owen [22]

velocity in the mainstream did not affect significantly the sealing effectiveness (see Fig. 1.9). The decrease of the radial gap width was confirmed to result in a significant improvement in sealing effectiveness compared to an increase of the axial overlap of the seal. Later, Bohn and Wolff [24] published an improved correlation based on measurements in a 1.5-stage gas turbine and demonstrated the dominant impact of the rim seal geometry on the minimum required coolant flow. The correlation proposed alleviated the knowledge of $C_{w,min}$ as in the experiments of Phadke and Owen [22]. These correlations were extrapolated to real engine conditions, and are relevant for a rough first estimate in a design process as shown by Teuber et al. [25].

1.2.3 Non-axisymmetric pressure distribution

Non-axisymmetric and time-dependent pressure distribution in the main annulus is due to rotor/stator system and interaction. The high turning/swirling flow in-

duced by blades cannot be responsible for the ingress process and non-axisymmetric disturbances observed in the experiments and pushed towards further investigations.

1.2.3.1 The origin of non-axisymmetric pressure distribution for a turbine stage

For a rotor/stator configuration with a cavity in-between, Dadkhah et al. [26] and Bohn et al. [24] were able to demonstrate that the pressure asymmetry in the mainstream flow was mainly due to the imposed vane pressure field that modulated the level of mainstream gas ingress. The nozzle guide vanes induce circumferential pressure asymmetry in the downstream region leading to alternating regions of ingestion and blowing occurring at the rim seal interface depending on the local pressure. The

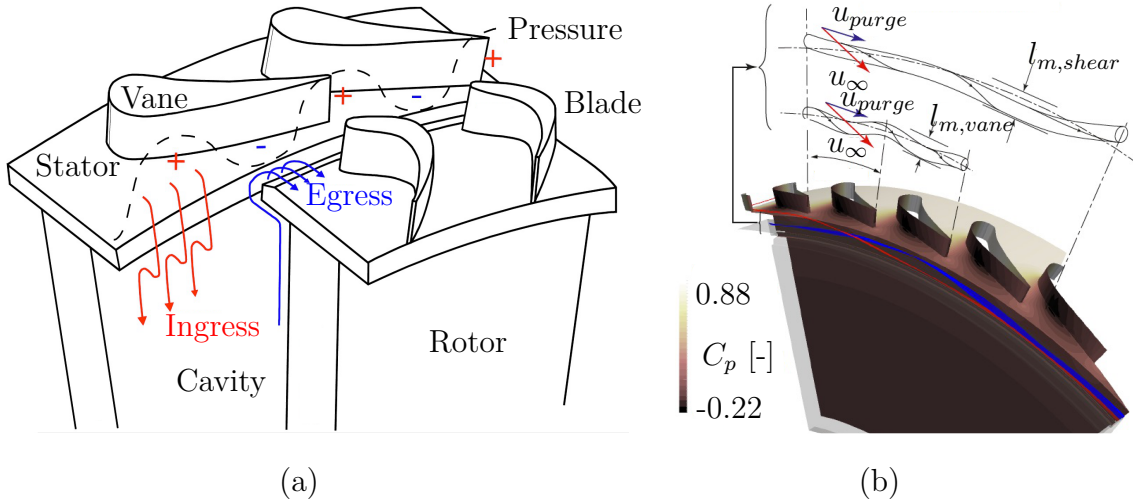


Figure 1.10: Ingress/egress process at the rim seal interface due to wake and potential effects. From Sangan et al. [27] (a). Streamlines of mainstream gas (red) and rim seal gas (blue) indicating a toroidal recirculation in the rim seal. From Savov et al. [28] (b)

rotating rotor row also generates pressure asymmetry in the upstream flow region due to potential effect (see Fig. 1.10a). However, the influence on the ingress process at rim seal interface was not as clear as with the vane effect, as it was dependent on rim seal geometry. Bohn et al. [29] and Turner [30] experimentally studied the addition of the rotor blade and showed an increase of the sealing effectiveness for the axial rim seal, but a reduction for an open rotor/stator configuration. The influence of the geometry was also reported by Savov et al. [31]. They showed a significant sealing efficiency modification for a single overlapping rim seal when adding downstream blade, while the efficiency was less sensitive for double overlapping. Nevertheless, the time instantaneous pressure field, which contains blade passing component was shown to be important for ingress, as stated by Roy et al. [25], who measured the time averaged unsteady pressure signal at various locations in the mainstream between the vane blade row. Savov et al. [31] concluded that the ingress process is dominated by the peak-to-trough vane pressure field and is modulated by the unsteady potential pressure field imposed by the downstream blade row.

1.2.3.2 The effect of non-axisymmetric pressure on ingress process

Unlike swirling motion, pressure asymmetries were shown to promote ingestion process as stated early by Abe et al. [32] who reported experimental measurements of ingress in the cavity downstream the vanes row. As stated by Phadke and Owen [22], the ingestion process was shown to be mainly driven by the external flow at sufficiently high Reynolds number compared to the rotational one. It was unclear to the authors at that time whether the ingress process was due to the flow itself, or to potential pressure flow inhomogeneity, since they were only able to derive a quasi-symmetric flow with relatively low pressure fluctuations. Additional experiments conducted with main flow-driven ingress with spatially aperiodic pressure distribution showed that $C_{w,min}$ increased with the peak-to-trough pressure asymmetry amplitude. The authors were able to show that the externally induced ingress was mainly fed by pressure asymmetry in the mainstream.

Carrying these experiments, the authors remarked that after ingress had occurred,

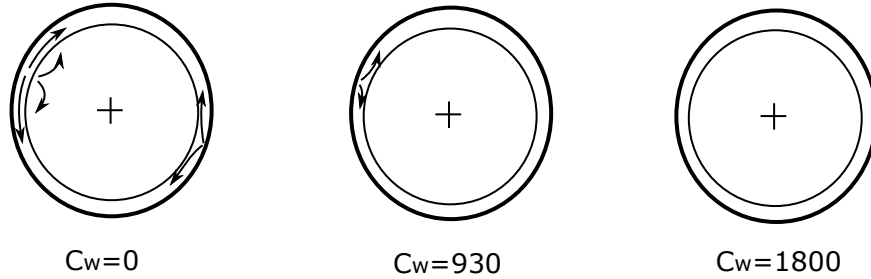


Figure 1.11: The effect of C_w on the observed flow patterns in the wheel space for $Gc = 0.01$, $Re_\theta = 0$, $Re_u = 0.2 \times 10^6$

the fluid migrated transversely across the wheel space characterized by a tangential instability of the flow and static pressure lobes. Double axial overlapping available showed that this "ring road" created by the rim seal enabled the transfer of most of the flow from the high to the low pressure regions in the external-flow annulus compared to simple gap geometries (see Fig. 1.6 and 1.11).

1.2.3.3 Unsteadiness at the rim seal interface

Experiments of simple gap seal with and without vanes upstream of the seal showed that approximatively twice the coolant flow is required to maintain a given disc cavity coolant effectiveness for a seal located downstream of the vanes compared to a seal with axial flow across the rim seal, as stated by Green and Turner [30]. The distance between the trailing edge and the rim seal was also shown to have an impact on coolant requirements since driving the wake residual strength: the experiments conducted by Chew et al. [33] showed that the coolant required to obtain 70 to 80% of cooling effectiveness was increased by 50 to 70% when the trailing edges of the vanes were positioned at the rim seal compared to 60% axial chord upstream. The increased ingress tendency when the blade to vane distance was reduced was attributed to stronger unsteady interaction between the wake and potential effect leading to strong pressure fluctuation in the rim seal region.

Inclusion of the mainstream flow leads to two competing phenomena for the ingress process: the rotational effect due to the rotor disc depicted in last subsection and the externally induced effect. The latter effect is mainly related to the pressure asymmetry in the main annulus imposed by the vane pressure field and modulated by the rotating blades. For cavity typically encountered in real applications, the main annulus effect is generally dominant.

1.3 Local effects at the rim seal interface

1.3.1 Shear layer

Unsteadiness in the main annulus was shown to have strong influence on the ingress process at the rim seal interface. Even at the rim seal interface, unsteady flow features were shown to develop. De la Rosa Blanco et al. [34] studied the effect of purge flow injection from an upstream rim seal clearance on hub endwall flows development. They observed a shear layer spanning the rim seal gap and rolling up in series of vortices. These vortices were subsequently convected in the inter-blade passage. This observation promotes the idea of unsteady interaction. Rabs et al. [35] reported similar vortex structures and concluded on the development of Kelvin-Helmholtz instability in the shear layer due to differences in tangential velocity components between the main annulus and the rim seal flow. The instability leads to periodical vortex shedding in the rotor passage. The shedding process frequency was shown to be influenced by the rim seal geometry as stated by Chilla et al. [36] as well as Savov et al. [28]. The unsteady activity due to Kelvin-Helmholtz instability intensifies and increases ingress occurrence for high levels of velocity mismatch between the mainstream and rim seal flows as stated by Savov et al. [28].

1.3.2 Turbulent mass transport

In addition to the shear layer process at the rim seal interface, the interaction of the mainstream and rim seal flow results in a recirculation zone in the rim seal mixing the flow, as reported in early studies of Ko et al. [37, 38]. This recirculation zone is a toroidal vortex that spans the annulus and is named as gap recirculation zone (see Fig. 1.10b). The vane pressure distribution modulates the recirculation. However, the flow being essentially in the tangential direction, a modeling of the recirculation by a turbulent process mixing has been proposed. This observation was supported by the large wavelength of the vortical structure which are of greater amplitude compared to the perturbation due to the vane pressure field. The recirculation zone which was early on not fully understood have seen the emergence of turbulent transport models assuming that the dominant source of mixing in the rim seal is driven by the recirculating flow. The ingestion is treated as a turbulent transport process for a given seal, assuming an effective eddy viscosity (representing the overall effect of all the length scales of ingress) acting across the difference in seal effectiveness between

the cavity value (one) and the mainstream value (zero). Under this hypothesis, numerous studies have been devoted to build orifice models.

The flow in rim seal region is characterized by a toroidal vortex spanning in the annulus, leading to a zone of strong mixing under turbulent processes. This has promoted the development of orifice models to characterize experimentally various rim seal geometries based on turbulent mixing assumption.

1.4 Large scale flow structures in the cavity

The previous description of cavity, main annulus and rim seal flows from theoretical and experimental developments gave further insights on the main underlying phenomena promoting ingress/egress processes. The levels of ingress were mainly evaluated on experimental analysis and empirical models to predict flow rates to seal the cavities in simplified configurations. Even though these models are used in the design phase, some flow mechanisms remain unknown and the highly unsteady interaction in real configurations remains challenging to tackle with experimental studies, as they give scarce insight of the flow physics. Thus, they are generally not sufficient to obtain improvement in sealing process understanding. Therefore, numerical studies of the rim seal flow, mainly based on a Reynolds-averaged Navier-Stokes (RANS) or Unsteady Reynolds-averaged Navier-Stokes (URANS) have been conducted as first numerical approach due to the low computational costs. At the time, it was noted that the flow field inside the rotor-stator wheel space converges much slowly compared to the main annulus flow that could be partially explained by the local low Mach number as compared to the higher Mach number in the main annulus. Overall, the investigations based on (U)RANS formalism were able to predict some trends. However, prediction of sealing effectiveness with early CFD was proven to be challenging as stated by O'Mahoney [39] reporting under-prediction of ingestion with small sector configuration conducted with RANS simulation compared to experiments. Numerical simulations and experimental studies indicated important unsteady flow effects that explained some differences identified in comparing predicted and measured sealing effectiveness. Among the complex unsteadiness processes occurring in the mainstream flow passage, relatively large structures rotating in the cavity were observed. Accounting for these structures showed improved results regarding experimental data [29].

1.4.1 The main features of the large scale flow structures

The description of large scale flow structures is generally challenging from a numerical point of view since full annulus is needed and very high accuracy in time integration to avoid dispersion problems. Bohn et al. was among the first to observe a local ingestion zone rotating at approximately half the rotor speed using URANS simulation over a one stage axial turbine with a cavity in-between. In early full annulus URANS simulations and corresponding experiments of Cao et al. [33] and

Jakoby et al. [40], energetic large-scale rotating structures inside the wheel space have been evidenced. More recently, Savov et al. [28] as well as Beard et al. [41] reported rotating structures in the cavity. The number of lobes of these large scale structures were shown to be uncorrelated with the blade or vane number that supports the theory of instability that may be triggered by the azimuthal gradients. An example of radial velocity and pressure contours on an axial plane are shown

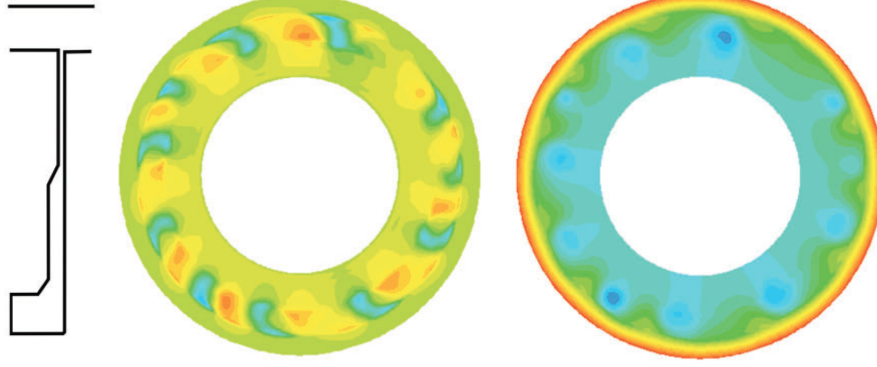


Figure 1.12: Instantaneous radial velocities (left: -70 to 50 m.s^{-1}) and pressure (right: -15 to 15 kPa), $Re_\theta = 6 \times 10^6$. From Cao et al. [33]

in Fig. 1.12 from URANS simulation performed by Cao et al. [33]. These large scale structures were observed both with and without a forced main annulus flow as stated by Boudet et al. [42], Cao et al. [33], as well as Jakoby et al. [40]. This suggests that this process is inherently initiated by the cavity. Depending on the configuration, related unsteady fluctuations confined to the small rim seal region or extended further in the disc cavity and the main annulus with potential interaction. The low frequency content was shown to possibly have the stronger spatial interaction with fluctuations, overcoming pressure fluctuations induced by the main flow. This generates non-negligible noise in the mainstream as stated by Schädler et al. [36]. Despite large scale structures being generated by the cavity, they can interact with mainstream under a non-linear process leading to a modification of the main frequencies of the process, as stated by Boudet et al. [43]. The purge flow was shown to have a damping effect on large scale flow structures with potential cancelling of the phenomenon as stated by Julien et al. [44] and Wang et al. [45].

1.4.2 The different likely initial mechanisms

The first possible path leading to large scale flow structure are the inertial waves due to Coriolis forces imposed to the inviscid core flow by the rotation of the disc. At the rim seal interface, De la Rosa Blanco et al. [34] studied the effect of purge flow injection from an upstream rim seal clearance on hub endwall flows development. They observed a shear layer spanning the rim seal gap and rolling up in series of vortices. Rabs et al. [35] reported similar vortex structures and concluded on the development of Kelvin-Helmholtz instability in the shear layer due to differences in the tangential velocity components between the main annulus and the rim seal flow. This effect has been observed to be the strongest and clearest at high purge

flow rates and has been associated with unsteady measurements in the outer seal region. Wlassow [46] observed oscillations at 0.8 times the frequency of rotation in a configuration with cavity at shroud, the author attributed this unsteadiness to Helmholtz-type instability. For seals with extended axial overlapping, the rim seal region is similar to a Taylor-Couette configuration (fluid confined in the gap between two rotating cylinders), hence the flow instabilities are expected to occur based on the Rayleigh criterion. Taylor-type structures have been observed in LES simulation by Gao et al. [47]. These rotating flow modes have been attributed to either intrinsic unsteadiness of the rim seal flow or interactions of the sealing and the annulus, or cavity flows. In some conditions it is clear that these modes play a dominant role in ingestion. In other cases, their significance relatively to other effects, such as vane and blade pressure generated asymmetries, is not clear. The number of vortex pairs appear to be geometry related. Capturing these large scale flow structures in numerical simulation is challenging since the results were shown to be dependent on the turbulence model used when performing (U)RANS simulations. The dependence to turbulence model can be reduced through the use of LES. O'Mahoney et al. [39] conducted numerical computations based on an URANS and a LES approach demonstrating a significant improvement of the numerical results for the LES approach, which showed a much closer agreement with experimental measurements of the cooling effectiveness. Another main uncertainty source in many previous studies is the periodicity assumption in the circumferential direction which may suppress the development of large-scale structures inside the wheel space, as stated by Jakoby et al. [40].

Despite significant contributions from analytical and experimental developments, some lack of knowledge remains in the ingestion process with difficulty to predict ingress amounts. Based mainly on numerical simulation and experiments devoted to the analysis of the flow in the cavity, large scale flow structures were observed in the cavity with frequencies and lobe number which were shown to be uncorrelated to the blade number and the rotation rate of the gas turbine. These large scale flow structures were shown to potentially induce strong pressure variation in the cavity, and could propagate in the mainstream with amplitudes of the order of magnitude of those observed in the main annulus. The cascade of effects leading to these structures remains an open problem, with hydrodynamic instabilities identified as a likely mechanism by some studies.

The ingestion and blowing processes at the rim seal interface is influenced mainly by three mechanisms: the positive radial pressure gradient in the cavity that is induced by the central inviscid rotating core flow between stator and rotor disc wall, the core flow imposing a pressure distribution underneath the rim seal that drives the rotationally induced ingress phenomenon, superimposed instability phenomena in the cavity strongly modifying the pressure distribution with frequency and pattern periodicity often decorrelated from geometrical feature (number of nozzle guide vanes, blades). On the other side of the rim seal, the pressure distribution is mainly imposed in the main annulus by the upstream wake and potential effect of downstream blade. The ingestion/blowing process induced by this phenomenon (externally induced ingress) is generally in competition or dominant at Reynolds number encountered in gas turbine applications. The pressure distribution imposed by the cavity and main annulus flow is three-dimensional and unsteady, inducing a complex ingestion and blowing process at rim seal interface. For an imposed pressure distribution up and down the cavity the amount of flow crossing the rim seal is controlled by the geometry of the rim seal and localized turbulent effects. The importance of these effects have pushed towards the use of orifice models based on turbulent transport across the rim seal to characterize the amount of ingress/egress across the rim seal and have shown to recover the proper values obtained experimentally.

Say little about what you know and nothing at all about what you don't know. Why not simply say more often : I don't know.

— Sadi Carnot

2

Analyzing losses in the flow field

Efficiency can be the most important parameter for gas turbine and characterizing the losses which determine the efficiency is a critical aspect in the analysis of this device with complex flows. A difficulty that generally emerges in efficiency purposes is the difficulty to link global efficiency of the gas turbine obtained from general thermodynamic considerations with the loss induced locally in the different components and processes encountered by the flow in the gas turbine. In the current study, it may be not obvious to relate the potential increase in combustion chamber temperature (benefit for thermal efficiency) with the loss induced by more flow collected at the compressor and the loss incurred by purge flow in the turbine. In this chapter is introduced an approach based on exergy (energy available to generate work) to put on a same basis these different phenomena impacting the efficiency of the gas turbine at different scales. A description of the main source of losses in a gas turbine (at current stage of knowledge and available in the literature) with special emphasis for the account of cavity flow will be presented. This description will be held by increasing complexity from two-dimensional flow field to three-dimensional effects including purge flow.

2.1	Loss accounting and tracking using an exergy formula-	
	tion	20
2.1.1	The general thermodynamic laws	21
2.1.2	Exergy: a link between loss and gas turbine efficiency	24
2.1.3	Balance equations for exergy and useful work	31
2.1.4	The application of exergy to numerical simulation	40
2.2	Losses in a turbine	49
2.2.1	Unsteadiness in gas turbine flows	49

2.2.2	The flow in near-wall region	52
2.2.3	Blade losses	59
2.2.4	Endwall losses	64
2.2.5	Tip clearance leakage flow	70
2.2.6	Transport of upstream non-uniform flow structures in a downstream cascade	72
2.3	Influence of purge flow blowing in the mainstream . . .	75
2.3.1	Viscous shear layer	75
2.3.2	Losses due to change of reaction	76
2.3.3	Influence on turbine secondary flow	77

2.1 Loss accounting and tracking using an exergy formulation

A definition of loss in a turbomachine has been proposed by Denton [48] that is generally agreed and defined as any flow feature that reduces the efficiency of the turbomachine. It is commonly accepted for example that the trailing shed vortex process downstream a blade of a turbine is a loss and may be measured by a decrease of total pressure. However, it is generally difficult to draw a link between this local phenomenon and a reduced efficiency for the gas turbine that would be, according to Denton, a loss for the gas turbine. A second difficulty that emerges from this notion of loss is the variability in the nature of the physical phenomena (heat transfers, mixing processes, etc.) inducing loss. Also, the possibility to add in a same balance the contributions measured locally (for example the trailing shed vortex process downstream a blade) and at higher scale (for example at the scale of the component based on global thermodynamic considerations) would be desirable. This section will be devoted to provide a general framework to put on a same basis these different phenomena for which different levels of measures are used (while all the phenomena occur locally) in the purpose to see how it affects the thermal efficiency of the gas turbine. The framework that has been chosen to be used in current study is based on the notion of exergy. The exergy is a composite quantity depending of the state of the flow with the enthalpy quantity and the level of irreversibility of the flow with the entropy quantity. These last two quantities will be first introduced by recalling the general thermodynamic laws that are essential equality to understand the work and heat transfers occurring between the flow crossing the gas turbine and the gas turbine itself as well as the irreversibility transported by the flow. A special emphasis will be given to the entropy quantity since this quantity is generally the one used to track loss generated in the gas turbine as it was popularized by Denton [48]. Then, the notion of exergy will be more explicitly defined as a thermodynamic quantity. The purpose will be to draw a link between the exergy levels at a certain scale for example locally in the fluid or at the scale of the component studied and its general impact on the efficiency of the gas turbine. An example of this approach will be provided for a whole gas turbine. Finally, a transport equation for exergy will be derived that is particularly suitable for numerical simulation since balance can be performed at each grid point to highlight locally regions of loss generation. The

influence of turbulence in the loss generation will be also accounted at the end of this section.

2.1.1 The general thermodynamic laws

In order to introduce the notion of exergy, general thermodynamic laws will be introduced. Mass and momentum conservation equations from Navier-Stokes equations are supplemented by total energy equation that was derived in the framework of thermodynamics. Thermodynamics deals with the study of work and heat transfer of a fluid system with a surrounding system. This approach is based on the notion of equilibrium state making possible to use a limited number of quantity like pressure and temperature for example to describe all other properties of the flow. The notion of equilibrium state refers to the absence of unbalanced forces, chemical reactions and temperature for the system. The whole fluid in a component of a gas turbine for example have quantities such as pressure which vary throughout, so that there is no single value that characterizes all the material within the device. If so, the conditions for the three types of equilibrium to hold on a global basis are not satisfied when the complete region of interest is seen as a whole. To deal with this difficulty, the flow field can be divided in a large number of small mass elements, over which the pressure, temperature, etc. have negligible variation, and consider each of these elements a different system with its own local properties. In defining the behavior of the different systems the working assumption is that the local instantaneous relation between the thermodynamic properties of each element is the same as for a uniform system in equilibrium.

2.1.1.1 First principle of thermodynamic

The first principle of thermodynamics applied to the considered fluid system that states on the total energy conservation can be written in differential form as:

$$d(E_{tot}) = d(e + E_k + E_p) = \delta W + \delta Q \quad (2.1)$$

where E_{tot} , e , E_k , E_p , W and Q are respectively total, internal, kinetic energy, potential energy of the fluid, the work and the amount of heat transferred between surrounding and the fluid system. The convention is taken as positive when work or heat is given to the fluid. From current equation was derived the total energy conservation of Navier-Stokes equation set eq.(A.1.2) proposed in Sec. A.8c with the account of potential energy¹. For the flow in a turbomachine, W can be the work given to the fluid by the rotor blades for a compressor (positive work) or extracted from the fluid by the turbine (negative work). W can also be the pressure work associated to the pressure variation of the fluid during a compression or expansion process. The heat Q can be transferred with the flow at the wall of the turbomachine. These transfers of work and heat modify the total energy of the fluid that can be stored and transferred in the different forms of energy. The notations d and δ

¹The potential energy variation related to gas turbine flows is generally gravity but this contribution is very small compared to kinetic and internal energy variations and so omitted since low or no altitude variations is experienced by the fluid in the gas turbine

denote conceptual and physical differences between the terms. Changes in E_{tot} represent state changes which do not depend on the path taken to achieve the change. Work and heat are not state variables and are only defined in terms of interactions with the system. The first principle was originally proposed by Sadi Carnot (1796-1832) in 1824 in his unique book *Reflections on the Motive Power of Fire* [49]. Almost thirty years were needed before the main ideas of this author were understood and popularized by Lord Kelvin introducing the thermodynamic of systems (Latin expression literally standing for work production by heat) to this field.

2.1.1.2 Second principle of thermodynamic

The first principle stated the conservation of energy for dynamical systems following conservation laws from the fundamental laws of dynamics introduced by Newton. In addition to this energy conservation law was proposed the second principle that can be expressed in two parts. The first part is a definition of a thermodynamic property: entropy of the system, denoted s , introduced by Rudolf Clausius (1822-1888). If δQ_{rev} is the heat transferred to the system during a reversible incremental state transformation, and T is the temperature of the system, the resulting change in entropy is:

$$ds = \frac{\delta Q_{rev}}{T}. \quad (2.2)$$

The second part of the second law known as Clausius inequality states that for any process, the change in entropy for the system is

$$ds \geq \frac{\delta Q}{T}. \quad (2.3)$$

The equality occurs for a reversible process. The concepts of reversibility and irreversibility are important in the analysis of gas turbine plants. A closed system (as the flow moving in a control volume of the turbomachine) moving slowly through a series of stable states is said to undergo a reversible process if that process can be completely reversed in all thermodynamic aspects, i.e. if the original state of the system itself can be recovered (internal reversibility) and its surroundings can be restored (external reversibility). An irreversible process is one that cannot be reversed in this way. The idea behind the second principle is that despite energy conservation from first principle, energy experiences quality degradation in the purpose to generate work that prevent from recovering reversible process. Entropy is used as a measure of this energy quality degradation. Entropy is generally an unfamiliar quantity because no absolute reference, as opposed to most quantities that the fluid mechanics deals with like velocity (defined with reference to the reference frame of the study) and temperature (with reference to the absolute zero or to the temperature at which water freezes). Also, it cannot be seen or measured directly, its value can only be inferred by measuring other properties. The fluid considered is a simple compressible substance. The thermodynamic state of this fluid is specified when two independent intensive thermodynamic properties (pressure and temperature, for example) are known. Any other thermodynamic quantities of the fluid

can be recovered with among them entropy. Therefore, the purpose is to derive an expression for entropy based on these two independent quantities. For incremental reversible processes in a simple compressible substance, the heat addition to the fluid is

$$\delta Q = Tds. \quad (2.4)$$

Under the assumption of a reversible process, the only force producing work onto the system is pressure force onto the volume V of the system

$$\delta W = pdV. \quad (2.5)$$

Although the association of work with pdV and heat addition with Tds is only true for a reversible process. The sum of these quantities, as expressed by the first law, is a state change which means that it does not depend on the path to achieve this change especially irreversible ones. For an infinitesimal process where the variation of kinetic and potential energy are negligible, total energy conservation eq.(2.1) leads to the equality (known as Gibbs equation) that holds for irreversible processes:

$$de = Tds - pdV \quad (2.6)$$

where the convention is taken positive when energy is supplied to the system. When pressure forces are applied onto the surface of the fluid system, the first principle of thermodynamics can be written as:

$$d(e + E_k + E_p) = dp/\rho + \delta W_{non-pressure} + \delta Q \quad (2.7)$$

where $W_{non-pressure}$ refers to non-pressure works. A convenient practice is to add pressure forces to internal energy to obtain a quantity known as enthalpy h :

$$h = e + p/\rho \quad (2.8)$$

that gives:

$$d(h + E_k + E_p) = \delta W_{non-pressure} + \delta Q. \quad (2.9)$$

Neglecting the potential energy compared to kinetic and internal energy, this makes possible to write the variation of total enthalpy $h_{tot} = h + E_k$:

$$d(h_{tot}) = \delta W_{non-pressure} + \delta Q. \quad (2.10)$$

This last quantity is of particular interest in the context of gas turbine flows. For example, for compression or expansion processes where no heat is transferred ($Q = 0$), total enthalpy is conserved along a stator row while reduced to W_{shaft} in a rotor row. More generally, in real processes, this quantity is relevant of the potential energy of the flow as the sum of the main energy contributions that are internal,

kinetic energy and work transfer with pressure. Similarly to the internal energy, the enthalpy can be expressed as a function of entropy:

$$\begin{aligned}
dh &= d(e + p/\rho) = de + (1/\rho)dp + pd(1/\rho) \\
&= Tds - pd(1/\rho) + (1/\rho)dp + pd(1/\rho) \\
&= Tds + (1/\rho)dp.
\end{aligned} \tag{2.11}$$

For a perfect gas, i.e. following perfect gas equation, the enthalpy depends only on temperature

$$dh = c_p dT \tag{2.12}$$

and an explicit expression can be derived for entropy based on thermodynamics quantities as

$$ds = c_p \frac{dT}{T} - r \frac{dp}{p} \tag{2.13}$$

where r is the molar gas constant that holds for a c_p function of the temperature. Assuming c_p independent of T gives by integrating last equation:

$$\Delta s = s - s_{ref} = c_p \ln \frac{T}{T_{ref}} - r \ln \frac{p}{p_{ref}}. \tag{2.14}$$

Alternatively, entropy can be expressed in terms of temperature and density by:

$$\Delta s = c_v \ln \frac{T}{T_{ref}} + r \ln \frac{\rho}{\rho_{ref}}. \tag{2.15}$$

These equations only give changes of entropy relatively to a reference state s_{ref} . The absolute value of entropy is always arbitrary. The temperatures, pressures and densities used in these equations may be either all static values or all stagnation (total) values because by definition the change from static to stagnation conditions is isentropic, meaning that the passage from static to total quantities in the expression of entropy does not incur any entropy change.

2.1.2 Exergy: a link between loss and gas turbine efficiency

From last subsection, enthalpy and entropy are shown to be two important quantities. The enthalpy that deals with the heat and work transfer of the flow with the gas turbine (first law of thermodynamic). Entropy (second law of thermodynamic) that is an indicator of deficiency in the flow field, i.e irreversibility generated in the flow field. It remains two issues that need to be clarified at current stage. The first concerns the relation between this entropy change due to irreversibility and the lost opportunity to produce or extract useful work for the gas turbine. Indeed, an important question is the relation between the (local) loss measures for components i.e

entropy that can be measured locally from thermodynamic property and loss measures based on global system (i.e. thermodynamic cycle) considerations exposed in the introduction of the thesis. The second issue concerns the loss measurement method that can be adopted and the way to put on a same basis this measure performed at different scales, i.e. locally in the flow, at the scale of a whole component or the gas turbine since the flow locally or at the scale of the components typically operate as a part of a more complex fluid system.

To deal with these last two requirements, we consider a steady-flow device, which can exchange heat Q and shaft work W_{shaft} with the surroundings during a process from an initial state X to a subsequent state Y is according to eq.(2.10):

$$W_{shaft} = Q + (h_{tot,X} - h_{tot,Y}) \quad (2.16)$$

Without loss of generality, this may represent the steady flow in a gas turbine that can exchange work with the shaft and heat provided to the flow by the combustion of fuel or heat transfer at the wall of the gas turbine in contact with the fluid. For given initial and final states, the change in stagnation enthalpy is specified. The first law gives no information concerning the magnitude of the heat addition Q but the larger the heat addition the larger the shaft work. The second law, however, puts a bound on the maximum heat addition and thus the maximum work that can be obtained for a given state change. This upper limit can be determined by examining a situation in which the mainstream flow exchanges heat only with a reservoir at temperature T_{res} . For current study, we will mainly consider two types of reservoir. A first reservoir at temperature T_0 corresponding to the calm atmosphere at condition (p_0, T_0) in which the turbomachine operates. A second reservoir at temperature T that is a total temperature. This can be seen as the situation of a component of the turbomachine operating in between other components and where T corresponds to either local temperature of the wall or the exit temperature of the component. Let's consider first the case of a reservoir at T_0 .

2.1.2.1 Heat transfer with a reservoir at T_0

For the considered process between X and Y, the entropy change of the reservoir is $\Delta s = -Q_0/T_0$. From the second law, the entropy change of the stream flow between inlet and outlet must be such that the total entropy changes occurring in the device plus the environment equal to or is greater than zero. Any difference from zero represents the departure from reversibility. The second law, applied to the fluid system which passes from state X to state Y is:

$$(s_Y - s_X) - \frac{Q_0}{T_0} = \Delta s_{irrev} \geq 0 \quad (2.17)$$

$Q_{rev} = (s_Y - s_X)T_0$ being the outwards heat transfer between X and Y with surrounding atmosphere at T_0 . The quantity Δs_{irrev} is the entropy generated as a result of irreversible processes. Combining eq.(2.16) and (2.17) leads to:

$$[W_{shaft}]_{real} = (h_{tot_X} - T_0 s_X) - (h_{tot_Y} - T_0 s_Y) - T_0 \Delta s_{irrev}. \quad (2.18)$$

The entropy change s_{irrev} is equal to zero or positive. The maximum shaft work that can be obtained for a state change from X to Y is therefore the difference in the quantity $h_{tot} - T_0s$,

$$[W_{shaft}]_{reversible} = (h_{totX} - T_0s_X) - (h_{totY} - T_0s_Y). \quad (2.19)$$

The notation of maximum and reversible are used indifferently since the maximum work extracted is obtained for the reversible process. The comparison of eq.(2.18) and (2.19) shows that for the given state change, the difference between the maximum shaft work and the shaft work actually obtained is $T_0\Delta s_{irrev}$ which is the lost work for the process or equivalently the heat generated during the process due to irreversibilities. The quantity $h_{tot} - T_0s$ is known as the steady-flow availability function denoted B as defined by Horlock [50]. It is a composite property which depends on both the state of the fluid (with the total enthalpy h_{tot}) and the temperature of the reservoir (here T_0). Based on availability function B, the maximum work that can be extracted from a fluid at initial state X can be defined. This quantity known as exergy denoted χ corresponds to the availability function at beginning of the process B_X minus the availability function of the reservoir $B_Y = B_0$ with which heat transfer can occur, here the atmosphere at the so-called "dead-state" (p_0, T_0):

$$\chi_X = B_X - B_0. \quad (2.20)$$

Exergy can be equally used to obtain the maximum shaft work that can be obtained for a state change from X to Y since:

$$[W_{shaft}]_{rev} = B_X - B_Y = (B_X - B_0) - (B_Y - B_0) = \chi_X - \chi_Y \quad (2.21)$$

$$[W_{shaft}]_{real} = \chi_X - \chi_Y - T_0\Delta s_{irrev}. \quad (2.22)$$

2.1.2.2 Heat transfer with a reservoir at T

As stated, in some configuration, the temperature of the flow heat transfer is not the environment one (locally the heat transfer with the wall of the main annulus for example). When the reversible heat is released at temperature T in the presence of an environment at T_0 , the heat transferred Q_{rev} supplies a reversible heat engine, delivering external work $(W_e)_{rev}$ and rejecting heat $(Q_0)_{rev}$ to the environment. The total work output from the extended control volume is $(B_X - B_Y)$, if the flow is again between states X and Y. But the work from the reversible external engine is

$$[W_e]_{reversible} = \int_X^Y \left(\frac{T - T_0}{T} \right) dQ_{rev}. \quad (2.23)$$

The maximum reversible work obtained from the inner control volume V is therefore equal to

$$[W_{shaft}]_{reversible} = B_X - B_Y - (W_e)_{rev} = \chi_X - \chi_Y - \int_X^Y \left(\frac{T - T_0}{T} \right) dQ_{rev}. \quad (2.24)$$

For a real irreversible flow process in the control volume V between fluid states X and Y with the sum of heat rejected at temperature T ($Q = Q_{rev}$), the work output is W . Heat Q_0 may also be transferred from V directly to the environment at T_0 . From the steady-flow energy equation, one can obtain:

$$[W_{shaft}]_{real} = h_{tot,X} - h_{tot,Y} - Q - Q_0. \quad (2.25)$$

The entropy flux from the control volume associated with the heat transfer is:

$$\int_X^Y \frac{dQ}{T} + \frac{Q_0}{T_0} \quad (2.26)$$

so the entropy increase is given by:

$$s_Y - s_X = \Delta s_{created} - \int_X^Y \frac{dQ}{T} - \frac{Q_0}{T_0}. \quad (2.27)$$

The lost work due to irreversibility within the control volume is

$$\begin{aligned} [W_{shaft}]_{reversible} - [W_{shaft}]_{real} &= (B_X - B_Y) - (h_{tot,X} - h_{tot,Y} - Q - Q_0) \\ &= B_X - B_Y - \int_X^Y \left(\frac{T - T_0}{T} \right) dQ - ((h_{tot,X} - h_{tot,Y}) - Q - Q_0) \\ &= T_0(s_Y - s_X) + T_0 \int_X^Y \frac{dQ}{T} + Q_0 = T_0 \Delta s_{created}. \end{aligned} \quad (2.28)$$

Thus, the work lost due to internal irreversibility within the control volume when heat transfer takes place at T is still $T_0 \Delta s_{irrev}$, as when the heat transfer is limited to transfer with reservoir at T_0 . The actual work output in a real irreversible process between stable states X and Y is therefore

$$\begin{aligned} [W_{shaft}]_{real} &= [W_{shaft}]_{reversible} - \int_X^Y \left(\frac{T - T_0}{T} \right) dQ - T_0 \Delta s_{irrev} \\ &= B_X - B_Y - \int_X^Y \left(\frac{T - T_0}{T} \right) dQ - T_0 \Delta s_{irrev} \\ &= \chi_X - \chi_Y - \chi_{out}^Q - T_0 \Delta s_{irrev} \end{aligned} \quad (2.29)$$

with $\chi_{out}^Q = \int_X^Y (T - T_0)/T dQ$ being the work potential, sometimes called the thermal energy of the heat rejected. In gas turbine processes, the transformation of part of the exhaust thermal energy into useful work can be or not performed, both situations being found in practice. Considering an exhaust nozzle for example, there is no chance to recover additional directly work from a stream that emerges in the atmosphere at a temperature T greater than T_0 ². For a high pressure turbine, the

²In electrical power plant, the heat released at the nozzle can be transferred to the incoming flow by a heat exchanger making possible to partially used the energy available in the exhaust gas

heat transferred at the walls will be transmitted to the environment by conduction and this available heat will be lost. At the outlet of the high pressure turbine however, heat released passing in the low pressure turbine and nozzle will be partially expanded to generate useful work. The thermal energy is also generally important when dealing with the efficiency assessment or work extracted by a component and depends on the perspective taken. From the component perspective, operating in an environment at T_0 and releasing heat at $T > T_0$, the potential work available in the thermal energy between T and T_0 (χ_{out}^Q) will be released in the atmosphere and lost for the turbine if none of the work represented by the hypothetical Carnot cycle is realized. Conversely, considering the turbine component as part of a more complex system including for example additional downstream turbine stages or nozzle, the thermal energy at the outlet of the turbine will be possibly transformed partially or fully in useful work in these components and the thermal energy is here no more a loss for the turbine. An additional implication of thermal energy available is the blade row inefficiencies in multi-stage turbines. The work output of the succeeding blade rows is higher than if the upstream rows were isentropic. Irreversibility in first stages provides additional heat to the flow compared to the isentropic process that can be expanded in downstream stages since still under pressure (this phenomenon is responsible for the higher efficiency obtained from a polytropic analysis of the multi-stage configuration compared to an isentropic one, better known as the reheat effect). The above analysis has been concerned with heat transfer from the control volume to the reservoir. To account for all heat transfers with the reservoir, one has to address the possible heat supplied by the reservoir to the fluid system. Without loss of generality, this heat supplied can correspond to the combustion of fuel in the combustion chamber releasing heat that is here hypothetically supplied by the reservoir to the fluid system. In electrical power plant, the heat available at exhaust of the gas turbine can travel into a heat exchanger to transfer thermal energy to the flow before entering in the burner to increase thermal efficiency (recuperative cycle). Therefore, we consider heat $dQ = dQ_{rev}$ transferred from a reservoir to the control volume. Then that heat could be reversibly pumped to the control volume (at temperature T) from the atmosphere (at temperature T_0) by a reversed Carnot engine. This would require work input:

$$(W_e)_{reversible} = \int_X^Y \left(\frac{T - T_0}{T} \right) dQ. \quad (2.30)$$

Under this new arrangement, eq.(2.24) for the reversible work delivered from V would become

$$W_{rev} = (\chi_X - \chi_Y) + \int_X^Y \left(\frac{T - T_0}{T} \right) dQ_{rev} \quad (2.31)$$

and eq.(2.29) for the work output from the actual process would be

$$W = (\chi_X - \chi_Y) + \chi_{in}^Q - I_{created} \quad (2.32)$$

where $I_{created} = T_0 \Delta s_{created}$ and χ_{in}^Q is the work potential or thermal energy of the heat supplied to the control volume V

$$\chi_{in}^Q = \int_X^Y \left(\frac{T - T_0}{T} \right) dQ. \quad (2.33)$$

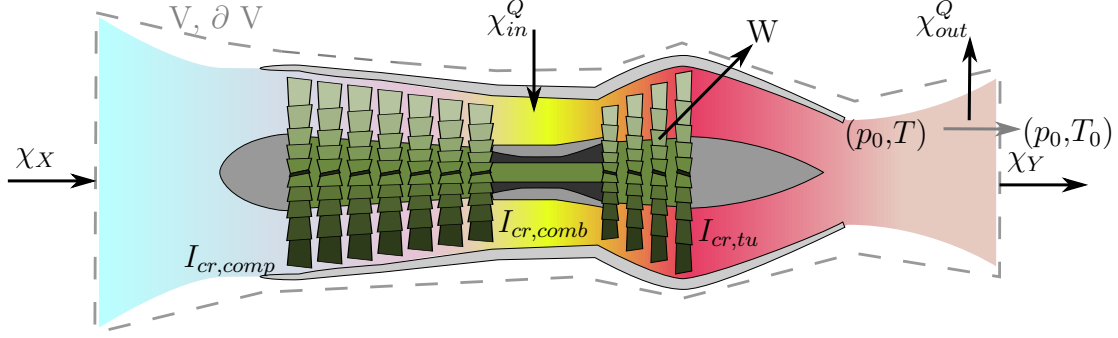


Figure 2.1: Exergy fluxes in a turbomachine

If heat were both transferred to and rejected from control volume V , then a combination of eq.(2.29) and eq.(2.32) would give

$$W = (\chi_X - \chi_Y) + \chi_{in}^Q - \chi_{out}^Q - T_0 \Delta s_{created} \quad (2.34)$$

This last equation can be interpreted in terms of exergy flow χ_X , work output W and work potential by

$$\chi_X = W + (\chi_{out}^Q - \chi_{in}^Q) + T_0 \Delta s_{created} + \chi_Y. \quad (2.35)$$

This equation makes possible to have a sight in the energy transformation processes from the entering flow. The available exergy χ_X can be transformed in:

- the actual work output W ;
- the thermal exergy $(\chi_{out}^Q - \chi_{in}^Q)$ of the heat rejected less the heat supplied;
- the work lost due to internal irreversibility $T_0 \Delta s_{created}$;
- the leaving exergy χ_Y .

A sight of these different contributions for the turbomachine is proposed in Fig. 2.1. Based on the lost work due to irreversibility in the different components $I_{created}$, if the heat transferred from the control volume is not used externally to create work, but is simply lost to the atmosphere in which further entropy is created, then χ_{out}^Q can be said to be equal to I_{out}^Q : the lost work term due to external irreversibility. This is typically what happens when the flow of the turbomachine from an aircraft is released in the atmosphere. The hot gas potential work cannot be recovered. Another form of eq.(2.35) is thus

$$\chi_X + \chi_{in}^Q = W + \sum I_{created} + I_{out}^Q + \chi_Y. \quad (2.36)$$

This steady-flow equation can be used to obtain the difference between the maximum work possible from the fuel and the actual work (or work equivalent) obtained from the turbomachine. This may be done at the scale of the turbomachine or dividing arbitrarily in regions (e.g. components: inlet, compressor, combustion chamber, turbine, nozzle) and summing the contributions making possible to obtain an exergy

statement for the whole turbomachine.

To give the reader an idea of these different contributions, Horlock [50] proposed to look at realistic Joule-Brayton cycle of a turbomachine with main characteristics: pressure ratio 12:1, maximum to inlet temperature ratio 5:1 ($T_{max} = 1450$ K, $T_0 = 290$ K), the compressor and turbine having polytropic efficiencies of 0.9 and the combustion pressure loss being taken as 3% of the inlet pressure to the chamber. The corresponding contributions as a fraction of the fuel exergy (the maximum reversible work) are given in Fig. 2.2. The thermal efficiency indicating the work

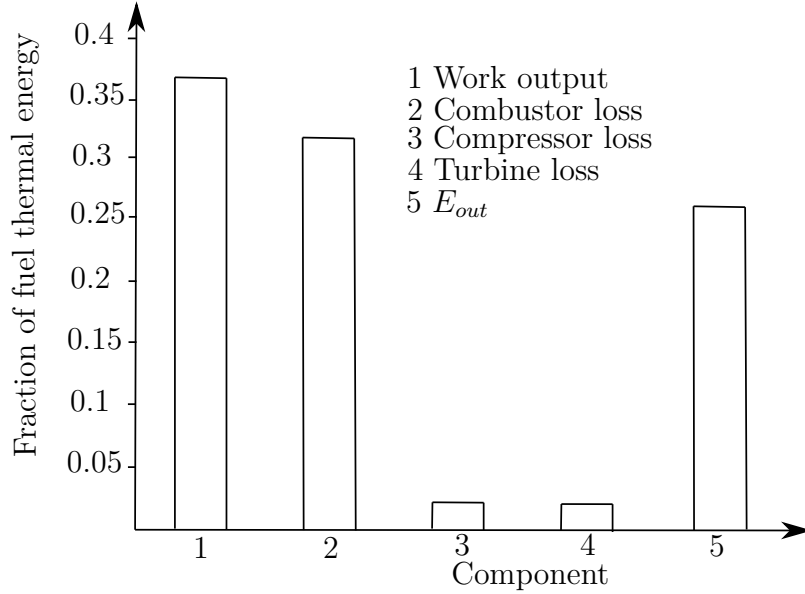


Figure 2.2: Example of work output and exergy losses in a gas turbine as a fraction of the fuel exergy

output (1) is shown to be around thirty five percent. In the combustion chamber contribution (2) has been added the natural limit provided by Carnot stating that between a hot source at T_{max} (in the combustion chamber) and a cold source at T_0 (the atmosphere) only $1 - (T_0/T_{max})$ of thermal energy provided by the combustion process can be converted useful work. For the present case, since $(T_0/T_{max}) = 1/5$, 20% of fuel energy originally available as the heat supplied by the combustion of the fuel is lost and the corresponding remaining energy available to produce work is χ_{in}^Q . The remaining contribution is related to internal irreversibility in the combustion chamber producing entropy. The term (5) corresponds to the energy transferred at the wall of the gas turbine and at the outlet of the gas turbine in terms of thermal energy and available exergy at the outlet of the gas turbine χ_{out}^Q . The thermal energy is associated to the heat transfer of the fluid with the wall of the gas turbine and the exiting flow from the gas turbine that is still hot compared to atmosphere (potential thermal work lost). Compressor and turbine loss (3 and 4) have relatively lower contributions compared to these last two sources of loss and correspond to internal irreversibility in these components. However, since the net power output is the difference between the turbine work and the compressor work that is roughly in the ratio 2:1, a small change in the power output of the turbine (by increasing its efficiency) causes a much larger proportional change in the gas turbine power

output

From this analysis, several observations can be made about exergy. Exergy is a composite quantity between total energy in the flow with total enthalpy (h_{tot}) and the subtracted entropy term (T_0s). Thus, exergy provides the available energy in the purpose to generate work. Conversely to energy, exergy is always destroyed during conversions because of the irreversible nature of energy conversion process. It depends on properties of both a matter or energy flow and the environment since the available work of the environment B_0 has been subtracted ($\chi=B-B_0$). The atmosphere contains a tremendous amount of energy but because the atmosphere is in a dead state, the energy contained has no work potential. The greater the difference between the temperature T of a given state and the temperature T_0 of the environment, the greater the value of for exergy.

2.1.3 Balance equations for exergy and useful work

Last subsection showed that performing balance of exergy at the inlet and outlet of the considered domain or component and linking the different domains/components together, it was possible to draw an exergy balance for the gas turbine that explicitly makes reference to the heat supplied to the gas turbine due to the burnt fuel Q_b (or the exergy available to generate work from this heat released χ_{in}^Q), the extracted work W and so to the efficiency of the gas turbine as the ratio of these two quantities. It remains that the flux balance of total enthalpy and entropy at inlet and outlet of the considered domain/component obtained from the thermodynamic definition of total enthalpy and entropy (eq.(2.11) and eq.(2.14)) providing the exergy balance for the component is not a local measure as it would be expected for example as proposed earlier to measure the loss of the local vortex shedding process downstream of a blade trailing edge. To alleviate this current issue, the purpose is to derive transport equations for total enthalpy, entropy and as a composite quantity of these two for exergy in order to obtain a local balance (for numerical simulation for example, it means that one could draw balance of exergy at the scale of the grid point). In the following is proposed a transport equation for exergy and an analysis of the different contributions over control volumes. The details of the derivation of the different equations is given in App. C and only final expressions are given in this chapter. As stated in eq.(2.20), the exergy is defined relatively to the dead-state environment denoted 0 by

$$\chi = B - B_0 = (h_{tot} - h_0) - T_0(s - s_0). \quad (2.37)$$

2.1.3.1 Transport equation for total enthalpy

Total enthalpy is obtained relatively to total energy according to eq.(2.8) by

$$h_{tot} = E_{tot} + p/\rho. \quad (2.38)$$

From the energy balance of the Navier-Stokes equations, one can derive a transport equation for total enthalpy by:

$$\frac{\partial(\rho h_{tot})}{\partial t} + \frac{\partial(\rho h_{tot} u_j)}{\partial x_j} = \frac{\partial}{\partial x_j}(\tau_{ij} u_j - q_j) + \frac{\partial p}{\partial t} \quad (2.39)$$

2.1.3.2 Entropy transport equation from energy conservation equations

Previous subsection provided a measure of entropy based on thermodynamic quantities. Entropy, through the second law of thermodynamics, was shown to measure irreversibility as transfers between different energy nature (kinetic, thermal) that cannot be recovered and used to produce work for the gas turbine. The idea is to look at balance equation of these different energy contributions to draw a balance equation for entropy. As mentioned, only the final expressions for balance equations are given in the section but the derivation of these different equations is proposed in App. C. The total energy transport equation corresponding to the energy conservation of the Navier-Stokes set of equation eq.(A.8c) introduced in Sec. A.1.2 is written as:

$$\frac{\partial(\rho E_{tot})}{\partial t} + \frac{\partial}{\partial x_j}(\rho E_{tot} u_j + p u_j - \tau_{ij} u_j + q_j) = \rho F_j u_j + \dot{Q}. \quad (2.40)$$

Transport equation for kinetic energy E_k can be derived by multiplying momentum equation eq.(A.8b) introduced in same section with u_i :

$$\frac{\partial(\rho E_k)}{\partial t} + \frac{\partial}{\partial x_j}(\rho u_j E_k + p u_j - u_i \tau_{ij}) = \rho u_j F_j + p \frac{\partial u_j}{\partial x_j} - \tau_{ij} \frac{\partial u_i}{\partial x_j}. \quad (2.41)$$

Subtracting kinetic energy equation to total energy equation gives transport equation for internal energy:

$$\frac{\partial(\rho e)}{\partial t} + \frac{\partial}{\partial x_j}(\rho u_j e + q_j) = \dot{Q} - p \frac{\partial u_j}{\partial x_j} + \tau_{ij} \frac{\partial u_i}{\partial x_j}. \quad (2.42)$$

The last two equations makes possible to draw the energy transfers between internal and kinetic energy of the fluid. It is to be noticed that the last two equations for internal and kinetic energy have been written in a particular manner to make correspond right-hand side of these two equations. However additional terms transferred left-hand side can be found. Internal (or thermal) energy equation right-hand term provides two terms with a sink term related to pressure work that can be transferred to kinetic energy. For example, when a fluid system is heated by a combustion process, the internal energy of the fluid is increased. The expansion process in the turbine lead to transfer toward kinetic energy by pressure work that is a useful work for the turbine. The second term is a source term for internal energy and is related to the transfer of kinetic energy to internal energy due to velocity gradients and viscosity of the fluid. The velocity gradients locally increase internal energy of the flow. Based on thermodynamic relation introduced in last subsection and equation energy conservation, the purpose is to derive a transport equation for entropy. The

enthalpy form of the Gibbs equality given in eq.(2.11) yields to $d(\rho h) = Td(\rho s) + dp$ that holds for all small changes. This equality can be used to express the entropy changes $(d(\rho s)/dt)$ experienced by a fluid particle

$$T \frac{d(\rho s)}{dt} = \frac{d(\rho h)}{dt} - \frac{dp}{dt}. \quad (2.43)$$

From the energy balance of the Navier-Stokes equations, one can derive a transport equation for total enthalpy by:

$$\begin{aligned} \frac{\partial(\rho h_{tot})}{\partial t} + \frac{\partial(\rho h_{tot})}{\partial x_j} &= \frac{\partial(\rho E_{tot})}{\partial t} + \frac{\partial(\rho E_{tot})}{\partial x_j} + \frac{\partial p}{\partial t} + \frac{\partial(\rho u_j)}{\partial x_j} \\ &= \frac{\partial}{\partial x_j}(\tau_{ij} u_j - q_j) + \frac{\partial p}{\partial t} + \dot{Q}. \end{aligned} \quad (2.44)$$

Substituting the expression of enthalpy in eq.(2.43) leads to

$$T \frac{d(\rho s)}{dt} = \tau_{ij} \frac{\partial u_i}{\partial x_j} - \frac{\partial q_i}{\partial x_i} + \dot{Q}. \quad (2.45)$$

Under the assumption that the fluid follows the Fourier's law ($q_i = -k(\partial T/\partial x_i)$ for heat transfer), one can obtain

$$\frac{d(\rho s)}{dt} = \frac{1}{T} \tau_{ij} \frac{\partial u_i}{\partial x_j} - \frac{1}{T} \frac{\partial}{\partial x_i} \left(-k \frac{\partial T}{\partial x_i} \right). \quad (2.46)$$

Integrating throughout a control volume $V_{sys}(t)$ enclosed in the surface $\partial V_{sys}(t) = A_{sys}(t)$ moving with the fluid and integrating by part the term related to temperature gradient leads to:

$$\int_V \frac{d(\rho s)}{dt} = \int_V \frac{1}{T} \tau_{ij} \frac{\partial u_i}{\partial x_j} + \int_V \frac{k}{T^2} \left(\frac{\partial T}{\partial x_i} \right)^2 + \int_V \frac{\dot{Q}}{T} + \int_A \frac{k}{T} \frac{\partial T}{\partial x_i} n_i dA. \quad (2.47)$$

Writing back the Fourier's law for last right-hand term ($q_i = -k(\partial T/\partial x_i)$), the transport equation for entropy can be finally written in differential form as

$$\underbrace{\frac{\partial(\rho s)}{\partial t}}_{(1)} + \underbrace{\frac{\partial(\rho s u_i)}{\partial x_i}}_{(2)} + \underbrace{\frac{\partial(q_i/T)}{\partial x_i}}_{(3)} = \underbrace{\frac{1}{T} \tau_{ij} \frac{\partial u_i}{\partial x_j}}_{(4)} + \underbrace{\frac{\lambda}{T^2} \left(\frac{\partial T}{\partial x_i} \right)^2}_{(5)} + \underbrace{\frac{\dot{Q}}{T}}_{(6)} \quad (2.48)$$

with:

- (1) temporal variation of entropy;
- (2) convective term of entropy;
- (3) entropy due to thermal transfer in and out of the volume and can be positive or negative. The entropy of a fluid particle can thus decrease only if there is heat conducted out of the particle, the entropy being transferred to the surrounding. The

second law of thermodynamics however still holds since entropy for the considered volume and surrounding is zero or increases;

(4) the local entropy generation due to viscous dissipation that means the degradation of mechanical energy into internal energy due to shear process;

(5) entropy generation due to heat transfer across temperature differences in the fluid;

(6) entropy generation due to heat source in the volume.

It can be noticed that pressure forces have no effect on entropy generation meaning that the transfer of internal energy to kinetic energy through pressure work does not induce entropy creation. Conversely, the transfer of kinetic energy to internal energy through the viscous term induces entropy creation. Body forces have no influence on entropy production. This last equation shows that all entropy variation cannot be associated to irreversibility in the domain. Indeed, terms (3) and (6) are related to heat transfers or production, meaning that these processes can occur while not inducing any loss generation for the flow system of interest. On the contrary, terms (4) and (5) induce entropy production under irreversible process leading to loss generation. Based on transport equation for total enthalpy eq.(2.44) and entropy eq.(2.48), one can write a transport equation for exergy:

$$\frac{\partial(\rho\chi)}{\partial t} + \frac{\partial(\rho\chi u_j)}{\partial x_j} = \frac{\partial}{\partial x_j}(\tau_{ij}u_j - (1 - \frac{T_0}{T})q_j) - \frac{T_0}{T}\tau_{ij}\frac{\partial u_i}{\partial x_j} - \frac{\lambda T_0}{T^2}\left(\frac{\partial T}{\partial x_i}\right)^2 + \frac{\partial p}{\partial t} \quad (2.49)$$

This equation can be integrated over a control volume V (the detail of the integration of the different terms is given in Sec. B.2.2.3 of App. B), and yields to

$$\frac{d}{dt} \iiint (\rho\chi) dV + \oint (\rho\chi) u_j n_j dA_{IO} = P_{shaft} + \chi_q + \Phi_{\nabla u} + \Phi_{\nabla T} + \frac{d}{dt} \iiint p dV \quad (2.50)$$

with

- $P_{shaft} = -\oint ((p - p_0)u_{w,j}n_j - (\tau_{ij}u_{w,j})n_j) dA_{MW}$. This is the integrand of force with velocity on all moving subsurfaces and hence the net total shaft power due to either pressure or shear forces. This term will be positive for a compressor and negative for a turbine;
- $\chi_q = \iiint \partial/\partial x_j (1 - (T_0/T))q_j dV$. This is the rate of transfer of mechanical work potential. It is associated with the heat transfer across the surface of the control volume. For a fixed dead state pressure p_0 , its value depends on the pressure p at the location at which the heat is added;
- $\Phi_{\nabla u} = -\iiint (T_0/T)\tau_{ij}(\partial u_i/\partial x_j) dV$ that is the rate at which the kinetic energy of the flow is converted into internal energy inside the control volume. The dissipation mechanism involves viscous stresses working against fluid deformation;
- $\Phi_{\nabla T} = -\iiint \lambda(T_0/T^2)(\partial T/\partial x_i)^2 dV$ is the rate of energy generation by thermal mixing which reduces any differences in temperature in the flow field.

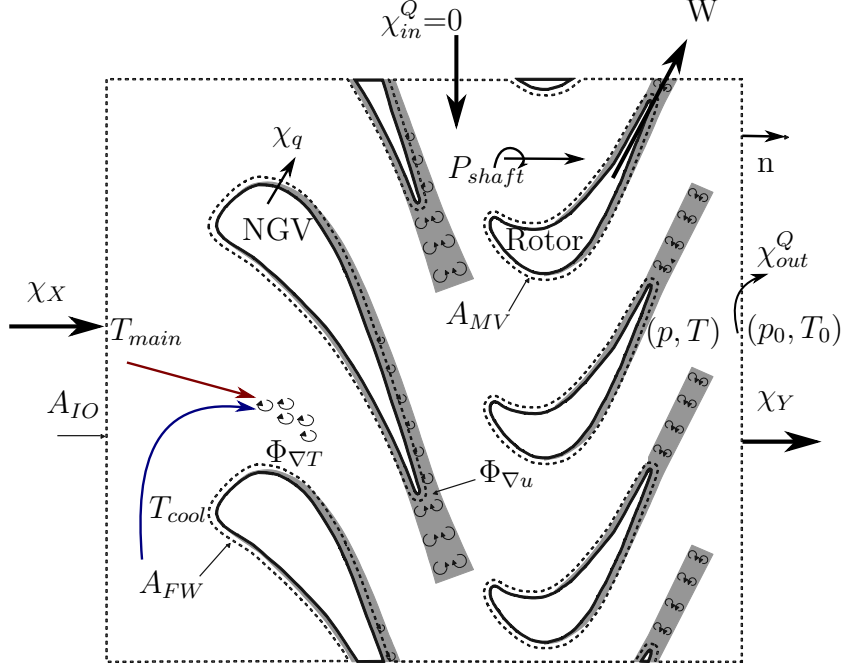


Figure 2.3: Control volume located around a turbine stage. Example of viscous and thermal irreversibility creation from exergy approach. Adapted from Miller [51]

The last two terms are responsible for the degradation of energy. This equation is also suitable for shock waves handling. Indeed, a shock wave is a thin layer over which the quantities vary deeply but continuously. The associated loss generated corresponds to velocity and temperature gradients contained in the terms $\Phi_{\nabla u}$ and $\Phi_{\nabla T}$. In the framework of numerical simulations, when one wants to properly evaluate the loss related to the shock based on viscous and thermal dissipation, the shock thickness must be discretized by several grid points that is generally impracticable in real configurations since shock thickness is in the order of the mean free path ($\simeq 6 \times 10^{-8}$ m for air at ambient conditions). To deal with this issue, a jump condition for entropy is generally applied, leading to

$$\dot{\Phi}_{s.w} = -T_0 \oint_{A_w} [\rho \delta s (v_j - u_j)] \cdot n_j dA_{s.w}. \quad (2.51)$$

at the location of the shock wave. The location of the shock wave can be obtained by a shock sensor for example. More details are given in App. B Sec. B.2.2.3. Figure 2.4 provides a sketch with these different contributions in the case of a turbine. Exergy balance provides a general framework for accounting the potential work that can be transferred between the fluid and its environment as well as the different contributions. When looking at the different contributions of exergy balance for a turbine, $\Phi_{\nabla u}$ is associated to local velocity gradients and viscosity of the fluid that depends on local temperature. Velocity gradients come from several contributions: the formation of a boundary layer over wetted surfaces (hub, shroud, blades) that induces velocity gradients from the wall where velocity is zero to free stream velocity; acceleration and deceleration processes induced by the blade; shear layer downstream of the blade trailing edge or at the rim seal interface; secondary

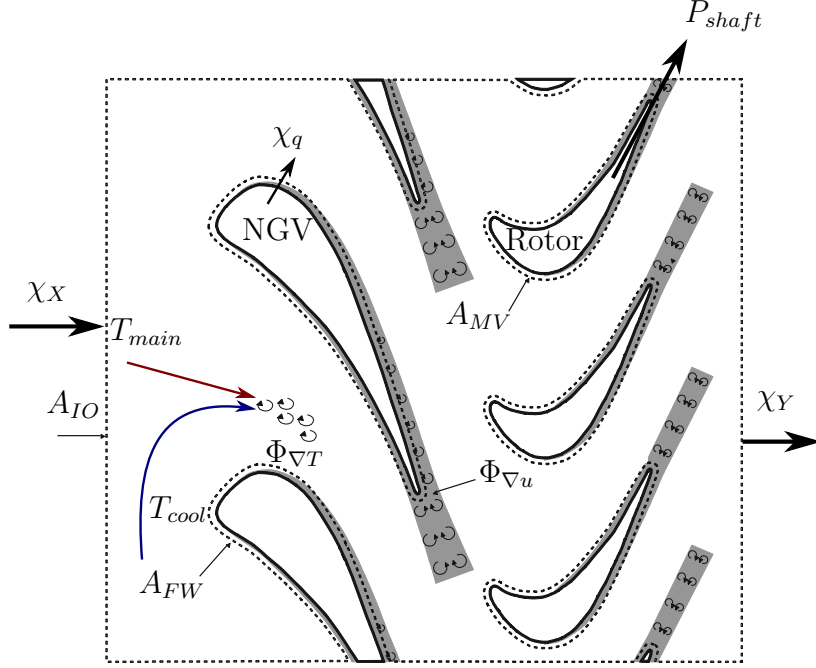


Figure 2.4: Control volume located around a turbine stage. Example of viscous and thermal irreversibility creation from exergy approach. Adapted from Miller [51]

vortices with velocity gradients from the center of rotation to outer radius of the structure. These contributions will be more detailed in Sec. 2.2 about the losses in a turbine. In addition, turbulence transports kinetic energy from large scales to small scale flow structures where energy is dissipated in thermal energy. More details about this contribution are given in Sec. 2.1.4. This expression also shows that the loss associated with viscous dissipation is lower when the temperature at which it occurs is higher. A given velocity distribution and related velocity gradients at high temperature is less crucial than at lower temperature (incurs less loss). The heat transfer with borders is generally performed partially with the walls of the gas turbine (hub, shroud and blade) that are generally at lower temperature than the mainstream flow and that can be increased by cooling. This means that some heat flux through the term χ_q is taken by the walls to the flow. This induces a decrease of the thermal energy of the flow and so less thermal energy will be transferred to the useful kinetic energy. This is typically what happens when the flow transfers locally heat with a system at temperature T (the system being the wall). Mainly by conduction processes, the heat is evacuated by the wall to the nacelle of the gas turbine in contact with the ambient environment (reservoir at T_0). Since no Carnot engine can be used, this thermal energy is lost. In gas turbine, the heat transfer is generally low compared to work transfers but this statement can become wrong especially in low-diameter gas turbine where surface exchange with walls are important in magnitude compared to the potential work to be extracted. At the scale of the turbine component as proposed in Fig. 2.4, the heat transfer is not only performed with the wall but with downstream components at the outlet of the domain. In this case, the heat work available between T (temperature of the outlet border) and T_0 the ambient one depends on the perspective adopted.

- If we consider the turbine as part of the gas turbine with downstream other turbine stages or a nozzle, the heat available at temperature T and flow at pressure $p > p_0$ will be possibly transformed into useful work in the downstream components since expansion is still possible. In this case, the potential work between T and T_0 is not a loss for the turbine.
- When considering the turbine as an isolated component transferring heat with outlet at T and all this potential heat transferred to the ambient at T_0 , the potential work between T and T_0 will be here a loss for the turbine.

The third term that needs to be further detailed is the one related to temperature gradients $\Phi_{\nabla T}$. In a gas turbine, the heat transfer at the wall introduced previously can promote temperature gradients from the wall to the free stream. The purge flow supplied to the blade, hub or cavities is generally provided at a lower temperature compared to the mainstream one. In the case of high pressure turbine, hot streaks can be produced by the combustion chamber. Also, compressibility effect at relatively high Mach number can induce temperature gradients in the flow field. The thermal gradients induce entropy rise through the thermal dissipation term $\Phi_{\nabla T}$. The terms $\Phi_{\nabla u}$ and $\Phi_{\nabla T}$ correspond to contributions contained in entropy transport equation and are useless in the perspective of producing work. The terminology used in the literature for these two terms is the viscous and thermal anergy (exergy being associated to a useful contribution while anergy being useless in a work extracting perspective). In other words, when the exergy decreases of some amount, the anergy increases of this same amount. Since the exergy balance eq.(2.50) is homogeneous with a power balance, it may be more rigorous to call $\Phi_{\nabla u}$ and $\Phi_{\nabla T}$ as anergy production rates that are proportional to the velocity and temperature fields disuniformities. But, over a same period of time in steady conditions, this equation simply states that the variation of exergy between inlet and outlet of the domain corresponds to thermal heat transfer in the domain, energy transferred with the shaft, and irreversible anergy produced due to thermal and velocity gradients. In the following, viscous/thermal entropy or anergy will be used indifferently but one has to remind that these two quantities are equal when viscous or thermal entropy is multiplied by the reference temperature of the environment leading to a quantity homogeneous with an energy: the anergy. The effect of heat transfer at the wall compared to adiabatic one was assessed by Shyang Maw Lim et al. [52] that studied the turbine of a turbocharger. An exergy balance showed that heat transfer, thermal irreversibility were increased and potential work extracted decreased when the temperature of the wall was colder. The entropy production due to thermal gradients can be important especially in components with high temperature gradients. For example, by considering the Bejan number [53] that compares entropy production related to temperature and velocity gradients: $Be = (\Phi_{\nabla T})/(\Phi_{\nabla u} + \Phi_{\nabla T})$, this quantity can be up to 0.4 in a high pressure turbine. The entropy production and potential loss of extractable work can be reasonably understood for velocity gradients contribution where higher quality energy (mechanical energy) is transformed into lower quality energy (thermal energy) from an extracting work perspective. For the contribution related to temperature gradients, entropy is clearly generated from this quantity but this is more difficult to ascertain the impact on work extracted by

the shaft since already a thermal form of energy. Shyang Maw Lim et al. [52] showed that when the cooling was increased in the turbocharger, heat flux and thermal entropy were increased but with small impact on work extracted on the shaft. Some information on this observation are provided by Miller [51]. The author studied analytically (based on thermodynamic consideration) an isentropic turbine operating between the particular fluid state and a fixed dead state static pressure p_0 . This means that the author is in the perspective of considering the turbine as an isolated system transferring heat with surrounding at pressure and temperature (p_0, T_0) . From this perspective, as stated earlier, the exit temperature of the turbine may be above the dead state temperature. It follows that extra useful work could still be theoretically extracted from exhaust by a Carnot engine exhausting to dead state temperature and recovering exergy. However, a turbine can only extract work by pressure or shear forces acting on moving surfaces and so a turbomachinery designer has no access to this component (see Fig. 2.5a). This approach can be considered as a so-called "figure of merit". A figure of merit consists in factoring out one or several contributions to exergy balance when considering that this quantity will not be recovered or recovered by another system³. The associated work that could be extracted by an isentropic turbine operating between the particular fluid state (p, T) and fixed dead state temperature is the "flow mechanical work potential" denoted in this study Ξ . A transport equation can be derived for flow mechanical work po-

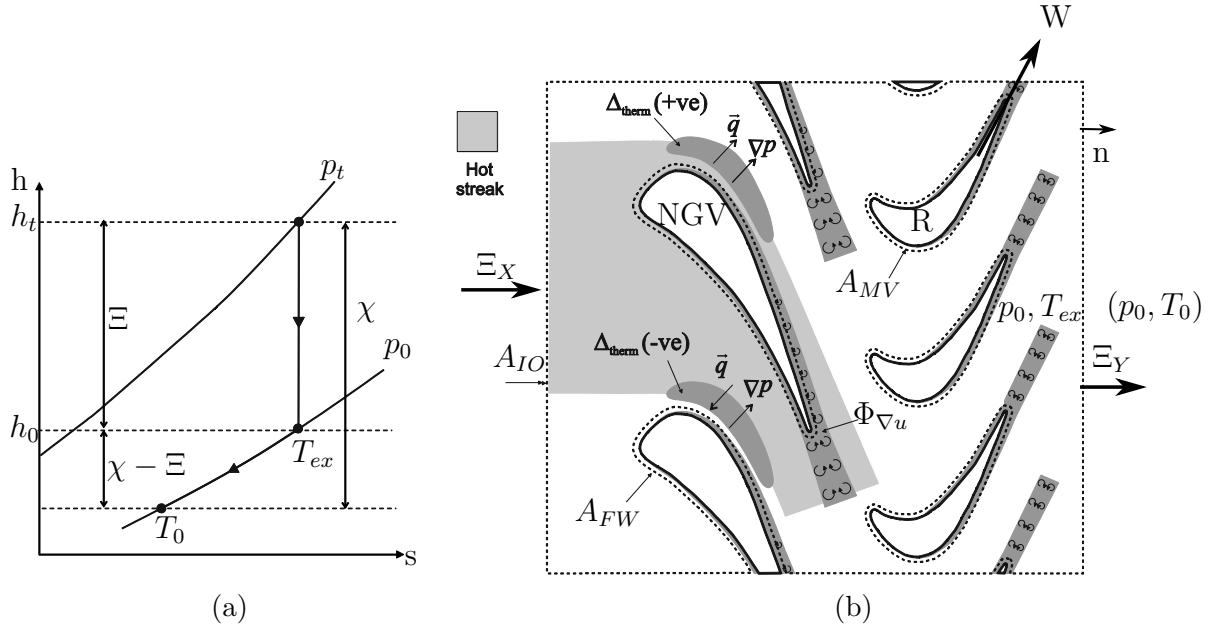


Figure 2.5: The split of exergy χ in the flow mechanical work potential Ξ and flow thermal work potential, marked on a h - s diagram (a) and a control volume located around a turbine stage exhibiting the thermal creation from the flow mechanical work potential approach (b). Adapted from Miller [51]

³It has been found that application of this approach to jet propulsion devices concludes that the largest exergy losses are due to non-equilibrium combustion, exhaust heat and kinetic energy. However, it appears that optimization of a thrust-producing device to promote maximum exergy output may lead to less-than-optimal result if the objective is to produce thrust for propulsion (decrease of thermal efficiency to the benefit of propulsive efficiency).

tential Ξ similarly to exergy equation. The details of the derivation are proposed in Sec. B.2.2.4. The reference temperature is no more the dead state temperature T_0 but the isentropic exhaust temperature T_{ex} :

$$T_{ex} = T \left(\frac{p_0}{p} \right)^{\frac{\gamma-1}{\gamma}} \quad (2.52)$$

$$\iiint \frac{\partial(\rho\Xi)}{\partial t} dV + \oint (\rho\Xi) u_j n_j dA_{IO} = P_{shaft} + \chi_{q,T_{ex}} + \Phi_{\nabla u} + \Psi_{therm} + \Psi_{reheat} + \Psi_{recool} \quad (2.53)$$

In this equation the net rate of work input P_{shaft} and rate of viscous dissipation $\Phi_{\nabla u}$ are the same as for exergy. The net rate of transfer of mechanical work by heat to the control volume surface $\chi_{q,T_{ex}}$ is the same as for exergy except that the temperature is at T_{ex} , temperature at the end of isentropic expansion process. This equality shows that entropy creation by thermal mixing (temperature gradients) has no effect on turbine work but new thermal creation terms appear. The new terms involved are:

- $\Psi_{therm} = \iiint (\gamma - 1/\gamma)(1/p)(\partial p/\partial x_j) q_j dV$ is the rate of thermal creation. This is the rate at which mechanical power potential is created by internal heat transfer across a finite pressure gradient within the fluid. The term is positive if heat flows across a positive pressure gradient, and negative if it flows across a negative pressure gradient;
- $\Psi_{reheat} = \iiint (1 - (T_{ex}/T)) \tau_{ij} (\partial u_i/\partial x_j) dV$ is the viscous reheat. This is the "reheat effect" which causes the polytropic efficiency of a machine to be different from the isentropic efficiency. The effect results from dissipation of kinetic energy raising the internal energy locally with the fluid. The effect is known as the "reheat effect" as it is identical to a heat being added locally in the flow. If this "reheat" occurs at a pressure above the ambient one, then mechanical work potential is created locally in the flow. This is the reason why dissipation of the same amount of kinetic energy in a high pressure turbine, or compressor, stage has a less deleterious effect on isentropic efficiency than if it had occurred in a low pressure stage;
- $\Psi_{recool} = \iiint (1 - (T_{ex}/T)) (\gamma - 1/\gamma)(1/p)(\partial p/\partial x_j) q_j dV$ ⁴ is the thermal recool. This is similar to the viscous reheat term, but it is instead caused by the thermal creation term. When this term is positive it reduces the internal energy locally within the fluid. The effect is known as the "recool effect" as it is identical to a heat being extracted locally within the flow. If the pressure at the location at which it occurs is above the ambient then the local mechanical work potential of the flow is reduced. Once again this is similar to a reversible Carnot engine extracting heat locally from the flow. It can be noticed that this term can also be negative and in this case the thermal recool term changes sign.

⁴At a one-dimensional level these last two terms could be explained following Rayleigh theory

This last equation provides two main important features. The anergy produced by velocity gradients and subsequent mixing (transformation of kinetic into thermal energy) can be residually recovered (as a second order term) since increasing locally temperature of the flow (if still under pressure) and some expansion can be used to generate work. This equation shows that a second heat transfer term, "thermal creation" does modify the mechanical work potential of the flow. This term is shown to occur in regions of the turbine where heat transfer occurs across a finite pressure difference. Miller [51] conducted numerical simulations on bent pipe and high pressure turbine blade. Applying this approach the author was able to show that convective cooling can raise efficiency by around 0.5% and therefore should be considered as part of the design process. Also, thermal mixing in the free stream has a negligible effect on efficiency and thus can be ignored in the design process. This approach proposed by Miller further explains why Zlatinov [54] only studied velocity gradient term for entropy production in the perspective to study the performance of a high pressure turbine.

The following subsection will be devoted to the application of this approach and equations to numerical simulation in order to track losses in the simulation domain. As it was suggested, irreversibility appearing in exergy balance equation emanates from viscous and thermal non-uniformity that are held by the entropy transport equation and also referred as anergy terms when entropy term is multiplied by the reference temperature. Therefore, this analysis will be led using the transport equation for entropy since volume viscous dissipation and thermal dissipation appear in this equation. Furthermore, this equation has received further developments from a numerical point of view making possible to more properly be used numerically. It is to be noted once again that the account of the thermal heat transfer χ_q depends on the perspective taken and the possibility to transform the thermal work in useful work. For the thermal mixing term $\Phi_{\nabla T}$, it depends on considering the general exergy equation or a figure of merit like the useful work for a turbine. In the general framework that will be used, these different contributions will be taken into account.

2.1.4 The application of exergy to numerical simulation

When using entropy to track loss generation, mainly two approaches have been developed. A first approach where the different terms of entropy transport equation are evaluated from temperature and velocity gradients of the flow field and referred as direct method. A second method in which the entropy transport equation is integrated over small control volumes. This second approach known as indirect method is obtained, under some assumptions that will be discussed, with classical expression for entropy based on two independent thermodynamic quantities as proposed in eq.(2.14).

2.1.4.1 Direct method and the account of turbulence

In the direct method, the entropy production terms on the right-hand side of eq.(2.48) are to be calculated based on numerical simulation performed. In laminar flow, shear work due to velocity or temperature gradients results directly in

entropy production, there is no intermediate. In turbulent flow, however, the transfer of mechanical energy to turbulent kinetic energy stores energy in one position, while its conversion into heat may happen downstream due to the convection of turbulent kinetic energy. This process has mainly two consequences. In turbulent flow, shear work at one point in the flow can result in entropy production downstream losing locality of entropy production as in laminar flow. Also, part of the shear work is hold by turbulent contribution. In other word, part of viscous and thermal entropy production are due to turbulent fluctuations. As suggested in App.A about the numerical methods to deal with turbulent flows, turbomachinery flows are at sufficiently high Reynolds number so that the flow would face predominant effects of turbulence.

When dealing with turbulent flows, different approaches can be applied from fully resolved simulation containing all the turbulent spectrum (DNS) to partially or fully modeled turbulence (LES and RANS) (see Sec. A.2). For DNS, terms (4) and (5) of eq.(2.48) related to viscous and thermal dissipation can be evaluated since turbulent contribution is contained in the output of the simulation. For (U)RANS approach, the output of the simulation contains only the mean contribution and additional treatment must generally be performed to recover the turbulent contribution. For LES, the situation is in-between. Part of the turbulent cascade is solved meaning that the direct output of the simulation contains the mean flow contribution and part of the turbulent one. Some part of turbulence contribution is modeled (small eddies) and similarly to RANS additional processing must be performed to recover this contribution to entropy production.

2.1.4.1.1 (U)RANS approach The case of RANS modeling is first studied by applying Reynolds averaging to the entropy transport equation (2.48) which lead to the equation known as Reynolds averaged Clausius-Duhem equality [55]. The resulting equation can be shown to be:

$$\begin{aligned}
\underbrace{\frac{\partial}{\partial t} (\bar{\rho s})}_{(1)} + \underbrace{\frac{\partial}{\partial x_i} (\bar{\rho u_i s})}_{(2)} + \underbrace{\frac{\partial}{\partial x_i} (\bar{\rho u'_i s'})}_{(3)} + \underbrace{\frac{\partial}{\partial x_i} \left(\bar{\frac{q}{T}} \right)}_{(4)} = \underbrace{\bar{\tau}_{ij} \frac{1}{\bar{T}} \frac{\partial \bar{u}_i}{\partial x_j}}_{(5)} + \underbrace{\overline{\tau'_{ij} \frac{1}{T} \frac{\partial u'_i}{\partial x_j}}}_{(6)} \\
+ \frac{\lambda}{\bar{T}^2} \left[\underbrace{\left(\frac{\partial \bar{T}}{\partial x_j} \right)^2}_{(7)} + \underbrace{\overline{\left(\frac{\partial T'}{\partial x_j} \right)^2}}_{(8)} \right]
\end{aligned} \tag{2.54}$$

where is reminded that $\bar{\cdot}$ and \cdot' correspond to the Reynolds mean quantities and fluctuations with:

- (1) temporal variation of mean entropy;
- (2) convective term of mean entropy;
- (3) convective term of fluctuating entropy;
- (4) turbulent flux of viscous entropy (correlation of entropy/velocity fluctuation);
- (5) entropy production by direct dissipation;

- (6) entropy production by turbulent dissipation;
- (7) entropy production by heat transfer with mean temperatures;
- (8) entropy production by heat transfer with fluctuating temperatures.

Terms (5) and (7) can be directly computed since they are only composed by mean quantities as direct output of the (U)RANS simulation. If only the mean (resolved) part of the flow field is used to evaluate right-hand side terms of the equation, entropy production could be underestimated. The discrepancy can be important as stated by Wheeler et al. [56] which performed DNS and RANS simulations of a high pressure turbine blade and splitted entropy source term in mean and fluctuating parts. Over the whole domain, entropy production due to fluctuations was shown to contribute to 40% of entropy production even if the boundary layer around the blade was laminar for most part of the blade. The account of modeled fluctuations in RANS formalism is therefore important to accurately estimate entropy production. Several approaches have been developed to evaluate terms (6) and (8) of Reynolds averaged transport entropy equation eq.(2.54). with for example the separate time averaging approach. A detailed description of the method can be found in Adeyinka and Naterer [57]. However, these methods introduced complexity and additional terms that cannot generally be obtained readily from the numerical simulation. This observation has pushed the way towards simplified models based on classical RANS closure approaches and linear eddy viscosity model that assumes a Boussinesq relationship between turbulent stresses and the mean strain rate through an isotropic eddy viscosity. The purpose is to obtain an expression for terms (6) and (8) of eq.(2.54) in terms of mean quantities and equivalent turbulent viscosity μ_{turb} . The viscous stress tensor can be expanded as:

$$\tau_{ij} = \mu \left(\frac{du_i}{dx_j} + \frac{du_j}{dx_i} \right) - \mu' \frac{du_i}{dx_i}. \quad (2.55)$$

The second term on the right-hand side represents the viscous stress associated with the bulk viscosity μ' and this term is usually negligible in turbomachinery flows except in presence of large density gradients (for example locally within shock waves) that may give large velocity divergence and since a normal stress may be considered as a pressure. For the purpose, terms (5) and (6) of eq.(2.54) can be then expressed as:

$$\overline{\tau_{ij} \frac{d\bar{u}_i}{dx_j}} = \mu \left(\frac{d\bar{u}_i}{dx_j} + \frac{d\bar{u}_j}{dx_i} \right) \frac{d\bar{u}_i}{dx_j} \quad (2.56)$$

$$\overline{\tau'_{ij} \frac{\partial u'_i}{\partial x_j}} = \mu \left(\frac{du'_i}{dx_j} + \frac{du'_j}{dx_i} \right) \frac{du'_i}{dx_j}. \quad (2.57)$$

Based on the transport equation for turbulent kinetic energy $k = 1/2 \overline{(u'_i)^2}$:

$$\begin{aligned}
\underbrace{\frac{\partial k}{\partial t}}_{\text{Local derivative}} + \underbrace{\bar{u}_j \frac{\partial k}{\partial x_j}}_{\text{Advection}} = & - \underbrace{\frac{1}{\rho_o} \frac{\partial \overline{u'_i p'}}{\partial x_i}}_{\text{Pressure diffusion}} - \underbrace{\frac{1}{2} \frac{\partial \overline{u'_j u'_j u'_i}}{\partial x_i}}_{\text{Turbulent transport}} + \underbrace{\nu \frac{\partial^2 k}{\partial x_j^2}}_{\text{Molecular transport}} \\
& - \underbrace{\overline{u'_i u'_j} \frac{\partial \bar{u}_i}{\partial x_j}}_{\text{Production}} - \underbrace{\nu \frac{\partial \bar{u}'_i}{\partial x_j} \frac{\partial \bar{u}'_i}{\partial x_j}}_{\text{Dissipation } \varepsilon} - \underbrace{\frac{g}{\rho_o} \overline{\rho' u'_i} \delta_{i3}}_{\text{Buoyancy flux}}
\end{aligned} \tag{2.58}$$

it can be noticed that dissipation ε appears in eq.(2.57) meaning that one can write:

$$\begin{aligned}
\overline{\tau'_{ij} \frac{\partial u'_i}{\partial x_j}} &= \frac{\mu}{\nu} \nu \frac{\partial \bar{u}'_i}{\partial x_j} \frac{\partial \bar{u}'_i}{\partial x_j} \\
&= \rho \varepsilon.
\end{aligned} \tag{2.59}$$

This kind of approach has been applied by several authors with among them Kramer-Bevan [58] and Kock and Herwig [59] onto a fully developed laminar and turbulent heated pipe. In the turbulent case, due to steep gradients of \bar{T} close to the wall, entropy production was shown to be accumulated in this part of the flow field. This was due to insufficiently resolved meshes close to the wall and enforced the use of analytical expression for entropy production terms in the immediate vicinity of the wall. Alternatively, the assumption can be made that the rate of production of turbulence kinetic energy equals the rate of its dissipation to produce entropy. This leads to a new expression for eq.(2.57):

$$\overline{\tau'_{ij} \frac{\partial u'_i}{\partial x_j}} = \rho \overline{u'_i u'_j} \frac{\partial \bar{u}_i}{\partial x_j}. \tag{2.60}$$

A classical practice in RANS averaging is to write the Reynolds stress tensor $\rho u'_i u'_j$ as:

$$\overline{\rho u'_i u'_j} = -\mu_t \left(\frac{\partial \bar{u}_i}{\partial x_j} + \frac{\partial \bar{u}_j}{\partial x_i} \right) + \frac{2}{3} \left[\mu_t (\nabla \cdot \bar{u}) + \frac{\rho k^2}{2} \right] \delta_{ij} \tag{2.61}$$

by making the assumption that the turbulence field driving normal stresses (that can be seen as an addition to static pressure) and that gradients of density in the flow direction are negligible (the second term on the right-hand side is neglected). Under this assumption, eq.(2.57) can be written as:

$$\overline{\tau'_{ij} \frac{\partial u'_i}{\partial x_j}} = \mu_{turb} \left(\frac{\partial \bar{u}_i}{\partial x_j} + \frac{\partial \bar{u}_j}{\partial x_i} \right) \frac{\partial \bar{u}_i}{\partial x_j} \tag{2.62}$$

where μ_{turb} is an equivalent turbulent molecular viscosity. This approach was proposed by Moore and Moore [60] leading to express the turbulent viscous dissipation

in terms of the mean quantities and an equivalent turbulent viscosity μ_t similarly to RANS approach itself. In addition, the same approach can be applied to the thermal turbulent contribution leading to:

$$\lambda \left(\frac{\overline{\partial T'}}{\partial x_j} \right)^2 = \lambda_{turb} \left(\frac{\partial \bar{T}}{\partial x_j} \right)^2 \quad (2.63)$$

where $\lambda_{turb} = c_p \mu_{turb} / Pr_{turb}$ is the turbulent molecular conductivity with $Pr_{turb} = 0.9$ the turbulent Prandtl number.

In addition, the turbulent entropy flux $\overline{u'_i s'}$ is generally neglected since it generally cannot be obtained from turbulence models. The Reynolds averaged of entropy flux is generally simplified under the assumption of low thermal turbulence that leads to:

$$\overline{\left(\frac{q}{T} \right)} = \frac{\bar{q}}{\bar{T}}. \quad (2.64)$$

Since the Reynolds averaging of entropy is not available from conservative and turbulent quantities from the simulation, this variable is replaced by entropy of the mean field. This leads to a new formulation for Reynolds averaged entropy transport equation:

$$\frac{\partial}{\partial t} (\bar{\rho} \bar{s}) + \frac{\partial}{\partial x_i} \left(\bar{\rho} \bar{u}_i \bar{s} + \frac{\bar{q}}{\bar{T}} \right) = (\mu + \mu_{turb}) \left(\frac{\partial \bar{u}_i}{\partial x_j} + \frac{\partial \bar{u}_j}{\partial x_i} \right) \frac{1}{\bar{T}} \frac{\partial \bar{u}_i}{\partial x_j} + \frac{\lambda + \lambda_{turb}}{\bar{T}^2} \left(\frac{\partial \bar{T}}{\partial x_j} \right)^2. \quad (2.65)$$

This approach has been used originally by Moore and Moore [60] considering the notion of effective viscosity by $\mu_{eff} = \mu + \mu_{turb}$ and in the context of tracking losses in turbomachine by Tailliez and Arntz [61] and Zlatinov [54]. Although these models attempt to minimize complexity, it is difficult to ascertain if the essence of relevant irreversibilities has been captured with sufficient accuracy with these approaches. It should be particularly noticed that this model makes several assumptions: the temperature fluctuations are small compared to the mean temperature. Turbulent dissipation/temperature fluctuation equilibrates turbulent production while there are local regions in boundary layers, for example, where turbulence kinetic energy and temperature fluctuations do build up without balance with dissipation.

2.1.4.1.2 LES approach In LES approach, the RANS formalism applied to entropy transport equation gives a potential modeling for unresolved scales. An equivalent turbulent viscosity/diffusivity is given by the subgrid scale model and velocity/temperature gradients are given by the resolved part of the flow as a direct output of the simulation. Equation 2.65 can be then used to recover the turbulent contribution not resolved by LES approach. However, it should be emphasized that this contribution is not the total contribution of turbulence as in RANS but only some part of the turbulence production. This contribution depends on the local mesh refinement. Based on the entropy transport equation in RANS formalism eq.(2.54), terms (6) and (8) can however be computed from the output of the

LES simulation since fluctuating quantities can be obtained from a temporal averaging. Lengani et al. [62] conducted LES simulation onto T106A low-pressure turbine profile configuration and applied direct entropy approach to track losses. For this configuration, LES simulation of half blade height was performed with very dense mesh ($X^+ < 30$, $Y^+ < 1$ and $Z^+ < 8$) with high order spatial and temporal scheme (4th order). For this mesh approaching 500 million points, 98% of turbulent spectrum energy as shown to be resolved. The present author expressed mean fluctuating terms as a direct output of the simulation by a temporal averaging over the fluctuating quantities.

2.1.4.1.3 Indirect evaluation of entropy production Entropy production can also be estimated from the imbalance of the left-hand side of eq.(2.54). The entropy production that will be noted S_{gen} in differential form can be written as:

$$s_{gen} = \frac{\partial}{\partial t} (\bar{\rho}\bar{s}) + \frac{\partial}{\partial x_i} (\bar{\rho}\tilde{u}_i\bar{s}) + \frac{\partial}{\partial x_i} (\bar{\rho}\overline{u'_i s'}) + \frac{\partial}{\partial x_i} \left(\frac{\bar{q}}{\bar{T}} \right). \quad (2.66)$$

Integrating former equation spatially over the simulation domain leads to:

$$\iiint_V s_{gen} dV = \iiint_V \frac{\partial}{\partial t} (\bar{\rho}\bar{s}) dV + \iint_{\partial V} \bar{\rho}\bar{s}\bar{u}_i dA_i + \iint_{\partial V} \bar{\rho}'\overline{u'_i s'} dA_i + \int \int_S \frac{\bar{q}}{\bar{T}} dA_i \quad (2.67)$$

and integrating over a period of unsteady phenomena Δt_u , one can obtain:

$$\begin{aligned} \overbrace{\frac{1}{\Delta t_u} \int_{\Delta t_u} \iiint_V s_{gen} dV dt}^{(1)} &= \overbrace{\frac{1}{\Delta t_u} \int_{\Delta t_u} \iiint_V \frac{\partial}{\partial t} (\bar{\rho}\bar{s}) dV dt}^{(2)} + \overbrace{\frac{1}{\Delta t_u} \int_{\Delta t_u} \iint_{\partial V} \bar{\rho}\bar{s}\bar{u}_i dA_i dt}^{(3)} \\ &\quad + \underbrace{\frac{1}{\Delta t_u} \int_{\Delta t_u} \iint_{\partial V} \bar{\rho}'\overline{u'_i s'} dA_i dt}_{(4)} + \underbrace{\frac{1}{\Delta t_u} \int_{\Delta t_u} \iint_{\partial V} \frac{\bar{q}}{\bar{T}} dA_i dt}_{(5)}. \end{aligned} \quad (2.68)$$

Term (1) corresponds to the mean entropy production within the considered volume V over a period of time Δt_u . Term (2) refers to the integral over a period of time Δt_u of phenomena having the same period. Therefore, this term is equal to zero or a statistically steady flow. Terms (4) and (5) are equal to zero at the wall of the domain, fluctuation of velocity and temperature being equal to zero. It remains the contribution at free boundary of the volume V . Making the assumption that thermal fluxes and fluctuation of entropy-velocity are negligible, one can finally express entropy production per unit of volume and time by:

$$\frac{1}{\Delta t_u} \int_{\Delta t_u} \iiint_V s_{gen} dV dt = \iint_{\partial V} \bar{\rho}\bar{s}\bar{u}_i dA_i = \dot{m}(s_{out} - s_{in}). \quad (2.69)$$

The entropy generated inside a control volume is then the difference between entropy flowing in and out. Entropy at inlet and outlet of the control volume can be

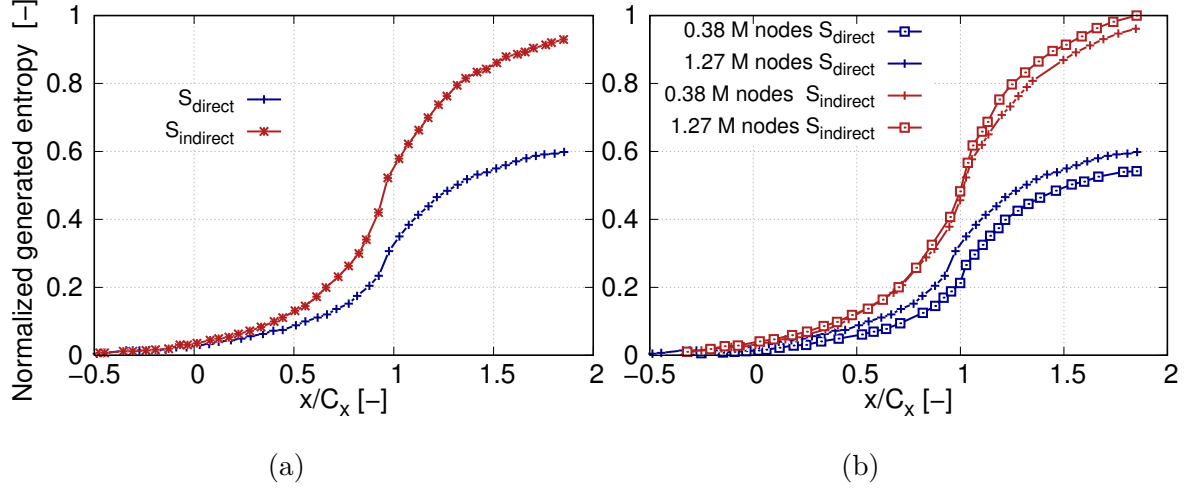


Figure 2.6: Accumulated entropy in a rotor configuration, based on entropy flux through axial cut from volume integral of direct entropy generation S_{direct} from eq.(2.48) and volume integral of indirect entropy $S_{indirect}$ from eq.(2.69) (a). Comparison of direct and indirect methods for entropy using two different meshes (b). Adapted From Zlatinov [54]

evaluated using an explicit formulation of s based on two thermodynamic quantities as proposed in eq. (2.14) ($s = s_{ref} + c_p \ln(T_s/T_{ref}) - r \ln(p/p_{ref})$). An interpretation of entropy has been proposed by Denton [48]: *Entropy may be considered to be like "smoke" that is created within the flow whenever something deleterious to machine efficiency is taking place. [...] Once created, the "smoke" cannot be destroyed and it is convected downstream through the machine and diffuses in the surrounding flow. The concentration of "smoke" at the exit from the machine includes contribution from every source within the machine and the loss of the machine efficiency is proportion to the average concentration of "smoke" at its exit.* Entropy based on two thermodynamic quantities measures a concentration of smoke accumulated from the reference (increases monotonically all along the domain). Spatial derivative of this quantity gives entropy production that can be either zero or positive. At the scale of the cell, direct entropy production based on velocity and temperature gradients that provides entropy production should be equivalent to a flux integration at the boundaries of the cell with entropy from two thermodynamic quantities. Bejan [53] compared direct and indirect method neglecting turbulent flux in indirect method for a turbulent flow in a pipe and showed good agreement of the two methods. However, Herwig and Kock [63] showed that in a highly turbulent flow this approximation can lead to strong discrepancy compared to the direct method. Zlatinov [54] compared direct and indirect methods on a RANS simulation of rotor-stator high pressure turbine stage. He showed that indirect approach can give accurate entropy production estimation when integrated over axial planes of the domain (see Fig. 2.6a). However, this method can give negative entropy generation when looking at a particular cell of the domain.⁵ For the direct method, the quadratic dependence of source terms in

⁵The author postulated that the cause of the local inconsistency is that the CFX finite volume code he used conserved mass, energy and momentum but not necessarily entropy.

velocity and temperature gradient, the computational domain meshes are often too low (see Fig. 2.6b). Between the two meshes used only 3% in total loss and 1% in change in net purge flow losses was observed while an underestimate of 53% and 41% of entropy production was observed in entropy production. Direct method converges to the correct value of dissipation only for high grid densities. This is especially due to secondary flows that introduce regions of high gradients away from the relatively well resolved endwall regions. The regions out of boundary layers and wakes being generally coarsened. This observation was also earlier stated by Kock [59]. The discrepancy in entropy production is due to additional numerical viscosity due to spatio-temporal discretization (see Sec. B.3 in App. B). Indirect method used to obtain entropy evolution in the domain is shown to be less dependant to the mesh than direct one. This trend observed in the literature remains difficult to justify as the inlet-to-exit values are the result of what is produced/destroyed in the domain. Since the indirect method can locally give wrong entropy production with negative values, the ability for the indirect method to recover better entropy generation levels is difficult to ascertain.

2.1.4.2 The use of entropy compared to pressure or enthalpy to track losses

The assessment of loss generation in a component is generally performed using total pressure measurements at the inlet $p_{tot,in}$ and outlet planes $p_{tot,out}$. These quantities being non-dimensionalized by various quantities, for example dynamic pressure at the inlet of the domain ($p_{tot,in} - p_{in}$) to build a loss coefficient ζ_p :

$$\zeta_p = \frac{p_{tot,out} - p_{tot,in}}{p_{tot,in} - p_{in}}. \quad (2.70)$$

This practice comes from viewing turbine blade rows as nozzles (rotor can also be seen as a nozzle where the incident quantity are the relative ones) with the purpose of accelerating working fluid with a minimal drop in stagnation pressure. This approach is also convenient from experiments since this quantity is readily obtainable. For adiabatic flow through a stationary blade row, total temperature is constant and so entropy changes depend only on total pressure changes by

$$\Delta s = -r \ln \frac{p_{tot}}{p_{tot,ref}} \quad (2.71)$$

or, for small changes in stagnation pressure⁶

$$\Delta s = -r \frac{p_{tot} - p_{tot,ref}}{p_{tot,ref}}. \quad (2.72)$$

The use of total pressure loss coefficient to track losses in a steady RANS simulation with adiabatic walls is then equivalent to the use of entropy. However, this observation is generally not true in the general case. Experiment research done by Mansour

⁶When the variation of p_{tot} is small around $p_{tot,ref}$, using a linear approximation $\ln(p_{tot}/p_{tot,ref}) = \ln((p_{tot} - p_{tot,ref}) + p_{tot,ref})/p_{tot,ref}) = \ln(1 + (p_{tot} - p_{tot,ref})/p_{tot,ref}) \simeq (p_{tot} - p_{tot,ref})/p_{tot,ref}$

et al. [64] showed that the overall losses and the loss distributions are misrepresented by the stagnation pressure loss coefficient since the overall losses were overestimated by more than 69% using the stagnation pressure loss coefficient. This observation was corroborated by studies of losses due to secondary flows where it was pointed out that the losses generated by secondary flow losses (tip leakage vortex, lower and upper passage vortex) were not correctly estimated by total pressure approach and entropy approach. The reason for this phenomenon is the isotropic rearrangement of the temperature and pressure, known as energy separation (Greitzer et al. [65]). The stagnation enthalpy of a particle changes as it traverses an inviscid flow where the static pressure fluctuates. This may be written as

$$\frac{dh}{dt} = \frac{1}{\rho} \frac{\partial p}{\partial t} \quad (2.73)$$

and the second law of thermodynamics relates changes in stagnation pressure and stagnation enthalpy by

$$Tds = dh - \frac{1}{\rho} dp. \quad (2.74)$$

From eq.(2.73) and (2.74), it can be seen that pressure changes with time not only influence the distribution of stagnation temperature, but also influence the stagnation pressure distribution by stagnation enthalpy. Also, entropy is a particularly convenient measure because, unlike stagnation pressure or stagnation enthalpy its value does not depend on whether it is viewed from a rotating or a stationary blade row that is of particular interest in multi-row configuration where entropy continuously increases. Relatively to rotating rows, the loss coefficient based on enthalpy ζ_h can be written as:

$$\zeta_h = \frac{h_{tot\ s,out} - h_{tot,out}}{h_{tot,in} - h_{in}} \quad (2.75)$$

where h_{tot} and $h_{tot\ s}$ refer to the actual (measured) total enthalpy and the one that could have been obtained from an isentropic process leading to same thermodynamic conditions as actual one. However, this coefficient can lead to wrong conclusions in rotating rows since the relative stagnation pressure and the relative stagnation enthalpy can change as a result of changes in radius without there being any implied loss of efficiency. It follows that the assessment of loss in turbomachinery where unsteadiness, thermal effects and rotating parts can occur, should be dealt with a measure of entropy because taking into account these different contributions.

An exergy formulation and transport equation were derived based on two quantities used in thermodynamic: enthalpy and entropy. This approach makes possible to take into account locally (in each point of the mesh for a numerical simulation) the contribution modifying the available energy in the purpose to generate work. These contributions integrated at the scale of the considered domain/component corresponds to the exergy flux balance between inlet and outlet of the domain. This approach applied to

the different components of the gas turbine makes possible to draw a general assessment for the contributions provided to the gas turbine (generally the heat supplied by the combustion of fuel in the combustion chamber) in conjunction with contributions that are extracted to the fluid or lost by irreversibility. Since this general balance makes explicitly reference to the potential extract work and heat supplied (i.e. the efficiency of the gas turbine), the link between local loss in the component and turbine efficiency is more properly drawn. The application of this approach to numerical simulation and turbulent flows requires some adaptation to the account of turbulence in the exergy balance in each point of the mesh (direct method). The indirect method based on exergy flux balance in the domain based on thermodynamic definitions of enthalpy and entropy is compliant with the direct method but some discrepancy can exist especially in RANS approach since the meshes are generally not sufficiently fine.

2.2 Losses in a turbine

The last section introduced a methodology to track the generation of losses using an exergy formulation based on thermodynamic and control volume analysis performed on transport equation without a description of macroscopic phenomena occurring in the gas turbine. This section introduces the different physical phenomena known at current stage of knowledge and available in the literature as generating potential losses for the turbine. The section is initiated with two topics of primary importance to understand loss generation that are unsteadiness and flow behavior in near-wall region. Following that, losses in gas turbine will be depicted by classifying losses from a macroscopic point of view. Despite all the losses considered in a low pressure turbine are related to viscous and thermal dissipation at relatively small scale, this classification makes possible to gather some common features. It also enables a study/description of each phenomena despite these different type of loss sources are seldom independent.

The flow in near-wall region and unsteadiness is first introduced since losses are strongly related to developing fluid around wetted surfaces and unsteady environment of the turbomachine. The description of losses will be made following an increasing complexity from losses related to the two-dimensional profile of the blade, influence of hub and shroud that enable the development of secondary flow, tip gap losses related to rotor blade. Once these baseline losses are described, the new mechanisms induced by cavity and rim seal as well as the impact of purge flow on losses will be introduced.

2.2.1 Unsteadiness in gas turbine flows

Unsteadiness in turbomachine generally includes several meanings and characteristic flow structures:

- the possible transient operation of the turbomachine that lead to variation of main annulus flow field in time;

- instability of the flow field such as fluttering, rotating stall, surge⁷ or flow distortion that is generally to be prevented since possibly damaging for the turbomachine;
- effects related to turbulence, trailing shed vortex process and boundary layer transition (see Sec. 2.2.2 and 2.2.6);
- inherent unsteadiness due to the relative motion of rotor/stator blade rows in a multi-stage environment where structures are strongly correlated to blade passing frequency and its harmonic.

Figure 2.7 provides the main unsteady processes in gas turbine introduced with their domain of characteristic length scale and frequency. The focus will be given to this

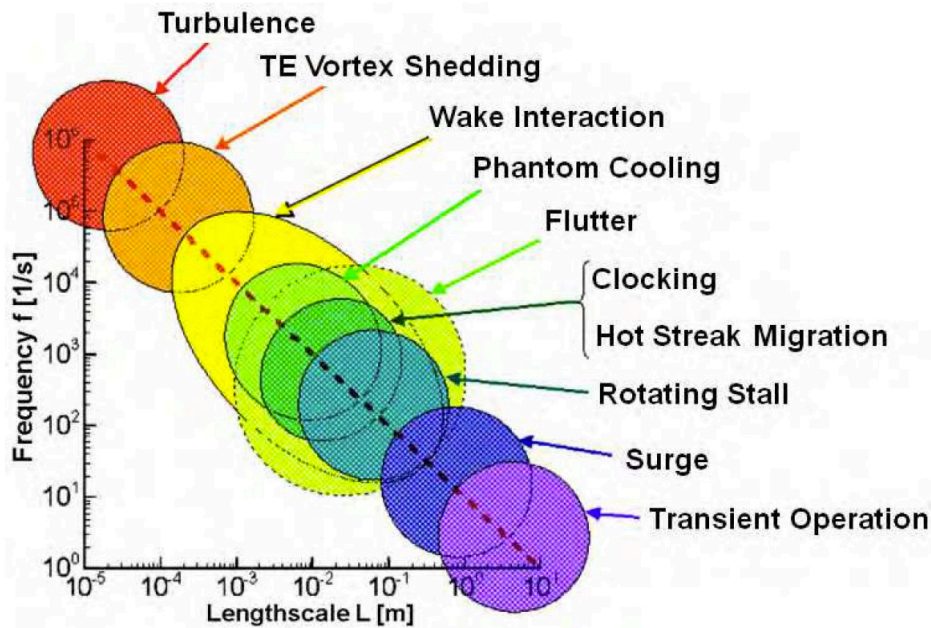


Figure 2.7: Unsteady flow structures with corresponding characteristic length scale and frequency. From Lagraff et al. [66]

last category. Unsteadiness has important consequences on generation of losses as it will be depicted in this section as well as on operating life due to heat transfer issues, thermal fatigue and noise generation. Section 1.2.3 describes the influence of wake transport and potential effects on ingress process at rim seal interface. More generally these two phenomena are responsible for an important part of unsteadiness in the main annulus.

⁷Fluttering: interaction between the flow and the structure that can lead to resonance and potential damaging. Rotating stall arises when a small proportion of airfoils experience stall, disrupting the local airflow without destabilizing the component, generally compressor. Compressor surge is when the air pressure after the compressor is actually higher than what the compressor itself can physically maintain leading to reverse flow

2.2.1.1 Characteristic parameters of unsteady flows

The influence and strength of flow unsteadiness can be evaluated by the Strouhal number as

$$St = \frac{L}{u_0 t} \quad \text{or} \quad St = \frac{L\omega}{u_0} \quad (2.76)$$

for a periodic phenomenon of frequency ω . In turbomachinery, the Strouhal number is equivalent to the frequency of unsteady disturbance sources that is the reduced frequency $\bar{\omega}$. The reduced frequency is parameter that has to be conserved when dealing with dynamic similarity of unsteady flow as stated in Sec. A.1.2. The reduced frequency is the ratio of the time taken by the given particle to be convected in the blade passage to the time taken for the rotor to sweep past one stator passage and is expressed as

$$\bar{\omega} = \frac{\omega L_{pitch}}{u} \quad (2.77)$$

where L_{pitch} is the blade pitch. The magnitude of the reduced frequency is a measure of the degree of unsteady effects compared to quasi-steady effects. If $\bar{\omega} \gg 1$, unsteady effects are significant and dominate the flow field. When $\bar{\omega} \simeq 1$, unsteady and quasi-steady effects coexist. The reduced frequency $\bar{\omega}$ also represents the number of wakes (or other upstream unsteady features) found in a single blade passage at any instant in time.

2.2.1.2 Potential effects

The potential effects are created by the presence of an obstacle in the flow that are here the blades. They propagate upstream and downstream at the speed of sound and induces a non-uniform field in pitchwise direction. Due to relative motion of stator cascades relatively to rotor ones, it induces an unsteady flow field composed of pressure waves propagating upstream and downstream. Parker and Watson [67] were among the first to propose the exponential decay of potential effects based on axial distance. Leboeuf [68] proposed a relation to describe the decay of potential effect with distance:

$$\frac{\partial p}{\rho u^2} = \frac{\sqrt{1 - M^2}}{\sqrt{1 - M_x^2}} \exp \left[-2\pi \frac{\sqrt{1 - M^2}}{\sqrt{1 - M_x^2}} \frac{x}{\theta_p} \right] \quad (2.78)$$

where M , M_x are the Mach and axial Mach number, p the pressure, u the velocity magnitude and θ_p the blade passage pitch. Similarly to the rotor/stator interaction, due to rotor/stator gap decrease, the potential effect can have significant effects. Penin et al. [69] experimentally studied the upstream potential effect generated by downstream moving cylindrical rods on an upstream turbine at Reynolds Number $Re = 1.6 \times 10^5$. The authors showed that potential effect has an impact of boundary layer state, they showed that potential effect of downstream rod was able to suppress periodically transition on blade suction side observed on a case where the rods were set further downstream. Potential interactions are generally weaker than wake interactions in most low pressure turbines as stated by Hodson and Howell [70].

2.2.1.3 Wake transport mechanism

The convection of wakes in the passage of downstream rows is detailed in Sec. 2.2.6.1. The emphasis of this paragraph is to deal with the unsteady nature of wake transport. Wake can be primarily considered as any flow deficit in the relative frame of the considered body beyond which this pattern develops. Conversely to potential effect, blade wake is only convected downstream. The velocity field is decreased in the disturbed region compared to undisturbed value and static pressure does not usually vary significantly. A wake looks like a facing backward jet when moving with the wake. The negative jet is one of the main unsteady transport mechanisms in axial turbines since the downstream rows face alternating zones of low momentum (wake) and undisturbed velocity field. Similarly to the ingress process that is dominated by the wake effect unsteadiness, the wakes from upstream blade rows provide one of the dominant sources of unsteadiness and is modulated by the downstream blade row potential effect.

2.2.2 The flow in near-wall region

The near-wall region is generally the main problem encountered in gas turbine flows due to the strong diversity of physical phenomena that can occur in this region. For the viscous fluid that can be either air for the compressing components or burnt gas for turbine components that flows on the wetted surfaces of the turbomachine (mainly hub, shroud and blade surfaces in the mainstream passage), an essential condition is that the velocity at any point on the wall surface is zero. This concept of boundary layer was first introduced by Ludwig Prandtl (1875-1953) in 1904. The extent to which this condition modifies the general character of the flow depends upon the value of the viscosity of the fluid. For the considered surfaces and fluid in gas turbine, the modifying effect appears to be confined within narrow regions adjacent to the solid surfaces that are called boundary layers. The boundary layer is characterized by rapid wall-normal fluid velocity changes from the skin surface where the velocity has to be zero and the free stream velocity of the fluid. The frictional effects experienced by the fluid are limited to the boundary layer while outside the boundary layer the flow is essentially an inviscid flow where Euler equations could apply. A boundary layer can mainly be in two states referred as laminar and turbulent that are characterized by very different behavior. The boundary layer can experience transition from laminar to turbulent nature and is referred as transitional one.

2.2.2.1 Laminar boundary layer

Laminar boundary layer refers to the organized and layered nature of the boundary layer where streamwise velocity changes uniformly as one moves away from the wetted surface. Laminar boundary layer has received strong analytical developments with earlier study of the steady two-dimensional incompressible laminar boundary layer developing over flat plate. It was analytically possible to derive the incompressible two-dimensional laminar boundary layer profile (known as Blasius profile) solution of the partial derivative set of equations (known as Falkner-Skan equations).

Boundary layer profile approximation based on a polynomial expansion was also derived known as Pohlhausen's method. These methods provide analytical tool to the evolution of boundary layer thickness, skin friction and energy dissipation associated to the laminar boundary layer. Extensions have been also proposed to account for compressibility effects and three-dimensionality. More details on Falker-Skan set of equations are given in App. C. In gas turbine application, such analytical methods make possible to account for the effect of pressure gradient on boundary layer profile. This can be accounted through the factor m that describe velocity at the edge of the boundary layer by $u_{edge} = C x^m$, with C a constant (see Fig. 2.8a).

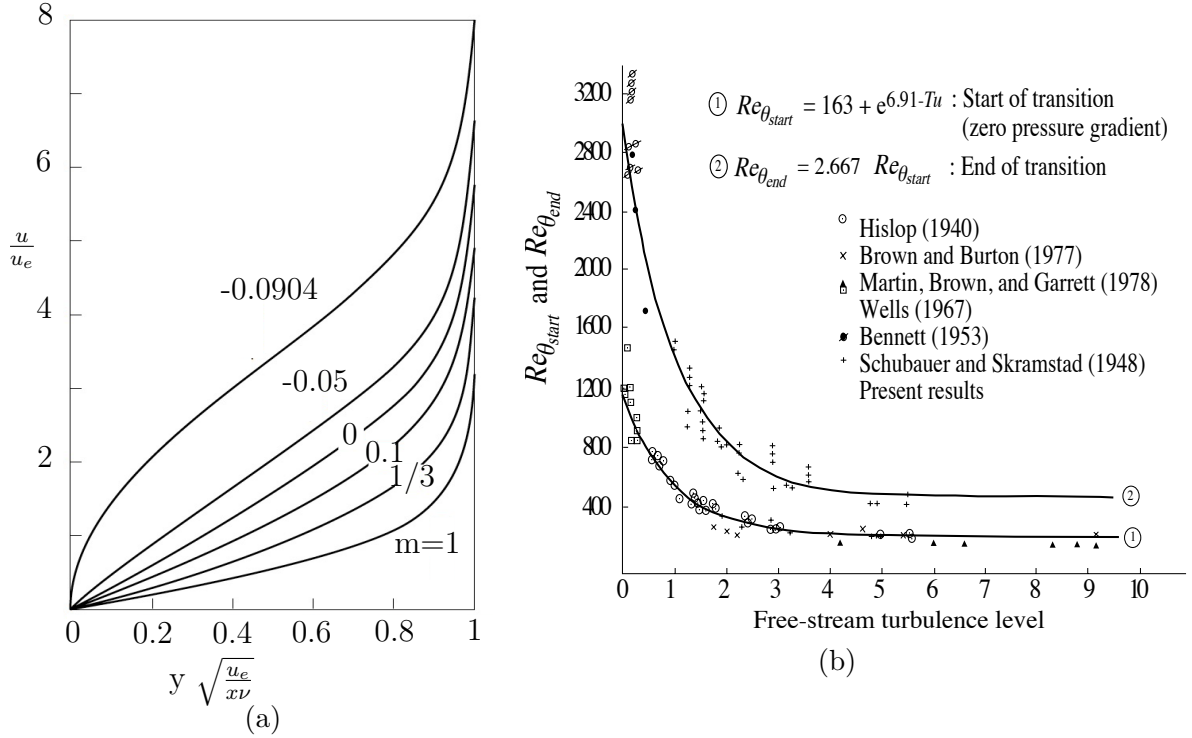


Figure 2.8: Blasius boundary layer profile for various pressure gradients (a) and start ($Re_{\theta_{start}}$)/end ($Re_{\theta_{end}}$) of transition based on momentum thickness Reynolds number over a flat plate without pressure gradient depending on the free stream turbulence (b). From Abu-Ghannam and Shaw [71]

2.2.2.2 Turbulent boundary layer

A turbulent boundary layers is characterized by a loss of coherency and organization compared to the laminar one. A turbulent boundary layer is classically divided in different sublayers (see Fig. 2.9a). The near-wall region where convection and turbulent terms are low is referred as the linear sublayer and is dominated by laminar viscous forces. The velocity profile is supposed to evolve linearly with the characteristic wall-normal coordinate y^+ ($y^+ = 0$ to 5). Going farther from the wall, the turbulent effects become the main contribution compared to the laminar one and the velocity profile evolves as the logarithm of y^+ ($y^+ = 50$ to 0.1δ). In between, the intermediate region known as buffer layer, where both viscous and inertial forces

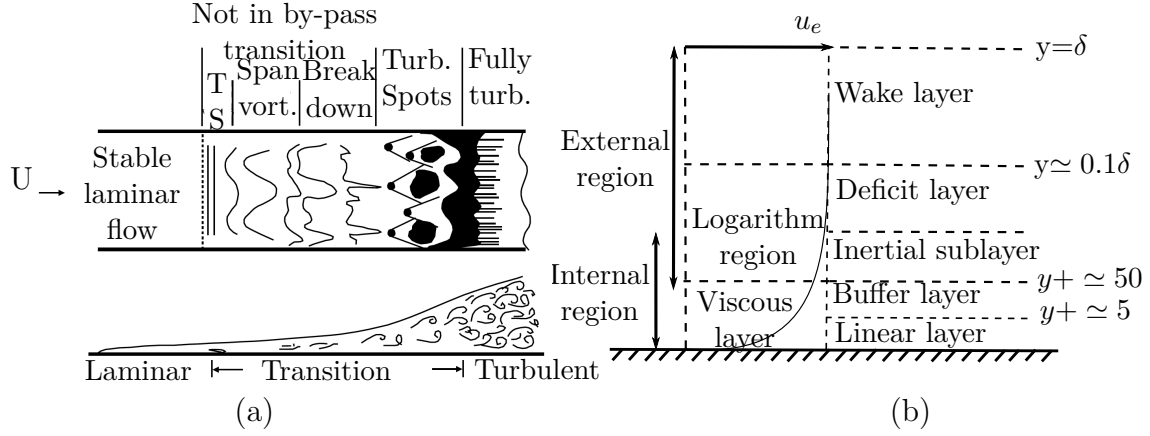


Figure 2.9: Sketch of natural and bypass transition processes (a). From White [72]. Sketch of the different layers composing a turbulent boundary layer (b)

account ($y^+ = 5$ to 50). These layers form the internal region. The viscous sublayer is dominated by streamlines tricks referred as "streaks". Due to high strain rate, strong velocity fluctuations and gradient in wall normal direction makes low momentum fluid initially close to the wall moves to higher momentum regions leading to long streamwise zones of negative fluctuation velocities that are represented by counter rotating streamwise vortices close to the wall from which streaks originate. This description of the turbulent velocity profile is valid based on the assumption of incompressible, two-dimensional, statistically steady without pressure gradient and at infinite Reynolds number flow.

The accurate prediction of transition process and position of transition to turbulence are critical to properly describe the flow around wetted surfaces that are mainly blade, hub shroud and eventually technological effects. For all existing flows, it has been early known that there is a value of the Reynolds number that triggers transition to a turbulent state. However, transition location is difficult to be accurately obtained since very dependent on free-stream turbulence, surface roughness and pressure gradients that are shown to be possibly important and diverse in gas turbine environment. It may be emphasized that concerning the free-stream turbulence, the turbulence length scale is another parameter of importance as it not only controls the decay of the turbulent kinetic energy, but it may influence the receptivity of the boundary layer to external disturbances. Furthermore, for aircraft engines operating at altitude the turbine inlet Reynolds number will be reduced to about one half compared to sea level which means that potentially various boundary layer states can be observed during the mission of the engine (see Fig. A.6b). The prediction of transition location is an important feature since the boundary layer state modifies locally the properties of the flow, the wall friction and heat transfer are higher and the stall is delayed for a turbulent boundary layer compared to a laminar one. In order to better understand the transition process to turbulence, a description of the main features and paths to the transition process are described in next section.

2.2.2.3 Boundary layer transition

Laminar-to-turbulence transition corresponds to the change from a laminar state to a turbulent one. This process is performed over some axial extent (see for example Fig. 2.8b with start and end of transition) where the flow is said to be transitional. Four important modes of transition are generally considered in turbomachine. The first mode is known as natural transition. The second one as bypass transition, third and fourth one are referred as separated flow transition and periodic wake unsteady transition. This section will be mainly focused on effects associated to low pressure turbine but a more complete description of transition in the various components of a gas turbine has been proposed by Mayle [73] and Walker [74].

2.2.2.3.1 Natural transition Since a turbulent boundary layer has generally experienced a laminar state, this has led many authors to study the stability of laminar flow and identify the perturbation that could give rise to this transition [8]. In the absence of external perturbations and pressure gradient, for the laminar boundary layer developing on a surface, the mechanism that can lead to turbulence is nowadays fairly well accepted. The initial stage of the natural transition process is known as the receptivity. At sufficiently high Reynolds number, the laminar boundary layer becomes susceptible to small disturbances both acoustic (sound) and vortical structures often unmeasurable. Acoustic disturbances tend to excite two-dimensional instabilities such as Tollmien-Schlichting (TS) waves, while vortical disturbances lead to the growth of three-dimensional phenomena such as the crossflow instability. The instability amplifies within the layer to a point where three-dimensional instabilities grow and develop in loop vortices with large fluctuations. Linear stability analysis is generally well able to capture the growth rate of disturbances in the linear regimes as well as predict critical Reynolds number of canonical flows above which the laminar boundary layer can become turbulent. Finally, the highly fluctuating portions of the flow evolve into turbulent spots which then grow and convect downstream within the laminar boundary layer under a non-linear process to eventually coalesce into a fully-developed turbulent boundary layer (see Fig. 2.9a). The natural transition process has been extensively experimentally studied over aircraft wings with low turbulence level. These studies have been complemented by linear stability analysis of the boundary layer developing on the leading edge of the wing based on the Falkner-Skan-Cooke base flow (three-dimensional steady laminar boundary layer extension of Falkner-Skan flow that forms around blade leading edge). Conversely, gas turbine field has received low experimental studies except the works of Walker and Gostelow [75] that studied the effect of adverse pressure gradient that can be encountered in gas turbine application on a boundary layer subject to low free stream turbulence. The authors were able to detect waves at the Tollmien-Schlichting frequency. However, the adverse pressure gradient remained modest conversely to real applications. A widely accepted rule is that the flow in gas turbine becomes turbulent when the Reynolds number based on the streamwise distance on the surface is roughly 350 000 (Reynolds number based on momentum

thickness⁸ $Re_{\theta_{trans}} = 0.664\sqrt{Re} \simeq 400$) while the natural transition would have occurred at higher Reynolds number (see for example momentum Reynolds number at zero free stream turbulence in Fig. 2.8b). This means that the transition process of laminar boundary layer to turbulent one is generally not the natural one.

2.2.2.3.2 Bypass transition Bypass transition is the common mode of transition in gas turbine. The flow in gas turbine engines has generally moderate or strong turbulence intensity. Under free-stream turbulence intensities of 1 % or more, it is observed experimentally that transition occurs rapidly under this process. Events which are generally occurring in natural laminar-turbulent transition, such as generation of two-dimensional Tollmien-Schlichting waves, spanwise vorticity and three-dimensional vortex breakdown are bypassed. External perturbations enter the boundary layer as very low frequency and low amplitude perturbation and tend to form elongated streaks in the streamwise component of velocity fluctuations. As the boundary develops, these perturbations cause an increase in the instability of the boundary layer leading to the formation of small spots which are turbulent. The spots, initially minuscule in size, tend to grow longitudinally and spread laterally. The turbulent spots ultimately become large and fully turbulent and lead to a fully turbulent boundary layer. Based on the works of Abu-Ghannam and Shaw [71] on a flat plate with pressure gradient and inlet turbulence, the transition Reynolds number may become insensitive to free stream turbulence above $T_u \simeq 3\text{-}4\%$ (see Fig. 2.8b) and the pressure gradient has a less significant effect on transition process as the turbulence level increases (as soon as $T_u \simeq 3\text{-}4\%$, the pressure gradient has almost no effect any more). At low free stream turbulence, a negative streamwise pressure gradient has a stabilizing effect on the boundary layer while destabilizing for an adverse (positive) pressure gradient. The boundary layer acceleration parameter sets a threshold on the receptivity of the BL to external disturbances. When the acceleration is very large, the receptivity to external disturbances drastically reduces in the boundary layer remains in a non-turbulent state. It is also interesting to observe in the limit case of high free stream turbulence that the momentum Reynolds number for start and end of transition is typically $Re_{\theta_{start}} \simeq 300$ and $Re_{\theta_{end}} \simeq 500$. In terms of axial coordinate Reynolds number, this provides $Re_{start} \simeq 200\,000$ and $Re_{end} \simeq 500\,000$. For a typical medium-sized low pressure turbine at cruise (see Fig. A.6b p.234), $Re \simeq 100\,000$ meaning that the boundary layer over blades may be fully laminar no matter the turbulence level (excepting a potential separated flow transition). Even at take off where the Reynolds number is higher typically $Re \simeq 400\,000$, the boundary layer may be transitional.

2.2.2.3.3 Separated flow transition The streamwise pressure gradient imposed on boundary layer induces a flatter (in the case of favourable pressure gradient $dp/dx < 0$) and thinner (in the case of adverse pressure gradient $dp/dx > 0$) boundary layer close to the wall as suggested in Fig. 2.8a. At sufficiently low Reynolds number for gas turbine as generally encountered in low pressure turbine and/or low

⁸We use here the evolution of the laminar boundary layer momentum thickness with axial coordinate over a flat plate without pressure gradient $\theta/x \simeq 0.664\sqrt{1/Re_x}$ providing $Re_{\theta} \simeq 0.664\sqrt{Re_x}$

free stream turbulence, in an adverse pressure gradient region, the laminar boundary layer developing on a surface could separate (inversion of boundary layer profile close to the wall). This causes the flow to locally transition and may reattach further downstream due to high mixing forming a laminar-separation/turbulent-reattachment "bubble" on the surface (see Fig. 2.10a).

2.2.2.3.4 Periodic wake unsteady transition Periodic unsteady transition is caused by the impingement of upstream periodic waves. Disturbances generated by the wake impact downstream blade and can lead to an early transition of the downstream blade boundary layer. The wake-induced transition can be seen as a particular case of bypass transition since the transition is strongly related to the turbulence intensity in the wake. Next paragraph is devoted to describe the transition processes that are commonly observed in low pressure turbine blades according to the different paths to a turbulent boundary layer introduced in last subsection. The description is led by splitting suction and pressure side surfaces since the mechanisms are generally different.

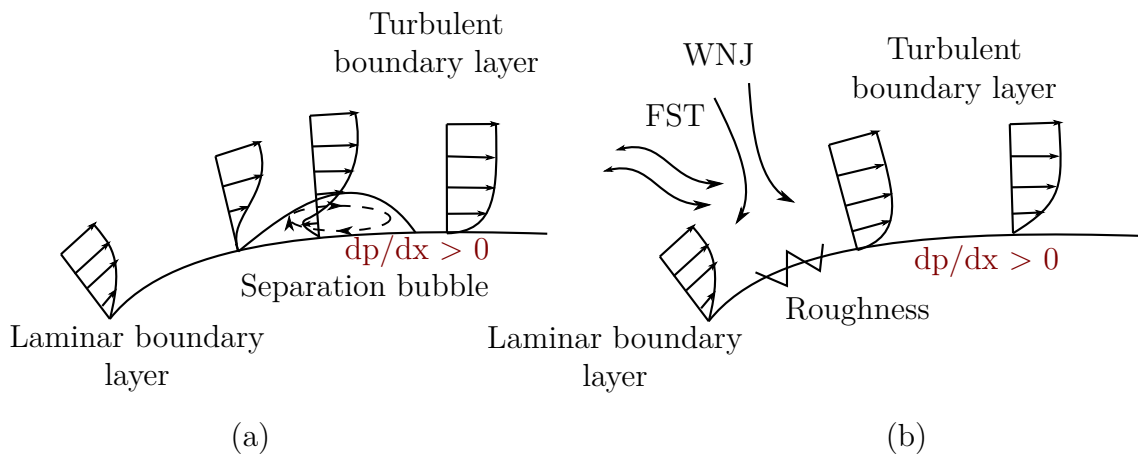


Figure 2.10: Sketch of possible transition process on aft part of low pressure turbine suction side depending on external disturbances (FST: Free Stream Turbulence, WNJ: Wake Negative Jet). Adapted from Cui et al. [76]

2.2.2.3.5 Transition process over low pressure turbine suction surface

The low pressure turbine blade design has generally favourable pressure gradients up to the throat on the suction side and the flow switches over an adverse-pressure gradient on the remaining portion of the suction side known as "diffusion" portion. At relatively low free stream turbulence/Reynolds number, the laminar boundary layer developing over the suction surface of a low pressure turbine can separate on its aft part due to adverse pressure gradient. The separated flow is inherently unstable and undergoes transition to turbulence enclosing a separation bubble (separated flow transition, see Fig. 2.10a). The size of separation bubble and related losses is strongly sensitive to the unsteady environment faced by low pressure turbine blade. If the separation extends until the suction side trailing edge, the boundary layer momentum thickness is large, and losses are large as well. This induces generally

a plateau for pressure coefficient around the blade in the separation bubble region. When incoming wake is added, the wake acts like a negative-jet intensifying Kelvin-Helmholtz roll-up vortices in the separated region and inducing large oscillation of pressure coefficient close to the separated bubble. This process can cause alternatively early transition for the boundary layer leading to a possible suppression of the separation process. The turbulent boundary layer being less prone to the adverse pressure gradient since more momentum is given to the boundary layer due to turbulence (see Fig. 2.10b). At high free stream turbulence, stronger streamwise Klebanoff streaks are induced in the boundary layer that suppress the tendency to form Kelvin-Helmholtz vortices and related flow separation. The boundary layer is no more alternatively laminar and turbulent as for wake effects but can experience early transition steadily. This configuration can be observed in some low pressure turbine where free stream turbulence is important. The majority of losses are generated in the diffusing part of the suction side, and therefore the design of the pressure side focuses mostly on controlling the suction side pressure gradient.

2.2.2.3.6 Transition process over low pressure turbine pressure surface

At relatively low free stream turbulence over the pressure surface, due to concave curvature, there is a possibility of Görtler instability under counter-rotating longitudinal Görtler vortices. The key parameter is the Görtler number $G = (U_{bl} \theta) (\theta/R)^{1/2}$. According to Saric [77], the Blasius boundary layer becomes unstable on a concave surface when $G \simeq 0.3$ and the Görtler vortices are shown to be detected at $G \simeq 5$. At low free stream turbulence, coherent elongated vortices have been observed by Cui et al. [76] as well as Wang et al. [78] with a Görtler number around 5 while at higher free stream turbulence where the Görtler number was lower, no evidence of elongated vortices were pointed out. These vortices are characterized by a mushroom-shaped streamwise velocity due to the transport of low-momentum fluid away from the fluid promoted by a pair of counter-rotating vortices. Wu and Durbin [79] as well as Wissink [80] proposed a different explanation for the formation of these elongated structures. Since their study took into account wake at low free stream turbulence, they proposed the selective intensification of vortices originally contained in the wake that are selectively developing in the pressure side boundary layer. At relatively higher free stream turbulence, transition on pressure side is mainly forced by bypass transition process.

2.2.2.3.7 Transition handling in numerical simulation

Transition process is intrinsically contained in the equations of fluid motion and can be captured in DNS simulation and LES simulations for fine enough grids. RANS approach is generally not able to capture transition process except some extensions proposed for example by Jones and Launder [81] that introduced the turbulent kinetic energy gradients in the so-called low-Reynolds number versions of the $k-\epsilon$ model allowing to capture transition without a dedicated transition model. The transition models used is the $\gamma-Re_\theta$ model of Langtry and Menter [82] which models the intermittency and transition momentum thickness Reynolds number is also an example of the account for transition in RANS approach. The laminar kinetic energy model from Walter et al. [83] determines the laminar, transition and turbulent flow regimes with the help

of a concept known as laminar kinetic energy. Laminar kinetic energy or laminar fluctuations are the fluctuations created by Tollmien-Schlichting waves in the pre-transitional boundary-layers. The description of losses in a turbine can be difficult to evaluate since the flow in a turbine is complex and a variety of phenomena can induce losses. In order to introduce the interaction between main and purge and its influence on low pressure turbine aerodynamic losses, it can be useful to have a sight of the different losses phenomena that occur in a turbine without technological effects and purge flow blowing into the mainstream.

According to the loss generation and exergy analysis led earlier in the chapter, irreversibility occurs due to the following fluid dynamic processes:

- viscous friction in either boundary layers or free shear layers. The latter include the mixing processes;
- heat transfer across finite temperature differences due to heat transfer at wall, compressibility effects, coolant flow;
- non-equilibrium processes such as very rapid expansions or shock waves. In low pressure turbines, these phenomena have generally less occurrence than in high pressure ones.

From these processes performed at relatively low scales, the mechanisms of loss have generally been split at macroscopic scale to make isolated study. The historical breakdown of loss in profile loss, endwall and leakage loss continues to be widely used although it is now clearly recognized that the loss mechanisms are seldom really independent as stated by Denton [48]. These different mechanisms of loss will be as far as possible quantified in terms of entropy/anergy since shown as a good indicator of loss generation. The profile loss will be first studied as from a two-dimensional analysis. Endwall losses will be split in the contribution of the boundary layer developing at hub and shroud and the secondary flows induced by the interaction of such boundary layer with blade. Leakage flow that refers to the flow field in between blade tip and casing will be finally introduced.

2.2.3 Blade losses

2.2.3.1 Two-dimensional flow field

In mid-span regions located away from endwalls, the radial flow is often considered as almost negligible and the flow assumed to be two-dimensional. The loss may be based on two-dimensional cascade tests or boundary layer calculations. When studying the losses related to the two-dimensional flow of a blade, a common idea would be to define a notion of drag similarly to external aerodynamics. The local surface normal force contribution of the flow is the pressure work while tangential one is the friction contribution. Projected on the incoming velocity direction gives the pressure and friction drag contribution forming total drag when no shocks are taken into account. The choice of this direction is obvious for external flows but is not at all obvious in turbomachinery where a force acting in the direction of blade motion is essential for work transfer and a force acting in the meridional direction is

essential for pressure changes. For example, the skin friction force acting on a highly staggered⁹ compressor blade has a large component in the opposite direction to rotation and so contributes to the work input. It is not immediately clear whether or not this work input contributes to the pressure rise. This difficulty further explained the necessity to use a different approach as the one based on exergy and entropy. For this two-dimensional configuration, Denton [48] derived an expression for entropy production per unit chord area $s_{bl,blade}$

$$s_{bl,blade} = \frac{d}{dx} \int_0^\delta \rho u_x (s - s_\delta) dy = \int_0^\delta \frac{1}{T} \tau_{yx} du_x \quad (2.79)$$

where δ is the boundary layer thickness. Since the velocity in the boundary layer

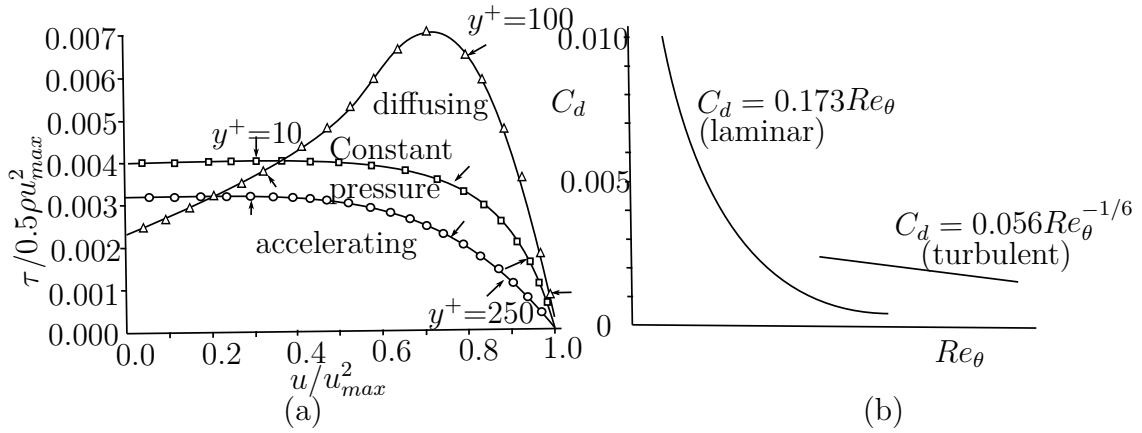


Figure 2.11: Variation of the shear stress with velocity in the boundary layer with $Re_\theta = 1000$ (a) and evolution of the dissipation coefficient for laminar and turbulent boundary layers based on the momentum thickness Reynolds number (b)

changes mostly near to the surface, most of the entropy generation is concentrated in the inner part of the boundary layer. The evolution of viscous shear stress in boundary layer as proposed in Fig. 2.11 for various boundary layers profiles shows that the viscous stress tensor is almost constant or vary slowly in the inner part of the boundary layer. This observation has pushed towards approximating entropy production at a considered Reynolds number by a constant value non-dimensionalized by the loss coefficient C_d :

$$C_d = \frac{T s_{bl,blade}}{\rho u_\delta^3} \quad (2.80)$$

where u_δ is the velocity at the edge of the boundary layer and $s_{bl,blade}$ is the entropy produced in the blade boundary layer at a considered abscissa. The evolution of the loss coefficient was shown to have different behavior depending on the nature of the boundary layer.

For fully developed turbulent boundary layers where much of the entropy creation occurs within the laminar sublayer and the logarithmic region, constant value of

⁹Angle between the chord line and the turbine axial direction

entropy production is generally good approximation for turbulent boundary layer profiles subject to a variety of pressure gradients. The well-characterized "universal velocity profile" of the boundary layer shows that only the external region of the layer (see Fig. 2.9b and 2.11b) is greatly affected by the streamwise pressure gradient. Since this portion generates little of the entropy, this result suggests that the entropy generation may be relatively insensitive to the detailed state of the turbulent boundary layer. Several experiments proposed a relation between loss coefficient and momentum thickness Reynolds by (see Schlichting [8]):

$$C_d = 0.0056 Re_\theta^{-1/6} \quad (2.81)$$

that is well suitable for $10^3 < Re_\theta < 10^4$ and shape factor¹⁰ $1.2 < H_f < 2.0$ (turbulent boundary layer with various pressure effects). This comparison suggests that for $Re_\theta > 500$, the dissipation coefficient is relatively insensitive to the boundary layer thickness since proportional to $\theta^{-1/6}$. In the range $500 < Re_\theta < 1000$ (typical of high pressure turbine for example), it is also relatively insensitive to the shape factor of the boundary layer. For many turbomachine blades where the average Re_θ is of order 1000, a reasonable approximation is to take $C_d = 0.002$ as a constant for turbulent boundary layers.

For low pressure turbine at lower Re_θ and potentially laminar boundary layer, the dissipation coefficient is more dependent on boundary layer thickness. Truckenbrodt reported results showing

$$C_d = \beta Re_\theta^{-1} \quad (2.82)$$

where the value of β varies little with the shape factor, about 0.17 for typical laminar boundary layers. An analytical result can be derived for laminar boundary layers by integrating the well-known Pohlhausen family of velocity profiles (Schlichting [8]) to give

$$C_d = Re_\theta^{-1}(0.1746 + 0.0029\iota + 0.000076\iota^2) \quad (2.83)$$

where terms with higher power of ι have been neglected. ι is the Pohlhausen pressure gradient parameter whose value ranges from 12 for a highly accelerated boundary layer to -12 at separation. The corresponding range of C_d is 0.22 to 0.151. Equation (2.83) shows that the dissipation coefficient is in fact relatively insensitive to the state of the boundary layer, the dissipation being marginally increased in an accelerating boundary layer and reduced in one near separation. Since laminar boundary layers are much more likely to exist on turbomachinery blades with favourable pressure gradients, i.e. with ι positive, a typical value of $\beta = 0.2$ is realistic. The variation of C_d with Re_θ obtained from eq.(2.81) and (2.82) is shown in Fig. 2.11. In the range of Re_θ where either a laminar or a turbulent boundary layer could exist that is to say $300 < Re_\theta < 1000$ due to envioning conditions, the dissipation in the

¹⁰ $H_f = \delta/\theta$. The shape factor of a laminar boundary layer over a flat plate without pressure gradient is generally around $H_f = 2.59$ (Blasius boundary layer) while for turbulent one $H_f = 1.3-1.4$

laminar boundary layer is much less (by a factor of between 2 and 5) than that in the turbulent one¹¹. This large difference highlights the importance of predicting boundary layer transition on turbomachine blades. From the loss coefficient, the total entropy generation in the blade boundary layers can be evaluated by

$$s_{bl,blade} = \int_0^x \frac{\rho u_\delta^3 C_d}{T} dx = \sum L_s \int_0^1 \frac{\rho u_0^3 C_d}{T} d(x/L_s) \quad (2.84)$$

where the summation is for both blade surfaces, x is the surface distance and L_s is the total length of the surface. The value of entropy production is dominated by the location of the transition point where C_d undergoes a rapid change, as shown in Fig. 2.11. In order to minimize the loss the boundary layers should be kept laminar as long as possible. The extent of the laminar boundary layer will depend mainly on the Reynolds number, turbulence level and on the detailed surface velocity distribution. At high turbulence levels prevalent in turbomachines, transition is likely to occur in the Re_θ range 300-500 whilst Re_θ at the trailing edge is usually in the range 200-500 for low pressure turbines and 500-2000 for high pressure ones. The approximation of loss coefficient with constant value has to be made with care when used to predict systematic trends for the variation of loss with blade and stage design. The blade surface boundary layer loss varies significantly with Reynolds number and surface roughness. The variation with Re_θ is, as suggested by Fig. 2.11 with the loss increasing rapidly at very low Re ($Re < 10^5$), due to the high dissipation in laminar boundary layers and possible laminar separation of the boundary layer. Within the transition region, $2 \times 10^5 < Re < 5 \times 10^5$, the variation is complex and depends on the details of the surface velocity distribution. The net result being a combination of the general decrease in loss with increasing Re and an increase in loss as the transition point moves upstream. At $Re > 6 \times 10^5$ the loss varies approximately as $Re_\theta^{-1/6}$ for very smooth blades. However, in this regime, the turbulent boundary layer is significantly influenced by the surface roughness so that for machines that operate at very high Re the surface finish of the blades is very important.

2.2.3.1.1 Three-dimensional boundary layer The former analysis assumed two-dimensional flow in the blade surface boundary layers. The same approach can be applied to three-dimensional boundary layers where the convergence or divergence of the surface streamlines may thicken or make thinner the layer. Although this can have a considerable effect on the boundary layer thickness, it should not have a large effect on the entropy creation per unit surface area, unless convergence of the surface streamlines causes the boundary layer to separate. Hence it is suggested that eq.(2.84) can be modified to estimate the entropy production over the whole blade surface, even in three-dimensional flow.

2.2.3.1.2 Trailing edge loss The other major contribution to blade loss comes from the trailing edge. The boundary layers developing on the blade pressure and

¹¹Not only skin friction is increased with turbulent boundary layer but boundary layer thickness is also increased. For example, at equivalent Reynolds number, for a 0.3 meter long duct at a velocity of 50 $m.s^{-1}$ (Reynolds number of 10^6), the thickness of the laminar and turbulent boundary layers are approximately 1.5 mm and 7 mm, respectively.

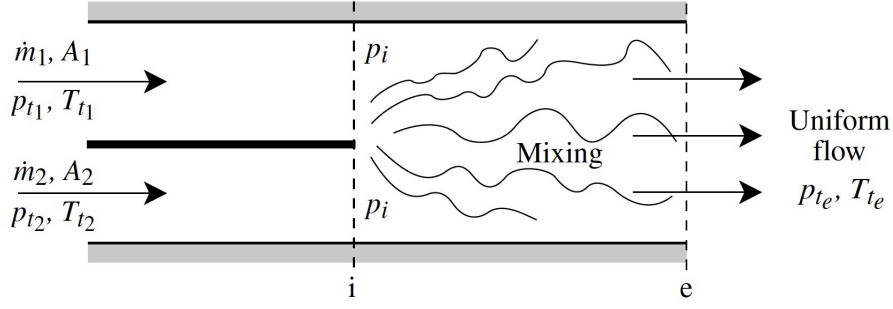


Figure 2.12: Mixing of two streams in a constant area duct corresponding to a simplified configuration of mixing process downstream a blade trailing edge. From Greitzer et al. [65]

suction side tend to separate at the blade trailing edge or slightly upstream since turbine blade trailing edge are generally thick for thermo-mechanical reasons. The mixing out of the surface boundary layers behind trailing edge induces relatively high rates of shearing behind the trailing edge in vortices with unsteady phenomena like the formation of Kelvin-Helmholtz instability and Karman vortex streets. Since usually associated with turbulent flow, the effective viscosity may be large, typically two order of magnitude higher the laminar viscosity. The loss generation is mainly brought by the mixing process of vortices when convected further downstream in the main annulus. The majority of entropy is produced within few trailing edge thickness. Entropy generation associated with trailing shed vortex can be assessed, from a simple view by considering the mixing of two co-flowing streams with different stagnation conditions corresponding to the flow on pressure and suction side. A model of this configuration is the constant area mixing of two streams $(\dot{m}_1, p_{tot1}, T_{tot1})$, $(\dot{m}_2, p_{tot2}, T_{tot2})$ of different stagnation temperature and pressure as shown in Fig. 2.12. The mixing process can be analysed using a control volume approach. This approach consists in applying conservation equation of mass, momentum and energy to a control volume from the unmixed two streams to the location where the two streams are fully mixed at conditions $(\dot{m}_e, p_{tot e}, T_{tot e})$ where $\dot{m}_e = \dot{m}_1 + \dot{m}_2$ and $T_{tot e} = (\dot{m}_1 T_{tot1} + \dot{m}_2 T_{tot2}) / (\dot{m}_1 + \dot{m}_2)$. For this configuration, entropy at the fully mixed plane s_e compared to entropy at the blade trailing edge s_i can be expressed by:

$$\frac{(s_e - s_i)}{c_p} = \left[\left(\frac{\dot{m}_1}{\dot{m}_e} \right) \ln \left(\frac{T_{tot e}}{T_{tot1}} \right) + \left(\frac{\dot{m}_2}{\dot{m}_e} \right) \ln \left(\frac{T_{tot e}}{T_{tot2}} \right) \right] - \frac{(\gamma - 1)}{\gamma} \ln \left(\frac{p_{tot e}}{p_{tot i}} \right). \quad (2.85)$$

A demonstration of this equality is proposed for example in Greitzer et al. [65]. The change in entropy measures not only the effect due to viscous dissipation but also the lost work associated with the thermal mixing of the two streams. This configuration makes possible to emphasis on the notion of perspective for loss generation in a component discussed previously depending on whether one is interested only in the degradation of the mechanical energy within a fluid component or in the overall system losses. In the first case, only loss associated to mechanical energy degradation should be taken into account for the variation of total pressure. In the latter

case the entropy change associated with heat transfer across a finite temperature difference must be added: someone has paid to have one fluid heated or cooled, and a comprehensive system accounting must include this. Alternatively, Denton [48] proposed simplified model to take into account trailing edge losses based on the state of boundary layer at trailing edge. The entropy that has been created in the boundary layers upstream of the trailing edge is measured by the entropy thickness which, in incompressible flow, is identical to their energy thickness, so the entropy level just before the trailing edge is

$$T\Delta s_{te} = 0.5\rho u_{te}\delta_e. \quad (2.86)$$

The total entropy created associated with blade and trailing edge losses can be related to momentum thickness for a blade with zero trailing edge thickness by

$$T\Delta s = 0.5\rho u_{te}(2\theta). \quad (2.87)$$

The loss related to the trailing edge can be finally obtained by making the difference of these last two contributions: $T\Delta s = 0.5\rho u_{te}(2\theta - \delta_e)$. The ratio θ/δ_e is a type of shape factor whose value depends on the state of the boundary layer. For a typical turbulent boundary layer its value is about 1.7 and so, for thin trailing edges, the ratio of the entropy level just before the trailing edge to that present far downstream is typically 0.85, that is to say about 15% of the total entropy is created behind the trailing edge. For boundary layers near separation, this proportion can rise to about 25%. For separated boundary layers and thick trailing edges, an even greater proportion of the entropy is generated downstream. Since trailing edge are generally not thin, a common value observed for the loss behind trailing edge due to mixing is about thirty percent of total loss generated by a two-dimensional blade profile. The entropy generation due to the mixing process can be obtained by subtracting total entropy generation downstream blade to the contribution of blade boundary layer calculated with the method introduced earlier in the section. It may be emphasized however that the extra losses downstream of the trailing edge caused by the wake mixing-out are not constant, as they depend on the static pressure gradients downstream, typically governed by a downstream blade row as stated by Marconcini et al. [84], Michelassi et al. [85], Pichler et al. [86].

2.2.4 Endwall losses

Endwall losses refer to several process related to the development of a boundary layer at hub and shroud of mainstream passage both within and outside of the blade passage. The flow at endwall is highly three-dimensional and more complex than those encountered at mid-span of the blade introduced previously. The boundary layer induces loss due to wall-normal velocity gradients and the interaction of the boundary layer with blade leads to the development of three-dimensional structures often referred as secondary flows. The term secondary arose since it was thought originally that it was a result of turning and stretching of the incoming boundary layer onto the blade as stated by Denton and Pullan [87]. Endwall losses are generally used in preference to "secondary loss" to also consider the loss arising on the

annulus walls both within and outside of the blade passage. The boundary layer at the endwall, especially in the passage, is strongly related to cross-passage pressure gradients and subsequent secondary vortices. Hence, the development of these secondary flow structures will be first introduced. The losses related to the friction processes at endwalls and associated to the secondary flows will be then described.

2.2.4.1 Secondary flows

The three-dimensional flow structure close to hub/shroud endwall has been investigated essentially for loss generation purposes with annular vane/blade configurations with or without rotation. Studies of the complex flow at hub/shroud has also been simulated using stationary cascades with three-dimensional blade geometry. Qualitative assessments have been given to the flow structures in the inter-blade channel with passage crossflow, vortices induced by the blade leading edge, the corners and supplied coolant flow. Most of the observations have been considered to be similar in rotating cases except mainly that cross flow vortices are alleged to be stronger in rotating configuration due to higher turning. A comprehensive review of the secondary flow structures in turbine cascades has been presented by Sieverding [88] and Langston [89]. Detailed experimental studies concerning secondary flows and the main pattern have been led successively by Langston et al. [90], Yamamoto [91], Goldstein et al. [92]. Figure 2.13 shows the different secondary structures that can be observed in a four blade linear cascade passage at Reynolds Number $Re = 2.7 \times 10^4$ proposed by Wang et al. [93]. Close to endwall, the boundary layer separates as

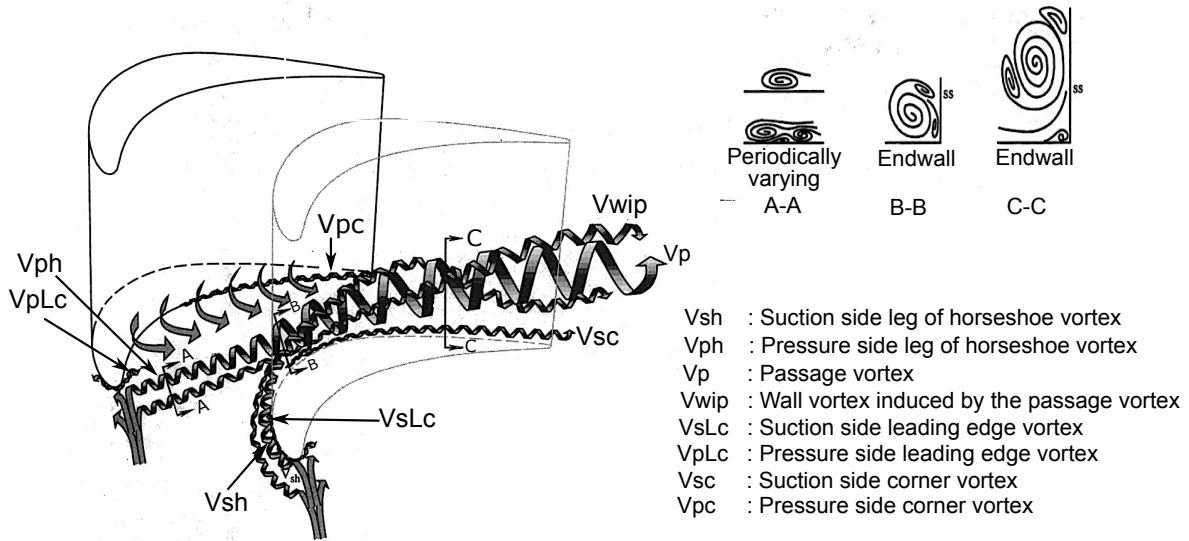


Figure 2.13: Secondary flow structures in the passage proposed by Wang et al. [93]

it approaches the leading edge stagnation point and rolls-up into a horse shoe vortex similarly to the one observed classically in most of the junction flows of blunt bodies [94, 95, 96, 97] or between fuselage and wing for aircraft for example. This process is due to the low momentum of the boundary layer at endwall that cannot reach blade leading edge due to high stagnation pressure. Multiple separations occurs front of the leading edge forming trains of vortices. The leading vortex in the

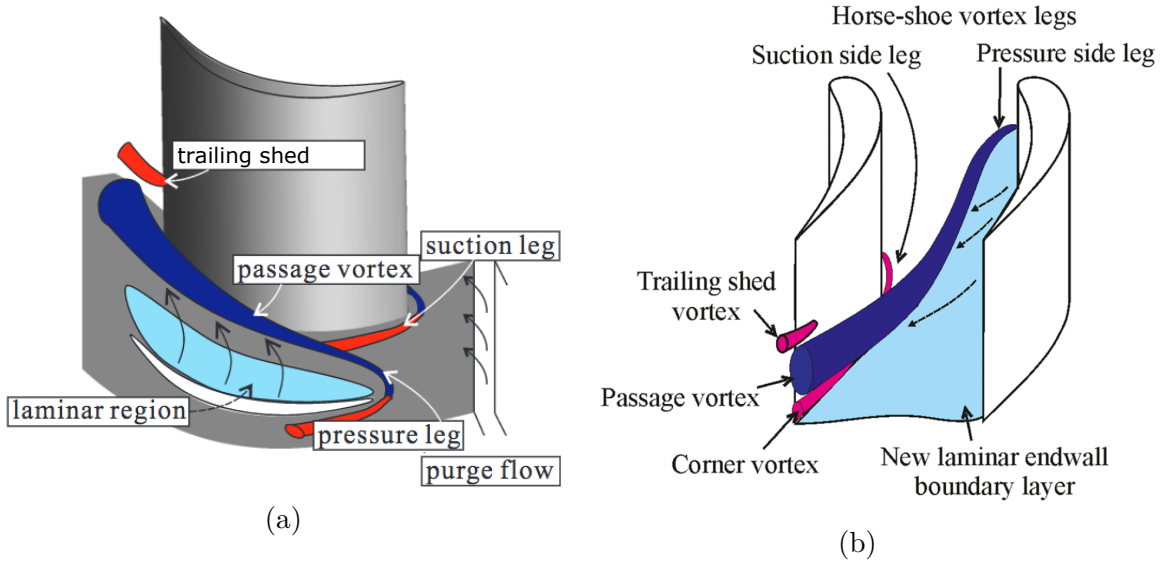


Figure 2.14: Side (a) and downstream view (b) of simplified secondary flow structures in the passage proposed by Cui et al. [76]

periodic separation process diminishes over time as it get closer to blade leading edge. The following vortex experiences a local favourable pressure gradient due to leading vortex and is convected towards the leading edge. The horse shoe vortices convected downstream impact periodically the blade at a frequency that depends mainly on the boundary layer edge velocity u_{bl} and equivalent diameter of blade leading edge. These vortices are chopped by the blade leading edge into two legs, one leg on the blade suction side and the other on the blade pressure side. The suction side leg of the horse shoe vortex (V_{sh}) remains close to blade suction side. Far from endwall, an equilibrium between pitchwise pressure gradient and centrifugal forces is applied on the fluid element. This equilibrium breaks close to the end-wall due to a low-momentum endwall boundary layer while cross-passage pressure gradient remains high. Hence, the pressure side leg of the horse shoe vortex (V_{ph}) close to endwall travel across the inter-blade channel due to this transverse pressure gradient. This vortex trajectory defines a separation line where the upstream boundary layer is swept onto the blade suction side surface and a new-born boundary layer must start to develop at endwall downstream of the separation lines. The boundary layer is subject to a strong cross pressure gradient and to the entrainment effect of secondary flows. These two effects make the boundary layer highly three-dimensional and drive it towards the suction surface. As a result, fluid is continually removed from this boundary layer and swept onto the suction surface so that the new endwall boundary layer itself stays thin. The measurements of Harrison [98] and Holley [99] suggest that this extremely thin boundary layer is laminar over an extended portion of the endwall in the passage. The pressure side leg of the horse shoe vortex strengthens as is entrains this thin passage boundary layer. Pressure and suction side leg of the horse shoe vortex merge close to blade suction side. The greater the blade turning and loading, the sooner the pressure side leg and end-wall boundary layer fluid moves onto the suction surface. At the two-leg merging

point, the interaction among different flow components, such as the counter-rotating horseshoe legs, the incoming boundary layer, the endwall crossflow, and the mainstream, form an even stronger vortex in the passage, which is called the passage vortex (V_p). Since the pressure leg has the same sense of rotation as the passage vortex, Langston [100] credited this pressure leg as part of the passage vortex. The passage vortex stays close to the suction surface, and rotates in a counter-clockwise direction when viewed in the flow direction. The sense of rotation of the suction side leg is clockwise when viewed in the flow direction and starts to rotate around passage vortex forming a counter-rotating vortex pair. Additional vortices with small spatial extent are created as the counter part of the vortices introduced previously mainly at the junctions of endwall and blade. At the blade leading edge, counter vortices with respect to pressure and suction side of horse shoe vortex respectively referred as suction and pressure side leading edge corner vortex (V_{sLc} and V_{pLc}) are observed. Further downstream, two additional vortices are created at suction and pressure side leg merge. The wall vortex (V_{wip}) is a very intense vortex that starts to rotate around passage vortex similarly to the suction side leg of the horse shoe vortex. The strong crossflow in the passage also induces a small intense corner vortex that remains close to hub and blade suction side (V_{sLc}). In addition, at the trailing edge of the blade row, a shear layer is formed between the fluid from suction side that has a significant spanwise velocity component compared to pressure surface that has little or slightly negative spanwise velocity. This induces vorticity rolls up behind the trailing edge often called counter vortex and contributes to the trailing shed vortex process (see Fig. 2.14b). Once the passage vortex has started to develop, it is gradually lifted away from the endwall as it travels downstream, remaining close to blade suction side and is the most energetic vortical structure in the inter-blade passage. Yamamoto [91] presented experimental results for two cascades with different turnings. In the case with 110° turning representative of a typical rotor blade row, the corner vortex is seen as a result of the overturning close to the endwall. For a lower turning case (68°) representative of a stator cascade, the experimental results did not exhibit this result. The author concluded that a corner vortex only develops at a certain level of blade turning. Conversely, underturning is observed some distance away from the endwall which is one of the most obvious signs of secondary flow downstream blade.

2.2.4.2 Losses related to friction process at hub and shroud

Similarly to blade surface, a boundary layer develops at hub and shroud. Endwall losses correspond to the dissipation of mechanical energy due to the boundary layer developing on the wetted endwall surfaces (hub and casing of the turbine). As introduced in former section, the endwall boundary layer is still very thin at the trailing edge. In a cascade, it continues to grow relatively undisturbed downstream of the blade row and becomes more two-dimensional as the passage vortex and the cross stream pressure gradient decay. Similarly, the incoming boundary layer is relatively undisturbed until the horse shoe vortex processes. Furthermore, in a turbine, the boundary layer will have to cross the gap separating the stationary and rotating parts of the endwall and will then find itself adjacent to a surface moving with a different velocity before it enters the next blade row. As a result of this

change of reference frame, the endwall boundary layers entering all except the first blade row in a turbine will be skewed relative to the mainstream flow. Hence, in cascade tests, which usually have a comparatively thick collateral endwall boundary layer may not be representative of conditions in a turbine. The conjunction of the passage pressure gradient and discontinuous endwall then strongly influences the amount of loss generated by endwall boundary layer due to wall-normal velocity gradient. The direction of the boundary layer skew in a turbine induces negative incidence on the blade row and so the direction of the relative inlet flow in the boundary layer reinforces the secondary flows. Unless the inlet boundary layer is very thick, the effects of the skew on blade loading are not large and so the local negative incidence does not significantly reduce the cross passage pressure gradient driving the secondary flows. The effects of skewing of the inlet boundary layer on the flow and loss have been examined. Skewing in the direction found in a turbine greatly increased the magnitude of the secondary flow the loss by about 50% whilst skewing in the opposite direction reduced both as stated by Walsh et al. [101]. The question that arise when dealing with loss related to endwall boundary layer is the possibility to apply formulation developed for blade boundary layer with entropy generation per unit of area and a simple approximation of the loss coefficient C_d . The main difficulty is related to the strong cross flow component of boundary layer since strongly skewed that makes difficult to use only τ_{yx} component for the evaluation of C_d . Based on measurements with 0 and 50° skew, Harrison [102] showed that the skew changes the dissipation by at most 10% suggesting that the dissipation rate on the endwalls is unlikely to be greatly different from that in a collateral boundary layer with the same Re_θ and the use of loss coefficient can be good approximation for endwall boundary layer. Upstream the passage and downstream of the blade boundary layer are generally to be treated separately since of different nature. After the separation line, the boundary layer is likely to be laminar with a very low value of Re_θ , Harrison [102] found that it remained laminar over most of the region near to the pressure surface but became turbulent in the higher velocity region near to the suction surface. A rough idea of the magnitude of the dissipation on the endwalls can be obtained by assuming constant value for loss coefficient, for example $C_d = 0.002$ and that the relative velocity varies linearly across the pitch from the suction surface (s) to the pressure surface (p). If the endwall is not moving relatively to the blades, the entropy production rate can then be integrated across the pitch to give

$$s_{endwall,p} = 0.25 \int_0^{C_x} \frac{C_d}{T} \left(\frac{u_s^4 - u_p^4}{u_s - u_p} \right) \rho dx \quad (2.88)$$

where x is the axial distance. The endwalls downstream of a turbine blade are subject to the full blade exit velocity and so the entropy generation rate per unit area will be comparable to the maximum value on the suction surface. In a turbine the downstream endwalls typically extend about 1/4 of an axial chord behind the blades before the relative velocity between the flow and the wall is reduced by the change from stationary to rotating walls, or vice-versa. Thus, the entropy generation in this region is comparable to that on the endwall within the blade row. This is a significant loss component which can only be reduced by minimizing the area of endwall exposed to the full blade exit flow velocity. The endwalls upstream of a

turbine blade are subject to the relative inlet velocity which is usually significantly less than the exit velocity. The axial extent of these walls is unlikely to be more than about $1/4$ of an axial chord and so the entropy generated in the inlet boundary layers is usually much less than that on the downstream endwalls. Hence it seems that the total entropy generation in the endwall boundary layers, upstream, within, and downstream of the blade row can only explain about $2/3$ of the observed endwall loss.

2.2.4.3 Losses related to secondary flow structures

Once the loss related to wall-normal velocity gradients on the blade and endwall have been factored out, it remains that the total loss is generally not recovered. A first phenomenon that was possibly inducing additional losses was the mixing of the inlet boundary layer in the passage. Butler showed that this source of loss remained almost constant as the thickness of the inlet boundary layer was changed. This implied that this source of loss is a low contributor. Due to the blade turning, the inlet boundary layer skewing and new endwall boundary layer developing into the passage, some secondary flows are generated as stated in last subsection. A measure of its amplitude is generally the secondary kinetic energy associated with the velocity component perpendicular to the primary mainstream flow. The development of secondary flows is an inviscid process and so does not initially produces entropy (from the point of view of a turbomachine it does not cause loss). When the mean flow is accelerated in the passage, the secondary kinetic energy increases since, for an inviscid flow, the secondary kinetic energy is proportional to the square length of the vortex, the vortex being elongated by the acceleration process. The process of loss generation is then mainly due to this vortex core stretching that induces strong velocity gradient close to its central core. Some of the related dissipation occurs within the blade row but the dissipation continues downstream and will incur additional loss. Secondary flows are strong contributors to aerodynamic losses in the turbine passage, requiring special considerations by turbine designers. Methods to predict secondary losses were originally developed on correlations from experimental data with seldom attempts to model physical processes generating losses. These different methods were gathered and analysed by Dunham [103] that showed strong discrepancies between the results and correlation prediction. To overcome these prediction difficulties, numerical simulation have quickly been used to predict secondary flow and their subsequent losses but it is well known until nowadays that they are scarcely accurately captured by numerical simulation. Denton and Pullan [87] performed RANS simulations of an experimental large-scale low-speed turbine and applied the direct entropy method to find the regions where losses are generated in the domain. The losses related to secondary flows were shown to be almost negligible upstream of the developing horse shoe vortex. Losses increased as the pressure side leg of the horse shoe vortex crosses the passage especially when it started to interact with the suction surface. Losses due to the thin passage boundary layer were shown relatively small. Downstream, important losses were generated on the blade suction surface where the passage vortex climb up and in the core of the passage vortex reaching a maximum at $x/C_x = 0.9$. Losses then decreased before additional localized losses immediately downstream of the blade trailing edge due

to the trailing shed vortex process. Downstream of the blade trailing edge, losses related to the passage vortex decrease but the vortices were still high so the net losses are still significant. One of the main parameters driving the development of secondary vortices is the development of the inlet boundary layer before interacting with blade. Gregory-Smith et al. [104] and more recently Cui et al. [76] studied the effect of boundary layer state at inlet on secondary vortices development. For the turbulent boundary layer, pressure and suction side leg of the horse shoe vortex are move further downstream in the passage compared to laminar one at similar thickness. The turbulent boundary layer being more unlikely to separate due to the adverse pressure promoted by blade leading edge potential effect since additional momentum is provided close to the wall to the turbulent boundary layer compared to laminar one. Downstream the blade, the passage vortex and trailing shed vortex are moved farther in span direction for a turbulent boundary layer compared to a laminar one. The boundary layer is also shown to have a strong influence on secondary flow development. The transition between the combustion chamber and the first high-pressure turbine nozzle guide vane no is shaped to control the endwall boundary layers, both velocity and thermal. For a downstream rotor blade and subsequent stages of a multistage turbine, the boundary layer is generally thin since developing over a low distance downstream rim seal. The secondary flow near the endwall may be consequently reduced and has a beneficial effect on losses related to secondary flows according to Denton and Pullan [87]. The proportion of endwall loss generation depends on inlet boundary layer thickness and skew and on blade turning and blade loading but generally 2/3 of it comes from entropy generation in the annulus wall boundary layers within, upstream of and downstream of the blade row. The loss associated with the secondary kinetic energy is in the order of 1/4 of the total endwall loss while the remaining can be attributed to mixing of the inlet boundary layer in the passage. This ratio may change from high pressure to low pressure turbine and it essentially depends on the endwall aerodynamic load and the blade aspect ratio.

2.2.5 Tip clearance leakage flow

The various losses introduced previously represent the different loss processes encountered in static row (nozzle guide vane). For unshrouded rotor blade rows, an additional process known as tip clearance leakage flow can occur. Mainly two types of blade tip architectures can be found: unshrouded and shrouded blades where a tip seal is added. Between the tip of a rotor blade and the casing, a tiny space called the tip gap is necessary to ensure the rotation of the rotor cascade. The pressure gap over the blade tip between the pressure and suction surfaces of the blade induces some flow to move through this gap from pressure to suction side. For unshrouded blades, the pressure difference driving the leakage flow is the one between the pressure and suction surfaces of the blades whilst for shrouded blades it is the overall pressure change over the blade tip. For most blade rows these two pressure differences are similar and so, for the same tip clearance, the leakage flow rates will be similar for shrouded and for unshrouded blades. However, for low reaction rotor blades, the pressure drop over the blade row becomes much less than that between

the blade surfaces and so, shrouded blades will have a lower leakage flow rate. Due to a generally high pressure gradient, the flow is highly accelerated in the tip gap. This process is mitigated by the rotation of rotor blade where some flow would be naturally deviated from suction to pressure side at the tip. The tip leakage flow separates at the pressure side sharp edge of the blade tip and is contracted in a narrow stream jet between the separation region and shroud endwall. The area of the jet being lower than the seal clearance by a contraction coefficient whose value is typically about 0.6. The tip leakage flow becomes generally turbulent in the clearance space and the mixing process is irreversible, creating entropy before additional mixing along the chord evolution. Downstream of the gap, the tip leakage flow separates from the endwall due to the adverse pressure gradient and travels in the inter-blade channel as a vortex structure convected downstream. The tip leakage flow is not turned similarly to the stream in the passage, it rather follows the blade-to-blade transverse pressure gradient. The leakage flow being re-injected into the main flow, due to differences in both the meridional velocity and the swirl velocity of the two flows, more mixing losses are generated. The leakage streams that bypass the passage does not yield to work extraction since the flow is widely underturning at the tip. The tip gap over the blade generally eliminates the potential effect of the blade leading edge. Therefore, no horse shoe vortex processes are encountered unless when the gap is very small. The flow at the tip approaching the blade leading edge is divided in two streams, one part going to the tip gap over the blade and a stream going across the passage. This last stream rolls-up in the passage and is referred to the tip passage vortex. The tip passage vortex and tip leakage vortex are counter-rotating vortical structures where the tip leakage structure is dominant with a circulation that is often several times larger than the passage vortex. The tip leakage region is characterized by a high level of flow turbulence where the production and dissipation of turbulent kinetic energy are significant sources of flow losses. In addition, the flow direction is not changed until blade trailing edge which indicates that no work can be extracted from the tip flow.

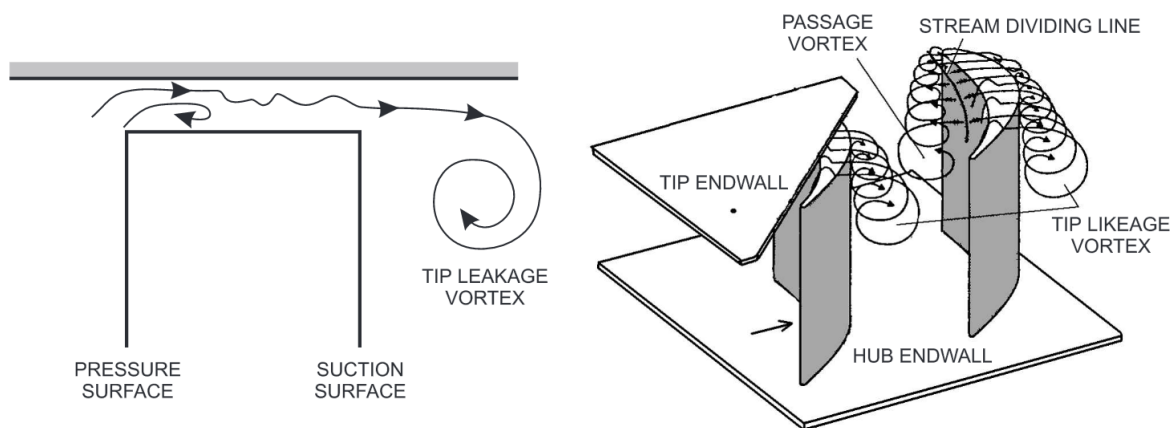


Figure 2.15: Sketch of the tip leakage process over a rotor blade. From P. Lampart [105]

2.2.6 Transport of upstream non-uniform flow structures in a downstream cascade

The mechanisms of losses introduced previously rely on approaches where only an isolated cascade is taken under consideration. This approach has been widely used to estimate losses since the coupling of several cascades could be difficult to perform, often computer demanding and more difficult to analyse. Furthermore, the assumption was made that the rotor and stator rows were spaced far enough apart such that the flow in each is steady that is to say that there is no unsteadiness of any sort due to rotor-stator aerodynamic interaction and the flow is sufficiently homogenized by mixing process downstream of the blade. However, turbine components are generally composed of several stages, each stage being composed of a stator and rotor cascade. The rows of current turbines (and compressors) are already very closely spaced. Axial gaps between adjacent rows of approximately $1/4$ to $1/2$ of the airfoil chord are common practice. Thus, the problem of rotor-stator interaction is having an impact on existing turbine designs. Future designs with higher loading and lower aspect ratios that is to say fewer and bigger airfoils, and the ever present desire to minimize engine length or compactness, will aggravate this condition even further. Interaction between cascade rows will therefore keep increasing and need to be taken into account in loss generation estimation. Wakes, vortices from separation process and secondary flow structures are the main structures emanating from an upstream cascade that can have different influence on loss generation. Since the blade loading is expected to increased due to decreased blade number, pressure gradients in transverse and radial directions are expected to increase and lead to stronger secondary flow losses.

2.2.6.1 Wake transport in a downstream cascade rows

Section 2.2.1.3 dealt with the unsteady nature of wake transport. This paragraph deals with the subsequent losses induced by the wake transport in the downstream rows. A downstream cascade faces periodically a wake from upstream cascade and the flow from an open channel. As stated in Sec. 2.2.1.3, wake can be primarily considered as a flow with same velocity direction than the free stream one but with a momentum deficit and turbulence carried. The balance between inertia and radial pressure equilibrium is not fulfilled and the wake is deviated downwards towards hub. An analysis based on the velocity triangle shows that this velocity deficit leads to underturning of the flow in the downstream cascade frame. The underturning generally means that less work will be extracted by the blade to the flow since the profile is no more adapted. The wake is chopped by downstream cascade leading edge and curved since the flow at middle of the passage goes faster than close to blade leading edge. Since the wake is low momentum flow, this flow is more influenced by acceleration processes in the passage. The wake undergoes bowing, dilatation, stretching and compression processes within the blade passage that lead to turbulent kinetic energy production by the shear and strain action of these processes as stated by Michelassi et al. [85]. The velocities near the suction surface are higher than near the pressure surface, and therefore, fluid near the suction surface is convected in the passage more rapidly, resulting in a reorientation of the wake segment. The

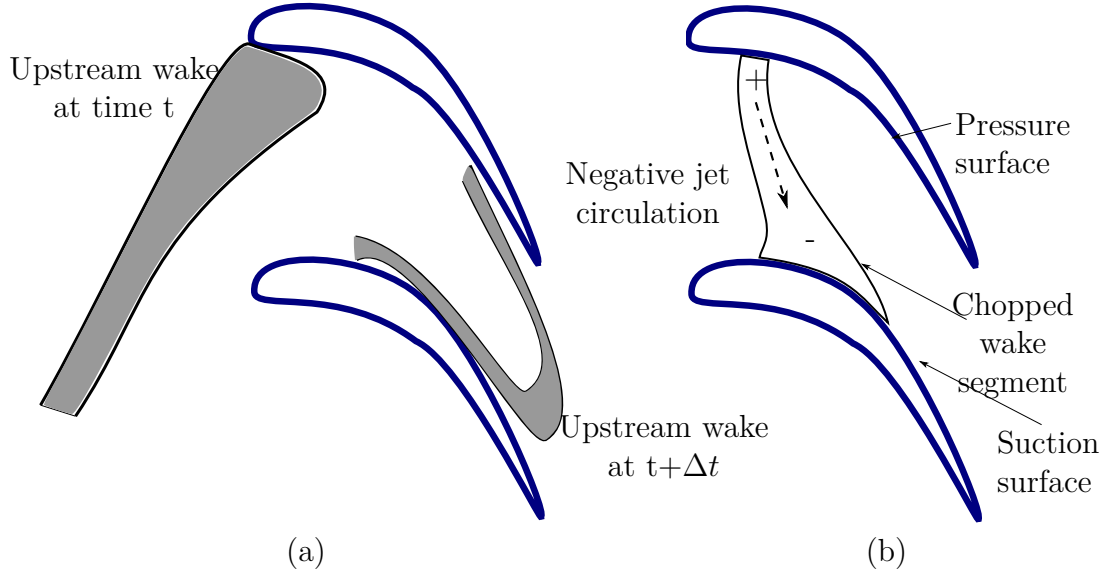


Figure 2.16: Evolution of an upstream wake in the passage of a downstream row, contours of entropy (a) and negative jet phenomenon (b). Adapted from Pullan [106]

gap in convective velocities also causes the wake segment to elongate, and this, in turn, decreases the wake width to conserve the vorticity of the wake fluid. From simple view, by neglecting viscosity, as the wake convects the circulation in the vortex sheets, bounding a fixed quantity of fluid must remain constant by Kelvin's theorem and so if the wake is stretched the velocity difference between its centreline and the mainstream is decreased. The implication is that the dissipation in the wake will be reduced by mixing in a downstream blade row relative to that when mixing in a uniform flow. Since the mixing loss of a wake is comparatively small and most of the mixing takes place very close to the trailing edge this is probably not a very important effect. However, considering that it is very difficult to further reduce profile losses, while still some hope exists to reduce such kind of unsteady losses studied for example by Pichler et al. [86]. This also leads to a negative jet phenomenon where the wake on blade pressure side tends to be deviated on blade suction side due to azimuthal pressure gradient induced between two adjacent blades and increase blade loading.

Wake can also have an impact on the boundary layer state of the subsequent blade row. Due to relatively low Reynolds number encountered in low pressure turbine, the boundary layer transition and/or separation plays an important role on loss generation. The open separation of boundary layer (without reattachment) is especially a key parameter to be controlled in low pressure turbine with relatively low Reynolds number. The turbulent intensity of the wake is higher than in the free stream one and carry a dense population of streaky structures that may further alter the stability of boundary layer by exciting the transition process of the downstream blade boundary layer. This mechanism can be especially observed in low pressure turbine since the Reynolds number can be low enough to have a laminar boundary layer on main part of blade suction side. An early transition may happen and a positive impact on the blade efficiency if it suppresses the boundary layer separa-

tion that can sometimes appear onto blade suction side close to the trailing edge due to the adverse pressure gradient at sufficiently high blade loading. Conversely, a detrimental effect on the overall performance can be observed if no flow separation was induced in the calmed region since a turbulent boundary layer induces addition friction compared to a laminar one. The blade suction side structure of the boundary layer can therefore be alternatively laminar and turbulent. Incoming wake and intrinsic unsteadiness were shown to have low impact on losses generated in blade suction side boundary layer under viscous process as well as in the mixing region downstream blade trailing edge as stated by Lengani et al. [62]. However, unsteady losses related to the rear part on blade suction side was shown to be due to mid-range modes carried by the wake in the boundary layer. The same argument developed for wake can be applied to a flow separation which is in effect only a large wake, however, the mixing loss of a separation can be large and so any reduction may be significant.

2.2.6.2 Transport of secondary flows from an upstream

Similarly to wake, secondary flow structures from an upstream cascade are generally not dissipated when approaching a downstream cascade. This is especially true for secondary structures that are large scale coherent structures that can be convected over great distance before to be fully mixed. The passage vortex experiences similar process than the endwall boundary layer by being alternatively chopped by blade leading edge and inducing the separation of the passage vortex into a pair of contra-rotating vortices in the downstream cascade. Denton and Pullan [87] studied this process onto a RANS simulation of a stator-rotor configuration. The upstream passage vortex at around 35% span was shown to be separated by the rotor blade into a lower vortex migrating downstream at 30% span and an upper vortex convected to higher radii onto the rotor suction surface boundary layer at 60% span (see Fig. 2.17). The transport of these vortical structures rotating mainly around

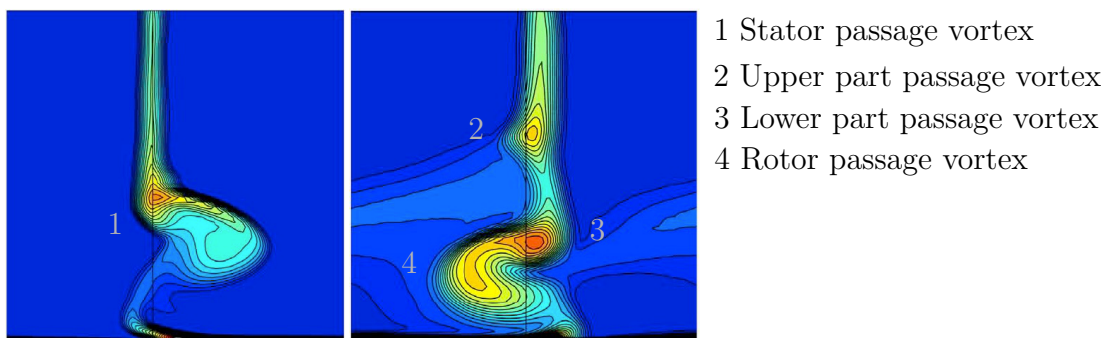


Figure 2.17: Entropy contour at exit of the stator (left) and rotor (right). From Denton and Pullan [87]

the stream direction have different implications for loss compared to wake. Using once again Kelvin's theorem from simple view, the circulation around a stream tube remains constant and so if the diameter of the tube is reduced by stretching the streamwise vorticity is amplified that is typically what happens for convected secondary flow structures in a downstream passage. When a vortex is stretched or

compressed longitudinally it can be shown that its secondary kinetic energy will vary as the square of its length. Hence, stretching a vortex will greatly amplify its secondary kinetic energy and when this is subsequently dissipated by viscous effects it will increase the loss. The magnitude of this effect is not known but if the kinetic energy of secondary flow vortices is significant, it could have important implications. Koschichow et al. [107] who run linear cascade tests and DNS of a low pressure turbine endwall flow with incoming wakes generated by cylindrical rods discovered that the unsteadiness from the inlet periodic wakes barely survived in the endwall region, while it was very evident at midspan.

Losses are related to processes at micro scales. In gas turbine, losses are generally split in different categories at macro scale. The boundary layer developing on the wetted surfaces is primarily a process related to all category of losses: profile loss, secondary flow losses, tip-leakage flow for rotor rows. Additional losses can be incurred by the wake transport of an upstream row unsteadiness.

2.3 Influence of purge flow blowing in the mainstream

This thesis aims at studying the interaction process between the mainstream and inter-disc cavities into a low pressure turbine with the emphasis to get a better understanding to the additional mechanisms of losses. Despite the study of Pau et al. [108] that observed a beneficial effect of purge flow on the loss generation in the cascade, the majority of the literature dealing with purge flow influence on mainstream have shown detrimental effects of purge flow. This section introduces the influence of this technological effect on losses mechanisms introduced previously and the new loss processes induced by purge flow.

2.3.1 Viscous shear layer

Purge air exhibits strong differences of velocity in both direction and magnitude compared to the flow in the mainstream. The axial component is very low despite some rim seal geometries with axial arms that can promote partially the flow to blow into mainstream with an axial velocity component. The radial velocity component is low too due to the low mass flow of purge air compared to the mainstream (typically in the order of magnitude of 1% of the mainstream mass flow rate) and relatively large rim seal gaps to ensure the sustainability of low pressure turbine. Purge flow has also a velocity deficit in the tangential direction. The boundary layer developing on the rotating disc (rotor) in the cavity "pumps" the flow tangentially and can draw annulus gas into the rim seal. The tangential velocity of the purge air flow is typically in the order of magnitude of half the rotational velocity of the rotor disc known as entrainment effect. The velocity gap of the purge flow compared to the main annulus one results in a shear layer at the rim seal interface, with velocity

gradients that are dissipated under a viscous process. In conjunction, cavity flow (c) temperature is generally lower than mainstream one (m) inducing temperature gradients that tend to be homogenized. Similarly to the two stream configuration to estimate entropy production downstream blade trailing edge, a control volume analysis can be led by considering the main and cavity stream as the two streams that fully homogenize in the mainstream after some distance. Young and Wilcock [109] furnished the corresponding entropy production until full mixing for two-dimensional configurations by:

$$\Delta s_{irrev} = \frac{\dot{m}_c}{m_m} \left\{ \left[\frac{(u_{x_m} - u_{x_c})^2 + (u_{y_c})^2}{2T} \right] + \left[\int_T^{T_{in}} \left(\frac{1}{T} - \frac{1}{\hat{T}} \right) d\hat{T} \right] \right\}. \quad (2.89)$$

The first square bracket represents the entropy change from mixing of two streams at different velocities, i.e. the dissipation of the bulk kinetic energy as the mainstream and injection flows mix to a uniform state. The first quadratic term in the bracket refers to velocity equilibration in the mainstream direction x . The second shows that in the mixing process all the kinetic energy associated with the injection normal to the mainstream is entirely converted into heat. The second square bracket is the entropy change associated with thermal mixing of the injected flow and the mainstream to a uniform temperature. This term, multiplied by $\dot{m}_c p T$ is the power that could theoretically be obtained from a Carnot engine coupled between the mainstream flow at constant temperature T and the injected flow as the temperature of the latter changes from T_c to T . Zlatinov [54] extended this equation for three-dimensional flow in a polar coordinate system taking into account the tangential velocity component and eventual velocity in the radial direction:

$$\Delta s_{irrev} = \frac{\dot{m}_c}{m_m} \left\{ \left[\frac{(u_{x_m} - u_{x_c})^2 + (u_{\theta_m} - u_{\theta_c})^2 + (u_{r_m} - u_{r_c})^2}{2T} \right] + \left[\int_T^{T_{in}} \left(\frac{1}{T} - \frac{1}{\hat{T}} \right) d\hat{T} \right] \right\} \quad (2.90)$$

2.3.2 Losses due to change of reaction

The purge flow blowing in the mainstream induces a velocity decrease of the flow upstream in the stator stage close to the hub. Reid et al. [110] observed a decrease of losses for a nozzle guide vane with an upstream cavity and purge flow. The loss decrease was attributed to a pressure drop along the blade and a decreased degree of reaction close to the hub as a consequence of the blockage effect introduced with the purge air flow. Conversely, the degree of reaction in the downstream rotor cascade is increased and the losses are higher compared to a configuration without purge flow. In addition, purge flow modifies flow angle close to hub for the downstream rotor cascade that lead to over and under incidence of the flow close to rotor blade leading edge. Zlatinov observed that for a rotor/stator configuration with cavity purge flow, loss decrease does not compensate additional losses in the downstream rotor cascade.

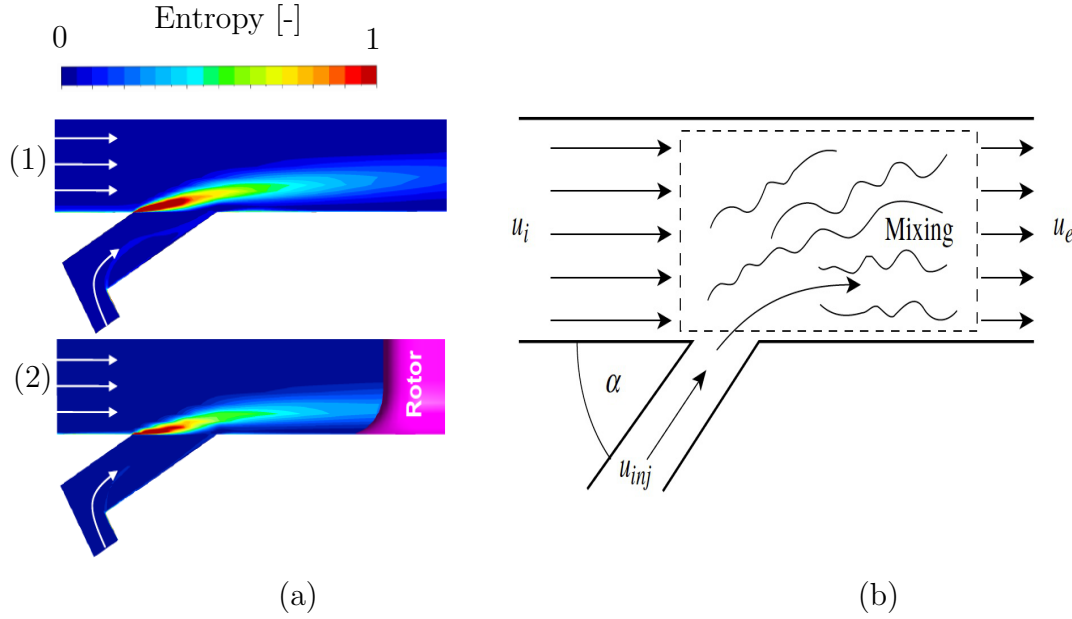


Figure 2.18: Generation of entropy due to shear layer in an axisymmetric (1)/3D configuration (2) (a). From Zlatinov [54]. Sketch of the mixing of two streams (b). From Greitzer et al. [65]

2.3.3 Influence on turbine secondary flow

Secondary flow developing in the passage was originally studied in endwall/blade configuration where boundary layer could develop on the endwall as introduced in Sec. 2.2.4.1. When purge flow and cavity is accounted, a new-born boundary layer starts to develop between rim-seal right corner and blade leading edge. Due to relatively low distance, the boundary layer is relatively thin and could make expect relatively low secondary flow to develop. However, when purge flow was supplied at the hub, the additional loss incurred usually exceeded what would be expected from mixing out of shear layer and change of reaction as stated by Zlatinov [54]. Evidences of increased secondary flows were reported when the cavity and purge flow were taken into account compared to a same configuration with simple endwall. Kost et al. [111], Paniagua et al. [112], de la Rosa Blanco et al. [34] and Ong [113] exhibited the potential interaction of purge flow with secondary flow structure and its potential loss increase. Schuler et al. [114] investigated experimentally the influence of different rim seal geometries for the linear cascade configuration. The author pointed out the increase of the passage vortex and counter vortex with an increase of the purge mass flow rate. Purge flow was shown to move radially secondary flow structures and its influence on mainstream flow was shown to remain within the lower 60% span of mainstream. The increase of secondary flow was not entirely due to purge flow since Abo El Ella et al. [115] showed an increase of secondary flow losses for a configuration with cavity but without purge flow, indicating that the cavity itself influence secondary flow losses. Purge flow does not remain close to hub endwall as stated by Popovic et al. [116] showing that purge flow can only marginally cool down the hub of a high pressure turbine configuration. Purge flow rather induces a modification of horse shoe vortex process as stated by Gallier [117]. Purge flow

is entrained by pressure side leg of horse shoe vortex leading to stronger secondary structures. Also, in the reference frame of the downstream blade, a strong crossflow component is observed at the hub by the blade compared to a configuration without cavity since the swirl fraction of cavity flow is generally lower than in mainstream. This crossflow has been shown to drive passage vortex development by giving an early start to secondary flows and could explain the stronger radial movement of secondary vortices as stated by Zlatinov et al. [54]. Stronger secondary vortices does not yield directly to stronger losses since entropy generation does not coincide with the main vortex cores indicating that the vortex itself is not the direct loss generation mechanism as stated by Zlatinov et al. [54]. The strong cross flow component at the inlet of the passage being accelerated when moving further downstream, the passage vortex induces a blockage effect generating high radial velocities. Associated loss generation is then mainly due to cross and radial velocity gradient occurring between passage vortex and blade suction side. However, by measuring the pressure distribution around the blades at different height, he concluded that the impact of purge air flow remained onto the first 50% of the blade. He noticed that regions of pressure losses corresponded with the location of secondary vortices. These observations were also reported by Paniagua et al. [112] and de la Rosa Blanco [34]. Using thermographic measurements and applying a different temperature between the mainstream and purge flow, Schuler [114] was able to show that purge flow was literally feeding the passage vortex.

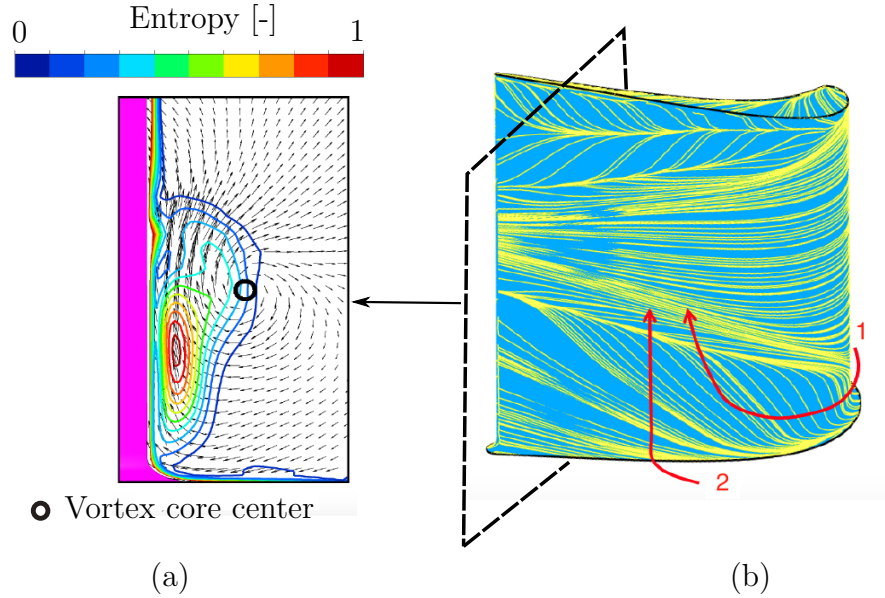


Figure 2.19: Regions of entropy generation in an axial plane with vortex center (a). Radial velocity across the blade due to crossflow (1), blockage (2) contributions (b)

The radial velocity can be associated with two effects: the crossflow component of the flow directed radially as it comes up against the blade (see (1) in Fig. 2.19b) and streamwise component of the flow deviated as a consequence of flow blockage (see (2) in Fig 2.19b). When purge flow blows into the mainstream without swirl or with a lower swirl than the mainstream, in the frame of the subsequent blade row, this purge flow has a strong crossflow component. The crossflow layer near the hub, and

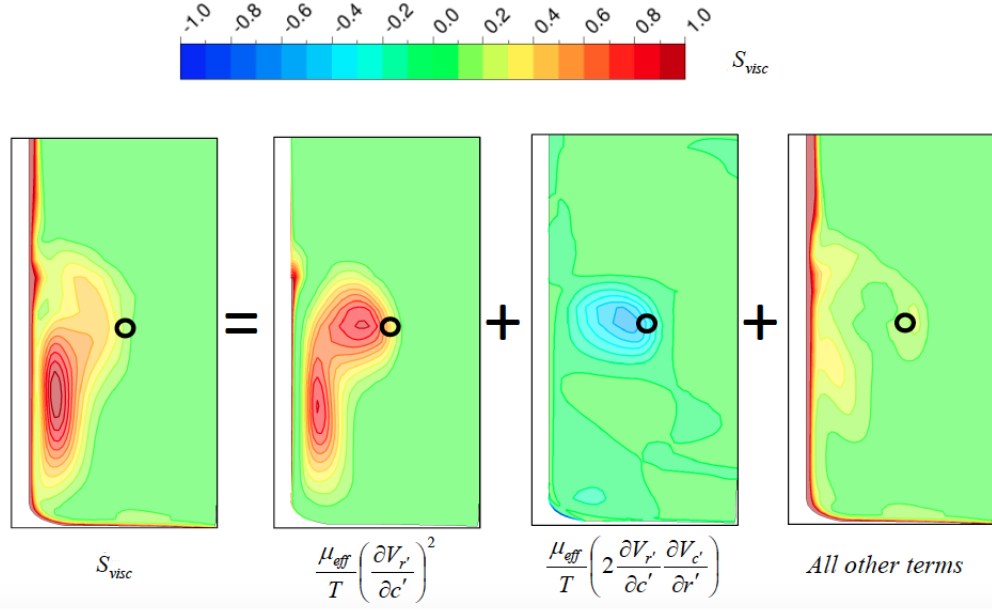


Figure 2.20: Decomposition of entropy production according to the velocity gradients (see eq.(3.12) p.146 for more details). From Zlatinov et al. [54]

consequently the passage vortex are given an early start due to purge flow blowing. As a consequence, the passage vortex core migrates toward mid-span as observed in experiments. Early development and radial migration of the passage vortex has two consequence: more fluid is swept by the vortex towards the blade suction surface and the blockage effect associated with the vortex is increased. These two features enhance the generation of radial flow on the blade suction surface and subsequent losses. The swirl component of purge flow is therefore an important parameter in loss generation for secondary flow as well as the migration of the passage vortex. These detrimental effects can be reduced by increasing swirl of purge flow.

Additional losses incurred by the purge flow blowing into the mainstream are first induced at the rim seal interface due to a mixing layer. The purge flow promotes a local blockage effect for the upstream row close to the hub while potential higher reaction rate in downstream row. Cavity flow experiences entrainment effect by the developing pressure leg of the horse shoe vortex that strengthen secondary vortices, secondary kinetic energy and the subsequent related losses.

Losses generated in a gas turbine can be analyzed based on the first and second law of thermodynamics leading to a composite quantity between the state of the flow and the level of irreversibility known as exergy that quantify the available energy in the purpose to generate work. This analysis makes possible to set under a same basis the different phenomena that contribute to modification of the available work for the gas turbine at the different scale including the local one at which they occur. For current applications at large Reynolds numbers, the turbulence needs to be accounted in the analysis since delaying the direct relation between dissipation of mechanical energy into heat. The phenomena inducing loss in a gas turbine that occur locally are generally treated at a larger scale in the literature to be more easily characterized. These physical mechanisms are strongly related to the incoming unsteadiness and the boundary layer development on the wetted surfaces. Blade, hub and shroud boundary layers contribute to loss generation due to wall-normal velocity gradients and additional losses emanating from the secondary vortices induced by the interaction of hub/shroud boundary layer with blades. The purge flow induces losses at the rim seal interface, due to mixing processes, change of reaction rate and increased secondary vortices.

A mathematician will recognise Cauchy, Gauss, Jacobi or Helmholtz after reading a few pages, just as musicians recognise, from the first few bars, Mozart, Beethoven or Schubert.

— Ludwig Boltzmann

3

Linear cascade configuration

This chapter is focused on the numerical simulation of a low speed linear cascade with an upstream cavity including different rim seal geometries and purge flow rates. This simplified configuration compared to real geometries makes possible to isolate the pressure asymmetry effect in the mainstream compared to the additional pumping effect that could have been incurred by a rotating configuration. Based on the comparison with experiments conducted on this configuration, the purpose is to assess the ability of different numerical solvers to recover the physical phenomena that occur in this configuration. Then, the flow field obtained numerically will be detailed to obtain insights and a better understanding of the interaction between purge and mainstream flow.

3.1	Experimental setup	82
3.1.1	Inlet parameters	83
3.1.2	Experimental data	84
3.2	Numerical setup and convergence	86
3.2.1	Numerical setup	86
3.2.2	Convergence	94
3.3	Experimental/numerical comparison	99
3.3.1	Flow around the blade	100
3.3.2	Pressure loss coefficient downstream blade	104
3.4	Main flow feature	106
3.4.1	Incoming boundary layer at shroud	106
3.4.2	Incoming boundary layer at hub	109
3.4.3	Blade flow feature	112
3.4.4	Flow downstream of the blade	113
3.5	Unsteady phenomena within the cascade	115

3.5.1	Horse shoe vortex process at shroud	115
3.5.2	Horse shoe vortex and Kelvin-Helmholtz process at hub	116
3.6	The influence of turbulence	118
3.6.1	Turbulence modeling	118
3.6.2	Turbulence injection in LES simulation using AVBP	125
3.7	Application of exergy formulation to track losses	129
3.7.1	Exergy analysis in the simulation domain	130
3.7.2	Influence of purge flow rate	151
3.7.3	Influence of rim seal geometry	156
3.7.4	Entropy generation from LES simulation	159

3.1 Experimental setup

Purge air flow contribution to turbine losses has been investigated during the European project MAGPI between 2007 and 2011 in which several industrials (Rolls-Royce, Siemens, Alstom, Industria de Turbo Propulsores S.A. (ITP), MTU, Avio, Turbomeca) and universities (Technische Universität Darmstadt, Karlsruhe Institute of Technology, Universidad Politecnica Madrid, University of Surrey, Università di Firenze) have been involved. The purpose was to improve qualitative and quantitative understanding of rim seal design and purge flow amount on aerodynamic performance of the turbine and sealing effectiveness. This study was based on two configurations extensively tested experimentally. These two configurations are studied during this chapter and in Chap. 4. The first configuration under investigation is a low-Mach linear cascade composed of five nozzle guide vanes set up at Karlsruhe university, Germany (see Fig. 3.1). The rig is set in an open circuit which includes an upstream honeycomb settling chamber, a centrifugal blower and a venturi pipe to target the desired inflow conditions. Upstream of the blade leading edge, the rim seal is included in a cavity module linked to the test section allowing to easily set different rim seal designs. The purge flow is supplied to the cavity as a fraction of the mainstream flow, respectively $\dot{m}_s/\dot{m}_m = 0, 0.5$ or 1% with a tangential component $\gamma = 45^\circ$ with respect to the span direction that mimic the entrainment effect of a rotor disc on the sealing flow. Main rig characteristics are gathered in Tab. 3.1. In order to promote periodic conditions on lateral sections of each blade of the cascade, adjustable tailboards were moved along rig channel's wall. Their position was moved until reach a low discrepancy for the pressure distribution around the blade for the three inner blade. The tolerated pressure coefficient mismatch at mid-span was set to 1% . This requirement is necessary to ensure that the comparison with numerical simulation for which only the central blade is simulated and periodic conditions are applied on the lateral sections is compliant. Three different rim seal geometries are studied during the experiments with a first geometries composed of an axial clearance (A) and two geometry using axial overlapping, simple (S) and double (D) (see Fig. 3.2).

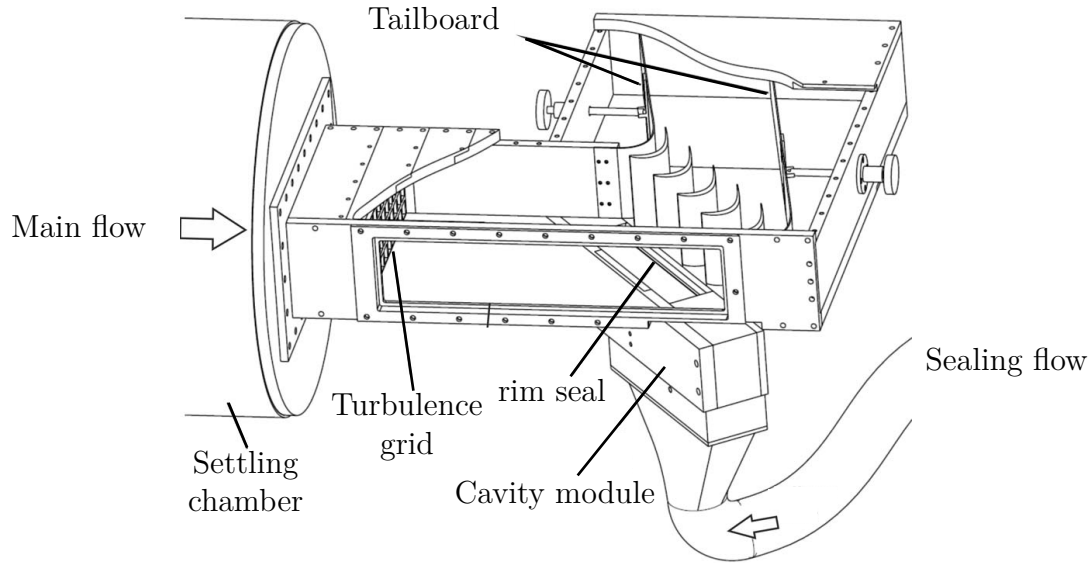


Figure 3.1: View of the experimental set up. Adapted from Schuler [114]

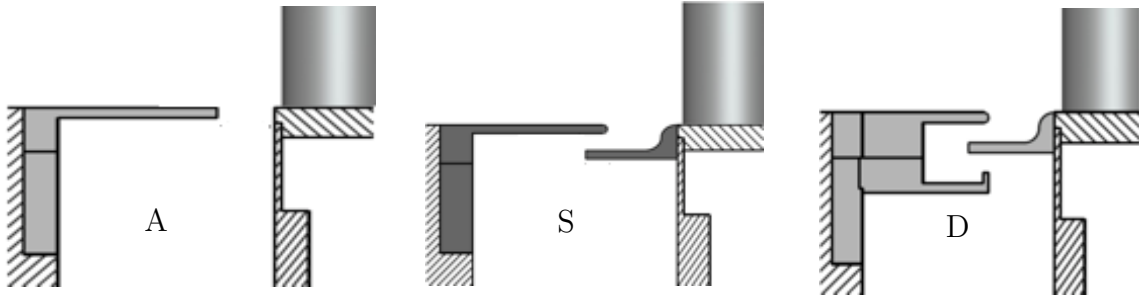


Figure 3.2: Rim seal geometry

3.1.1 Inlet parameters

Total pressure, temperature, azimuthal α and radial β angles profiles are provided at one axial chord length upstream of the blade leading edge by the experiments (see Fig. 3.3). Measurements of turbulence intensity have been conducted by means of a hot-wire probe upstream of the cascade. Free stream turbulence is produced by a turbulence grid positioned at seven axial chord length upstream of the blade leading edge. The grid has been designed to correspond to the correlation published by Roach et al. [118] on turbulence decay behind a grid and consists in 8 mm squared bars with an aperture of 25 mm. Measurements of turbulence intensity have been conducted at two different locations upstream of the leading edge at 50% blade height. This correlation and the experimental decay provides additional informations on the characteristic length of turbulence produced by the turbulence grid since influencing the decay rate. In Figure 3.4a, the decrease of resulting turbulence intensity is shown and compared to the correlation. The axis of abscissa represents the distance from the measurement point to the upstream turbulence grid. The turbulence intensity measured in the experiments agrees well with the correlation. In addition, the turbulence intensity at one axial chord length upstream of the blade leading edge ($x = 400$ mm) is shown to be $Tu = 6\%$.

Table 3.1: Characteristics of the cascade rig

cascade details		nominal conditions	
Inlet blade angle α_0	37.9 °	Re chord	5.6×10^5
Outlet blade angle	66.3 °	Exit Mach	0.22
C_x	75 mm	\dot{m}_m	1.13 kg/s
Aspect ratio	1.3	$p_{tot,in}/P_{out}$	1.035
h_{NGV}/C_x		\dot{m}_m/\dot{m}_s	0 - 0.5 - 1 %
s/C_x	0.884		

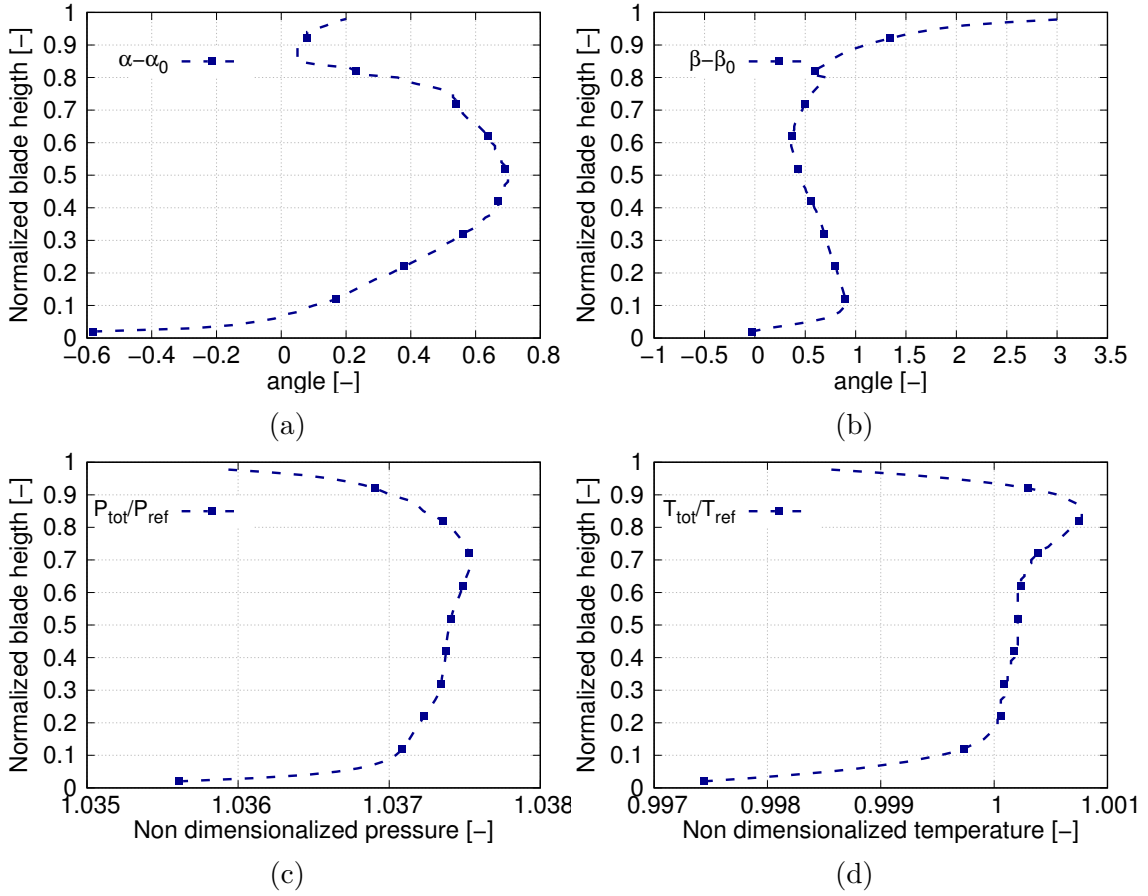


Figure 3.3: Inlet profiles at one axial chord length upstream of the blade leading edge: (a): azimuthal angle, (b): radial angle, (c): inlet total pressure (d): inlet total temperature. The height has been normalized by the height of the main annulus. $(P_{ref}, T_{ref}) = (101\,325\text{ Pa}, 300\text{ K})$

3.1.2 Experimental data

Measurements have been conducted by means of a calibrated five-holes probe. This kind of probe allows the complete determination of local total and static pressures as

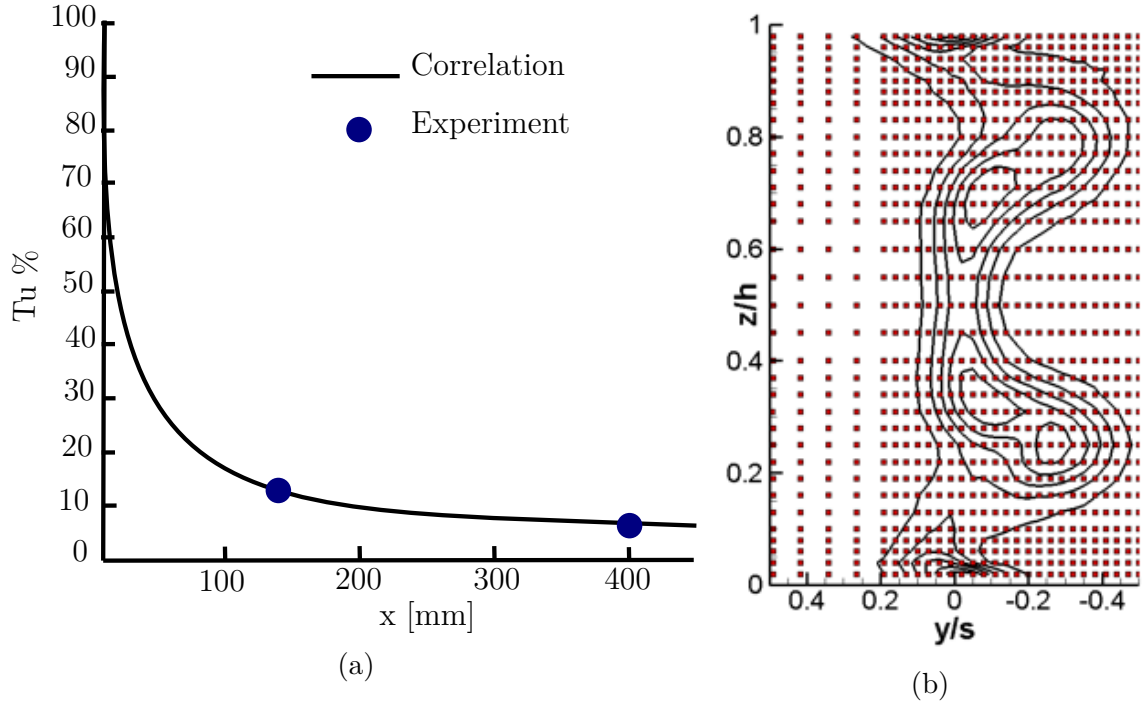


Figure 3.4: Turbulence intensity decay in the axial direction downstream the turbulence grid (a) and five-holes probe measurement positions (b)

well as relative flow directions at a point in a flow. The experimental determination of the total pressure loss is based on measurements in two planes, one axial chord upstream of the blade leading edge (station 1 in Fig. 3.5) and 25% axial chord downstream of the cascade, respectively (station 2 in Fig. 3.5). The five-holes probe has been moved inside these planes by means of a stepper motor and a traversing system over one pitch and the entire channel height. The resolution of the measurement grid in each plane is locally optimized and refined corresponding to the location of high total pressure gradients inside the flow (see Fig. 3.4b). The step-size varied between 2 and 5 mm considering that the boundary layer thickness at the outlet of the blade represents around 2 mm, while the endwall boundary layer and the regions corresponding to secondary vortices were traversed with minimum step-size.

Measurements of static pressure distribution around the blade surface at three different blade height 4, 6 and 50% have been performed. For this purpose, pressure tabs have been instrumented on the central blade. The instrumentation of the blades was confined to 80% of the axial chord-length, as the thin trailing edge did not permit to set any pressure tab. From experimental measurements, the pressure coefficient around the central blade the at 4, 6, 50% span and the total pressure loss coefficient 25% axial chord downstream of the blade defined as follows

$$C_p(x, z) = \frac{\bar{p}_{tot,1}(z) - p_{blade}(x, z)}{\bar{p}_{tot,2}(z) - \bar{p}_2(z)}, \quad (3.1)$$

$$\zeta(z) = \frac{\bar{p}_{tot,1}(z) - \bar{p}_{tot,2}(z)}{\bar{p}_{tot,2}(z) - \bar{p}_2(z)}, \quad (3.2)$$

have been used to compare blade loading as well as aerodynamic efficiency along the different parameters compared during this study. $\overline{p_{blade}}$ is the static pressure around the blade. The overline indicates that pressure is pitch-wise area averaged according to the two-dimensional measurement grid (azimuthal mean). Subscripts 1 and 2 refer respectively to a position one axial chord upstream of the blade leading edge and 25% downstream of the blade trailing edge (see Fig. 3.5). The experimental uncertainty was estimated to be $\zeta \pm 0.015$ for the pressure loss downstream of the blade and $C_p \pm 0.03$ for the pressure coefficient around the blade.

3.2 Numerical setup and convergence

3.2.1 Numerical setup

3.2.1.1 Simulation domain

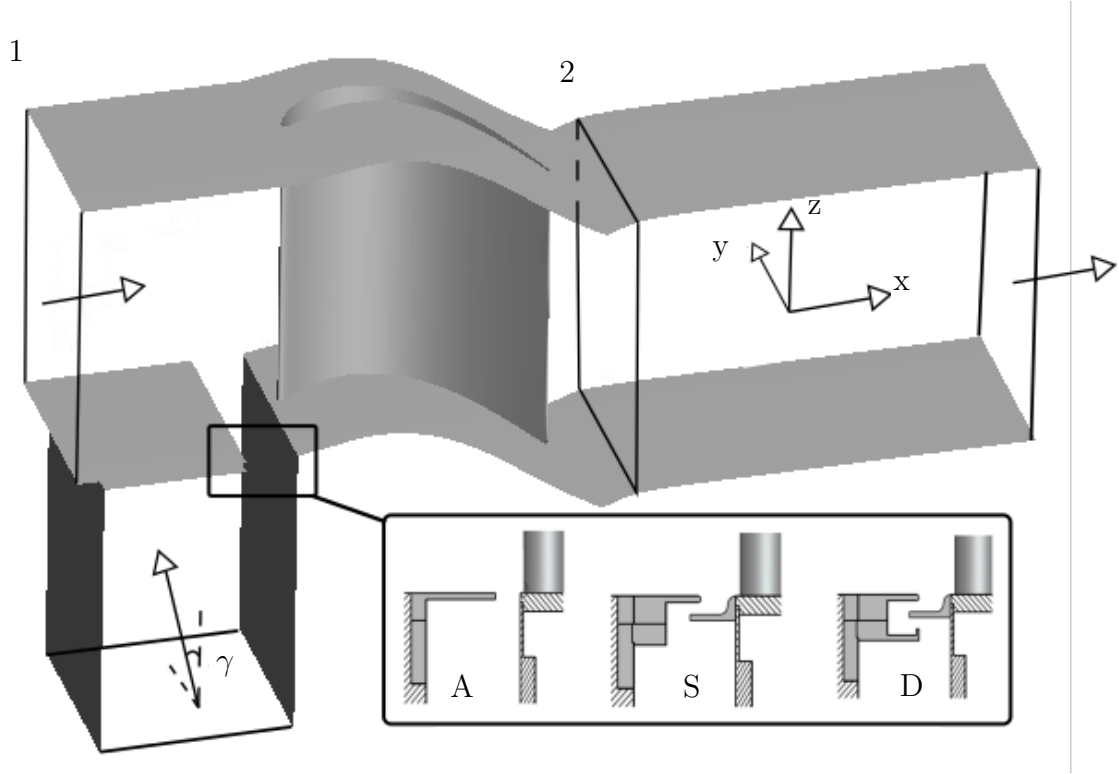


Figure 3.5: Simulation domain

For the present study, the simulation domain is composed of one blade and is focused on the flow around the central nozzle guide vane of the experimental test rig. The rim seal is set one axial chord downstream of the inlet to isolate the rim seal flow feature from inlet boundary. The outlet is located two axial chord-length behind blade trailing edge to avoid wave reflection issues. In this chapter, the different cases studied with the different geometries and purge flow rates will be denoted by a letter for the rim seal geometry (A: axial, S: simple overlapping, D: Double overlapping) and a figure for the purge flow rate (0: 0%, 05: 0.5%, 1: 1%). For

example, the configuration A05 stands for the axial rim seal geometry with 0.5% of the mainstream flow supplied in the cavity.

3.2.1.2 Boundary conditions

The linear cascade normal Mach number of the fluid at the inlet is lower than unity. Subsonic boundary conditions are applied at the inlet and outlet of the domain. At the inlet, total pressure, total temperature and velocity direction profiles are applied according to the experimental data introduced previously. Uniform velocity and temperature profiles are applied at the bottom of the cavity to meet desired purge flow (0, 0.5 or 1% of the mainstream flow). The purge flow is supplied radially with a tangential component ($\gamma = 45^\circ$, see Fig. 3.1) at a slightly lower temperature than the mainstream one to follow the purge flow mixing with the main annulus one ($T_{cavity}/T_{main} = 0.9$). This temperature ratio between the mainstream and cavity flow is higher than in real low pressure turbine configurations where the ratio can be in the order of magnitude of 0.6 at the first low pressure turbine stage. This value increases along the stages. Periodic conditions are applied on the lateral boundaries (y-axis direction)¹ and walls are considered as adiabatic. This last condition should be representative of the experiments since the temperature gap between the mainstream and cavity flow is quite low and in a steady state. The wall temperature should be close to the mainstream one. Wlassow [46] that performed coupled (aerodynamic and thermal) high-pressure turbine simulations showed the low influence of the heat flux at the wall on aerodynamic since the thermal power is generally low compared to the power extracted by the turbine to the flow. Denton [48] discussed the influence of heat flux at wall and observed that these effects are generally negligible but can be important in relatively low-diameter gas turbine where wetted surfaces and thermal power can become important compared to the work extracted.

3.2.1.2.1 RANS

The turbulent quantities are prescribed for the RANS simulations based on the turbulence intensity provided in the experiments $T_u = 6\%$ and a characteristic length based on the width of the squared section grid used to generate upstream turbulence. The outlet is modeled by a throttle condition to target the experimental mass flow by a variation of the throttle parameter λ ,

$$p_{out}(t) = p_{ref} + \lambda \dot{m}^2(t) \quad (3.3)$$

with p_{ref} a reference pressure taken at an arbitrary radius R_{ref} .

3.2.1.2.2 LES

Conversely to the RANS simulations, the inlet and outlet conditions for elsA LES

¹It may be emphasized that applying periodic boundary conditions on lateral sections induce a phase synchronization for the flow along the different nozzle guide vanes of the linear cascade that may be not the case in the experimental configuration. However, this impact has not been considered. This effect becomes a source of inaccuracies generally in presence of very large scale turbulence and/or in presence of large flow separations.

and AVBP solvers, former conditions are coupled with the Navier-Stokes Characteristics Boundary Condition (NSCBC) [119] to avoid wave reflection in the simulation domain in conjunction with a shift of the outlet position.

3.2.1.2.3 LES-LBM

The experimental pressure and velocity profiles are applied at the inlet since the solver is based on a weakly-incompressible formulation around a reference temperature.

Without any additional mention, the figures related to the meshing and convergence criteria that will be showed in the next subsection are based on the axial rim seal geometry at an intermediate purge flow (A05 case) since the geometry and purge flow rate induce marginal deviation for these quantities.

3.2.1.3 Meshing strategy

3.2.1.3.1 RANS

The simulations have been performed using the ONERA code elsA [120] solving the compressible Navier-Stokes equations over multi-block structured grids. This approach is generally suitable for configuration where only the mainstream is taken into account or with relatively simple technological effects. The take into account of more complex geometries and technological effects using structured grids are generally made by using a chimera approach (see for example Wlassow [46] and Tang [121] for high-pressure turbine applications) or hybrid methods coupling structured and unstructured meshes in the simulation domain (see for example Tucker et al. [122]). The main annulus domain is discretized in same way for all three rim seal geometries based on a multi-block approach using a O-6H meshing strategy for the nozzle guide vane. The O-block around the blade makes possible to describe accurately

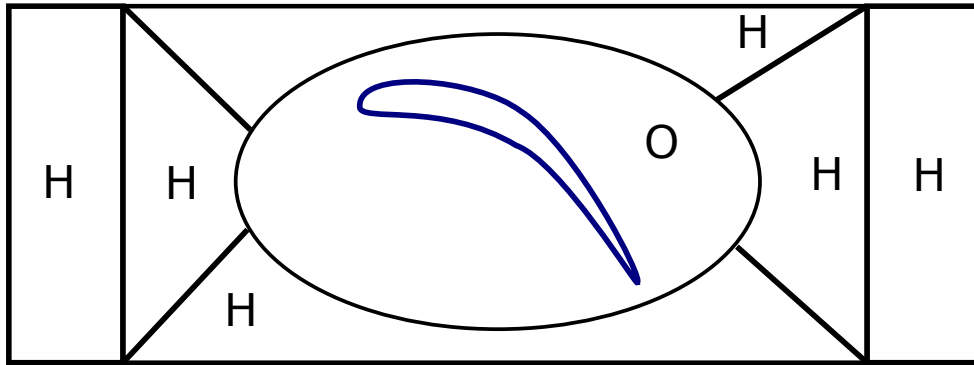


Figure 3.6: Structured multi-block O-6H topology

the boundary layer keeping orthogonality errors as low as possible. The 6 H-block around the O-block discretizes the remaining domain. The topology for the nozzle guide vane is built to have an orthogonality² higher than 30°, aspect ratio³ lower than 1000. In near-wall region, these criteria are checked to have orthogonality higher

²The angle between two contiguous faces of the considered cell

³The ratio between the longer and shorter edge of the cell

than 80° , lower than 500 for aspect ratio and an expansion ratio⁴ lower than 1.2 (see Fig. 3.8a). The geometry with the cavity is meshed using a matching approach without any chimera approach. The mesh size close to the wall is set to 5×10^{-6} m in order to reach the quality requirements for a wall-resolved simulation $y^+ < 1$ (see Sec. A.3.2.3 p.246). Figure 3.7 shows y^+ distribution around the blade, at the hub and shroud obtained from the RANS simulation. y^+ remains below unity for the different wetted surfaces. The mesh is refined at the blade leading and trailing edge, in the wake region and at the interface between the cavity and mainstream. The mesh is coarsened when approaching the outlet of the domain to prevent any reflection of wake structures on the outlet condition. The mesh is composed of around 7 million cells for the different geometries. Pau et al. [123] used a similar number of grid points in a high pressure turbine at $Re=1.1 \times 10^6$ with the same structured flow solver.

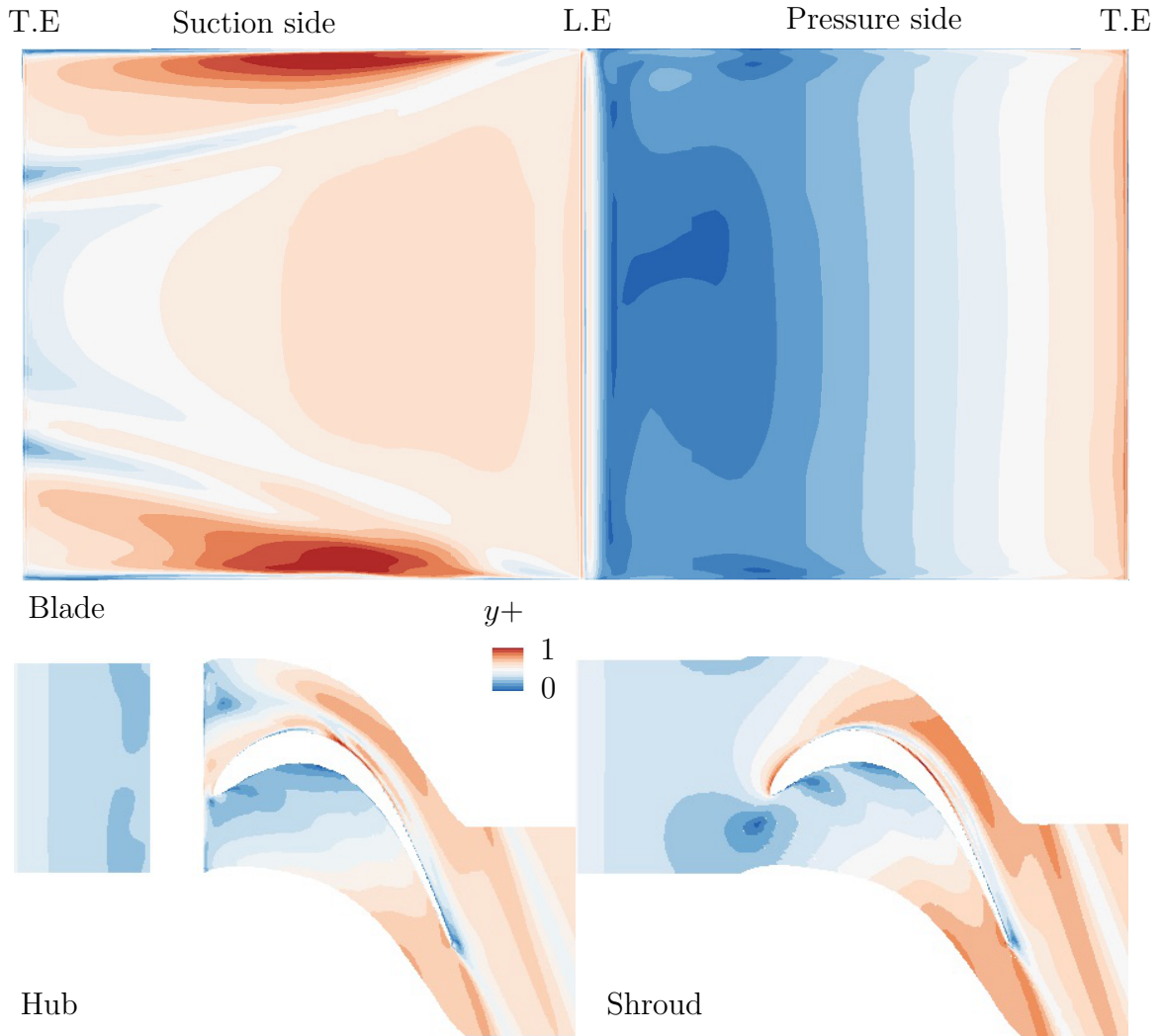


Figure 3.7: y^+ distribution around the wetted surfaces: unwrapped blade (top), hub and shroud (bottom) for the RANS simulation. LE and TE stand respectively for leading and trailing edge

⁴The ratio of the edge length between two successive cells

3.2.1.3.2 LES

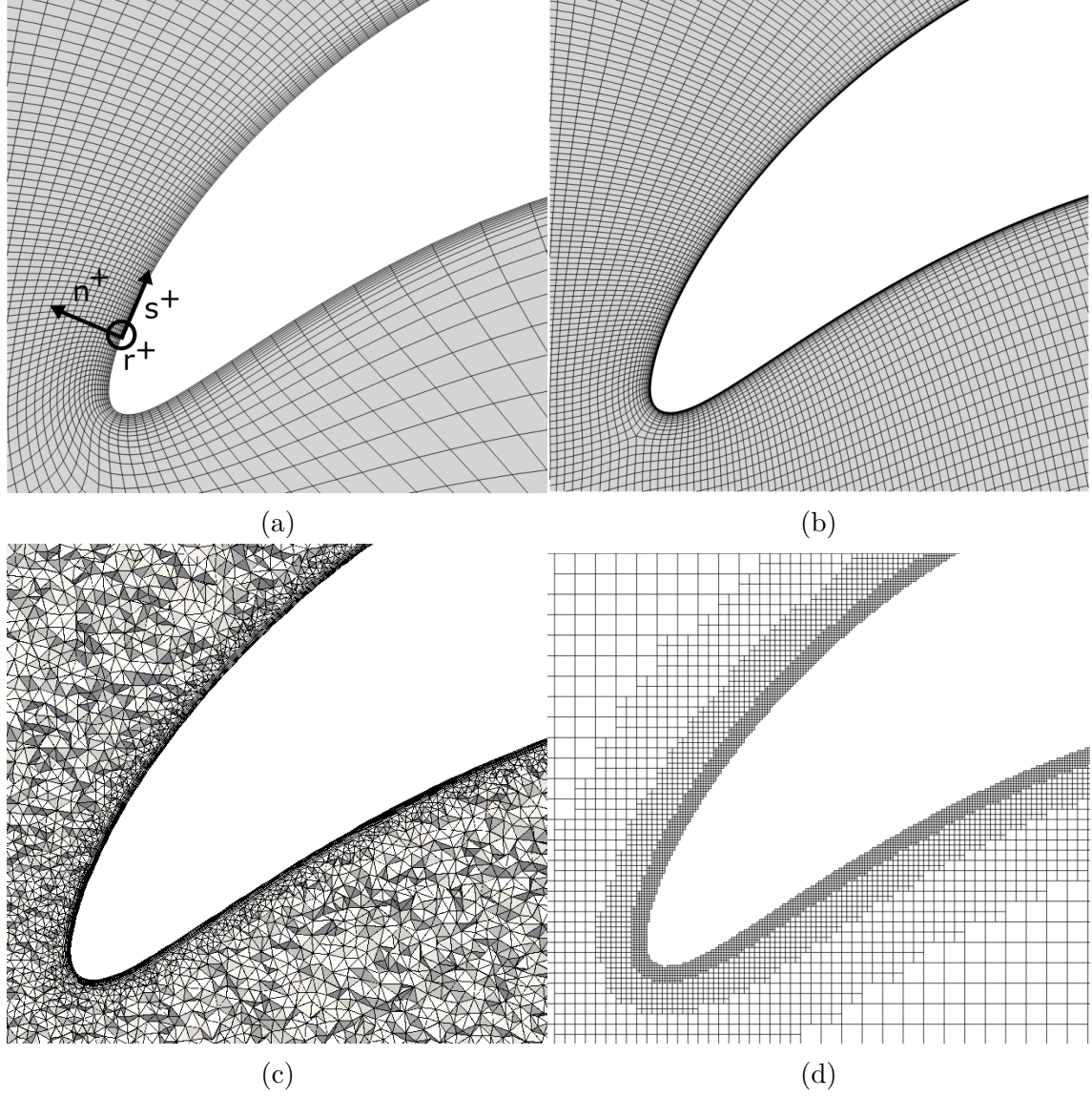


Figure 3.8: Leading edge discretization (a) : RANS elsA, (b) : LES elsA, (c) : LES AVBP, (d) : LES-LBM Pro-LB

elsA The meshing strategy for the LES solver based on structured grid keeps the same topology as for the RANS simulation described previously (see Fig. 3.8b). LES mesh quality requirements close to the blade and wakes have to be as high as possible to prevent insufficient gradient resolution. For the T106C configuration simulation, Pichler et al. [124] provided almost perfect orthogonality around blade and deviation by more than 15 degrees in the wake region. The stretching ratio between the size of neighbouring cells was set below 1.04. For the current study, minimum orthogonality remains higher than 30° with orthogonality around 80° in near-wall regions. The aspect ratio is also decreased compared to the RANS approach by applying the criteria furnished in the literature to fulfil recommendation

for wall-resolved LES in near-wall region [125][126] proposed in Sec. A.3.2 (p.245). These criteria were first set to $50 \leq s^+ \leq 150$; $n^+ \leq 1$; $15 \leq r^+ \leq 40$, where (s^+, n^+, r^+) is the local curvilinear coordinate system close to the wall. The notation y^+ and n^+ will be used indifferently, y^+ being generally used for Cartesian coordinates considering wall-normal coordinate as y (notation generally used for the study of a boundary layer over a flat plate) while n^+ is generally used when wall-normal direction is not y and along curved surface where the wall-normal component can change along the surface. More recent works are alleged to show that these values need to be lowered especially in the spanwise direction to capture the streaks aligned with the streamlines in the near-wall region. LES simulation conducted by Cui et al. [76] on the T106A configuration set grid requirements close to the wall to $s^+ \leq 30$; $n^+ \leq 1$; $r^+ \leq 30$. Similarly, Pichler et al. [124] performed LES simulation over T106C configuration where the grid requirements close to the wall were set to $s^+ \leq 50$; $n^+ \leq 2$; $r^+ \leq 15-20$. For the current study, mesh refinement criteria close to the wall have been refined to reach $s^+ \leq 80$; $n^+ \leq 1$; $15 \leq r^+ \leq 25$ (see Fig. 3.9, and 3.10) leading to a mesh of around 60 million cells.

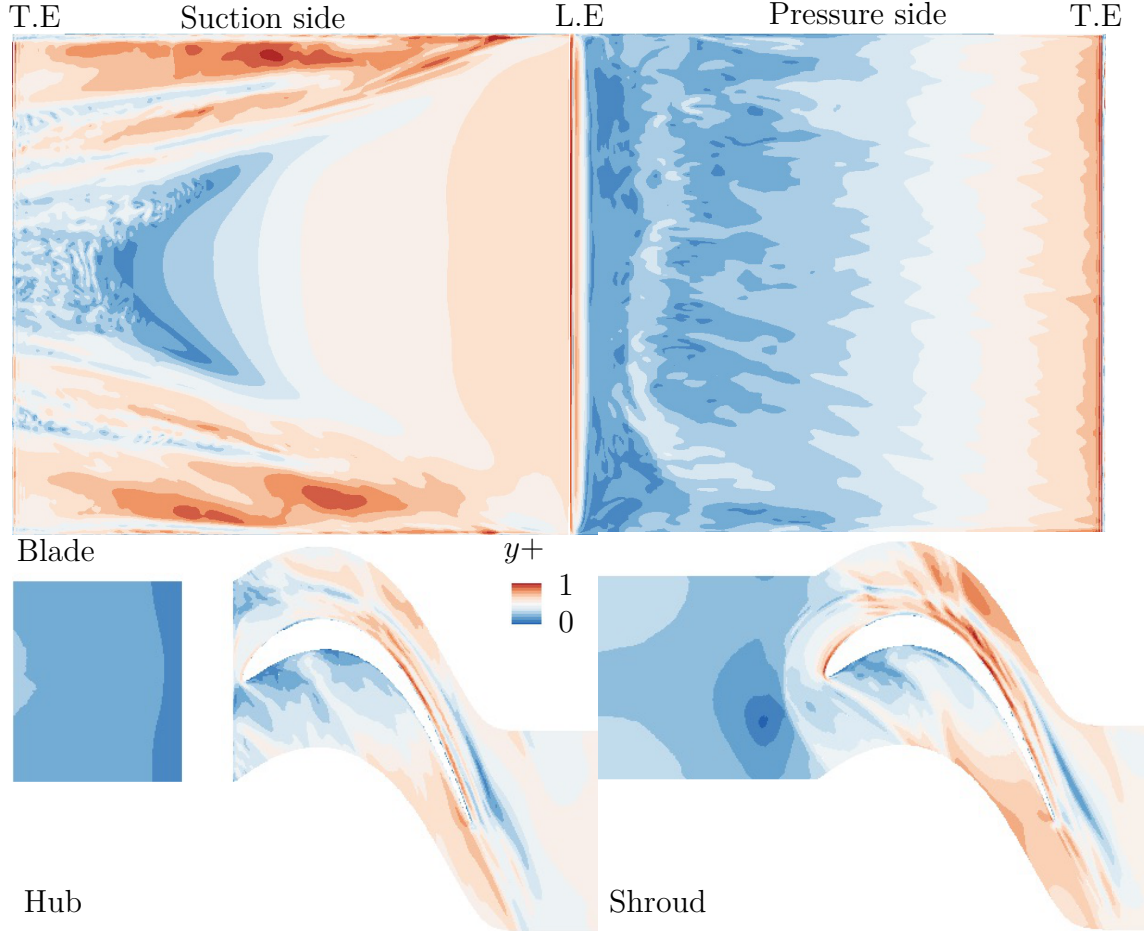


Figure 3.9: y^+ distribution around the wetted surfaces: unwrapped blade (top), hub and shroud (bottom) for the LES elsA simulation (temporal average). LE and TE stand respectively for leading and trailing edge

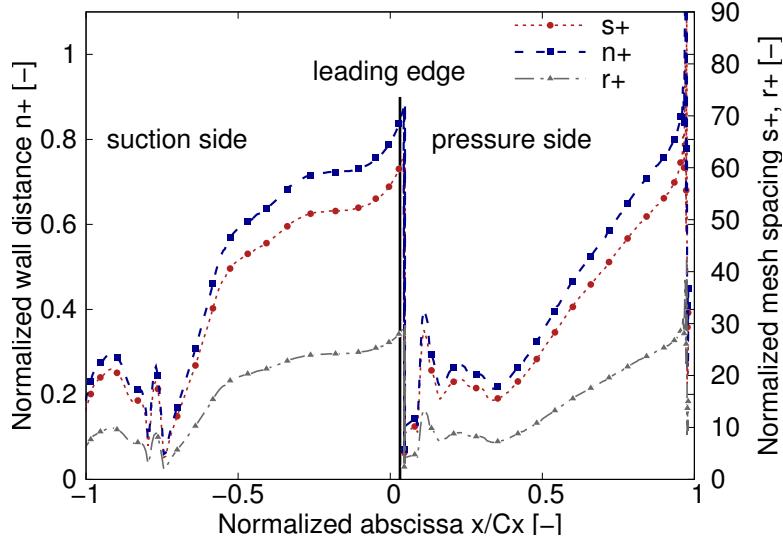


Figure 3.10: Averaged grid dimension at the wall for the LES elsA simulation, s^+ : streamwise, n^+ : normal, r^+ : spanwise

AVBP For the unstructured LES approach, a layer of 15 prisms in near-wall regions is applied with an expansion ratio of 1.05 and a maximum $y^+ \simeq 3$ on blade suction side. Tetrahedra elements fill the remaining domain (see Fig. 3.8c). In addition, pyramids are used in some locations to allow for a transition between the prisms and the tetrahedra. Since an explicit temporal scheme is only available for this approach, CFL number has been set to 0.7 to ensure the stability of the numerical simulation

LES-LBM Unlike former described domain discretization based on a body-fitted approach, LES-LBM approach is based on an Immersed Boundary Model (IBM) with octree elements and multi-domain grids refinement (see Fig. 3.8d). Since the mesh size is the same in all three directions, a wall-resolved simulation is not possible at a reasonable cost for the current Reynolds number because no stretching of the cell is tolerated in axial and span direction as it was done for finite volume approaches. Furthermore, a filter used in the solver to improve the stability prevent from having layer with same characteristic length lower than six cells (no expansion ratio possible in the layer conversely to the finite volume approaches). The Mesh is then unrefined close to the wall to recover a similar number of degree of freedom and physical time step compared to the other LES approaches leading to a $y^+ \simeq 40$. The law of the wall treatment derived by Afzal [127] is used to correctly recover the flow behaviour (friction velocity and velocity profile) at the first fluid node above the wall.

3.2.1.4 Numerical parameters

3.2.1.4.1 RANS

An upwind Roe scheme with third-order limiter is used for the convective terms [128]. Diffusive fluxes are computed with a second-order centred scheme. The Wilcox $k-\omega$

two-equations model with Zheng’s limiter is used to evaluate turbulent quantities while avoiding strong sensitivity to free stream conditions. This turbulence model was selected since widely used and calibrated for turbomachine application at Cerfacs, see for example Daroukh et al. [129] and good practises were developed by Gourdain et al. [130, 131] in a turbomachinery context. Menter also showed that the $k-\omega$ model does well for flows with adverse pressure gradients [132] that are supposed to occur on the aft (diffusion) portion of the blade suction side and along pressure side close to the leading edge.

3.2.1.4.2 LES

elsA The mesh quality in current application was not high enough to use the sixth-order compact finite-volume scheme [133] available in elsA to solve convective fluxes and promoted the use of a second order centred scheme with the Jameson artificial viscosity [134] ($\kappa_{jam.}^4 = 0.002$). This scheme is generally preferable to Roe schemes used for RANS simulation because, despite of a lower order, it avoids the dissipative nature of upwind scheme. Subgrid scale model is the Wall-Adapting Local Eddy-viscosity (WALE) [135] specifically designed to compute turbulent effects in wall-bounded flows by recovering the proper y^3 near-wall scaling for eddy viscosity. The time step is adapted to mesh resolution close to the wall $\Delta t^+ = \Delta t u_\infty / C_x = 10^{-5}$ (i.e. 1 500 time steps per axial chord length). The temporal integration is achieved with a Dual Time Step (DTS) approach based on an implicit backward Euler scheme with sub-iteration Newton’s algorithm (second order accurate). The maximum CFL number based on the cubic root of the smallest cell volume in the domain remains lower than 11 out of the near-wall region. In addition, the same simulation has been performed with a time step $\Delta t^+ = 4 \times 10^{-5}$, residuals in the sub-iterations of the implicit loop were difficult to converge and are alleged to indicate that the time step close to $\Delta t^+ = 10^{-5}$ used for the different approaches is compliant with the configuration studied.

AVBP The convective operator is discretized by the two-step Taylor-Galerkin scheme [136] that is the high-order numerical scheme available in AVBP compared to the Lax-Wendroff scheme. The diffusion operator is discretized using a method close to the Galerkin finite element method (second order accurate). The simulation time step based on the explicit time advancement is $\Delta t^+ \simeq 10^{-6}$.

LES-LBM Pro-LB The particle velocity space is discretized using the D3Q19 lattice. A main implication is that no difference in temperature can be set between the main and cavity flow since solving the isothermal, incompressible Navier-Stokes equations. The spatio-temporal resolution is based on the characteristic method while a regularized BGK method is used for the collision operator. The subgrid scale model is the Approximate Deconvolution Model (ADM) [137] based on an explicit selective spatial filtering that have shown good behaviour in LES of incompressible wall-bounded flows [138]. A summary of the numerical parameters for the various solvers is given in Tab. 3.2 and 3.3.

Table 3.2: Numerical setup for the Navier-Stokes numerical approaches

Numerical approach	Convective scheme	Temporal scheme	Turbulence model/SGS
RANS	Upwind (3^{rd} order) Centered (2^{nd} order)	DTS	k- ω Wilcox
LES elsA	Jameson ($\kappa_{jam.}^4 = 0.002$)	DTS ($\Delta t^+ = 10^{-5}$)	WALE
LES AVBP	TTGC (3^{rd} order)	Explicit (CFL = 0.7) $\Delta t^+ \simeq 10^{-6}$	σ -model

Table 3.3: Numerical setup for the LBM numerical approach

Lattice	Space/Time discretization	Collision operator	SGS
D3Q19	Characteristic method	BGK scheme + regularization step $\Delta t^+ \simeq 1.6 \times 10^{-5}$	ADM

3.2.2 Convergence

3.2.2.1 Numerical convergence

3.2.2.1.1 RANS

The convergence is shown here for A05 configuration only but all other rim seal geometries and purge mass flow rate showed similar behaviour. The evolution of the normalized mass flow rate at the inlet, cavity inlet and outlet are given in Fig. 3.11. After approximately 20 000 iterations, the inlet mass flow rate reaches a plateau and the sum with inlet cavity leads to differences lower than 0.1% compared to the outlet mass flow rate. Figure 3.12 shows the residual convergence of continuum, first momentum, energy and turbulent quantity equations. The increase at approximately 250 000 iterations corresponds to the passage from Van Albada to a third order limiter. All residuals have decreased their magnitude of more than three orders and reached a plateau. According to the convergence criteria proposed in Sec.A.4.1 (p.249), RANS simulations have reached a converged state.

3.2.2.1.2 LES

elsA According to the numerical convergence criteria for unsteady simulation exposed in Sec. A.4.2 (p.249), the simulation time is expressed in terms of flow

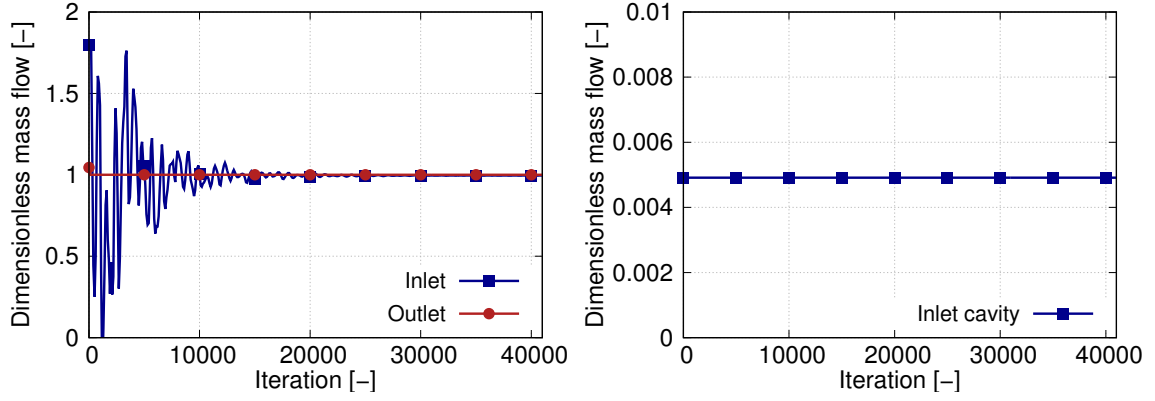


Figure 3.11: Evolution of the mass flow rate at the inlet, cavity inlet and outlet based on the number of iterations performed (RANS)

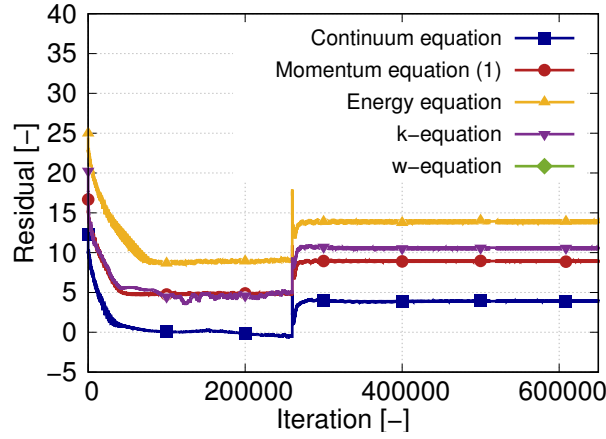


Figure 3.12: Convergence of continuum, first momentum, energy and turbulent residuals (logarithm scale) for the RANS simulation

through i.e. the characteristic time for a particle to move along the cavity at a convection velocity corresponding to the one in the cavity plus the time for the particle to move from the rim seal to the exit of the mainstream domain, $t_{chara.} = h_{cav}/u_{cav} + L_{main}/u_{main}$ where h_{cav} , L_{main} , u_{cav} and u_{main} are respectively cavity height, mainstream axial width, mean velocity in the cavity and in the mainstream. Since the cavity convective velocity is very low compared to the mainstream one, the characteristic time is mainly the transport time in the cavity. The convergence time is generally higher for simulations taking into account the cavity compared to smooth configurations because the flow in the cavity needs more time to converge. The convergence is shown here for the A05 configuration only but all other rim seal geometries and purge mass flow rates showed similar behavior. The evolution of the normalized mass flow rate at the inlet, cavity inlet and outlet are given in Fig. 3.13 in terms of particles that would have travel along the domain at fluid velocity speed (one flow through). The domain of fluctuation for the inlet is higher than for outlet due to larger sponge zone at the outlet than at the inlet.

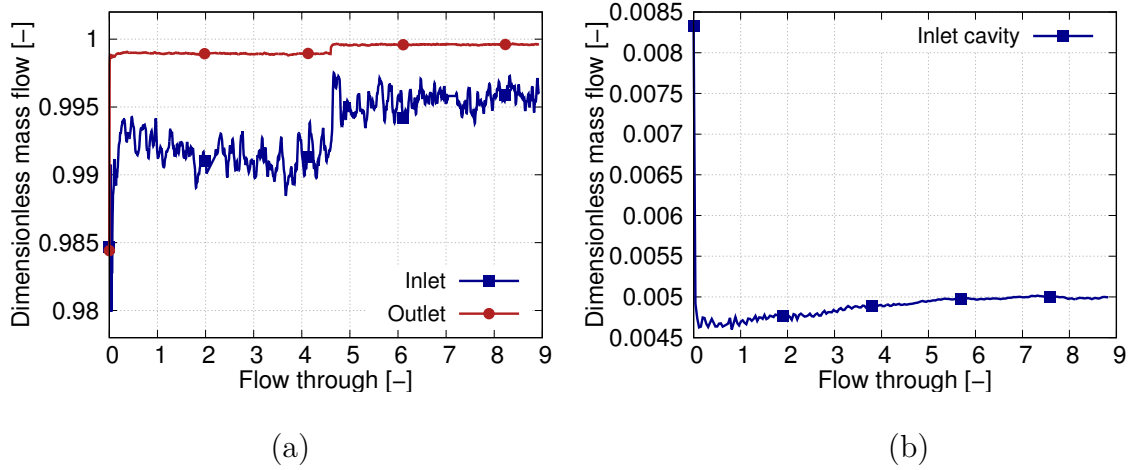


Figure 3.13: Evolution of the mass flow rate at the inlet, outlet (a) and cavity inlet (b) in time for the LES elsA simulation

AVBP Similarly to elsA LES approach, the evolution of the mass flow rate at the inlet and outlet of the domain for the AVBP simulation is proposed in Fig. 3.14. After a similar number of flow through, the inlet and outlet purge flow rates converge towards the same value with a discrepancy lower than 0.1%. Table 3.4 shows the

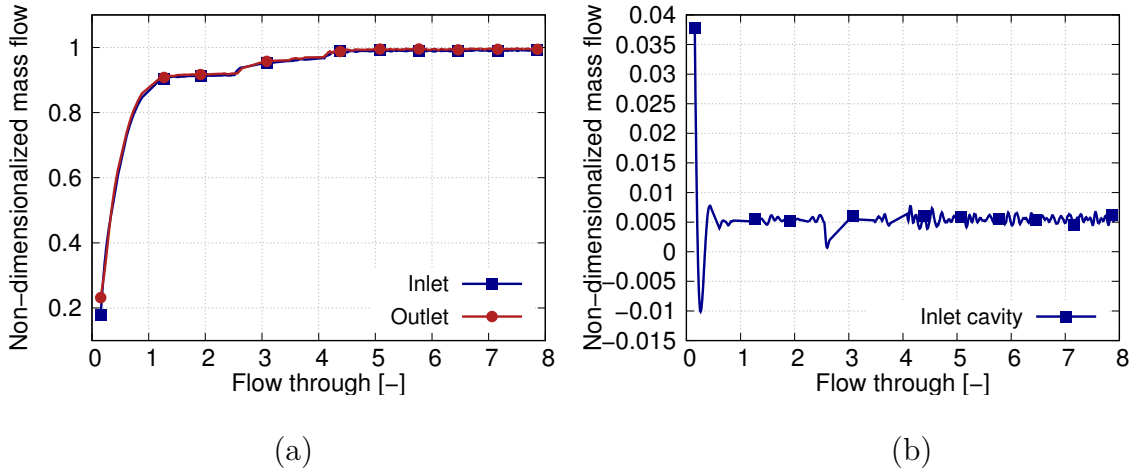


Figure 3.14: Evolution of the mass flow rate at the inlet, outlet (a) and cavity inlet (b) in time for the LES AVBP simulation

number of CPUs used for each simulation and the whole computational time.

3.2.2.2 Mesh dependency

The mesh convergence is proposed for the different numerical approaches by comparing the pressure coefficient around the blade and the pressure loss coefficient downstream of the blade for the standard and a refined mesh used only for the mesh convergence study. Most of the published studies related to turbine stages use the mean blade pressure distribution and pressure loss profiles downstream blades. These quantities give an assessment of the ability of the mesh to properly capture

Table 3.4: Evalation of computational cost

	RANS	LES-LBM	LES AVBP	LES elsA
Flow through	-	13	11	11
Number of CPUs	96	360	360	360
Cost/flow through	-	1600	9000	12 000
Total cost (CPUh)	1100	20 800	99 000	132 000

the different gradients in the flow field that will affect the aerodynamic quantities and level of loss downstream blade. In addition, this quantity is readily extracted numerically and from experiments when available. However, in LES simulations, more stringent criteria based on turbulence statistics often emanating from DNS practice can be used to assess the convergence and give a more accurate indication of grid convergence. For the present study, the grid convergence is based on the pressure loss downstream of the blade but this last point will be discussed in more details in the section related to loss generation proposed in Sec. 3.7.

3.2.2.2.1 RANS

In order to assess the grid convergence for the RANS simulation, an additional grid has been generated where the transverse mesh size (s,r) have been refined and the expansion ratio in the wall normal direction has been decreased to 1.1. Figure 3.17 shows the pressure coefficient around the blade and the pressure coefficient downstream of the blade for A05 configuration for the standard and refined mesh grids. For the pressure coefficient around the blade, a local discrepancy of 5% can be observed on suction side close to the wall at 4 and 6% blade height (see Fig. 3.15a and 3.15b). For the pressure loss coefficient downstream of the blade, a similar local discrepancy can be observed especially in the two main peaks of loss. However, results for the standard and fine grids are in relatively good agreement to indicate grid convergence.

3.2.2.2.2 LES

In order to assess grid convergence, the simulations have been performed on refined grids for the various LES approaches with a similar number of cells (approximately 100 millions). The simulations are performed for the A05 configuration.

elsA The mesh has been mainly refined in the span direction to capture the streaks aligned with the streamlines in near-wall region ($r^+ \leq 15$). Additionally, the mesh has been refined in the streamwise direction ($s^+ \leq 50$) and the expansion ratio has been decreased to 1.03.

AVBP For the LES AVBP approach, the mesh has been refined in the wall normal direction to reach $n^+ \simeq 1$.

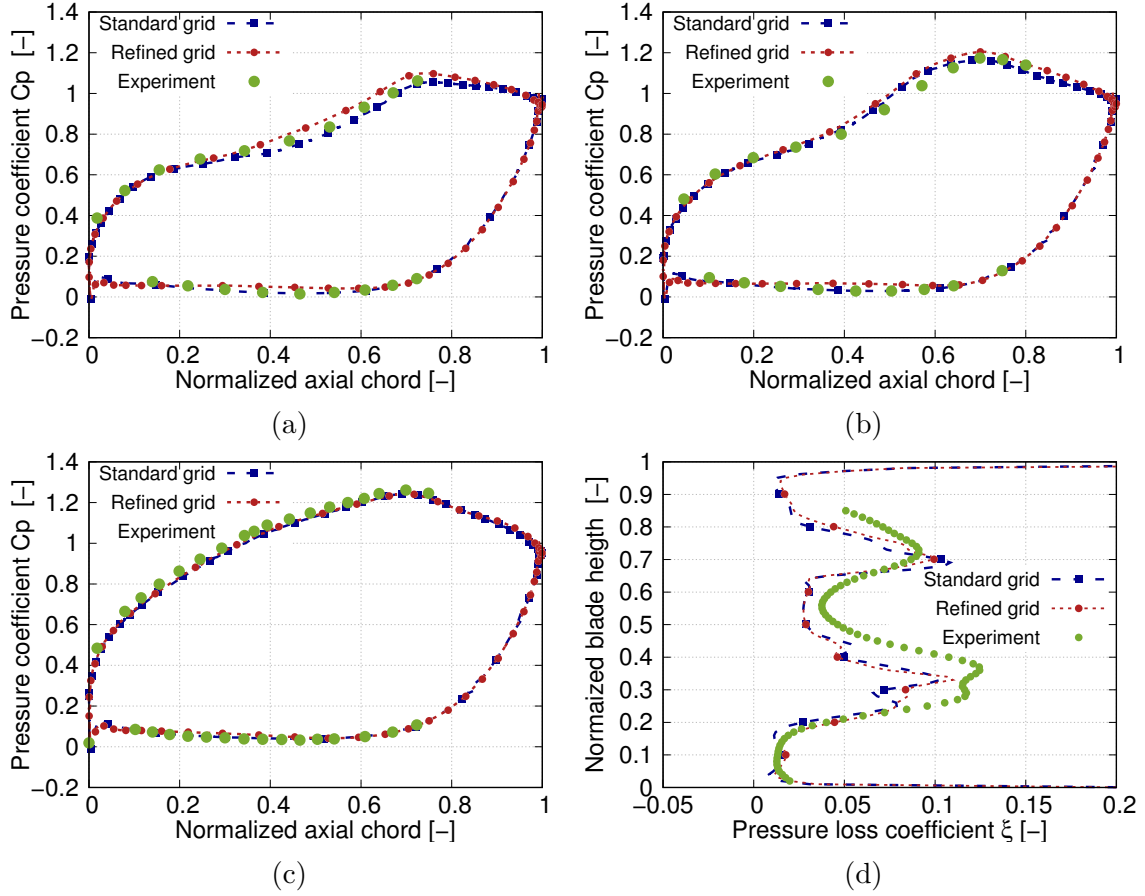


Figure 3.15: Comparison of the pressure coefficient distribution around the blade (a): 4%, (b): 6%, (c): 50% and pressure coefficient downstream of the blade (d) for the A05 configuration for the standard and refined mesh grid (RANS simulation)

LES-LBM For the LES-LBM approach, an increase in the mesh size in the same order of magnitude as other approaches has led to a decrease in the mesh size in near-wall region to $n^+ \simeq 25$. Figure 3.16 shows the comparison of pressure distribution downstream blade for the A05 configuration for the different LES approaches with the two mesh refinement. The change in mesh size shows local discrepancy in the order of magnitude of 5% in loss peak region for the elsA and AVBP approaches. For the LES-LBM approach, the discrepancy is slightly higher with locally differences of 8%. Despite these local differences, the results between standard and refined meshes are in relatively good agreement.

3.2.2.3 Influence of turbulence modeling

In order to assess the influence of the turbulence modeling on the RANS simulation, a simulation has been performed using the one equation Spalart-Allmaras model compared to the $k-\omega$ Wilcox two equations model used to perform the various simulations. Figures 3.17a, 3.17b and 3.17c show the pressure coefficient around the blade for the RANS simulation with $k-\omega$ turbulence and Spalart-Allmaras turbulence modeling for the A05 configuration. Pressure coefficients are close to each

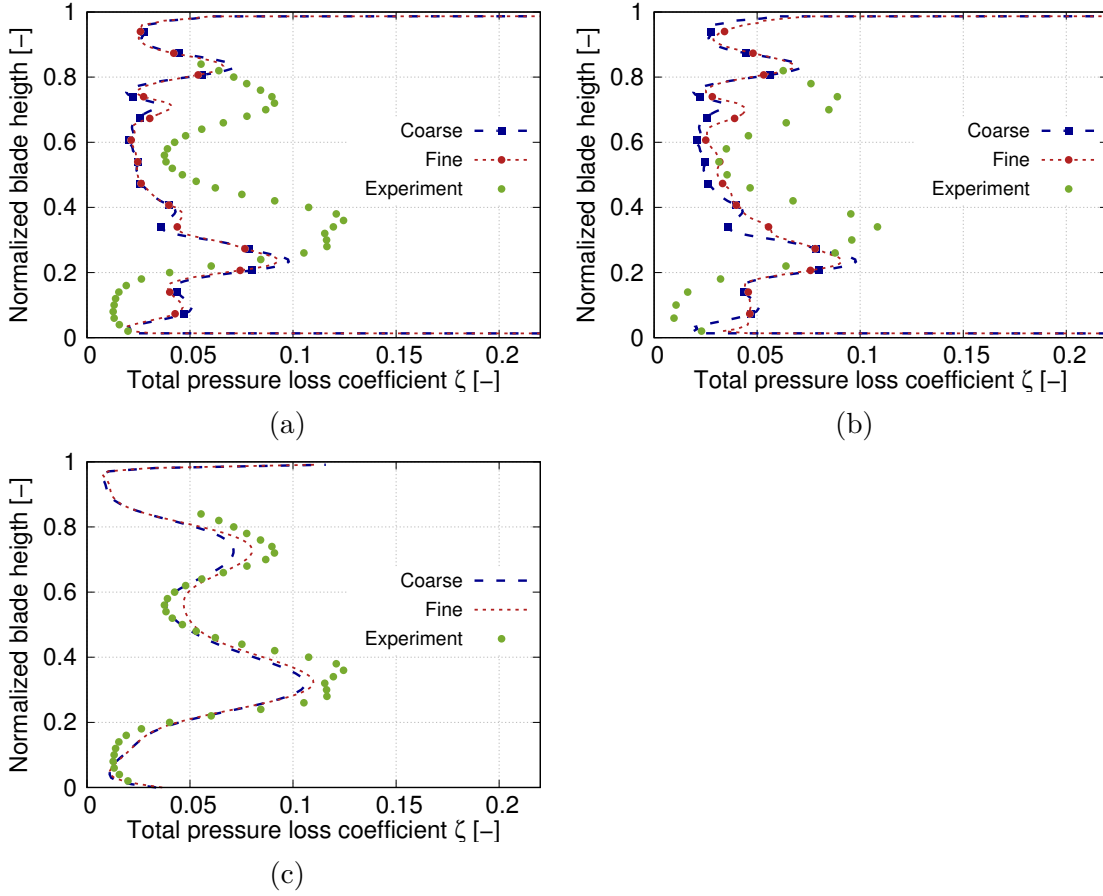


Figure 3.16: Comparison of the pressure loss coefficient downstream of the blade for the A05 configuration for coarse and fine grids, (a) : LES elsA, (b) : LES AVBP, (c) : LES-LBM Pro-LB

other except at 6% span where some discrepancy can be observed at around 60% chord. Concerning pressure loss coefficient downstream blade, the discrepancy in the results between the two different turbulence models are larger. In particular, the pressure losses are more important for Spalart-Allmaras turbulence modeling. An additional pressure loss is almost well distributed along blade span. The analysis of the boundary layer thickness based on a vorticity magnitude criterion (see Fig. 3.18) shows that the boundary layer is thicker for Spalart-Allmaras turbulence modeling than with $k-\omega$ model both on the blade suction and pressure side. Using a control volume analysis, Denton [48] has demonstrated that the profile loss on the suction surface of the aerofoil is proportional to the momentum thickness at the trailing edge θ_{te} (see Sec. 2.2.3.1). This trend is observed at different span and explains the main pressure loss difference between the two turbulence model.

3.3 Experimental/numerical comparison

The purpose of this section is to compare the numerical results obtained from the different solvers (RANS elsA, LES elsA, AVBP and LES-LBM Pro-LB) against ex-

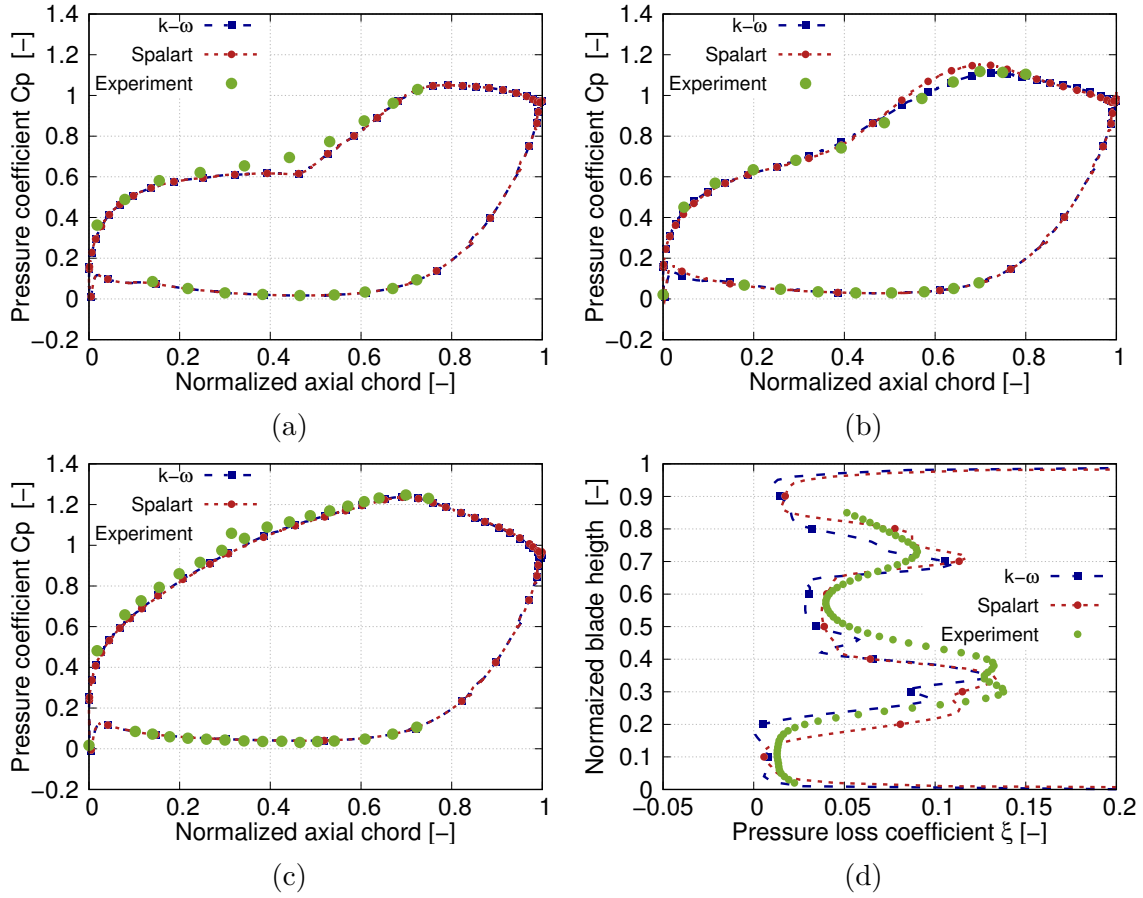


Figure 3.17: Comparison of the pressure coefficient distribution around the blade at (a): 4%, (b): 6%, (c): 50% span and pressure coefficient downstream of the blade for the A05 configuration for $k-\omega$ and Spalart-Allmaras turbulence model (RANS)

perimental results available. The comparison is conducted for the A05 configuration to assess the capability of the different codes to predict the correct trend with cavity and purge flow. Y-error bars are included in the plots to take into account experimental uncertainty described in Sec. 3.1.2 (p.86) that was estimated at $C_p \pm 0.03$. In the definition of the pressure coefficient C_p , the pressure around the blade p_{blade} is subtracted to the pressure at the inlet meaning that the suction side pressure coefficient is the top curve while the pressure side is the bottom one.

3.3.1 Flow around the blade

3.3.1.1 RANS

Figure 3.19 shows pressure coefficient blade at 4, 6 and 50% span for the A05 configuration. The comparison against experiment is first conducted at mid-span where the flow can be supposed to follow an ideal flow behaviour and endwall contributions are normally low (see Fig. 3.19c). However, the effect of endwalls may be visible at midspan due to the streamtube contraction effect driven by the growth of secondary flows. Its effect could be assessed by performing a purely 2D simu-

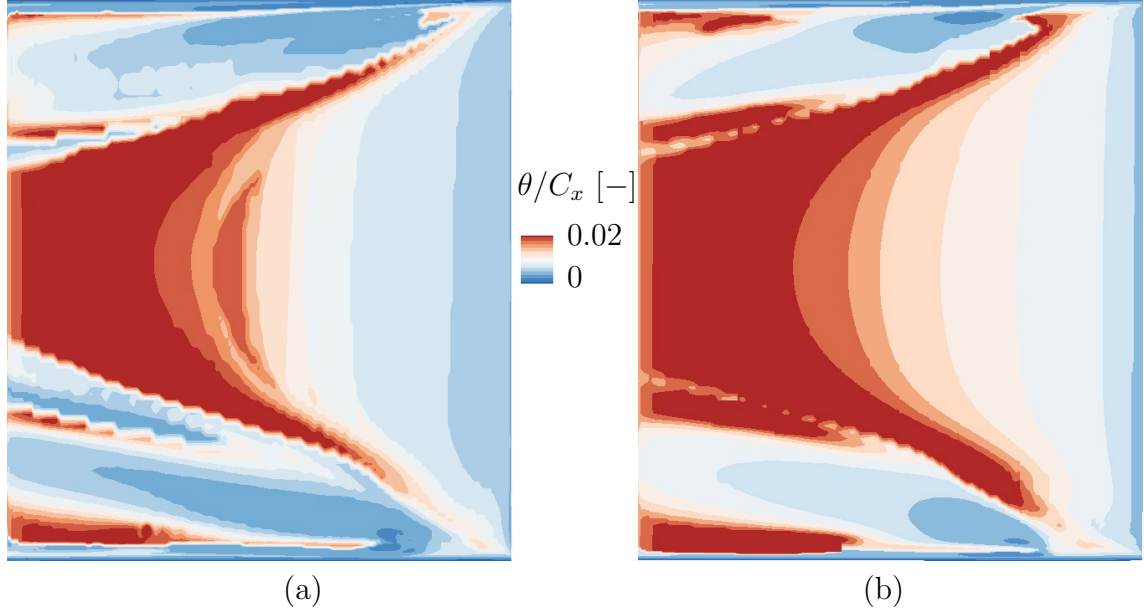


Figure 3.18: Suction side boundary layer thickness from k- ω turbulence model used in the study (a) and Spalart-Allmaras model (b)

lation. On the blade suction side (top curve), the flow initially accelerates on the favourable pressure gradient portion (decreasing pressure portion) until $x/C_x = 0.7$ that corresponds to the passage throat. Downstream, the flow velocity starts to decline when it encounters the adverse pressure gradient downstream of the throat until the blade trailing edge. This portion of the blade suction side is sometimes referred as the diffusion portion of the blade suction side. The pressure coefficient on the blade suction side is relatively well predicted by RANS simulation. Despite a lack of experimental pressure measurements downstream the throat, the trend inversion at this location shown by the experiments is predicted by the RANS simulation. On the blade pressure side, the RANS simulation agrees well with available experimental data between $x/C_x = 0$ and $x/C_x = 0.75$. The pressure coefficient on this portion is almost constant then increases steadily until the blade trailing edge with a positive pressure gradient. A localized adverse pressure gradient is observed close to the blade leading edge. The pressure coefficient on pressure side is almost insensitive to the span, while decreasing on the blade suction side when approaching the hub. Blade loading or lift that provides work on the turbine shaft being determined based on the area circumscribed by these pressure curves, it decreases close to the hub. Since the blade is two-dimensional in span, these differences in pressure coefficient are only due to the flow around the blade, which is more affected by the wall close to the hub.

Figures 3.19a and 3.19b show pressure coefficient around the blade at 4 and 6% span. A similar trend for suction and pressure side pressure coefficient can be observed compared to mid-span. The flow is well predicted by RANS simulation on the blade pressure and suction side. However, pressure coefficient is slightly overpredicted between $x/C_x = 0.4$ and $x/C_x = 0.7$ at 6% span.

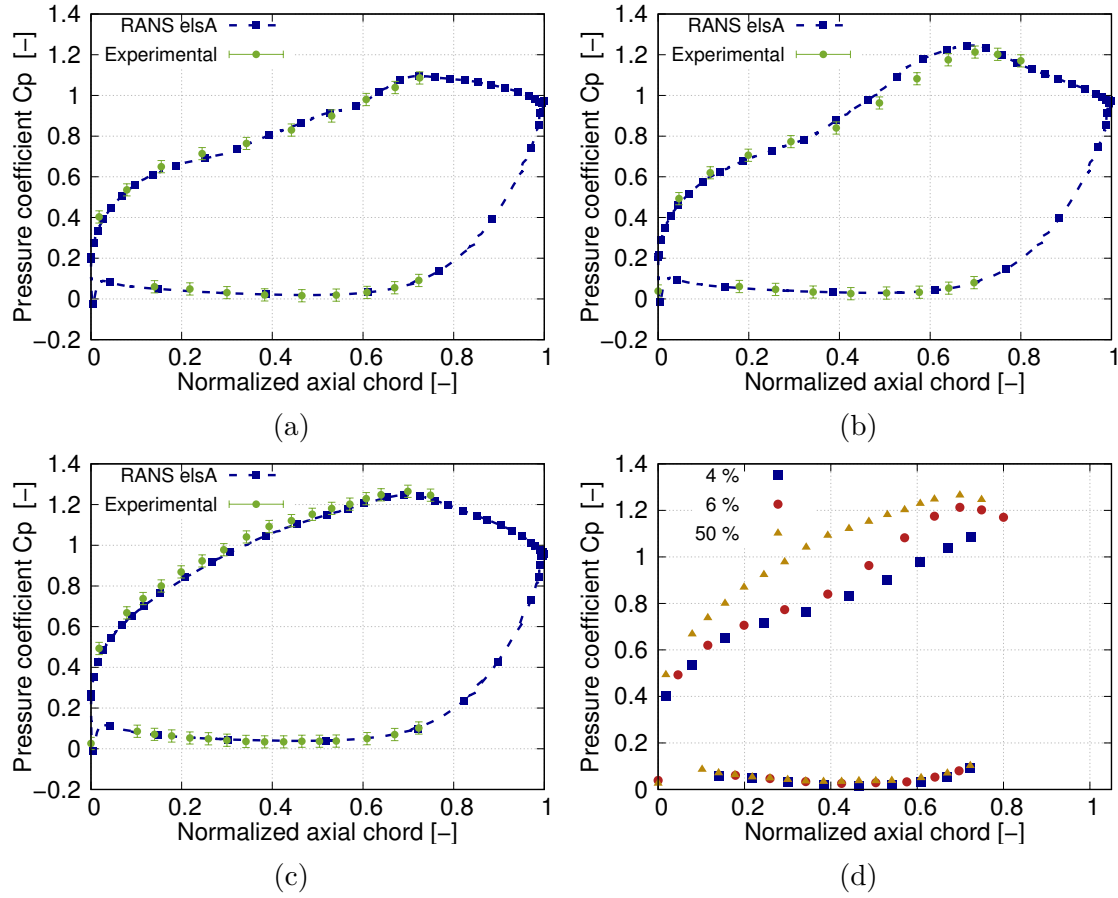


Figure 3.19: Pressure coefficient around the blade at (a): 4%, (b): 6%, (c): 50% span for the A05 configuration using RANS approach and experimental results at the different blade height (d)

3.3.1.2 LES

3.3.1.2.1 elsA Figure 3.20 shows the pressure coefficient around blade at 4, 6% and 50% span. At mid-span, pressure coefficients are in good agreement compared to the experiments. On the blade suction side, an inflectional portion can be observed that was not observed in the RANS simulation. Since no experimental data is available at this position, no conclusion can be drawn between the RANS and LES at current stage concerning this different behavior. Close to the hub (4 and 6% span), pressure side coefficient is well predicted by LES approach. On blade suction side, the pressure coefficient is slightly underpredicted until mid-chord then overpredicted but remains in good agreement with experiments.

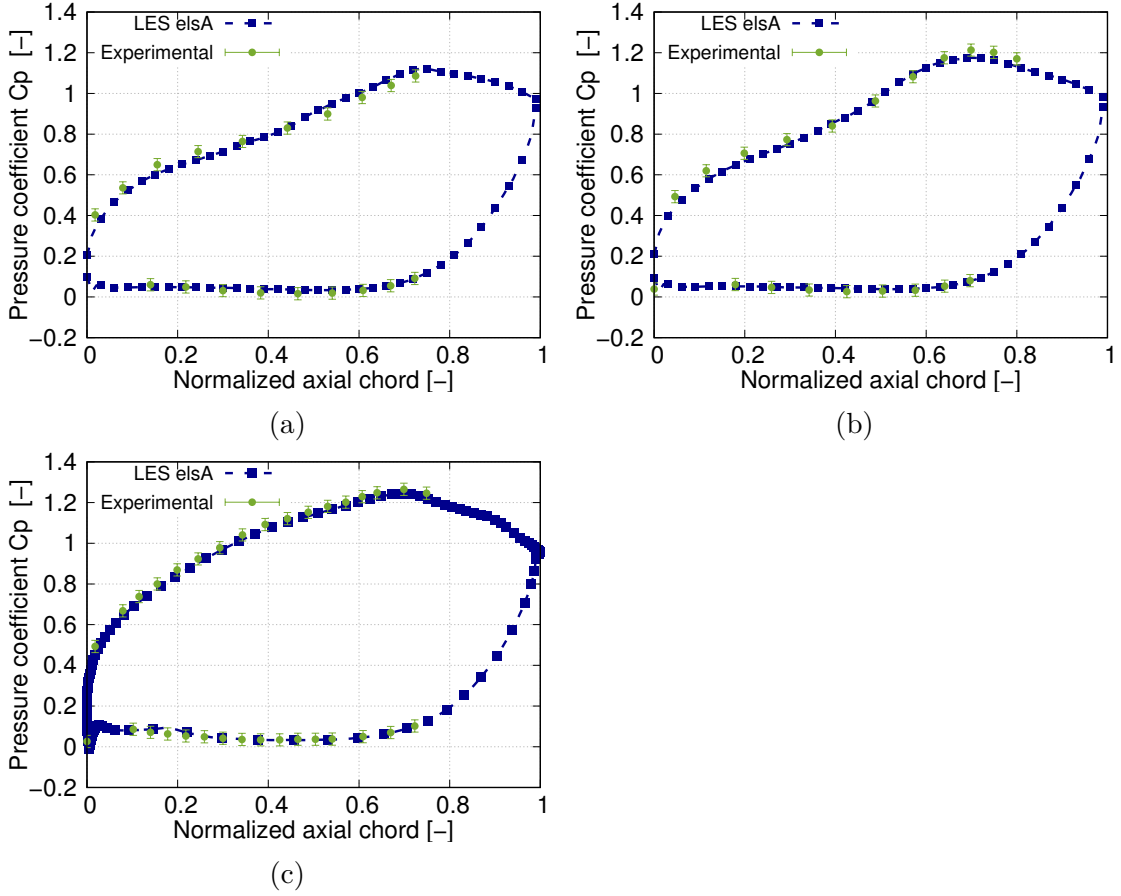


Figure 3.20: Pressure coefficient around the blade at 4, 6 and 50% span for the A05 configuration using the LES elsA approach

3.3.1.2.2 AVBP Figure 3.21 shows pressure coefficient around blade the A05 configuration based on LES AVBP simulation. At mid-span, the pressure coefficient distribution around the blade is in good agreement with the experiments. Similarly to the LES elsA simulation, an inflection of pressure loss coefficient is observed at around $x/C_x = 0.8$ in the adverse pressure gradient portion. Close to the hub, a similar trend can be observed compared to the LES elsA simulation with a pressure coefficient distribution underestimated in the first half blade length and overestimated elsewhere.

3.3.1.2.3 Pro-LB Figure 3.22 shows the pressure coefficient around the blade for the A05 configuration based on Pro-LB simulation. The pressure coefficient is slightly underestimated at mid-span (around 3% of discrepancy) without inflection point observed at mid-span compared to LES elsA and AVBP solvers. Close to the hub, pressure coefficients are in good agreement compared to the experiments at the locations where experimental measurements were available.

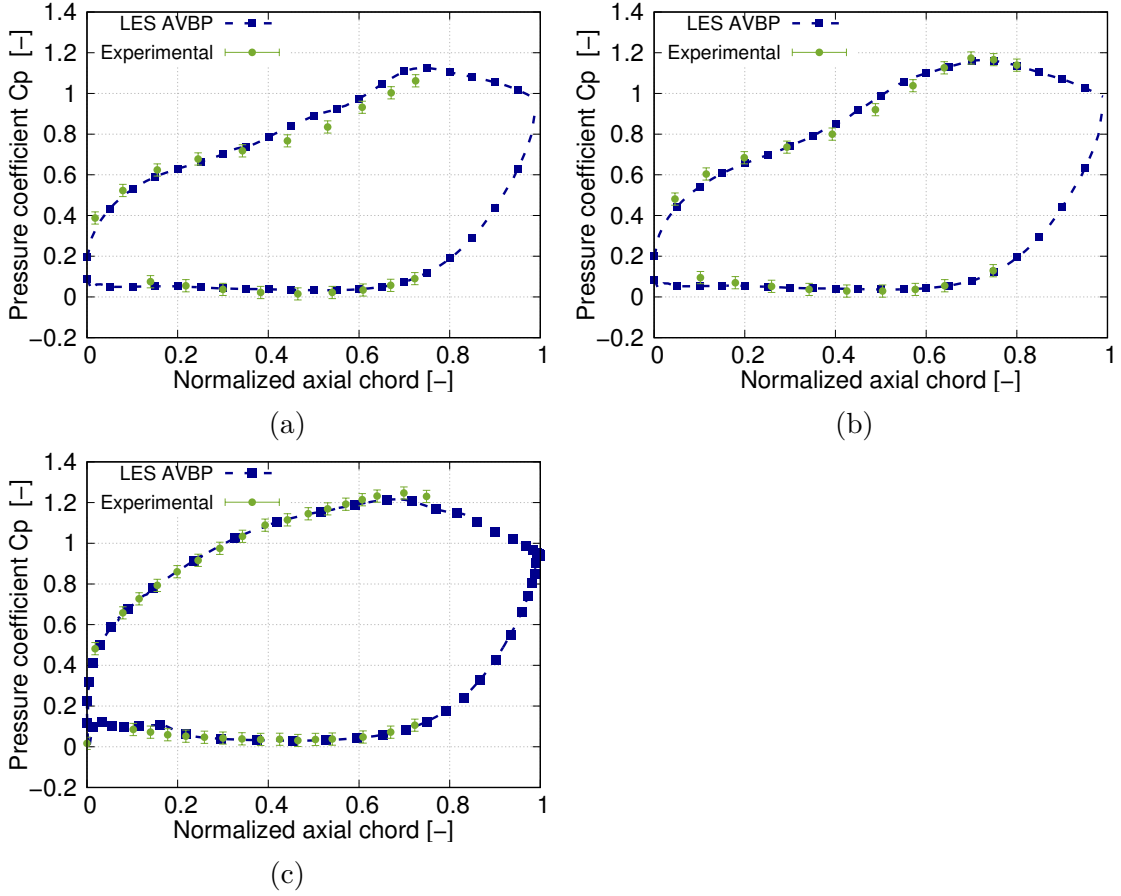


Figure 3.21: Pressure coefficient around the blade at (a): 4%, (b): 6%, (c): 50% span for the A05 configuration using the LES AVBP approach

3.3.2 Pressure loss coefficient downstream blade

Figure 3.23 shows the pressure loss coefficient downstream of the blade for the A05 configuration for the different numerical solvers used in this study.

3.3.2.1 RANS

Close to the hub and shroud, Fig. 3.23a high values of pressure loss coefficient that corresponds to the hub and shroud boundary layers where total pressure is lower than in the mainstream one. A pressure peak can be observed at approximately $h/H = 0.35$ that is relatively well captured by the RANS simulation both in terms of position and amplitude. In the mid-span region between $h/H = 0.4$ and $h/H = 0.6$, a region of low pressure loss coefficient can be observed. RANS simulation shows some discrepancies compared to the experiments with a flatter pressure distribution in this region. On the upper part of the blade, another pressure loss coefficient peak can be observed at around $h/H = 0.7$. The RANS simulation predicts a pressure peak with higher amplitude and slightly shifted towards mid-span compared to the experiments (around 4% of spanwise shift discrepancy).

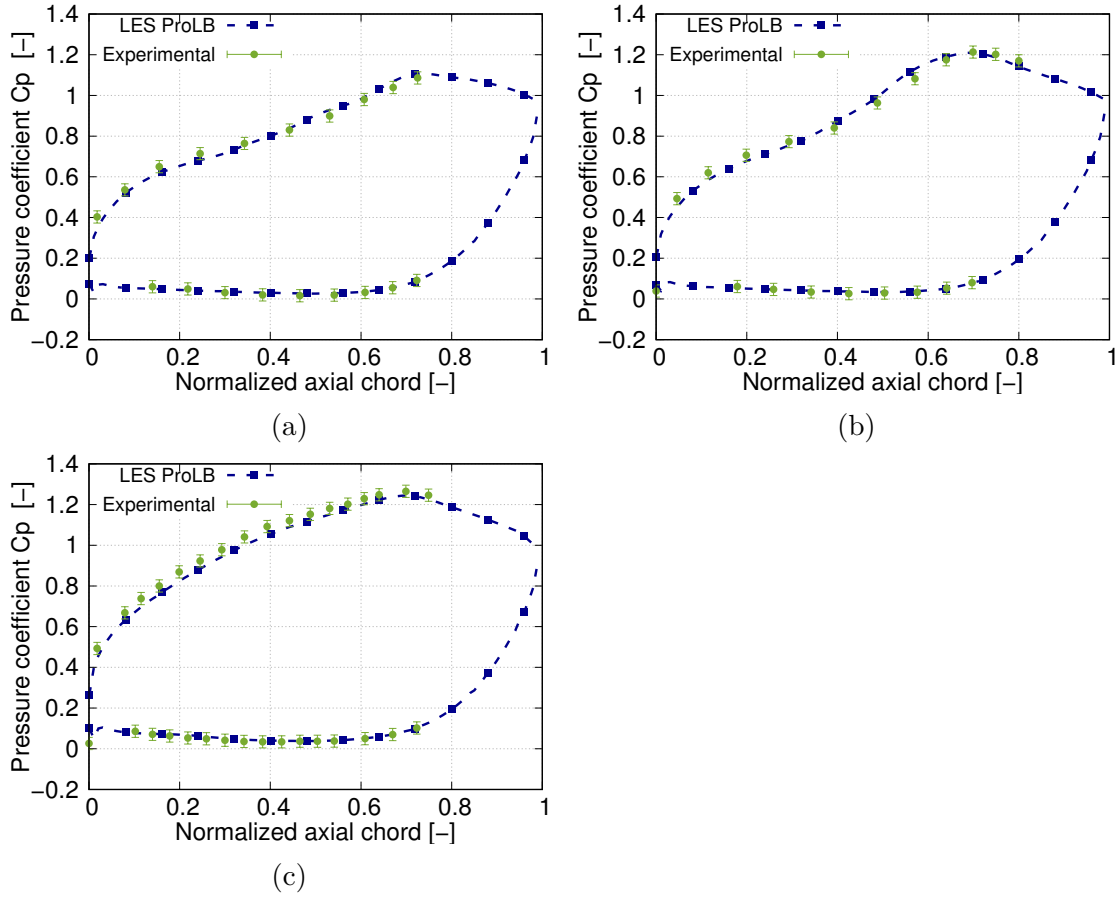


Figure 3.22: Pressure coefficient around the blade at (a): 4%, (b): 6%, (c): 50% span the A05 configuration using the LES Pro-LB approach

3.3.2.2 LES

For the LES solvers, Fig. 3.23b and 3.23c show a strong discrepancy of the pressure loss downstream of the blade for the LES elsA and AVBP solvers compared to experiments. From a general sight, the overall loss are underpredicted/overpredicted of 40% in some portions of the annulus. The position of the two main pressure loss peaks is too close to the wall compared to the experiments. A central region of constant pressure loss is observed but not in the experiments. Concerning the results from Pro-LB solver, the two main loss peaks of pressure loss are well predicted as well as the position of the two main pressure loss peaks.

+The comparison of the results for the different approaches led to the conclusion that the approaches with more modeling (turbulence for RANS) and near-wall region management for LES-LBM Pro-LB (law of the wall treatment) gave better results for losses downstream of the blade compared to the wall-resolved simulation LES elsA and AVBP. It seems acceptable that the poor results obtained from LES simulation AVBP and elsA would not be due to a poorly resolved simulation because the two simulation are in good agreement with each other concerning the pressure coefficient around the blade and pressure loss coefficient downstream the blade. The next section will focus on the flow behavior in the cascade to better understand the

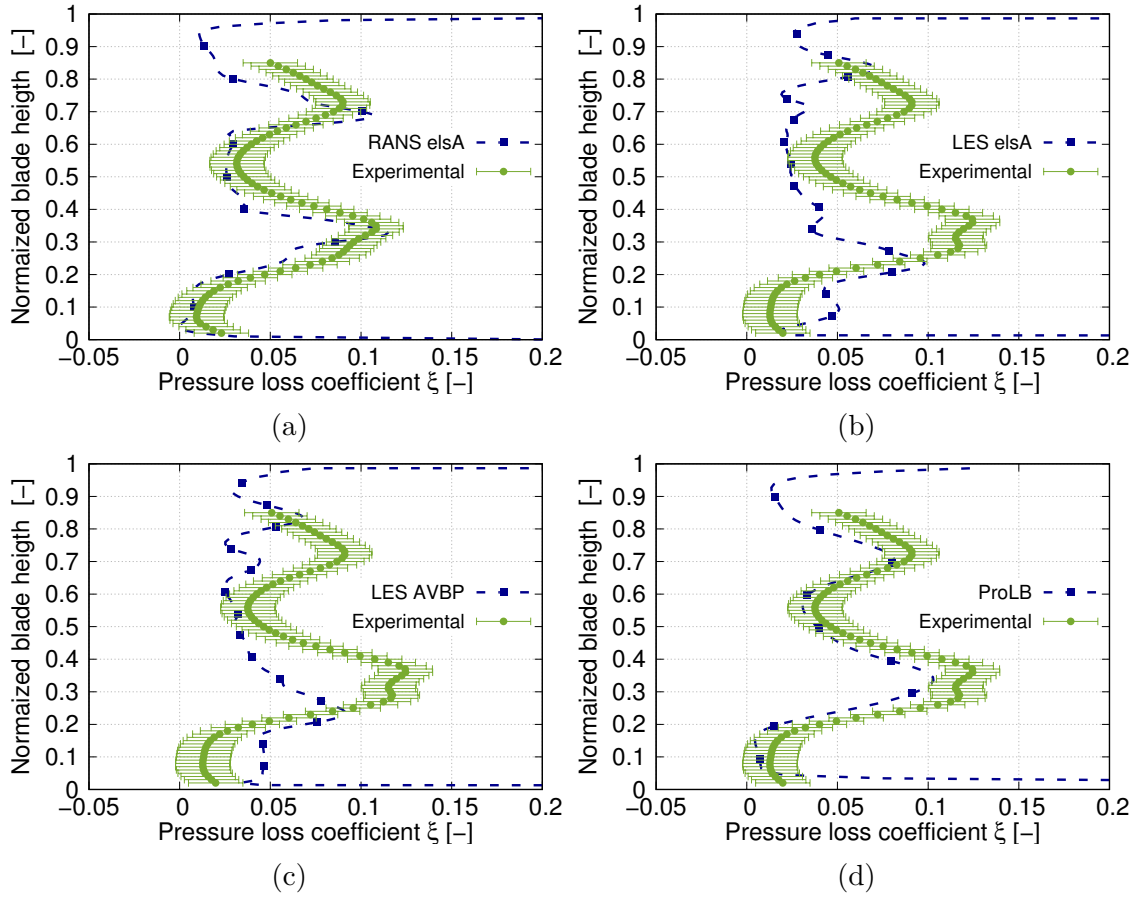


Figure 3.23: Pressure loss coefficient downstream the blade for the A05 configuration for the different solvers (a): RANS, (b): LES elsA, (c): LES AVBP, (d): Pro-LB

mechanisms of loss and explain the differences between the different simulations performed.

3.4 Main flow feature

The purpose of this section is to describe the main flow feature obtained first by the steady RANS simulation and temporally averaged LES solvers in conjunction with the knowledge learnt from the literature concerning the flow along a linear cascade. The emphasis is given to further understand the pressure distribution around and downstream of the blade that have been used for the comparison with experiments and the influence of purge flow and rim seal geometry. The description is made as much as possible by following the flow in the linear cascade. The interaction of the shroud boundary layer with the blade leading edge will be first studied.

3.4.1 Incoming boundary layer at shroud

The interaction of endwall boundary layer with blade has been deeply studied [111, 139, 88] especially with the emphasis to describe secondary flow development

in the passage as proposed in Sec. 2.2.4.1 (p.65). The scope of this subsection is to verify that the main mechanisms previously observed in these former studies can be observed in this configuration. This section is used to draw the differences with a hub where the endwall is partially replaced by a cavity upstream of the blade including an emerging purge flow.

Figure 3.24b shows the boundary layer thickness at shroud obtained from the RANS simulation. At the inlet of the domain, the boundary layer has a non-zero initial thickness due to the imposed experimental inlet profile that mimic an existing boundary layer that had started to develop downstream of the turbulent grid. Fig-

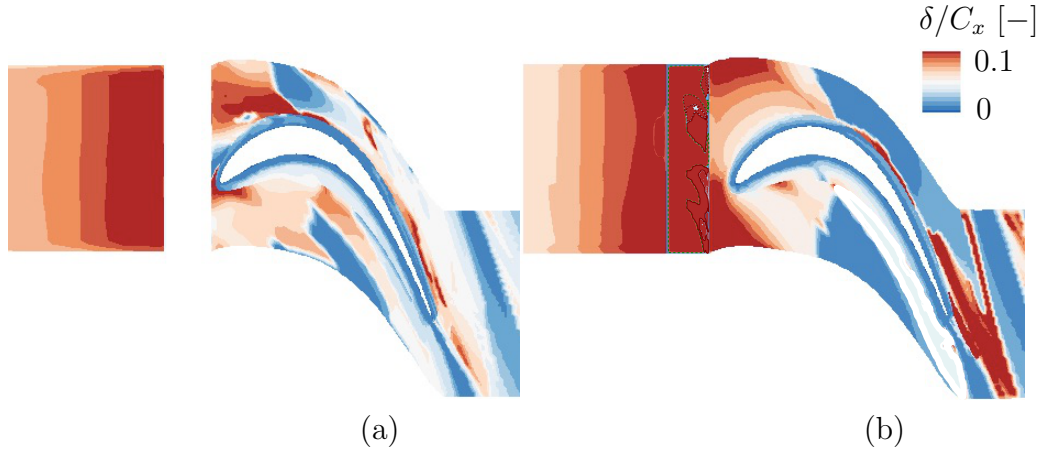


Figure 3.24: Hub (a) and shroud (b) boundary layer thickness from the RANS simulation

Figure 3.25a shows streak lines obtained from friction vectors at the shroud endwall. The flow at the inlet is supplied with a tangential component that mimics a hypothetical upstream rotor stage and that corresponds to an adapted (zero incidence) profile for the nozzle guide vane cascade under consideration. Streak lines bifurcation can be observed when approaching the blade leading edge (see Fig. 3.25a). This observation corresponds to the shroud boundary layer approaching the blade that detaches due to an increase of the static pressure from the blade potential effect and low momentum of the shroud boundary layer compared to the free stream one. At this location known as saddle point and all along the separation line, the boundary layer detachment induces the formation of vortical flow structures almost orthogonal to the mainstream flow direction immediately downstream the separation line. Figure 3.25b shows the wall friction at the shroud where elongated structures upstream of the blade leading edge can be observed since these structures locally increase the wall shear stress. This observation indicates the rolling structures development from the boundary layer detachment that travels until the blade leading edge before to impact it. This vortex structure termed as horseshoe vortex is split by the blade leading edge and propagates downstream in the passage on both pressure and suction side forming two legs. According to the streak lines at the shroud, the suction side leg horse shoe vortex remains close to suction side wall while the pressure side leg travel along the inter-blade channel due to the cross pressure gradient (induced by a high pressure pressure side and low pressure suction side of the adjacent blade). The pressure side leg azimuthal and axial migration induces a separation line where

the flow close to shroud is entrained by the pressure side leg and downstream a new-born boundary layer starts to develop [98]. This process is related to the equilibrium between pitchwise pressure gradient and centrifugal forces on the fluid element that breaks down close to endwall due to the low momentum boundary layer and pressure forces that are dominant as stated by Acharya et al. [140]. Downstream of the blade

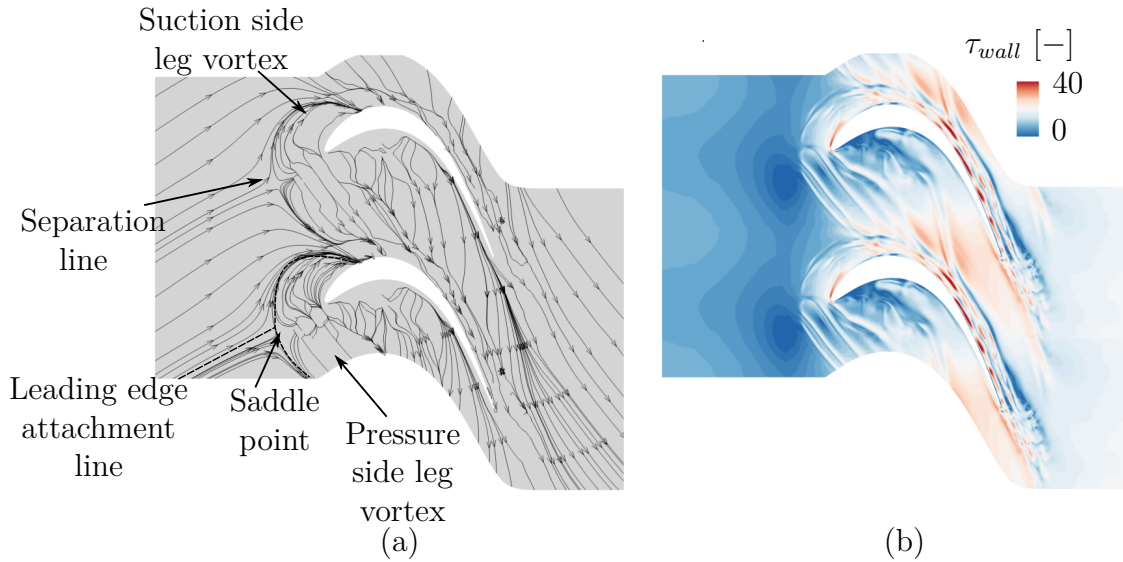


Figure 3.25: Streak lines (a) and skin friction (b) at the shroud wall exhibiting rolling process of the horse shoe vortices from the LES simulation

leading edge, streak lines at shroud indicate that the suction side and pressure side leg merge together in the region where the two separation lines meet close to blade suction side and initiate the formation of the vortex known as passage vortex (see Fig. 3.25a at around 30% axial chord length). On the blade suction side, the flow is less accelerated in the boundary layer than in the free stream. A negative spanwise pressure gradient is induced from the endwall to free stream. Figure 3.26 shows streak lines around the blade suction side and pressure side. Near to the shroud on the blade suction side, a streamline deviation can be observed that indicates the migration of the passage vortex along the blade suction side due to the spanwise pressure gradient. The migration is characterized by a three-dimensional turbulent flow travelling on the blade and skewed as stated by Dominy et al. [141]. The pressure and suction side leg merge at the shroud induces the formation of an additional vortex structure slightly downstream the initial migration location of the passage vortex that remains close to the shroud called corner vortex that can be seen on the streak lines of Fig. 3.26. This vortical structure is a small but very intense structure as stated by Wang et al. [93].

The interaction of the shroud boundary layer with the blade leading edge and the subsequent development of secondary structures has been described and made possible to observe some of the different phenomena described by former studies especially in linear cascade experiments. At the hub, the configuration is similar to the shroud except that part of the wall is replaced by a cavity and rim seal upstream of the blade leading edge.

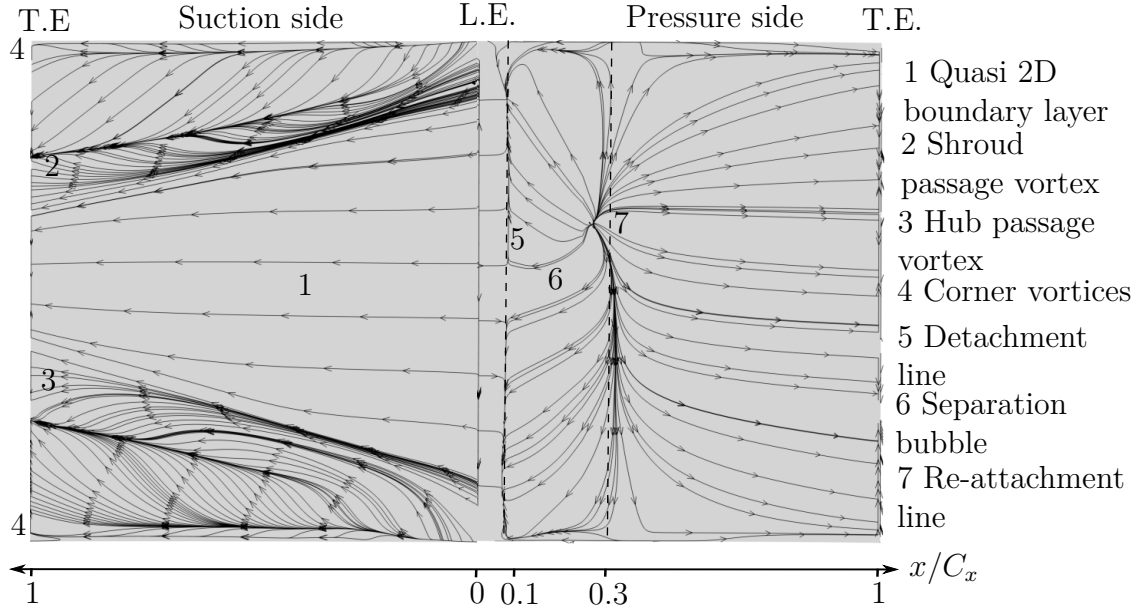


Figure 3.26: Streak lines on the suction (left) and pressure side (right) for the A05 configuration from the RANS simulation (unwrapped blade)

3.4.2 Incoming boundary layer at hub

The boundary layer developing at the hub, upstream of the cascade, separates when approaching the cavity rim seal left corner. For the axial rim seal, the flow in the cavity is entrained by the mainstream flow. This process is similar to academic entrained cavity where a base flow onto a cavity induces a clockwise vortical structure in the whole cavity. The additional momentum provided to the cavity flow at the interface by the main annulus flow is progressively spread all over the cavity under a viscous process. Figure 3.27a and 3.27b show velocity vector in the upper part of the axial rim seal face to the blade leading edge and at the center of the passage with top part of this rotating core. For simple (S) and double overlapping rim seal geometries (D) that are more representative of real engine geometries, the overlapping partially breaks the entrainment effect on whole cavity restricting the influence and rotating core to the flow in the rim seal (see Fig. 3.27c and 3.27d). According to these different velocity vector plots at the rim seal interface, the velocity adaptation between the cavity and mainstream flow is performed at the top of the rim seal over a small height typically in the order of magnitude of the incident boundary layer. The strongest velocity gap being observed at the rim seal left corner and decreasing all along the axial direction due to the entrainment effect. This small region of velocity adaptation is a shear layer in both axial (see Fig. 3.27) and azimuthal velocity component at a radius corresponding to the rim seal left corner. This shear layer will be more deeply analysed in the Sec. 3.5 related to unsteady phenomena with the possible development of Kelvin-Helmholtz instability in the case of low free stream turbulence. Since less flow is entrained for the single (S) and double axial overlapping rim seal geometries (D) compared to the axial one (A), the velocity deficit of the rim seal flow compared to the mainstream flow is lower for overlapping geometries than axial one and therefore promotes a less intense shear layer (see Fig. 3.27a and

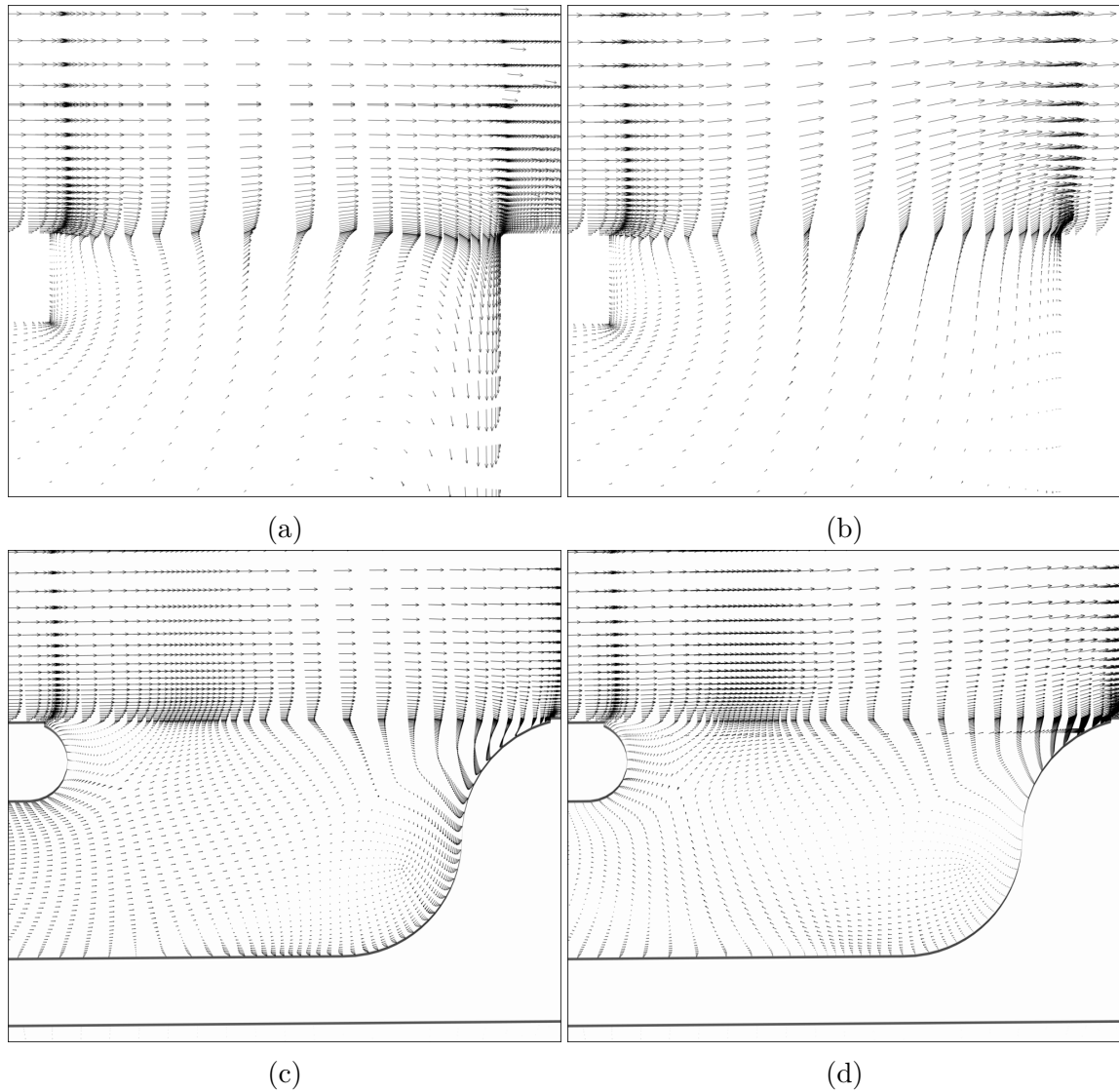


Figure 3.27: Velocity vector close to the rim seal: face to leading edge (a)(c) and at the center of the channel (b)(d) for the A05 and S05 configuration

3.27c). Between the single (S) and double overlapping geometries (D), relatively low differences were observed compared to the flow topology at the rim seal interface. The first axial overlap (single overlap) promotes a reduced entrainment of the whole cavity flow to reduce the shear layer at the rim seal interface. Similarly, the second arm of the double overlapping geometry and radial tooth is a discourager of flow transfer between the cavity flow and rim seal one that is shown to have relatively low influence in current static configuration. However, as stated in Sec. 1.1.3 (p. 8) the second (bottom) arm (see rim seal geometry D in Fig. 3.2 p.83) has a considerable importance in rotating cavity configurations. The entrainment effect in the cavity producing the central core and the positive radial pressure gradient in the cavity is damped by this second arm inducing less pressure asymmetry and pressure gradient across the rim seal. The flow at the rim seal interface is generally asymmetric due to upstream effects with alternating wakes and free stream flow when an upstream

cascade is considered or potential effects of downstream row. In this configuration, only the potential effect of the downstream blade is taken into account. The effect of wakes will be developed in the next chapter (see Sec. 4.4.3). Figure 3.27a shows velocity vector face to the blade. When approaching blade leading edge, the flow at the rim seal interface is deviated downwards in the rim seal and cavity due to the potential effect of downstream blade and high stagnation pressure. Figure 3.27a and 3.27c show velocity vector at the rim seal interface face to the blade and at center of the passage in Fig. 3.27b and 3.27d showing that part of the flow is deviated into the cavity when facing the blade (velocity vectors oriented upstream close to rim seal right corner) while the flow can freely go into the mainstream at the center of the passage where pressure is low (velocity vectors oriented downstream close to rim seal right corner). Based on a mass conservation balance for the cavity including the rim seal, since some flow enters in the cavity face to the blade, an equivalent amount of flow must blow into the mainstream. When purge flow is added, this additional mass flow has to blow into the main annulus. Since the cavity flow was supplied at a lower temperature than the mainstream one ($T_c/T_m \simeq 0.9$), temperature can be used as a passive scalar to track the blowing and mixing of the cavity flow in the mainstream. Figure 3.28a shows the total temperature profile at hub where the flow emerges into the mainstream. The blowing process is mainly performed where the main annulus pressure is more favourable, i.e. where pressure at the hub of the main annulus is lower. Along the azimuthal direction, pressure is lower at the center of the inter-blade channel and close to the suction side. The cavity flow then travels and is rolled up towards the blade suction side due to the cross pressure gradient. These structures interact with the vortical structures emanating from the horse shoe vortex especially the horse shoe pressure side leg (see Fig. 3.28b). Due

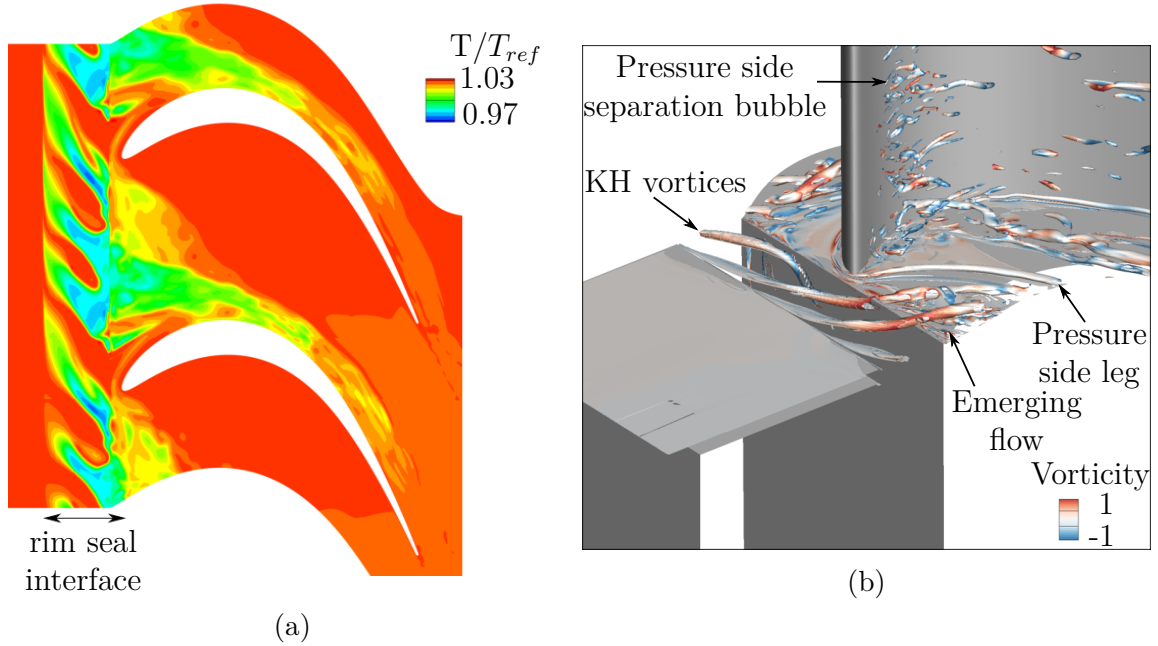


Figure 3.28: Total temperature distribution at the hub (a) and horseshoe vortex interaction with the cavity flow based on a iso q -criterion $q = 10^6$ colored by the streamwise vorticity from an instantaneous LES solution (b)

to the rim seal at hub, a new boundary layer starts to develop at the rim seal right corner on the hub platform of the nozzle guide vane. This boundary layer is very thin when approaching blade leading edge compared to the shroud due to the proximity between the rim seal right corner and blade leading edge. Similarly to the process at the shroud, the horse shoe vortex at hub emanates from the developing hub boundary layer. The pressure side of the horse shoe vortex travels along the passage and is strengthened by the new-born passage boundary layer similarly to the process at shroud. In addition, the emerging low-velocity cavity flow is entrained by the pressure side horse shoe vortex promoting a stronger rotating core structure. The different mechanisms described at the shroud leading to the development of passage and corner vortices are the same at the hub except that these secondary flow structures have higher extensions/secondary kinetic energy due to the purge flow.

3.4.3 Blade flow feature

Based on Fig. 3.26 introduced previously showing streamlines related to the blade suction and pressure side, the boundary layer on the blade pressure side separates at around ten percent chord length (5 in Fig. 3.26) and is characterized by a loss of organization of the flow. This is confirmed by a local constant / slightly increasing isentropic Mach number in this region of the pressure side (see Fig. 3.29). The

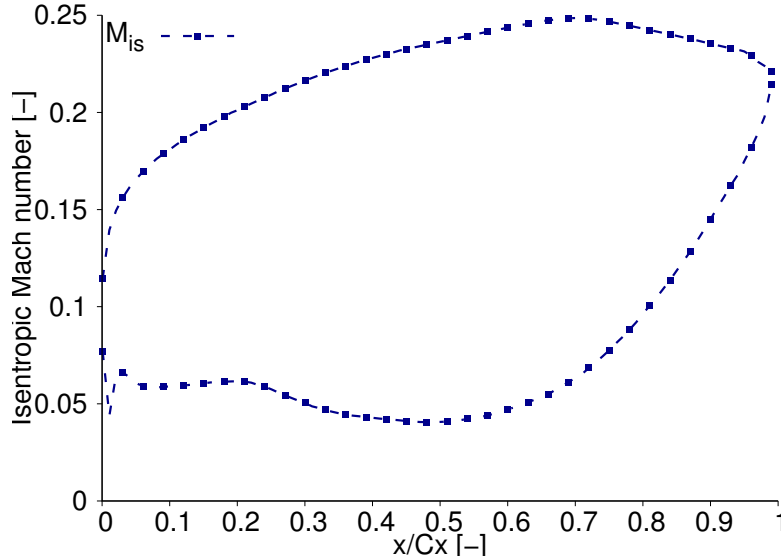


Figure 3.29: Isentropic Mach number at mid span for LES simulation

adverse pressure gradient inducing a closed separation bubble along most of the span (6) that reattaches at around thirty percent axial chord length (7). Downstream, the boundary layer remains attached until blade trailing edge. The flow on the blade pressure side is essentially two-dimensional and not influenced by secondary vortices. The quasi-uniform pressure distribution all along the pressure surface span and very weak interaction of the boundary layers between the pressure surface and endwall are responsible for this flow behavior. On the blade suction side, the developing boundary layer is relatively insensitive to wall effects in a cup shape region from the

blade leading edge (1). The influence of secondary vortices can be observed at the hub and shroud with migrating passage vortices (2-3) and corner vortices close to the hub and shroud (4) in a delta shape region.

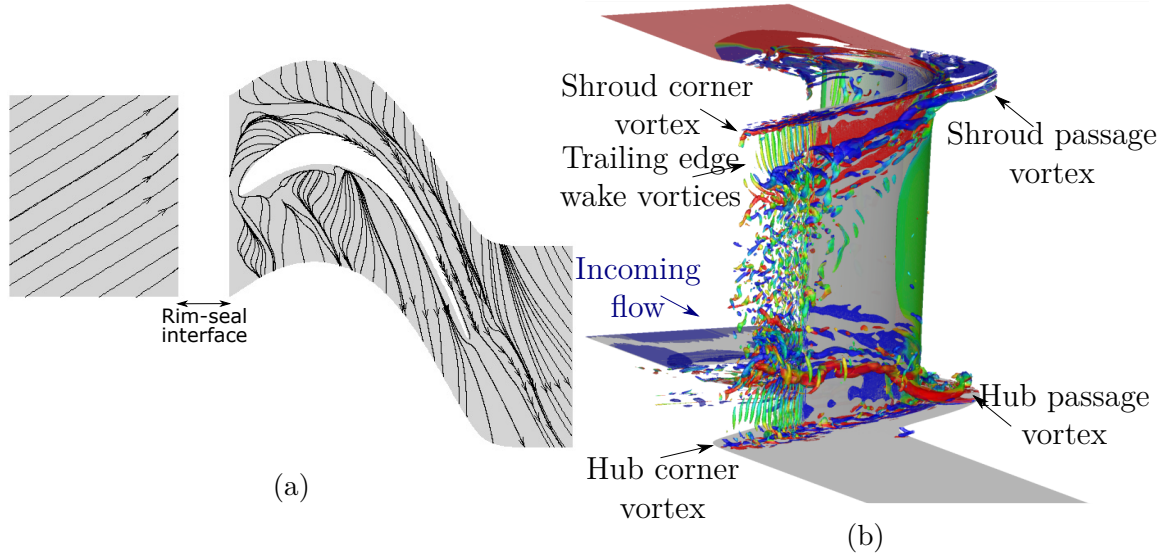


Figure 3.30: Streak lines at the hub from the temporally averaged LES (a) and sight from downstream to upstream of the secondary flows in the passage obtained using iso q -criterion $q = 10^6$ colored by vorticity from instantaneous LES solution (b)

3.4.4 Flow downstream of the blade

Figure 3.30b shows an iso q -criterion colored by the streamwise vorticity in a down to upstream view where some of the vortical flow structures developed in the passage can be highlighted. The hub and shroud passage vortices can be identified as migrating structures on the blade suction side. Hub and shroud passage vortices have opposite sign vorticity. Similarly, close to the hub and shroud boundary layer, corner vortices can be identified. Close to the blade trailing edge, pressure and suction side boundary layer separate and mixes out due to a velocity gap between pressure and suction side exiting velocity producing trailing edge wake vortices. Between corner and passage vortex, where the flow is relatively undisturbed by secondary vortices, the wake vortices are characterized by elongated roll-up structures aligned with the radial direction characterizing stream velocity differences. At locations where secondary flow structures leave the blade, these structures cannot be clearly identified due to the interaction with secondary flow structures, mainly the corner and passage vortices. At this location, elongated structures aligned with the stream direction are rather observed due to the shear layer formed between the fluid from the suction surface, which has a significant spanwise velocity and the fluid from the pressure surface with little or slightly negative spanwise velocity. The vorticity in this shear layer rolls up into a vortex behind the trailing edge generally referred as the counter vortex with opposite sign to the main passage vortex (see Fig. 2.14a p.66). For the case where a separation bubble occurs on the blade suction side, the separation also induces vortices that interact with the trailing edge vortices leading to complex

three-dimensional structures.

From this last description of the flow, a first qualitative assessment of the loss

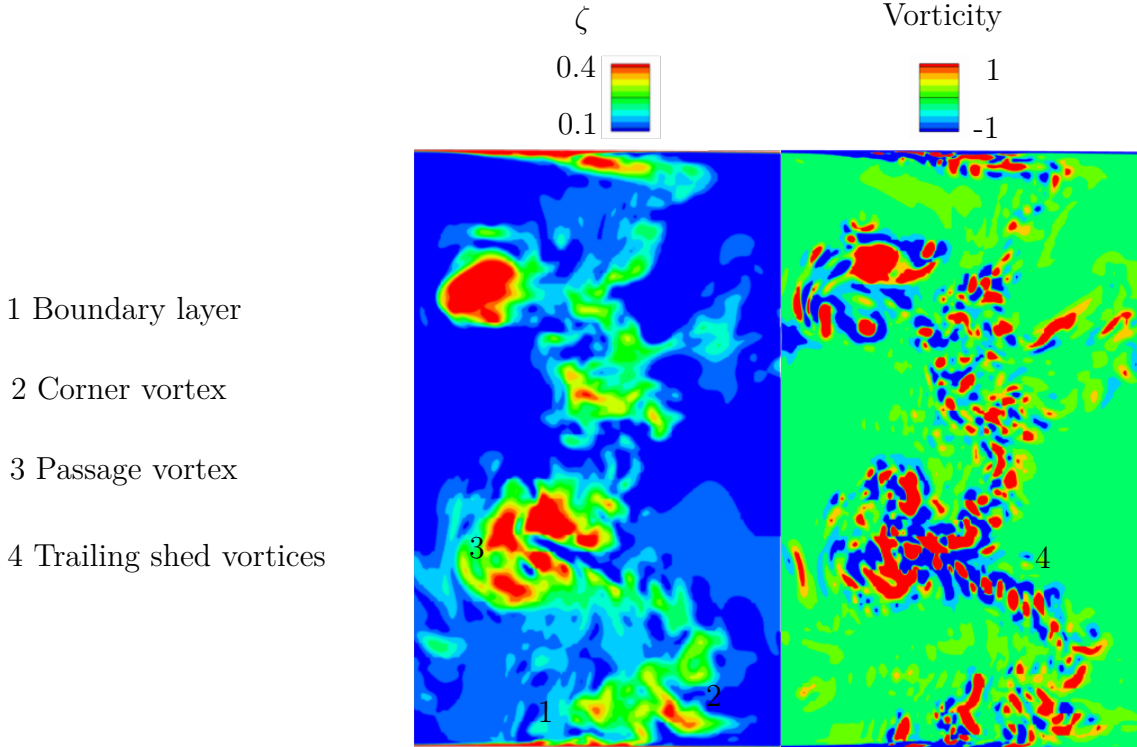


Figure 3.31: Pressure coefficient and vorticity downstream the blade from instantaneous LES solution where experimental measurements have been performed

sources leading to a pressure drop downstream of the blade where experimental measurements have been performed can be proposed. Figure 3.31 shows the non-dimensional pressure and vorticity at 25% axial chord length downstream of the blade trailing edge where the experimental pressure measurements have been performed. By performing an azimuthal averaging, one can recover the curves of pressure coefficient as a function of blade height used to compare the simulations against experiments. This figure makes possible to see the loss history of the flow in the linear cascade since the total pressure decrease can be seen as an accumulation of irreversibility generated upstream. A first possible mechanism contributing to the pressure loss is the shear layer at the rim seal interface. The boundary layer developing along the hub and shroud is expected to produce pressure loss localized close to the wall (1). Out of the hub and shroud boundary layers, part of losses can be related to the blade boundary layer contributions and trailing shed vortex process (4). The last type of contribution that could be inferred in this configuration are the secondary flows that are associated to low pressure regions close to their center of rotation and large vortical structures (hub and shroud corner vortices (2), passage vortices (3)).

3.5 Unsteady phenomena within the cascade

3.5.1 Horse shoe vortex process at shroud

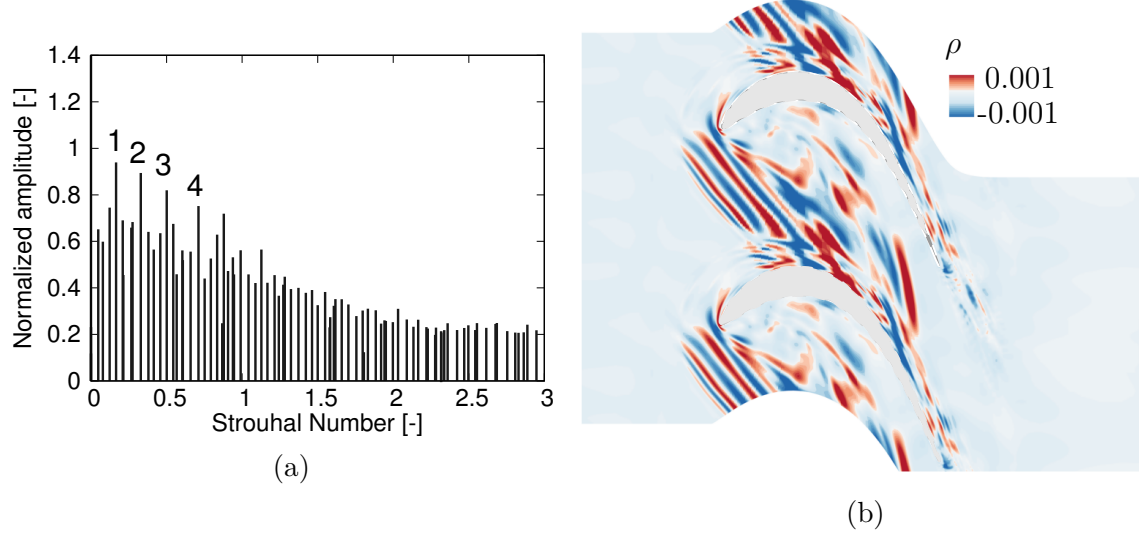


Figure 3.32: Spectrum and corresponding summed modes (1, 2, 3 and 4) related to the horse shoe vortex process at the shroud obtained from Dynamical Mode Decomposition (LES simulation)

Horse shoe vortices developing at the shroud impact periodically the blade leading edge initiating pressure and suction side leg horse shoe vortices. The frequency depends on the boundary layer edge velocity u_{bl} and equivalent diameter of the blade leading edge as stated by Cui et al. [76]. A Dynamical Mode Decomposition (DMD) performed at the shroud have made possible to identify a few modes with a large amplification showed in Fig. 3.32 and related to the periodic horse shoe vortex development. The main harmonic of the phenomenon is set at Strouhal number $St = (f_r D)/u_{bl} = (250 \cdot 0.02)/30 = 0.2$ where f_r is the frequency, D the distance from saddle point to blade leading edge. The corresponding reconstructed mode is shown in Fig 3.32b with alternating high and low density modes associated to shroud boundary layer separation and horse shoe vortices generation. The location where horse shoe vortex develops and the pressure side leg of the horse shoe vortex migrates are associated to strong pressure standard deviation σ_p (see Fig. 3.33b top). On the blade, the strongest pressure deviations are observed where the passage vortex migrates on the blade suction side and close to the shroud where the corner vortex travels (see Fig. 3.33a). Even downstream of the blade, the pressure loss coefficient experiences amplitude fluctuations in particular in regions of strong losses related to the passage vortices (see Fig. 3.35b). A spectral content analysis have been conducted with the two-dimensional temporal signal associated to the shroud wall, skin blade where passage and corner vortices travel and downstream of the blade where the pressure loss experimental measurements have been performed. This last position was convenient in the purpose to analyse the beating frequency of the passage vortex downstream blade. The position is relatively far from the blade

trailing edge to reduce the influence of the trailing shed vortex characteristic frequency and close enough to have secondary flow structures still relatively coherent. The modes related to the horse shoe vortex process are shown to be propagating in the secondary structures leading to unsteadiness around the blade suction side where the secondary flows travel. Downstream of the blade, amplitude and azimuthal position variations of the passage vortices were shown to be related to the horse shoe vortex process (see Fig. 3.36 with HS standing for horse shoe-related modes). Therefore, the horse shoe vortex process and subsequent secondary vortices development in the blade passage is a source of unsteadiness for the cascade.

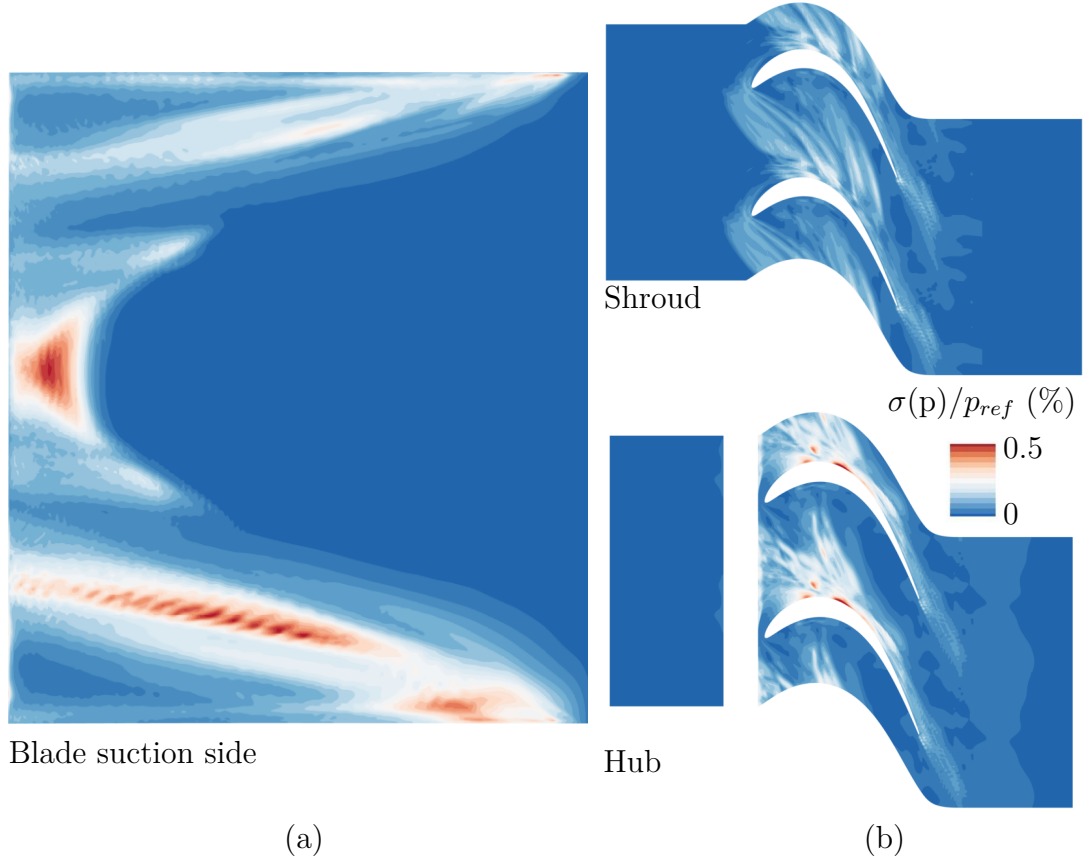


Figure 3.33: Pressure standard deviation $\sigma(p)$ around the blade suction side (a), at hub and shroud (b)

3.5.2 Horse shoe vortex and Kelvin-Helmholtz process at hub

At the hub, due to tangential and axial velocity gap between the mainstream and cavity, a shear layer takes place at the rim seal interface. Under low free stream turbulence, the shear layer induces Kelvin-Helmholtz instability. A three-dimensional DMD has been performed using fully three-dimensional snapshots in time and made possible to isolate a few modes initiated at the rim seal interface and considered as the instability. The spatial reconstruction of this mode can be seen in Fig. 3.34a

characterized by alternating positive and negative density modes at the rim seal interface. Once generated and amplified in the axial extent of the rim seal, alternat-

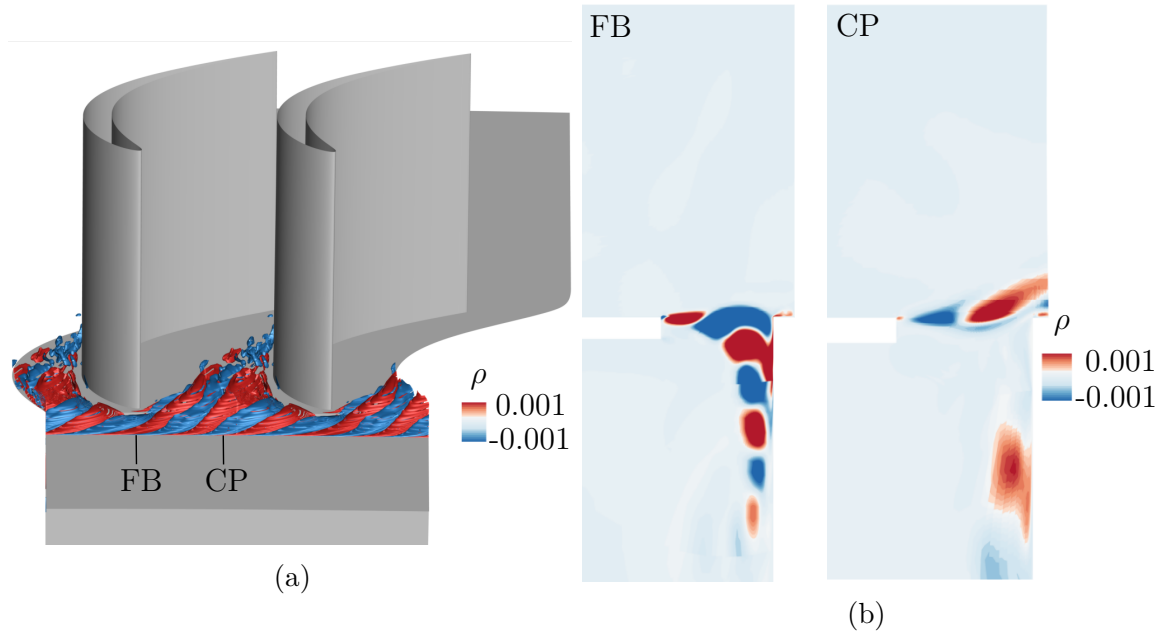


Figure 3.34: Three-dimensional (a) and two-dimensional modes related to Kelvin-Helmholtz instability based on fully three-dimensional and two-dimensional meridional plane face to the blade leading edge (FB) and at the center of the passage (CP) (b)

ing vortical flow structures extending along the whole azimuthal direction are either deviated downward into the rim seal when facing the nozzle guide vane due to high stagnation pressure or remain in the mainstream due to cavity purge flow blowing into mainstream and relatively lower pressure. The flow structures entering into the cavity tend to weaken and vanish when going further downstream in the cavity for the axial rim seal and in the rim seal for overlapping geometries. At the center of inter-blade channel, these flow patterns emerge into the mainstream (see Fig. 3.34b and 3.28b). The blade-to-blade pressure gradient induces the migration of these modes from the center of the passage to the suction side of the adjacent blade under the entrainment effect of pressure side horse shoe vortex. Additional entrainment flow given to the pressure side horse shoe vortex and Kelvin-Helmholtz instability induce higher pressure standard deviation compared to the shroud (see Fig. 3.33b bottom). Similarly, around the blade, the pressure unsteadiness is stronger where the secondary vortices travel compared to the shroud (see Fig. 3.33 left and 3.35a showing pressure fluctuations around the mean value at 4% span). Similarly to the spectral analysis performed at the shroud, the sources of unsteadiness observed at the hub, on the blade suction side where the passage vortex migrates and downstream of the blade where passage vortex decays have been conducted. The horse shoe vortex process is the dominant source of unsteadiness even at the hub. The Kelvin-Helmholtz instability occurs at higher frequency, typically four times higher than the horse shoe vortex process (see Fig. 3.36 with KH standing for Kelvin-Helmholtz-related modes). Based on these observations, a reduction of the shear

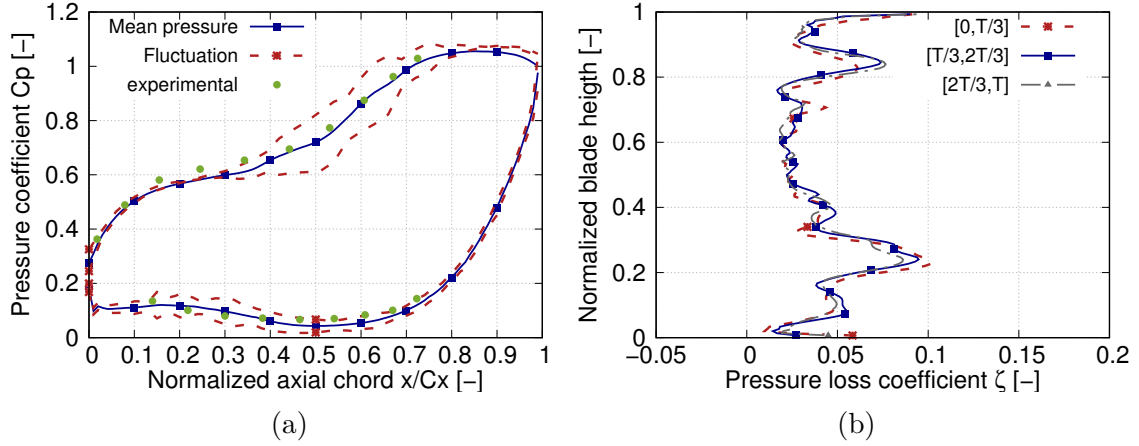


Figure 3.35: Pressure coefficient and domain of fluctuation at 4% blade height (a) and downstream blade (b) where the characteristic time T corresponds to the time for a particle to be convected of one axial chord

layer intensity close to the rim seal could reduce unsteadiness on the blade suction side at the hub. This could be achieved by reducing the tangential and axial velocity gap between the mainstream and rim seal flow by increasing swirl in the cavity or longer rim seal arms to increase rim seal axial flow component.

The last description was dedicated to show the common flow feature in the linear cascade that were observed with the different numerical simulation performed (RANS and LES) and the unsteady phenomenon observed in the LES simulation. Next section will be focused on the influence of turbulence modeling on the processes occurring in the linear cascade described previously. This study is made with the emphasis to better understand the difference observed between the different numerical solvers, in particular the discrepancy in pressure loss downstream of the blade. The influence of turbulence will be assessed in two ways. At first by comparing turbulence modeling approaches: RANS simulation against LES simulations performed with elsA and AVBP. Then, as a second step, by comparing LES simulations from elsA and AVBP without turbulence injection compared to the same simulation where turbulence is injected at the inlet of the domain (AVBP).

3.6 The influence of turbulence

Based on the common flow features described in the last section no matter of the approach chosen, the purpose of this section is to describe the differences observed between the different simulations with the objective to better understand the differences observed especially the pressure loss coefficient downstream of the blade.

3.6.1 Turbulence modeling

At the hub and shroud, a boundary layer develops from the inlet of the simulation domain with an initial thickness imposed according to the experiments. Figure 3.38

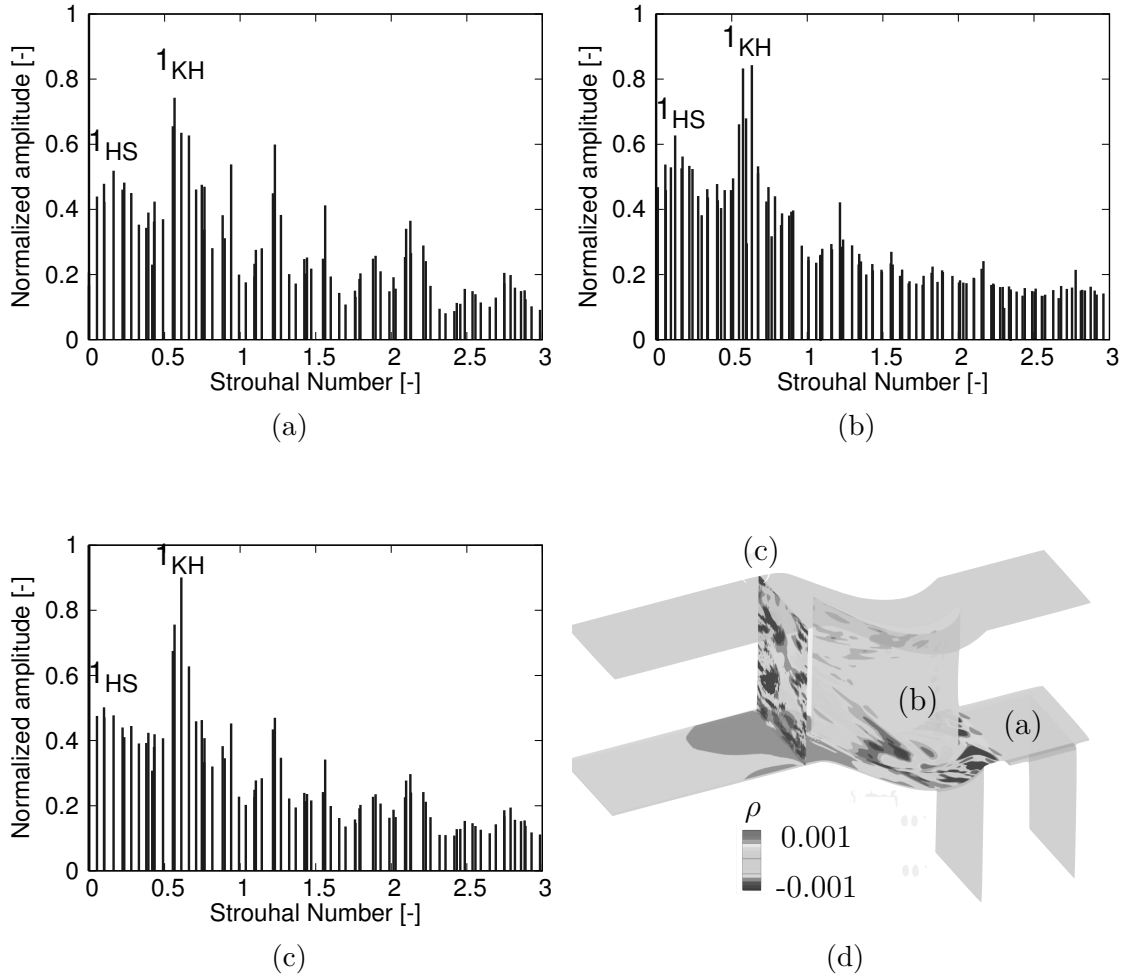


Figure 3.36: Density frequency spectrum in x, z cuts and around the blade with the A05 configuration and corresponding to the fundamental Kelvin-Helmholtz density mode

shows the boundary layer profiles on the hub endwall at the various axial positions for the RANS and LES simulations before the rim seal. The positions where the boundary layer profiles have been extracted are given in Fig. 3.37. In addition, the Blasius analytical solution without pressure gradient for a laminar boundary layer has been added to the profiles related to the LES simulation and power law turbulent boundary layer profiles $(u/u_{edge}) = (y/\delta)^{1/7}$ for the RANS simulation. The wall-normal coordinate and velocity in the boundary layer have been non-dimensionalized by the boundary layer thickness δ and velocity at the edge of the boundary layer u_{edge} . This process is used since the Blasius profile, solution of the laminar boundary layer on a flat plate, is a self similar function. However, it is reminded that the boundary layer thickens with the axial coordinate and the same process is also used for the turbulent boundary layer profiles. The boundary layer at the hub for the RANS simulation (Fig. 3.38a) has a profile close to a turbulent one with lower momentum close to the wall until $y/\delta < 0.08$ but higher momentum above. The hub is relatively close to a flat plate configuration with a very low favourable pressure gradient and due to the RANS modeling, this boundary layer profile is essentially what could have been

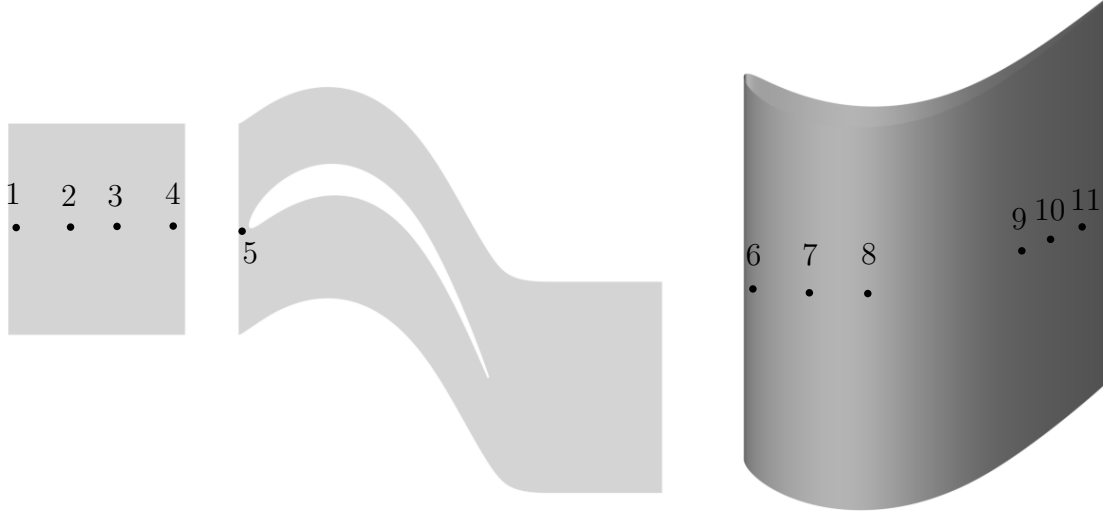


Figure 3.37: Positions in the linear cascade where the boundary layer profiles have been extracted for the RANS and LES simulations

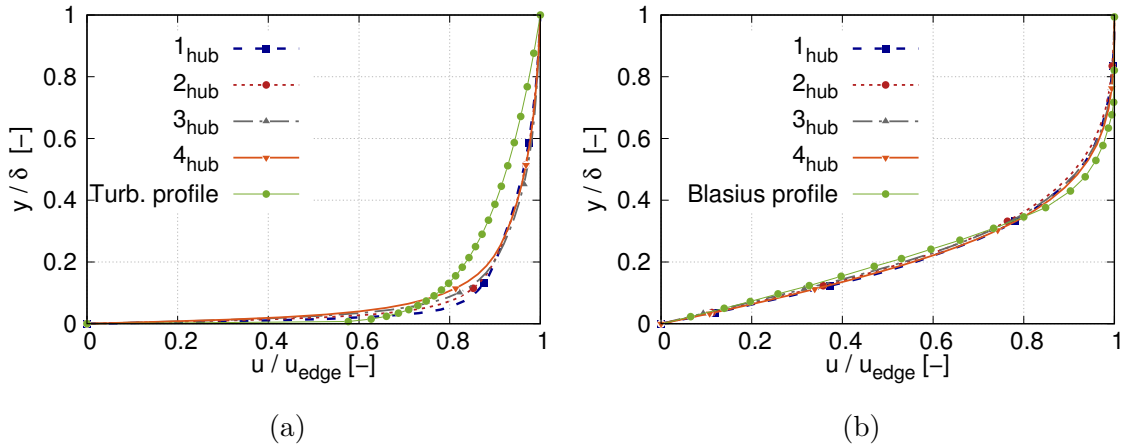


Figure 3.38: Inlet hub boundary layer profiles for RANS (a) and LES simulations (b), see Fig. 3.37 for the corresponding extraction positions

expected. For the LES simulation (Fig. 3.38b), the boundary layer profile is close to a laminar boundary layer profile over a flat plate. Since no turbulence injection was performed and for the current Reynolds number ($Re \simeq 500\,000$ or $Re_\theta \simeq 500$) at the trailing edge, this is in agreement with the works of Abu-Ghannam and Shaw [71] (p.53) for which the boundary layer over a flat plate remained laminar at the considered Reynolds number without turbulence injection. According to streak lines at shroud from the RANS (3.25) and LES simulations (Fig. 3.30a), the separation line is closer to the blade leading edge for the RANS simulation. The turbulent boundary layer is more resistant to an adverse pressure gradient since the fluctuating velocities in the turbulent boundary layer greatly increase the transfer of momentum and energy towards the wall and is less prone to separate when facing an increasing stagnation pressure due to the blade compared to a laminar boundary layer as stated by Cui et al. [76]. Figure 3.39 shows the boundary layer profile upstream of the

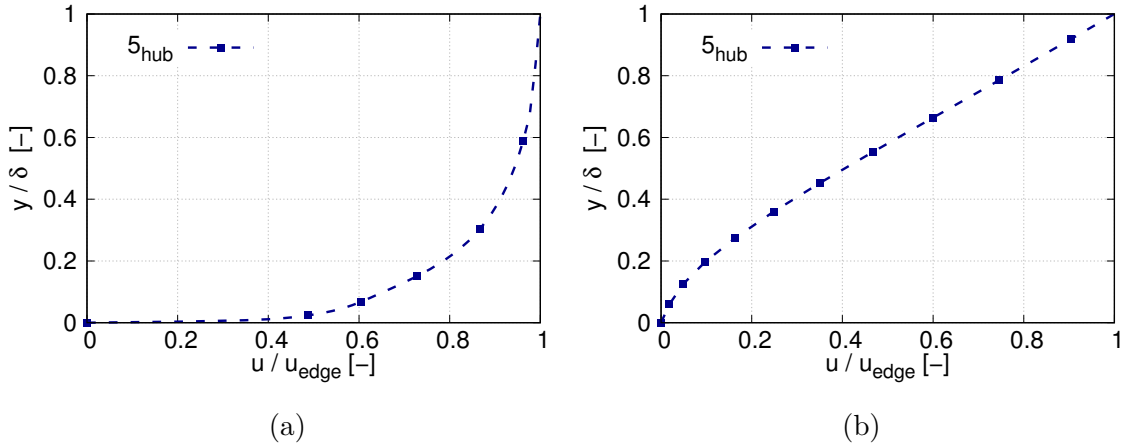


Figure 3.39: Boundary layer profiles for the RANS (a) and LES simulation (b) upstream of the blade leading edge, see 5 in Fig. 3.37 for the corresponding extraction position

blade leading edge for the RANS simulation (position 5 in Fig. 3.37 between rim seal right corner and blade leading edge). While the boundary layer profile for the RANS simulation is close to separation due to the adverse pressure gradient (the velocity profile rise up close to the wall in Fig. 3.39a), the boundary layer module provide a profile that may indicate that the boundary layer has already separated in the LES simulation. Since no boundary layer thickness can be obtained due to a non converging value far from the wall, the profile has been set to the RANS boundary layer thickness. (Fig. 3.39b). A main consequence is that the pressure

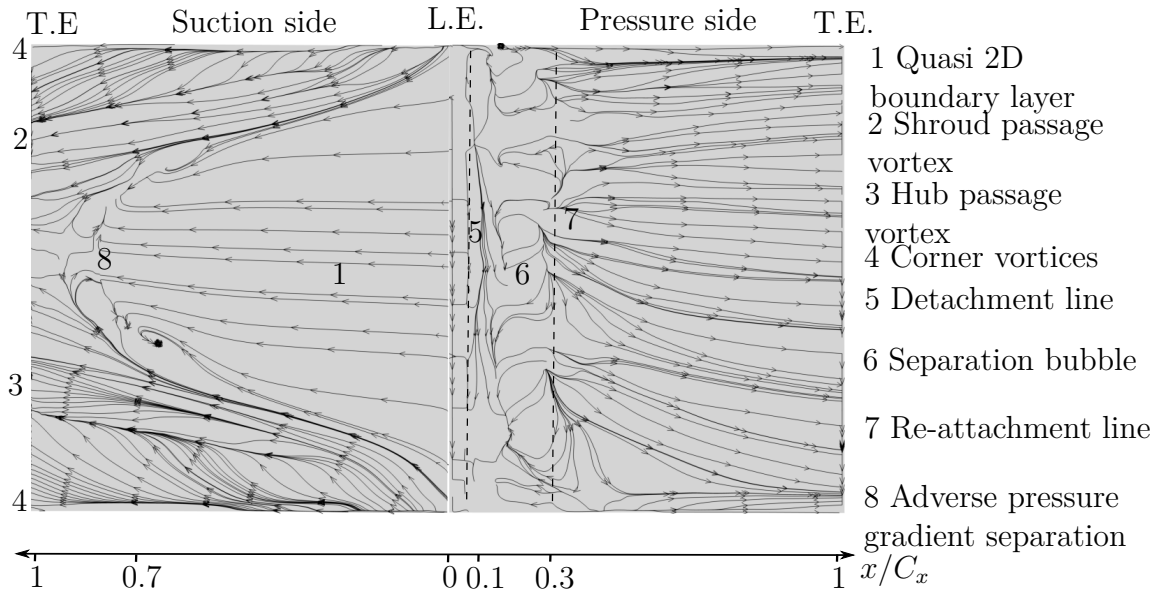


Figure 3.40: Streak lines on the suction and pressure side for the A05 configuration from the LES simulation (unwrapped blade)

side leg of the horse shoe vortex reaches the adjacent blade suction side earlier in the LES than RANS. The migration of the passage vortex is initiated earlier on the

blade suction side. At same time, based on the streak lines around the blade, the angle of migration of the passage vortex is less important for the LES (around 18° between the x axis and the stramline direction in the passage vortex) than RANS simulation (around 25° see Fig. 3.26 for RANS and 3.40 for LES). The two main loss peaks downstream of the blade associated to hub and shroud boundary layers are moved farther from the endwall for RANS, i.e. shifted more strongly towards half span for the RANS simulation. This phenomenon was previously observed by Cui et al. [76]. Around the blade, similar flow topology is observed on the pressure side with a separation bubble at around 10% of axial chord, reattachment at around 30% of axial chord and a nearly two-dimensional flow downstream (see Fig. 3.40). The experimental measurements have been supplemented with oil-painting visual-

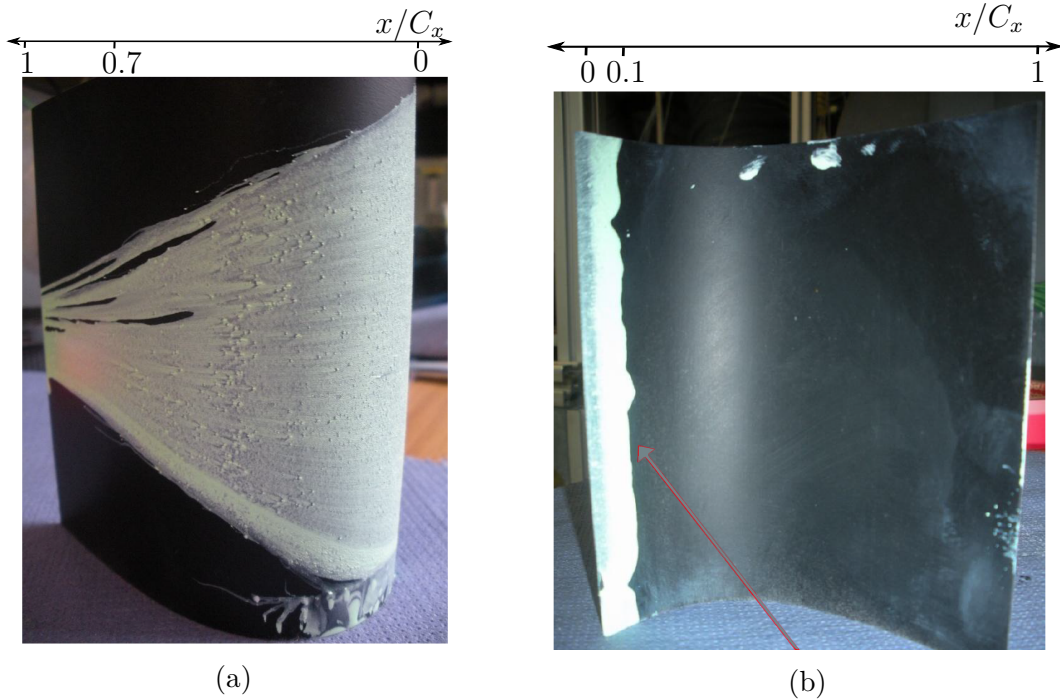


Figure 3.41: Oil-painting visualization on the blade suction (a) and pressure side (b)

izations to characterize the boundary layer nature over the different wetted surfaces. For the laminar boundary layer region, the friction at the wall is low enough so that the oil-painting would be maintained while for turbulent boundary layer region, the friction at the wall is supposed to be high enough to prevent it. Figure 3.41 shows oil-painting visualization obtained experimentally around the blade pressure side. The high friction due to a closed separation bubble on the blade pressure side leads to an oil-painting that cannot be maintained on the surface. The LES, RANS simulations and experiments are allegedly to capture similar flow behavior on the pressure side with a separation bubble between $x/C_x = 0.1$ and $x/C_x = 0.3$. On the blade suction side, based on the streak lines around the blade, the RANS, LES and experiments predict regions of strong friction levels associated to the migrating passage and corner vortices. Also, the cup shape of the boundary layer is in agreement for all three approaches. Figure 3.42 provides the boundary layer profiles around the blade suc-

tion side in the favourable pressure gradient part (from $x/C_x = 0$ to $x/C_x = 0.7$, $dp/dx < 0$) for the RANS and LES simulation. Similarly to the hub, a power law turbulent profile has been provided for RANS. For LES, the Blasius profile without and with pressure gradient $m = 0.1$ has been added. The boundary layer profiles

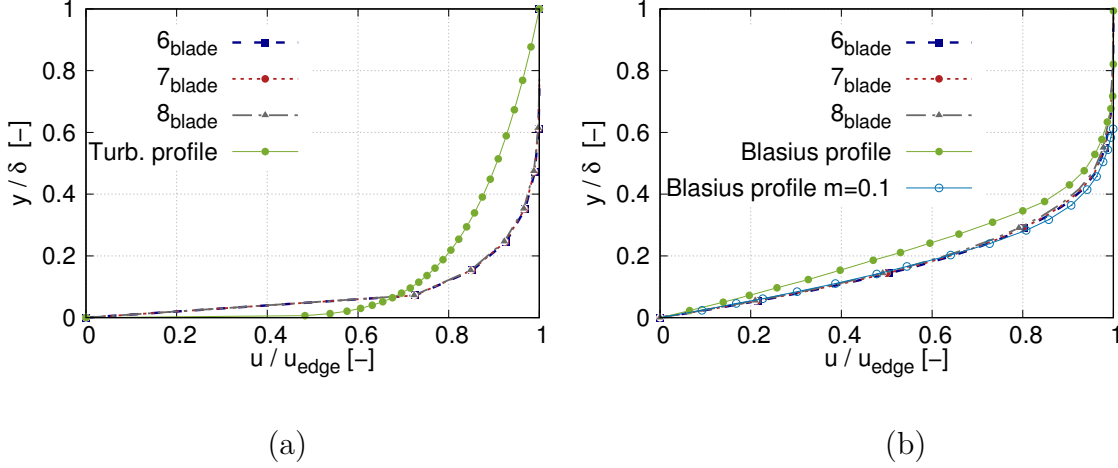


Figure 3.42: Boundary layer profiles on the blade suction side in the favourable pressure gradient portion for the RANS (a) and the LES simulations (b), see position 6, 7 and 8 in Fig. 3.37

around the blade for the RANS simulation displays some differences compared to the power-law turbulent boundary layer profile. According to the author, this may be due to the relatively low friction Reynolds number $Re_\tau = (u_\tau \delta)/\nu$ where u_τ is the friction velocity. For the considered profile extraction location $Re_\tau \simeq 250$ while the description made of a fully turbulent boundary layer with established logarithm region (see Sec. 2.2.2.2 p.53) is generally considered to be valid for $Re_\tau > 500$ that is not fulfilled in current configuration. This is due to relatively low axial Reynolds number and length over which the boundary layer has developed. For this case the viscous layer occupies a larger portion of the near-wall region. This profile is almost unmodified around the blade. For the boundary layer profile extracted from the LES simulation, the profile is close to the Blasius one with favourable pressure gradient $m = 0.1^5$. Similarly to the RANS simulation, the boundary layer profile is almost unmodified on the blade suction side in the favourable pressure gradient portion. Figure 3.43 shows boundary layer profiles for the RANS and LES simulations (extractions 9, 10 and 11) around the blade suction in the adverse pressure gradient portion $x/C_x = 0.7$ to $x/C_x = 1$, $dp/dx > 0$. For the RANS simulation (Fig. 3.43a), the boundary layer profiles are shifted from the wall indicating the adverse pressure gradient effects on the boundary layer. For the LES simulation (Fig. 3.43b), the boundary layer separates characterized by an inversion of the velocity profile indicating a separation bubble due to the adverse pressure gradient. The laminar boundary layer separates at around 80% axial chord without reattaching. Hodson and Dominy [142] also reported the formation of a separation bubble on the blade

⁵The value of m corresponds to the power value of velocity at the edge of boundary layer $u_{edge} = x^m$ before to be injected in the boundary layer equations

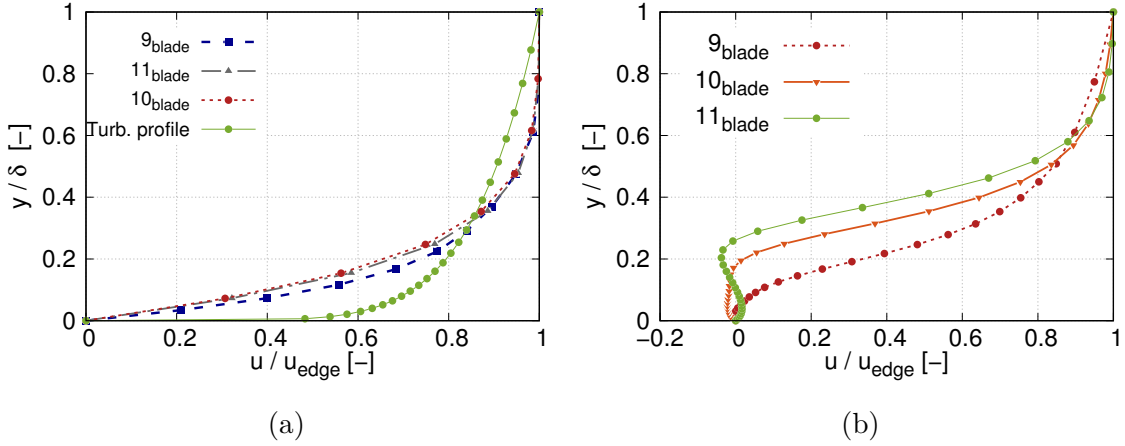


Figure 3.43: Boundary layer profiles on the blade suction side in the adverse pressure gradient portion for the RANS (a) and LES simulations (b), see 9, 10, 11 in Fig. 3.37 for the corresponding extraction positions

suction side at around $x/C_x = 0.7$ at lower Reynolds number $Re = 1.8 \times 10^5$ and low free stream turbulence. According to the oil flow visualization in Fig. 3.41a, this boundary layer separation is not observed. Due to the relatively high free stream turbulence (around 6% when approaching blade), the hub and shroud boundary layers are supposed to turn turbulent since similar angles of migration of passage vortices at the hub and shroud between the RANS and experiments are observed. On the blade suction side, the boundary layer is allegedly to become turbulent and no separation bubble would be observed because the turbulent boundary layer is less prone to separate under adverse pressure gradient. It remains that the oil-painting should have been removed from blade suction side due to turbulent boundary layer. According to the partial information reporting the experiments, streaks structures were observed on the blade suction side with oil-painting. Oil-painting being progressively removed from suction side. It is the author's view that the boundary layer may be transitional/turbulent on the suction side but since the wall shear is less important than at the pressure side separation bubble and along the migrating suction side secondary vortices, the oil-painting is progressively removed. The turbulent nature of the incoming hub and shroud boundary layers as well as around the blade seems to be confirmed since the experimental total pressure loss downstream blade are in better agreement with the RANS than LES simulation. In particular, the position of the main loss peaks associated to the hub and shroud passage vortices are in better agreement indicating that boundary layer close to hub and shroud boundary layer is better predicted in the RANS than LES. The levels of loss downstream of the blade are underpredicted by the LES simulation all over the span. Since the laminar boundary layer induces less loss than a turbulent one at equivalent thickness, this would indicate that the boundary layer over the suction side would be mainly transitional/turbulent.

The comparison between the RANS, LES simulations without turbulence injection and experiments have shown that the flow field is poorly resolved by the LES simulations without turbulence injection. Indeed, turbulence has a significant influence

on the physical phenomena in the linear cascade as observed in the comparison between RANS and LES. Turbulence modifies the nature of the hub and shroud boundary layer, the position of the passage vortex and subsequent losses as well as the boundary layer around the blade. However, these last observations suffer from a lack of predictability and the idea was to perform the same LES simulation but with turbulent injection in order to see if the different assumptions made were correct and if it was possible to recover the proper level of losses downstream of the blade.

3.6.2 Turbulence injection in LES simulation using AVBP

Turbulence injection at the inlet of the LES simulation is made in conjunction to NSCBC conditions of AVBP solver proposed in Sec. A.3.1 (p.241) (see Fig. 3.44a). Velocity fluctuations are generated using a synthetic eddy viscosity method. The details of the method is proposed in Smirnov et al. [143] but a brief description is given. A set of modes is randomly chosen from a Normal distribution on each component of κ , the wave number corresponding to the two direction over which is defined the boundary layer plane. The corresponding energy $E(\kappa)$ is computed using the turbulent spectrum for each mode and the related velocity coefficients in the spectral domain are then computed. The velocity signal and its time derivatives are rebuilt in physical space using a Taylor assumption with a bulk velocity. Different parameters need to be set in the turbulence injection: the characteristic integral length scale, the spectrum of turbulence and the characteristic mesh size at the inlet of the domain. These parameters have significant effects on the flow in the configuration. The parameters have been chosen following the numerical study of Segui [144] using the same flow solver AVBP, turbulence injection and a configuration (LS89) with a turbulent grid upstream of a turbine cascade. The integral length scale has been set to 7 mm that corresponds to the experimental measurements on the LS89 configuration [145] for which the turbulence grid and distance to the cascade was similar to the current configuration. The cut-off length scale is set to 0.2 mm and corresponds to the characteristic length scale of the mesh from the inlet to the blade since the mesh cannot transport structures with characteristic length lower than the characteristic cell size. Once the turbulence is generated (using a grid for experiments and at the inlet boundary for the simulation), turbulence experiences a spatial decay in the axial direction. The integral scale set is here an important parameter since the decay rate is inversely proportional to the integral length scale. That's why setting the inlet length scale is important to make sure that a realistic turbulence level reaches the airfoil. The decay of turbulence is then compared to the analytical law resulting from the decay of a homogeneous isotropic turbulent field [146] in order to reach similar values of turbulence intensity at the blade leading edge compared to the experiments. The analysis is based on the initial turbulent kinetic energy $E_{k_{turb}}(t_0)$ and initial turbulent dissipation $\epsilon_{k_{turb}}(t_0)$ at the inlet of the domain. The time evolution of E_k is:

$$E_{k_{turb}}(t) = E_{k_{turb}}(t_0) \left(1 + \left(C_{\epsilon_{k_{turb}}} - 1 \right) \frac{t}{\tau_0} \right)^{\left(-\frac{1}{C_{\epsilon_{k_{turb}}} - 1} \right)} \quad (3.4)$$

with $\tau_0 = (E_{k_{turb}}(t_0)/\epsilon_{k_{turb}}(t_0))$ and the analytical model constant $C_{\epsilon_{k_{turb}}} = 1.92$. From the integral length scale, the initial turbulent dissipation $\epsilon_{k_{turb}}(t_0)$ is estimated at $\epsilon_{k_{turb}}(t_0) = 2.1 \cdot 10^6 m^2 s^{-3}$. The time evolution can then be transformed to a spatial evolution along a streamline using the Taylor hypothesis [146], i.e $x = u_0 t$ with u_0 the velocity at the inlet to be compared to the spatial prediction. Figure 3.44b shows the turbulent kinetic energy decay from the inlet of the domain $x/C_x = -1$ to blade leading edge $x/C_x = 0$ obtained by integrating the turbulent kinetic energy on axial planes. The turbulence decay is stronger in the simulation compared to the theoretical one. This may be due to two effects. Since turbulence is injected from a synthetic eddy viscosity method, turbulence is not initially a homogeneous and isotropic turbulence (HIT) meaning that some axial extent is required to reach this state [144] while the theory supposes HIT as soon as the inlet. A second contribution may be due to the mesh. Despite a refined mesh from the inlet to the blade leading edge to carry turbulent structures, part of the structures are possibly dissipated by numerics (spatial scheme and subgrid scale model). The ratio $E_{k_{turb}}(x)/E_{k_{turb}}(0)$ is

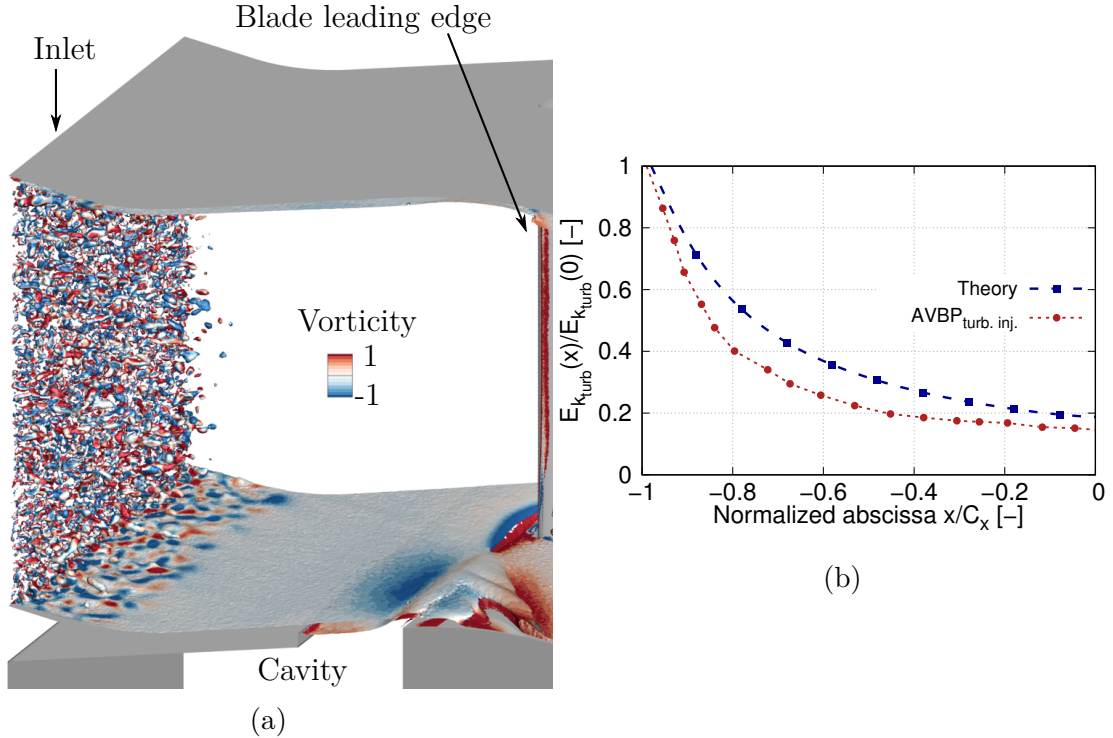


Figure 3.44: Iso q -criterion $q = 10^7$ colored by the vorticity showing the turbulence injection at the inlet of the domain in the first time steps of the AVBP simulation (a) and the turbulent kinetic energy decay from the inlet of the domain to the blade leading edge based on a theoretical HIT decay and obtained in AVBP simulation (b)

around 0.2 meaning that the velocity fluctuations between the inlet and blade leading edge is around $u'_{inlet}/u'_{LE} = 0.4$, the turbulent fluctuations injected at inlet of the domain have been set to $Tu \simeq 15\%$ to reach the turbulence level at the blade leading edge measured experimentally $Tu = 6\%$. The value of the turbulence intensity at the blade leading edge has been checked by setting a probe giving a turbulence

intensity of 6.5%. For the considered turbulence intensity and momentum thickness $Re_\theta \simeq 350$, the boundary layer should be transitional according to the works of Abu-Ghannam and Shaw [71]. Figure 3.45a shows the boundary layer profile at positions 1,2,3 and 4 provided previously and power-law turbulent profile. The boundary layer profiles are close to a turbulent boundary layer profile. The levels of turbulence injection is not relevant above 5% for the transition process according to the study of Abu-Ghannam and Shaw [71] but the inlet turbulence injection around 15% at the inlet of the domain may have played in favour of an earlier transition to turbulence. The Kelvin-Helmholtz instability that was developing at the rim seal

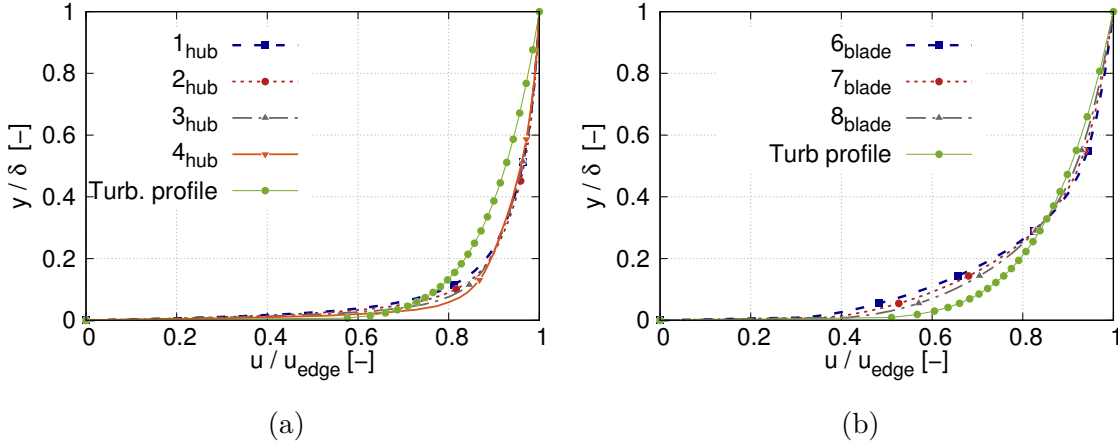


Figure 3.45: Boundary layer profiles on the hub endwall (a) and around the blade (b) for the LES simulation AVBP with turbulence injection. The boundary layer profile extraction location is provided in Fig. 3.37

interface in the LES without turbulence injection is not observed in the case with turbulence injection since no rolling up process is observed. This may be due to the cancelling of this instability phenomenon at a sufficiently high free stream turbulence since this instability is a natural instability of the flow that can be fully bypassed in relatively high free stream turbulence. From the spectral content, only the horse shoe vortex process remains at the hub. The boundary layer at the hub and shroud is seen to be separating closer to the blade leading edge due to the adverse pressure gradient compared to the LES simulation with a radial migration less important, closer to the RANS simulation (see Fig. 3.47b). On the blade pressure side, the topology is similar between the RANS and LES simulations with a separation bubble in the adverse pressure gradient region close to the blade leading edge reattaching downstream. On the blade suction side, the boundary layer profile at position 6, 7 and 8 (see Fig. 3.37) is shown in Fig. 3.45b. The boundary layer profile is not clearly a turbulent boundary layer since less momentum is provided to the near-wall region but may be considered as a transitional one. A main consequence shown in Fig. 3.47a is that for the pressure coefficient around the blade at mid-span, no inflectional point can be observed at $x/C_x = 0.8$ indicating that the separation bubble observed in the LES without turbulence injection has been cancelled, the transitional boundary layer being less prone to separate in the adverse pressure gradient portion (see Fig. 3.46). Figure 3.47b shows the pressure loss coefficient

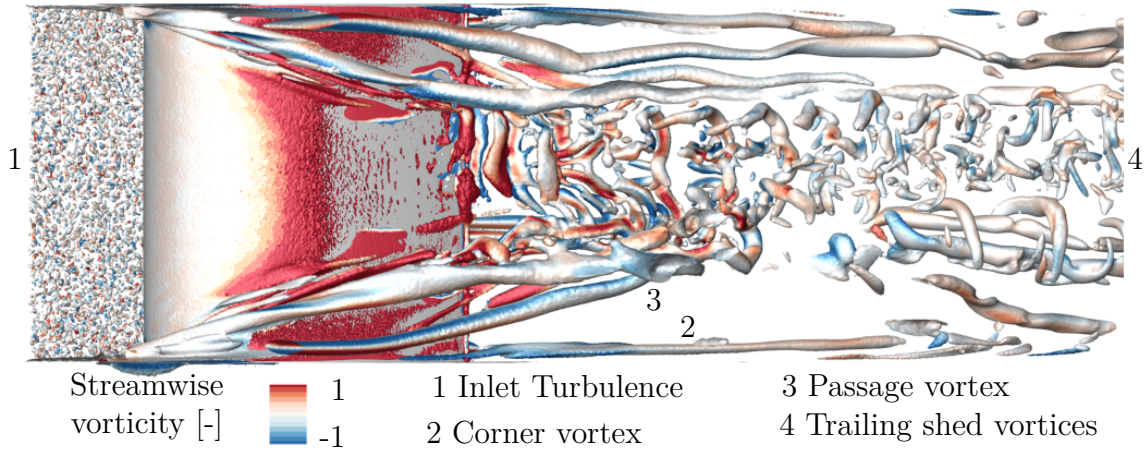


Figure 3.46: Lateral sight of blade suction side with iso q -criterion $q = 10^6$ colored by streamwise vorticity for the LES simulation AVBP with turbulence injection at the inlet

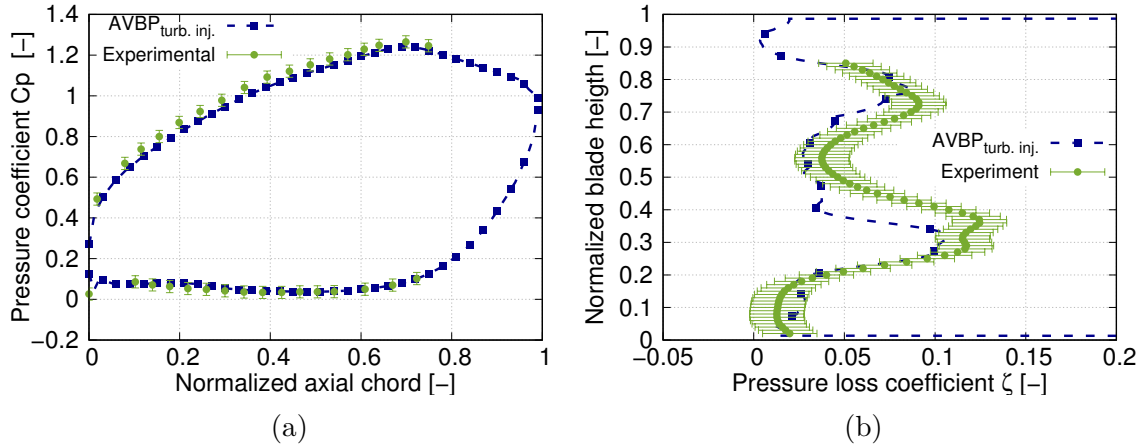


Figure 3.47: Pressure coefficient around the blade at mid-span (a) and pressure loss coefficient downstream of the blade for the axial rim seal at an intermediate purge flow rate for the LES simulation AVBP with turbulence injection at the inlet (b)

downstream of the blade for the A05 configuration and turbulence injection. The two main loss peaks are moved towards mid-span and the levels of loss are larger than the LES simulation without turbulent injection. Some discrepancy can be still observed compared to the experiments but turbulence injection promotes a better agreement with experiments for the position of the two main loss peaks and loss levels. This observation is in favour of the turbulent state proposed for the hub and shroud boundary layer as well as the suction side boundary layer. The comparison between the RANS, LES simulations without turbulence injection and experiments indicated that the flow field was not properly recovered by LES simulations without turbulence injection leading to a poor estimation of losses downstream blade. In this configuration, this is mainly due to the relatively high free stream turbulence that plays a major role in the development of secondary flow structures and topology around the blade suction side that cannot be properly captured by the current LES

approach since no turbulence injection was provided. Turbulence injection made possible to recover levels of losses similar to the experiments. RANS and Pro-LB approaches gave relatively good results since, the hub, shroud and blade boundary layers are turbulent in the experiments meaning that the modeling approach of RANS and law of the wall treatment for the Pro-LB simulation can relatively well approach the flow in the experimental configuration.

The effect of turbulence on the physical phenomena in a linear cascade with upstream hub cavity has been assessed by comparing RANS, LES and LES with turbulence injection at the inlet of the domain. In conjunction with experiments, the numerical results show that the hub and shroud boundary layers approaching the blade leading edge turn turbulent under a bypass process due to the free stream turbulence. The main effects are a stronger migration towards mid-span of the hub and shroud passage vortices compared to a laminar boundary layer and the cancelling of the natural Kelvin-Helmholtz instability at the interface between main annulus and cavity due to the shear layer observed in the LES simulation without turbulence injection. Also, the suction side boundary layer is allegedly to become transitional/turbulent. This information is supported by the cancelling of the suction side pressure bubble separation observed in the LES simulation without turbulence injection (laminar boundary layer) while not observed in the experiments and LES with turbulence injection. Furthermore, the levels of losses downstream of the blade for the LES simulation without turbulence injection are underestimated compared to the experiments that could indicate that the boundary layer is indeed turbulent and generate more losses than the laminar one.

3.7 Application of exergy formulation to track losses

In the current section, the exergy formulation is applied to the linear cascade configuration. The analysis is first conducted by looking at the decrease of useful work (exergy) along the simulation domain due to irreversibility. Then, the emphasis is given to the influence of the different contributions to exergy decrease along the domain: the effects of turbulence, the contribution of the viscous and thermal dissipation. Once described, a closer look is given to the contributions of the boundary layers over the wetted surfaces (hub, shroud and blade) by restricting the analysis to these subdomains and in the remaining domain (the full domain where the subdomains related to boundary layers have been removed) where secondary flows are known to develop and contribute to loss in the turbine. All these elements will be used to obtain the regions and mechanisms inducing loss in the turbine. These subsections are followed by the influence of the purge flow rate and rim seal geometry on the loss mechanisms previously described. The study is performed first on the RANS simulation for the axial rim seal at intermediate purge flow rate (A05), the same analysis on the LES simulation being proposed at the end of this section.

3.7.1 Exergy analysis in the simulation domain

Exergy formulation described in Sec. 2.1.3 (p.34) is used in this section to highlight the regions of loss production. The general equation for exergy proposed in eq.(2.50) can be written as:

$$\frac{d}{dt} \iiint (\rho\chi) dV + \oint (\rho\chi) u_j n_j dA_{IO} = P_{shaft} + \chi_q + \Phi_{\nabla u} + \Phi_{\nabla T} + \frac{d}{dt} \iiint p dV. \quad (3.5)$$

Considering steady flow conditions, this equation can be written as

$$\oint (\rho\chi) u_j n_j dA_{IO} = P_{shaft} + \chi_q + \Phi_{\nabla u} + \Phi_{\nabla T} + \Phi_{sw}. \quad (3.6)$$

This equation gives a power balance between enthalpy, entropy flux balance (with exergy) at the inlet and outlet of the domain (left-hand side of the equation) and the power associated to the heat flux (χ_q), work transferred with the shaft (P_{shaft}), and the irreversibility in the domain ($\Phi_{\nabla u} + \Phi_{\nabla T} + \Phi_{sw}$). The current configuration is low Mach meaning that no shocks are expected $\Phi_{sw} = 0$. Since the configuration is static, no work is transferred with the fluid similarly to a stator row leading to $P_{shaft} = 0$. Finally, no heat is transferred at the border of the domain (since adiabatic wall), no heat due to a combustion process for example leading to $\chi_q = 0$. Thus, the exergy variation between inlet and outlet of the domain can only decrease due to viscous $\Phi_{\nabla u}$ and thermal $\Phi_{\nabla T}$ gradient contributions.

It may be useful to recall here the composite nature of exergy $\chi = (h_{tot} - h_0) - T_0(s - s_0)$ composed of the total enthalpy and entropy. The total enthalpy in last equation eq.(3.6) provides in right-hand side of the equation non-pressure related work, here expressed in terms of power extracted/supplied on the shaft P_{shaft} and heat added/collected for the fluid (see eq.(2.10) p.23). In the current configuration, since none of these contributions appear, the total enthalpy is conserved along the cascade. This means that the flux of total enthalpy at the inlet of the main annulus plus the cavity inlet one equals the flux of enthalpy at the outlet of the domain. This statement is true in current configuration and more generally in static configuration with no heat exchanged. Some useful work stored in kinetic energy and pressure work is transferred to internal energy under irreversibility and since total enthalpy is the sum of all these three contributions, the total enthalpy is conserved. However, from the purpose to generate work, since kinetic energy and pressure that can be fully used to generate work have been transformed partially in internal energy that can only be partially transformed in useful work (the Carnot cycle for example), loss is generated (in the purpose to generate work). With exergy, the entropy term added to the total enthalpy makes possible to take into account this degradation of energy quality (in the purpose to generate work) with the velocity and thermal mixing $\Phi_{\nabla u}$ and $\Phi_{\nabla T}$ held by the entropy transport equation eq.(2.48) (p.33). The entropy production in the domain multiplied by the temperature at which irreversibility occurs T_s provides the equivalent heat supplied Q to the fluid increasing its internal energy and equal to the decrease of pressure and kinetic energy terms. This term being subtracted to the total enthalpy in the definition of exergy. An additional feature of exergy is its definition relatively to a reference state (h_0, s_0). The potential energy contained in

the fluid of the cascade could be hypothetically used to generate work by expanding the fluid towards zero pressure (the total energy contained in the fluid). However, since the majority of applications are performed on earth used as the reference or dead state, the energy contained between atmospheric and zero energy cannot be used to generate work and further explains why exergy is defined with a reference state. It should be emphasized that the reference state could be any other reference state than atmosphere like exit conditions of the turbine for example.

The description of this notion of exergy makes also possible to recall the procedure of averaging that should be used if one had only access to a value of pressure and temperature at the inlet and outlet plane of the domain to properly analyse the losses generated in the averaged flow field of the turbine. The exergy quantity is here shown to be relevant for tracking losses. Since a composite quantity of total enthalpy and entropy, the flux of these two quantities must be conserved between the non-uniform inlet/outlet plane and the one dimensional quantities at these same planes. Since the flow field can be described by any other two intensive independent variables like pressure and temperature commonly used in gas turbine. It was shown that the conservation of total enthalpy is obtained for mass averaged temperature while following the work averaging procedure for pressure to ensure a conservation of entropy flux. Following this averaging procedure, the conservation of exergy fluxes at the inlet and outlet planes is ensured between the non-uniform plane and one dimensional value on these same planes (see Sec. A.5 p.250).

Figure 3.48a shows the exergy decrease of the flow along the simulation domain where the environment has been taken at conditions ($p_0 = 101\,325\text{ Pa}$, $T_0 = 300\text{ K}$) since the exergy is defined with a reference state. It is reminded that inlet to rim seal left corner extends from $x/C_x = -1$ to -0.26 , rim seal region from $x/C_x = -0.26$ to -0.04 , blade domain from $x/C_x = 0$ to 1 and blade trailing edge to two axial chord downstream blade (outlet) from $x/C_x = 1$ to 3 (see Fig. 3.50). This figure is obtained by subtracting to the total exergy at the inlet of the domain (here normalized to one), the contributions related to velocity and temperature gradients $\Phi_{\nabla u}$ and $\Phi_{\nabla T}$. These contributions that decrease the exergy of the flow restricted here to these last two terms are generally said to produce anergy. The anergy is the useless energy (for the purpose to generate work) obtained from the gradients transformed into thermal energy. The viscous and thermal anergy evolutions along the simulation are given in Fig. 3.48b where the left-hand side abscissa corresponds to viscous term and right-hand side to the thermal one. The exergy of the flow at a position x is obtained by subtracting the viscous and thermal anergy at position x from the exergy available at inlet of the domain. The viscous and thermal anergy are obtained by performing a volume integration of the velocity and temperature gradients from the inlet to the considered position x :

$$\Phi_{\nabla u}(x) = \iiint_{V,0 \rightarrow x} \frac{\tau_{ij,eff}}{\bar{T}} \frac{T_0}{\bar{T}} \frac{\partial \bar{u}_i}{\partial x_j} dV; \quad \Phi_{\nabla T}(x) = \iiint_{V,0 \rightarrow x} (\lambda + \lambda_{turb}) \frac{T_0}{\bar{T}^2} \left(\frac{\partial \bar{T}}{\partial x_j} \right)^2 dV \quad (3.7)$$

where $\tau_{ij,eff} = (\mu + \mu_{turb})(\partial u_i / \partial x_j + \partial u_j / \partial x_i)$ is the effective viscous stress tensor. In addition, the derivative according to the axial coordinate of the anergy that is here referred as anergy production at station x of the domain and denoted $d\phi/dx$ can be obtained by splitting the whole domain in axial subdomains of characteristic length

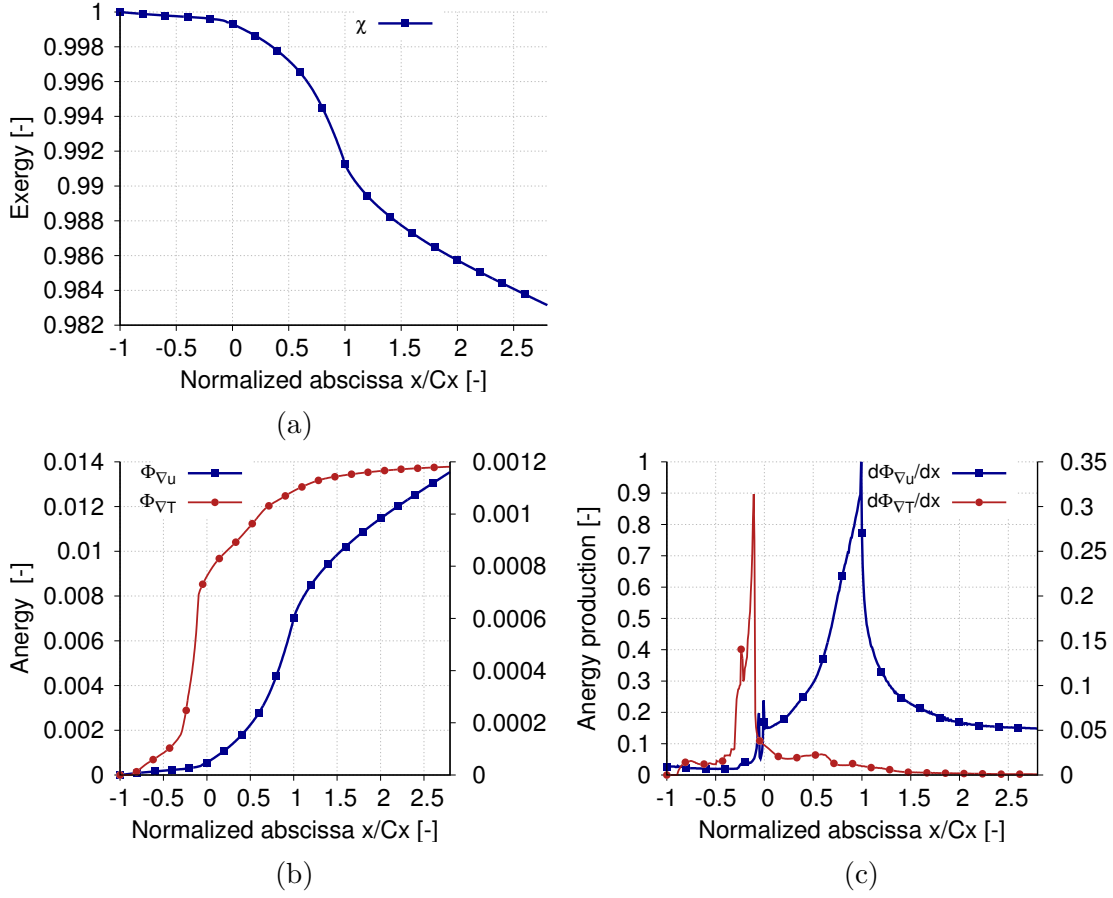


Figure 3.48: Evolution of the flow exergy from the inlet to outlet of the domain (a). Evolution of anergy along the simulation domain including viscous $\Phi_{\nabla u}$, thermal contribution $\Phi_{\nabla T}$ (b) and anergy production along the axial evolution $d\Phi_{\nabla u}/dx$ $d\Phi_{\nabla T}/dx$ (c). The right axis refers to thermal contribution and left axis to viscous contribution

dx (see Fig. 3.50). Integrating the velocity and temperature gradient terms over these subvolumes for which the characteristic length tends towards zero provides the local production:

$$\frac{d\Phi_{\nabla u}}{dx}(x) = \iiint_{V,x}^{x+dx} \frac{T_0}{\tau_{ij,eff} \bar{T}} \frac{\partial \bar{u}_i}{\partial x_j} dV; \quad \frac{d\Phi_{\nabla T}}{dx}(x) = \iiint_{V,x}^{x+dx} (\lambda + \lambda_{turb}) \frac{T_0}{\bar{T}^2} \left(\frac{\partial \bar{T}}{\partial x_j} \right)^2 dV. \quad (3.8)$$

The corresponding anergy production is shown in Fig. 3.48c. These different plots that provide the evolution of exergy/anergy in the domain makes possible to observe the main regions all along the main axis x contributing to loss generation before to look more precisely at local points in the three-dimensional domain. From these last figures, it can be pointed out that the decrease in exergy of the flow (or equivalently increase in anergy) is not performed linearly in the simulation domain. The viscous and thermal anergy are shown to have different behavior. For the thermal anergy production, the main regions of production corresponds to the extension of the rim seal and downstream along the blade. The viscous anergy production is relatively

	$T_0 = 300 \text{ K},$ $p_0 = 101325 \text{ Pa}, s_0 = 1050$	$T_0 = 295 \text{ K},$ $p_0 = 95000 \text{ Pa}, s_0 = 1050$
$\oint \rho(h_{tot} - h_0)u_j n_j dA_I$	9135	10227
$\oint \rho(h_{tot} - h_0)u_j n_j dA_0$	9135	10227
$\oint \rho T_0(s - s_0)u_j n_j dA_I$	7202	6753
$\oint \rho T_0(s - s_0)u_j n_j dA_0$	7236	6788
$\oint (\rho\chi)u_j n_j dA_I$	1897	3508
$\oint (\rho\chi)u_j n_j dA_O$	1833	3474
$\oint (\rho\chi)u_j n_j dA_{I0}$	34	34
$\frac{\oint (\rho\chi)u_j n_j dA_{I0}}{\oint (\rho\chi)u_j n_j dA_I} [\%]$	1.8	0.8

Table 3.5: Exergy balance at two different reference conditions

low from the inlet to rim seal, increases sharply along the rim seal and blade extensions before to return towards intermediate levels of anergy production downstream of the blade. The viscous anergy production does not tend towards zero while the thermal contribution is almost zero as soon as one axial chord downstream of the the nozzle guide vane ($x/C_x = 2$) (see Fig. 3.48c). In magnitude, the thermal contribution is in the order of magnitude of ten times lower than the viscous contribution (see Fig. 3.48b). At the outlet of the domain, the remaining exergy is around 98.2% of the exergy available at inlet of the domain (compared to the reference state). It corresponds to the remaining exergy compared to the reference state that is still available and could be extracted by expansion between pressure at outlet of the domain and reference pressure. Alternatively, the linear cascade is shown to deteriorate 1.8% of the exergy available at the inlet of the domain by viscous and temperature dissipation process in order to accelerate the flow by transfer of potential pressure forces to kinetic energy. A detail of the enthalpy flux at the inlet, outlet and entropy flux that are constituent of exergy is proposed in Tab 3.5. It can be noticed that the flux of enthalpy between the inlet (main annulus and cavity) equals the enthalpy flux at the outlet and that the evolution of exergy is only held by the changes in entropy. The same exergy flux balance between inlet and outlet of the domain has been performed for a reference state at a same disorganization level $s_0 = 1050 [kg.m^2.s^{-2}.K^{-1}]$ but with lower enthalpy ($T_0 = 295 \text{ K}, p_0 = 95000 \text{ Pa}$). In this case, the entropy generated along the domain is still the same, but the ratio of exergy decrease between inlet and outlet compared to the exergy available at inlet of the domain is lower than the case ($T_0 = 300 \text{ K}, p_0 = 101325 \text{ Pa}$) since more exergy is available due to a lower enthalpy magnitude for the reference state (see Tab.3.5).

3.7.1.1 Anergy production splitting between mean and turbulent contribution

Last figures provided the total contribution (mean and modeled turbulent contribution) of viscous and thermal anergy. This total contribution was obtained by using the notion of effective viscosity/diffusivity (μ_{eff}/λ_{eff}) that is the sum of the natural

viscosity/diffusivity of the fluid (μ/λ) provided by the mean flow and a turbulent contribution modeled with an equivalent turbulent viscosity/diffusivity ($\mu_{turb}/\lambda_{turb}$) as proposed in Sec. 2.1.4.1 (p.40). These different contributions can be written for viscous and thermal energy as:

$$\Phi_{\nabla u, mean} = \iiint_{\mathcal{V}} \mu \left(\frac{\partial \bar{u}_i}{\partial x_j} + \frac{\partial \bar{u}_j}{\partial x_i} \right) \frac{T_0}{\bar{T}} \frac{\partial \bar{u}_i}{\partial x_j} d\mathcal{V}; \quad \Phi_{\nabla u, turb} = \iiint_{\mathcal{V}} \mu_{turb} \left(\frac{\partial \bar{u}_i}{\partial x_j} + \frac{\partial \bar{u}_j}{\partial x_i} \right) \frac{T_0}{\bar{T}} \frac{\partial \bar{u}_i}{\partial x_j} d\mathcal{V} \quad (3.9)$$

$$\Phi_{\nabla T, mean} = \iiint_{\mathcal{V}} \lambda \frac{T_0}{\bar{T}^2} \left(\frac{\partial \bar{T}}{\partial x_j} \right)^2 d\mathcal{V} \quad \Phi_{\nabla T, turb} = \iiint_{\mathcal{V}} \lambda_{turb} \frac{T_0}{\bar{T}^2} \left(\frac{\partial \bar{T}}{\partial x_j} \right)^2 d\mathcal{V}. \quad (3.10)$$

Figure 3.49 provides the mean and turbulent contributions to the viscous and ther-

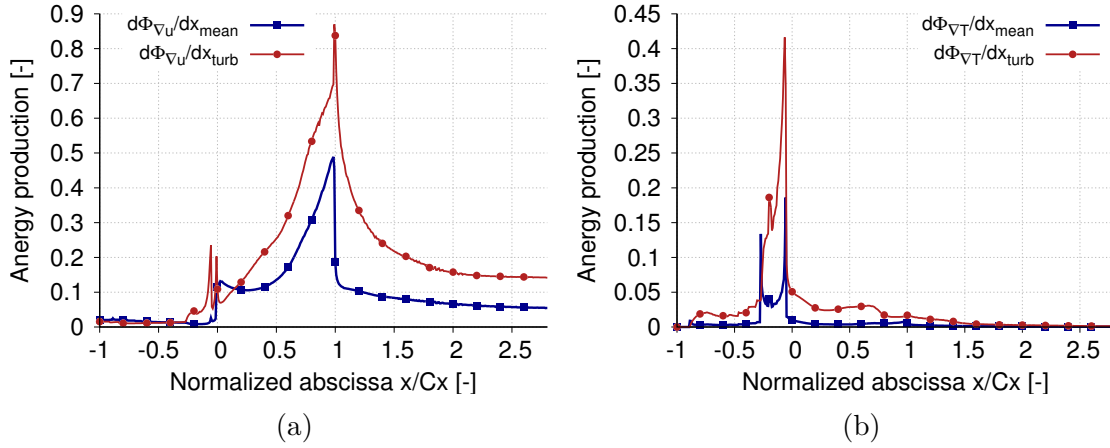


Figure 3.49: Evolution of the energy production along the simulation domain for viscous $d\Phi_{\nabla u}/dx$ (a) and thermal contributions $d\Phi_{\nabla T}/dx$ (b) including the mean and turbulent contributions

mal energy production. As proposed in Sec. 2.1.4.1 (p.40) or Lengani et al. [147], the viscous and thermal energy production (or equivalently entropy since these two terms are held by the entropy transport equation) in a turbulent flow corresponds to a mean contribution sometimes called laminar contribution and a turbulent one. This former contribution is only due to the mean flow distortion. The second contribution is provided by turbulence that under transfer of energy from large to small scales is dissipated in internal energy (heat). This induces the non locality between mean energy flow lost and equivalent heat generated at small scales. But, similarly to the mean contribution, as soon as mean kinetic energy is transferred to turbulence this contribution will not be recovered in the purpose to generate work. The turbulent production is larger than mean contribution for both viscous and thermal contributions at the current Reynolds number. Mean and turbulent contributions, despite of different magnitudes, provide a similar trend in the domain.

3.7.1.2 Anergy production splitting between different regions of the flow

The boundary layer module introduced in App. C makes possible to obtain the boundary layer thickness over the different wetted surfaces: hub shroud and blade.

Based on the boundary layer thickness available over the different surfaces of the configuration, the volume related to the hub (\mathcal{V}_{hub}), shroud (\mathcal{V}_{shroud}) and blade boundary layer (\mathcal{V}_{blade}) can be extracted from the three-dimensional domain as well as the remaining domain ($\mathcal{V}_{rem.}$) i.e. the full domain (\mathcal{V}) without the boundary layers of the wetted surfaces ($\mathcal{V}_{hub} \cup \mathcal{V}_{shroud} \cup \mathcal{V}_{blade}$) (see Fig. 3.50). From this decomposition is built contiguous volumes that map the whole volume. Anergy production along the domain can be then split according to these different contributions. For example, for the viscous anergy evolution, the integral can be split according to the different contributions:

$$\Phi_{\nabla u}(x) = \iiint_{\mathcal{V}_{hub} + \mathcal{V}_{shroud} + \mathcal{V}_{blade} + \mathcal{V}_{rem.}, 0 \rightarrow x} (\mu + \mu_{turb}) \left(\frac{\partial \bar{u}_i}{\partial x_j} + \frac{\partial \bar{u}_j}{\partial x_i} \right) \frac{T_0}{\bar{T}} \frac{\partial \bar{u}_i}{\partial x_j} d\mathcal{V}. \quad (3.11)$$

The computational domain can be split in axial subvolumes to obtain anergy production along the domain as performed previously. The same procedure applied to the volumes restricted to the boundary layer and remaining domains can be used to obtained anergy production restricted to these different contributions. This procedure is used in the following of the section. It is to be noticed in the remaining of the section that we will deal indifferently with entropy production or anergy production to characterize the regions of loss generation. Anergy and entropy production can be used indifferently to follow the loss generation along the domain since related by a constant that is the reference temperature T_0 : $d\Phi_{\nabla u}/dx = T_0 s_{visc}$, $d\Phi_{\nabla T}/dx = T_0 s_{therm}$. We use here these two terms since the anergy production along the domain is held by contributions that appear in the entropy transport equation (eq.(2.48) p. 33). It is reminded that if one wants to lead an exergy analysis, the quantities obtained with entropy are simply to be multiplied by T_0 to draw the exergy balance. Furthermore, as shown in Tab. 3.5, the ratio of exergy decrease along the domain compared to the inlet one depends on the reference state while the entropy production term depends only on local quantities (temperature, velocity, viscosity and diffusivity) that may be more intuitive when one wants to deal with local loss. The analysis is first conducted on the viscous entropy production then on the thermal entropy production (where viscous and thermal anergy are simply recovered by multiplying this result by the reference temperature). The different figures related to the contributions of the boundary layers and remaining domain are given in conjunction with the total contribution of the domain at a same abscissa (denoted $s_{visc,total}$) to give the reader the magnitude of the contribution to the total one.

3.7.1.2.1 Viscous entropy production Figure 3.51 shows viscous entropy production related to the boundary layers of the different wetted surface (hub, shroud, blade) and the remaining term that is the difference of the total viscous entropy production less boundary layers contributions. From the inlet $x/C_x = -1$ to the rim seal left corner $x/C_x = -0.26$, the viscous entropy is produced by hub and shroud boundary layers (see Fig. 3.51c and 3.51d for contributions of hub, shroud and cumulated contributions). This can be understood as the development of a boundary layer over the hub and shroud that induces velocity gradients close to the

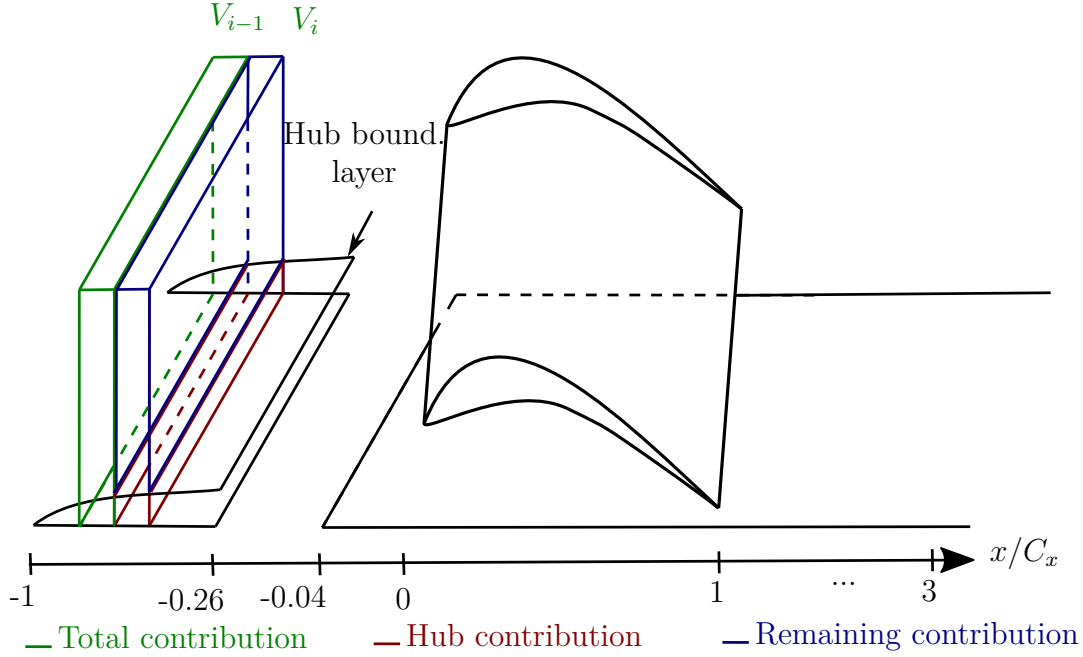


Figure 3.50: Example of a simulation domain discretized in axial subvolumes V_i (green). For a simple configuration where only the hub boundary layer is considered, V_i can be split in a subvolume associated to the hub boundary layer (red) and a remaining domain that is simply the subvolume V_i minus the subvolume associated to the hub boundary layer (blue)

wall and as a consequence the viscous entropy. Since the hub and shroud contributions almost equal the total contribution along this portion, it may be concluded that negligible viscous entropy is generated in the free stream (i.e. the velocity gradients must be low). Along the blade domain, viscous entropy production is split between the contributions of the blade, hub and shroud boundary layers as well as remaining term (see Fig. 3.51). The notion of remaining domain and remaining term is used here since this subdomain can contain and cover various phenomena. The main underlying phenomena that may happen out of the boundary layers are, according to the description of the flow in the cascade proposed in Sec. 3.4 (p.106), the shear layer at rim seal interface (p.109), secondary vortices produced in the passage (p.112) and the trailing shed vortices at blade trailing edge (p.113). Depending on the axial position in the domain, one or other contribution may be dominant. For example, at the rim seal interface, the main contribution could be attributed to the shear layer since no secondary vortices and trailing shed vortices have been produced yet. However, at the blade trailing edge for example, trailing shed vortex process and secondary vortices mixing/dissipation could contribute to this notion of remaining term. Downstream of the blade, the viscous entropy production is mainly brought by the hub, shroud and remaining term. The entropy production is almost entirely due to hub and shroud boundary layers at around one axial chord downstream of the blade trailing edge ($x/C_x = 2$). The entropy production related to the boundary layer downstream of the blade is greater of a factor 5 compared to the upstream blade. This observation agrees with Denton [48] stating that the loss

associated to the hub and shroud boundary layers downstream of the nozzle guide vane are generally greater than upstream of the vane since the flow has experienced acceleration in the passage and more losses are to be expected (see Fig. 3.51b and 3.51d). The platform extent downstream of the blade being important to shorten to reduce losses. An additional observation that can be made is that the hub and shroud boundary layers generate a similar levels of viscous entropy in the domain. From the inlet $x/C_x = -1$ to the rim seal $x/C_x = -0.26$, since the prescribed inlet profile gave a similar inlet boundary layer thickness and state at the hub and shroud, the associated loss should be comparable. Along and downstream of the blade, the comparable magnitude observed is less obvious to understand since, at the hub, the cavity induces a boundary layer separation at the rim seal left corner $x/C_x = -0.26$ and a new born boundary layer at the rim seal right corner $x/C_x = -0.04$ that is not induced at the shroud. However, this similar viscous entropy generation can be understood by the similar horse shoe vortex process at the hub and shroud that induces a boundary layer separation at the saddle point upstream of the blade leading edge line and a new boundary layer initiated downstream of the blade leading edge at the hub and shroud. The new born boundary layers at the hub and shroud are then skewed similarly in the passage due to the cross pressure gradient and entrainment in the pressure side of the horse shoe vortex process. These two boundary layers experiencing similar processes, a similar nature and thickness is expected and consequently a similar viscous entropy until the outlet of the domain. Downstream of the trailing edge, the total contribution to viscous entropy becomes equal to the hub and shroud boundary layers after around one axial chord at $x/C_x = 1$ (see Fig. 3.51d). Between the trailing edge and one axial chord downstream of the trailing edge, the additional contribution emanates from the remaining term. At the blade trailing edge, according to the description of the flow proposed in Sec. 3.4.4 (p.113), two main contributions can be associated to the remaining term that are the secondary vortices produced in the passage and the trailing shed vortices produced at blade trailing edge. From Fig. 3.51b, the decay of these structures under a mixing process generates entropy and are mainly dissipated over one axial chord downstream blade, the contribution becoming very low between $x/C_x = 2$ and $x/C_x = 3$.

Similarly to the total anergy production where the mean and turbulent contributions have been split as proposed in Fig 3.49, this same process can be applied for the viscous entropy production to the different subdomains defined. The entropy generation related to the hub and shroud boundary layer is almost equally balanced between mean and turbulent contributions with a similar trend along the domain (see Fig. 3.52). For the blade boundary layer contribution, mean and turbulent part contribute almost equally to the total entropy production with an increasing entropy production trend on the blade. However, it is observed that the mean contribution increases strongly close to leading edge and is a phenomenon not observed in the turbulent contribution that increase linearly all along the blade (see Fig. 3.53). Figure 3.54 shows the contribution of the blade boundary layer split in pressure and suction side of the blade. The major part of the entropy is produced on the blade suction side (see Fig 3.54a and 3.54c). This observation agrees with the statement of Denton [48] showing that main part of the loss contribution to the blade boundary layer is brought by the suction side essentially because acceleration and velocity

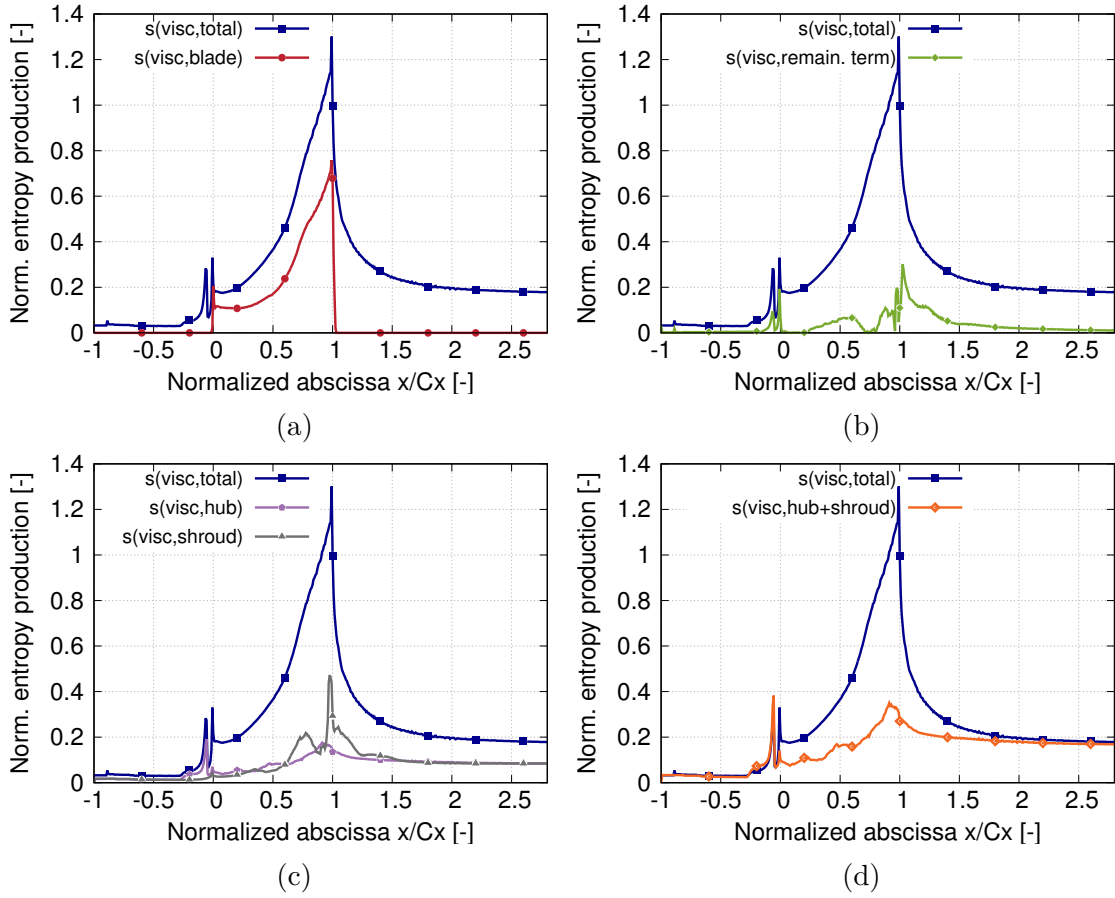


Figure 3.51: Mean, turbulent and total entropy production for the different subdomains

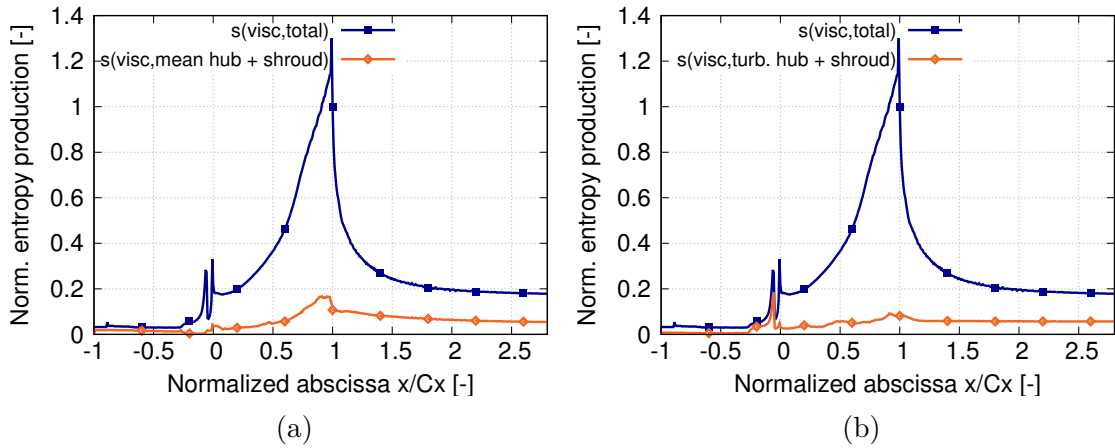


Figure 3.52: Entropy production associated to mean and turbulent contributions for the hub and shroud

are stronger on the blade suction side. The contribution of the pressure side is relatively low until $x/C_x = 0.5$ corresponding to the decelerating flow portion and may explain why the viscous entropy production is almost zero. This relatively low contribution may be also explained by the boundary layer thickness estimation

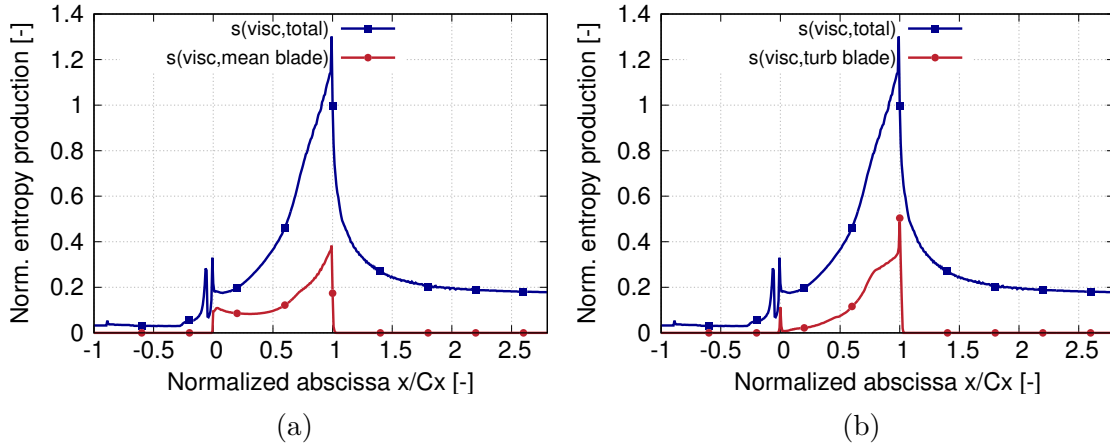


Figure 3.53: Mean and turbulent contribution to the blade boundary layer entropy production

on this portion. Indeed, a separation bubble was observed on the blade pressure side between ten and thirty percent axial chord (see Sec. 3.4.3 p.112). Providing a boundary layer thickness in this region is rather challenging for the boundary layer module since the boundary layer is not properly defined. The entropy production then increases corresponding to the accelerating flow portion of the pressure side until the blade trailing edge (see Fig. 3.54b and 3.54d). Close to the blade trailing edge ($x/C_x = 1$), a sharp increase in entropy production can be observed for the blade contribution. This may be explained by the possible separation process of the pressure and suction side boundary layer slightly upstream of the trailing edge (around $x/C_x = 0.95$) due to a thick trailing edge enforcing the boundary layer to separate upstream. Also, the methodology used to capture the blade boundary layer that may contain a short portion of the flow downstream blade trailing edge where shedding vortex process occurs.

The total viscous contribution in entropy production is, as stated previously, dominated by turbulent contribution with a mean contribution lower. The study of the different boundary layers shows, however, that the contributions between turbulent and mean contributions are in the same order of magnitude. This means that the additional contribution to the turbulent part must be provided by the remaining domain without boundary layers. Figure 3.55 shows viscous entropy production related to this remaining term. The turbulent contribution is clearly seen to be the largest. The mean and turbulent contributions of the remaining term are zero before the rim seal that is as stated previously, indicating that the velocity gradients in the free-stream are low. Two localized entropy peaks can be observed corresponding to a portion close to rim seal right corner $x/C_x = -0.04$ and in front of the blade leading edge $x/C_x = 0$. For the first peak, some main annulus flow can enter the cavity due to the potential effect of the blade leading edge and cavity flow emerges close to the center of the passage that may explain velocity gradients in this region. The second peak is associated to the portion between the rim seal right corner and blade leading edge. This peak may be associated to the horse shoe vortex process at the hub and shroud initiating the formation of secondary vortices in the passage. A first observation is that between $x/C_x = 0$ and $x/C_x = 0.2$, negligible entropy

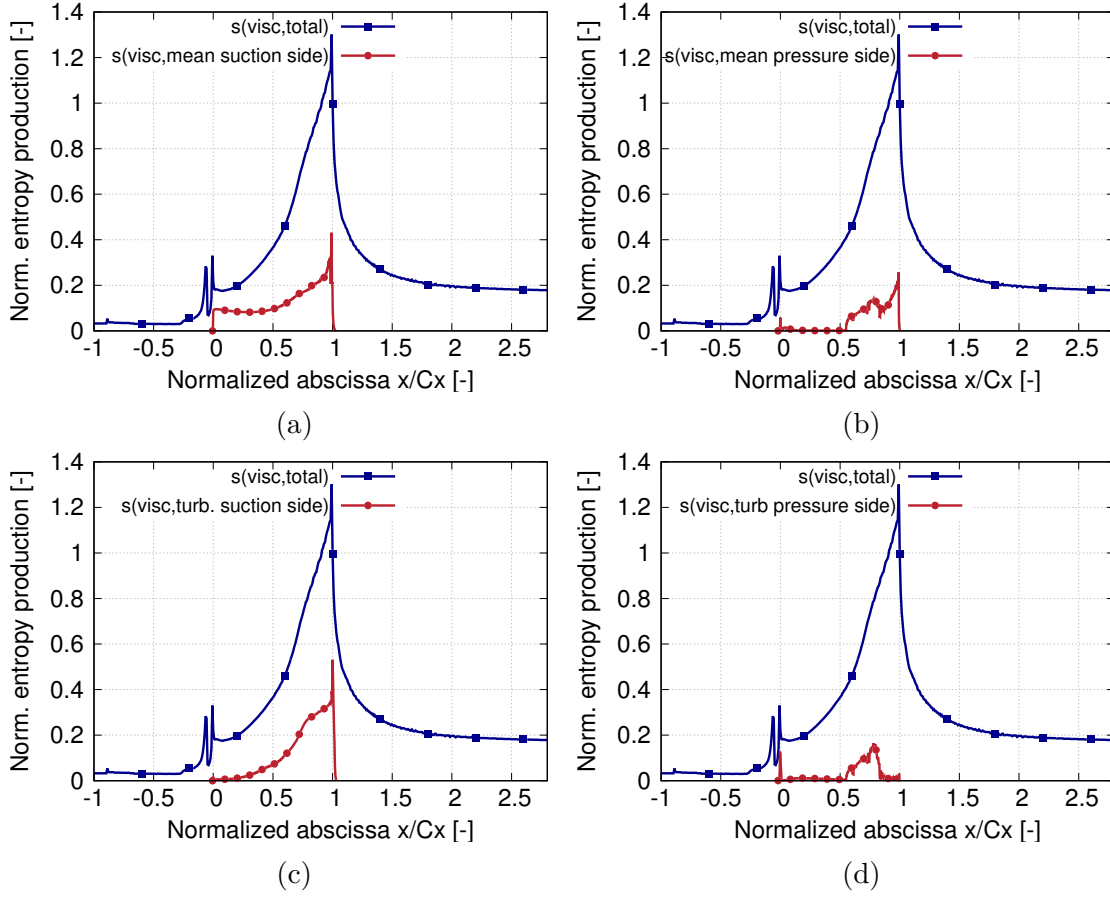


Figure 3.54: Pressure and suction side contribution to the viscous entropy production

due to secondary flow structures is generated indicating that from the horse shoe vortex process at the blade leading edge, the generation of loss is not immediately initiated. Downstream, the turbulent contribution increases as soon as $x/C_x = 0.2$ corresponding to the migration of the pressure side of the horse shoe vortex. For the mean contribution, the increase starts at around $x/C_x = 0.5$ where pressure and suction side of the horse shoe vortex have already merged and the migration of the passage vortex have been initiated. The mean and turbulent contributions then increase until trailing edge meaning that the secondary vortices are continuously fed by the cross flow component induced by the blade-to-blade pressure gradient and dissipate this additional momentum along the passage. At the trailing edge, the mean contribution becomes negligible while a peak of turbulent entropy can be observed associated to the trailing shed vortex process. Downstream, the entropy generation decreases, the secondary vortices are no more fed by the passage pressure gradient and trailing shed vortices decrease. The dissipation process of these structures is made mainly by turbulence and over one axial chord. The entropy production related to this remaining term becoming negligible downstream $x/C_x = 2$. A point that also needs to be addressed is the decomposition of the full domain in different subdomains related to the different boundary layers over the wetted surfaces and remaining domain. A main consequence of that decomposition is that no interaction

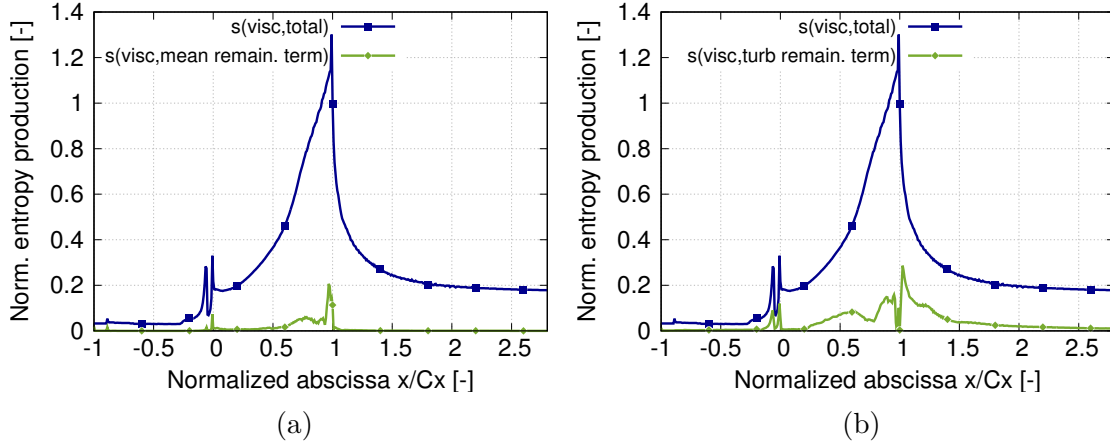


Figure 3.55: Mean and turbulent contribution to the viscous entropy production for the remaining term

can proceed between for example the remaining term and the boundary layer contributions. However, some interactions can be exhibited between the secondary flows in the passage that are supposed to be captured by the remaining domain and the boundary layers. Figure 3.56 shows the entropy production at the hub and shroud for mean and turbulent contributions in the boundary layers. Regions of high entropy production in the hub and shroud boundary layers correspond to the regions where the pressure side of the horse shoe vortex travels in the passage and further downstream where corner vortex migrates. The vortices induce additional friction close to the wall and more entropy is generated in the hub/shroud boundary layer contribution. Figure 3.57 shows the entropy production in the blade boundary layer. Similarly to the hub and shroud, regions of high entropy production correspond to the regions where passage and corner vortices migrate. Secondary vortices developing in the passage induce additional entropy production in the hub, shroud and blade boundary layers by a friction process of the vortical structures on the wetted surfaces. This means that part of the viscous entropy generated in the hub, shroud and blade boundary can be attributed to the friction of the secondary vortices on these surfaces. Then, secondary vortices can be seen to have two main mechanisms of loss generation. A first mechanism related to the mixing process and viscous dissipation of the secondary kinetic energy (energy contained in the cross contributions to the stream one) in the vortices and the friction of these structures on the different walls of the turbomachine where these structures travel. This observation was previously made by Denton and Pullan [87] studying the endwall sources of loss in a rotor/stator configuration based on an entropy formulation. The regions of high entropy production close to the endwall were shown to correspond to the horseshoe vortex system, especially the pressure side leg as it crosses the passage towards the suction surface and on the blade suction surface with the passage vortex.

3.7.1.2.2 Entropy production in the boundary layer in the wall-normal direction Previous paragraphs were devoted to study the evolution of entropy relatively to the axial coordinate in the different regions of the flows including the

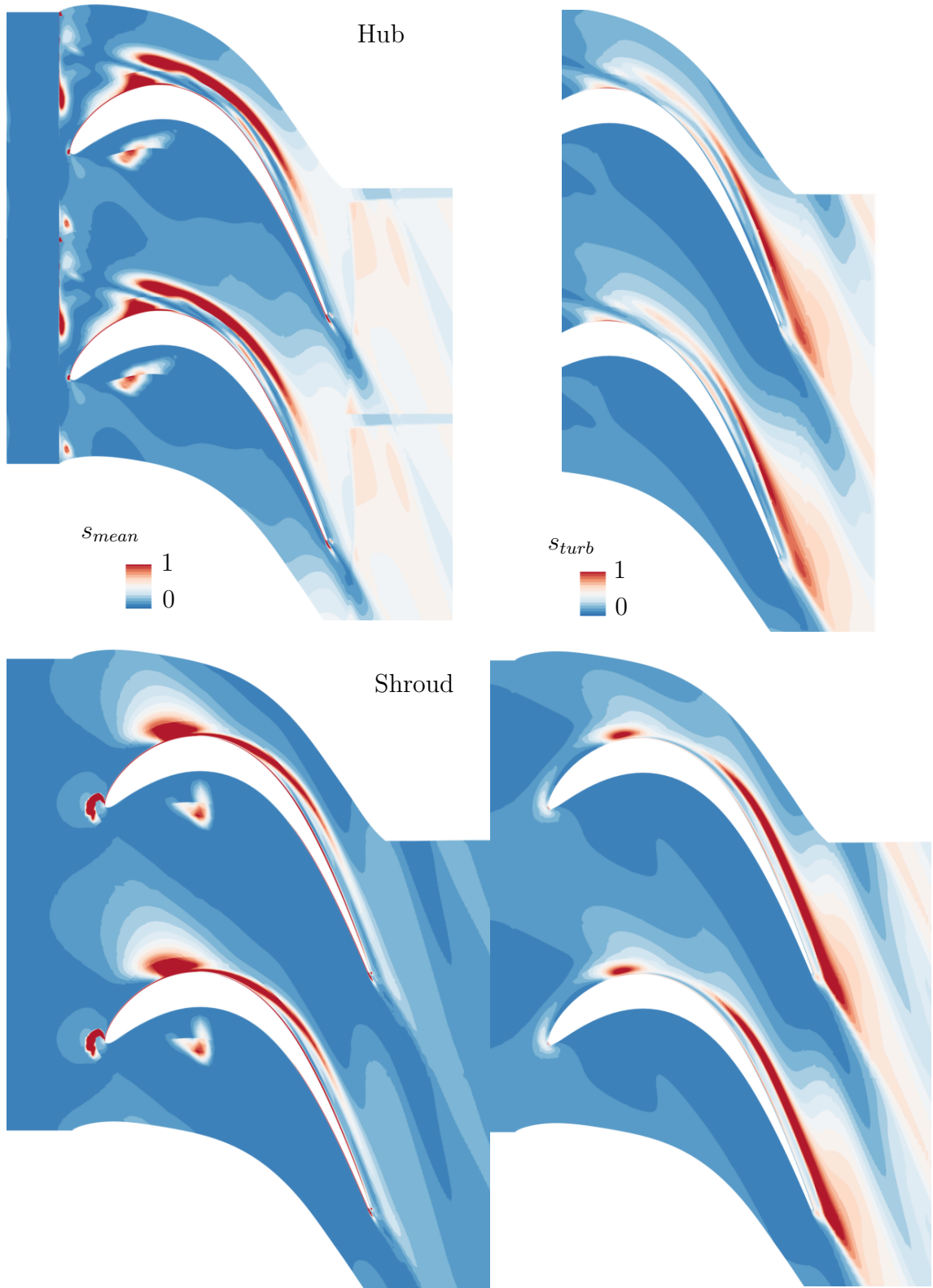


Figure 3.56: Mean and turbulent entropy production related to the hub and shroud in the boundary layer at a constant distance from the wall ($y^+ = 30$)

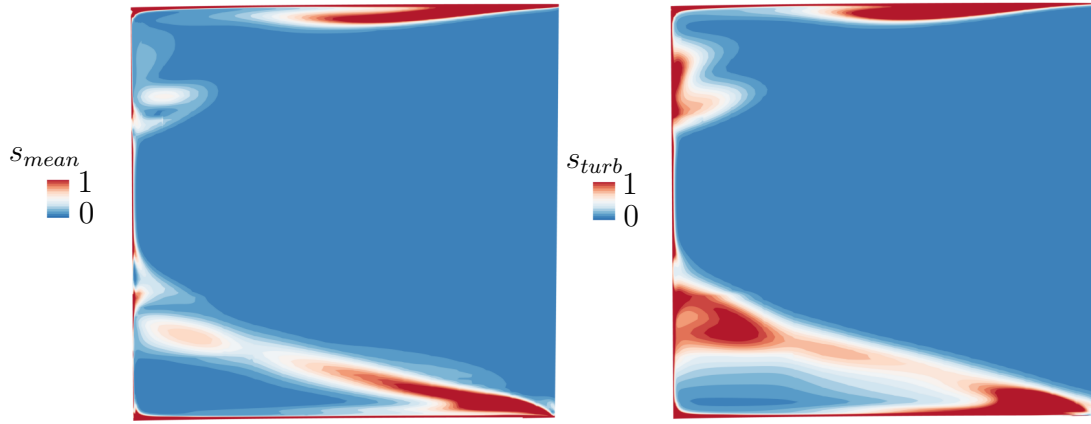


Figure 3.57: Mean and turbulent viscous entropy production related to the suction side blade in the boundary layer at a constant distance from the wall ($y^+ = 30$)

boundary layers. The purpose of this paragraph is to study the evolution of entropy production with the wall-normal coordinate. This analysis is performed at mid-chord and span on the blade suction side. According to the turbulent velocity profile

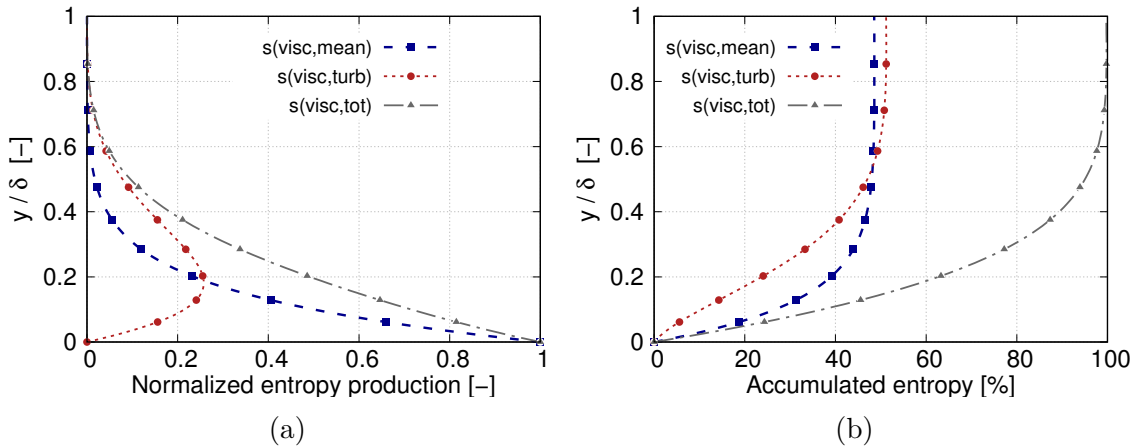


Figure 3.58: Mean, turbulent and total entropy production in the boundary layer at mid-span, mid-height of blade suction side (a) and accumulated entropy production relatively to the wall-normal coordinate (b)

around the blade suction side provided in Fig. 3.42a (p.123), the mean entropy production is large close to the wall due to wall-normal gradients that is observed in Fig. 3.58a where the entropy production is maximum at the wall and decrease to become zero at around $y/\delta = 0.6$. The turbulent entropy contribution is identically zero at the wall since no turbulent fluctuations and increases until $y/\delta = 0.2$ where the mean and turbulent curves cross. The turbulent contribution becomes negligible at $y/\delta = 0.8$. The total entropy production is dominated by mean contribution between $\delta = 0$ to 0.2 and by turbulent contribution between $\delta = 0.2$ to 1 . In addition, the cumulated entropy from the wall can be plotted relatively to the wall-normal coordinate for the mean, turbulent and total entropy production as shown in Fig. 3.58b. The mean and turbulent contributions contribute almost equally to the

total entropy production for the considered abscissa as observed in Fig. 3.54a and 3.54c at the abscissa $x/C_x = 0.5$. At the considered location, the friction Reynolds Number $Re_\tau \simeq 250$ that is low to consider a fully developed turbulent boundary layer as proposed in Sec. 2.2.2.2 (p.53). The main consequence at the considered abscissa and for the relatively low Reynolds number encountered in current low pressure turbine configuration, the viscous layer has a larger extension in the boundary layer. However, it may be interesting to draw a parallel with the observations of Denton [48] at an higher friction Reynolds number ($Re_\tau \simeq 500-1000$) for the boundary layers over high pressure turbine blades for example. It provides a good understanding on how entropy and consequently loss is generated in the boundary layer. For developed turbulent boundary layers, much of the viscous entropy creation occurs within the laminar sublayer and the logarithmic region since the strongest velocity gradients occur in this region (about 90% of the entropy generation occurs within the inner part of the layer). Since only the outer part of the boundary layer is affected by pressure gradient that may be important in gas turbine (see Fig. 2.11a p.60), the dissipation coefficient was then shown to slowly vary with the Reynolds number encountered in gas turbines (see Fig. 2.11b p.60) and pushed towards the use of the constant value $C_d = 0.002$ that integrated over a an axial line of a blade for example provided the two-dimensional loss related to the boundary layer on this surface (see Sec. 2.2.3.1 p.59). The laminar boundary layer or in current configuration at relatively low friction Reynolds number, the related dissipation coefficient is more dependant to the Reynolds number. The conclusions of Denton [48] concerning the low influence of pressure gradient on loss generation at higher friction Reynolds number may found less applicability at current lower friction Reynolds number since as stated the large velocity gradients occur on a wider portion of the boundary layer where pressure effects may have a significant effect. In the current approach, since the boundary layers are isolated and the viscous entropy is integrated on the whole boundary layer thickness, it provides a path to fully account for the entropy produced including the pressure effects. Even in the case of a laminar boundary layer, for simulation that tolerate both laminar and turbulent boundary layers (in current study the wall-resolved LES simulation), this approach is suitable.

3.7.1.2.3 Thermal entropy production The similar analysis conducted for the viscous entropy production is performed for the thermal contribution. It is reminded that all the contributions (hub, shroud, blade boundary layer and remaining term) are plotted against the total contribution at a same abscissa. Figure 3.59 shows the total thermal entropy production and the contributions of the different subdomains (hub, shroud, blade and remaining domain). The entropy production at the shroud boundary layer is identically zero. Due to adiabatic wall and no influence of the purge flow supplied at the hub, temperature gradients are reduced to temperature inhomogeneity that are not negligible. For the contribution of the blade boundary layer, the contribution is almost zero except between $x/C_x = 0.5$ and $x/C_x = 1.0$. The two main contributions to the thermal entropy production are related to hub and remaining subdomain. These two contributions are in regions where the cavity flow at lower temperature than the mainstream one can interact with the main annulus one. The contribution of the hub boundary layer upstream

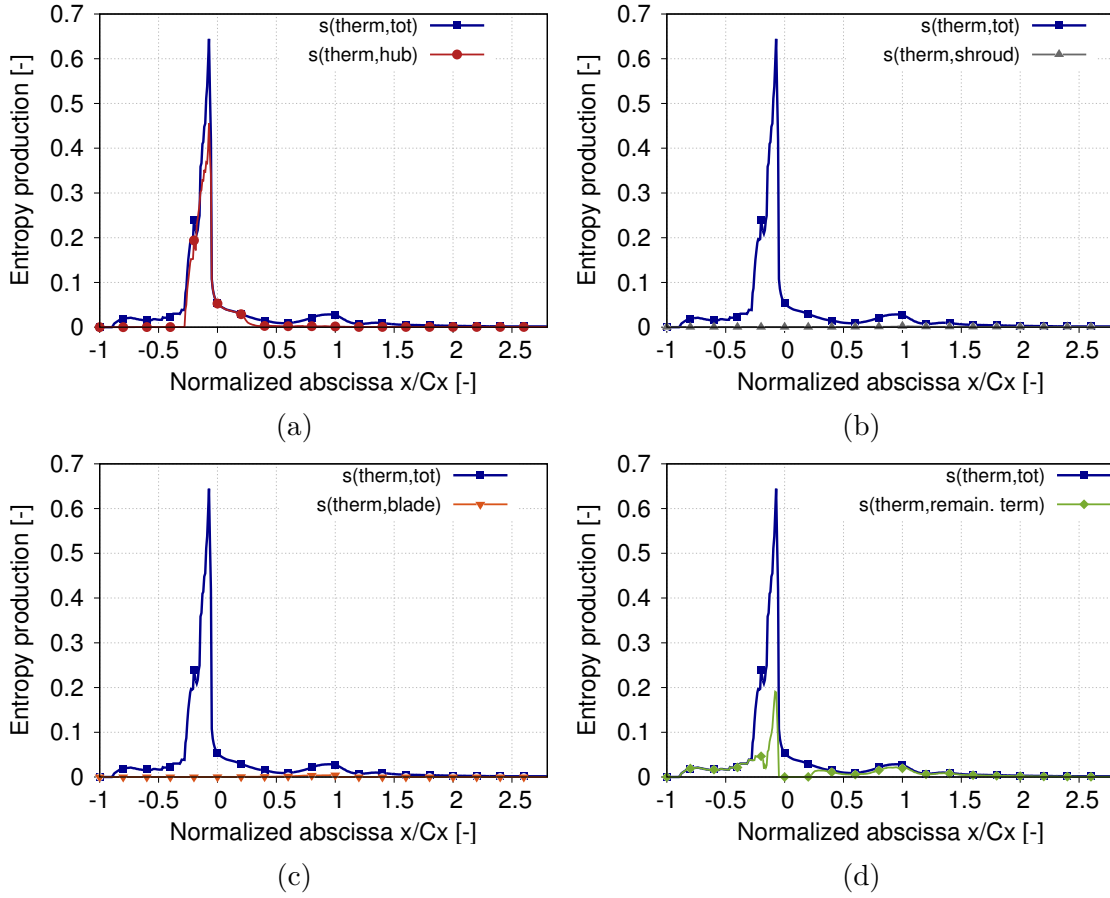


Figure 3.59: Total thermal entropy production and contributions of the subdomains (hub, shroud, blade) and remaining domain

of the rim seal is zero. The thermal entropy production increases close to the rim seal interface where the cavity and main annulus flow start to interact and where temperature gradients are the stronger. The entropy production then continuously decreases until reaches negligible values close to the trailing edge. The remaining term provides a similar trend with a strong increase at the rim seal interface corresponding to the mixing regions between the main annulus and cavity flow. As stated in Sec. 3.4.2 (p.109) about the description of the flow, the cavity flow is entrained by secondary vortices in the passage. Furthermore than dissipating kinetic energy due to a mixing process and generating viscous entropy, the secondary vortices also generate thermal entropy by homogenizing the cold cavity flow entrained with the main annulus flow (see Fig. 3.60a). This observation may be put in parallel with the viscous contribution. It was shown that out of the boundary layers, the secondary flow contribution to entropy generation was made until one axial chord downstream of the blade trailing. For thermal contribution, this thermal entropy production and temperature homogenization performed by the secondary vortices is performed on a shorter distance (until blade trailing edge).

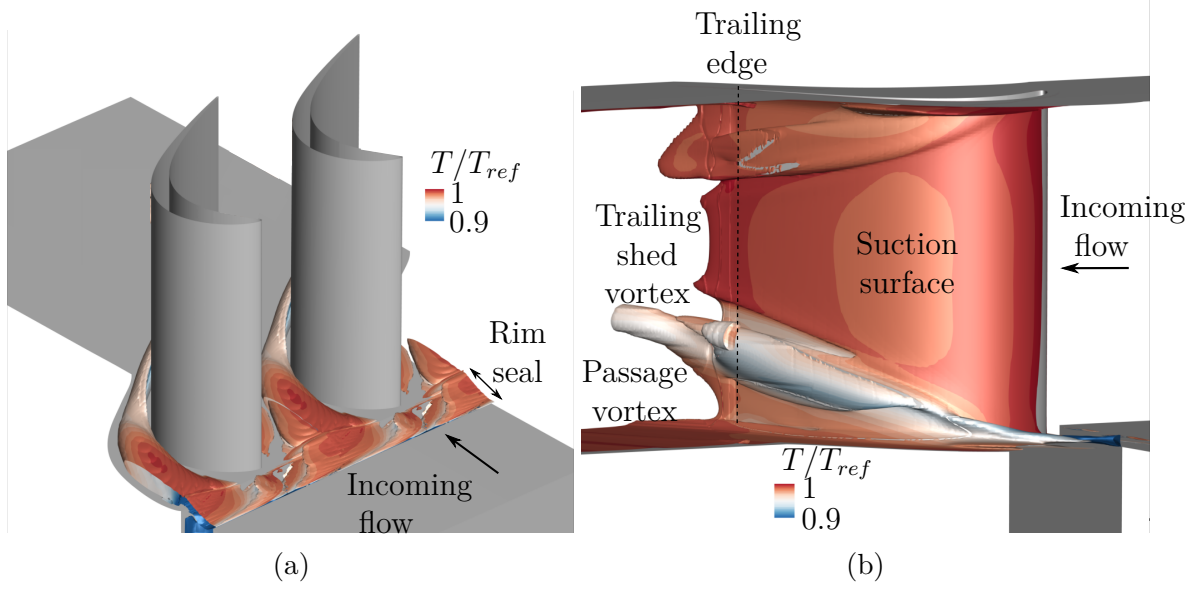


Figure 3.60: Iso-contour of the thermal entropy colored by temperature (a) and iso-contour of viscous entropy colored by temperature (b) exhibiting the secondary vortices downstream of the blade trailing edge (trailing shed and passage vortices)

3.7.1.3 The directional decomposition of entropy production

The viscous entropy production contains twelve terms that can be expended in any coordinates systems. The total viscous entropy production used earlier is independent of any coordinate system chosen because a scalar quantity. Similarly, the thermal entropy production contains three terms (the three derivatives of temperature according to the three coordinates). In the context of turbomachinery, the notion of secondary flow and related losses is often defined as the flow normal to the circumferentially averaged mean flow direction. It is then convenient to express the different entropy contributions in the polar streamline coordinates (stream, cross and radial components). In the current study of the linear cascade and more generally in high hub-to-tip ratio, it is convenient to approximate polar stream line coordinate by local Cartesian coordinate denoted (s , c , r). When expanding the viscous stress tensor in this coordinate system, the total viscous entropy production S_{visc} based on effective viscosity $\mu_{eff} = \mu + \mu_{turb}$ can be written as :

$$S_{visc} = \frac{\mu_{eff}}{T} \left[2 \left(\left(\frac{\partial u_s}{\partial s} \right)^2 + \left(\frac{\partial u_c}{\partial c} \right)^2 + \left(\frac{\partial u_r}{\partial r} \right)^2 \right) + \left(\frac{\partial u_s}{\partial c} \right)^2 + \left(2 \frac{\partial u_s}{\partial c} \frac{\partial u_c}{\partial s} \right) + \left(\frac{\partial u_c}{\partial s} \right)^2 + \left(\frac{\partial u_s}{\partial r} \right)^2 + \left(2 \frac{\partial u_s}{\partial r} \frac{\partial u_r}{\partial s} \right) + \left(\frac{\partial u_r}{\partial s} \right)^2 + \left(\frac{\partial u_c}{\partial r} \right)^2 + \left(2 \frac{\partial u_c}{\partial r} \frac{\partial u_r}{\partial c} \right) + \left(\frac{\partial u_r}{\partial c} \right)^2 \right]. \quad (3.12)$$

Similarly the thermal entropy production, S_{therm} can be written as:

$$S_{therm} = \frac{\lambda_{eff}}{T^2} \left(\left(\frac{\partial T}{\partial s} \right)^2 + \left(\frac{\partial T}{\partial c} \right)^2 + \left(\frac{\partial T}{\partial r} \right)^2 \right). \quad (3.13)$$

This process makes possible to extract the direction over which entropy is produced since each of the twelve terms can be integrated for the viscous contribution and the three terms for the thermal entropy production.

3.7.1.3.1 The contributions of boundary layers Figure 3.61 shows the total entropy production related to the hub, shroud and the wall-normal contributions ($\partial u_s/\partial r$ and $\partial u_c/\partial r$) of entropy. Out of the blade domain extension, entropy production is due to the hub/shroud wall-normal contribution that makes possible to confirm that the entropy generation from the inlet to the rim seal is due to the development of boundary layers over hub and shroud inducing wall-normal gradients. In the blade passage domain, part of the entropy production is not due to wall-normal contribution. One of the main issues that could explain this difference is the difficulty to define the hub and shroud boundary layer in the passage where a new-born boundary layer starts to develop and is strongly skewed due to the cross pressure gradient. This difference between total and wall-normal entropy grows may be put in parallel with the growth of the streamwise vorticity, that is proportional to the growth of secondary flows. This induces a poor estimation of the boundary layer thickness and a bad evaluation of the entropy production. Figure 3.62

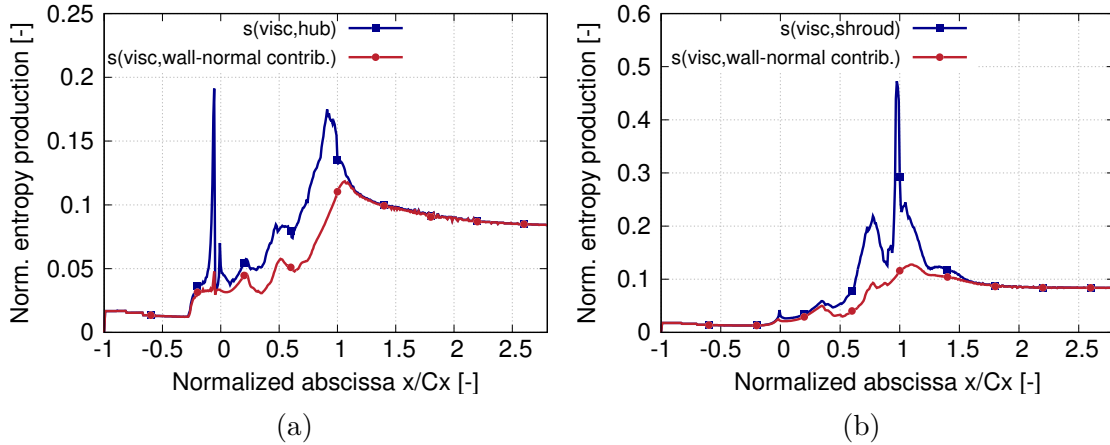


Figure 3.61: Hub and shroud boundary layer viscous entropy production with wall-normal contributions ($\partial u_s/\partial r$ and $\partial u_c/\partial r$)

shows total entropy production related to the blade boundary layer and wall-normal contribution ($\partial u_s/\partial c$). Similarly to the hub and shroud, the contribution to the entropy production in the boundary layer is due to wall-normal velocity gradients corresponding to the development of a boundary layer along the blade pressure and suction side.

3.7.1.3.2 The contributions to the remaining term In order to obtain the direction over which the gradients are generated in the remaining domain, the analysis is conducted by focusing on the different regions of the flow where different phenomena are supposed to happen. We first look at the rim seal interface from the rim seal left corner at $x/C_x = -0.26$ to the right corner at $x/C_x = -0.04$. Figure 3.63a shows the viscous entropy production related to the remaining term at

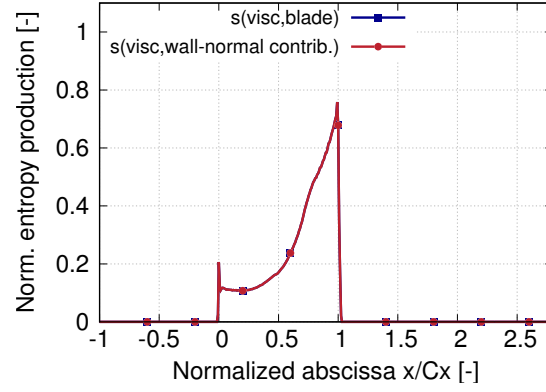


Figure 3.62: Blade boundary layer entropy production with wall-normal contribution (du_s/dc)

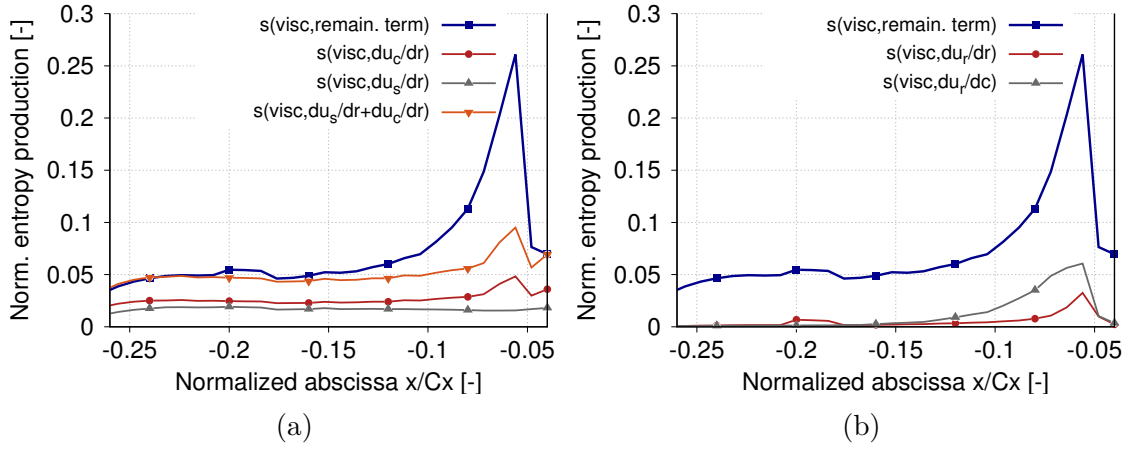


Figure 3.63: Entropy production at the rim seal interface between the left corner at $x/C_x = -0.26$ and right corner at $x/C_x = -0.04$ including the terms with high contribution to entropy: shear layer for axial and tangential velocity gap (du_c/dr and du_s/dr) (a) and variation of radial velocity u_r close to rim seal right corner (b)

the rim seal interface ($s_{visc,remain.term}$) and the contributions of radial evolution for stream (du_s/dr), cross components (du_c/dr) and the sum of these two contributions ($du_s/dr+du_c/dr$). These two contributions are responsible for the entropy production at the rim seal interface on the first 70% of axial extension of the rim seal (between $x/C_x = -0.26$ and $x/C_x = -0.12$). As described in Sec. 3.4.2 (p.109), this corresponds to the adaptation of the flow over a short layer at the rim seal interface between a cavity flow with low axial and tangential velocity components to a strong one corresponding to the main annulus flow that induces velocity gradients in the radial direction. Close to rim seal right corner between $x/C_x = -0.12$ and $x/C_x = -0.004$, the entropy production strongly increases of a factor five compared to the levels upstream. In addition to the shear layer contribution already described (radial evolution of stream and cross component), strong variations of radial velocity are shown to contribute to the entropy production (see Fig. 3.63b). The radial velocity variation with the radius close to the rim seal right corner is attributed to the cavity/rim seal flow emerging into the main annulus at the center of the pas-

sage. The analytical solution based on the three-dimensional shear layer providing an increase of the entropy in terms of radial evolution of the velocity components at the rim seal interface as proposed in eq.(2.90) of Sec. 2.3.1 (p.76) is here shown to be relevant. However, it may be observed that an additional contribution to entropy production is provided by the cross evolution of radial velocity (du_r/dc close to the rim seal right corner). Close to the rim seal right corner, alternating regions of ingested main annulus flow (upstream of the blade leading edge) and blowing at the center of the passage induce alternating regions of positive and negative radial velocity along the cross direction (see Fig. 3.74). This radial velocity distribution induces gradients in the cross direction that are observed in Fig. 3.63b. The en-

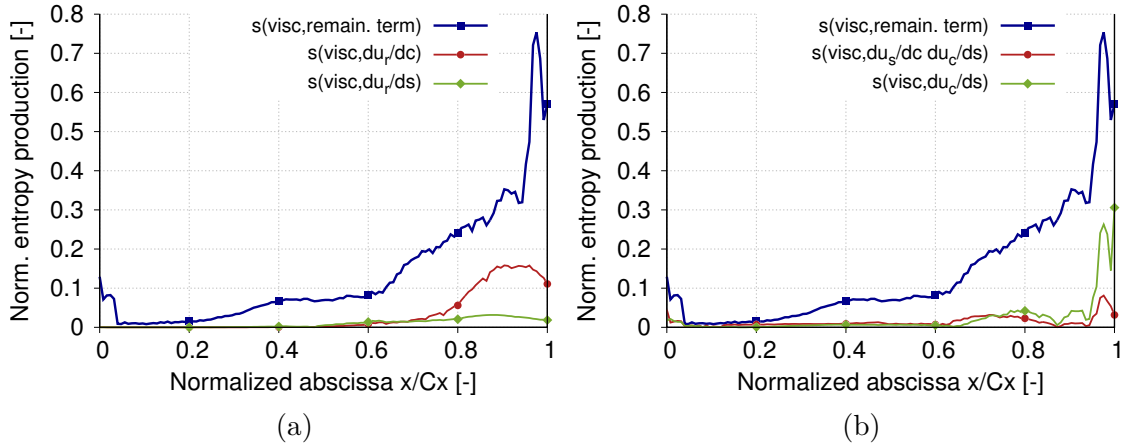


Figure 3.64: Viscous entropy production in the passage from the blade leading edge to trailing edge ($x/C_x = 0$ to $x/C_x = 1$) including the terms with high contribution to entropy: variation of radial velocity u_r in the passage (a) and u_c close to the trailing edge (b)

ropy production related to the remaining term in the passage is shown in Fig. 3.64b. As stated in last subsection, the entropy production related to the remaining term and the secondary vortices developing in the passage does not induce losses before $x/C_x = 0.2$ while some secondary vortices are initiated as soon as at the leading edge $x/C_x = 0.0$ for the horse shoe vortex process. A major contribution to secondary vortices in the passage is induced by strong variations of the radial velocity according to the stream and cross component. This observation was originally made by Zlatinov [54]. The author demonstrated that purge flow induces stronger secondary vortices in the passage. The secondary vortices generating loss and entropy close to their center of rotation but also under an additional process. The passage vortex migrating close to the blade suction side serves as a region of blockage, creating the effect of a nozzle that generates high radial velocities. However, the resulting interaction between this radial flow and the passage vortex is not purely a potential flow effect, and shearing occurs between the two flow features that can be observed in Fig. 3.64a between $x/C_x = 0.6$ and $x/C_x = 1$. Slightly upstream of the trailing edge (between $x/C_x = 0.95$ and $x/C_x = 1$), an increase of entropy related to cross velocity gradients can be observed in Fig. 3.64b. This may indicate a separation of the boundary layer on blade suction and pressure side slightly upstream of the trailing

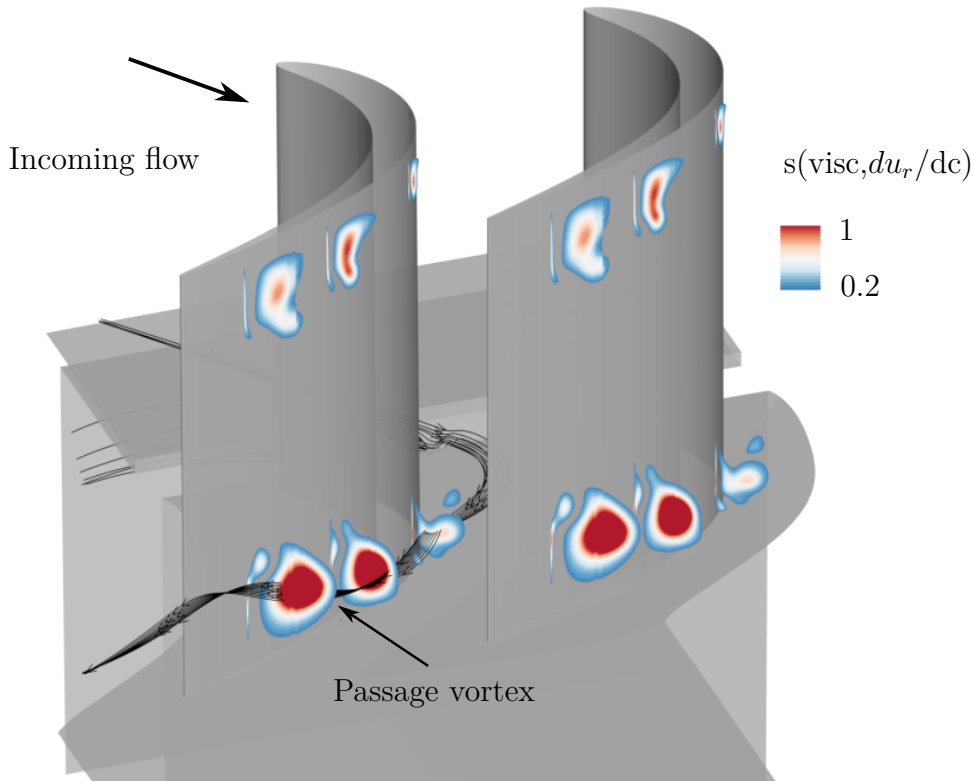


Figure 3.65: Axial cuts in the passage colored by viscous entropy production related to du_r/dc gradients

edge. At the blade trailing edge, the entropy production related to the remaining term decreases. The main contributions to the decay downstream of the trailing edge is twofold. A first contribution related to cross velocity gradients. The cross velocity gradient corresponds to the shear layer between the suction and pressure side flow promoting the formation of trailing shed vortices (see Fig. 3.60b). The contribution is strong close to the trailing edge with a quick decay since becoming almost zero as soon as $x/C_x = 1.4$ (see Fig. 3.66a). A second process related to the passage vortex that induce entropy production due to variation of radial velocity that is performed over a longer distance since becoming negligible around $x/C_x = 1.8-2$ (see Fig. 3.60b and Fig. 3.66b)

3.7.1.3.3 The contributions to thermal entropy production Thermal entropy production is mainly initiated at the rim seal interface and the contribution is mainly due to radial temperature gradients. Similarly to the velocity, at the rim seal interface, a mixing region is induced between hot main annulus flow and low temperature cavity flow inducing a radial temperature change (see Fig. 3.67).

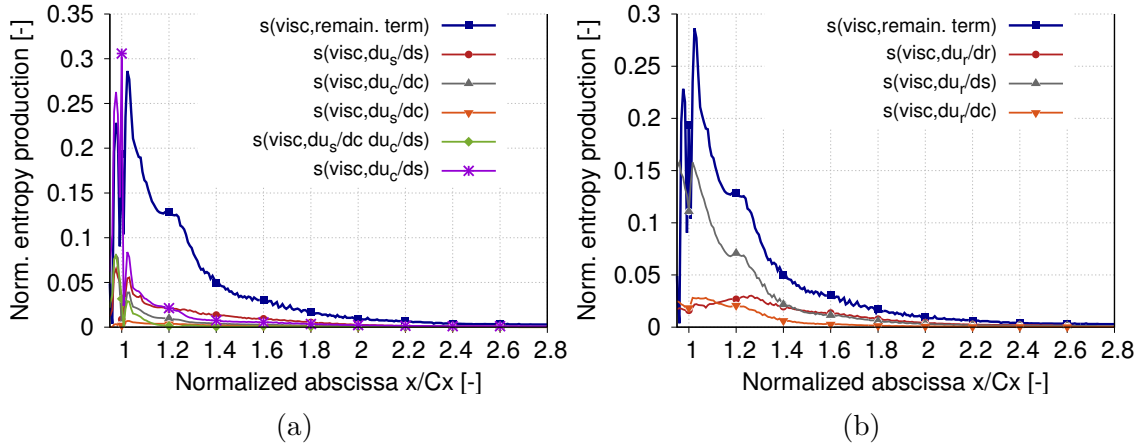


Figure 3.66: Viscous entropy production from upstream of the trailing edge $x/C_x = 0.9$ to the end of the domain $x/C_x = 3$ including the terms with high contribution to entropy: trailing shed vortex process (du_c/ds) (a) and radial velocity gradients (b)

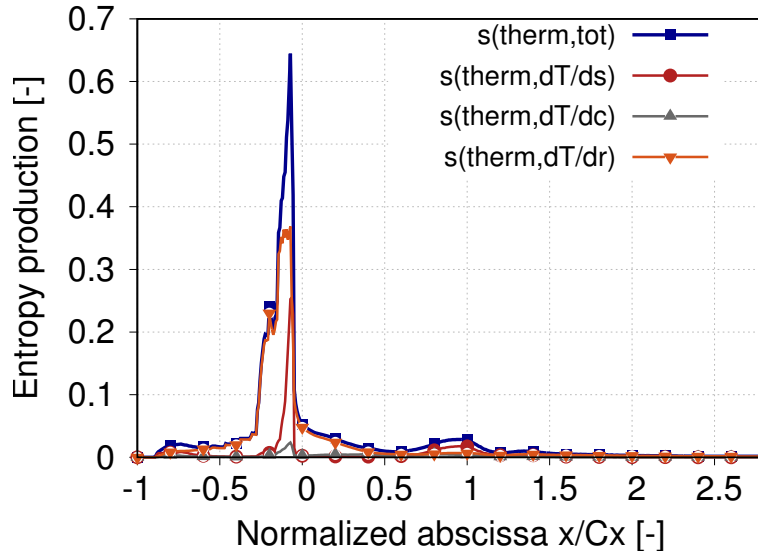


Figure 3.67: Thermal entropy production along the domain with the large contribution of the radial variation of temperature (dT/dr)

3.7.2 Influence of purge flow rate

3.7.2.1 Pressure coefficient around the blade

Figure 3.68 shows the pressure coefficient around blade at 4, 6 and 50% span for the axial rim seal at the different purge flow rates available for RANS and experiments. At mid-span, the RANS simulation as well as experiments show an unaffected pressure coefficient profile for the different purge flow rates. This observation indicates that no modification of blade loading is induced far from rim seal interface. This result is in agreement with Schuler et al. [114] showing that the purge flow influence on blade loading is generally limited to the first 20% of blade height for a common

purge flow rate around 1%. At 4 and 6% blade height, RANS and experiments do not show any influence of the purge flow on the blade pressure side pressure coefficient. Conversely, on blade suction side, experiments as well as RANS simulations show an increase of pressure coefficient with purge flow rate. This observation shows that the emerging purge flow is mainly deviated towards the blade suction side and additional flow leads to stronger acceleration on blade suction side which decreases the pressure coefficient on blade suction side (it is reminded in the pressure coefficient definition that the pressure around the blade is subtracted to the inlet pressure). The increase in the peak suction Mach number (decrease of pressure coefficient) in the endwall region with purge flow rate may be directly associated and proportional to added flow rate, although there may be an extra contribution due to additional blockage.

3.7.2.2 Pressure loss coefficient downstream of the blade

Figure 3.69 shows the pressure loss coefficient downstream of the blade for the axial rim seal at different purge flow rates obtained from RANS simulations (left) and experiments (right). The azimuthal averaging is performed with a mass averaging which ensure a conservation of total enthalpy between the axial cut total pressure and its azimuthal averaging. A main issue in the comparison between the different purge flow rate is that the total enthalpy in the flow field increases with increased purge flow rate that may have influence on the total pressure loss coefficient downstream of the blade. Based on the comparison, an increased purge flow rate leads to additional pressure loss for the turbine. Figure 3.70 shows the influence of the purge flow rate on the total entropy production and according to the various contributions. Similarly to the pressure loss downstream of the blade, the increase of purge flow rate increases the amount of entropy generation in the simulation domain. This observation is in agreement with the majority of turbine studies taking into account the purge flow that has a detrimental effect on loss generation. Above $h/H = 0.6$, no influence of the purge flow rate on the pressure loss coefficient can be seen according to experiments as well as in the RANS simulations. The pressure coefficient around the blade did not show an influence of the purge flow rate at mid-span which indicates that the pressure loss downstream of the blade cannot be only induced by blade pressure repartition and boundary layer. This observation is supported by Fig. 3.69 showing a very low influence of the purge flow rate on the blade boundary layer entropy production. Similarly, close to the hub between $h/H = 0$ and $h/H = 0.2$, the purge flow rate has a low influence on pressure loss downstream of the blade. The purge flow is entrained by the pressure side of the horse shoe vortex and further downstream by corner and passage vortices. The region between the corner and passage vortices should be then undisrupted by a variation of the purge flow rate that is indicated by an undisrupted pressure loss coefficient downstream of the blade at this location. According to the experiments, the purge flow rate mainly influences the bottom pressure loss peak related to the hub passage vortex. As stated, the purge flow is entrained by the secondary vortices in the passage and particularly in the passage vortex. The strengthened structures increase loss under a mixing process and induce more pressure loss downstream of the blade. The influence of purge flow on secondary vortices is supported by additional entropy

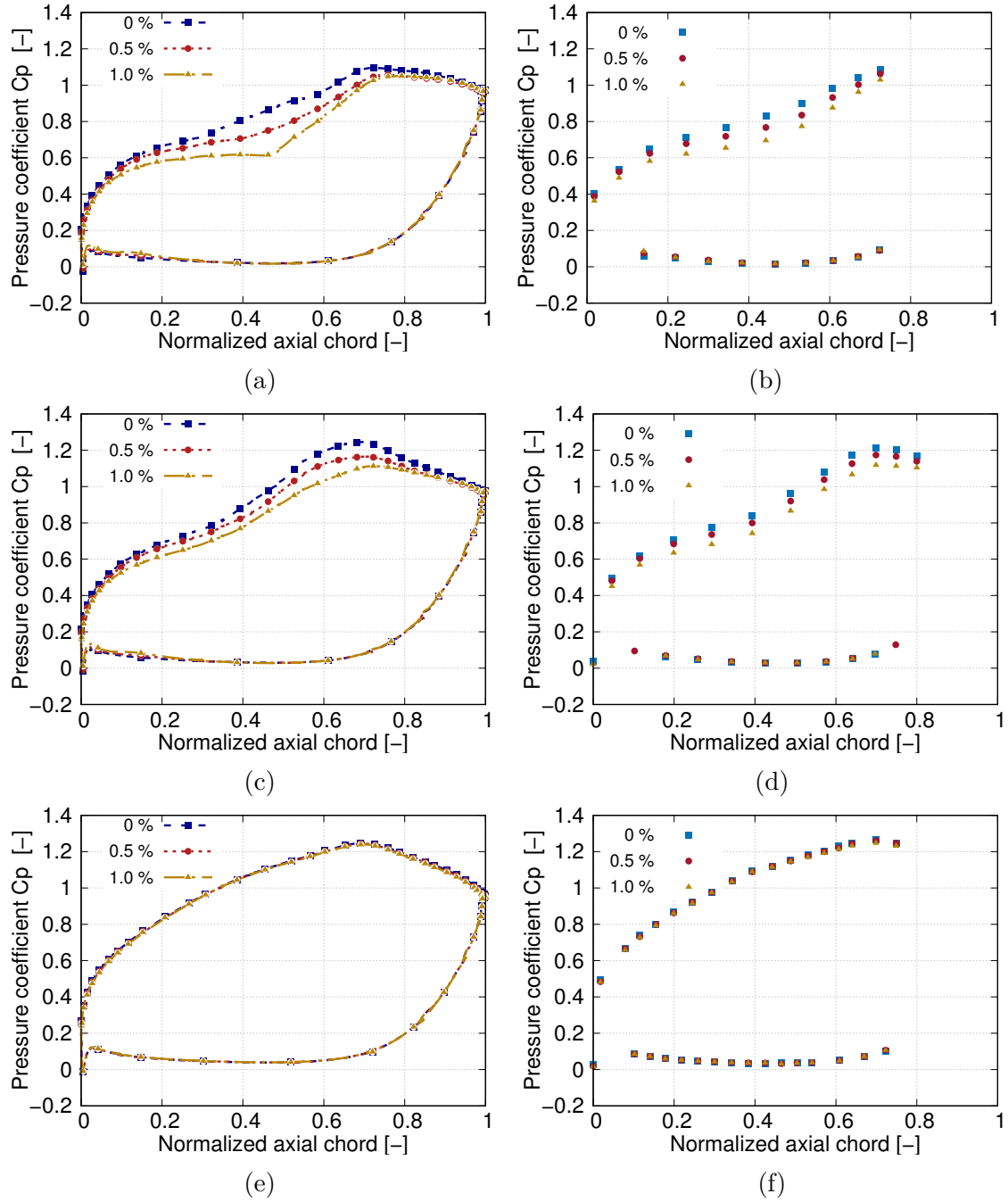


Figure 3.68: Pressure coefficient around the blade at (a)-(b): 4, (c)-(d): 6 and (e)-(f): 50% span for the axial rim seal at the different purge flow rates based on the RANS approach (left figures) and experiments (right figures)

production close to hub when purge flow is added (see Fig. 3.69). This contribution can be difficult to assess in the experiments because very close to the wall where no data are available. The entropy production related to the secondary vortices in the passage is also stronger (see Fig. 3.69) and can be associated to stronger corner and passage vortices identified on the pressure loss downstream blade by a stronger pressure loss peak.

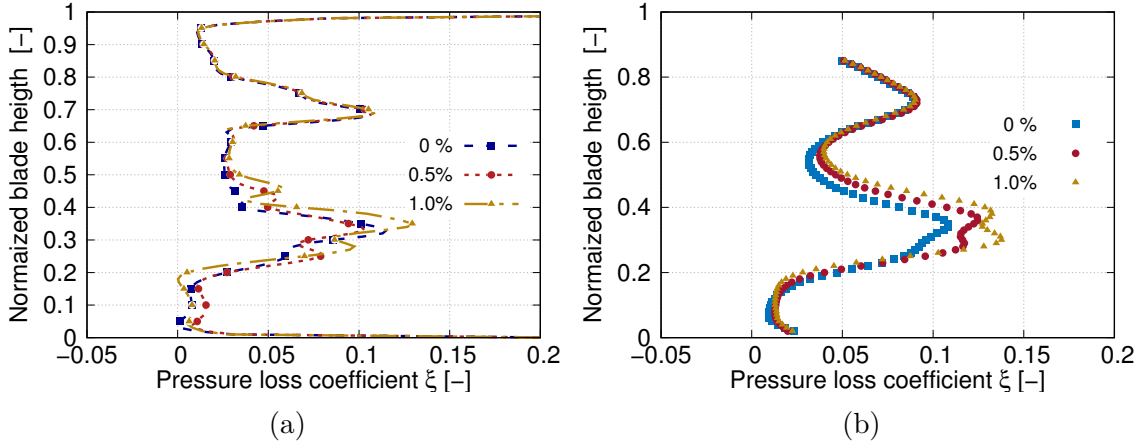


Figure 3.69: Pressure loss coefficient downstream of the blade for the axial rim seal at the different purge flow rates obtained from RANS simulations (a) and experiments (b)

3.7.2.3 Influence of purge flow rate on viscous entropy production

Figure 3.70 shows the viscous entropy production for the axial rim seal at the different purge flow rates including the contributions of the different subdomains (hub, shroud, blade, remaining term). The total entropy produced along the domain increases with an increased purge flow rate. This is compliant with the increase of pressure loss downstream of the blade observed in the last subsection and more generally with the studies dealing with influence of purge flow rate on turbine aerodynamics. The influence of the purge flow rate on the entropy production at shroud is shown to be negligible as shown in Fig. 3.70e. At the current purge flow rate, typically in the order of magnitude of 1% of the main annulus flow, the influence of purge flow rate is generally shown to be limited to the first of the 60% blade height and explains why no influence is shown in the loss related to the shroud boundary layer. The main contribution of purge flow rate is seen on the hub and remaining domain contribution. The purge flow rate increases entropy production in the blade passage from $x/C_x = 0$ to $x/C_x = 1$ and downstream blade. As stated in Sec. 3.7.1.3.2 (p.149), the entropy generated in the passage and downstream of the blade in the remaining domain may be attributed to secondary flows developing in the passage. The current observation supports a feeding process of the secondary vortices in the passage that as a consequence generates more entropy (see Fig. 3.70e). Also, as stated in Sec. 3.7.1.2.1 (p.141), the secondary vortices induce additional entropy generation on the hub boundary layer due to a friction process of the secondary vortices on these surfaces. Due to stronger secondary vortices, the friction process at the hub is also higher with a higher purge flow amount that is observed in Fig. 3.70c. However, it should be reminded that if the increasing entropy production trend with increased purge flow at the hub should be acceptable, it is difficult to ascertain on its magnitude for the reason already mentioned about the ability to properly evaluate the boundary layer thickness at the hub in the passage due to the strong cross-component velocity and entrainment effects. The additional friction process due to the additional purge flow rate should also be visible on the

blade boundary layer contribution. However, the contribution of this surface is relatively high and the difference between the different purge flow rate is very low (see Fig. 3.70b).

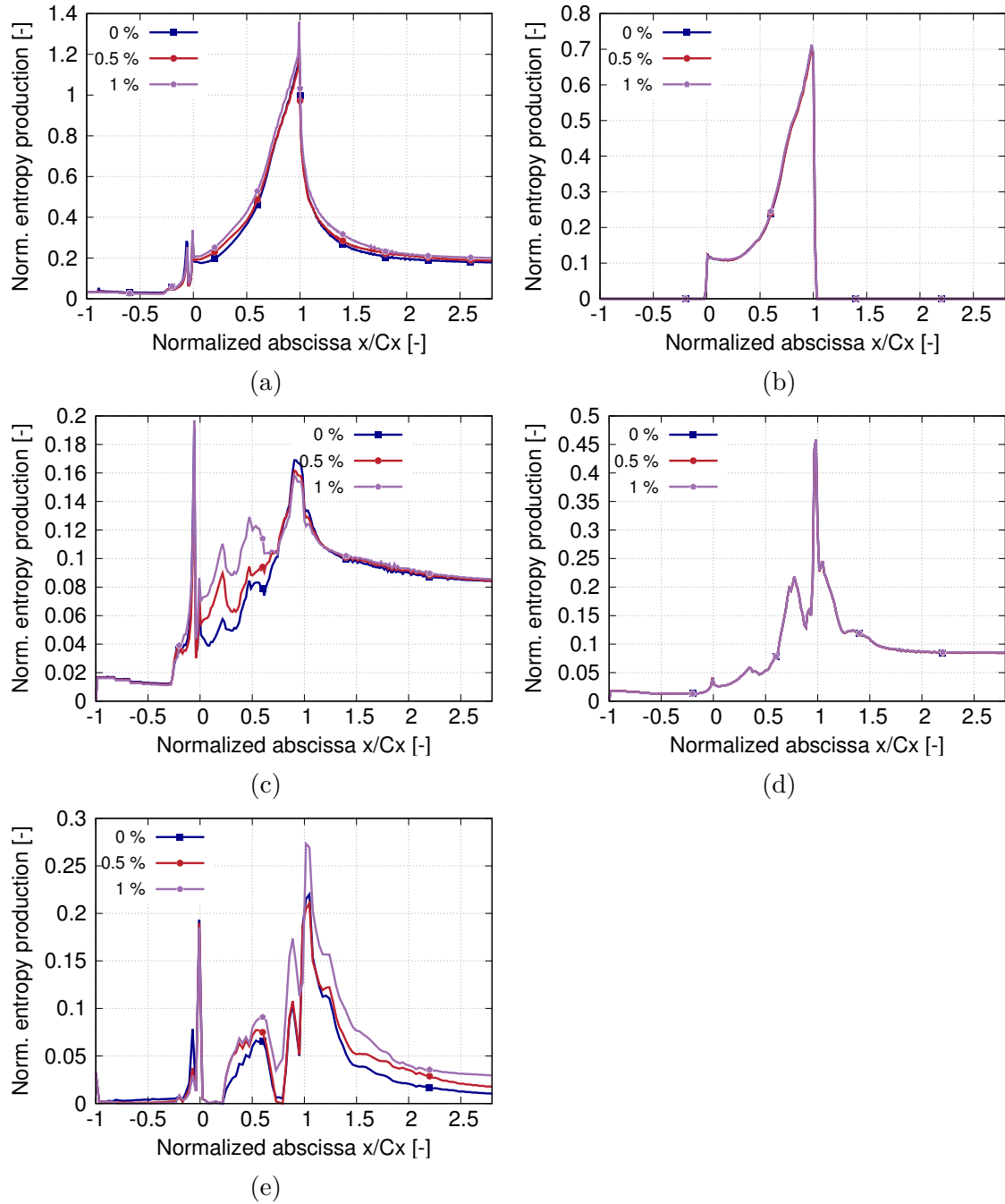


Figure 3.70: Influence of the purge flow rate on entropy production for the total (a), blade (b), hub (c), shroud (d) and remaining term (e) contributions

3.7.3 Influence of rim seal geometry

3.7.3.1 Pressure coefficient around blade

Figure 3.71 shows the pressure coefficient around the blade at 4, 6 and 50% span at the intermediate purge flow rate (0.5%) for the axial, simple and double overlapping geometries available for the RANS and experiments. Similarly to the purge flow rate, no influence of the rim seal geometry can be observed at mid-span and on blade pressure side at the different span height for the RANS simulations and experiments. Pressure coefficients on the blade suction side close to hub (4 and 6%) show almost no difference between the rim seal geometries in the experiments. Conversely, the RANS simulations shows some discrepancy of pressure coefficient on the blade suction side for the axial rim seal compared to single and double overlap rim seal geometries. At 4% span, between 30 and 50% chord length, and between 40 and 70% chord length at 6% span, the pressure coefficients are higher for overlapping geometries compared to the axial one. At equivalent purge flow rate, for the different rim seal geometries, a same amount of purge flow emerge into the mainstream and provides similar blade loading.

3.7.3.2 Pressure loss coefficient downstream of the blade

Figure 3.72 shows the pressure loss coefficient downstream of the blade at high purge flow rate (1%) for the different rim seal geometries (axial, single and double overlap) available for RANS and experiments. Similarly to the influence of purge flow rate, rim seal geometry does not affect pressure loss downstream of the blade over $h/H = 0.6$ and below $h/H = 0.2$. The rim seal geometry mainly influences the lower pressure peak with larger pressure losses related to the axial rim seal geometry (A). A similar trend is predicted by the RANS simulation. At the rim seal interface, simple (S) and double axial overlapping geometries (D) promote an axial momentum of the purge flow emerging into the mainstream and less localized than axial one. The main consequence is that the strengthening of the pressure side leg of the horse shoe vortex is delayed compared to the axial one. The passage vortex is then weaker for overlapping rim seal geometries and induce less pressure loss downstream of the blade.

3.7.3.3 Influence of rim seal geometry on viscous entropy production

Figure 3.73 shows the total viscous entropy production at an intermediate purge flow rate for axial and single overlapping rim seal geometries. The entropy production is shown to be decreased at the rim seal interface for the overlapping geometry. In addition, the entropy production is shown to be residually lower all along the blade extension and downstream of the blade compared to an axial geometry. Similarly to the purge flow rate, the rim seal geometry is shown to have no influence on losses generated in the shroud boundary layer and around the blade confirming that both purge flow rate and rim seal geometry have a limited influence on losses in the main annulus. The main influence is shown to be on the secondary flows. At the rim seal interface, the entropy production associated to azimuthal and axial

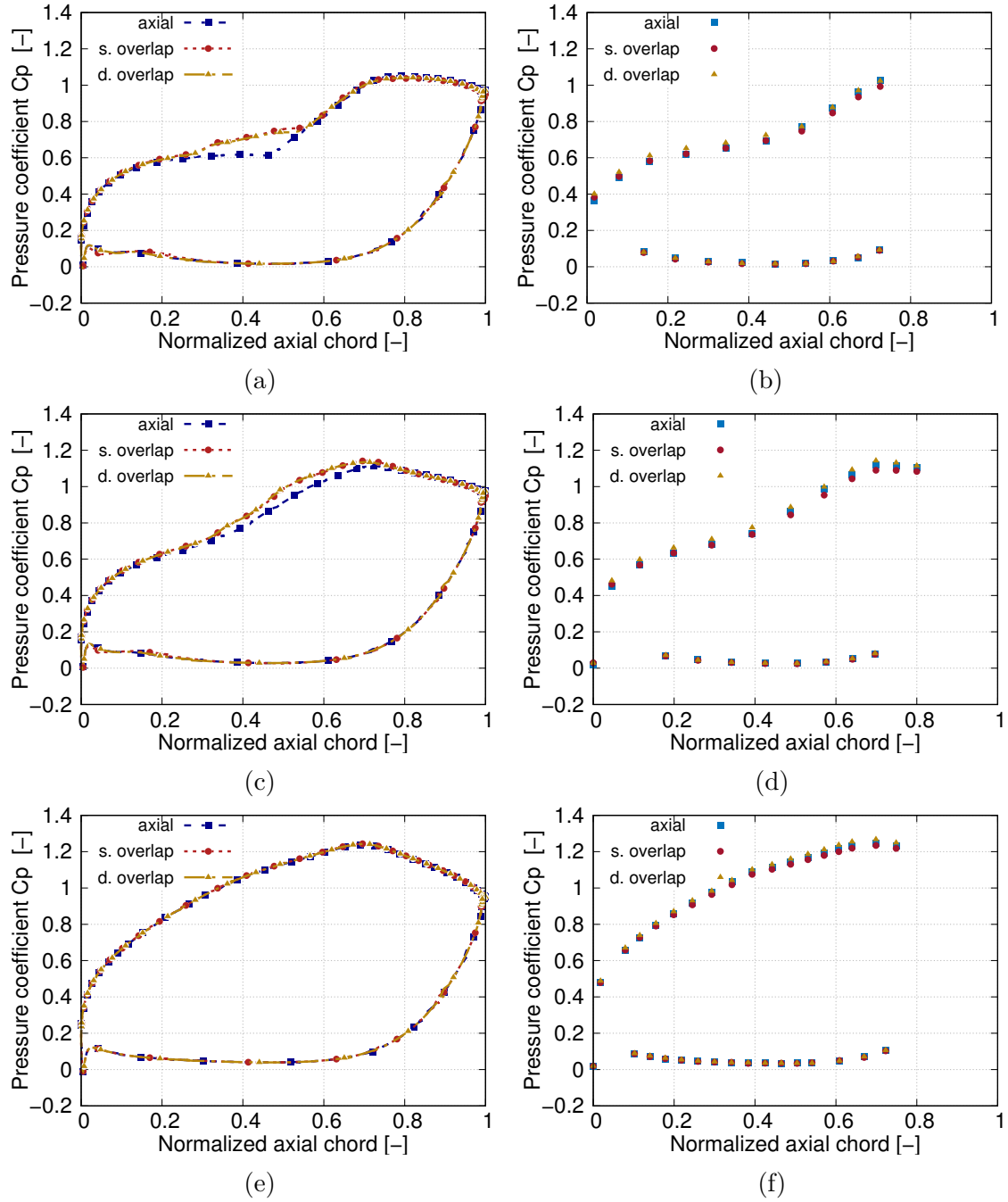


Figure 3.71: Pressure coefficient around blade at 4, 6 and 50% span for the different rim seal geometries at high purge flow rate (1%) based on the RANS approach and experiments

velocity gap between the main and rim seal flow is lower for the overlapping geometry. According to Sec.3.4.2 (p.109), this is due to the local recirculation zone for overlapping geometries that reduces the shear compared to the axial geometry. The overlapping geometry promotes an intense recirculation zone that homogenizes the flow at the rim seal interface. A main consequence is that the main annulus ingested flow (negative radial velocity close to rim seal interface) is made over an

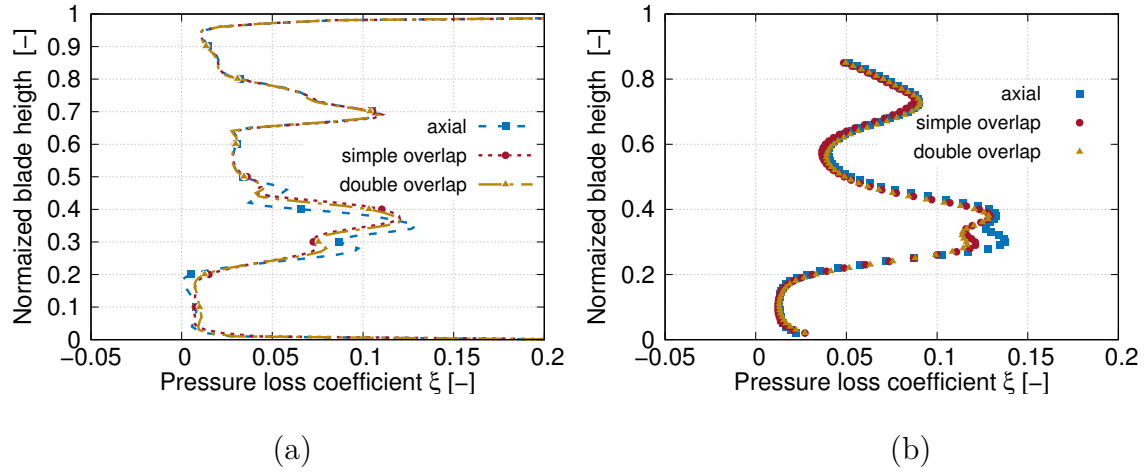


Figure 3.72: Pressure loss coefficient downstream of the blade at high purge flow rate (1%) for the different rim seal geometries obtained from RANS simulations (a) and experiments (b)

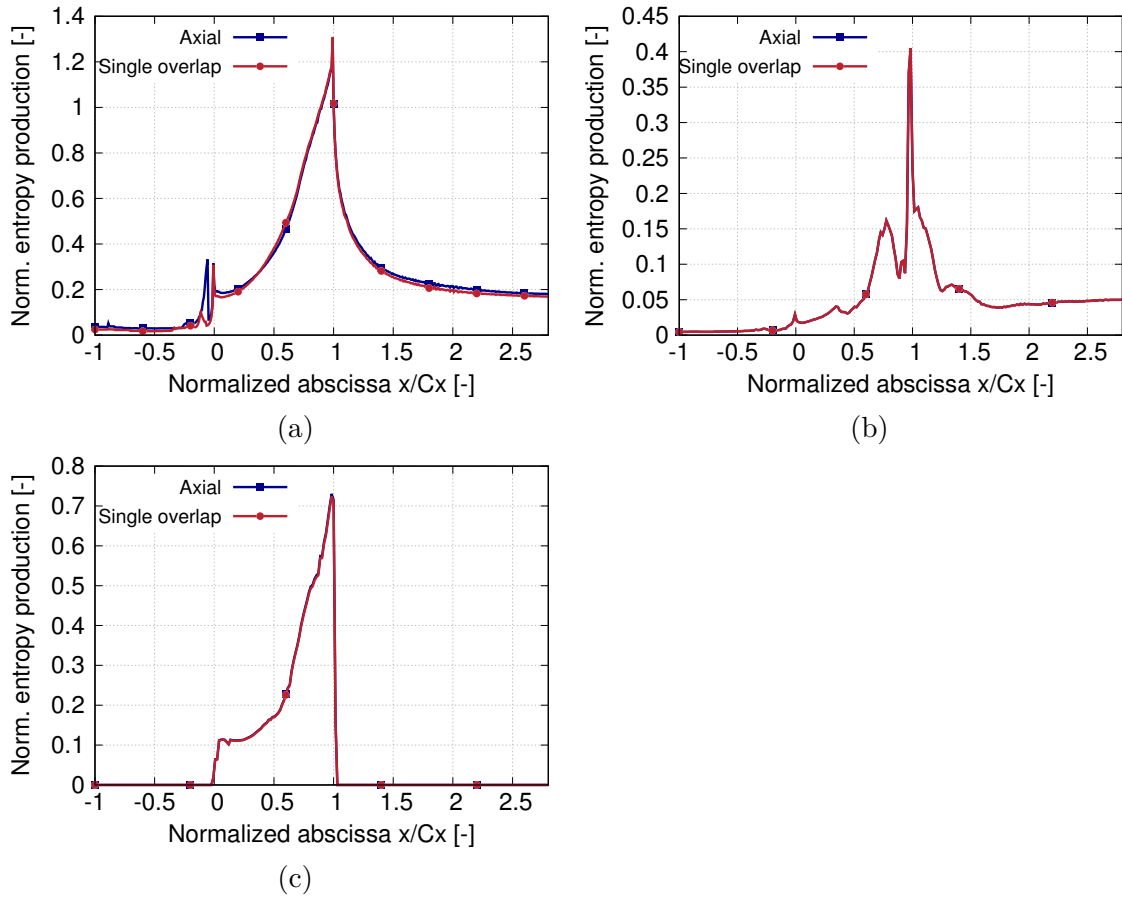


Figure 3.73: Influence of the rim seal geometry (axial and simple overlapping) on entropy production for total (a), blade (b), hub (c) contributions

axial extension lower for overlapping geometry than axial geometry (see Fig. 3.74a for axial geometry and Fig. 3.74b for overlapping geometry). Similarly, the cav-

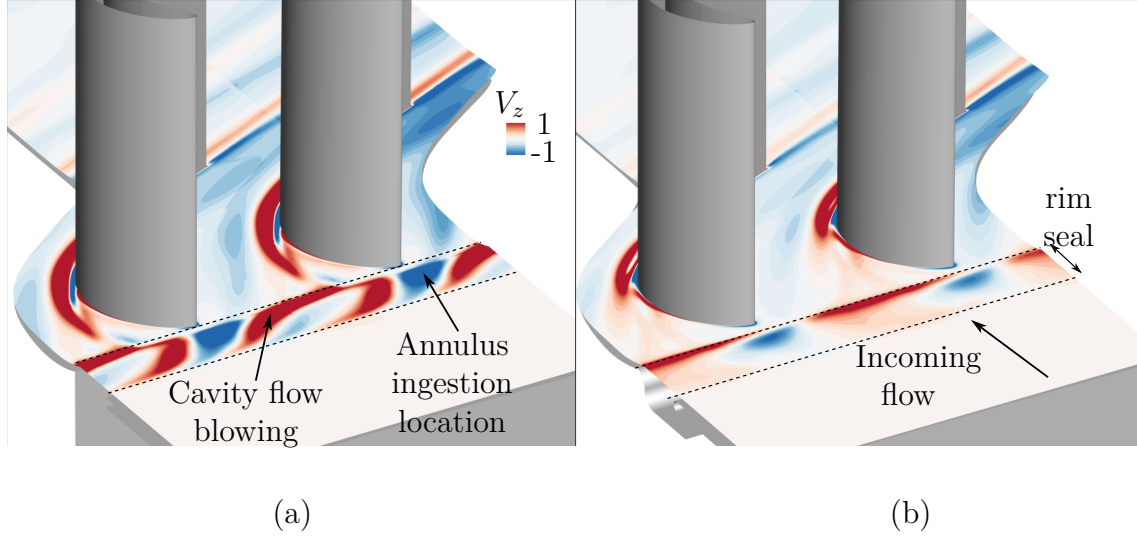


Figure 3.74: Radial cut close to the hub colored by the radial velocity for axial (a) and single overlapping geometry (b)

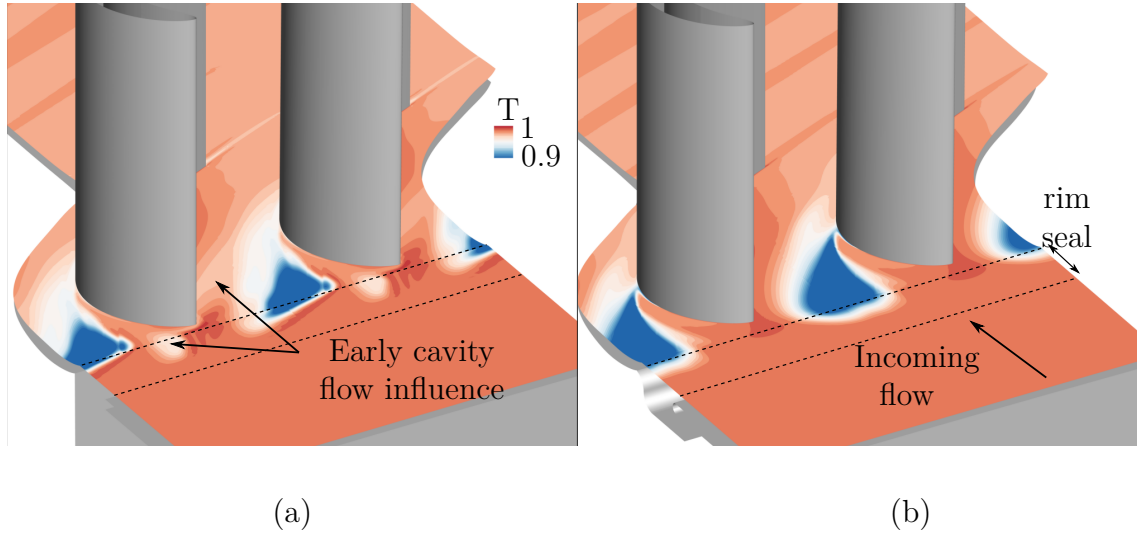


Figure 3.75: Radial cut close to the hub colored by temperature for axial (a) and single overlapping geometry (b)

ity/rim seal flow emerges earlier in the axial direction and closer to blade leading edge (see Fig.3.75). This induces an earlier development and strengthening of the horse shoe vortex process, pressure side of the horse shoe vortex process for axial geometry compared to overlapping one. The radial migration of secondary vortices along blade suction are initiated early for the axial rim seal geometry (see Fig. 3.74)

3.7.4 Entropy generation from LES simulation

3.7.4.1 LES without turbulence injection

Figure 3.76 shows viscous entropy production for the RANS and LES simulations without turbulence injection based on the A05 configuration. For the RANS simu-

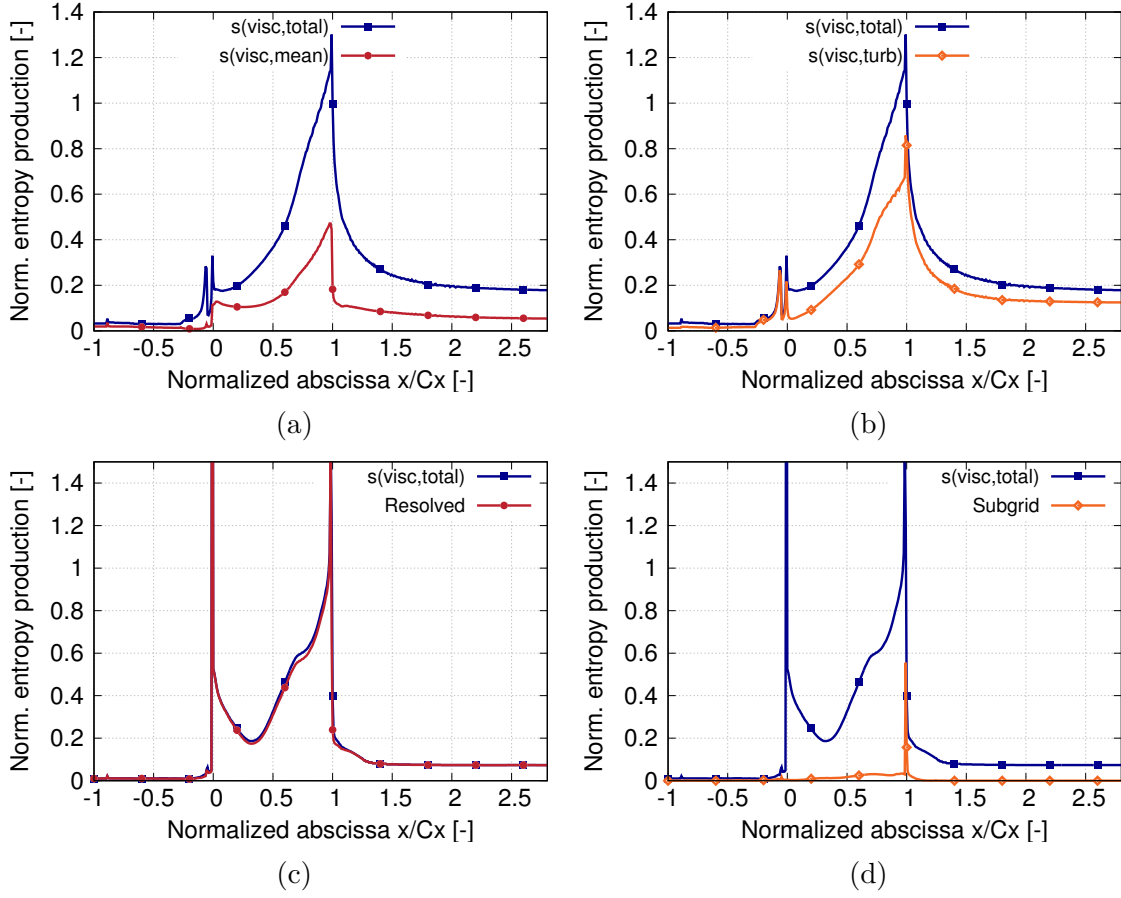


Figure 3.76: Mean and turbulent contribution to the viscous entropy from the RANS simulation (top). Resolved and subgrid contributions to the viscous entropy production based on the LES simulation without turbulence injection (bottom)

lation, the total contribution can be split between mean and turbulent contribution. For the LES simulation, the splitting operation is performed between resolved (by the mesh grid) and unresolved contributions for which an equivalent turbulent viscosity is furnished by the subgrid scale model. The general trend of total entropy production between the RANS and LES simulations is similar excepts that the LES simulation predicts a much stronger peak close to the leading edge for $x/C_x = 0$. In addition, entropy production decreases until $x/C_x = 0.3$ while for the RANS, entropy production increases linearly in the blade domain. The entropy production related to hub and shroud boundary layers upstream of the cavity from $x/C_x = -1$ to from $x/C_x = -0.26$ and downstream blade when the secondary vortices have been dissipated where only hub and shroud boundary layer induce entropy production are shown to be twice less for LES simulation than for RANS simulation. The laminar nature of the boundary layer for LES simulation without turbulence injection shown in Sec. 3.6.1 (p.119) induces less entropy production compared to the turbulent one from RANS simulation. For the LES simulation, resolved and subgrid contributions acts quite differently than the mean and turbulent contribution of RANS simulation. Part of the turbulence is directly accounted in the resolved contribution. According to Fig. 3.76c and 3.76d, the subgrid scale model contribution is low compared to

the resolved one. It remains however that the subgrid scale model is triggered in the blade domain and at the trailing edge of the blade $x/C_x = 1$ where a strong peak can be observed. Despite a mesh refinement in the wake, the turbulence associated to the trailing shed vortex process seems to be not captured and induces the subgrid scale model to be triggered. The turbulent structures of the wake are then not properly propagated but dissipated by the subgrid scale model. A main consequence is that the decay of these structures is made over a shorter distance between $x/C_x = 1$ and $x/C_x = 1.4$ compared to the RANS simulation where the structures were dissipated on a larger axial extension.

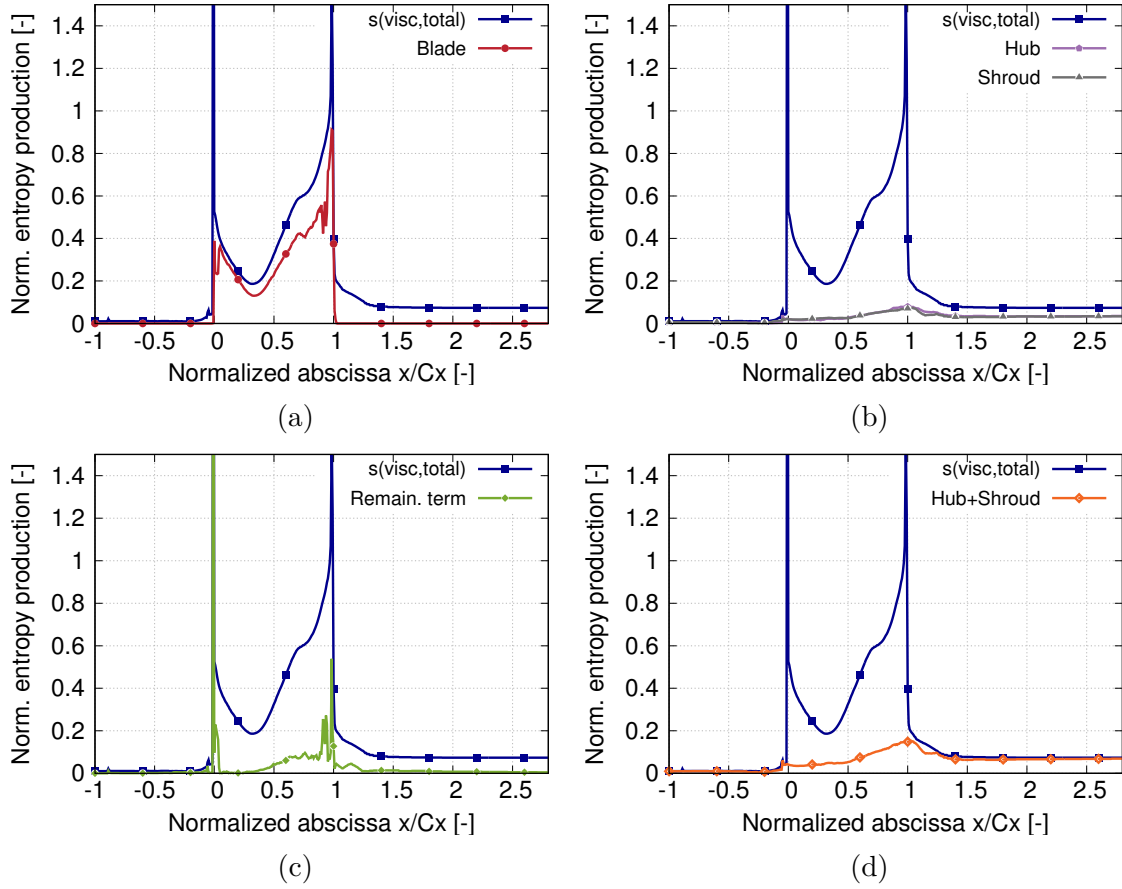


Figure 3.77: Total entropy production for the different subdomains in the LES simulation without turbulence injection

3.7.4.2 LES with turbulence injection

Compared to the LES simulation without turbulent injection (Fig. 3.77), the entropy production for the LES simulation with turbulent injection is larger (Fig. 3.78). This trend is consistent with the pressure loss downstream of the blade that were larger for the LES simulation with turbulence injection compared to without turbulence injection. The entropy production associated to the separation bubble on the blade suction side for the LES simulation without turbulence injection and observed in the blade (Fig. 3.77a) and remaining contribution (Fig. 3.77c) between $x/C_x = 0.7$ and

1 is no more visible in the case with turbulence injection (Fig. 3.78a and Fig. 3.78c) since the separation bubble was cancelled by the inlet turbulence. The entropy production between the inlet and the blade leading ($x/C_x = -1$ to 0) is non zero compared to the entropy production with turbulence injection and can be attributed to the inlet turbulence decay (see Fig. 3.78c). Also, the contribution of this same remaining term is higher in the passage domain ($x/C_x = 0$ and 1) compared to the case without turbulence injection.

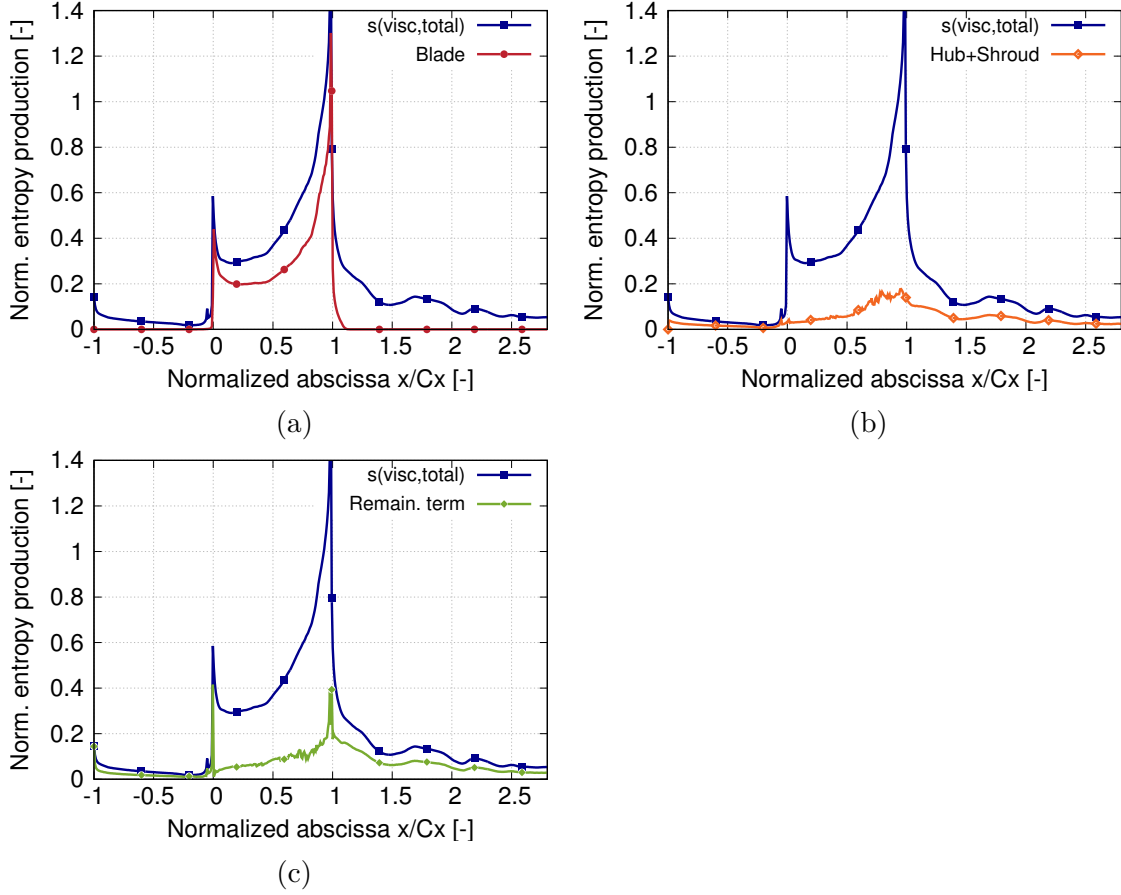


Figure 3.78: Total entropy production for the different subdomains in the LES simulation with turbulence injection

The exergy analysis applied to the linear cascade showed that the available energy to generate work could only decrease in the domain due to viscous and thermal anergy production. Based on the splitting operation between the mean and turbulent contributions of the RANS formalism, these two contributions were shown to contribute almost equally to anergy production. Upstream of the rim seal left corner, and one axial chord downstream of the blade, the contribution to viscous anergy was almost entirely due to boundary layers developing on the hub and shroud inducing wall-normal gradients. At the rim seal interface, viscous anergy is produced due to the shear layer between the cavity with low momentum flow and the main annulus flow with high momentum (both axial and azimuthal). Thermal anergy is also produced since the cavity flow with slightly lower temperature ($T_c/T_m \simeq 0.9$) mixes with higher temperature main annulus flow. Close to the rim seal right corner, the potential effect of the downstream blade induces main annulus ingestion and purge flow blowing at the center of the passage inducing azimuthal gradients of radial velocity. In the passage, several contributions to viscous anergy production can be found: the boundary layers at the hub, shroud and around the blade due to wall-normal gradients. Secondary flow losses that induce anergy production as soon as 20% axial chord under various mechanisms: a friction process on the wetted surfaces where secondary vortices travel especially the passage vortex on the blade suction side and the corner vortex at the hub and shroud; a blockage effect due to the passage vortex promoting strong cross radial velocity gradients. In addition, a mixing process close to the center of rotation of these structures induces thermal viscous anergy production since the cold flow emerging from the cavity is carried and mixed by the secondary vortices in the passage. This last contribution being limited to the blade passage. Downstream of the blade leading edge, mainly two contributions are added to the hub and shroud boundary layer: the vortex shedding process that induce velocity gradients of stream velocity in the cross direction. This contribution, mainly by a turbulent dissipation process induces anergy production until half chord downstream of the blade trailing edge. A second contribution, related to the decay of secondary vortices that is performed over a longer axial distance around one axial chord. The same analysis applied to LES simulations without turbulence injection shows that the contributions of the boundary layers are lower compared to RANS due to the laminar nature of the boundary layer and a lower thickness at a same axial coordinate. However, an additional contribution due to the separation bubble on blade suction side was highlighted both on the blade and remaining domain contribution. For the LES simulation with turbulence injection, losses are generated in the free stream domain until blade leading edge due to turbulence decay that was not observed in both RANS and LES without turbulence injection, the boundary layer contributions were also higher due to the turbulent nature of the boundary layer and no loss

related were incurred due to a separation bubble since cancelled by the free stream turbulence compared to the LES without turbulence injection.

The linear cascade configuration has been studied using several numerical approaches with different turbulence modeling. The different methods predicted similar pressure coefficient around the blade as in experiments. However some discrepancy was observed between the different numerical approaches regarding the pressure loss coefficient downstream of the blade. The numerical methods with lower turbulence modeling (LES without turbulence injection) gave less representative results than other approaches with more modeling (RANS and LES-LBM with law of the wall treatment). This difference was shown to be due to the importance impose the proper inlet profile and turbulence level that was not taken into account in the LES simulations without turbulence injection. The free stream turbulence was show to turn the hub and shroud boundary layers turbulent causing a stronger radial migration of the hub and shroud passage vortices on the blade suction side. Around the blade suction side, the boundary layer becomes turbulent and recovers a similar loss profile as in the experiments compared to a laminar one as obtained in LES simulation without turbulence injection. An exergy formulation has been applied to track the loss generated in the linear cascade including the contributions of the boundary layers over the wetted surfaces, the secondary flows developing in the passage and the directions over which the losses occur. This analysis made possible to observe the influence of the cavity, the rim seal geometry and the purge flow rate. The variation of purge flow rate supplied in the cavity promoted strengthened vortices with higher secondary kinetic energy inducing more loss by mixing and friction process on the linear cascade surfaces compared to a smooth configuration. The rim seal geometry was also shown to influence the levels of loss in the linear cascade. Axial geometries were shown to induce higher level of loss at the rim seal interface due to higher velocity deficit compared to overlapping geometries. In addition, the purge flow emerging earlier in the passage for axial geometry promoted early development of the secondary vortices in the main annulus and subsequently more losses due to secondary flow dissipation.

Gentlemen, I give you the Whittle engine.

— Frank Whittle

4

Two-stage annular configuration

This chapter is focused on the second configuration of the MAGPI project corresponding to a two-stage low speed annular cascade. Some insights have been obtained from the last chapter about the interaction process between the purge and main annulus flow and the subsequent generation of loss in a linear cascade. The purpose of this chapter is to obtain further knowledge about the mechanisms of interaction and loss in a more complex and realistic configuration. In particular, the pumping effect of the rotor discs and multiple row configuration will be studied as additional phenomena to be accounted compared to the linear cascade.

4.1	Experimental setup	166
4.1.1	Inlet parameters	168
4.1.2	Experimental data	168
4.2	Numerical setup and convergence	170
4.2.1	Numerical setup	170
4.2.2	Numerical parameters	173
4.2.3	Convergence	175
4.3	Experimental/numerical comparison	175
4.3.1	Flow around the blade	175
4.3.2	Pressure loss coefficient downstream of the blade	176
4.4	Phase-averaged flow field	177
4.4.1	Cavity flow field	178
4.4.2	Main annulus flow field	184
4.4.3	The flow at the interface between the cavity and the main annulus	190
4.5	Application of exergy formulation to track losses	194
4.5.1	The work extracted by rotor rows	195

4.5.2	Viscous and thermal energy production along the domain	196
4.5.3	Evolution of exergy in the simulation domain	202

4.1 Experimental setup

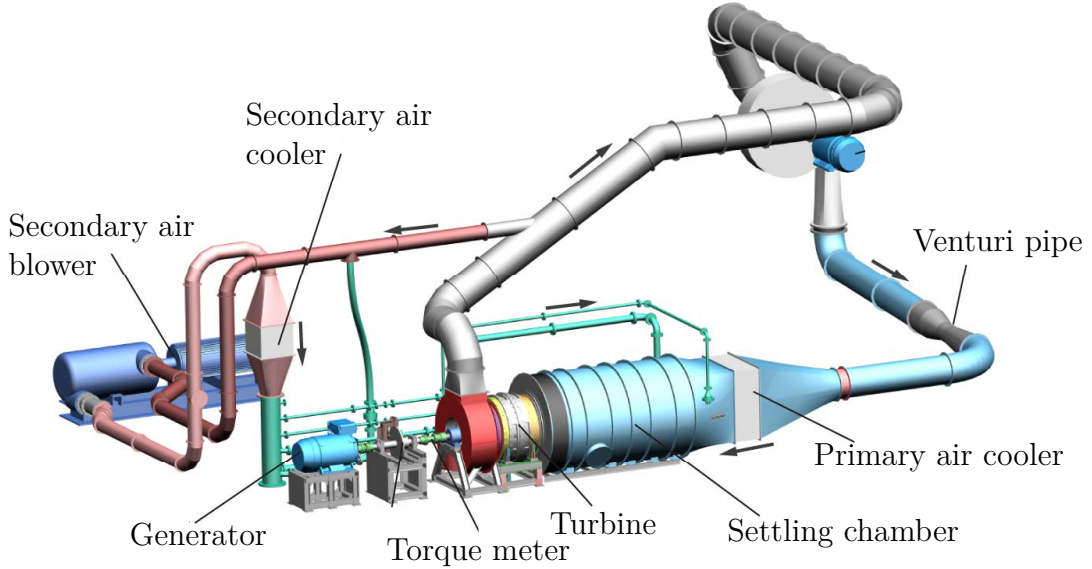


Figure 4.1: Low pressure turbine experimental test rig

The configuration under investigation is an experimental facility representing a high-diameter two-stage low pressure turbine equipped with a representative low pressure turbine blading set up in Darmstadt, Germany. The primary air circuit of the test rig is driven by a compressor which is designed to provide a mainstream mass flow rate up to 15 kg.s^{-1} at a pressure ratio of 1.55. Downstream of this primary air blower a Venturi pipe and a water driven air cooler are installed to measure the mass flow and adjust the turbine inlet temperature. A settlement chamber upstream of the turbine itself houses several screens and flow straighteners to generate a homogeneous pressure and temperature distribution at the inlet. The power of the turbine is absorbed by a generator which feeds the energy back to the primary air blower. To evaluate the efficiency of the turbine, a torquemeter is installed at the shaft between the main bearing of the turbine and the generator. The seal air is provided by an additional blower, which is designed for a mass flow up to 4 kg.s^{-1} and a pressure ratio up to 2.1. The temperature of the seal air is adjusted by another water driven air cooler. Downstream of the secondary air cooler, the seal air is separated into two flows to feed two cavities of the turbine configuration. Each of these seal air flows is controlled by its own valve and mass flow orifice (see Fig. 4.1). Figure 4.2 shows the general arrangement of the two-stage turbine including cavities underneath the hub platform. Blue parts indicate the nozzle guide vanes and light orange parts indicate blades. Grey and blue colors are associated to static parts while light orange ones describe rotating walls. The

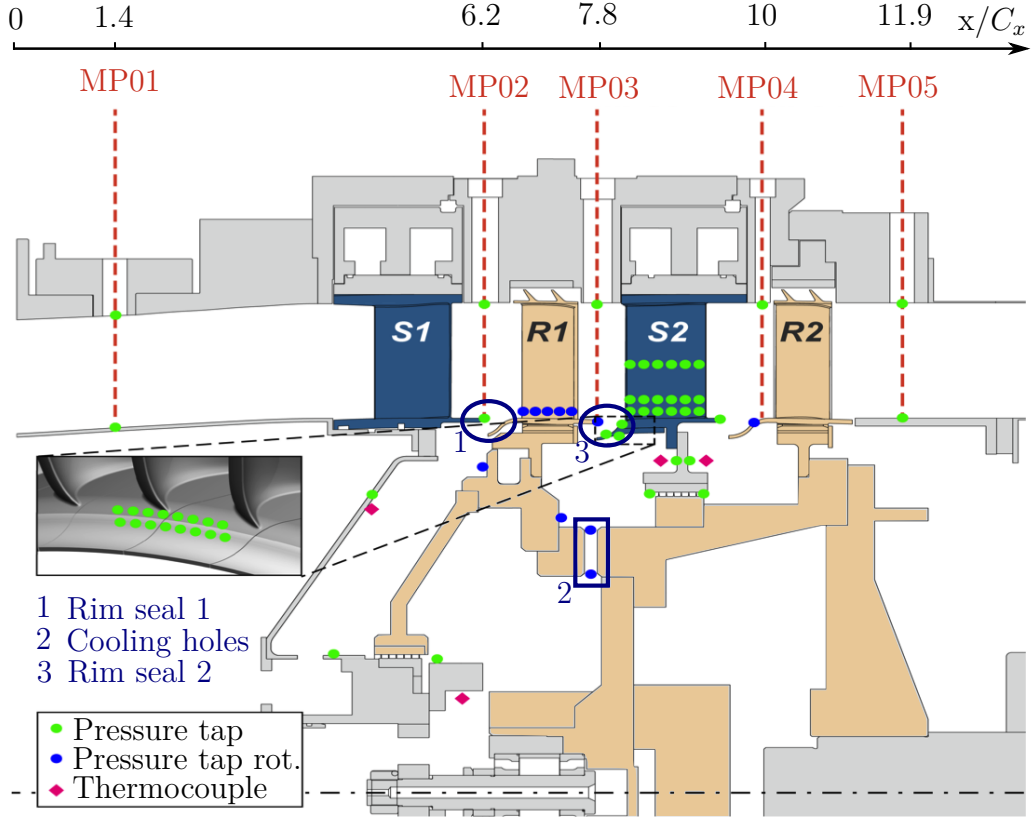


Figure 4.2: Sketch of the two-stage linear cascade including the pressure taps, thermocouples and total pressure experimental measurement planes (MP0I)

rim seal at the interface between the different platforms has been designed to be compliant with the rim seal geometries tested on the linear cascade configuration and are of single axial overlapping type with various axial and radial overlapping distance. The axial distance along the test rig is expressed in terms of the first stator axial chord C_x (see Fig. 4.2 top). Main rig characteristics are gathered for each row in Tab. 4.1, and for stage and full turbine in Tab. 4.2. The main features of this test rig are smaller blade aspect ratios (h/C_x) compared to the typical value for modern low pressure turbine. The main reason relies on the geometrical constraints of the rig as it was previously designed to run with high pressure turbine conditions for which the section height is low and the blades have high axial extent. The blades are designed without any creeping¹ due to experimental instrumentation. Stage work distribution is around 45% for the first stage and 55% for the second one. The stage reaction is around 45%, whereas in modern gas turbines a typical stage reaction is 50% (the expansion ratio is the same in stator and rotor row). In addition, the expansion ratio ($p_{tot,in}/p_{out} = 1.09$) and Mach number ($Ma \simeq 0.2$ on blade suction side) is lower than in real configuration. The turning for each row is around 100° , which is similar to current turbine design, except for the first stator due to the inlet flow characteristics (no upstream swirl). The Reynolds number corresponds to a medium-size configuration at take-off (see Fig. A.6b p.234).

¹the wavy pattern along the blade height at the leading and trailing edge

Table 4.1: Characteristics of the stator and rotor rows

Row	S1	R1	S2	R2
Number of blades	48	72	48	72
C_x [mm]	0.075	0.048	0.075	0.050
Aspect ratio h/C_x	1.77	2.77	1.77	2.66
Inlet blade angle ($^\circ$)	0	37.1	-36.0	39.6
Exit blade angle ($^\circ$)	65.2	-64.6	65.4	-66.4
Lift coefficient (Zweifel $2F_L/\rho u C_x$)	0.61	0.90	0.83	0.86
Exit Mach	0.19	0.19	0.20	0.21
Re_{chord}	544 000	354 000	581 000	405 000

4.1.1 Inlet parameters

The radial distribution of total pressure and temperature at the inlet of the domain (see MP01 in Fig. 4.2) are provided by the experiments based on two pressure and two temperature rakes, each containing 10 pressure or temperature keels in the radial direction. Azimuthal and radial angle (α, β) are set to zero producing a non swirled inlet profile. The static pressure at the outlet of the domain located approximatively 1.5 chord lengths downstream of rotor 2 trailing edge (see MP05 in Fig. 4.2) is also provided by the experiments from eight different circumferential positions. The design point is characterized by a pressure expansion $p_{tot,in}/p_{out} = 1.09$, a rotational speed of $750 \text{ rounds.min}^{-1}$ (78.5 rad.s^{-1}) and a main mass flow rate $\dot{m} = 14 \text{ kg.s}^{-1}$. For this operating point of the main annulus, several purge flow rates were supplied in the cavities. For the cavity between the stator 1 and rotor 1 (rim seal 1), a purge flow was supplied at the bottom of the cavity in circumferentially spread holes to reach a purge flow blowing into the mainstream of 0.5% of the mainstream flow rate for all the cases studied (rim seal 1 in Fig. 4.2). The purge flow rate in the cavity between rotor 1 and stator 2 (rim seal 2) was then the parameter changed to provide the different cases. Table 4.3 provides the purge flow rate in the cavity between rotor 1 and stator 2 (cooling holes in Fig. 4.2) and corresponding purge flow rate at the interface between the cavity and main annulus (rim seal 2 in Fig. 4.2). These different amounts of purge flow supplied correspond to different regimes observed experimentally from strong ingestion of the mainstream air into the cavity at low purge flow rate to a high leakage when a sufficient amount of purge flow is provided in the cavity by the holes shown in Fig. 4.3. In the current study, the numerical simulation is performed at the ingestion point.

4.1.2 Experimental data

Static pressure taps are set up at 5, 20 and 50% span of the second stator (static tap). Each blade contains six pressure taps on the pressure side and 8 taps on

Table 4.2: Characteristics of the annular test rig

	Stage 1	Stage 2		Full turbine
Stage spe. work (dh_{tot}/T) [$m^2.s^{-2}.K^{-1}$]	10.6	12.0	Mass flow [$kg.s^{-1}$]	14
Stage reaction	0.45	0.52	Rotational speed [$rad.s^{-1}$]	78.5
p_{tot}/p	1.042	1.047	p_{tot}/p	1.091
Stage loading parameter (dh_{tot}/U^2)	2.04	2.28		
Stage flow parameter	0.72	0.75		

	Cooling mass flows				
	No flow	Ingestion point	High leakage	High leakage WP3	Very high leakage
Rim seal cavity 1	0.5	0.5	0.5	0.5	0.5
Cooling holes 1	0	0.2	0.6	1.3	2.3
Rim seal cavity 2	-0.3	-0.1	0.3	1	2

Table 4.3: Purge mass flow rate ($kg.s^{-1}$) for the different cases studied

the suction side (see Fig. 4.2). In addition, several static pressure and temperature measurements are provided in the cavity. The flow field behind each row is monitored by five hole probe measurements providing total pressure, temperature and velocity direction (radial and tangential angles). The total number of measurement points is 1209 to cover 15° (test rig periodicity angle) and the mesh is refined at the lower 50% span to better account for the cavity flow influence. From experimental measurements, the pressure coefficient around the stator 2 nozzle guide vane at 5, 20, 50% span and the total pressure loss coefficient downstream the different rows defined as follows

$$C_p(x, z) = \frac{\bar{p}_{tot, MP03}(z) - p_{NGV}(x, z)}{\bar{p}_{tot, MP03}(z) - \bar{p}_{MP03}(z)}, \quad (4.1)$$

$$\zeta(z)_{MP0(I)} = \frac{\bar{p}_{tot, MP0(I-1)}(z) - \bar{p}_{tot, MP0(I)}(z)}{\bar{p}_{tot, MP0(I-1)}(z) - \bar{p}_{MP0(I-1)}(z)}, \quad (4.2)$$

have been used to compare the blade loading as well as aerodynamic efficiency for the different parameters compared in this study. \bar{p}_{NGV} is the static pressure around blade. The overline $\bar{\cdot}$ indicates that the pressure are pitch-wise area averaged values over the two-dimensional measurement grid. Subscript MPOI refers to the measurement plane I (see Fig 4.2). The experimental uncertainty was estimated to be $\zeta \pm 0.015$ for the pressure loss downstream of the blade and $C_p \pm 0.03$ for the pressure coefficient around the blade.

4.2 Numerical setup and convergence

4.2.1 Numerical setup

4.2.1.1 Simulation domain

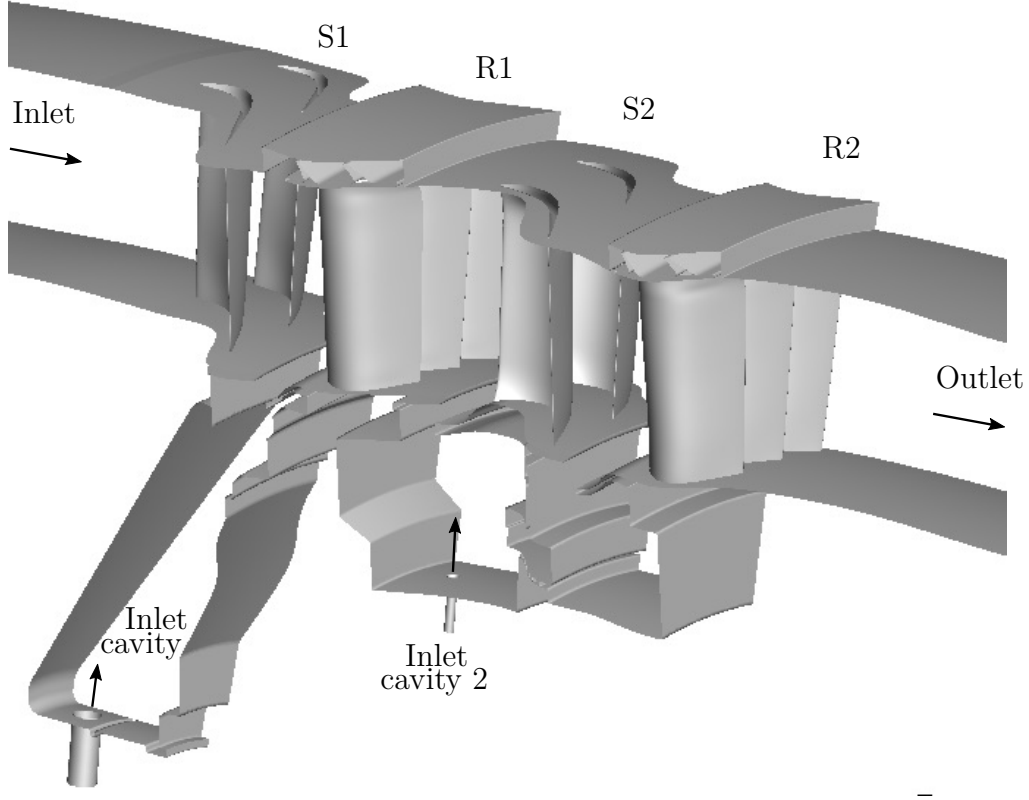


Figure 4.3: Simulation domain representing 1/24 of the full test rig

For the present study, the simulation domain is composed of two nozzle guide vanes of the stator row 1, three blades of the rotor row 1, two nozzle guide vanes of the stator row 2 and three blades of the rotor row 2. This configuration represents 15 degrees and 1/24 of the full domain since the configuration has been developed in such a way to provide a periodicity of 15 degrees based on the blade count (48 nozzle guide vanes, 72 blades, 48 nozzle guide vanes, 72 blades)². The inlet

²In real configurations, the blade count for the different rows is generally composed of coprime

boundary condition is set at MP01 plane where the inlet parameters are available in the experiments. The outlet is set four axial chord downstream of the blade trailing edge of the last blade row to avoid wave reflection issues. Since outlet measurements are provided at MP05 upstream outlet, the pressure outlet condition has been adjusted to reach the experimental mass flow rate and static pressure at MP05. Figure 4.3 provides a side view of the numerical simulation domain.

4.2.1.2 Boundary conditions

At the inlet, total pressure, total temperature and velocity direction profiles are applied according to the experimental data previously introduced. Conversely to the linear cascade configuration, no turbulence grid is used to increase the free stream turbulence and no turbulence is injected at the inlet of the domain. A non-rotating mass flow condition is applied at the bottom of the first hole (see Fig. 4.3) to meet the requirement of 0.5% of mainstream flow at the rim seal interface 1 (see Fig. 4.2). A rotating mass flow condition is applied at the bottom of the second hole (see Fig. 4.3) and was varied to reach the desired mass flow rate corresponding to ingestion point (0.2% of main annulus flow rate). The temperature of the purge flow rate supplied in these two holes is set at a value slightly lower than the mainstream ($T_c/T_m \simeq 0.95$) to be able to follow how the purge flow mixes with the main annulus one, consistently with the experiments. All these conditions are coupled with a Navier-Stokes Characteristics Boundary Condition (NSCBC) to avoid wave reflection in the simulation domain in conjunction with a shift of the outlet position. Periodic conditions are applied on the lateral sections (azimuthal direction) and walls are considered as adiabatic. Because the purge flow rate is low and cavity volume large, the flow in the cavity has been initialized with the temperature of the purge flow.

4.2.1.3 Meshing strategy

The simulation has been performed using the in-house code AVBP described in Sec. A.3.3 (p.248) and Sec. 3.2.1.4 for the linear cascade configuration. Two instances of AVBP (one for the static domain and the other for the rotating one) are coupled at interfaces between static and rotating domains. In each domain, an instance solves the Navier-Stokes equations and a data exchange is performed at the interface under a synchronous process. This current approach makes the mesh generation tractable in this complex geometry. A layer of 15 prisms in near-wall regions is applied around the different nozzle guide vanes/blades and tetrahedra fill the remaining domain. In addition, pyramids are used in some locations to allow for a transition between the prisms and the tetrahedra. The mesh is refined at the blade leading and trailing edge, in the wake region and at the interface between the cavity and the mainstream. The mesh is coarsened when approaching the outlet of the domain to prevent any reflection of wake structures on the outlet condition. The initial mesh is composed of around 150 million cells. This mesh has been used to perform the numerical convergence, reach the operating point and perform as much as possible rotations

numbers to prevent any amplification phenomena along the gas turbine related to common characteristic modes between rows

of the gas turbine in order to converge the flow in the cavity. The convergence rate in the cavity being generally slower than the main annulus. This point will be further detailed in Sec. 4.4.1.1 (p.148) of this chapter but this process has been used to follow the observations by Tang [121] studying the cavity over the rotor shroud on a high pressure turbine performance. A dozen of rotations were required to converge the flow in the cavity. From this simulation, the viscous dissipation term $\tau_{ij}(\partial u_i / \partial x_j)$ contributing to loss has been extracted. In the AVBP distribution, an automatic mesh refinement library called mmg3d [148] of INRIA Bordeaux has been used. The viscous dissipation term called "LIKE" (Loss In Kinetic Energy) in the AVBP code has been used. An isosurface of "LIKE" is provided in Fig. 4.4. This quantity is, as stated in last chapter 3 on the linear cascade, large in regions of strong velocity gradient: in the boundary layers, along the secondary vortices developing in the passage, downstream of the blade trailing edge and in the wake. The mesh refinement technique is currently available only for tetrahedral elements. The prism layers, interface with tetrahedral and azimuthal boundary nodes have been frozen to keep prisms and periodic nodes. This criterion is generally relevant in gas turbine simulations given that for an imposed pressure difference between the inlet and outlet of the domain, the corresponding mass flow rate (and so the operating point) is driven by the discharge (amount of loss) generated across the domain. Furthermore, in the scope of this study on loss generation, the regions where losses are generated need to be properly discretized to evaluate accurately the amount of loss generated for each phenomenon while keeping a computationally affordable numerical simulation. In addition, the mesh refinement technique was shown to provide a better quality mesh with improved skewness, smoothness and aspect ratio³ compared to the initial mesh, which may reduce numerical issues. The

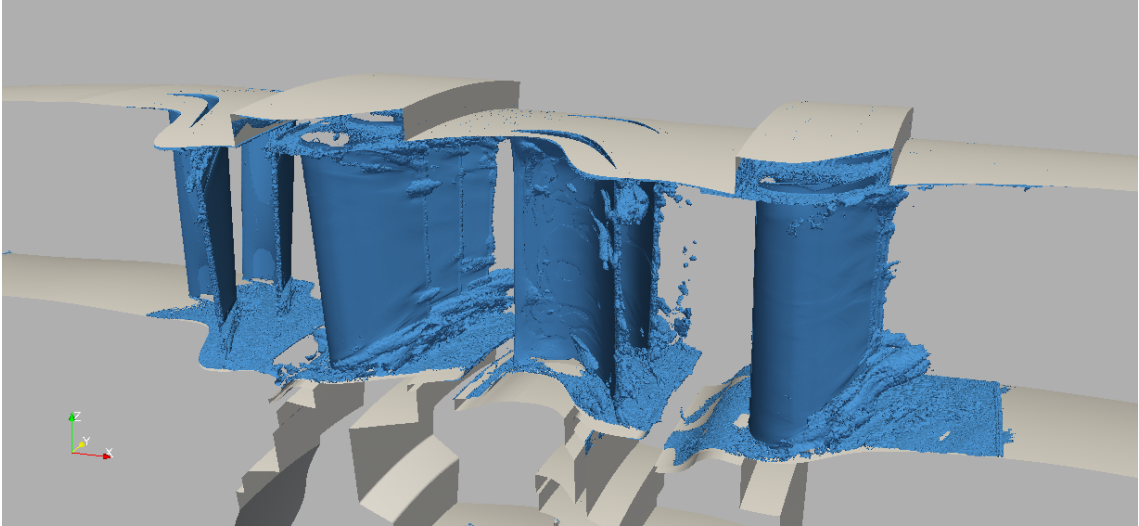


Figure 4.4: Iso-contour of quantity "LIKE"

quantity "LIKE" has been transformed into a metric given to mmg3d. In this metric,

³Respectively determines how close the actual cell is compared to the ideal one (i.e., equilateral or equiangular), the change in size between cells and the ratio of longest to the shortest side in a cell

a constraint of no mesh coarsening is imposed, and a refinement limitation of 0.4 the original characteristic length (tolerating a minimum volume around $(0.4)^3 \simeq 1/16$ the initial volume of the cell) to prevent the generation of very small cells that could strongly affect the explicit time step. The final mesh is composed of around 380 million cells. The mesh refinement at mid-span of the rotor 1 and in the cavities is given in Fig. 4.5. The mesh shows refinement in wake regions of upstream stator 1, rotor 1, in the boundary layers and in the inter-stage honeycomb labyrinth between cavity 2 and 3. The tetrahedral mesh is finally glued back to the prisms and periodic nodes. The mesh refinement in the near-wall region is provided in Fig. 4.2. On the

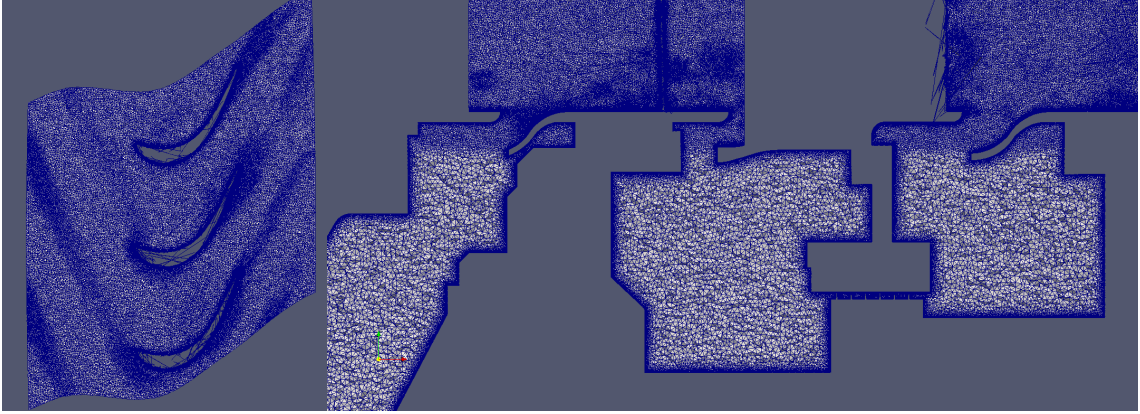


Figure 4.5: Grid refinement for rotor 1 including wake refinement of stator 1 and refinement in the cavities

hub endwall, y^+ resolution can go up to 30 into the passage, therefore a law of the wall treatment is applied. Around the blade, the use of prism layers enable to reach wall resolved requirements in terms of y^+ . For each cavity, the wall resolution has been estimated *a priori* by $\delta_{cav} = \sqrt{\mu/\Omega}$ that originates from the radius-independent Ekman layer representative of this standalone model flow and generally provides a good estimate of the boundary layer thickness over discs even in turbulent confined cases. The wall resolution is checked *a posteriori* by calculating the first grid node wall-normal coordinate y^+ (we use here the notation y^+ since no unique normal vector exists for the different cavities). Figure 4.7 shows the corresponding y^+ distribution for all three cavities. As the friction velocity u_τ increases with the radial position in the cavity, y^+ also increases with the radius, but in all layers the first mesh point is always located within the viscous sublayer (usually bounded by $y^+ < 5$). However, the y^+ value exceeds recommendation for wall-resolved simulation locally in the labyrinth.

4.2.2 Numerical parameters

The 150 million cells mesh used to converge the flow provided sufficiently light and high explicit time step. However, due to the automatic mesh refinement which impacts the mesh size and the physical time step, the simulation time step for explicit time-advancement is $\Delta t^+ = \Delta t u_\infty / C_x = 10^{-5}$. A simple analysis of the physical time required to converge (two full rotations) and extract data from the

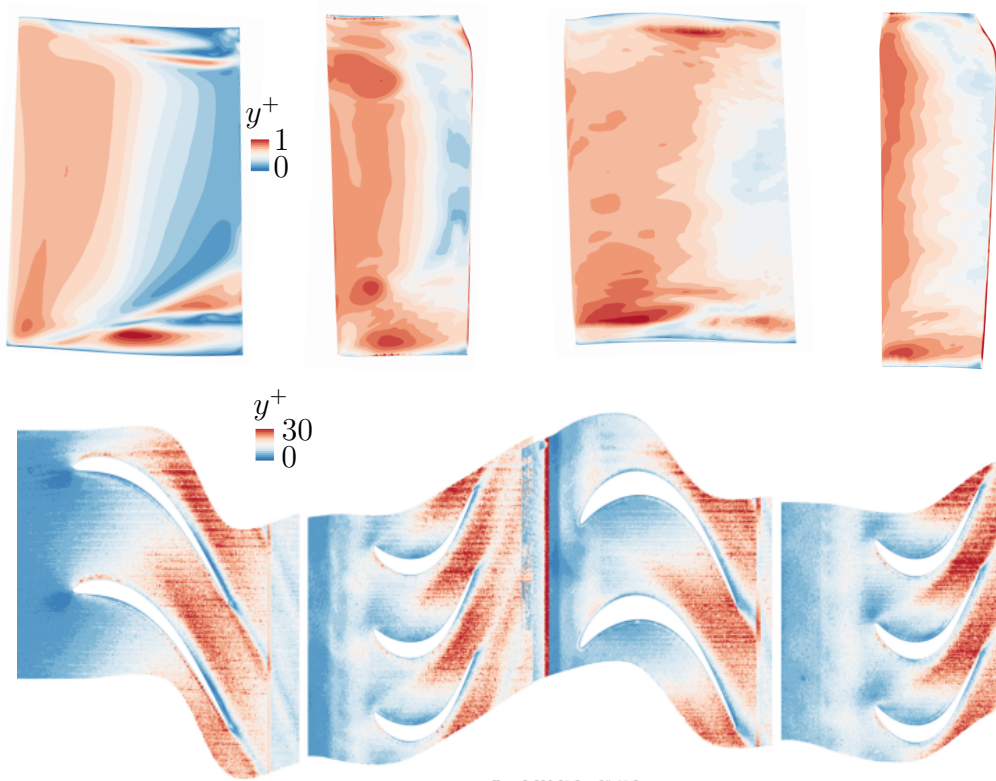


Figure 4.6: y^+ resolution around the different blade suction sides S1, R1, S2, R2 (top) and at the hub surface (bottom)

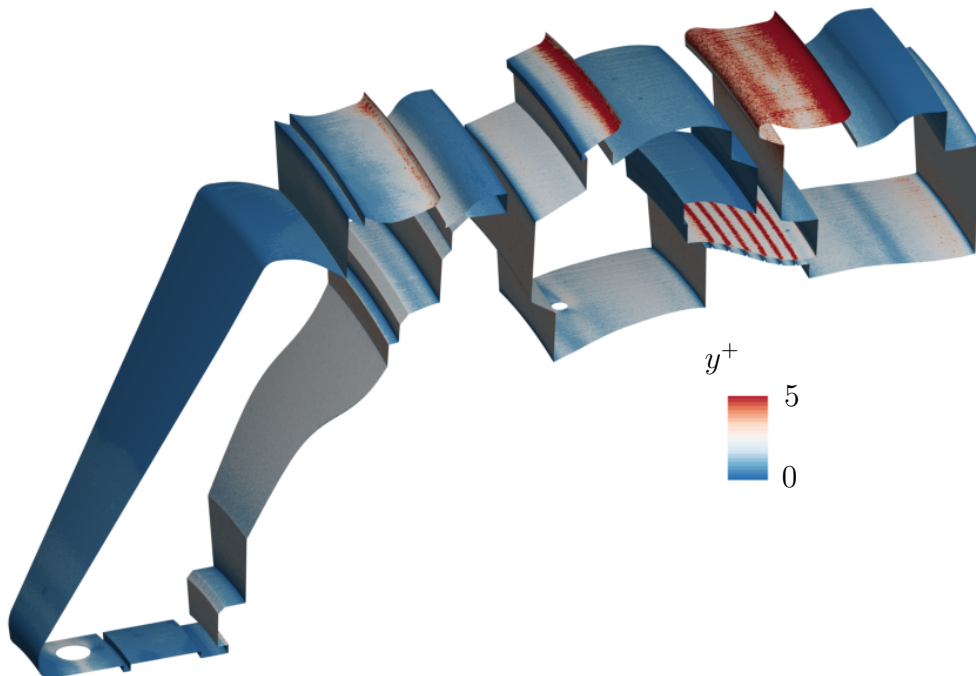


Figure 4.7: y^+ resolution at the cavity walls

simulation (two additional full rotations) shows that due to the low rotational speed of current configuration ($750 \text{ round.min}^{-1}$) compared to real engines, the number

of iteration is important for the considered time step. This constraint has led to the use of the second order accurate Lax-Wendroff scheme instead of the TTG family scheme (third order accurate) due to higher CPU cost compared to Lax-Wendroff scheme (2.5 to 3 times slower).

4.2.3 Convergence

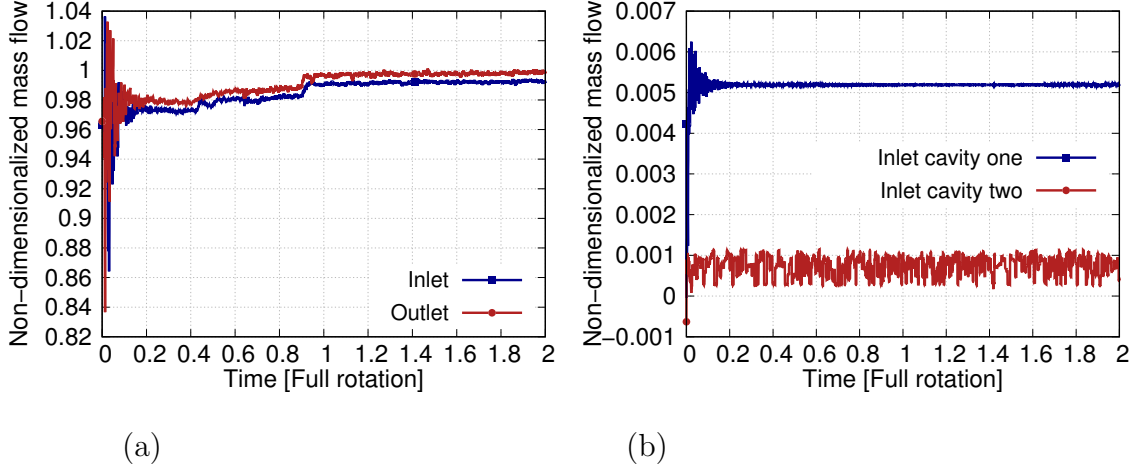


Figure 4.8: Temporal evolution of the mass flow rate at the inlet, outlet (a) and at the inlet of the cavities (b)

The evolution of the mass flow rate at the main annulus inlet, cavity 1, cavity 2 inlet holes and the outlet of the domain for the refined mesh is given in Fig. 4.8 for the time window corresponding to two full convergence rotations of the gas turbine on the refined mesh. The target mass flow rate corresponding to the operating point is reached after around one full rotation. The mass flow rate at the inlet of the domain and the contribution of the two purge flow rates supplied in the cavity differs less than 0.1% from the outlet mass flow rate. The mass flow supplied in the cavity 1 corresponds to a non-rotating inlet while the injection into the second cavity corresponds to a rotating inlet at lower mass flow rate that was shown to increase fluctuations.

4.3 Experimental/numerical comparison

The purpose of this section is to compare the results obtained from the numerical simulation on the refined mesh with experimental data available to assess the capability of the simulation to predict the physical phenomena observed during the experiments.

4.3.1 Flow around the blade

Figure 4.9 shows the pressure coefficient around the nozzle guide vane of stator 2 at 5, 20 and 50% blade height. At mid-span on the blade pressure side, the pressure

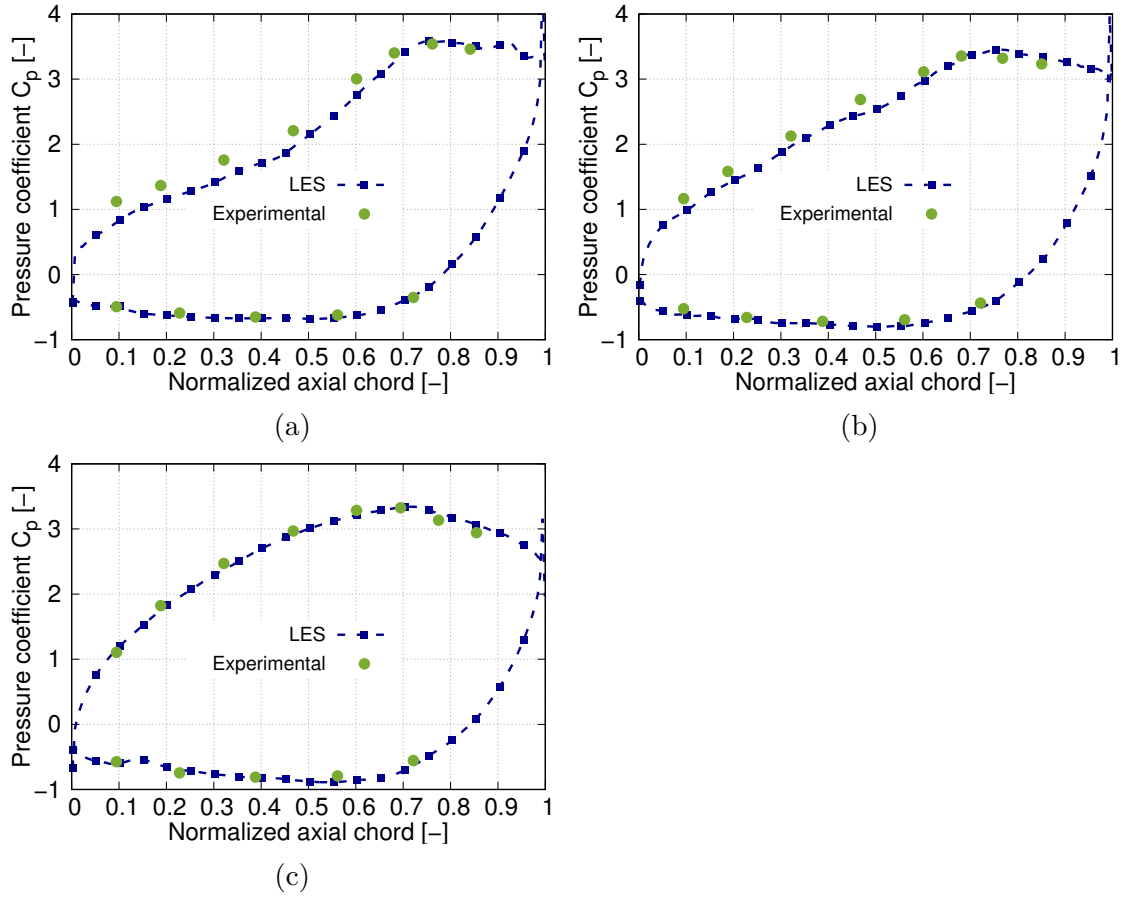


Figure 4.9: Pressure coefficient around the blade at (a): 5, (b): 20 and (c): 50% span of the stator 2 row and experimental measurements at the different nozzle guide vane height (d)

coefficient is correctly predicted. The pressure increase observed at $x/C_x = 0.15$ may indicate a separation bubble. This observation cannot be supported by the experiments because experimental measurements does not give enough measurements points at this location. On the blade suction side, the pressure coefficient is in agreement with the experiments on the accelerating portion until $x/C_x = 0.7$ but the simulation underpredicts the velocity decrease until the trailing edge on the diffusion portion. Close to the hub, the pressure coefficient obtained numerically is in agreement with the experiments on the blade pressure side. On the suction side, the pressure coefficient is underpredicted in the region of pressure decrease until $x/C_x = 0.7$ with a maximum discrepancy of around 5% at 4% span, then the pressure increase is correctly predicted until the trailing edge.

4.3.2 Pressure loss coefficient downstream of the blade

Figure 4.10 shows the one dimensional total and static pressure evolution all along the simulation domain including the experimental data available at measurements planes based on a mass averaging procedure. The expansion process along the different rows shows a good agreement compared to the experiments at the available

measurement planes. Figure 4.11 shows the pressure loss coefficient downstream

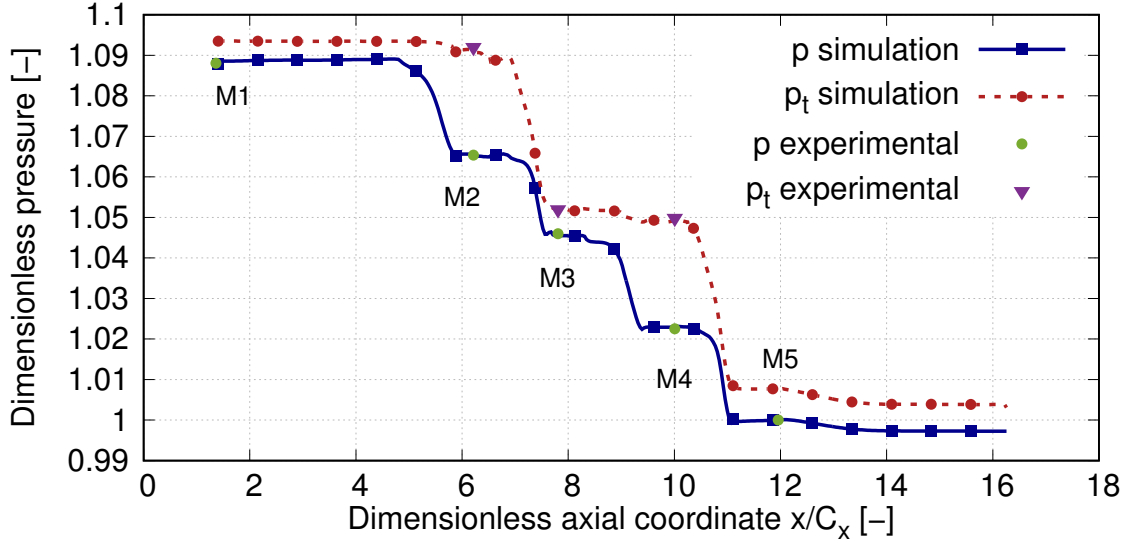


Figure 4.10: Evolution of the total and static pressure in the simulation domain compared to the experiments non-dimensionalized by the pressure at the outlet of the domain

of the stator row 1, rotor 1 and stator row 2. The pressure loss coefficient in span is slightly overpredicted in the numerical simulation (around 5% discrepancy in mid-span region) downstream of stator row 1. The two main pressure loss peaks are at a similar radial position $h/H = 0.1$ and $h/H = 0.85$ (see Fig. 4.11a). Downstream of the rotor 1, the constant pressure loss zone between $h/H = 0.2$ and $h/H = 0.8$ is in good agreement with the experiments except at $h/H = 0.3$ where the numerical simulation indicates additional losses. Close to the hub, the pressure loss is relatively well predicted. However, close to the shroud between $h/H = 0.8$ and 1, the pressure loss coefficient is strongly underpredicted compared to the experiments in the region corresponding to the blade tip with a maximum discrepancy of around 8% (see Fig. 4.11b). Downstream of the stator row 2, the linear increase in the pressure loss coefficient between hub and $h/H = 0.2$ is not properly recovered by the numerical simulation. The loss peak at $h/H = 0.35$ is not predicted by the simulation while the pressure peak at $h/H = 0.6$ is underpredicted by the simulation. This may be due to several contributions: the incoming flow on stator row 2 may be inhomogeneous due to the effects of stator and rotor 1 and the small gap between rotor 1 and stator 2 may prevent sufficient homogenizing of the flow. It should also be noted that the linear trend reported by the experiments close to the wall is also difficult to explain.

4.4 Phase-averaged flow field

The purpose of this section is to describe the flow field in the whole configuration based on a phase averaging performed over two complete rotations of the configu-

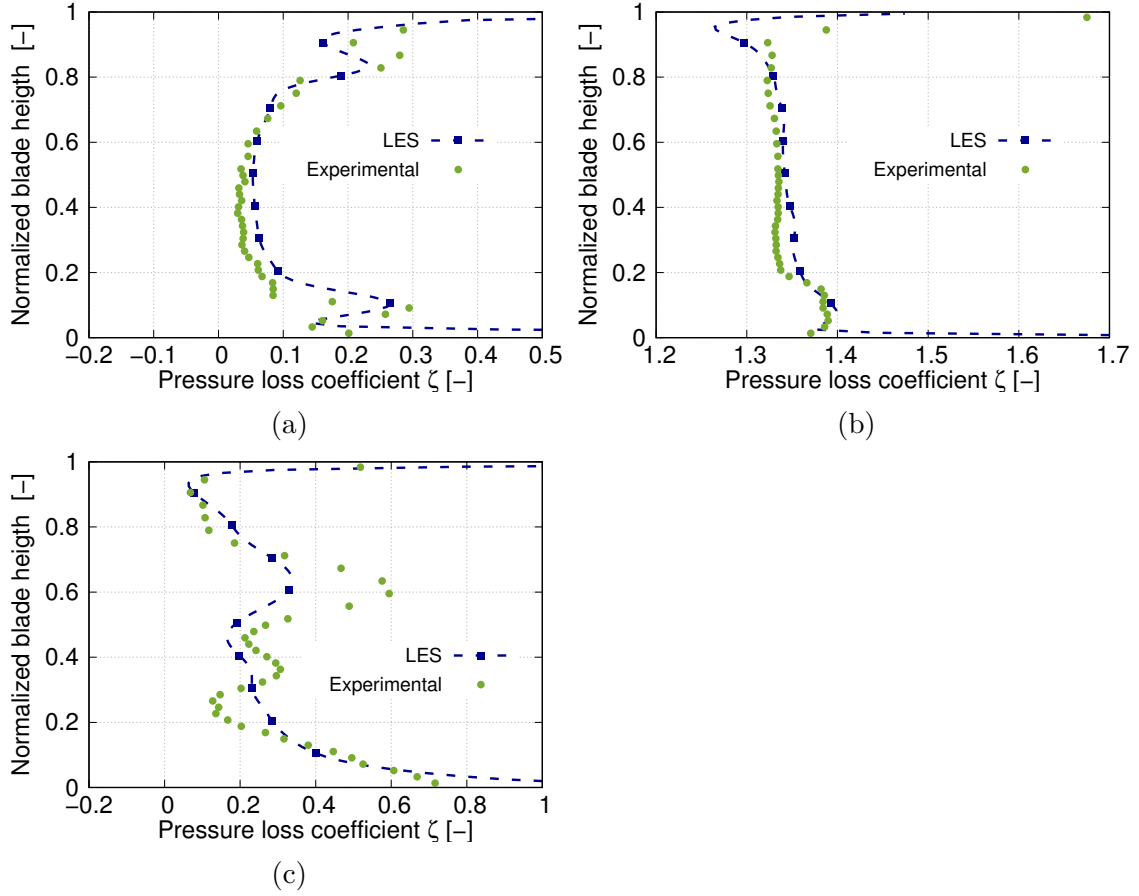


Figure 4.11: Pressure loss coefficient downstream of stator 1 (a), rotor 1 (b) and stator 2 (c) obtained numerically compared to experimental data

ration. Because 24 shifts of one passage are required to make a full rotation, the average is based on 48 snapshots. The description is first conducted in the three cavities underneath the main annulus, in the main annulus and at the different rim seal interfaces between the cavities and the main annulus.

4.4.1 Cavity flow field

4.4.1.1 General motion of the three cavities

In order to describe the flow in the cavity, we briefly recall the main mechanisms leading to the established laminar flow field in a two infinite facing disc configuration initially at rest. Despite being a crude simplification of the current configuration, it provides some guidelines, parallels and references with the flow observed in the configuration. From the fluid in the cavity initially at rest, the rotor is instantaneously brought to its rotation speed in the current numerical simulation. Due to the slip condition on the rotor disc, the flow close to the disc is driven in rotation inducing the formation of a boundary layer. Some air is pumped axially towards the rotating disc to be expelled radially outwards. This boundary layer on rotating disc corresponds to the Ekman family profile (flow initially at rest on a rotating

disc). The evolution of the kinetic energy for the fluid layer located immediately above the rotating disc of cavity 1 is provided in Fig. 4.12b. After approximately 0.1 full rotation of the gas turbine, the kinetic energy reaches a plateau. According to the study on the laminar flow over a rotating disc (Sec. 1.1.1.3 p.4), in addition to this short layer of fluid influenced by the disc, the rotating disc promotes at current Reynolds number the development of an inviscid core flow between the static and rotating disc where the radial velocity is close to zero and the tangential velocity is constant $u = K$, K being usually termed as the entrainment coefficient. This inviscid core flow generates the second type of characteristic flow observed near the static disc with a rotating flow on it (corresponding to the inviscid core flow) and referred as Bödewadt configuration. In this configuration, the flow migrates radially inwards from high radius to the center of the disc to generate an axial flow leaving the stator disc. The evolution of the kinetic energy for the fluid layer located immediately above the rotating disc of cavity 1 is provided in Fig. 4.12c. The layer close to the stationary discs have a delayed response and stay in its initial resting state for a longer time compared to the rotating disc (around 0.2 full rotation, see Fig 4.12c). This corresponds to the time required for the fluid in between stator and rotor walls to be set in rotation. However, the plateau observed for the kinetic energy on the stator side is only true at the initial state, it will progressively increase when the flow in between (inviscid core flow) will be increasingly put in rotation (over a much longer period of time). The axial flow extracted from the static cavity wall is pumped by the rotor disc. The studies of Bridel-Bertomeu [12] on industrial rotor/stator cavities of turbopump configuration, Tang [121] for the shroud cavity over a high pressure turbine stage reported a convergence of the flow field in the cavity after a dozen of full rotation at a similar cavity Reynolds number, the time required to have the former described phenomena established. The convergence time required to converge the flow field in the cavity can be further increased as stated by Pogorolev et al. [149] that studied instability in the cavity of a rotor/stator configuration with mainstream flow. The author showed that around 40 full rotation of the rotor were required to obtain a fully developed flow field inside the rotor/stator wheel space. The number of rotation required to make the flow into cavity converge can be of this magnitude when thermal effects are important. For example, in bore cooling, thermal instability like Rayleigh-Bénard instability can be a dominant phenomenon compared to convective ones and requires four or five dozen rotations to reach a converged state [150]. Figure 4.12 shows the temporal evolution of the total volume-averaged kinetic energy of the flow for the first cavity. The base flows of the rotor/stator cavities used in this investigation are then considered to have reached a converged state when the volume-averaged cavity kinetic energy reaches a plateau. For current configuration based on ten full rotation of coarse mesh, the volume-averaged cavity kinetic energy approaches a plateau that is in favour of a convergence of the flow in the cavity. This large time required to converge the total kinetic energy of the flow in cavity 1 corresponds to the time required to put the inviscid core flow between stator and rotor walls at the entrainment velocity. These observations are coherent with Tang [121] that showed a convergence in a shroud cavity in a high pressure turbine after around 14 full rotations. Regarding the transition to turbulence, this may be induced by relatively high free stream turbulence

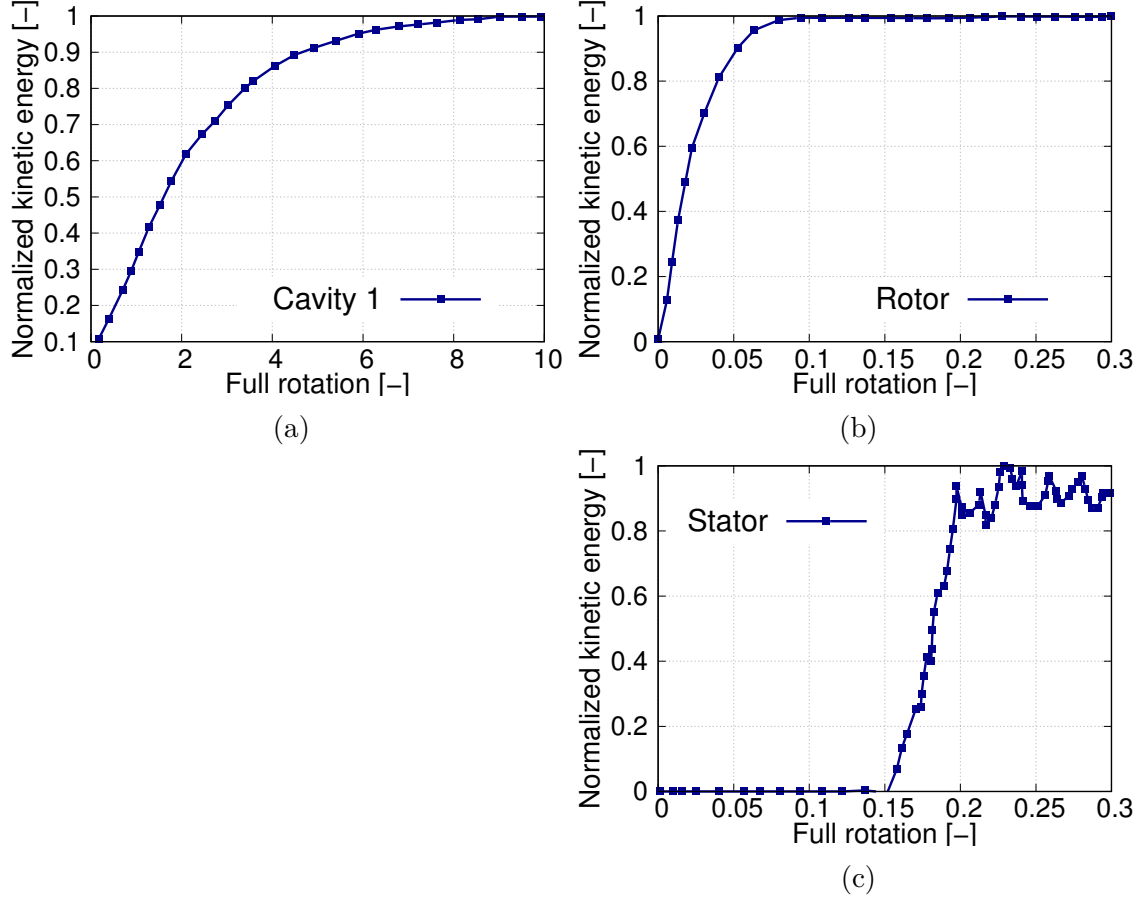


Figure 4.12: Evolution of the dimensionless volume-averaged kinetic energy for the entire cavity 1 (a) and evolution of the dimensionless kinetic energy of the rotor boundary layer (b) and stator boundary layer at the cavity mid-height (c)

that could onset the transition to turbulence under a bypass process. At relatively high Reynolds number and low free stream turbulence as in the current situation, several studies infer in favour of a natural destabilization of the flow field (hydrodynamic instability) [151]. The susceptibility of rotor/stator cavity flow to inviscid crossflow instability is to be expected from the inflectional nature of the velocity profiles close to rotating and stationary wall that might be responsible for the onset of turbulence in this configuration. These fluctuations are observed to form macro structures, born in the unstable stator boundary layer and extending to the homogeneous inviscid core and the rotating disc boundary layer, causing its instability. This phenomenon is generally enhanced by the inner shaft and reach the limit cycle (fully developed turbulent flow in the cavity) [12]. The natural destabilization process is supported by linear stability analysis showing similar transitional Reynolds number between theoretical and experimental value [152]. Cavity 1, 2 and 3 provide similar cavity aspect ratio $G = h_x/r_0 = 0.28$ and rotating Reynolds number at mid-height $Re_\omega = (r_0^2 \omega)/\mu = 7.37 \times 10^5$, where it is reminded that h_x is a characteristic length between the stator and rotor side (here in the axial direction), r_0 is the mean radius of the cavity and ω is the rotating angular velocity of the gas turbine. Given the cavity aspect ratio, Reynolds number Re_h and the analysis provided in Sec. 1.1.2

and Fig. 1.4, the flow in these cavities should be turbulent with separated boundary layers. The boundary layer profiles for the axial, radial and azimuthal velocity are provided at cavity mid-height for the cavities 1, 2 and 3 (see Fig. 4.16 and 4.14 for velocity profile extraction location). These profiles have been obtained by averaging azimuthally the flow field. In addition, the analytical profile for the laminar flow in a two infinite facing disc configuration without inner shaft (one static and the other rotating) is provided at $Re_h = 58\,000$ corresponding to the cavity Reynolds number. Radial and tangential velocity profiles in cavity 1, 2 and 3 are provided in

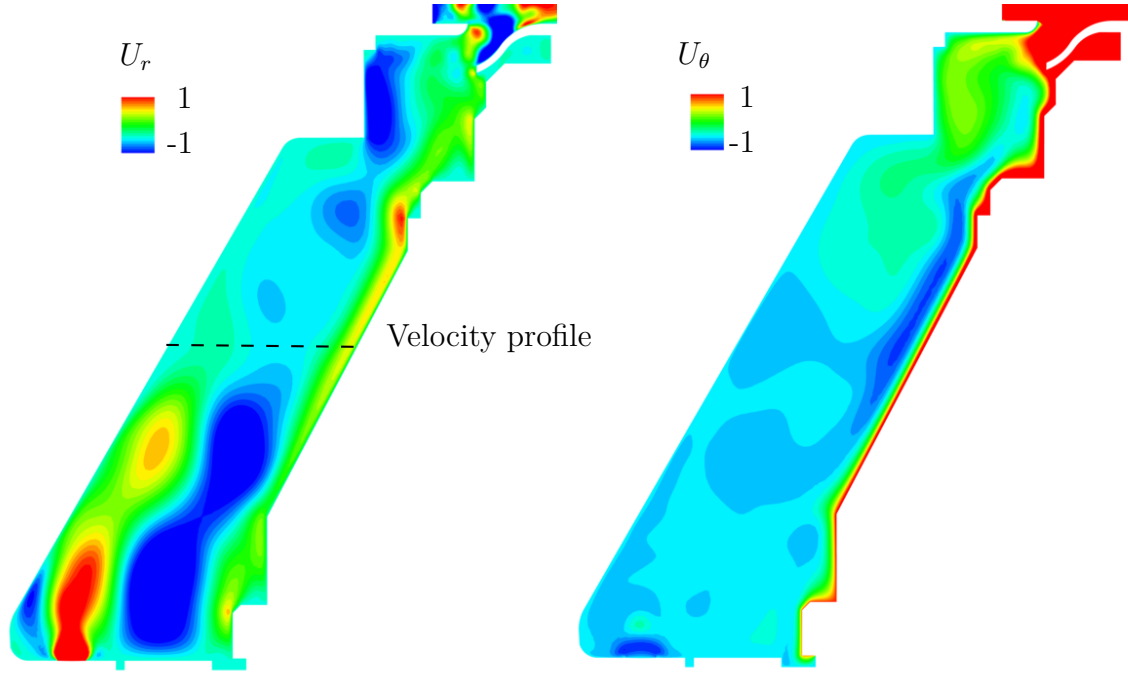


Figure 4.13: Radial and tangential velocities in the cavity 1 in a meridional plane

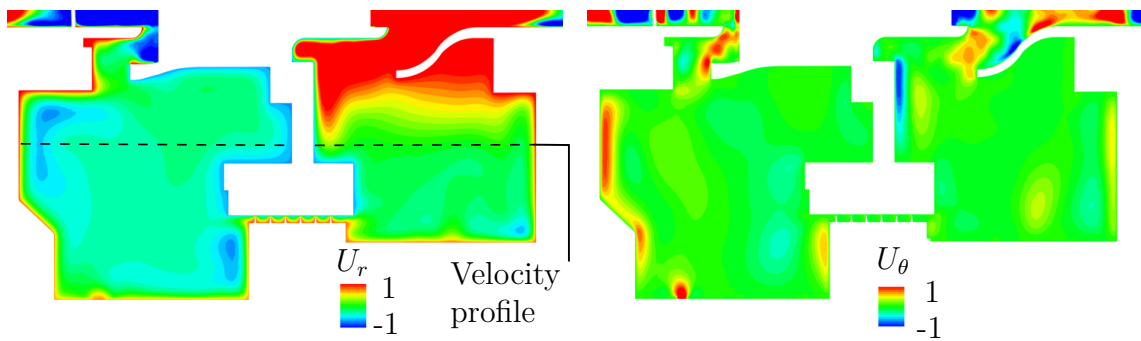


Figure 4.14: Radial and tangential velocities into the cavities 2 and 3 in a meridional plane

Fig. 4.13 and 4.14. Due to the rotation of the rotor discs that hold the blades, the azimuthal component of the flow near the rotor disc surfaces can be observed for all three cavities. The rotation of the disc induces radially outward expelled flow on the rotating disc and conversely radially inwards on static surfaces (see Fig. 4.13a

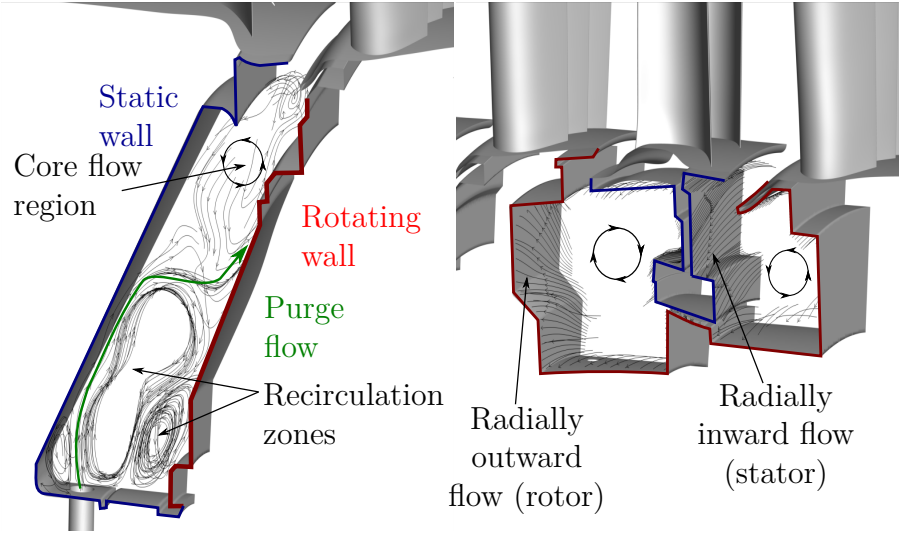


Figure 4.15: Three-dimensional streamlines in the cavities 1, 2 and 3

and 4.14b). In addition, streamlines in the cavities are provided for all three cavities in Fig. 4.15, the static walls being displayed in blue and rotating ones in red. For cavity 1, the purge flow supplied at the bottom of the cavity is shown to induce three recirculation zones with a center clockwise recirculation zone and two counter rotating structures on both side of this recirculation zone. These structures extend until around 40% of the cavity height. Above, the flow is shown to recover the structure of the flow in a rotor/stator cavity. The streamlines show two main contributing phenomena: the pumping effect where some flow is pumped towards the rotor disc at low radius, expelled radially outwards by rotor disc, travel towards the stator wall at high radius and is send radially inwards at low radius by the stator wall (see the streamlines on the static and rotating wall of the cavity 2 and 3 in Fig. 4.15). In a meridional plane, this generates the large scale flow structure rotating counter clockwise for cavities one and three (since the rotor disc is on right-hand side and static one on left-hand side), and clockwise for cavity two (rotor disc on left-hand side and static one on right-hand side). The second effect is the rotating central core which induces this large scale structure also rotating azimuthally. Figure 4.15 also provides the streamlines (green arrow) of the purge flow emerging from cooling holes at the bottom of the cavity. The purge flow first travels radially on the stator wall before migrating at around 40% cavity height on the rotation wall. The axial momentum may be explained by the von Kármán pumping effect induced by the rotating disc (see Sec. 1.1.1.1 p.2). When the flow reaches the rotating wall, the purge flow is sent radially outwards at higher radial locations before blowing in the main annulus in the upper loop induced by the rotor/stator configuration. In addition of the meridional planes provided for the three cavities, radial and tangential velocity profiles at mid-span is proposed in Fig. 4.16 for cavity 1 and in Fig. 4.18 for cavities 2 and 3. The theoretical profile for laminar flow over an infinite two-discs configuration is also provided in the same figures. For all three cavities, a central core with nearly zero radial velocity but non-zero entrainment velocity can be observed. This central core separates two regions of strongly varying radial and azimuthal velocity close

to rotor and stator walls. This observation shows some similarities with the prediction by Daily and Nece [17] for enclosed rotor/stator configuration. For the current Reynolds number Re_h and the aspect ratio of all three cavities ($Re_h = 5.8 \times 10^4$, $G = 0.28$), the mean flow exhibits separated boundary layers with a central core (regime IV in Fig. 1.4 p.6). However, it may be pointed out that the central core is not rotating at a purely constant velocity as for theoretical profiles. This may be due to the relatively complex geometry and the influence of purge flow blowing at the bottom of the cavities 1 and 2. In addition, the entrainment is shown to be lower than for the theoretical profile, around half the rotating velocity of the rotor disc. Also, the boundary layer profiles close to rotor and stator surfaces are shown to be different with respect to the theoretical laminar one. This may indicate the turbulent nature of the boundary layer over stator and rotor disc walls, as it is predicted by the experimental studies of Daily and Nece [17] (separated, turbulent boundary layers).

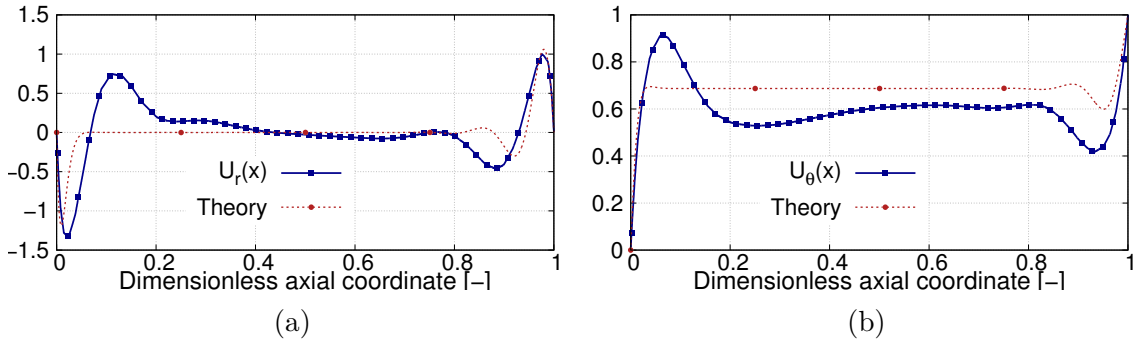


Figure 4.16: Azimuthally-averaged radial (a) and azimuthal (b) velocity profiles at cavity 1 mid-height

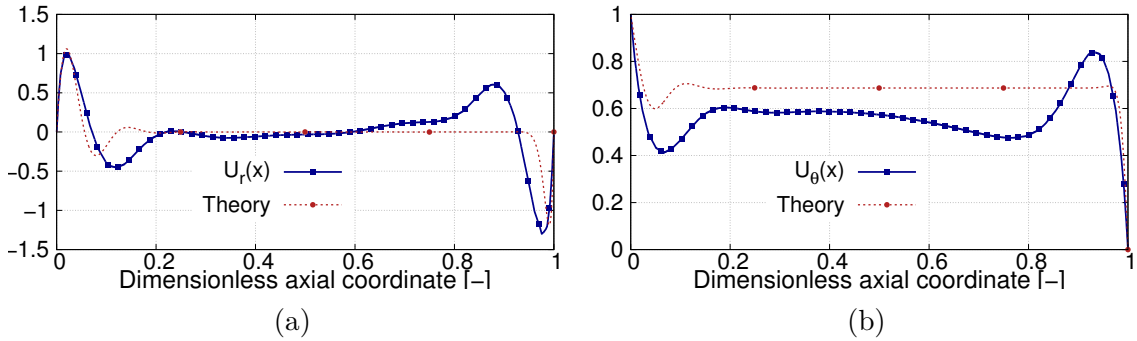


Figure 4.17: Azimuthally-averaged radial (a) and azimuthal (b) velocity profiles at cavity 2 mid-height

4.4.1.2 The flow transfer between cavities

Some purge flow is supplied into the cavity 1. Since this cavity is only linked to the main annulus, a mass balance for the cavity 1 shows that an ingestion (main annulus flow into cavity)/egress (cavity flow into main annulus) process can happen

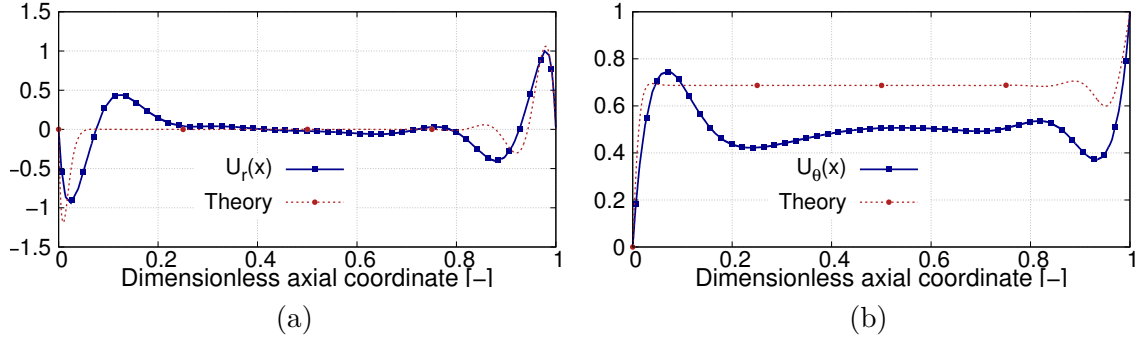


Figure 4.18: Azimuthally-averaged radial (a) and azimuthal (b) velocity profiles at cavity 3 mid-height

at the rim seal interface but the blowing will exceed the ingress of the main annulus flow by an amount corresponding to the mass flow supplied in the cavity. In the current configuration, it corresponds to 0.5% of the main annulus flow. In the cavity 2, some purge flow is also supplied at the bottom of the cavity. The second cavity is connected with the main annulus flow and cavity 3 by the inter-stage labyrinth seal. Figure 4.19a provides axial velocity in the labyrinth between cavity 2 and 3. The flow in the labyrinth is characterized by an increased velocity when approaching the tooth due to a section reduction. Regarding pressure distribution, between the teeth of the labyrinth, pressure is almost constant with jumps to ensure the pressure drop between cavity two and three (see Fig. 4.19b). The labyrinth seal used to reduce flow migration of flow between cavity 2 and 3 was shown to induce a mass flow rate between cavity 2 and 3 that is around 4% of the mass flow provided to the cavity 2 by the cooling holes. The main consequence is that the balance between ingress and blowing at the rim seal interface 2 is positive (blowing into the mainstream) corresponding to 96% of the cooling flow for the cavity 2, while the balance at the rim seal interface 3 represents 4% of the cooling flow for the cavity 2 (see Fig. 4.20).

4.4.2 Main annulus flow field

4.4.2.1 The flow field in stator rows

As introduced in Sec.4.1, the mainflow gas path of the current configuration corresponds to the main geometrical feature and Reynolds number of a medium-sized low pressure turbine at take-off (see Fig. A.6b p.234). The two stator and two rotor are similar in design (see Tab. 4.1 p.168). The flow at the inlet of the turbomachine is a purely axial flow without whirl (angle between axial axis and actual velocity vector projected in blade-to-blade plane) or radial angle (angle between radial axis and actual velocity vector projected in axial plane) for the first stator row while swirled for the second stator row (36° with respect to the axial direction). The first and second stator rows have geometrical feature similar to the previously studied linear cascade configuration, making possible to draw some parallels. The boundary layer at the hub and shroud separates when approaching the blade leading edge. This induces the development of a horse shoe vortex process with pressure side leg

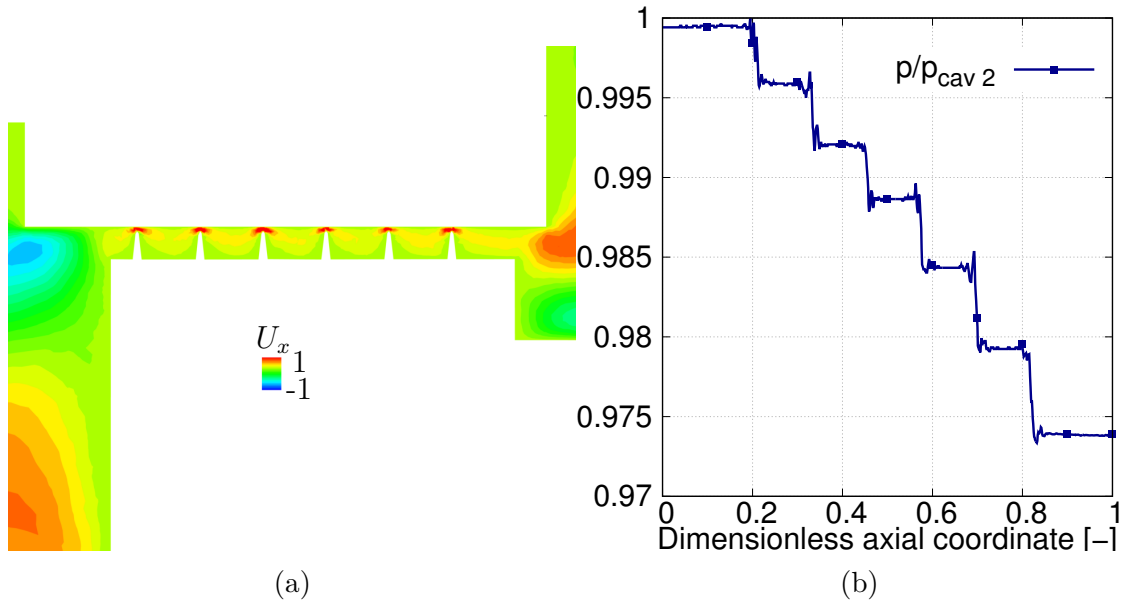


Figure 4.19: Axial velocity in the labyrinth (a) and pressure evolution normalized by pressure cavity 2 (b)

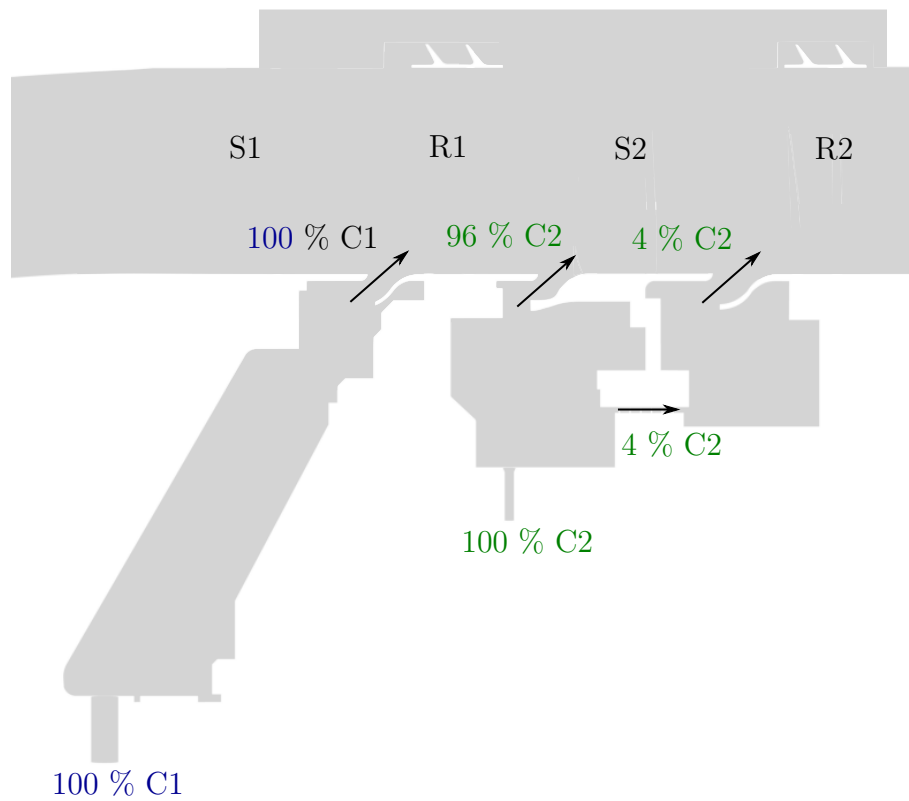


Figure 4.20: Repartition of cooling flow in cavity 1 and 2 on the three rim seal

and suction side leg emanating from the horse shoe vortex being chopped by the blade leading edge. The pressure side leg travels along the passage to reach the

blade suction side and initiates the migration along the blade suction side and subsequent passage vortex (see Fig. 4.21). At the shroud, due to decambering (nozzle guide vane less twisted), the cross pressure gradient is lower, the pressure side of the horse shoe vortex at shroud travels with a lower cross component velocity inducing the merge between the pressure and suction side horse shoe at a higher axial chord (see Fig. 4.21). In addition, the boundary layer thickness on the blade suction

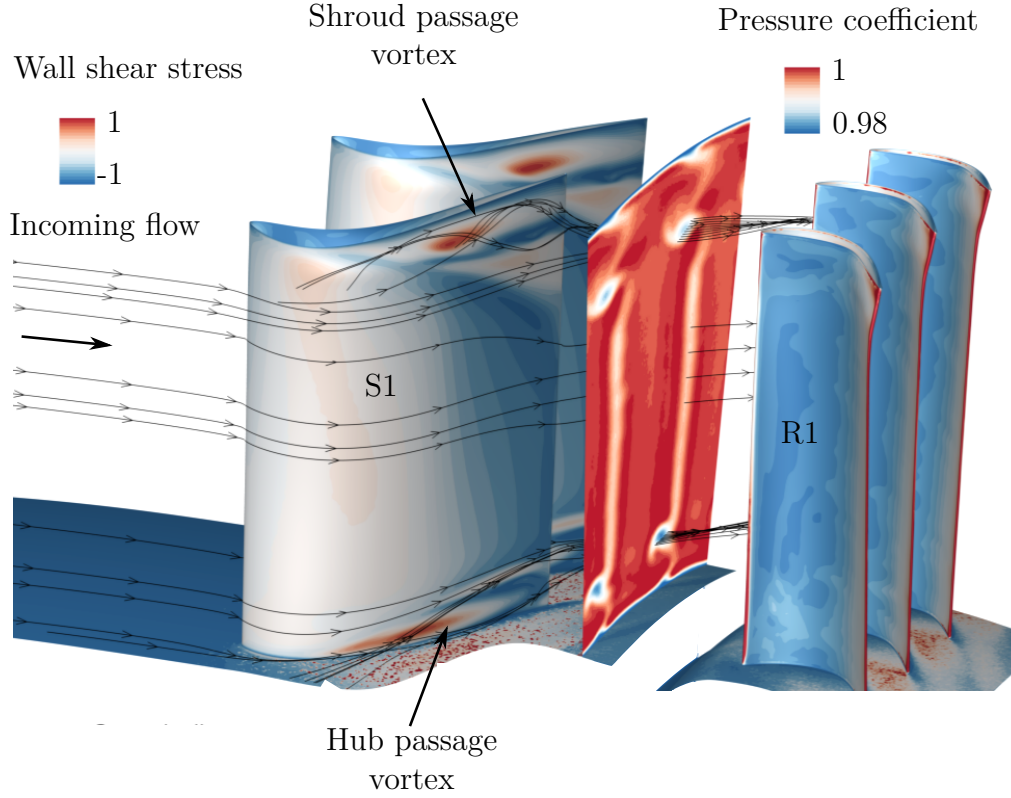


Figure 4.21: Wall friction on the surfaces of stator 1 and on an axial plane downstream of the blade with pressure coefficient. The shroud and cavities are omitted

side is provided for stator 1 and 2. Similarly to the linear cascade configuration, regions where secondary vortices travel along the blade suction side are shown to thicken the boundary layer profile predicted by the boundary layer module (see Sec. 3.2.2.3 p.98). The boundary layer profile on the blade suction side is provided at mid-span at different axial positions in conjunction with the Blasius profile of a laminar boundary layer for stator row 1 (see Fig. 4.22a) and 2 (see Fig. 4.22b). The boundary layer on the suction surface provides a similar profile compared to the theoretical Blasius laminar boundary layer profile. Based on the characteristic Reynolds number $Re \simeq 500\,000$ ($Re_\theta \simeq 470$) and no free stream turbulence, the boundary layer should remain laminar according to the works of Abu-Ghannam and Shaw [71] (p.53) that is confirmed on the stator 1 surface. On the stator 2 surface, despite an increased turbulence level due to stator 1 and rotor 1 wake, the boundary layer is shown to be laminar. Figure 4.24 provides the total pressure, whirl and ra-

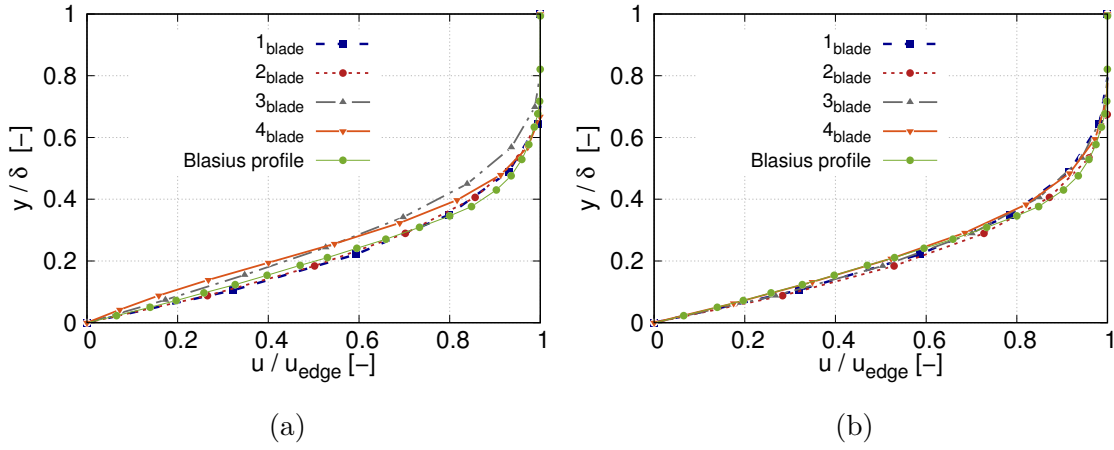


Figure 4.22: Boundary layer profile on the blade suction side at mid-span for stator row 1 (a) and 2 (b)

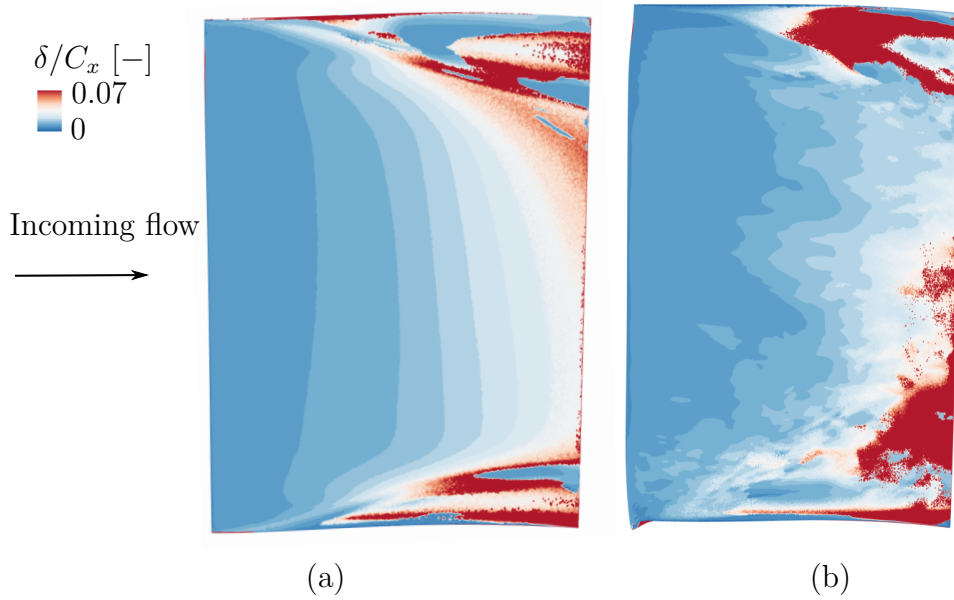


Figure 4.23: Suction side boundary layer thickness for stator 1 (a) and 2 (b)

dial angle downstream of the nozzle guide vane of the first stator row at MP02 plane for which experimental measurements are available. This same measurement plane is shown in Fig. 4.21 with the correspondence between low pressure coefficient region and streamlines emanating from the upstream nozzle guide vane. The pressure loss coefficient downstream of the blade employed in the linear cascade configuration is used in the current configuration in conjunction with Fig. 4.21 to correlate pressure loss coefficient and phenomena inducing the loss in total pressure. The regions of low pressure coefficient close to the hub and shroud can be attributed to the boundary layer over these surfaces. The central region of loss extending along the whole span can be related to the blade boundary layer and wake. The high pressure loss coefficient at 20% blade height at hub and shroud slightly shifted in the azimuthal direction from the wake region is attributed to hub and shroud passage vortices. The

position of strong pressure loss coefficient, corresponding to the passage vortex, is in good agreement with experiments both in terms of amplitude and position. The central region of intermediate pressure loss coefficient corresponds to the blade influence and the trailing shed vortices. At the shroud, a similar pressure loss peak can be observed corresponding to the shroud passage vortex. The azimuthal averaging on this axial plane is provided in Fig. 4.11a for MP02 plane. The whirl angle at the hub is also provided in the experiment. The region associated to the passage vortex induces overturning of the flow, the blade being design to provide a nominal whirl angle of -62.5° (the trigonometric convention is used). Under the region related to the passage vortex, a region of overturning is observed. This structure may be associated to corner vortex more prone to be influenced by cross pressure gradients near the wall. The secondary flow gives rise to a passage vortex in and downstream of the blade row. This overturning close to the endwall and underturning some distance away from the endwall is generally the most obvious evidence of a secondary flow from measurements downstream of a blade row. The numerical simulation underpredicts the azimuthal shift between these two structures. The turning of the flow decreases with radial distance in span because the blade is designed with decambering towards nozzle guide vane tip. Regarding radial angle downstream stator 1, the profile is relatively well predicted by the simulation with alternating negative, positive and negative structures close to the passage vortex. The positive radial angle in the region related to the passage vortex corresponds to the radial migration of the passage vortex. For the stator row 2, the development of secondary vortices

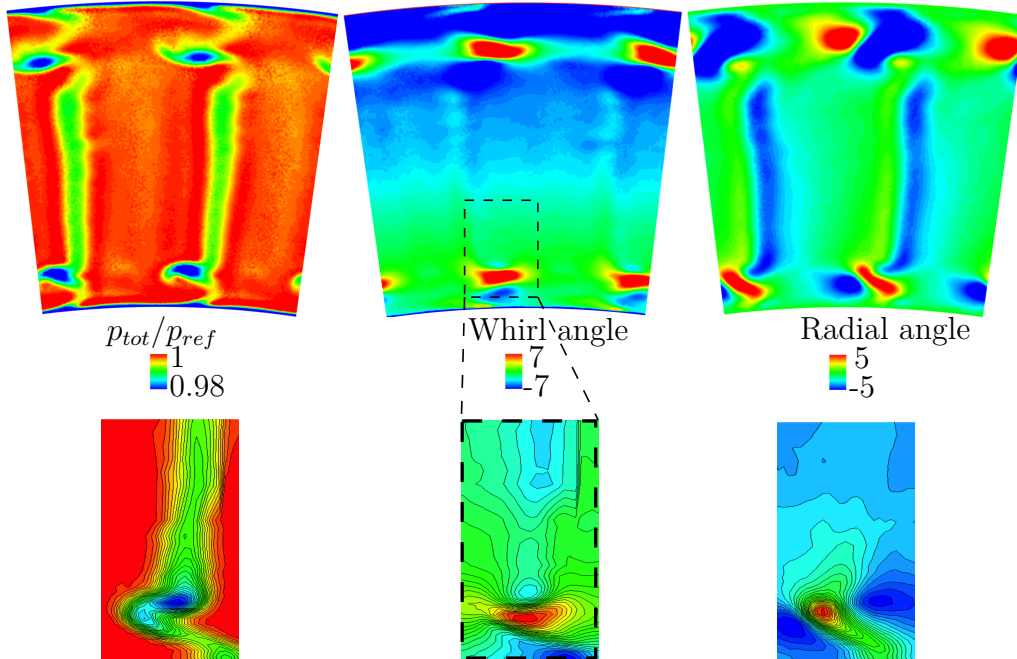


Figure 4.24: Total pressure, whirl and radial angle downstream of the first rotor row (compared to the nominal turning of the blade 64.6° and no radial angle) from simulation (top) and experiments (bottom) (MP02 plane)

is seen to be similar to the first stator row with hub and shroud passage vortices (see Fig. 4.25). However, several differences can be observed compared to the first

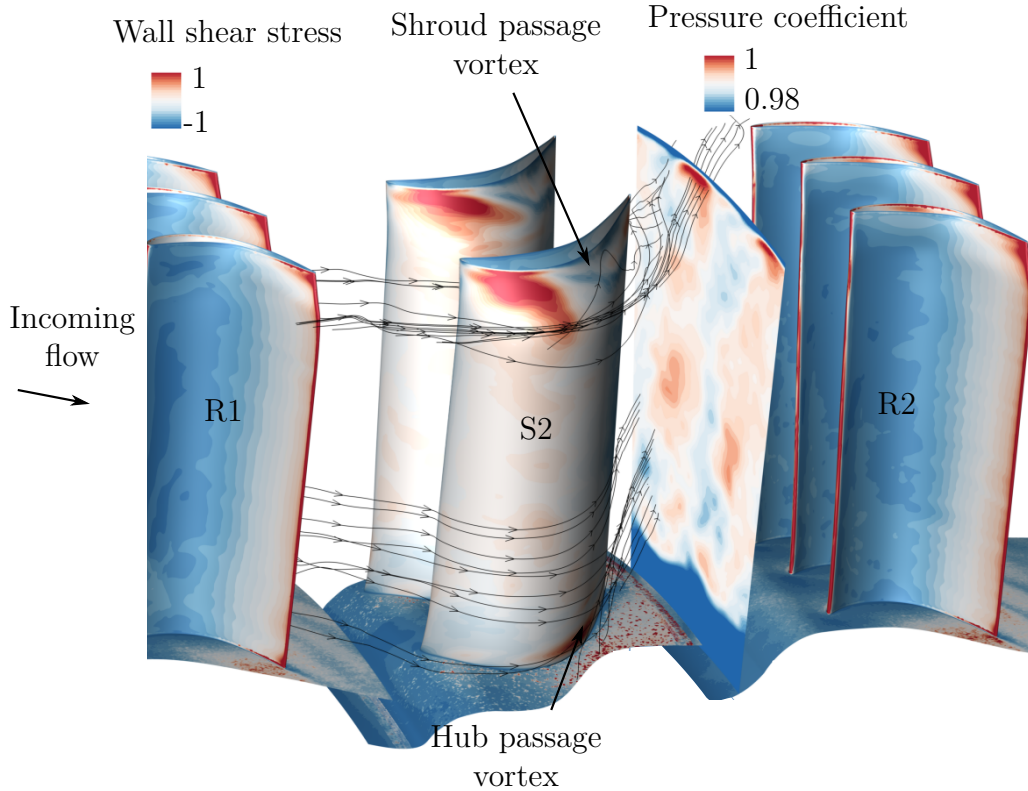


Figure 4.25: Wall friction on the surfaces of stator 2 and axial plane downstream of the blade with pressure coefficient. The casing, rotor shrouding and cavities are omitted

stator row. The incoming flow from rotor one is swirled. The wake and secondary vortices developed along the upstream rows are shown to influence the flow on the blade suction and pressure side. The boundary layer and pressure loss coefficient downstream of the blade more disrupted than in row 1 (see Fig. 4.23b). However, the boundary layer remains laminar despite upstream perturbations (see Fig. 4.22b).

4.4.2.2 The flow field in rotor rows

The first and second rotor row use an axis-symmetric full shroud. The shroud is composed of two inclined backward fins for the two rotor rows promoting a reduced tip leakage flow in the labyrinth between the shroud and casing compared to unshrouded blade and reduced associated loss. At the hub, the rim seal geometry is a simple axial overlapping with similar shape as the one introduced in the previous chapter on the linear cascade. Figure 4.40 shows streamlines and pressure loss coefficient downstream of rotor 1 blade. The development of secondary vortices in the rotor is shown to be similar to the stator rows since the shrouded rotor provides a similar configuration as a nozzle guide vane. The influence of hub/shroud boundary layers, wakes and secondary vortices can be identified in the pressure loss coefficient downstream blade similarly to stator rows. However, some differences in the pressure loss coefficient downstream of the blade can be drawn. Close to the shroud,

regions of high pressure can be observed related to the underturning of the blade close to the shroud. Similarly, a wide region of low total pressure is observed close to shroud. Figure 4.27 shows the corresponding streamlines emerging in this low pressure region that may be attributed to bypassed flow between the shroud with labyrinth and the casing. The flow entering this region separates along the teeth of the shroud labyrinth inducing recirculation zones downstream of the teeth, which is designed to reduce the flow in this region. The mass flow rate bypassed between the shroud and the casing was measured at 1.5% of main annulus flow rate for rotor 1 and 1.9% for rotor 2.

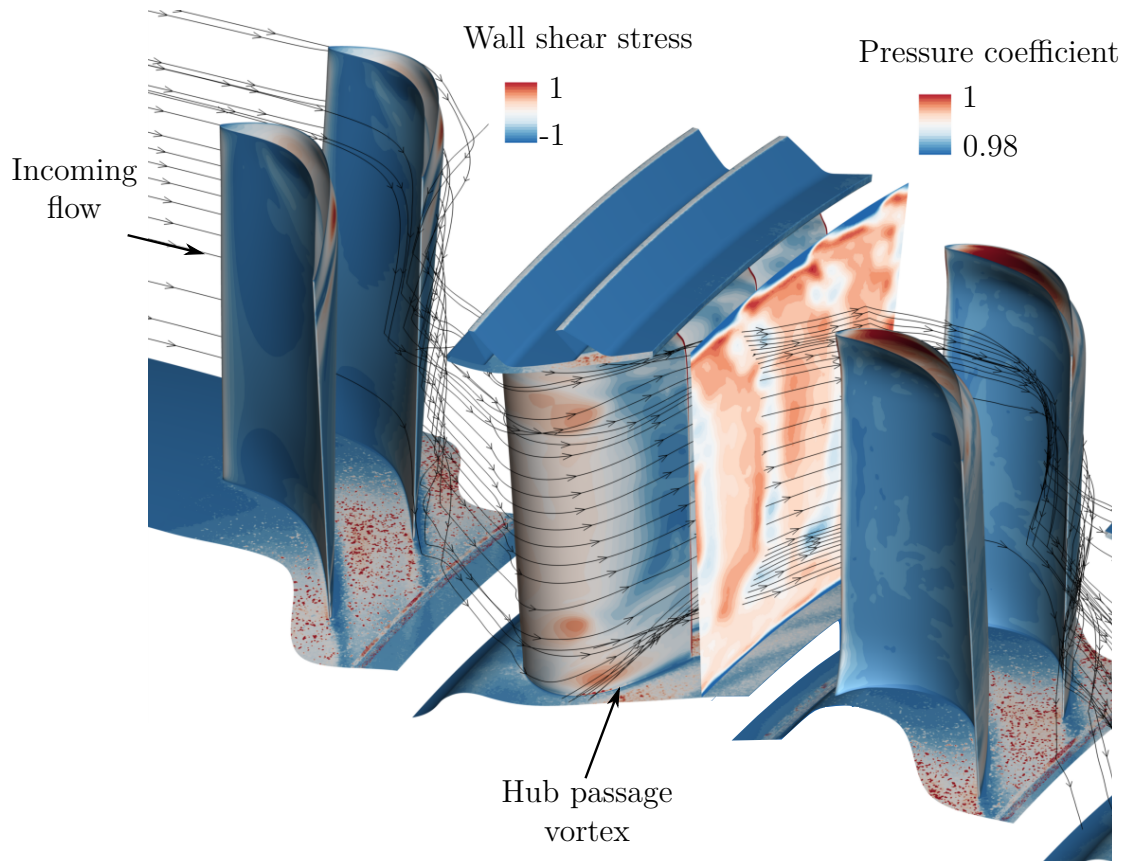


Figure 4.26: Wall friction on the surfaces of stator 1, rotor 1 and axial plane downstream of the blade with total pressure showing wakes and secondary flow influence on the pressure coefficient downstream of the blade. The casing, rotor shrouding and cavities are omitted

4.4.3 The flow at the interface between the cavity and the main annulus

Similarly to the linear cascade configuration (see Sec. 3.4.2 p.110), the main annulus flow close to hub is partially deflected downwards into the rim seal when facing a downstream blade leading edge. The potential effect can be observed close to the rim seal interface right corner with high stagnation pressure (see Fig. 4.29). The flow that

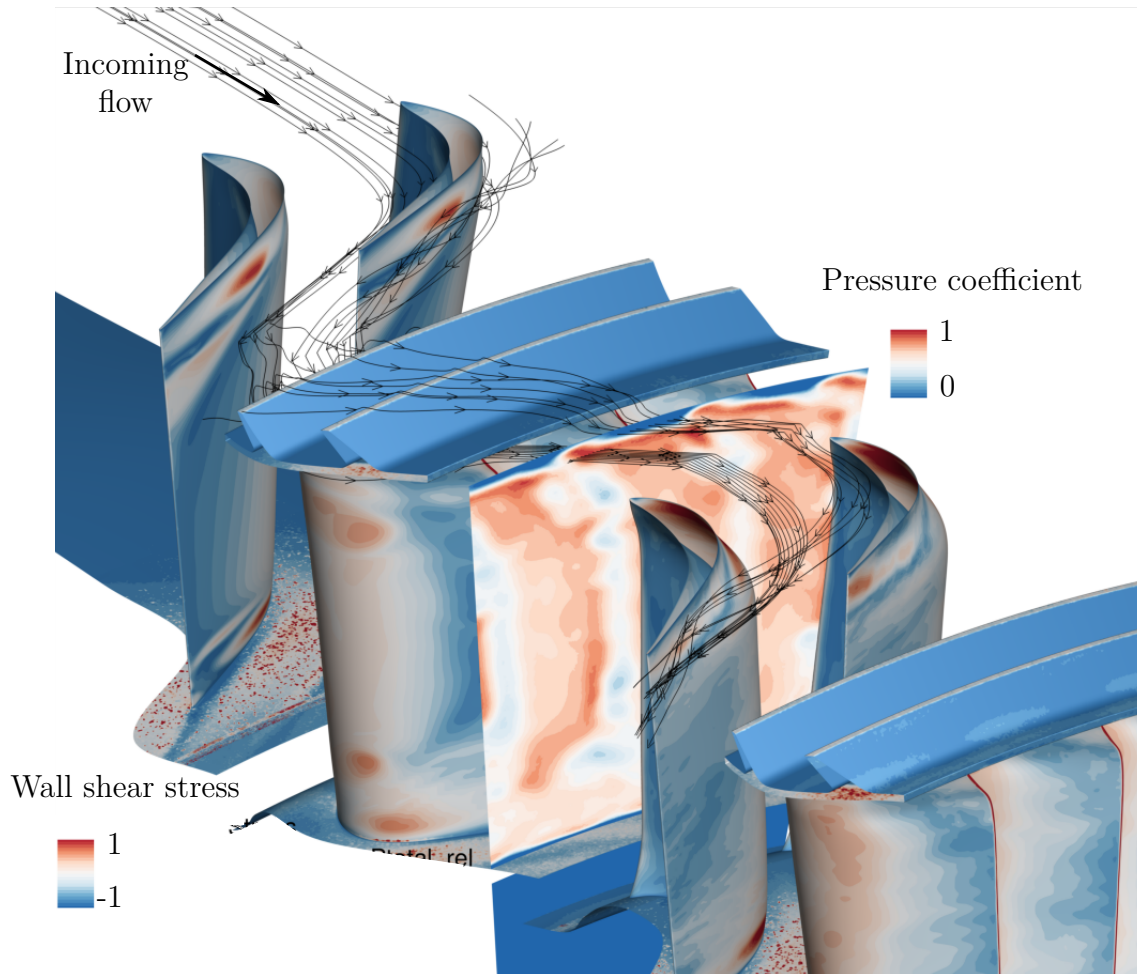


Figure 4.27: Wall friction on the surfaces of rotor 1 and axial plane downstream of the blade with total pressure showing wakes, secondary and bypassed flow influence on the pressure coefficient downstream of the blade. The casing and cavities are omitted

enters into the rim seal induces negative axial velocity at the bottom of the cavity, and is then expelled radially close to the rim seal left corner promoting the formation of a localized recirculation zone. The recirculation zone corresponds to this small amount of flow contained in the rim seal that is continuously entrained by the main annulus flow under a viscous process (see Fig. 4.28). As stated in Sec. 3.4.2 (p.110), the entrainment effect of the main annulus flow on the cavity/rim seal provides additional momentum to the flow at the interface that is progressively spread to the whole rim seal under viscous effect. When the axial and radial clearance (for axial overlapping geometries) are important (in the limit case, axial geometries with strong axial clearance) this additional momentum will be provided to the whole cavity meaning that the deficit of velocity will be higher at the interface for axial rim seal than for overlapping geometries. This difference was observed in the loss generation at the rim seal interface for axial and overlapping geometries where the loss induced were shown to be higher for axial rim seal than the overlapping geometries (see Sec. 3.7.3.3 p.156) due to higher tangential and axial velocity deficit. This effect

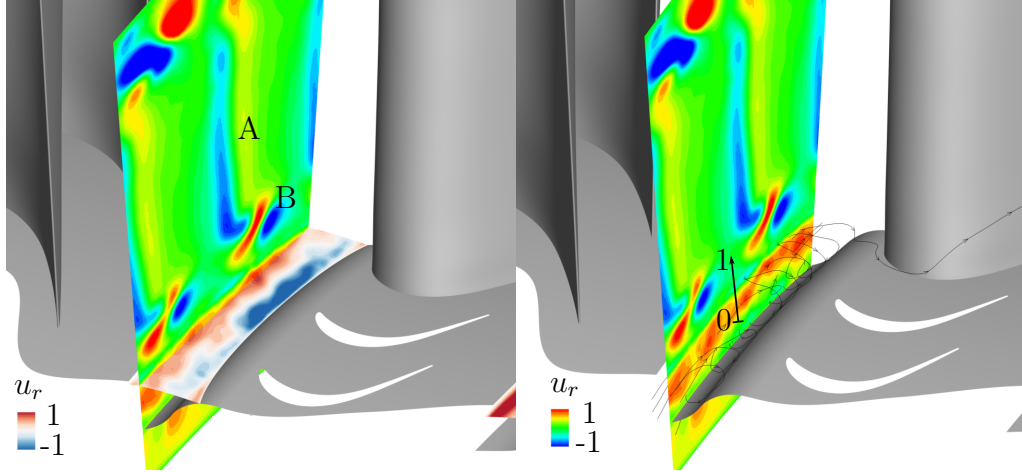


Figure 4.28: Radial velocity at the rim seal interface in a radial and axial plane (a). Streamlines showing the recirculation zone at rim seal interface S1-R1. A: wake region, B: passage vortex. Rotor blade 1 and 2 have been omitted

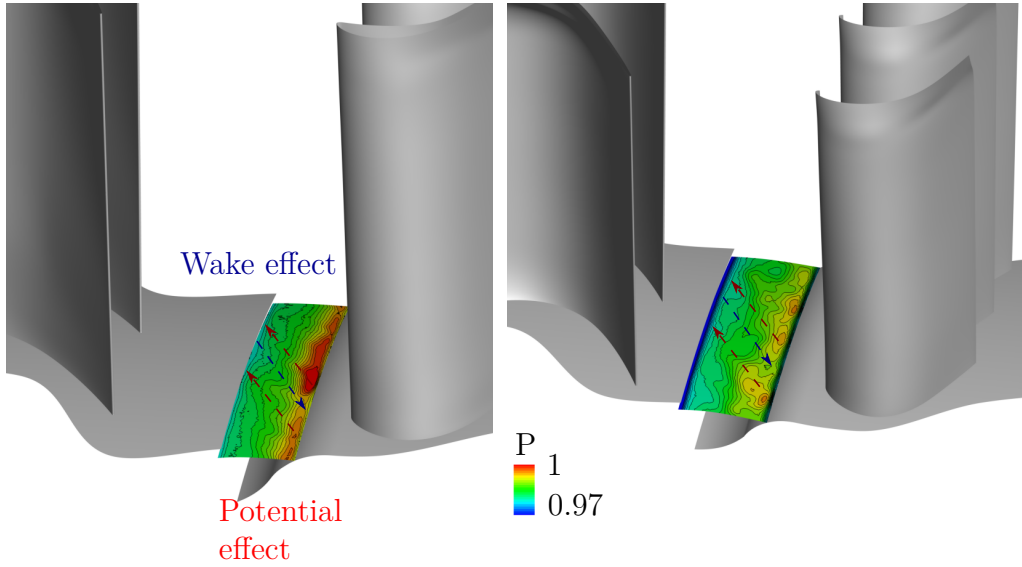


Figure 4.29: Pressure distribution at the rim seal interface 1 (S1-R1) and 3 (S2-R2)

is important when the flow into rim seal is partially isolated from the flow into cavity i.e. when the radial and axial clearance of the rim seal are low. The rotating disc in the cavity 1, 2 and 3 induce a central core with a rigid body rotation. The entrainment velocity corresponds to a portion of the rotating velocity (see Fig. 4.16b, 4.17b and 4.18b). Therefore, compared to the linear cascade configuration studied in Chap. 3, the flow in the cavity and the rim seal interface is shown to have reduced azimuthal velocity deficit compared to main annulus. Figure 4.30 shows the radial evolution at the rim seal of axial and tangential velocity profiles, temperature and total pressure at the beginning ($x/C_x = 6.3$), middle ($x/C_x = 6.4$) and end of the cavity ($x/C_x = 6.5$), the radial extension between 0 and 1 is provided in Fig. 4.28b. As stated, the rim seal used for the current rotating configuration is similar in terms of geometry to the single overlapping geometry used for the linear cascade, thus it

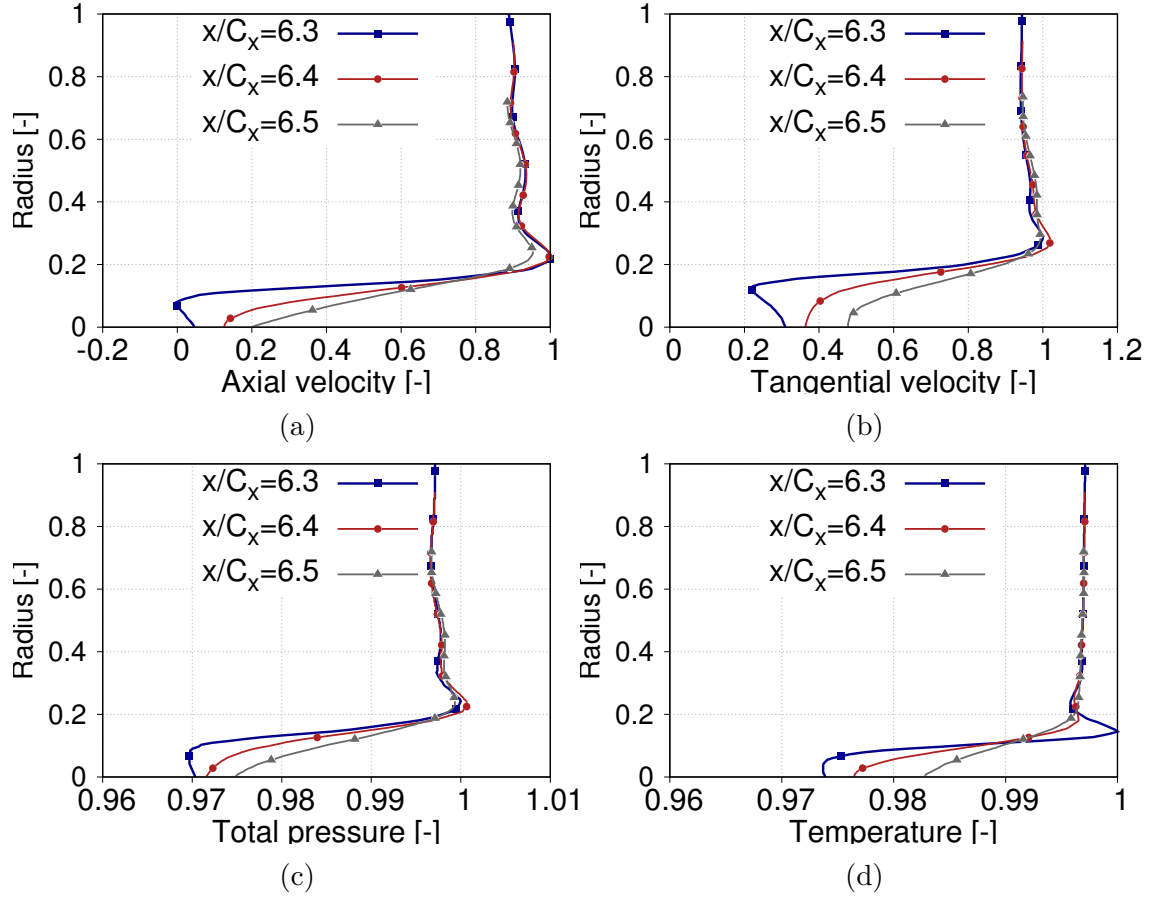


Figure 4.30: Radial evolution at the rim seal interface at the beginning ($x/C_x = 6.3$), middle ($x/C_x = 6.4$) and end of the cavity ($x/C_x = 6.5$) for axial (a), azimuthal (b), total pressure (c) and static temperature (d)

is possible to look at the influence of the rotation and especially the cavity core flow compared to the static configuration. The adaptation between tangential, axial velocity, total pressure and temperature at the rim seal interface is performed over a short layer at radius close to the rim seal left corner ($R = 0.15$ in Fig. 4.30) where hub boundary layer from stator platform separates. The thickness over which the field at the cavity adapts to the mean flow field is roughly 1 cm. At the rim seal left corner, the axial velocity is almost zero with the entrainment effect into cavity providing only residual axial velocity because the pumping is a low magnitude effect (see Fig. 4.30a). The tangential velocity deficit is shown to be lower compared to the linear cascade configuration. This is due to the entrainment effect of the flow into the cavity and at rim seal interface that corresponds to an entrainment of 0.3 the tangential velocity in the main annulus at the rim seal left corner (see Fig. 4.30b). From the left corner ($x/C_x = 6.3$) to the right corner of the rim seal ($x/C_x = 6.5$), velocity pressure and temperature deficits of the rim seal flow are reduced due to the mixing process into the rim seal that progressively homogenize the rim seal flow along the axial direction. The temperature of the purge flow supplied at the bottom of the cavity increases progressively along the rim seal (see Fig 4.30d) to accommodate the cavity flow at a temperature lower than in the main annulus one.

In the main annulus, the additional effects contributing to the ingestion and blowing process at rim seal interface is the wake travelling above the rim seal interface. The upstream wakes and secondary vortices induce locally along their trajectory a lower pressure close to the hub where some rim seal flow can blow into the main annulus (see blue arrows in Fig. 4.29). Conversely to the linear cascade where the rim seal flow emerged close to the rim seal right corner at the center of the passage, the rim seal flow can blow into the main annulus upstream. The wake and potential effects are two phenomena contributing to the asymmetric and unsteady purge flow blowing at the rim seal interface. The flow field at the rim seal interface remains however complex and these two phenomena alone appear not sufficient to fully explain the current ingestion/blowing distribution. In particular, it is difficult to ascertain the influence of the flow field in the cavity on the blowing process. It remains that the wakes promote a purge flow blowing slightly upstream the rim seal right corner compared to the linear cascade without upstream wakes. For the Reynolds number found in the main annulus and in the cavity, the externally induced ingress/egress due to the flow field imposed into main annulus (see Sec. 1.2.1 p.10) should be predominant, which seems to be the case in the current configuration.

The flow in the cavities of the two-stage turbine configurations is influenced by the rotating disc that holds blades. The rotating disc promotes a radially expelled flow on the rotor side and radially inwards flow on the stator side with a rotating central core flow region separating the stator and rotor side of all three cavities. The separated and possibly turbulent nature of the flow for the considered cavity Reynolds number is coherent with the literature, the laminar flow over infinite disc solution also providing a good match compared to current configuration for the velocity profiles in the cavity. In the main annulus, the two-stage annular turbine shows similar secondary vortices development process along the different blade rows, as expected from the linear cascade. Since the rotor rows are shrouded, secondary vortices similar to the nozzle guide vanes can be observed. At the rim seal interface, the flow entrained tangentially by the cavity accommodates with the main annulus flow over a short layer close to the rim seal left corner. The main annulus flow is ingested close to rim seal right corner due to potential effect of the downstream blades. This recirculated flow at the bottom of the cavity is expelled and blows into the main annulus in regions where the upstream row wakes travel.

4.5 Application of exergy formulation to track losses

Exergy formulation described in Sec. 2.1.3 is used in this section to highlight/extract regions of loss production. The general equation for exergy proposed in eq.(2.50) can be written under steady flow condition as

$$\oint (\rho\chi) u_j n_j dA_{IO} = P_{shaft} + \chi_q + \Phi_{\nabla u} + \Phi_{\nabla T} + \Phi_{sw}. \quad (4.3)$$

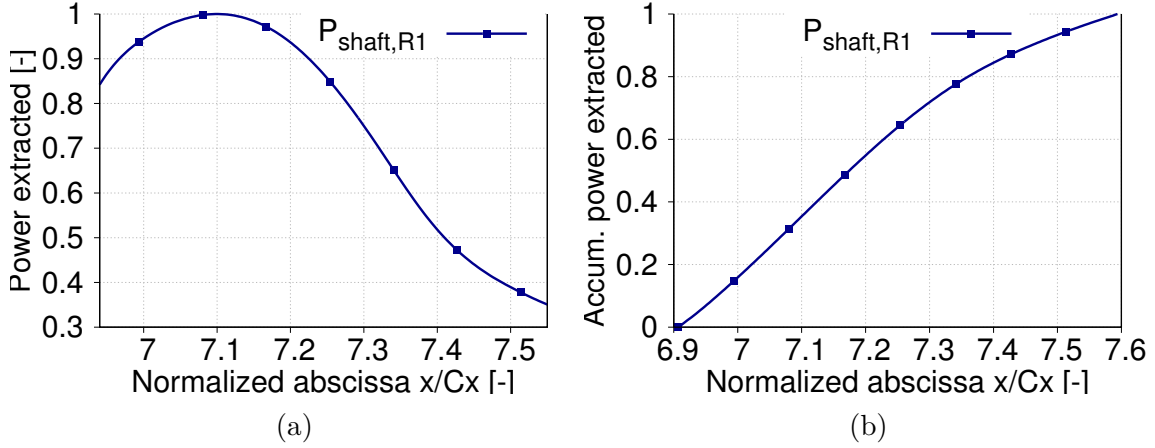


Figure 4.31: Extracted power on first rotor along blade (a) and cumulated power (b), the first rotor blade extends from $x/C_x = 6.9$ to 7.6

The current configuration is low Mach meaning that no shocks are to be expected, thus $\Phi_{sw} = 0$.

4.5.1 The work extracted by rotor rows

Similarly to the linear cascade configuration no work is transferred with the fluid at the first and second stator leading to $P_{shaft} = 0$. However, along the two rotor rows, some work is extracted meaning that $P_{shaft} < 0$ in the regions of rotor rows that is extracted from the total enthalpy of the flow. No heat is transferred at the border of the domain because of adiabatic wall conditions and there is no heat from a combustion process. Thus, the exergy variation between the inlet and outlet of the domain can only decrease due to $\Phi_{\nabla u}$, $\Phi_{\nabla T}$ terms (anergy production) and the work extracted by the shaft of the rotor rows. The power extracted on the shaft proposed in Sec. 2.1.3 (p.35) is written as $P_{shaft} = -\oint ((p - p_0)u_{w,j}n_j - (\tau_{ij}u_{w,j})n_j) dA_{MW}$. The pressure term is related to the local wall-normal contribution while the shear term corresponds to the local tangential one. Integrating pressure and shear forces on the surface of the blade and projecting according to the axial main axis provides the axial contributions that is absorbed by the bearings of the shaft. This contribution does not generate any work because orthogonal to the velocity of the blade. Conversely, the projection of pressure and shear forces in the azimuthal direction and multiplied by the velocity of the blade provides the work extracted by the shaft P_{shaft} , these two terms being collinear. Figure 4.31 and 4.32 show the extracted shaft power for rotor 1 and 2 along the blade (left figures) as well as the cumulated extracted shaft power (right figures). It is reminded that rotor 1 and 2 extend respectively from $x/C_x = 6.9$ to 7.6 and $x/C_x = 10.35$ to 11.1 .

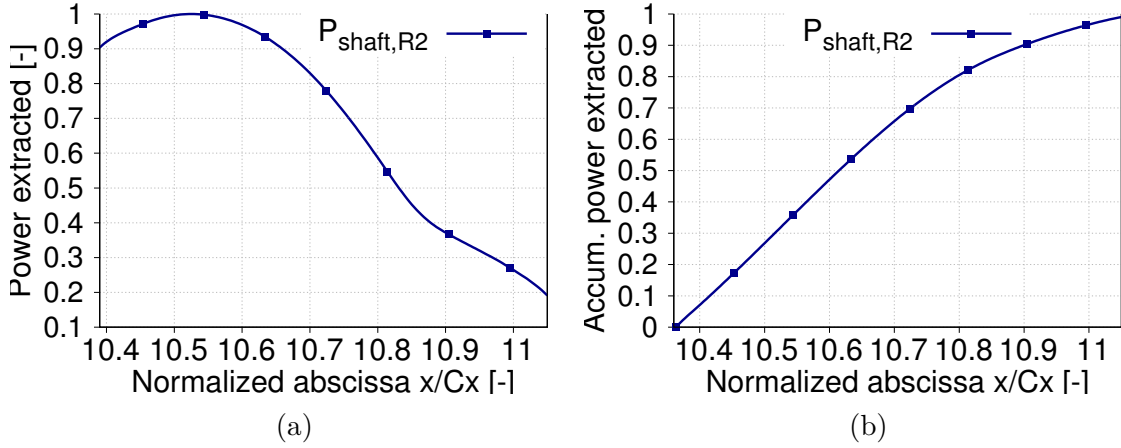


Figure 4.32: Extracted power on second rotor along blade (a) and cumulated power (b), the second rotor blade extends from $x/C_x = 10.35$ to 11.1

4.5.2 Viscous and thermal anergy production along the domain

4.5.2.1 General trend in the simulation domain

Similarly to the analysis conducted for the linear cascade in Sec. 3.7.1 (p.130), the viscous and thermal anergy production along the simulation domain can be obtained by integrating the viscous term from inlet to a given axial coordinate point x (main axis) of the domain. In addition, the simulation domain can be split in axial subdomains. When the characteristic axial length of the subdomain dx tends towards zero, integrating the viscous term provides the anergy production at considered point x . Figure 4.33 provides the total viscous anergy production in the domain (resolved and subgrid scale model contribution) and the subgrid scale model contribution only. The stator row 1 extends from $x/C_x = 4.7$ to $x/C_x = 5.9$, rotor 1 from $x/C_x = 6.9$ to 7.6, stator 2 from $x/C_x = 8.3$ to 9.4 and rotor 2 from $x/C_x = 10.35$ to 11.1. Similarly to the linear cascade configuration in Sec 3.7.4 (p.160), the contributions of the subgrid scale model providing an equivalent turbulent viscosity can be explicitly obtained from the LES simulation. The subgrid scale model in the current configuration is also shown to be triggered close to the trailing edge of the different rows. This may be due to the insufficiently resolved mesh in wake regions and strong contribution of turbulence in the wake. However, conversely to linear cascade configuration, the subgrid scale model is shown to be triggered along the different blade rows with non negligible contributions. Despite automatic mesh refinement, this observation is alleged to indicate that the mesh is not refined enough to properly resolved all scales of turbulence. A simple assessment of the number of mesh points used for the linear cascade shows that 60 million cells per blade were used in the linear cascade while in the current simulation around 350 million cells for ten blade ($\simeq 35$ million cells per blade). In the T106C configuration studied by Pichler et al. [124], which is a symmetric low pressure turbine blade profile, nearly 500 million cells were used to properly resolved the turbulence spectrum which is much higher than the 35 million cells per blade in current configuration meaning

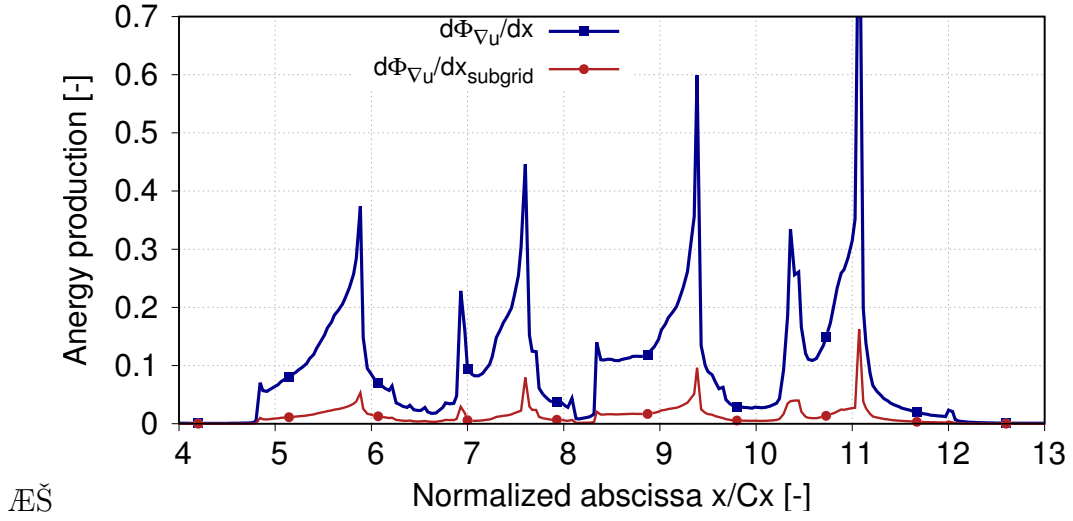


Figure 4.33: Evolution of total viscous anergy production (resolved+subgrid) along the domain including subgrid scale model contribution

that some care has to be taken regarding the results in the current configuration. Also, the spatio-temporal resolution was 4^{th} order both in time and space compared to the current 2^{nd} order accurate approach. In addition, in the AVBP code, artificial viscosity is often added to stabilize the numerical scheme. Depending on a sensor that detects node-to-node non-linear behaviour of pressure events, additional viscosity can be triggered locally. As described in App. B Sec. B.3.1, the spatio-temporal discretization induces additional equivalent viscosity to the fluid to which we have generally no access but which is contained in the total contribution shown in Fig. 4.33. In current simulation, no access is given to this numerical viscosity contribution except the contribution to stabilize the convective scheme. The added artificial viscosity is applied according to the sensor model proposed by Colin [153]. The corresponding artificial viscosity contribution to anergy is provided in Fig. 4.31. Similarly to the subgrid scale model contribution, the artificial viscosity is not negligible, as it is triggered in regions related to the different rows and at the trailing edge similarly to the subgrid scale model contribution. Based on this general view of anergy production in the simulation domain, peaks of viscous anergy production are observed at location $x/C_x = 6.2, 8.1, 9.6$ and 12 . These locations correspond to the overlapping regions where informations are exchanged between static and rotating instance of AVBP. The data exchange between the two instances is performed using a third order interpolation in the overlapping regions that are not coincident. This interpolation induces local additional viscosity to the fluid. A general observation shows that the viscous anergy production is low upstream stator one ($x/C_x = 4.7$) and around $1.5 C_x$ downstream rotor 2 ($x/C_x = 12.5$). The main regions of viscous anergy production correspond to the different row domains and downstream of these rows in wake regions. The viscous anergy production increases in the different rows. The anergy production for the different rows has a similar trend compared to the linear cascade configuration with a sharp increase at the leading edge, continuous increase along the blade until the trailing edge before to decay downstream. For the thermal entropy production, the trend is similar to the linear cascade con-

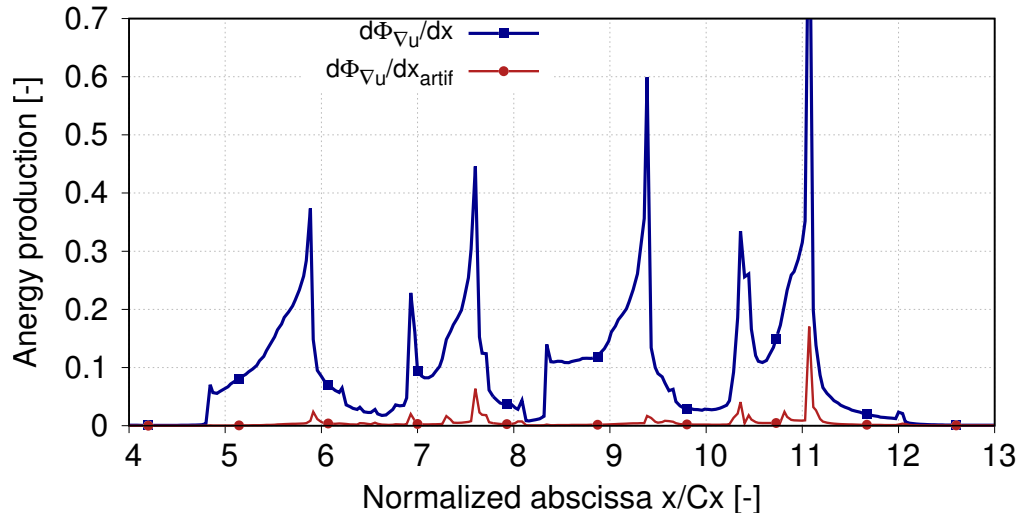


Figure 4.34: Evolution of total energy production (resolved+subgrid) along the domain including the artificial contribution

figuration with strong entropy production at the different rim seal interfaces and a decrease in the passage of the downstream row with an influence limited to the blade row extension (see Fig. 4.35). A similar feeding process of the secondary flows developing in the passage by the cavity flow is observed with the cold flow being entrained by the passage vortex (see Fig. 4.36).

4.5.2.2 The analysis for the different rows based on a directional analysis

Obtaining the boundary layer domains related to the hub, shroud and the different blades is difficult to performed in the current configuration because the number of grid points is important. Indeed, in the process of three-dimensional boundary layer extraction, all the grid points of the simulation domain must be checked to evaluate whether they are in or out of the boundary layer of a given surface. Therefore, in the current subsection the analysis is not conducted by splitting the whole domain according to the different contributions (hub, shroud, blade boundary layer and remaining domain) but based on the gradients direction over which anergy is produced. Indeed, based on the linear cascade study, the different mechanisms of loss were shown to occur in directions that are generally independent. Similarly to the linear cascade configuration, the entropy production is shown for each contribution and including the total contribution to give the relative magnitude of the different contributions.

Figure 4.37 shows the entropy production at the inlet and outlet of the domain at one axial chord downstream of rotor 2 blade trailing edge including wall normal contributions. The entropy production at the inlet and outlet of the domain one axial chord downstream of the rotor 2 blade is due to the hub and shroud wall-normal contributions related to the boundary layers over these surfaces (see Fig. 4.39 for an iso-contour of viscous entropy restricted to hub/shroud wall-normal contribution du_s/dr). The levels of entropy production between boundary layers at the inlet and outlet of the domain have comparable magnitudes. In the linear

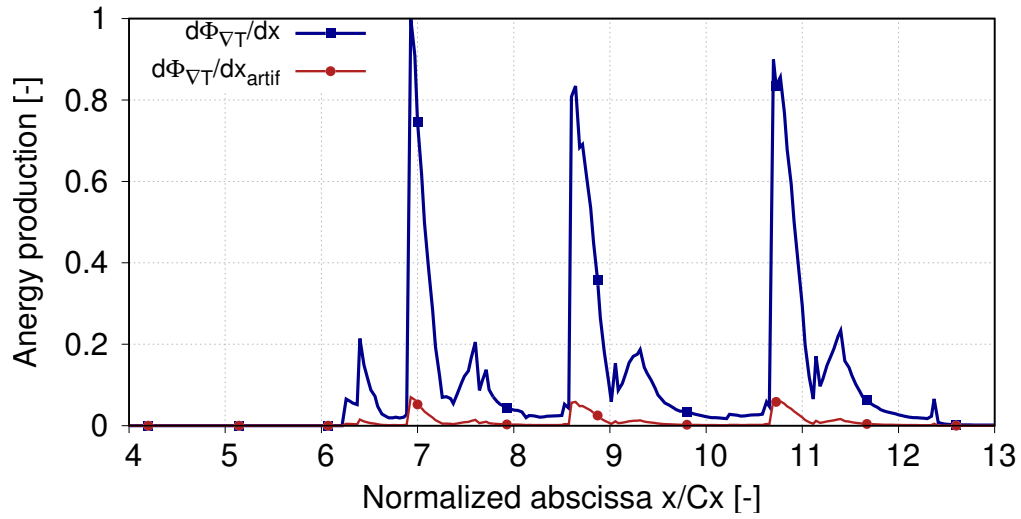


Figure 4.35: Evolution of total thermal energy production (resolved+subgrid) along the domain including subgrid scale model contribution

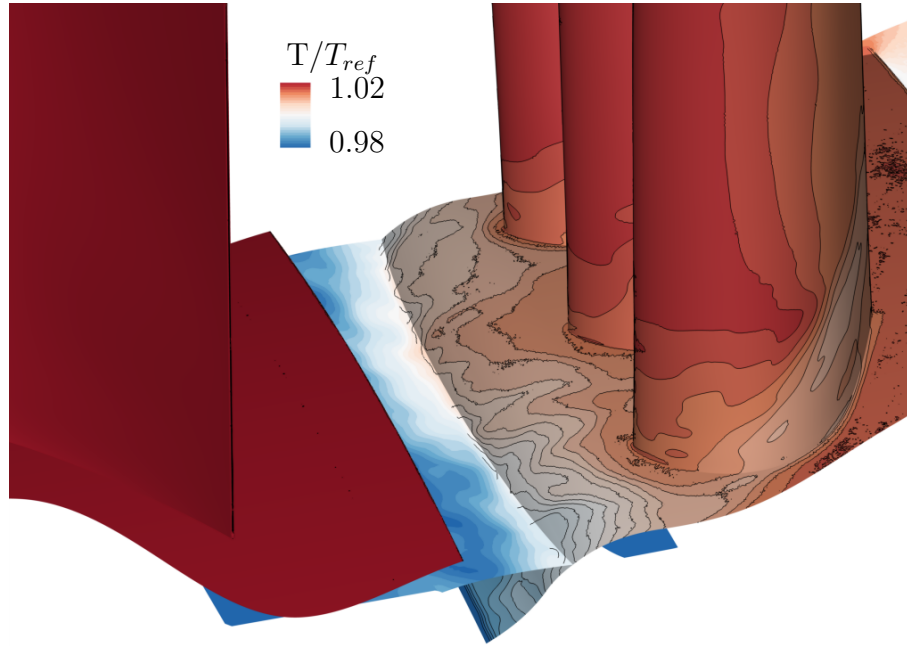


Figure 4.36: Temperature at the rim seal interface, along the hub and rotor 1 blade with migrating cavity flow on blade suction side

cascade configuration, the entropy production related to the boundary layers over hub and shroud downstream of the nozzle guide vane showed entropy production levels five times higher compared to the inlet due to accelerated flow in the passage (see Sec.3.7.1.2.1 p.136). In the current configuration, the work extracted by the second rotor that slow down the flow induces lower losses to the hub and the shroud boundary layer at the outlet. The entropy production along the domain due to the hub and shroud boundary layer generates wall-normal gradients (see Fig. 4.38) and similar magnitude to the linear cascade for the different rows with a slightly higher contribution along the passages of rotor rows ($x/C_x = 6.9$ to 7.6 and $x/C_x = 10.35$

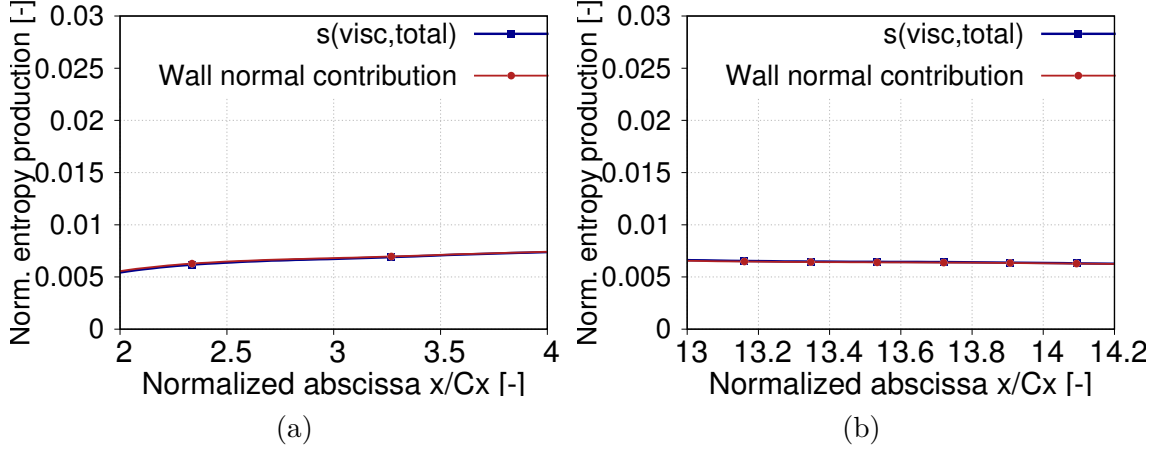


Figure 4.37: Total entropy production at the inlet (a) and outlet (b) of the domain one axial chord downstream of rotor 2 blade trailing edge including wall normal contributions

to 11.1) than stator rows ($x/C_x = 4.7$ to 5.9 and $x/C_x = 8.3$ to 9.4). In addition, the cross hub/shroud wall normal contribution (du_c/dr) increases in the passage due to skewed boundary layer in the azimuthal direction of the different rows (see Fig. 4.41 and 4.39b). The contribution of blade wall-normal gradients (du_s/dc) that were attributed to the development of a boundary layer over the nozzle guide vane in the linear cascade configuration (see Sec. 3.7.1.3.1 p.147) is shown for current annular configuration in Fig. 4.42. The contribution of the blade boundary layer is important in the different rows, around 40% in the passage. This contribution increases at the different blade trailing edge, and correspond to the vortex shedding process slightly upstream of the trailing edge (see Fig. 2.14b and Fig. 4.39). The contribution of du_r/dc velocity gradients that was attributed to blockage effect of passage vortex in the linear cascade configuration (see Sec. 3.7.1.3.2 p.147) is also observed in the current configuration (see Fig. 4.44). The higher contribution in the rotor rows may be attributed to stronger cross passage pressure gradients and higher secondary kinetic energy to develop secondary vortices in the passage (see Fig. 4.45). Downstream of the different blade, the total viscous entropy production does not tends towards zero (i.e no entropy production). This is due to several processes: the shear layer at the rim seal interface that induces stream and cross velocity gradients in the radial direction (see Fig. 4.38 and 4.45) similarly to the loss observed at the rim seal interface of upstream blades in the linear cascade (see Sec. 3.7.1.3.2 p.147). The vortices downstream of the rows show an exponential decay. The first mechanism of vortex decay downstream of the blade is the trailing shed vortex process where the loss are mainly due to a velocity gap between pressure and suction side flows. The velocity gap in the streamwise direction induces vortices aligned with the radial direction (see Fig. 4.43 and Fig. 3.30b for the linear cascade configuration) and the radial velocity difference induces vortices aligned with stream velocity (see sketch in Fig. 2.14b and Fig. 4.41 for related loss). Losses are also induced by the dissipation of the passage vortex. These structures are not fully dissipated before reaching downstream rows. This interaction process between upstream secondary vortices and downstream rows can be seen in Fig. 4.46. The secondary vortices are

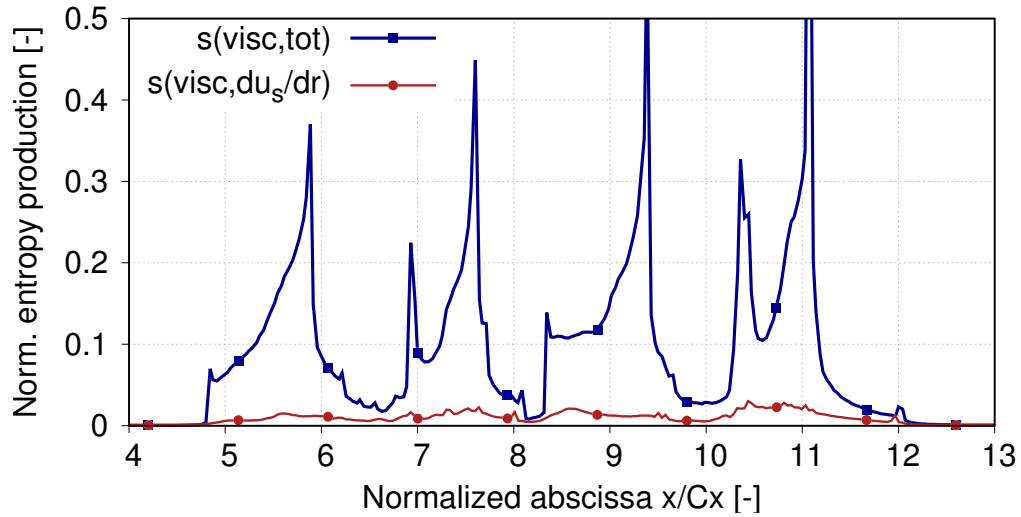


Figure 4.38: Evolution of the total viscous entropy production along the simulation and restricted to the hub/shroud wall normal contribution (du_s/dr)

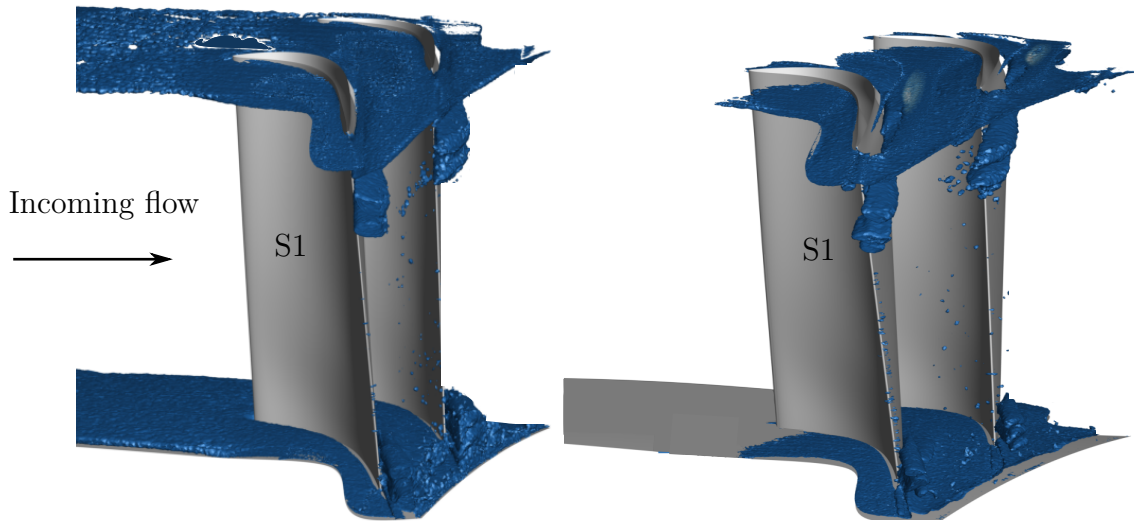


Figure 4.39: Iso-contour of entropy production along first stator row for the contribution du_s/dr (left) and du_c/dr (right)

chopped by the blade leading edge and induce additional friction on the blade suction side. Upstream secondary vortices interact with developing secondary structures of the rotor. Figure 4.47 shows the pressure loss coefficient downstream of the first rotor row. The shrouding at the tip of the blade provides a similar configuration as static rows where an horse shoe vortex process and passage vortex can develop in the passage. The hub passage vortex and equivalent shroud passage vortex can be observed with regions of lower total pressure. In addition, two additional peak can be observed. When upstream passage vortex is chopped by the rotor leading edge apart of this structure migrates radially upwards while another part migrates downwards. It can be discussed that these two structures impact the pressure loss downstream of the blade.

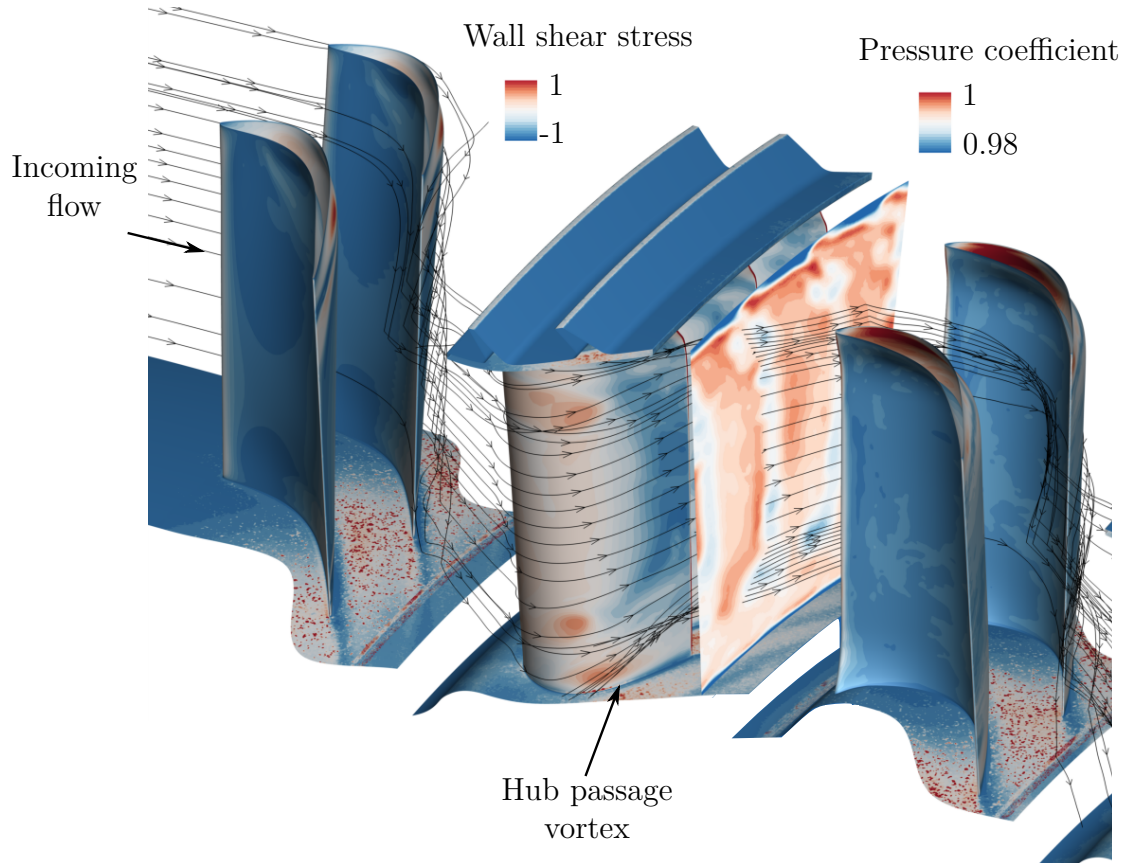


Figure 4.40: Wall friction on the surfaces of stator one rotor one and axial plane downstream blade with total pressure showing wakes and secondary flow influence on pressure coefficient downstream blade. The shroud is omitted

4.5.3 Evolution of exergy in the simulation domain

Since the contributions of shaft, viscous and thermal irreversibility have been obtained along the domain, it is possible to extract the decrease of exergy (normalized to one at the inlet of the domain) due to these different contributions. Figure 4.48a provides the decrease of exergy restricted to the contribution of viscous anergy, Fig. 4.48b due to the thermal anergy and Fig. 4.49a due to the work extracted by the shaft. This last figure makes possible to confirm in the numerical simulation that around 45% of the work extracted by the shaft is performed by rotor 1 ($x/C_x = 6.9$ to 7.6) and 55% by rotor 2 ($x/C_x = 10.35$ to 11.1). Finally, all these contributions can be summed to obtain the exergy decrease along the domain due to all of these contributions (see Fig. 4.49b).

The exergy analysis performed on the two-stage annular configuration is characterized by a transfer of energy from the flow to the shaft along the two rotor rows, decreasing total enthalpy of the flow. Along the domain, the decrease of exergy is also associated with entropy production due to viscous and thermal mixing. The viscous entropy production is originates from

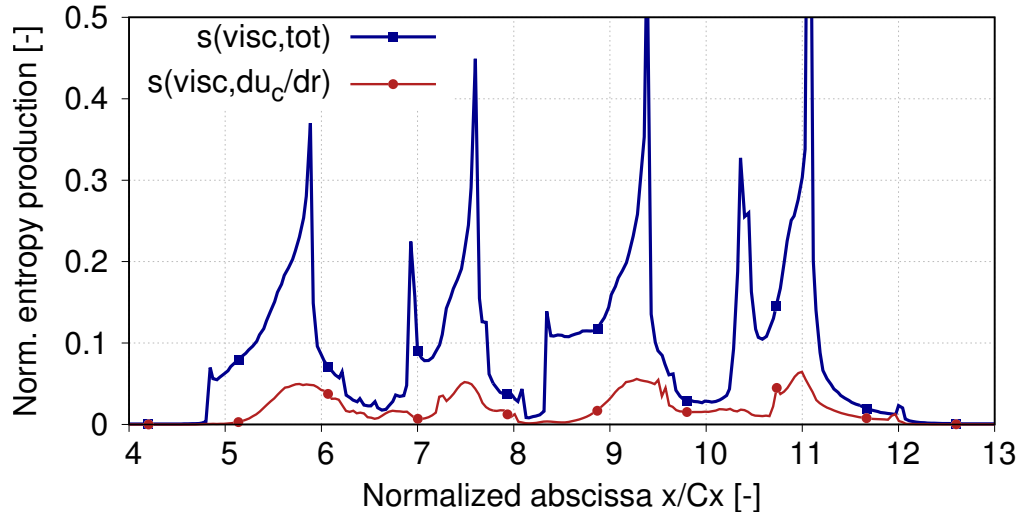


Figure 4.41: Evolution of the total viscous entropy production along the simulation and restricted to the hub/shroud wall normal contribution (du_c/dr)

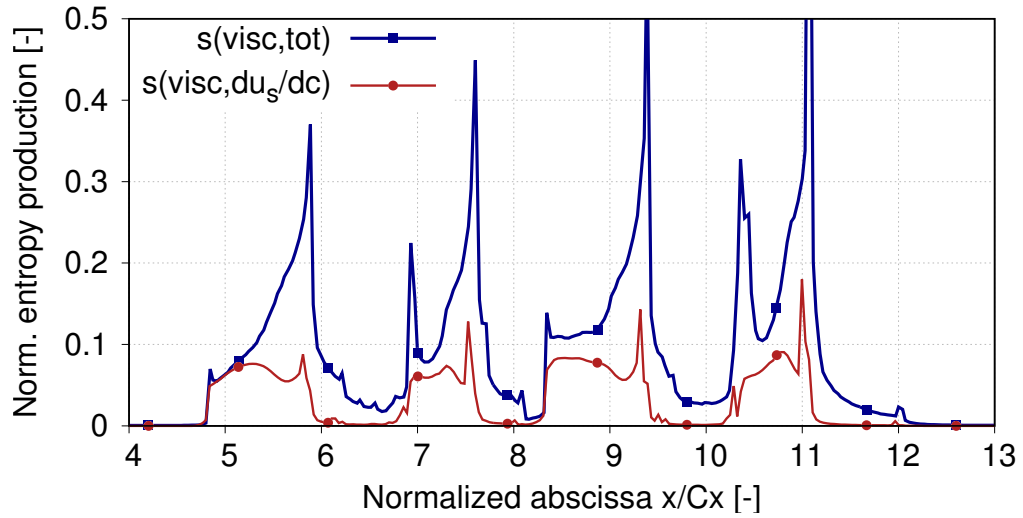


Figure 4.42: Total entropy production along the domain and blade wall normal contribution (du_s/dc)

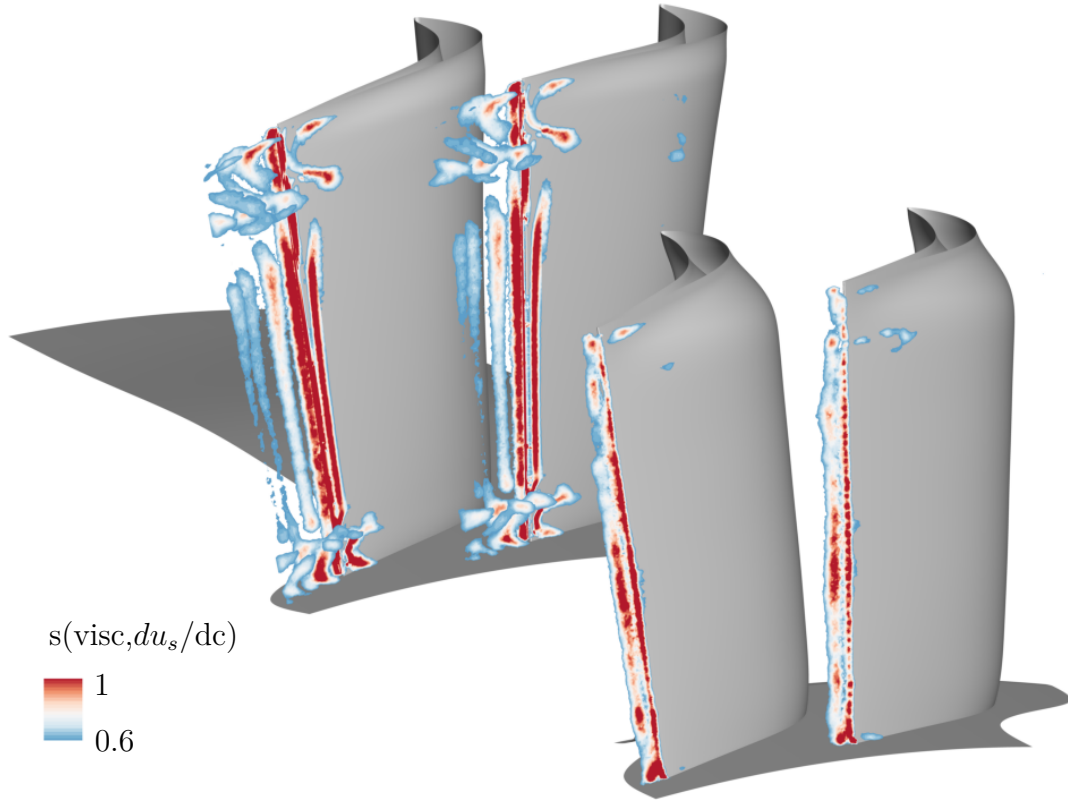


Figure 4.43: Axial cuts at the trailing edge colored by viscous entropy production related to du_s/dc gradient for stator 1 and 2

to wall-normal velocity gradients along hub, shroud and blade boundary layers of the different rows. Secondary vortices developing in the passage induce entropy production due to the blockage effect of passage vortex, trailing shed vortex process due to the mixing of pressure and suction side flow and overturning/overturning flow. Downstream of the different rows, these structures decay, inducing additional entropy production. At the rim seal interface, the entropy production is mainly due to velocity gradients following the radial direction associated to the shear layer at the rim seal interface.

The two-stage annular configuration provides more realistic and additional insights in the interaction process of the purge flow with the main annulus flow compared to the linear cascade configuration introduced in Chap. 3.

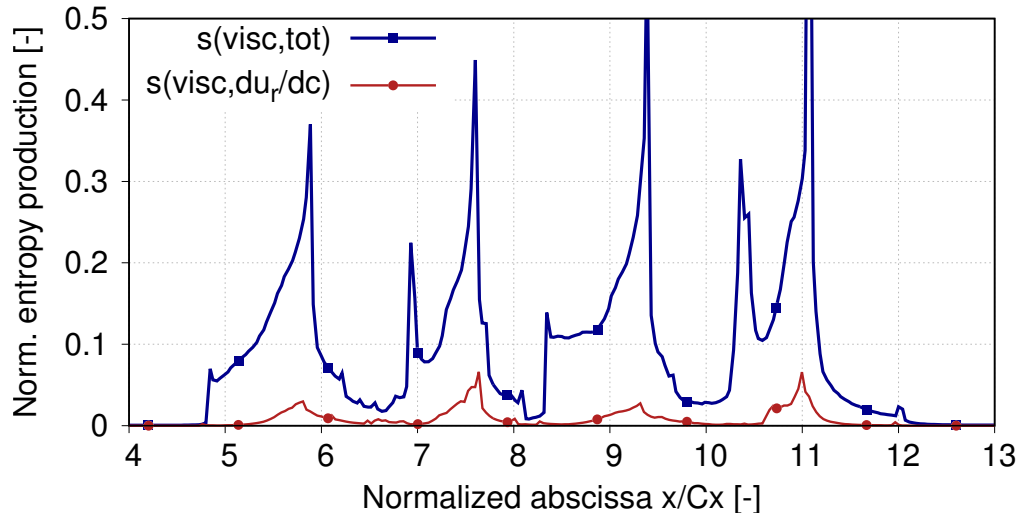


Figure 4.44: Total entropy production along the domain and entropy production related to du_r/dc gradients

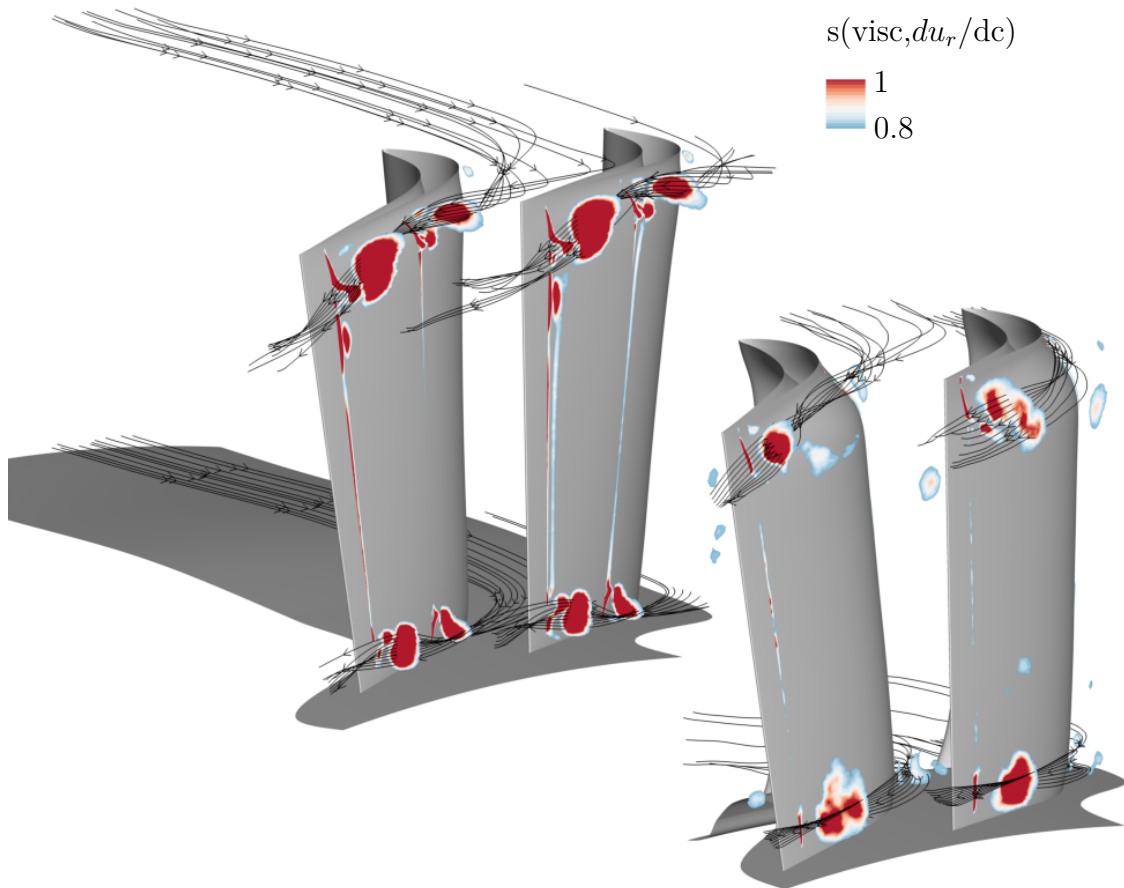


Figure 4.45: Axial cuts along the passage domain colored by viscous entropy production related to du_r/dc gradient for stator one and two

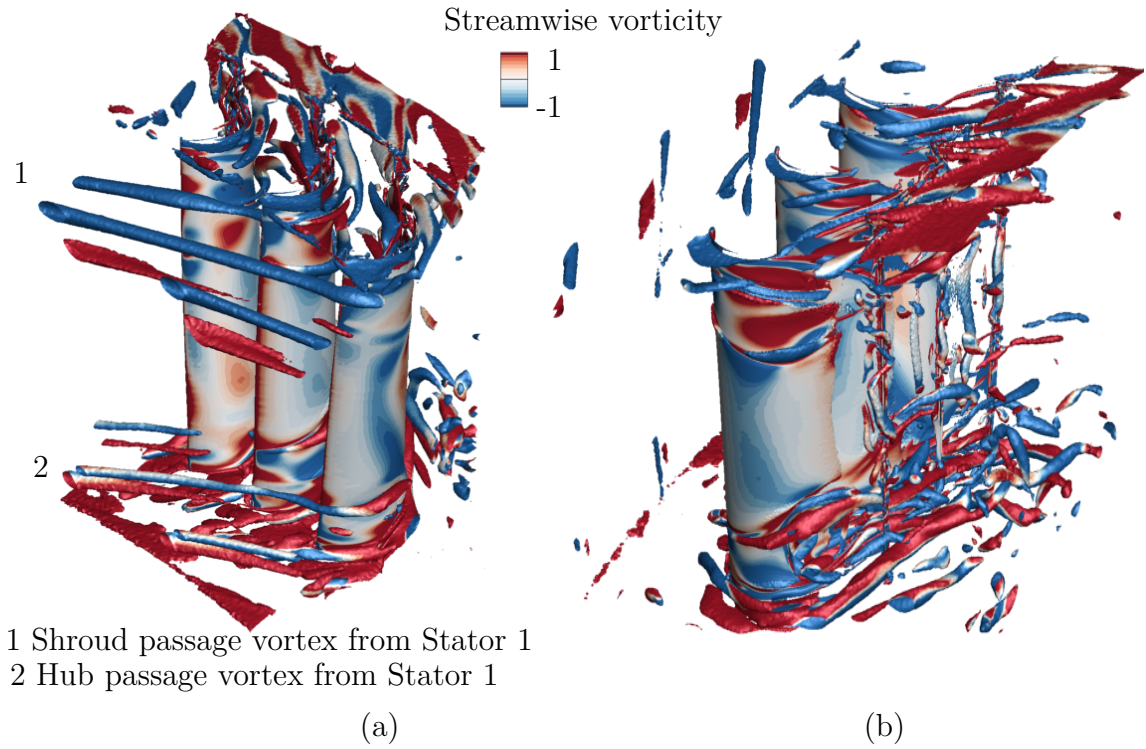


Figure 4.46: Iso-surface of q -criterion colored by streamwise vorticity showing upstream secondary vortices from stator 1 impacting rotor 1 in an upstream (a) and side view (b)

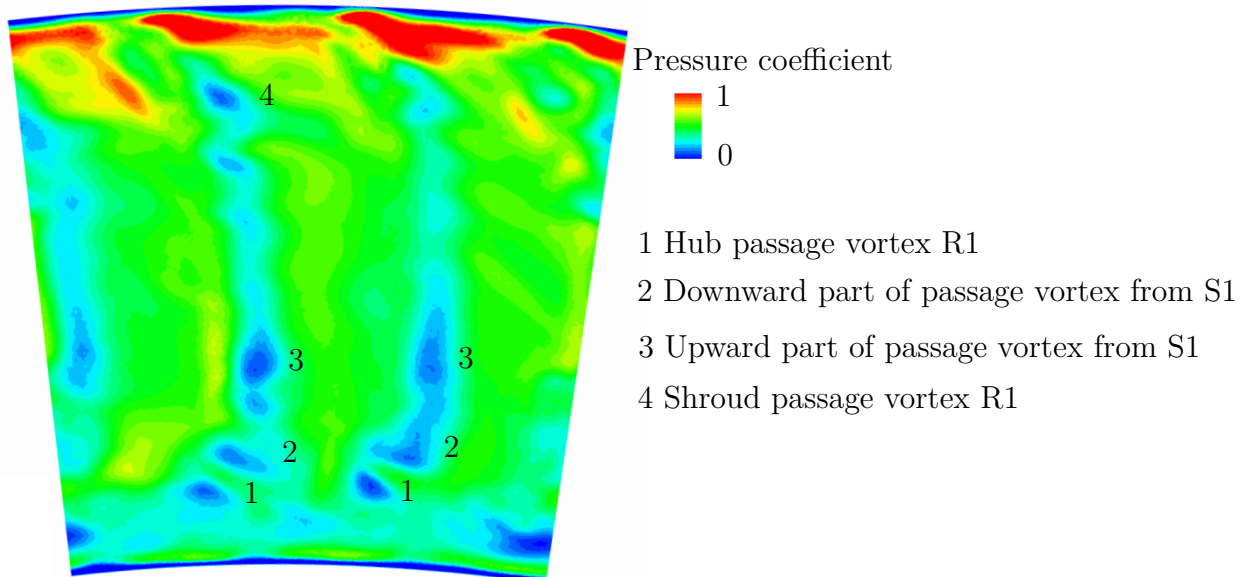


Figure 4.47: Pressure coefficient downstream of the rotor 1

The ingestion and blowing processes at the rim seal interface shows a similar influence of the potential effect of the downstream blades as observed in the linear cascade configuration. In addition, the wake transport from upstream rows promotes the blowing of the cavity flow in the main annulus. The

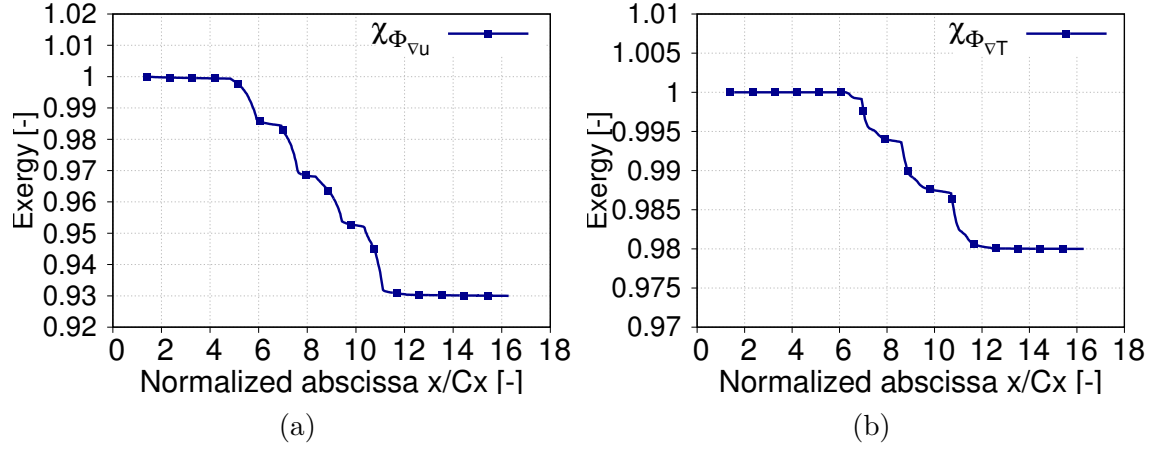


Figure 4.48: Contribution of viscous and thermal anergy to the decrease of exergy or the flow

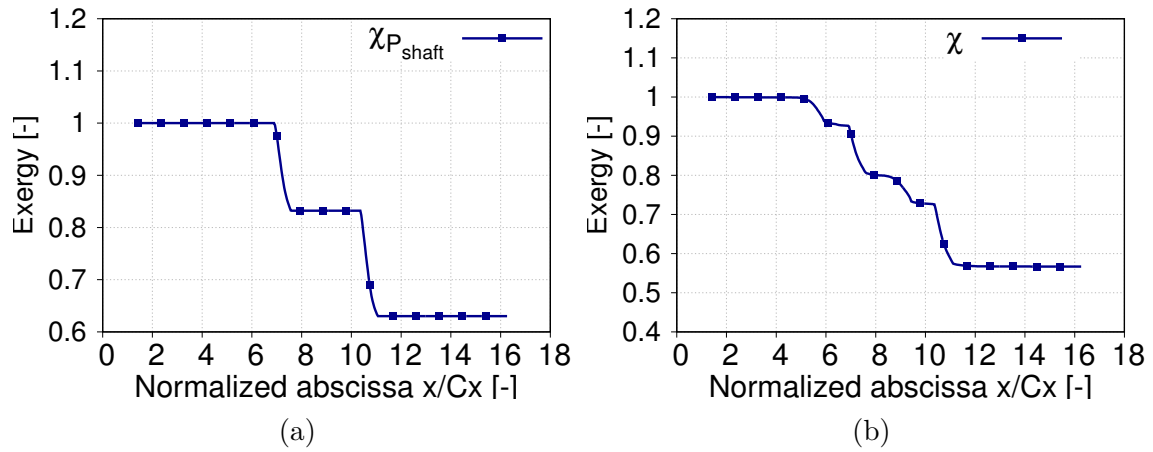


Figure 4.49: Contribution of the work extracted on the shaft to the decrease of exergy of the flow

entrainment effect of the disk in the cavity promotes a reduced shear layer at the rim seal interface. The influence of this process on the ingress/egress distribution at the rim seal interface is more difficult to establish. Regarding the influence of the purge flow blowing into the main annulus on the the generation of loss, the main mechanisms observed are the shear layer at the rim seal interface between the different rows, an increased blockage effect in the passage due to more energetic secondary flow structures. The analysis of the work extracted by the two rotor rows and irreversibility induced by velocity and thermal gradients mixing made possible to draw the decrease of available energy in the purpose to generate work all along the domain.

Conclusions and perspectives

Recalling the objectives

The present thesis deals with the influence of the purge flow blowing at the hub on turbine aerodynamics. The purge flow supplied in the turbine component emanates from the increased temperature in the combustion chamber to improve the natural limit conversion of thermal energy from the combustion to useful work. The main drawback is this additional flow taken at the compressor to cool down turbine that comes as a net loss since not used in the thermodynamic cycle. The bleed air system makes possible to maintain a quiescent environment for the components downstream of the combustion chamber while maintaining a high thermal efficiency. This thesis has been developed to provide a general framework to take into account the benefits of a thermal efficiency increase promoted by a increased temperature as well as the losses related to the air collected at the compressor that does not contribute to the thermodynamic cycle and additional losses due to the mixing of the purge flow with the mainstream flow in the turbine. This general framework is based on the notion of exergy that consists in energy balance at local, component or whole turbine scale compared to a dead state, generally the environment for gas turbine studies. When assessing the possible benefits of an increased combustion temperature with the side effect of an higher purge mass flow rate required, mainly three contribution must be balanced. First, the benefit of an increased temperature that enhances the conversion of thermal energy into work. Due to an increased temperature in the combustion chamber, the temperature in the turbine will increase and additional purge mass flow rate must be collected at the compressor. Based on an aero-thermal analysis, the additional amount of purge flow required to cool down the blades, rotor discs, etc. can be obtained. The cost in the exergy balance can be assessed since the amount of flow collected is known from the former analysis and the work (pressure) given to the fluid can be obtained depending on the station where air is collected. The purge flow supplied in the turbine generally provides a residual work to the turbine since still under pressure but at a relatively low temperature. The last contribution that needs to be quantified is the detrimental effect of an additional purge flow for the turbine by interaction with the main annulus. Since the interaction mechanisms are not currently fully understood, this thesis has been devoted to provide a better understanding of the mixing processes between the main annulus and cavity flow as well as the underlying mechanisms of loss in order to provide an

accurate estimate of the loss incurred. The main strength of the exergy analysis is that the additional useful work obtained from an increased thermal efficiency, the work lost for compressing purge flow that are global quantities can be put in a same analysis with the local losses in the turbine induced by the mixing of the purge flow with the main annulus turbine flow (from the numerical simulation, the exergy balance can be applied in each grid point of the domain).

Conclusion from a methodological point of view

The exergy formulation

The exergy formulation used in this study to take into account the losses generated in a gas turbine is a composite quantity between the state of the flow with the total enthalpy and the degradation of current energy in the purpose to generate work measured by entropy. From a general purpose, exergy formulation makes possible to balance between different nature of energy (kinetic, internal, potential pressure, etc.) in a same framework. This quantity is defined relatively to a dead reference state that provides the lower limit of energy extraction. Compared to a more common energy balance assessment, the exergy formulation takes into account the energy that cannot be used to generate work (anergy) in this study and held by the entropy term. This approach can be used at the different scales of the turbomachine. At the scale of the full gas turbine, this approach gives a sight in the conversion of the heat provided by the fuel in the combustion chamber into useful work, heat released into the atmosphere at the outlet, etc. as proposed in Sec. 2.1.2 (p.24). At the scale of the component, the exergy balance performed in Chap. 3 and 4 gives access to the transformation of exergy available at the inlet of the domain in the different contributions (work extracted on the shaft, heat transfers at the wall of the component, losses in the flow, exergy available at the outlet of the component) to provide a better insight in the energy transfer for the component. This assessment is obtained locally based on an exergy transport equation (Sec. 2.1.3 p.31). For numerical simulations, each of the contributions to the exergy transport equation can be obtained in each point of the mesh. In the purpose to study the losses generated in the turbine due to purge flow, two of the contributions are of particular interest: the viscous and thermal anergy terms denoted $\Phi_{\nabla u}$ and $\Phi_{\nabla T}$ in this study that are induced by velocity and temperature gradients and held by entropy. Since these two terms were available in each grid point it was convenient to split the whole simulation domain in contiguous subdomains. The splitting strategy proposed in current thesis is based on isolating the boundary layer domains developing on the wetted surfaces (hub, shroud, cavity, blades) and a remaining domain that is the whole domain minus the subdomains related to the boundary layers. This strategy has been chosen since the boundary layer is known to be a contributor to anergy/loss generation since the flow has to adapt between a no slip condition at the wall and the free stream velocity inducing strong velocity gradients. Furthermore, the remaining domain composed of the full domain minus the boundary layer contributions contains the contributions of secondary flows (cross components with respect to the stream direction) that are also known to contribute to losses and can be more properly studied in the

remaining subdomain. Finally, the exergy formulation is particularly adapted to study the losses generated in the simulation domain since providing a local measure (in each grid cell) with an access to the gradient directions inducing loss.

Numerical approach

The LES-LBM approach used in the linear cascade configuration described in Chap. 3 gives access to higher computing efficiency compared to classical finite volume approaches for low-Mach flows. The Cartesian grid provides an easy meshing strategy (sometimes referred as meshless approach) since the non body fitted meshing of the configuration can be performed automatically especially when complex geometries are considered like technological effects and cavities for the current study. However, the isotropic mesh prevent generally from having wall-resolved simulation for the Reynolds number encountered in low pressure turbines and a law of the wall treatment needs to be added. This approach can be adapted when the boundary layer is turbulent on a wide portion of the wetted surfaces. But in low pressure turbine where the boundary layer can be depending on the free stream turbulence, Reynolds number and surface roughness, laminar on a large portion of the surfaces, this approach may be more questionable. The more classical finite volume approaches used for current LES simulations are suitable for handling low pressure turbine flows. The Reynolds number encountered makes possible to perform wall-resolved simulation at a high but more and more affordable computational cost. For relatively simple geometries as the one encountered in chap. 3 concerning the linear cascade, the structured approach is suitable since providing well posed problem and high order schemes can be derived more easily. For more complicated geometries as the one encountered when technological effects like cavities of the two stage annular cascade of Chap. 4, an unstructured approach is more suitable. The finite volume approaches can also reduce the sources of uncertainty that can be numerous: wall-resolved LES simulation makes possible for dense enough grids to predict the laminar, transitional or turbulent nature of the boundary layer over the wetted surfaces. High order schemes with explicit time stepping reduce numerical errors. The automatic mesh refinement makes possible to increase the spatial discretization in regions of interest. Finally, turbulence injection at the inlet of the domain is important for predicting the flow in near-wall despite some improvement still need to be made in the turbulence spectrum content injected and its possible intermittent nature.

Conclusion from a physical point of view

The study of loss generation in the main annulus due to cavity flow has been conducted based on two configurations. A first configuration based on a low-Mach linear cascade with an upstream cavity providing different rim seal geometries and purge flow rates detailed in Chap. 3. The numerical simulations performed showed a better agreement of RANS with experiments compared to LES simulations without turbulence injection (Sec. 3.3 p.99). The turbulence was shown to be an important parameter for the physical mechanisms and subsequent losses in the cascade especially due to an upstream grid that artificially increased the turbulence intensity of

the flow facing the cascade. The high free stream turbulence was shown to drive the state of the boundary layers at the hub, shroud and around the blade by triggering the onset to turbulence while remaining laminar without free stream turbulence. The LES simulation performed with turbulence injection was then shown to give a better agreement with experiments (Sec. 3.6 p.118). The influence of purge flow and rim seal geometry on losses generated was assessed using the exergy formulation. This analysis showed the influence of the shear layer at rim seal interface, more energetic secondary vortices in the passage as additional paths for more losses generated in the cascade compared to a smooth configuration. The second configuration studied during this thesis in Chap. 4 was a two stage low-Mach annular turbine with cavities at hub. This configuration made possible to add the entrainment effect of the rotor discs on the cavity flow and the influence of upstream rows and wakes on the flow at rim seal interface compared to the first configuration. A similar feeding process of secondary vortices by cavity flow was observed in this configuration as well as similar physical mechanisms in the main annulus compared to the linear cascade. This configuration made possible to have a look into the possible interaction (transport of vortices) between the different rows as well as the energy transferred to the rotor rows in the exergy analysis.

Future work

From a numerical point of view, the influence of spatio-temporal discretization on the viscous and thermal entropy production needs to be assessed accurately. The main issue is the additional viscosity and diffusivity induced by the discretization. The entropy production is higher than the one that would be obtained from continuous equations. The numerical viscosity is not uniform in the domain and depends on the discretization and physical phenomenon occurring in the region of interest. An a posteriori method similarly to the one suggested in App. B should make possible to evaluate this numerical viscosity, without dependence on the numerical scheme used but based on the numerical solution. A major difficulty faced in the current study is the determination of the boundary layer when complex phenomena occur. Indeed, the boundary layer thickness estimate gave very thick boundary layer on the blade suction side where the passage vortex travels or in the separation bubble region on the diffusion portion for the LES simulation without turbulence injection. This observation comes from the difficulty to define the notion of boundary layer in these regions. However, since the boundary layer thickness is used to split the domain in the different contribution, a more reliable method would be required if one want to prevent to see part of these contributions accounted in boundary layers while not purely related to the development of a boundary layer on these surfaces. From a physical point of view, it would be interesting to look at the terms appearing in the exergy balance but simplified in the two configurations of this thesis. At first, an increased Mach number in order to look at the compressibility effects and especially the transfer of energy since thermal and convective contribution are no more decoupled as in the two low Mach configurations studied. At higher Mach number, the shock handling from a numerical point of view with the use of sensors would provide a more general framework to tackle this kind of flow. The other

contribution that was not been taken into account in this study is the heat transfer at wall. This term can either provide or extract heat to the flow depending on the temperature of the wall compared to the flow. Furthermore, non adiabatic wall would induce temperature gradients that could be interesting to study with an exergy balance.



Numerical methods

In the gas turbine, the flow experiences a strong variety of behaviour along the channel with complex phenomena, interaction processes over a wide range of temporal and spatial scales. At the same time, experimental measures are often difficult to perform due to compactness and complexity that make difficult an accurate description of the flow. A further improvement of aeronautical engines and future breakthrough requires a better understanding of the flow behavior. In the past decades, with the emergence and increasing capacity of supercomputers, the numerical simulations have become a path for a better understanding of the flow in the gas turbine. This chapter introduces a framework used to deal with the numerical simulation of turbulent flows encountered in gas turbines. The numerical simulation of the fluid motion requires a model that is supposed to describe the flow. A first part is devoted to introduce the Navier-Stokes and lattice-Boltzmann method approaches that have been used along this study. The treatment of turbulence is an important feature that strongly affects the quality of the numerical simulation and the computational cost. Different approaches from fully resolved turbulence (DNS) to fully modeled turbulence ((U)RANS) with intermediate level of modeling (LES) are presented. From the temporally and spatially continuous governing equations obtained from the modeling approach, equations are discretized on the simulation domain in discrete points forming a mesh and are solved through the use of numerical scheme that approximate the continuous equations. The end of the chapter is devoted to the understanding of numerical schemes, parameters and boundary conditions used and required to ensure a proper study of the flow field obtained numerically. The application of exergy method and description of physical phenomena inducing loss detailed in Chap 2 requires a proper convergence assessment of the simulations. Once converged,

the output of the simulation generally needs to be reduced temporally for unsteady methods ((U)RANS, LES and DNS) and spatially. This process needs to be carefully performed to enable a correct analysis of the flow field and in order to be compliant with the exergy approach. These notions of numerical convergence and data extraction are discussed at the end of this section.

A.1 Equations in fluid dynamics	216
A.1.1 Early development of fluid dynamics	216
A.1.2 Navier-Stokes equations	219
A.1.3 Lattice-Boltzmann Method	222
A.2 Turbulence modeling	231
A.2.1 Direct numerical simulation	233
A.2.2 (U)RANS simulation	234
A.2.3 Large Eddy Simulation (LES)	237
A.3 Discretization of the equations	240
A.3.1 Boundary conditions	240
A.3.2 Meshing strategy	245
A.3.3 Numerical parameters and flow solvers	247
A.4 Numerical convergence	249
A.4.1 RANS	249
A.4.2 LES	249
A.5 Reducing information by averaging	250
A.5.1 Statistical convergence	251
A.5.2 Temporal averaging: the comparison against experiment .	253
A.5.3 Quantities to be temporally and spatially averaged	254
A.5.4 Performance quantities	255

A.1 Equations in fluid dynamics

This section introduces modeling approaches of the flow motion based on the Navier-Stokes and lattice-Boltzmann Method. These models have emerged after a long period of time and thanks to different contributions. A quick journey back over the development of fluid dynamics leading to the first governing equations proposed to model turbulent flows known as Navier-Stokes equations is introduced. The section is followed by the introduction of lattice-Boltzmann Method that propose an alternative modeling strategy of the flow based on developments obtained from the end of nineteen and along the twentieth century.

A.1.1 Early development of fluid dynamics

Fluid dynamics refers to the study of fluid motion. Early studies were led by Archimedes (287-212 BC) that introduced some basic ideas in static fluid and Hero of Alexandria (10-70 AD) on the notion of pressure with the first steam-powered devices. Later on, Leonardo Da Vinci (1452-1419) observed and drew sketches of

canonical (jets, vortices, surface waves) and complex flows over objects in streams. All these statements were based purely on observation at the time. Quantitative physical and mathematical understanding of the fluid flow began only along the seventeenth century with the works of Isaac Newton (1642-1726). In his *Principia Mathematica* (1687), Newton proposed a direct link between the movement of a solid and the forces applied to the solid (second principle of the dynamics). With the contributions of Gottfried Wilhelm Leibniz (1646-1716) on the differential calculus, partial differential equations that describe the dynamics of a system in time and space were derived for a variety of systems. Book II of the *Principia Mathematica* (1687) from Isaac Newton was exclusively devoted to the examination of static and dynamic fluids. However, the application of these developments to fluid dynamics remained difficult until the contribution of Leonhard Euler (1707-1783). At the time, the purpose of the fluid dynamics was to be able to track the position of a fluid composed of particle initially at position X_0 at time t_0 to obtain the successive positions (trajectory) at any time step Δt of same particle until time t , $X(x, t)$. This representation of the fluid motion is now known as Lagrangian description. Euler was able to show from a mathematical point of view that for a fluid in motion, the ability to know the trajectory of fluid particle in time is equivalent to know the velocity field $u_i = (u_1, u_2, u_3)$ in any position and successive time step until time t . This representation is known as Eulerian description. Based on the works of Daniel Bernoulli (1700-1782) and Jean d'Alembert (1717-1783), Euler was able to conceptualize the mathematical description of a fluid flow by modeling the flow as a continuous collection of infinitesimally small fluid elements. By applying the basic principles of mass conservation and Newton's second law on small fluid elements, Euler obtained two coupled, non-linear partial differential equations for an incompressible flow of density ρ_0 subject to body forces F^1

$$\frac{\partial u_j}{\partial x_j} = 0 \quad (\text{A.1})$$

$$\rho_0 \left(\frac{\partial u_i}{\partial t} + u_i \frac{\partial u_j}{\partial x_j} \right) = \rho_0 F_i \quad (\text{A.2})$$

where t and $x_i = (x_1, x_2, x_3)$ are respectively time and coordinates. From the former system of equation, mathematical inconsistency was observed by Jean d'Alembert. Assuming the external body forces known, the above set of two equations contained three unknowns ρu_i for four equations. Furthermore, when divergence operator is applied to eq.(A.2), it can be shown that the left-hand side is non-zero while divergence applied to a constant body force is zero. From this ill-posed problem, Euler proposed to add the gradient of a quantity p called pressure that could overpass the last two inconsistencies with a constitutive law where pressure should only depends on density (barotropic fluid, $p = p(\rho)$) leading to the final incompressible Euler

¹A body force is a force that acts throughout the volume of a body in contrast with contact forces or surface forces which are exerted to the surface of an object. Forces due to gravity, electric fields and magnetic fields are examples of body forces.

equations proposed in 1755:

$$\frac{\partial u_j}{\partial x_j} = 0 \quad (\text{A.3})$$

$$\rho_0 \left(\frac{\partial u_i}{\partial t} + u_i \frac{\partial u_j}{\partial x_j} \right) = - \frac{\partial p}{\partial x_i} + \rho_0 F_i. \quad (\text{A.4})$$

Using Euler equations without external body forces ($F = 0$) and looking at the time derivative of kinetic energy for a fluid in motion in the domain of volume V expressed as $\partial/\partial t \left(\iiint_V \rho_0 u_i^2 dx_i \right)$, it can be shown that this quantity is identically zero. This result promoted the use of perfect fluid for the flow following the Euler equations since energy is conserved along the movement. Jean D'Alembert was able to find particular analytical solutions from steady incompressible Euler equations and showed that the drag force was zero on a body moving with constant velocity relatively to the fluid what was not observed and known as D'Alembert's paradox. To solve this paradox, a first correction to Euler momentum equation was proposed by Claude-Louis Navier (1785-1836) in 1821 for incompressible flows. Its purpose was to take into account viscous forces applying to an object moving at a constant speed in this kind of flow. An heuristic term known as viscous stress tensor τ was added to the Euler equations to account for the effect of internal friction within the flow field with a viscous dissipation. A more general derivation of the momentum equation for compressible flows was later given by Augustin Louis Cauchy (1789-1857) in 1829. In his work, he derived a general equation of motion that included non normal (shear) deformations based on continuum mechanic theory. In 1845, George Stokes (1819-1903) expressed the compressible momentum equation in the fluid mechanics framework, leading to the set of equations:

$$\frac{\partial \rho}{\partial t} + \frac{\partial(\rho u_j)}{\partial x_j} = 0 \quad (\text{A.5a})$$

$$\frac{\partial(\rho u_i)}{\partial t} + \frac{\partial}{\partial x_j} (\rho u_i u_j + p \delta_{ij} - \tau_{ij}) = \rho F_i \quad i = 1, 2, 3. \quad (\text{A.5b})$$

Kinetic energy for the fluid in motion described by latter equations is not conserved since one can obtain:

$$\frac{\partial}{\partial t} \left(\iiint_V \rho_0 u_i^2 dx_i \right) = - \iiint_V \tau_{ij} u_i dx_i. \quad (\text{A.6})$$

Despite this further extension of fluid flow modeling, some shortcomings still remained since several phenomena, such as the conversion of mechanical energy into heat by viscosity through the viscous stress tensor were still not taken into account. Following the developments of the thermodynamics, an additional equation was added to the system of equations that stated for the conversion of the total

energy denoted e_{tot} by possible transfer of kinetic energy to internal energy for the fluid denoted e . Jean-Baptiste Joseph Fourier (1768-1830) was among the first to be interested in temperature fluctuations inside an inviscid and incompressible flow. He proposed to take into account these fluctuations through an energy equation. In 1868, Kirschoff (1824-1887) further included the impact of small viscous effects in the fluid mechanics framework:

$$\frac{\partial(\rho E_{tot})}{\partial t} + \frac{\partial}{\partial x_j}(\rho E_{tot} u_j + p u_j - \tau u_j + q_j) = \rho F_j u_j + \dot{Q} \quad (\text{A.7})$$

where q and \dot{Q} are heat transfer and internal heat source.

This paragraph introduced the main chronological steps leading to a possible description of the fluid motion. The next subsection introduces the set of Navier-Stokes equations at the current stage of knowledge including phenomenological laws to close the Navier-Stokes equations. The lattice-Boltzmann approach will be then introduced as another possible path to model fluid motion. The related development are more recent, essentially at the end on nineteen and twentieth century.

A.1.2 Navier-Stokes equations

The Navier-Stokes equations are nowadays used to describe the physics of many phenomena of scientific and engineering interest with among them the weather, ocean currents, pipe flow or flow around a wing. These equations are also of interest from a pure mathematical point of view. Despite its wide use, it has not yet been proven whether solutions always exist in three dimensions and, if they do exist, whether they are smooth (they are infinitely differentiable at all points in the domain). The Navier-Stokes equations in their current form can be written as:

$$\frac{\partial \rho}{\partial t} + \frac{\partial}{\partial x_j}(\rho u_j) = 0 \quad (\text{A.8a})$$

$$\frac{\partial(\rho u_i)}{\partial t} + \frac{\partial}{\partial x_j}(\rho u_i u_j + p \delta_{ij} - \tau_{ij}) = \rho F_i \quad i = 1, 2, 3 \quad (\text{A.8b})$$

$$\frac{\partial(\rho E_{tot})}{\partial t} + \frac{\partial}{\partial x_j}(\rho E_{tot} u_j + p u_j - \tau_{ij} u_j + q_j) = \rho F_j u_j + \dot{Q}. \quad (\text{A.8c})$$

The main concern of computational fluid dynamics is to obtain a representative flow of a given configuration determined by the boundary conditions, the geometry, the set of equation and its discretization. According to the historical steps for modeling fluid dynamics introduced previously, a set of equation capable of representing the fluid behaviour are the Navier-Stokes equations. The fluid under consideration is assumed to be monoatomic and compressible which means that the density can vary in time and space. Navier-Stokes equations are a set of conservative equations for the mass eq.(A.8a), momentum eq.(A.8b) and total energy eq.(A.8c). Since the system

is composed of eight unknown for five equations, the system needs to be closed using three additional equations. To close these equations, it is necessary to determine the pressure p , the viscous stress tensor τ , the dynamic viscosity μ contained in the viscous stress tensor and the heat flux q . For this purpose, the following state laws and behavior laws are used.

A.1.2.1 State law

The fluid is assumed to follow to the ideal gas law known as perfect gas²

$$p_s = \rho r T_s \quad (\text{A.9})$$

where $r = R/M = c_p/c_v$ is the specific mixture gas constant ($r = 287.058 [m^2.s^{-2}.K^{-1}]$ for air mixture). R is the universal gas constant ($R = 8.3145 [kg.m^2.s^{-2}.K^{-1}.mol^{-1}]$) and M the molecular weight of the gas. c_p and c_v are the constant pressure and volume specific heat capacity. Equation (A.9) holds for air and other gases over a wide range of temperatures and pressures. For a perfect gas, the internal energy of the fluid e and heat capacity only depend on temperature. The flow will be considered as calorifically perfect that lead to constant values for c_p and c_v . The total energy of the fluid can be then written as

$$E_{tot} = \frac{rT}{\gamma - 1} + \frac{1}{2}\rho ||u||^2 \quad (\text{A.10})$$

with $\gamma = c_p/c_v$ the ratio of specific heat capacity. The assumption of constant temperature and pressure heat capacity is convenient to integrate internal energy between two states since it depends on the temperature difference of these two states. It remains that these two quantities rigorously evolve with temperature and must be taken into account when dealing with accuracy requirements or high temperature flows such as in combustion chamber or turbine. The mid-way solution often used is the semi-perfect gas assumption where a constant value of γ is taken for the compressor side ($\gamma = 1.4$) and the turbine side ($\gamma = 1.3$).

A.1.2.2 behavior laws

The behavior laws are used to model the momentum and heat transfer at the fluid particle scale. The Newtonian fluid hypothesis is generally used and assumes that

²The ideal gas law was originally introduced by Emile Clapeyron (1799-1864) and later Kirschoff to relate pressure to temperature through a proper equation of state since only isobaric relation was proposed at the time. For ideal gases, it is assumed that there are no intermolecular forces and that the molecules themselves take up no volume. This is quite true at low pressures and in majority of flows encountered in turbomachine, because the spacing between the molecules is so large that they rarely collide. Also, low pressure usually means that there is little of them or that the volume of the container is very large, so the space taken up by the actual molecules is negligible. For example, air at a pressure of 30 atmospheres and a temperature of 1650 K that are conditions representative of the exit of the combustion chamber in a gas turbine, the ratio $p/\rho r T$ would be approximately 1.03. For dense gas, alternative law must be used referred as real gas laws.

the viscous stresses arising from the flow are linearly proportional to the local strain rate at every point:

$$\tau_{ij} = -\frac{3}{2}\mu' \left(\frac{\partial u_i}{\partial x_j} + \frac{\partial u_j}{\partial x_i} \right) - \frac{2}{3}\mu \left(\frac{\partial u_i}{\partial x_i} \right) \delta_{ij} \quad (\text{A.11})$$

where μ' is the coefficient of bulk viscosity and μ is the dynamic viscosity of the fluid. For a fluid following the Stokes hypothesis, these two quantities can be related by:

$$\mu' + \frac{2}{3}\mu = 0. \quad (\text{A.12})$$

The viscous stress tensor can be finally expressed as:

$$\tau_{ij} = \mu \left(\frac{\partial u_i}{\partial x_j} + \frac{\partial u_j}{\partial x_i} \right) - \frac{2}{3}\mu \left(\frac{\partial u_i}{\partial x_i} \right) \delta_{ij}. \quad (\text{A.13})$$

The evolution of the dynamic viscosity of the fluid is obtained using the Sutherland law:

$$\mu(T) = \mu_{ref} \left(\frac{T}{T_{ref}} \right)^{\frac{3}{2}} \frac{T_{ref} + S}{T + S} \quad (\text{A.14})$$

where $\mu_{ref} = 1.711 \cdot 10^{-5} [kg.m^2.s^{-1}]$ is the dynamic viscosity at reference temperature $T_{ref} = 273.15 [K]$ and the constant for air $S = 110.4 [K]$ obtained experimentally. The thermal transfers due to the conduction are modeled using the Fourier law that relate the heat flux and the temperature gradient

$$q_i = -\lambda \frac{\partial T}{\partial x_i} \quad (\text{A.15})$$

where λ is the thermal conductivity. This value is obtained along this study by assuming that the Prandtl number Pr defined as :

$$Pr = \frac{\mu c_p}{\lambda}. \quad (\text{A.16})$$

is constant and equal to 0.72.

An important non dimensional number in fluid dynamics is the Reynolds number denoted R_e that was first introduced by Stokes in 1851 and popularized by Osborne Reynolds (1842-1912) along his famous pipe flow studies [154]. Reynolds number appears naturally in the Navier-Stokes set of equations by casting the equations in non-dimensional form and comparing viscous and inertial forces in the fluid. The Reynolds number being the ratio of these two quantities

$$R_e = \frac{\rho u L}{\mu} \quad (\text{A.17})$$

where ρ , u , L and μ are characteristic density, velocity, length and viscosity of the considered configuration. This number is of particular interest when dealing with the conditions that have to be fulfilled in order that the informations about one flow field could apply to another with different parameters. This situation can happen for example when a real configuration have high dimensions (aircraft or gas turbine) such that the configuration could not be studied experimentally in a wind tunnel and reduced scale model has to be used. For the reduced scale model under study, the idea is to know which parameters of the flow have to be tuned in order to observe similar phenomena as in real configuration. The two configuration have to be kinematic similar which means geometrical parameters such as blade profile, blade stagger angle, blade spacing/chord ratio and hub/tip radius ratio are kept the same for a gas turbine. For a steady incompressible flow around two kinematic similar models, the behavior of the flow depends only of the Reynolds number³ (dynamic similarity). For a reduced model gas turbine with characteristic length L half the real configuration, cinematic viscosity of the fluid $\nu = \mu/\rho$ could be divided by two to be dynamically equivalent to the first configuration, by cooling down the incoming flow for example.

Fluid motion modeling can be led at different scales from approaches where any particle of the fluid is tracked to fluid volumes as developed in current section for the Navier-Stokes equations. In-between, the statistical behavior of a group of particle can be described and is at the basis of the lattice-Boltzmann Method.

A.1.3 Lattice-Boltzmann Method

Another approach capable of representing the fluid behaviour is the Boltzmann equation. This equation is based on a fluid description at an intermediate scale between microscopic scale where motion of individual particle is tracked in time and macroscopic scale where the fluid is described with control volumes that contain a very large number of imperceptible particles forming a continuum as in the Navier-Stokes equations previously introduced (see Fig. A.1). The numerical resolution of this equation is made with the lattice-Boltzmann method.

A.1.3.1 Kinetic theory of gases

The Boltzmann equation was derived in the framework of the kinetic theory of gas along the nineteen century thanks to strong contributions of Josiah Willard Gibbs (1839-1903), Lord Kelvin (1824-1907), James Clerk Maxwell (1831-1879) and Ludwig Eduard Boltzmann (1844-1906). The purpose of the kinetic theory of gas was to describe the evolution of probability density functions in time and space of particles. This analysis was led at mesoscopic scale of fluid that lies in between microscopic and macroscopic worlds. For the former, the evolution of each particle is tracked, while the latter describes the evolution of fluid particles with constant characteristics in the considered particle volume. The purpose of kinetic theory

³Note that true dynamic similitude may require matching other dimensionless numbers as well. For unsteady flows, the reduced frequency $\beta = (\omega L)/U$. For compressible flows, the Mach, Stanton or Nusselt number.

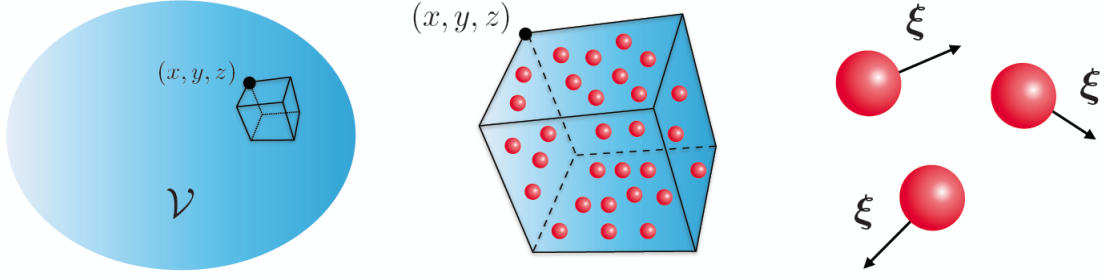


Figure A.1: Illustration of different scales to describe a flow. From left to right, macroscopic, mesoscopic and microscopic scales

being to draw the statistical behavior of particles in the considered volume. The probability density function or velocity distribution function $f(M, \vec{\xi}, t)$ evaluates the number of particles at point $M(x, y, z)$ of the domain and time t travelling at particle speed $\vec{\xi} = (\xi_1, \xi_2, \xi_3)$. From current approach, the total number of particles N in a volume V can be expressed as:

$$N = \int_V \int_{\xi} f_N(M, \vec{\xi}, t) d^3 M d^3 \xi. \quad (\text{A.18})$$

If all the particles have the same mass m , the total mass m_{tot} of the considered volume is

$$m_{tot} = \int_V \int_{\xi} \underbrace{m f_N(M, \vec{\xi}, t)}_{f(M, \vec{\xi}, t)} d^3 M d^3 \xi. \quad (\text{A.19})$$

By identification with the macroscopic density ρ

$$m_{tot} = \int_V \rho(M, t) d^3 M, \quad (\text{A.20})$$

one can write density in terms of distribution function as:

$$\rho(M, t) = \int_{\xi} f(M, \vec{\xi}, t) d^3 \xi. \quad (\text{A.21})$$

More generally, the macroscopic conservative quantities can be expressed as the stochastic moments of the distribution function with respect to the particle velocity $\vec{\xi}$, i.e. by integrating over the whole velocity particle domain.

$$\begin{bmatrix} \rho(M, t) \\ \rho(M, t) \vec{u}(M, t) \\ \rho(M, t) e(M, t) \end{bmatrix} = \int \begin{bmatrix} 1 \\ \vec{\xi} \\ \frac{1}{2} |\vec{\xi} - \vec{u}|^2 \end{bmatrix} f(M, \vec{\xi}, t) d^3 \xi. \quad (\text{A.22})$$

Maxwell and Boltzmann were able to derive an equation that governs the evolution of the velocity distribution function in time and space. For packets of particles whose

velocities distribution is described by f , affected by either external body forces F or collision occurring between particles, the space-time evolution of f is governed by the advection-collision Boltzmann equation:

$$\frac{\partial f}{\partial t} + \xi_j \frac{\partial f}{\partial x_j} + F_j \cdot \frac{\partial f}{\partial \xi_j} = \Omega(f). \quad (\text{A.23})$$

The left-hand side term corresponds to the advective part in both geometrical ($\xi_i \partial f / \partial x_i$) and velocity ($F_j \partial f / \partial \xi_j$) spaces, whereas the right-hand side term is linked to the change of f originating from collisions. The main difficulty lies in the definition of the collision term $\Omega(f)$, which contains all the underlying physics. Since the Boltzmann original collision operator $\Omega(f)$ relied on a complicated double integral over velocity and space, the idea has been to propose a simplified modeling of the collision operator.

A.1.3.2 Modeling the collision operator

Maxwell and Boltzmann were first able to derive a particular velocity distribution function denoted f_{eq} solution of the Boltzmann equation that maximize disorder (or entropy production) and can be seen as the local thermodynamic equilibrium distribution function of particles after collisions. Maxwell-Boltzmann equilibrium function can be expressed as

$$f_{eq} = \frac{\rho}{(2\pi RT)^{D/2}} e^{-|\xi - u|^2 / (2RT)} \quad (\text{A.24})$$

with D standing for the dimension of space. Based on the Maxwell-Boltzmann equilibrium function, Bhatnagar, Gross and Krook (1954) proposed a collision operator. This collision operator relies on the idea that collision induces a deviation with respect to the local thermodynamic equilibrium state. The local equilibrium is recovered after a time t_{relax} called relaxation time. The mathematical expression of this operator can be read as

$$\Omega^{BGK}(f) = -\frac{1}{t_{relax}}(f - f_{eq}). \quad (\text{A.25})$$

Similarly to the distribution functions, it can be shown that the collision operator stochastic moments integrated over the whole particle velocity domain ensure mass, momentum conservation and elastic collisions since $\int \vec{\xi}^i \Omega(f) d^3 \xi = 0$ for $i = 0, 1, 2$. The Boltzmann equation eq.(A.23) and BGK collision operator from eq.(A.25) form the Boltzmann-BGK equation. A natural analytical development to be performed is to look at the stochastic moments of the Boltzmann-BGK equation to draw a link with the macroscopic quantities. For the sake of clarity and simplicity, no external body forces are considered ($F = 0$).

$$\int \begin{bmatrix} 1 \\ \xi \\ \xi^2 \end{bmatrix} \left(\frac{\partial f}{\partial t} + \xi \frac{\partial f}{\partial x_j} \right) d^3 \xi = - \int \begin{bmatrix} 1 \\ \xi \\ \xi^2 \end{bmatrix} \left(\frac{1}{t_{relax}} (f - f_{eq}) \right) d^3 \xi. \quad (\text{A.26})$$

Rewriting the different contributions in terms of macroscopic quantities when they are known lead to:

$$\frac{\partial}{\partial t} \begin{bmatrix} \rho \\ \rho u_i \\ \int \xi^2 f d^3 \xi \end{bmatrix} + \frac{\partial}{\partial x_j} \begin{bmatrix} \rho u_j \\ \int \xi^2 f d^3 \xi \\ \int \xi^3 f d^3 \xi \end{bmatrix} = \begin{bmatrix} 0 \\ 0 \\ -\frac{1}{t_{relax}} \int \xi^3 (f - f_{eq}) d^3 \xi \end{bmatrix}. \quad (\text{A.27})$$

Chapman and Enskog (1920) made the assumption that the relaxation time t_{relax} corresponding to the mean time between two collisions is small compared to the characteristic time of local equilibrium. Moreover, f can be approximated by f_{eq} , i.e. the probability density function is not far from the equilibrium function. This corresponds to make a Taylor Expansion (TE) of f around the equilibrium function:

$$f = \sum_{k=0}^N K_n^k f^k \quad (\text{A.28})$$

truncated at first order in N_{TE} (or equivalently at zero order in K_n), where K_n is the Knudsen number. This number compares the free mean path L_{free} to a macroscopic characteristic length related to the flow L_{char} by

$$K_n = \frac{L_{free}}{L_{char}}. \quad (\text{A.29})$$

Under this truncation assumption it can be shown that

$$\int \xi^2 f d^3 \xi \simeq \int \xi^2 f_{eq} d^3 \xi = \rho u_i u_j + \rho r T \delta_{ij} \quad (\text{A.30})$$

$$\int \xi^3 f d^3 \xi \simeq \int \xi^3 f_{eq} d^3 \xi = \rho E_{tot} u_i + \rho r T u_i \quad (\text{A.31})$$

and replaced in eq.(A.27) yields to

$$\frac{\partial \rho}{\partial t} + \frac{\partial(\rho u_j)}{\partial x_j} = 0 \quad (\text{A.32})$$

$$\frac{\partial(\rho u_i)}{\partial t} + \frac{\partial(\rho u_i u_j)}{\partial x_j} + \frac{\partial(\rho r T) \delta_{ij}}{\partial x_j} = 0 \quad (\text{A.33})$$

$$\frac{\partial(\rho E_{tot})}{\partial t} + \frac{\partial(\rho E_{tot} u_j)}{\partial x_j} + \frac{\partial(u_i \rho r T)}{\partial x_j} = 0 \quad (\text{A.34})$$

that is under the ideal gas law $p = \rho r T$, the Euler set of equations. Similarly, the distribution function expansion can be made until the second order in N_{TE} (or

equivalently first order in K_n) with $f \simeq f_{eq} + f_1$ and $f_1 \ll f_{eq}$. A new expression can be obtained for the second and third order moment of f :

$$\int \xi^2 f d^3\xi \simeq -t_{relax} p \left(\frac{\partial u_i}{\partial x_j} + \frac{\partial u_j}{\partial x_i} - \frac{2}{D} \frac{\partial u_i}{\partial x_i} \right) = -\tau_{ij} \quad (\text{A.35})$$

$$\int \xi^3 f d^3\xi = -D t_{relax} p r \frac{T}{2} \frac{\partial T}{\partial x_i} = -q_j. \quad (\text{A.36})$$

By setting

$$\mu = (-t_{relax} p) \quad (\text{A.37})$$

$$\lambda = (-D t_{relax} p r T/2) \quad (\text{A.38})$$

the viscosity and conductivity of the fluid, this yields to the set of equations:

$$\frac{\partial \rho}{\partial t} + \frac{\partial(\rho u_j)}{\partial x_j} = 0 \quad (\text{A.39})$$

$$\frac{\partial(\rho u_i)}{\partial t} + \boxed{\frac{\partial(\rho u_i u_j)}{\partial x_j}} + \frac{\partial(\rho r T)}{\partial x_j} = \boxed{\frac{\partial \tau_{ij}}{\partial x_j}} \quad (\text{A.40})$$

$$\frac{\partial(\rho E_{tot})}{\partial t} + \boxed{\frac{\partial(\rho E_{tot} u_j)}{\partial x_j}} + \boxed{\frac{\partial(u_i p r T)}{\partial x_j}} = \frac{\partial(\tau_{ij} u_i)}{\partial x_j} + \boxed{\frac{\partial(q_j)}{\partial x_j}} \quad (\text{A.41})$$

corresponding to the compressible Navier-Stokes set of equations. Extending the distribution to the third order in N_{TE} (or equivalently second order in K_n) leads to the Burnett set of equations particularly used for rarefied atmosphere as in low earth orbits. The former development of f needs to be further explained especially the quantity K_n used to perform the expansion process. High Knudsen numbers ($0.001 < K_n < 0.1$) are encountered when studying discrete systems such as rarefied gas. This explains the need to extend the distribution function until higher orders since a low number of collisions occur. This requires more accurate approximation of the distribution function to recover equilibrium. Small Knudsen numbers correspond to dense or continuous fields such as liquids. Fluid dynamics described by the Navier-Stokes equations considered as continuous is at relatively low Knudsen number $K_n < 0.001$. This explains the need to develop only until $N = 2$ the distribution function to recover this set of equations. From the current approach, the viscosity and the heat diffusivity of the flow depend on the relaxation time t_{relax} and Prandtl number $Pr = \mu c_p / \lambda = 1$. This differs from the value commonly used in Navier-Stokes approach ($Pr = 0.72$). This general statement based on the continuous Boltzmann-BGK equation then requires space, time and velocity discretization to be numerically solved.

A.1.3.3 The velocity discretization

When dealing with the numerical resolution of the Boltzmann-BGK equation, the continuous velocity space needs to be discretized. Since all the velocities from continuous space cannot be used for memory and computational cost, a limited number of velocities has to be chosen. The main idea behind the velocity discretization is the ability to find a set of Q discrete velocities ξ_α known as lattice that recovers the Taylor expansion of the continuous distribution function up a certain order (see Fig. A.2a) depending on the physic that is looked for (Euler with $N_{TE} = 1$, Navier-Stokes with $N_{TE} = 2$, Burnett with $N_{TE} = 3$). As shown from eq.(A.27) to (A.41), the ability to recover the desired flow physic depends on the ability to recover stochastic moments of the distribution function up to a certain order noted N_{DF} . The purpose is to conserve these equilibrium moments during the velocity discretization compared to the continuous one such that:

$$\begin{aligned}\xi &\rightarrow \xi_\alpha, \alpha \in [1, Q] \\ f(M, \xi, t) &\rightarrow f_\alpha(\xi, t), \alpha \in [1, Q] \\ \int \xi^n f_{eq} d\xi &= \sum_\alpha \xi_\alpha^n f_{eq, \alpha}.\end{aligned}\tag{A.42}$$

Since the recovery of macroscopic quantities is of interest when using lattice-Boltzmann Method to describe fluid dynamics, the distribution does not need be known but only ensure that the stochastic moments are conserved between continuous and discrete ones. This statement leads to approximate the distribution function by a polynomial function. Under the assumption of a polynomial behavior of the distribution function, it can be shown that the moments of the distribution function can be exactly recovered up to order N_{DF} by performing a Gauss-Hermite quadrature of the continuous distribution function

$$f_{eq, \alpha}^N(M, \vec{\xi}, t) = w_\alpha \sum_{n=0}^{N_{DF}} a_{n, eq}(M, t) \mathcal{H}_n(\vec{\xi}) \quad \text{with} \quad a_{n, eq} = \int f_{eq} \mathcal{H}_n(\vec{\xi}) d\xi \tag{A.43}$$

where w_α are the quadrature weight and \mathcal{H}_n the Hermite polynomials. In the three-

α	1	2-7	8-19
$\vec{\xi}_\alpha$	(0,0,0)	(0,0, ± 1) (± 1 ,0,0)	(0, ± 1 , ± 1) (± 1 , ± 1 ,0)
w_α	$\frac{1}{3}$	$\frac{1}{18}$	$\frac{1}{36}$

Table A.1: Velocity particle and weight of Gauss-Hermite quadrature of the D3Q19 lattice

dimensional space, the set of nineteen velocities (D3Q19) proposed in Fig. A.2b with weight furnished in Tab.A.1 makes possible to recover the second order moment of the distribution equilibrium function ($N_{DF} = 2$, see blue box in eq.(A.41)). A

consequence is that higher order moments cannot be accurately evaluated. This lead to a non-physical term that appears in viscous stress tensor:

$$\tau_{ij} = \mu S_{ij} - t_{relax} \frac{(\rho u_i u_j u_k)}{\partial x_k}. \quad (\text{A.44})$$

This additional error term in equivalent momentum Navier-Stokes equation evolves with $O(M^3)$. This error prevents from facing flows with Mach number higher than $M = 0.3$. This means that the current approach is equivalent to solve weakly compressible Navier-Stokes equations around a reference temperature (isothermal). This set of velocities is used in the solver Pro-LB and along this thesis. This limitation is alleviated with a particular set of 103 particle velocities (D3Q103) that recovers the third order moment distribution equilibrium function ($N_{DF} = 3$, see green box in eq.(A.41)) and corresponds to the isothermal fully compressible Navier-Stokes equations. Fully compressible Navier-Stokes equations with thermal effects are recovered with a particular set of 343 particle velocity (D3Q343) that is generally unaffordable ($N_{DF} = 4$, see red box in eq.(A.41)). When thermal effects are of interest, other approaches are generally used alleviate the cost related to the high number of particle velocity required. Mainly two methods can be used:

- double distribution function: a first distribution function is associated to the conservative mass an momentum quantities ($\rho, \rho u$) and a second distribution models thermal effects [155];
- hybrids methods: energy equation is solved using classical methods (finite volumes, differences or elements) [156].

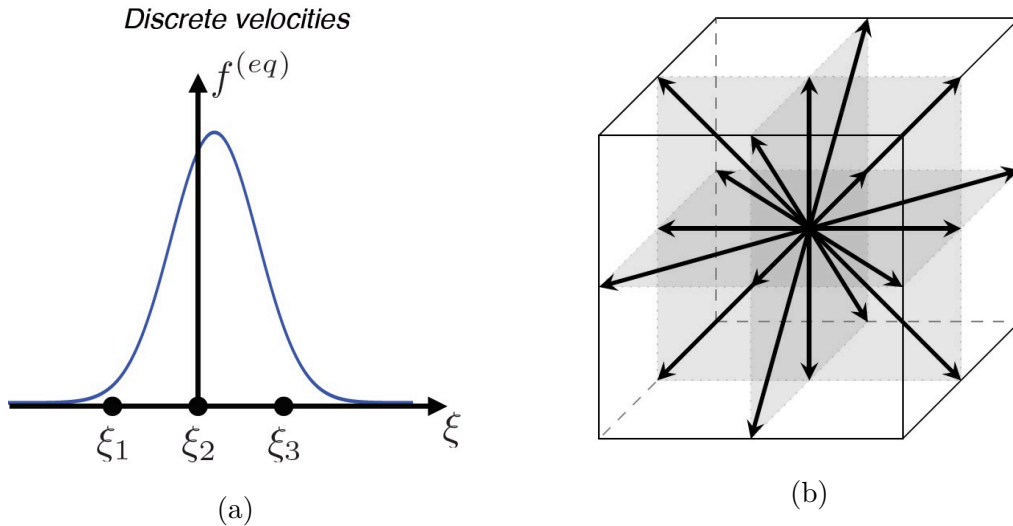


Figure A.2: One-dimensional continuous distribution function and discretization (D1Q3) to recover the exact integral value (a). Velocity distribution in three dimension (D3Q19) to recover the weakly compressible isothermal Navier-Stokes equations (b)

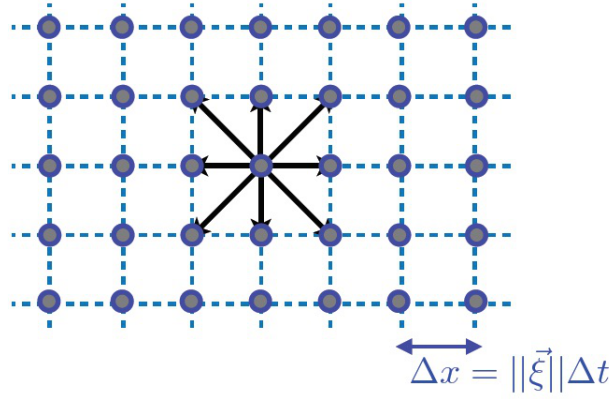


Figure A.3: Link between velocity, space and time discretization in a Cartesian grid

A.1.3.4 Spatio-temporal integration

Time and space discretization can be done in a smart way by considering that spatial nodes are set such that:

$$\|\vec{\xi}\| = \frac{\Delta x}{\Delta t}. \quad (\text{A.45})$$

This leads to a Cartesian mesh with a constant time step (see Fig. A.3). More generally, this approach is not restricted to Cartesian mesh, the method could be adapted to any kind of discretization, the cartesian mesh is generally used since it is particularly convenient and efficient. The time and space resolution over the Cartesian mesh is made by integration along a characteristic line (second order accurate in time and space):

$$f_\alpha(M + \vec{\xi}\Delta t, t + \Delta t) - f(M, t) = \int_0^{\Delta t} \Omega(M + \vec{\xi}s, t + s) ds. \quad (\text{A.46})$$

The collision term is computed using a trapezoidal rule

$$\int_0^{\Delta t} \Omega(M + \vec{\xi}s, t + s) ds \simeq \frac{\Delta t}{2} [\Omega(M, t) + \Omega(M + \vec{\xi}\Delta t, t + \Delta t)]. \quad (\text{A.47})$$

The implicitness of this spatio-temporal integration is removed by the use of a change of variable:

$$\overline{f}_\alpha = f_\alpha - \frac{\Delta t}{2} \Omega_\alpha \quad (\text{A.48})$$

since it can be shown that \overline{f}_α and f_α have the same distribution moments, this leads to the explicit integration:

$$\overline{f}_\alpha(M + \xi_i\Delta t, t + \Delta t) = \overline{f}_\alpha(M, t) + \Omega_i(M, t) - \frac{\Delta t}{t_{relax} + \Delta t/2} (\overline{f}_\alpha - f_{\alpha,eq}). \quad (\text{A.49})$$

The Boltzmann-BGK equation and the discretization in particle velocity, time and space of this equation are the constituent of the method known as lattice-Boltzmann Method (LBM).

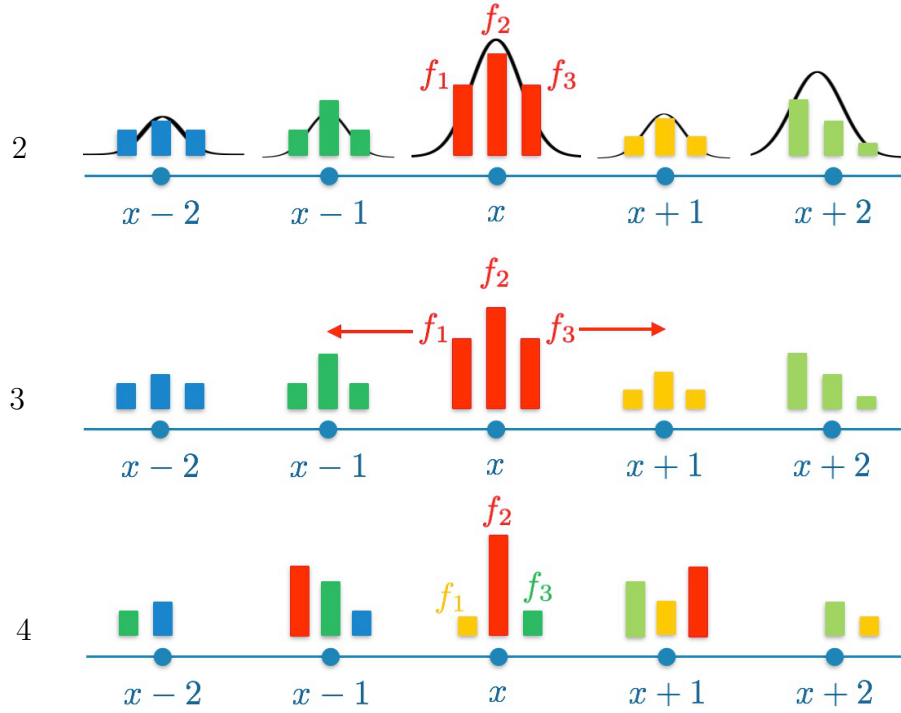


Figure A.4: Schematic view of steps 2 to 4 required to perform one iteration in LBM approach from a D1Q3 lattice. Courtesy of Coreixas [157]

A.1.3.5 The different steps to perform one iteration in LBM

The different steps corresponding to one iteration in the lattice-Boltzmann method over a one dimensional domain discretized by three velocities (D1Q3) $e_0 = \vec{0}$, $e_1 = \vec{x}$, $e_2 = -\vec{x}$ is proposed. The corresponding steps 2 to 4 are shown in Fig. A.4.

1. The meshing: the choice of space length δx and speed of sound c_a sets the time step δt while the choice of μ leads to set t_{relax} according to eq.(A.37);

2. the equilibrium distribution function is calculated from the macroscopic quantities with the initial field for the first iteration or obtained from the previous iteration for others;

3. the collision term is calculated for each discrete particle velocity: $f_\alpha := f_\alpha - \frac{1}{\tau}(f_\alpha - f_{\alpha,eq})$;

4. the spatio-temporal integration or streaming that consists in simply moving the distribution functions between the corresponding nodes. This operation is possible because of the Cartesian nature of the mesh and the particle velocities, space and temporal relation set by $\|\vec{\xi}\| = \Delta x / \Delta t$;

5. computation of macroscopic quantities at each node from the probability density functions $\rho = f_1 + f_2 + f_3$, $\rho u = f_3 - f_1$.

6. equilibrium function: determination of f_{eq} from ρ and u .

A.2 Turbulence modeling

From the Navier-Stokes equations, it can be noticed that these equations are non-linear partial differential equations. The non-linearity makes difficult an exact resolution of this set of equations. Furthermore, these non-linear terms indicate possible non-linearities in the flow. One main difficulty of fluid dynamics is turbulence. Turbulence refers to the time-dependent chaotic behavior seen in many fluid flows. By opposition, laminar flow are characterized by flows behaving in parallel layers, with no disruption between the layers. For a given configuration, the Reynolds number makes possible to predict the laminar or turbulent nature of the flow by a critical Reynolds number below which the flow is laminar and above turbulent. Reynolds [154], in his pipe flow studies observed that the fluid changed from an orderly predictable state to a chaotic and unpredictable one at $Re = 2300$. At low Reynolds numbers, flows tend to be dominated by laminar (sheet-like) flow (diffusion term), while at large Reynolds numbers, turbulence results from differences in the fluid speed and direction (convection term). Analytical solutions to the full non-linear equations exist such as the flow created by a uniformly rotating infinitely long plane disc known as von Kàrmàn swirling flow or an unsteady decaying vortex known as Taylor-Green vortex. However, solutions at sufficiently large Reynolds number where the flow is turbulent cannot be derived analytically due to strongly non-linear and stochastic turbulence dynamics. This limitation has motivated the development of numerical methods to solve either the Navier-Stokes or Boltzmann equations. The previous partial differential equations introduced are continuous equation that are generally discretized to be numerically solved. Depending on the discretization, more or less modeling process needs to be performed. One main issue that emerges when one want to solve these equations at sufficiently high Reynolds number is, as mentioned above, the treatment of turbulence. The treatment of turbulence is at the basis of the numerical methods developed to tackle flow motion in turbomachinery applications. The flow in gas turbines, due to high Reynolds number, transformation processes and geometrical arrangement, is generally strongly affected by turbulence. To obtain an accurate description of the flow, turbulence needs to be properly predicted numerically. A review of current turbulence handling in the framework of gas turbine flows is proposed by Tucker [158]. A spectrum of kinetic energy for homogeneous turbulence is proposed in Fig. A.5. The spectrum can be decomposed in three characteristic length scales:

- the integral length scale I , with wavenumber κ_I that corresponds to the length of the most energetics turbulent structures. These structures are the main contribution to the kinetic energy production. The integral scale varies slowly with the Reynolds number except in the boundary layers [160];
- the Taylor length scale with wavenumber κ_T that correspond to the characteristic length scale of the structures affected by the viscosity of the fluid leading to a dissipation of the fluctuating kinetic energy into heat;
- Kolmogorov length scale ν with wavenumber κ_ν that corresponds to the smallest scales of turbulence.

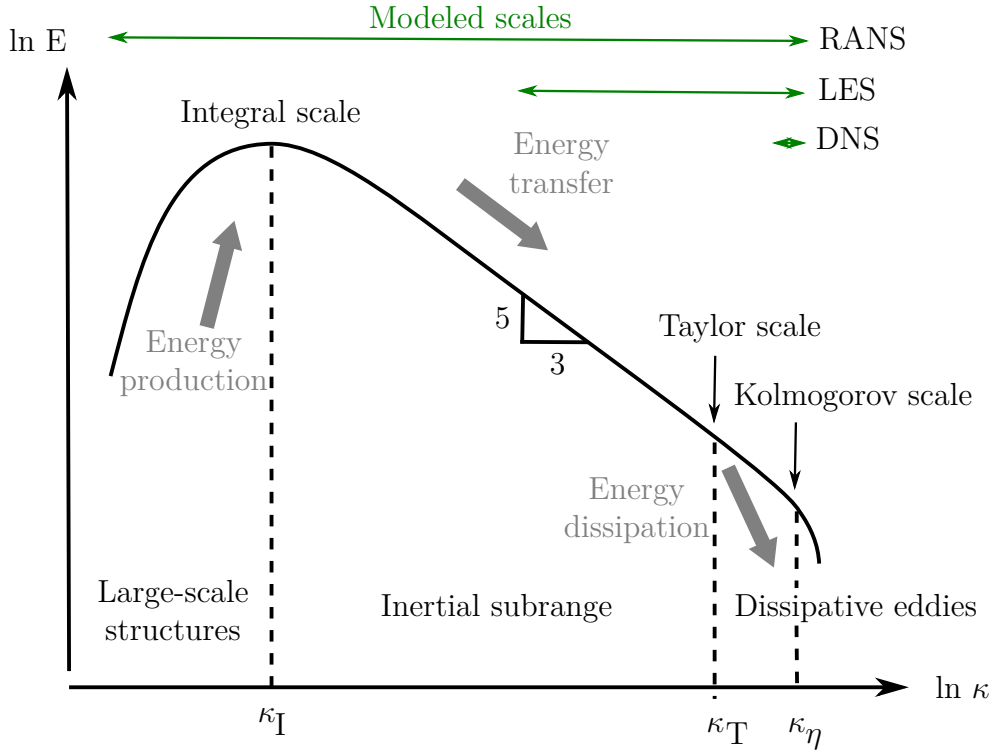


Figure A.5: Turbulent spectrum with degrees of modeling: DNS, LES and RANS. From Gravemeier et al. [159]

From this description based on turbulent scales, the spectrum can be divided into three regions according to the cascade concept introduced by Richardson [161]:

- an energy production zone for wavenumbers below k_I ;
- an energy transfer zone from big structures toward the small ones, also known as the inertial range. In this region between integral and Taylor length scale, the energy density spectrum decreases according to the Kolmogorov law for large Reynolds number ($E \sim k^{-5/3}$);
- an energy dissipative zone made by the small structures under a Joule heating process for wavenumbers above k_T .

Numerical resolution of the Navier-Stokes equations in addition with the closure equations make possible to simulate the three-dimensional turbulence if all turbulent length scales are resolved. This approach referred as Direct Numerical Simulation (DNS) requires very fine grids for complex and large Reynolds number in this kind of configurations. On the other side, turbulence can be fully modeled based on (U)RANS formalism. Between these two approaches, part of the turbulent cascade can be solved while small scales are modeled and is known as Large Eddy Simulation (LES) approach.

A.2.1 Direct numerical simulation

Direct Numerical simulations is a complete time-dependent solution of the Navier-Stokes equations that solves all the turbulent scales without any modeling. In a turbulent isotropic context, estimation of the length scales is based on the Kolmogorov theory [162]. The assumption of isotropic turbulence is fulfilled below a fixed length scale. To achieve the full scale resolution, the size of the mesh cells has to be in the order of magnitude of the smallest dissipative scales of turbulence (Kolmogorov scales ν) or smaller to have several grid points per wavelength. At the same time, the whole domain under consideration has to be discretized taking into account the largest structures that contain most of the kinetic energy (integral scales I). The ratio between these two scales makes possible to estimate the number of degree of freedom in each direction that can be related to the turbulent Reynolds number Re_I (based on fluctuating kinetic energy and integral length scale I , see Coleman [163]):

$$\frac{I}{\nu} \sim Re_I^{3/4}. \quad (\text{A.50})$$

Assuming that turbulent kinetic energy is related to the macroscopic deformation $Re_I \sim Re$ and for three-dimensional domains, this means that the number of cells needed is of magnitude $Re^{9/4}$. The additional time resolution of kolmogorov scale yields to a number of operation in the order of magnitude $Re^{11/4} \sim Re^3$. Due to computational cost, the first Direct Numerical Simulation have been focused on the study of canonical flows for which the analytical solution were available for the laminar flow but generally not in the turbulent regime at sufficiently large Reynolds number. DNS have been so conducted on channel flow for example with the contribution of Kim, Moin and Moser that studied a fully developed turbulent channel flow at $Re = 3300$ [164]. The computational Reynolds number of these canonical flows is becoming higher and higher thanks to improvement of computer technology and numerical method. DNS also contributes to the understanding of complex flow mechanisms like boundary layer transition depicted in Sec. 2.2.2 (see for example the works of Krishnan and Sandham [165] for turbulent spot development in supersonic boundary layer). For realistic, complex engineering flows, DNS is yet to become an established analysis tool because of computational domains with complicated geometries, and the very high computational power and memory requirements when Reynolds number is large. Figure A.6a shows Reynolds number evolution along axial direction for medium-sized gas turbine engine. The Reynolds number encountered in compressors and high-pressure turbine that can be in the order of magnitude of 10^6 - 10^7 is currently challenging when one wants to simulate the flow in these components. In the literature, due to relatively low Reynolds number (see Fig. A.6b) and Mach number, the flow past low pressure turbine blades is perhaps one of the practical engineering concern that was first investigated by DNS. This is because of the relatively lower computational power requirement, the Reynolds numbers being in the order of magnitude of 10^4 - 10^5 . Indeed, Wu and Durbin [79] were among the first to perform fully resolved turbomachinery simulation of a stator passage in 2001. They were quickly followed by other authors with among them Michelassi et al. [167]; Wissink [168]; Kalitzin et al. [169]; Wissink et al. [168]. Ranjan et

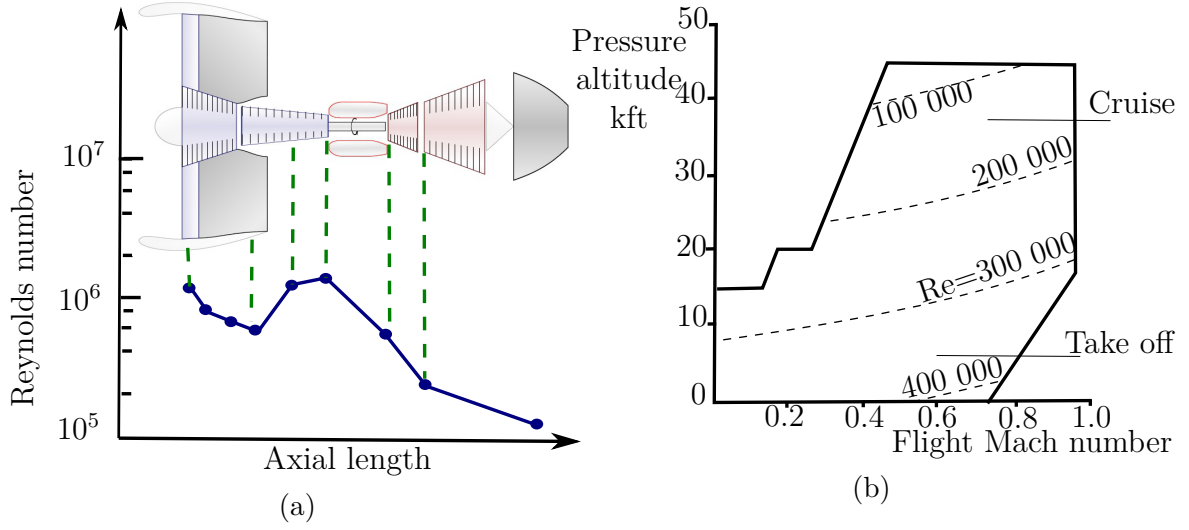


Figure A.6: Reynolds number variation in a medium-sized gas turbine engine (a) and engine flight envelope Reynolds number for a medium-sized low pressure turbine (b). Adapted from Hourmouziadis [166]

al. [170]; Michelassi et al. [85], Garai et al. [171]. Chen et al. [172] performed a DNS of a T106 profile⁴ investigated by Cardamone et al. [173] at Reynolds Number $Re = 60\,000$ to study the influence of incoming wake on the turbine performance as well as Ranjan et al. [170] that studied the influence of curvature effects. DNS of low pressure turbine configurations remain very costly especially since previous study took advantages of simplified geometries compared to industrial one (isolated blade, mid-span symmetry conditions) and are mainly focused on fundamental phenomena.

A.2.2 (U)RANS simulation

A.2.2.1 Averaged equations

Reynolds-averaged Navier-Stokes (RANS) approaches were proposed by Reynolds in 1895 and have been originally developed to simulate incompressible and stationary flows. The equations are obtained by time- (in steady flow) or ensemble-averaging (in unsteady flow) the Navier-Stokes equations providing a set of transport equations for the averaged momentum. They are based on a statistical approach of the turbulence where each instantaneous flow variable ϕ is decomposed into a mean part $\tilde{\phi}$ and a fluctuating part ϕ'

$$\phi(t) = \tilde{\phi} + \phi'. \quad (\text{A.51})$$

The mean part is defined as a statistical average called Reynolds averaging over N independent realization of the same hypothetical simulation:

$$\tilde{\phi} = \lim_{n \rightarrow \infty} \left(\frac{1}{N} \sum_{i=1}^N \phi_i \right). \quad (\text{A.52})$$

⁴The T106 low pressure blade turbine is a configuration extensively studied experimentally and numerically to deal with wake-blade interference

This averaging filters the random fluctuations of the flow and the effects of turbulence are entirely modeled, the fluctuations being such that $\tilde{\phi}' = 0$. Under the assumption of ergodicity stating that the mean value of a quantity obtained statistically is equal to the average of a great number of measures over time, this leads to replace the statistical averaging by a temporal average over a period T (longer than the turbulent characteristic time):

$$\tilde{\phi} = \lim_{T \rightarrow \infty} \left(\frac{1}{T} \int_0^T \phi(\tau) d\tau \right). \quad (\text{A.53})$$

In URANS incompressible simulations, the same principle is applied at the different time steps, a phase averaging is performed to take into account the unsteadiness related to the motion of the blades (URANS approach)

$$\tilde{\phi}(t) = \lim_{T \rightarrow \infty} \left(\frac{1}{T} \int_{t-T}^t \phi(\tau) d\tau \right). \quad (\text{A.54})$$

The period T must be appropriately chosen to be long enough to average the turbulent fluctuations but short enough to keep the unsteady features of the flow. When the Reynolds averaging is applied to the compressible Navier-Stokes equations, the equations become much more complex. To simplify them, a Favre averaging is generally applied [174] (Reynolds averaging weighted according to mass):

$$\phi = \bar{\phi} + \phi'' \quad (\text{A.55})$$

with:

$$\bar{\phi} = \frac{\widetilde{\rho\phi}}{\bar{\rho}}. \quad (\text{A.56})$$

The averaging process and steps leading to compressible RANS equations can be found in Aupoix [175]. Among the different steps of this averaging process, the molecular, turbulent transport of the turbulent kinetic energy and fluctuations of the molecular viscosity are neglected. Applying the Favre decomposition for u, E and h = e+p/ρ, the (U)RANS equations yields:

$$\frac{\partial \tilde{\rho}}{\partial t} + \frac{\partial}{\partial x_j} (\tilde{\rho} \tilde{u}_j) = 0 \quad (\text{A.57a})$$

$$\frac{\partial (\tilde{\rho} \tilde{u}_i)}{\partial t} + \frac{\partial}{\partial x_j} (\tilde{\rho} \tilde{u}_i \tilde{u}_j + \tilde{p} \delta_{ij} - \tilde{\tau}_{ij} - \tau_r) = \tilde{\rho} F_i \quad i = 1, 2, 3 \quad (\text{A.57b})$$

$$\frac{\partial (\tilde{\rho} (\overline{E_{tot}} + k))}{\partial t} + \frac{\partial}{\partial x_j} [(\tilde{\rho} (\overline{E_{tot}} + k) + \tilde{p}) \tilde{u}_j - (\tilde{\tau} + \tau_r) \tilde{u}_i + \tilde{q} + q_{turb}] = \tilde{\rho} \overline{F_j} \tilde{u}_j. \quad (\text{A.57c})$$

A.2.2.2 Closure of the equations

This averaging procedure leads to an open problem with additional terms induced by the non-linearity of momentum and energy conservation equations that have to be modeled in order to have a closed system for eq. (A.57). These terms are:

- the turbulent kinetic energy $k = \frac{1}{2} \rho \overline{|u_i''|^2} / \tilde{\rho}$;
- the Reynolds stress tensor $\tau_r = -\rho \overline{u_i'' u_j''}$;
- the turbulent heat transfer $q_{turb} = \rho \overline{u_i'' h_i''}$.

Generally, the turbulent kinetic energy k in the energy conservation equation is neglected. Based on an analogy with the viscous stress tensor, Boussinesq (1877) proposed a behavior law that links the Reynolds stress tensor to the strain by a turbulent viscosity μ_{turb} :

$$\tau_r = -\frac{2}{3}(\tilde{\rho}k + \mu_{turb} \frac{\partial \bar{u}_j}{\partial x_i}) + \mu_{turb} \left(\frac{\partial \bar{u}_i}{\partial x_j} + \frac{\partial \bar{u}_j}{\partial x_i} \right). \quad (A.58)$$

Similarly, to describe the turbulent heat flux, an analogy with the heat flux and Fourier's law was proposed:

$$q_t = -\lambda_{turb} \frac{\partial \bar{T}}{\partial x_i} \quad \text{with} \quad \lambda_{turb} = \frac{c_p \mu_{turb}}{Pr_{turb}} \quad (A.59)$$

where Pr_{turb} is the turbulent Prandtl number. Therefore, for approaches based on the Boussinesq hypothesis, the closure leads to evaluate μ_{turb} and Pr_{turb} . Generally, the turbulent Prandtl number Pr_{turb} is considered constant ($Pr_{turb} = 0.9$). Using a dimensional analysis, μ_{turb} is homogeneous to the product of a density, turbulent velocity and turbulent length scale. The turbulence model must give an estimation of turbulent length scales. A first approach called algebraic (or zero-equation model) uses geometrical data and mean flow to prescribe without any additional equation, the turbulent scales. Mixing length model or the Baldwin-Lomax model (1978) are example of algebraic models. A second approach uses one transport equation in order to evaluate the turbulent viscosity. The Spalart-Almaras model is an example of one equation transport model. The models based on two transport equations make possible to obtain two scales of turbulence to evaluate μ_{turb} . Several model of this type can be found as k - ϵ , k - ω or k - l model. These models are widely used in gas turbine simulations despite some limitations: isotropic turbulence hypothesis, equilibrium between turbulence production and dissipation, calibration of coefficients over simplified or canonical configurations. These model can be further modified to take into account rotating and curvature effects.

A second category with higher order closure of RANS equations have also been developed known as Reynolds Stress Models (RSM models) especially second order closure with Explicit Algebraic Reynolds Stress equation Models (EARSM). These models are more computational and memory demanding (seven transport equations

for the RSM model) and generally less robust.

Turbulence models have been the subject of many studies over the last 40 years, but no model was shown to provide accurate results in all flows without adjustments of the model constants leading to numerous turbulence models. This may be due to the fact that the large, energy-carrying eddies are much affected by the boundary conditions, and universal models that account for their dynamics may be impossible to develop. This observation has pushed toward developing approaches where less modeling is given to turbulence.

A.2.3 Large Eddy Simulation (LES)

Knowledge obtained from general turbulence considerations (Pope [176]) as well as lessons learned from DNS that have been conducted on canonical flows (Kim and Moin [164], Spalart [177]) suggest that different scales require different levels of resolution. For a range of flows, the energy content of the smallest scales is little. Therefore, if the focus of a simulation for this kind of flows is on quantities that are dominated by the energy content of the mean flow and large scales, resolving the small scales might not be necessary and computational resource requirements could be reduced compared to DNS requirements. Large Eddy Simulation (LES) approach is based on a scale splitting using a spatial filtering that takes benefit of this observation by solving only the large scale structures and modeling small scale structures. Small scale structures being less affected by the boundary conditions and having more isotropic, homogeneous behavior, they are most likely to follow universal models. Spatial filtering can be made explicitly or implicitly depending on the mesh over which LES approach is applied (see Fig. A.7). Sufficiently large and

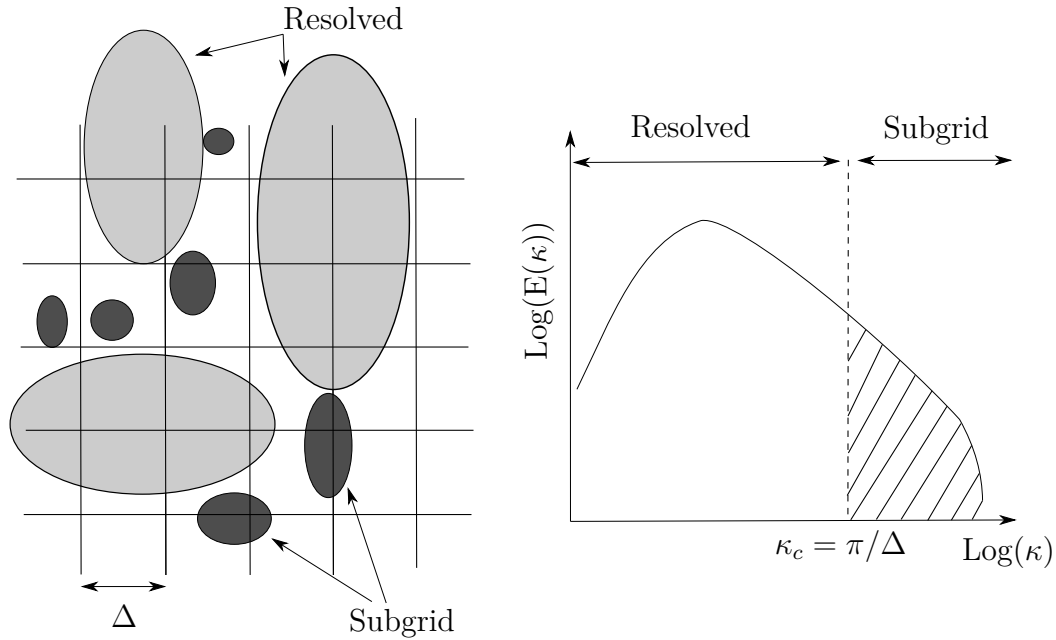


Figure A.7: Sketch of the scale splitting principle in LES due to the mesh. From Sagaut [178]

coherent structures are implicitly solved since the structures that are larger than a grid cell are solved while subgrid scale effects are explicitly modeled by adding additional terms to the fluid motion equations (subgrid scale models). The spatial cutoff frequency κ_c is directly related to the Nyquist frequency and considered cell size of the mesh by

$$\kappa_c = \frac{\pi}{\Delta} \quad (\text{A.60})$$

with:

$$\Delta = (\Delta_i \Delta_j \Delta_k)^{\frac{1}{3}} \quad (\text{A.61})$$

where Δ is the characteristic length of the mesh in the directions (i,j,k). Spatial scales with wavenumber lower than κ_c are solved. In order to only model the scales with a nearly universal behavior the cutoff wavelength must be ideally set between integral wavelength and Taylor wavelength. The mesh acts as a low-pass filter in the wavenumber domain. It can be noticed that the spatial filtering induces a temporal filtering of high frequencies. The following formalism used for LES is built to be the same as for (U)RANS formalism to keep notation as simple as possible but one has to remind that the filtering process is different. A quantity ϕ is decomposed into a resolved part $\bar{\phi}$ and a modeled part ϕ' :

$$\phi = \bar{\phi} + \phi'. \quad (\text{A.62})$$

Similarly to (U)RANS formalism, the filtering follows a Favre operation to account for compressible flows applied to u, E and h quantities leading to

$$\phi = \bar{\phi} + \phi'' \quad (\text{A.63})$$

that reduces for the spatially, temporally and localized filter function under consideration to

$$\bar{\rho}(M, t) \bar{\phi}(M, t) = \overline{\rho(M, t) \phi(M, t)} = \int_{-\infty}^{+\infty} \rho(M', t) \phi(M', t) J(M - M') dM' \quad (\text{A.64})$$

where J denotes the low-pass filter function kernel. The filtered LES equations yields to

$$\frac{\partial \bar{\rho}}{\partial t} + \frac{\partial}{\partial x_j} (\bar{\rho} \widetilde{u_j}) = 0 \quad (\text{A.65a})$$

$$\frac{\partial (\bar{\rho} \widetilde{u_i})}{\partial t} + \frac{\partial}{\partial x_j} (\bar{\rho} \widetilde{u_i u_j} + \bar{p} \delta_{ij} - \bar{\tau}_{ij} - \tau_{ij}^{SGS}) = \bar{\rho} f_i \quad i = 1, 2, 3 \quad (\text{A.65b})$$

$$\frac{\partial (\bar{\rho} \widetilde{E_{tot}})}{\partial t} + \frac{\partial}{\partial x_j} (\bar{\rho} \widetilde{E_{tot} u_j} + \bar{p} \widetilde{u_j} + \bar{q_j} + q_j^{SGS} - \widetilde{u_i \tau_{ij}} - \widetilde{u_i \tau_{ij}^{SGS}}) = \bar{\rho} f_j \widetilde{u_j} \quad (\text{A.65c})$$

where τ_{ij}^{SGS} is the subgrid scale stress tensor and q_j^{SGS} the subgrid scale heat flux. Because of these two terms, the filtered equations are not closed. Subgrid scale models are used to model the effect of the smallest eddies. Various parameters that influence the quality of a LES have to be chosen by the user like the subgrid scale model or the size of the cells that will determine the filter. They are presented in the next paragraphs.

A.2.3.1 Subgrid scales models

In LES approach, mainly two approaches can be used to deal with subgrid terms. A filtering procedure alone as presented for the LES method known as explicit filtering and an implicit filtering where additional treatment is performed. When an explicit filtering of the equations is used, there is no need for subgrid scale modeling. For implicit filtering, two approaches exist:

- implicit methods, in which the dissipation linked to the smallest scales of eddy viscosity turbulence is done by the numerical schemes :
- explicit methods, in which these terms are modeled. This kind of method is the most widely used.

Among the explicit methods, there are structural models where the subgrid flow is computed but not discussed here, the functional methods. In the explicit methods, the effect of the subgrid is held by τ_{ij}^{SGS} and q_j^{SGS} . The most common models introduce a turbulent viscosity μ_{SGS} :

$$\tau_{ij}^{SGS} = 2\mu_{SGS} \left(\frac{\partial \tilde{u}_i}{\partial x_j} + \frac{\partial \tilde{u}_j}{\partial x_i} - \frac{2}{3} \frac{\partial \tilde{u}_k}{\partial x_k} \delta_{ij} \right) \quad (\text{A.66})$$

$$q_j^{SGS} = \frac{\bar{\rho} \mu_{SGS} C_p}{P_{rSGS}} \frac{\partial \tilde{T}}{\partial x_j}. \quad (\text{A.67})$$

A.2.3.1.1 Smagorinsky model The Smagorinsky subgrid scale model [179] expresses the subgrid viscosity as:

$$\mu_{SGS} = \bar{\rho} (C_s \Delta)^2 || \tilde{S} || \quad (\text{A.68})$$

where C_s is the Smagorinsky constant and:

$$|| \tilde{S} || = \sqrt{2 \tilde{S}_{ij} \tilde{S}_{ij}}. \quad (\text{A.69})$$

Assuming that the turbulence is homogeneous, isotropic and that there is an equilibrium between the production and the dissipation of turbulence, this constant can be set to $C_s = 0.18$. But Fujiwara et al. [180] showed that near the walls, this model is too dissipative and the transition to turbulence is poorly predicted. Some authors thus use lower values for the Smagorinsky constant like Leonard et al. [181] ($C_s = 0.09$) or McMullan and Page [182] ($C_s = 0.1$). Dynamic versions of the Smagorinsky model have been proposed, like the one of Germano et al. [183] in which the value of the constant is adapted to each point of the grid mesh depending on the flow physics.

A.2.3.1.2 Wale model In the WALE model [135], the subgrid viscosity yields:

$$\mu_{SGS} = (C_w \Delta)^2 \frac{(S_{ij}^d S_{ij}^d)}{(\tilde{S}_{ij} \tilde{S}_{ij})^{\frac{5}{2}} + (S_{ij}^d S_{ij}^d)^{\frac{5}{4}}} \quad (\text{A.70})$$

with:

$$S_{ij}^d = \frac{1}{2} (\tilde{g}_{ij}^2 - g_{ij}^2) - \frac{1}{3} \delta_{ij} \tilde{g}_{kk}^2 \text{ and } \tilde{g}_{ij}^2 = \frac{\partial \tilde{u}_i}{\partial x_k} \frac{\partial \tilde{u}_k}{\partial x_j}. \quad (\text{A.71})$$

The recommended value for the WALE constant C_w is 0.5. This model is compliant with the cubic decrease of the subgrid scale viscosity μ_{SGS} with the wall distance (turbulence behavior in near-wall region).

A.2.3.1.3 Implicit LES The implicit LES does not use a subgrid scale model and assumes that the numerical dissipation is sufficient. It is sometimes called Numerical LES (NLES) [176]. If the schemes used are dissipative, the use of a subgrid scale model can lead to an overestimation of the dissipation. But if they are not, the code may be unstable. Eastwood et al. [184] studied the effect of a change of subgrid scale model on the velocity and shear stress in a jet flow. They concluded that if the code used is dissipative, the choice of the subgrid scale model has little importance and can be omitted. Indeed, as 90 % of the turbulent kinetic energy is resolved, the modeling of the other 10 % has a limited influence. This kind of method has been successfully applied to turbomachinery configurations [184, 185]. However, these results are highly dependent on the numerical schemes used. Compared to RANS simulations, the time-dependent nature of LES enables the resolution of transient flow structures since a spatial filter is applied compared to a statistical one for (U)RANS formalism. RANS and URANS simulations are also generally not capable of predicting many turbulent unsteady effects such as transition or flow separation that are generally crucial to properly describe the flow motion while possibly captured by sufficiently resolved LES.

A.3 Discretization of the equations

A.3.1 Boundary conditions

Literature is rich about the number of physical variables to be set at each boundary to close the mathematical problem. In terms of physics, two possible conditions are to be imposed in a fluid problem.

A.3.1.1 Physical boundary conditions

The physical boundary conditions are imposed to set conditions at border of the domain of the partial differential equation system. Dirichlet boundary conditions lead to set directly the solution variable value. For example, a no-slip condition imposed at wall lead to impose zero velocity at wall ($\vec{u} \cdot \vec{t} = 0$) where \vec{t} is the tangential

vector. Neumann boundary conditions lead to apply condition on the first spatial derivative of the solution variable. Using again the case of a wall, considered here as adiabatic, the heat exchange must be equal to zero that is represented by $\nabla T \cdot \vec{n} = 0$ where \vec{n} is the normal vector. Mixed boundary condition can also be used where the gradient at the wall is linked to an imposed value. For example a heat flux as the difference between wall and fluid temperature above the wall.

A.3.1.2 Permeability boundary conditions

A.3.1.2.1 Imposed quantities Numerical simulations are generally performed over a limited spatial extent compared to real configuration that induces the need to impose inlet and outlet conditions known as permeability conditions where quantities are imposed to ensure compatibility with real field. For subsonic compressible three-dimensional flows described by Navier-Stokes equations, four quantities are imposed at inlet of the domain and one quantity at outlet of the domain corresponding to the five equation of the Navier-Stokes set. In turbomachinery application, a particularly convenient set of quantities imposed is total pressure, total temperature, velocity direction at inlet and static pressure at outlet. For the lattice-Boltzmann approach with standard D3Q19 velocity discretization, the simulation is performed around a reference temperature meaning that only three quantities are to be imposed at inlet of the domain. The macroscopic quantities imposed being transformed in equivalent distribution function in the solver at the nodes corresponding to the inlet. For RANS approaches, turbulent quantities are also provided at inlet to be compliant with additional turbulence equations. An analysis of compressible Euler or Navier-Stokes set of equations shows that intrinsically physical waves are being generated and propagated in the simulation domain. A proper implementation of inlet and outlet boundary conditions taking into account wave impacting the boundary condition is generally required. In RANS approaches, the quantities at inlet and outlet can generally be imposed directly in "hard way" since only a steady state is looked for and waves have to be eliminated. No interest being given to boundary as long as steady final state can be reached. Furthermore, turbulence modeling and low order numerical schemes generally used often eliminates waves before they could reach the boundary condition. In LES or DNS approaches, the situation is generally different since the methods are unsteady meaning that no steady state is to be reached and generally high order schemes used lead to non dissipated waves in the domain that can interact with boundary conditions. Special treatments have to be applied to control wave reflections at the boundary of the computational domain. This is especially true since unwanted wave reflection can lead to the development of spurious non-physical waves propagating back in the domain. This phenomenon has several implications such as numerical instability since amplification can occur when reflected waves impact successively inlet and outlet boundary conditions or a disturbed acoustic field when acoustic quantities are looked for. These waves can also possibly being coupled with many flow mechanisms like induced boundary layer transitions that would not have happened with a proper handling of wave reflection at boundaries.

A.3.1.2.2 Navier-Stokes Characteristics Boundary Conditions (NSCBC)

The Navier-Stokes Characteristics Boundary Conditions (NSCBC) [119] provides a path to deal with spurious waves by relaxing the solutions predicted by the scheme towards the target value. This approach is based on an analysis of waves entering and exiting the domain of simulation. The determination of generated waves contained in the Navier-Stokes set of equation is based on the simpler Euler set of equations for which is analytically possible to derive the characteristics waves. The Navier-Stokes equations are not hyperbolic⁵ as Euler set of equations due to viscous term but the main approximation is to assume that waves from Navier-Stokes equations are associated only with the hyperbolic part of this set of equations. The characteristic analysis of Thompson [186] for Euler equations consists in transforming the conservative variables $\phi_{cons} = (\rho, \rho u_1, \rho u_2, \rho u_3, \rho E)^T$ into primitive variables in the reference frame (n, t_1, t_2) of the boundary condition as: $\phi_{prim} = (u_n; u_{t1}; u_{t2}; p_s; \rho)^T$, and then transforming those primitives variables into characteristics variables. Writing the set of equations for primitive variable yields to:

$$\frac{\partial \phi_{prim}}{\partial t} + \mathbf{N} \frac{\partial \phi_{prim}}{\partial n} + \mathbf{T}_1 \frac{\partial \phi_{prim}}{\partial t_1} + \mathbf{T}_2 \frac{\partial \phi_{prim}}{\partial t_2} + \mathbf{S} = 0 \quad (\text{A.72})$$

where \mathbf{N} is the normal Jacobian, T_1 and T_2 are the two tangential Jacobian along

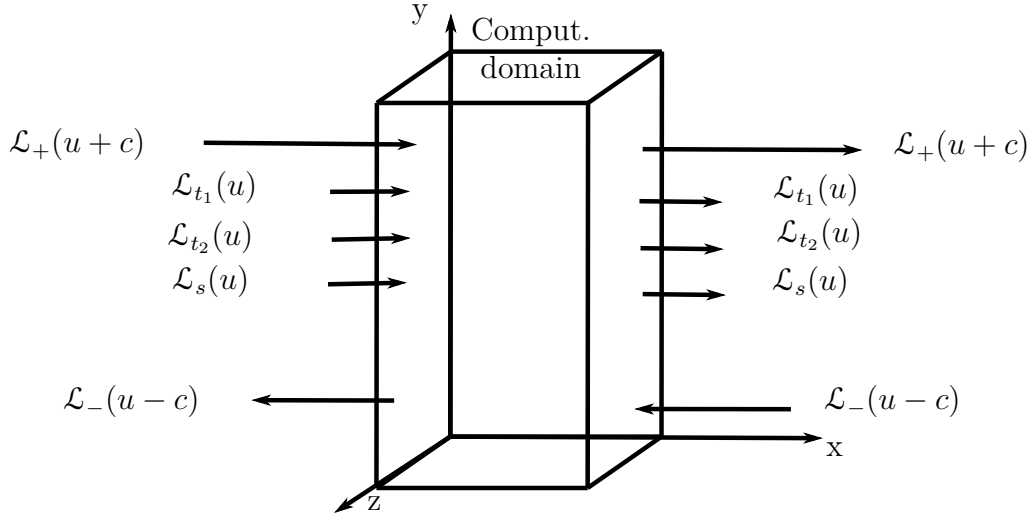


Figure A.8: Computational domain with incoming and outgoing waves at the inlet and outlet of the domain

t_1 and t_2 , and \mathbf{S} is the diffusion term. The transformation into the characteristics variables consists in diagonalizing the Jacobian \mathbf{N} and the corresponding singular

⁵The Navier-Stokes equations have a parabolic character because there is a non-zero diffusion term. But, in reality, we say that equations are "hyperbolic" when we mean that they are advection dominated, and "parabolic" when they are diffusion dominated, and the Navier-Stokes equations can be either one or the other depending on whether your Reynolds number is large or small. In current applications encountered, the Reynolds is generally large meaning close to hyperbolic set of equation

eigenvalues are the characteristic waves:

$$\begin{pmatrix} \mathcal{L}_+ \\ \mathcal{L}_- \\ \mathcal{L}_{t_1} \\ \mathcal{L}_{t_2} \\ \mathcal{L}_S \end{pmatrix} = \begin{pmatrix} (u_n + c) \left(\frac{\partial u_n}{\partial n} + \frac{1}{\rho c} \frac{\partial p_s}{\partial n} \right) \\ (u_n - c) \left(-\frac{\partial u_n}{\partial n} + \frac{1}{\rho c} \frac{\partial p_s}{\partial n} \right) \\ u_n \frac{\partial u_{t_1}}{\partial n} \\ u_n \frac{\partial u_{t_2}}{\partial n} \\ u_n \left(\frac{\partial \rho}{\partial n} - \frac{1}{c^2} \frac{\partial p_s}{\partial n} \right) \end{pmatrix} \quad (\text{A.73})$$

where \mathcal{L}_+ and \mathcal{L}_- are respectively the inward and the outward acoustic waves, \mathcal{L}_{t_1} and \mathcal{L}_{t_2} are transverse shear stress waves, and \mathcal{L}_S is the entropic wave (see Fig. A.8). The NSCBC strategy proposed by Poinso and Lele [119] consists in considering a Locally One-Dimensional Inviscid (LODI) flow on the boundary to specify the amplitude of ingoing waves. The characteristic system for the Navier-Stokes equations becomes (LODI relations):

$$\begin{aligned} \frac{\partial p}{\partial t} + \left(\mathcal{L}_S + \frac{\rho c}{2} (\mathcal{L}_+ + \mathcal{L}_-) \right) &= 0 \\ \frac{\partial p_s}{\partial t} + \frac{\rho c}{2} (\mathcal{L}_+ + \mathcal{L}_-) &= 0 \\ \frac{\partial u_n}{\partial t} + \frac{1}{2} (\mathcal{L}_+ - \mathcal{L}_-) &= 0 \\ \frac{\partial u_{t_1}}{\partial t} + \mathcal{L}_{t_2} &= 0 \\ \frac{\partial u_{t_2}}{\partial t} + \mathcal{L}_{t_1} &= 0 \end{aligned} \quad . \quad (\text{A.74})$$

Waves amplitudes are deduced using LODI relations, and then used on the boundary in equation eq.(A.72) to advance the solution in time. The equations presented before concerns imposing primitive variables. When the objective is to impose p_{tot} , T_{tot} and flow direction at inlet using NSCBC, it requires to express LODI equations for p_{tot} and T_{tot} . This can be done by some algebra and can be written for total pressure for example as (the demonstration can be find in Odier et al. [187]):

$$\begin{aligned} \frac{\partial p_{tot}}{\partial t} &= \mathcal{L}_+ \left(-\frac{\rho c}{2} \frac{p_{tot}}{p} + \frac{p_{tot}}{r T_{tot}} \left(\frac{\beta e_c}{2c} - \frac{u_n}{2} \right) \right) + \mathcal{L}_- \left(-\frac{\rho c}{2} \frac{p_{tot}}{p} + \frac{p_{tot}}{r T_{tot}} \left(\frac{\beta e_c}{2c} + \frac{u_n}{2} \right) \right) \\ &\quad - \mathcal{L}_{t_1} u_{t_1} \cdot \frac{p_{tot}}{r T_{tot}} - \mathcal{L}_{t_2} u_{t_2} \cdot \frac{p_{tot}}{r T_{tot}} - \frac{e_c}{\rho} \cdot \mathcal{L}_S \cdot \frac{p_{tot}}{r T_{tot}}. \end{aligned} \quad (\text{A.75})$$

A well-characterized drawback of characteristic methods is that they allow drifts of mean values which requires a modification of the baseline theory. In order to avoid experiencing a "drift" between the target value and the computed one, several authors have proposed linear relaxation methods. For a linear relaxation method, the temporal derivative of any quantity ϕ to be imposed at boundary is:

$$\frac{\partial \phi}{\partial t} = -\sigma_\phi (\phi_{predicted} - \phi_{target}) \quad (\text{A.76})$$

where σ_ϕ is a relaxation coefficient needed to be chosen by the user, $\phi_{predicted}$ predicted is the value of the variable ϕ predicted by the numerical scheme, and ϕ_{target}

is the target value imposed in the boundary condition. Non zero values of σ_ϕ lead to a boundary which is no longer non reflecting but partially non reflecting. In turbomachinery application, the value of σ_ϕ is generally set low at the beginning of the simulation then progressively increased to force the boundary condition to target the imposed condition. NSCBC condition can sometimes be not sufficient to prevent wave reflection for example when an outlet condition is set close to blade trailing edge and pressure waves emanating from trailing shed vortex process can impact the boundary. In this situation, sponge layers can be added that are limited areas of the domain, generally where the flow is not of interest where the artificial viscosity is set higher to dissipate waves. Sponge layers are often use close to inlet and outlet boundary conditions [188].

A.3.1.3 Turbulence injection

The incoming flow in a gas turbine can have relatively high free stream turbulence for example for a high-pressure turbine facing the flow from a combustion chamber or any row facing incoming waves from upstream rows. Turbulence injection consists in injecting fluctuation superimposed to the mean quantities at inlet of the domain. The transient and fidelity according to physical behavior of the flow at inlet requires fluctuations injection as stated by McMullan and Page [182]. The account for turbulence injection in the NSCBC can be made by adding unsteady velocity components (u_1, u_2, u_3) to the characteristic waves:

$$\mathcal{L}_{+turb} = \mathcal{L}_+ + \frac{\partial u'_1}{\partial t} \quad \mathcal{L}_{t_1turb} = \mathcal{L}_{t_1} + \frac{\partial u'_2}{\partial t} \quad \mathcal{L}_{t_2turb} = \mathcal{L}_{t_2} + \frac{\partial u'_3}{\partial t}. \quad (\text{A.77})$$

Unsteady field applied is mainly characterized by the fluctuation intensity, the characteristic turbulence spectrum and possible intermittency of turbulence for example when an upstream wake impacts periodically a downstream blade. These three characteristics are of primary importance and can widely influence the dissipation rates in the flow field as well as the state of the boundary layer developing on the wetted surface under a bypass mechanism as stated by Matsuura [185] et al., Gourdain et al. [2] and Segui Troth [144]. Turbulence intensity also influences the boundary layer state as described in Sec. 2.2.2 and 2.2.6. Turbulence intensity corresponds to the rate between the fluctuating velocity injected u' and mean velocity u :

$$T_u = u' / u \quad (\text{A.78})$$

Turbulence injection methods aim at imposing the proper fluctuating field according to the specific application at the inlet of the domain. A common expectation of these different methods is the ability to replicate a turbulence cascade spectrum. Different methods for turbulence injection have been proposed:

- Synthetic type injection methods [189] that require some adaptation distance to develop a physical energy spectrum;
- rescaling methods [190] that use the flow at the outlet of the domain. Using various processing especially a rescaling of the boundary layer thickness, the boundary layer profile is injected back to the inlet;

- precursor methods [144] that consists in performing an additional simulation with the same code then to couple it with the inlet of the domain.

The turbulence injection methods add to the difficulty of having an adequate boundary condition implementation (especially noise generation at inlet), an adequate grid resolution and numerical scheme able to transport the turbulent structures without being dissipated along the domain. A comprehensive review of the different turbulent injection methods is given by Dhamankar et al. [191].

A.3.2 Meshing strategy

Geometrical features as well as mesh grid quality and refinement are the most important elements of LES. The use of different numerical parameters (convection, temporal schemes, turbulence modeling/subgrid scale model) may lead to different solution for different meshes, more accurate results being reached for higher order schemes. However, a high-order scheme over an under resolved mesh in near wall region or without sufficiently fine cells to capture the structures of interest in the simulation will not provide the correct physics. An important aspect of the meshing strategy concerns the way the code will access the information stored at each degree of freedom. It generally defines two type of mesh approaches.

A.3.2.1 Structured mesh

The mesh has an implicit regular connectivity with a direct data addressing. The main strength of this meshing strategy is the possibility to construct high order schemes since neighbouring cells can be readily known. The main drawback of this meshing strategy is the difficulty to tackle complex geometry which in gas turbine context often limit the use to the meshing of mainstreams. In addition, the human time required to generate the mesh can be important (see Fig. A.9b).

A.3.2.2 Unstructured mesh

This approach is more computational demanding since it requires to read an irregular connectivity table to exchange data between elements compared to the direct addressing in structured mesh. The main advantage of this approach is the possibility to address complex geometries, especially technological effects in a gas turbine context. In addition, the human time required to generate mesh can be lower thanks to partially automatic mesh generation and local mesh refinements capability to better capture some region of the domain. Unstructured mesh makes possible to use several types of elements with in particular the use of prisms layer in near-wall region to resolve properly boundary layer and tetrahedra in the remaining domain (see Fig. A.9a)

A.3.2.3 Grid requirements

The mesh sensitivity is generally higher for LES than for (U)RANS simulations as stated by Gomar et al. [192]. One key feature is that for under-resolved LES, gradients in near-wall region can be poorly predicted and Eastwood et al. [184] showed

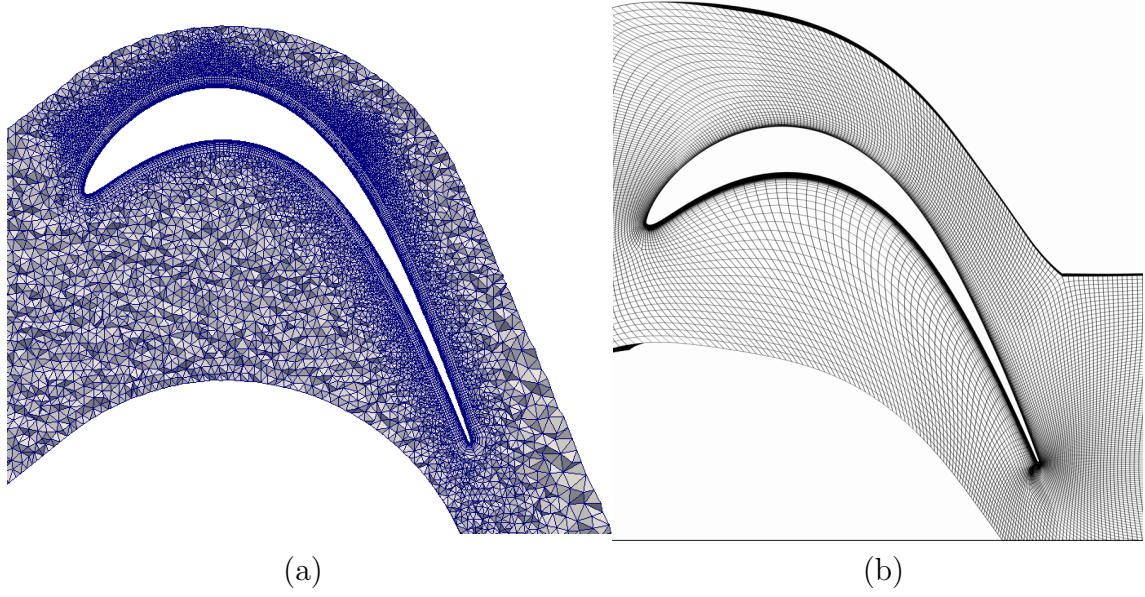


Figure A.9: Hybrid (a) and structured meshes (b) around a low pressure turbine blade at mid-span

that hybrid LES can help to recover a more accurate near wall region flow than pure LES. Within an extensive study of the different configurations and simulations performed in the context of hybrid LES and pure LES, Tucker et al. [122] proposed an estimation of the number of points according to the Reynolds number based on the chord Re_c required to discretize one blade passage for a wall-resolved LES simulation separated between the inner boundary layer ($y^+ < 100$, red long dashed lines in Fig. A.10a) and the outer boundary layer ($y^+ > 100$, green short dashed lines in Fig. A.10a). y^+ is the non-dimensional wall distance for a wall-bounded flow that can be expressed as $y^+ = u_\tau y / \nu$ where u_τ is the friction velocity at the wall. For low pressure turbine where Reynolds numbers based on axial chord are commonly around 100 000, the inner boundary layer is not dominant and the number of points required can be given by $N = 3000 \times u/c \times Re_c^{0.4}$. For high pressure turbine and compressors, the inner boundary layer becomes dominant and the number of points required scales towards $N = 5 \times 10^{-4} \times u/c \times Re_c^{1.8}$. Due to high computational cost in these kinds of configurations, geometries are generally simplified (without technological effects) and/or use methods to reduce the cost in near-wall region by using wall model [125], hybrid RANS-LES methods [193] or by a reduction of computational domain (reduction of blade number, chorochronic periodic conditions [194]). Low pressure turbines are characterized by very different flow region where the dominant scales are different in near wall region, wakes and free stream as stated by Cui et al. [76]. In free stream region, acoustic waves induce fluctuation in compressible simulation. The mesh must be able to transport incoming wakes if an upstream cascade is considered or incoming turbulence. In experiments, turbulence is generally generated with an upstream grid and can be seen as a decaying turbulence approaching the blade which have been strongly investigated [196]. Figure A.10b shows typical turbulence cascade obtained from two levels of grid refinement compared to a theoretical turbulence cascade. Close to the blade, flow conditions are

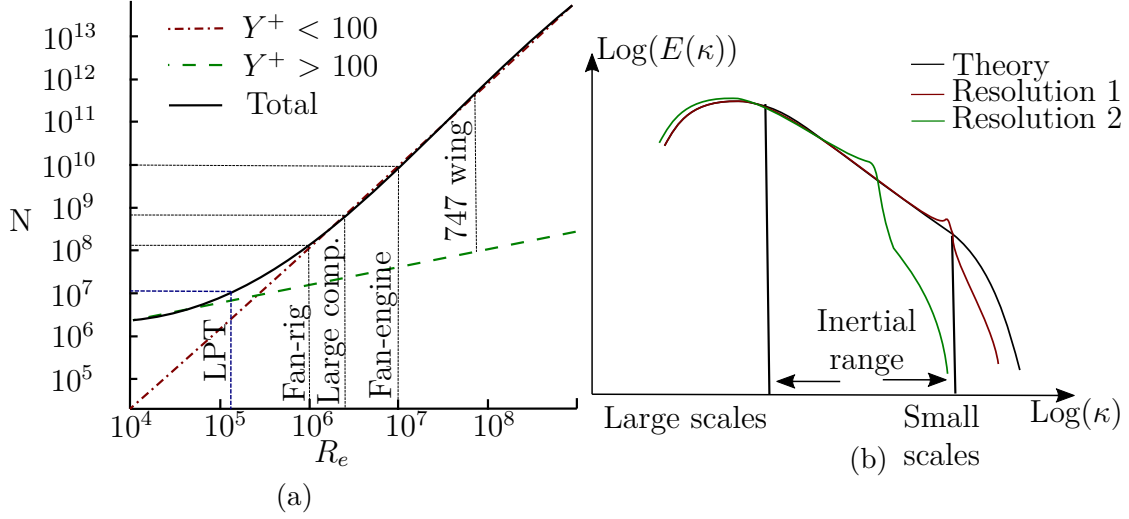


Figure A.10: Grid requirements for LES and hybrid RANS-LES following Piomelli and Balaras [195] and adapted from Tucker [158] (a). Sketch of the influence of the grid resolution on the theoretical turbulence cascade (b)

considerably different. The boundary layer is initially laminar but can be influenced by continuous free stream turbulence or intermittent upstream wakes that requires a sufficient resolution to correctly account to the forcing fluctuations onto the boundary layer. Since the flow around a blade can be seen in a simplified sight as a flat plate with adverse pressure gradient subject to upstream disturbances, the first grid quality requirements have emanated from this kind of configuration. and especially similarly to the turbulent boundary layer directly after transition. However, the Reynolds number are generally relatively low compared to these canonical configuration and partially explain why mesh grid requirements are coarsened compared to boundary layer or channel studies $s^+ \leq 5-10$; $n^+ \leq 0.5$; $6 \leq r^+ \leq 15$. These requirements are supposed to make possible to capture the streamwise aligned structures known as streaks that make a more stringent resolution in wall normal and spanwise direction.

In the wake region, the situation is supposed to be similar to the free-stream region, especially in fully developed wake at sufficiently large Reynolds number where turbulent cascade is to be recovered [197]. For the wake region close to thick blade trailing edge, vortex shedding can take place and will lead to turbulence production and redistribution of turbulent kinetic energy in the wake. The small structures are assumed to be influenced by large scales streaks that have developed in the blade boundary layer that have lost their streamwise orientation at the blade trailing edge [198].

A.3.3 Numerical parameters and flow solvers

A.3.3.1 elsA code

The solver used to perform RANS simulations and part of the LES simulations of the various configurations is the elsA (*Ensemble Logiciel de Simulation Numérique*)

software from ONERA. This software solves the compressible Navier-Stokes equations on structured-multi block mesh [120]. This single calculation code is able to solve internal and external, viscous and non-viscous as well as steady or unsteady flows. Perfect and real gas at equilibrium, low to hypersonic speeds can be solved by the code. For turbulent flows, RANS and LES versions are available. The account for complex geometry has been more recently tackled with hybrid (coexistence of structured and unstructured area) and chimera methods implemented. Thermal and aero-elastic coupling of fluid with structure is also available [199]. More specifically for turbomachine applications, mixing plane and frozen rotor for RANS simulations have been implemented at interface between static and rotating part. No match sliding mesh as well as chorochronic conditions [200] have also been developed for URANS/LES approaches.

A.3.3.2 AVBP code

The AVBP code is developed conjointly by CERFACS and IFPEN and is used in this thesis for LES simulation of the linear and annular cascade. This unstructured code is used both for basic research and applied research of industrial interest [201] with capability in combustion simulation. This parallel code solves the full compressible Navier-Stokes equations using a finite-element scheme TTGC [136] based on a two-step Taylor-Galerkin formulation or Lax-Wendroff from finite volume approaches. It relies on a cell-vertex formalism and schemes [202] specifically designed for LES on multi-element meshes (prisms, tetraedra and pyramids). The low diffusion and low dispersion properties of this explicit solver makes it suitable for LES by providing third order space and time accuracy for TTG scheme. The subgrid scale model available are the Smagorinsky, WALE [135] and Sigma models. For turbomachine applications, the simulation domain is split between static and rotating instances onto which the AVBP code solves the equations separately. Rotating and static instances transfer information in overlapping regions, the two instances being synchronous at each time step [203].

A.3.3.3 Pro-LB code

Pro-LB software, the code based on the lattice-Boltzmann Method, has been developed in a consortium of industrial companies (Renault, Airbus, CS), academic laboratories (Aix-Marseille University, École Centrale de Lyon, Laboratoire de Mathématiques d'Orsay) and partnerships with others entities (CERFACS, ONERA, Alstom, GANTHA, Matelys, Kalray) in two successive projects, namely, LaBS (2011-2014) and CLIMB (2015-2018) projects. This code relies on a D3Q19 particle velocity lattice. The particle populations are projected on a hermite base before the collision step for stability and accuracy purposes called regularized BGK [204]. Unstructured isotropic cells (known as octree) are used to discretized the domain (non body-fitted) in conjunction with grid refinement technique [205] for a better account of regions with strong gradients. Turbulence modeling is handled similarly to more classical Navier-Stokes large eddy simulation solvers [178], using either a dedicated subgrid scale model (the Shear Improved Smagorinsky Model SISM [206]) or model based on an explicit high-order selective spatial filtering that have shown good behaviour

in LES of incompressible wall-bounded flows [138]. Due to mesh isotropy and possible high Reynolds number, a wall law is available accounting for adverse pressure gradient and curvature effects.

The sources of loss and a method to track loss generation based on exergy/entropy were described in Sec. 3. From a numerical point of view, the analysis of the flow field and the application of this method requires a proper assessment of numerical convergence of the simulation. When converged, the data are generally reduced temporally for unsteady methods and spatially to be properly analysed. Next section will be devoted to describe these different notions.

A.4 Numerical convergence

This section introduces methods available in the literature to assess numerical convergence of a simulation. As first step, convergence methods for RANS formalism are introduced followed by convergence criteria for LES simulations.

A.4.1 RANS

A general convergence criterion has been proposed by Casey and Wintergerste [207] stating that a steady simulation can be considered as numerically converged if the following criteria are fulfilled:

- decrease of equations residuals of at least three order of magnitude, and stabilization;
- discrepancy between inlet and outlet mass flow rate lower than 0.1 %;
- the main global quantities of interest are stabilized (mass flow rate, expansion ratio, efficiency).

This criterion states on the numerical convergence of the simulation. The physical convergence of the phenomena in the simulation domain is generally strongly related to the numerical one. However, some studies of turbine annulus flows including the cavities have been shown to fulfil all three criterion for numerical convergence while not all the structures into the cavities had reached their steady state. Therefore, special attention have to be taken in the regions of the simulation domain where the physical convergence of the flow is generally slow compared to the mainstream one.

A.4.2 LES

For unsteady simulation, a general method used to assess the numerical convergence is based on a characteristic time of the simulation. This characteristic time (sometimes referred as "flow through" time) is based on a characteristic length scale of the domain L that can be the domain size or blade length for gas turbine application and a convection velocity u_0 . The characteristic time is then set to $t_{character.} = L/u_0$. Empirical values of flow through time are then generally proposed in each field of study above which the simulation has been considered to numerically converged.

Similarly to steady simulation, the convergence can also be assessed looking at the convergence of one-dimensional quantities like mass flow, efficiency or pressure ratio. These quantities are generally fluctuating in time but oscillation around a mean value can generally be obtained. More rigorous criteria have been proposed especially by Ahmed and Barber [208] stating that an unsteady simulation is numerically converged if physical frequencies emerge in the simulation and if these frequencies dominate when performing a Fourier transform. This process can be performed by setting different probes at different location in the simulation domain (in blade boundary layer, blade wake, etc.). Based on the analysis of Ahmed and Barber, Clark and Grover [209] have proposed another criterion based on several convergence criteria to be fulfilled:

- average convergence of the signal;
- amplitude convergence of the physical frequencies,
- phase convergence of the signal;
- correlation of two successive signals, especially over two blade period/revolution when dealing with gas turbine;
- convergence of the ratio between the power spectral density at the frequency of interest and the integral of the power spectral density.

This criterion gives a more accurate meaning to the numerical convergence but can remain difficult to apply since the frequencies of the phenomena in the simulation domain are scarcely known except some physical phenomena like trailing shed vortex process, Kelvin-Helmholtz instability that can be estimated analytically. Numerical convergence in unsteady simulation is strongly related to the quantity of interest to be extracted. The time of convergence generally needs to be increased when looking at higher moments of the flow field (mean quantities, fluctuations, skewness, kurtosis, etc.). When dealing with turbine flows where the cavities are taken into account, special care has to be taken regarding the convergence of the flow in the cavity since the dynamic is generally different than the mainstream one. More information on the convergence of the flow in turbine cavities is provided in Sec. 4.4.1.1.

A.5 Reducing information by averaging

In their general form, data extracted from turbomachine numerical simulations are unsteady non-uniform field for URANS or LES approaches and non-uniform field for RANS approach. Non-uniformities in the flow field emerge from different sources like blade-nozzle guide vane imposed field, boundary layer effects, inlet conditions like distortion or non-uniform flow exiting the combustion chamber. Similarly, the flow in a turbomachine is intrinsically unsteady due to relative motion or rotor-stator blade row, turbulence. A more detailed description of unsteadiness in gas turbine is proposed in Sec. 2.2.1. On the other hand, the assessment of component performance (pressure ratio, efficiency) are generally based on single values of pressure and temperature at inlet and outlet. Moreover, the analysis of the thermodynamic

cycle normally uses single values for pressure and temperature at different stations in the engine. The way that the non-uniform flow is represented by single values of temperature and pressure is, therefore, of considerable importance. Without reducing until zero-dimensional data, the analysis or comparison of data generally needs a dimension reduction of data from $\mathbb{R}^3 \times \mathbb{R}^+$ for LES/URANS or \mathbb{R}^3 data for RANS to lower dimension. Among the information reduction processes commonly used in turbomachine, temporally averaged solutions are used to exhibit the main features of the flow field or azimuthal averaging of axial planes to obtain one-dimensional radial evolution of some quantities of interest like the pressure loss downstream a blade row. The averaging procedure is generally performed in the scope to compare against experimental data, study a physical phenomenon in the simulated domain or for parametric studies over geometrical or physical parameters. It has generally been assumed that there must be a correct method of averaging that will be universally valid. Unfortunately, it does not seem to be the case at current state of knowledge. Whenever a dimension decrease is operated by averaging process, information is necessarily discarded. However, it is generally accepted that there is an appropriate method for each application that is not a matter of choice or preference. In the framework of this study, averaging procedure will be introduced with special attention to total pressure and temperature quantities with the use of the work average method since suitable for turbine components. Between temporal and spatial averaging, some differences exist especially since spatial averaging is to be performed onto a unique simulation domain solution while temporal one is based on a number of instantaneous solution distributed over a certain range of time. The number of instantaneous solution and time interval over which data are extracted are crucial parameters to ensure correct averaging known as statistical convergence and will be depicted in this section. A paragraph is devoted to the temporal averaging procedure where former rules introduced are generally not to be circumvented but performed as close as possible to the experimental procedure. It remains that temporal and spatial averaging face the problem of the quantities that are to be averaged to be compliant as close as possible with full solution/data and make correct assessment with averaged field. This common issue for temporal and spatial averaging is tackled at the end of the section.

A.5.1 Statistical convergence

The extraction of instantaneous data (or statistics) to perform temporal averaging can be performed when the numerical convergence of the simulation has been assessed according to convergence criteria proposed in previous Sec. A.4 for example. When dealing with temporal (statistical) convergence of the time evolving flow field, mainly three parameters have to be taken into account. The time interval over which the data extraction have to be performed, the number of snapshots to be extracted during this time interval and the quantity to be extracted. We first propose to deal with the two first requirements.

In gas turbine numerical simulations, the time step for the unsteady simulation is generally low with a cost per time step that is generally high due to mesh size, numerical schemes. A main consequence is that the physical time simulated and

consequently the available time of data extraction is low and a proper analysis of the physical time required to extract data has to be done. The gas turbine flow field can be split in steady contributions, for example an attached boundary layer over a blade without upstream variations and unsteady contributions that can be horse shoe vortex process, trailing shed vortex, turbulence, beating separation bubble or related to the relative motion of stator and rotor. The averaging procedure will mainly depends on the quantity that is looked for and unsteady phenomena influencing this quantity. To be more relevant, the example of pressure loss downstream a

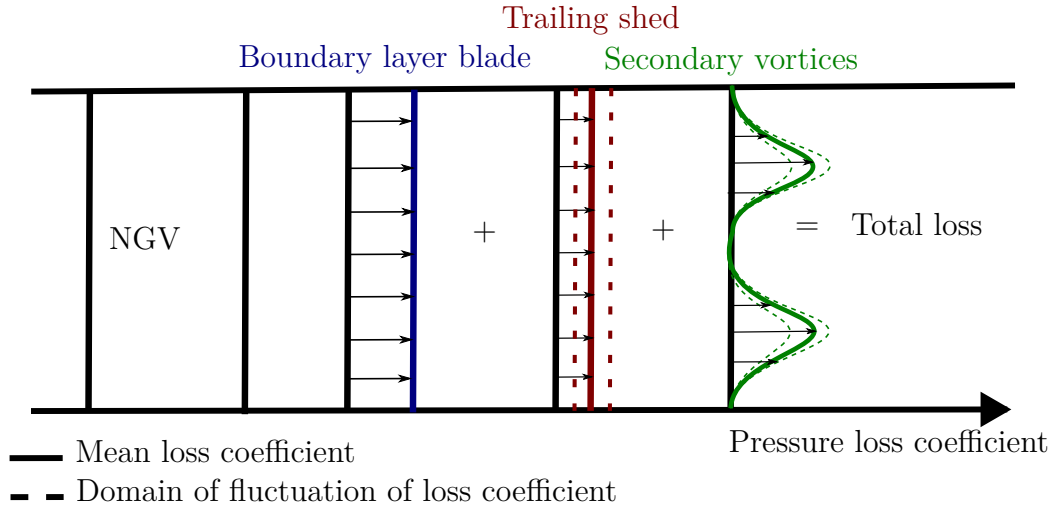


Figure A.11: Decomposition of the sources of pressure loss downstream of a blade in a simplified configuration

Nozzle Guide Vane or the one presented in Chap.3 is taken here (see Fig. A.11). For the sake of simplicity we consider that pressure loss downstream blade are mainly due to three contributions. A first contribution that is due to the boundary layer developing around the blade generating pressure loss due to wall normal velocity gradient close to the wall. We consider here that this contribution is steady, meaning no separation or unsteady phenomena (contribution in blue). From the statistical sight the mean contribution is the same as one snapshot. The second contribution is the trailing shed vortex process downstream blade that induces pressure loss under turbulent mixing process and is an unsteady phenomenon (contribution in red). The third effect is the formation of the passage vortex in blade passage that generates loss downstream blade by mixing process. The passage vortex beats at a frequency related to horse shoe vortex phenomenon and induces variation of pressure loss meaning that this phenomenon is unsteady (contribution in green). If one is interested in the contribution of trailing shed vortex process to downstream pressure loss, the time interval over which the data will be extracted will be lower than the corresponding to horse shoe vortex process. This is due to the fact that trailing shed vortex process is made at higher frequency than horse shoe vortex process. A lower amount of time is then required to obtain a representative amount of occurrences to build the statistic. However, if one is interested to have an average total pressure loss downstream blade taking into account all the unsteady effects, the time interval onto which statistics can be collected will be lower bounded by the lowest

frequencies with substantial energy, that is for this example, the horse shoe vortex process. From practical point of view, a good assessment of the time required to make the temporal mean can be done by comparing the temporally averaged solution of contiguous subsequent time intervals. When the same mean results is obtained over these time intervals, the solution can be considered as time converged or statistically converged. Related to this notion of time interval is the number of snapshots to be extracted during the time interval obtained. On one hand, if the data to be stored is not demanding from a storage point of view, snapshots can be performed at any time step. On the other hand, if the data requires strong storage resources, common values of snapshots to be extracted are in the order of magnitude of a hundred equally spread over the time interval of the phenomenon of interest. In the context of rotating configuration, the passage or rotation phase-locked averaging is commonly used to capture the flow field in a passage or a full rotation. This temporal averaging is performed by averaging the flow at any time interval Δt corresponding to the time necessary to turn of one passage of rotation. It is to be noticed that these different temporal averaging (ensemble, mass or phase) are only able to isolate the deterministic contribution. Despite temporal averaging that are generally performed to analyse the flow field, the unsteady content can have significant contribution to the flow field as stated by Lengani et al. [62] that proposed a Proper Orthogonal Decomposition (POD) storage to take account of unsteady effects onto a low-pressure turbine configuration. In addition to time interval and number of snapshots to be extracted in order to obtain a temporally averaged solution, the data to be extracted is an important issue since it can strongly affect the solution and analysis made over the temporally averaged solution.

A.5.2 Temporal averaging: the comparison against experiment

When numerical data can be compared against experiments, the averaging procedure should be as close as possible to the experimental one. The averaging is to be made on the same variable as the one measured by experiment. Area averaging is widely used for a practical reason, it is very often the best and only procedure available for averaging a limited number of pressure probes and thermocouples buried in an engine. For example, if static pressure is measured with a pressure tap, static pressure obtained numerically should be averaged, taking into account eventual experimental filtering. Since numerical solvers store generally conservative quantities (ρ , ρu , ρv , ρw , ρE), the temporal averaging process should not be made onto conservative quantities to extract temporal averaged pressure from these averaged conservative quantities. The frequency to extract data over time should be as close as possible to the one used in the experiments. Numerical simulations have generally low time step and same frequency as in the experiments can be chosen even for high frequency acquisition. However, the number of snapshots extracted must be high enough to have a statistically converged quantity which is generally more feasible from an experimental point of view since the available time of extraction is generally high compared to numerical simulation time.

It remains true today that in engine experimental data, there is frequently little

scope to average the data in any way more than a crude area averaging. Very often, the biggest inaccuracy of uncertainty comes from assumption necessary to extrapolate data close to walls. The advent of numerical simulations has led to a new need for averaging output and ample opportunity to select the correct averaging technique since in principle all the variables of the flow are available in greater density of coverage than in common experiments.

A.5.3 Quantities to be temporally and spatially averaged

When numerical results are not compared against experiments, the averaging process is generally performed to be as coherent as possible with the conservation of quantities over the considered domain between the averaged and initial raw solution. These are generally conservative quantities solution of a transport equation: ρ , ρu , ρv , ρw , ρE from Navier-Stokes equations written in conservative form⁶, ρh_{tot} and ρs . For example when one want to average the axial velocity component, a possible averaging process is

$$\langle u \rangle = \frac{\langle \rho u \rangle}{\langle \rho \rangle} \quad (\text{A.79})$$

where $\langle . \rangle$ is either temporal, spatial or both averaging operator. This averaging procedure ensure a conservation of axial momentum and mass between initial and averaged field in the case of a spatial averaging. In the case of a temporal averaging, the mean solution conserves mean axial momentum and mean mass between snapshots and time averaged field. Another averaging procedure could have been applied to conserve some other quantities. This averaging procedure seems preferential to a simple surface averaging where axial velocity is conserved which has no really physical meaning and rational basis. However, no universal averaging procedure can be found due to a loss of information in the averaging process. This observation has led to the development of averaging process "for a purpose" introduced by Cumpsty and Horlock [210] which mean that the averaging procedure will be performed in the scope to conserve some quantities of interest while some other quantities will not be conserved. A special attention is to be given to total pressure and temperature that are crucial quantities in turbomachinery since they are often used in the assessments of component performance and for thermodynamic cycle analysis. Furthermore, for a pure substance, such as air or combustion products of a particular chemical composition, all the gas properties may be obtained if two independent intensive⁷ properties are known, the two-property rule. In the context

⁶The structured and unstructured codes used during this thesis are based on a finite volume approach on which the equations are solved in their conservative form. For the LES-LBM approach the conservative equations are reconstructed from the velocity distribution functions.

⁷Physical properties of the fluid can often be categorized as being either intensive or extensive, according to how the property changes when the size (or extent) of the system changes. An intensive property means that it is a local physical property of a system that does not depend on the system size or the amount of material in the system (p, T, ρ , etc.). An extensive property means the system could be divided into any number of subsystems, and the extensive property measured for each subsystem; the value of the property for the system would be the sum of the property for each subsystem (m, V, e, S, etc.).

of turbomachine, total pressure and temperature are usual to represent these two independent properties. Since the quantities of interest are generally different between the components of a turbomachine several averaging procedure for these two quantities have been proposed for the different components of a turbomachine. A complete and detailed averaging procedure depending on the quantities to be conserved is proposed by Cumpsty and Horlock [210]. In the case of compressor/turbine, the interest is generally given to work input/output, pressure ratio and efficiency. Given an unsteady non-uniform flow and equivalent steady uniform flow that conserve mass, energy and generate the same amount of work over the interval Δt is looked for by a proper averaging of total temperature and pressure. Normally the appropriate average for stagnation temperature is the mass-average, since this gives the correct value of enthalpy flux, according to ideal-gas assumptions where total temperature is proportional to total enthalpy that is a convected quantity. This leads to apply mass averaged procedure when either time, space or both averaging must be performed for total temperature, These operations can be equally permuted (i.e performing spatial or temporal averaging first is equivalent). This statement can be expressed as:

$$\langle T_{tot} \rangle = \frac{\langle \rho T_{tot} \rangle}{\langle \rho \rangle} \quad (\text{A.80})$$

where $\langle . \rangle$ is either temporal, spatial or both averaging operator.

This last process makes possible to conserve mass and total enthalpy between the initial and space averaged quantity that together define the heat and shaft work exchanges with a fluid system that is to be conserved during the averaging. In the case of a temporal averaging, the mean solution conserves mean mass and mean total enthalpy between snapshots and time averaged field. For stagnation pressure, to fix the state of the substitute flow, we can obtain an appropriate averaging by following the derivation for work averaged pressure in steady flows from Cumpsty and Horlock [210]. Similarly to the mass averaging for total temperature, an equivalent total pressure is sought that will give the correct work input or output when the flow leaves an ideal turbine at a uniform outlet pressure. The basis of the approach is to consider flow non-uniformity by a two stream flow with conditions (P_a, T_a) and (P_b, T_b) mixed to a uniform pressure. This leads to the following expression for total pressure P_{tot}^{wa} obtained from the spatial averaging performed here over surface A:

$$p_{tot}^{wa} = \left[\frac{\int T_{tot} \rho u dA}{\int T_{tot} / p_{tot}^{\frac{\gamma-1}{\gamma}} d\rho u dA} \right]^{\frac{\gamma}{\gamma-1}} \quad (\text{A.81})$$

A.5.4 Performance quantities

As stated, the temporal and spatial averaging are common practices in turbomachine to obtain zero-dimensional quantities by an averaging process on axial planes across the turbomachine. The components of a gas turbine are generally studied separately over contiguous domains that are bounded by axial planes. In a turbine, the quantities that are commonly to be estimated are the following quantities:

- the power extracted to the fluid \dot{W} (under ideal gas law assumption):

$$\dot{W} = h_{tot,in} - h_{tot,out} = c_p \dot{m} (T_{tot,in} - T_{tot,out}) \quad (\text{A.82})$$

- the expansion ratio Π

$$\Pi_{tot-tot} = \frac{p_{tot,in}}{p_{tot,out}} \quad \Pi_{tot-sta} = \frac{p_{tot,in}}{p_{out}} \quad \Pi_{sta-t} = \frac{p_{in}}{p_{tot,out}} \quad \Pi_{sta-sta} = \frac{p_{in}}{p_{out}} \quad (\text{A.83})$$

- the efficiency that compares actual work to an hypothetical ideal work subscripted is. The efficiency can be both for cascade, blade row or full stage. Similarly to expansion ratio, the efficiency can be defined in terms of static to static quantities generally used for nozzles $\eta_{sta-sta}$ where actual increase in kinetic energy is compared to ideal increase. The total-to-static efficiency $\eta_{tot-sta}$ that compares the actual exit kinetic energy with the ideal exit kinetic energy. The full stage efficiency generally expressed in terms of total-to-total efficiency $\eta_{tot-tot}$ based on entry and exit total conditions:

$$\eta_{sta-sta} = \frac{h_{in} - h_{out}}{h_{in} - h_{out,is}} \quad \eta_{tot-sta} = \frac{h_{tot,in} - h_{out}}{h_{tot,in} - h_{out,is}} \quad \eta_{tot-tot} = \frac{h_{tot,in} - h_{tot,out}}{h_{tot,in} - h_{tot,out,is}} \quad (\text{A.84})$$

Total-to-total efficiency can be written in terms of total pressure and temperature as:

$$\eta_{is} = \frac{T_{tot,in} - T_{tot,out}}{T_{tot,in} \left[1 - \left(\frac{p_{tot,out}}{p_{tot,in}} \right)^{\frac{\gamma-1}{\gamma}} \right]}. \quad (\text{A.85})$$

These quantities makes possible to asses the performance of the considered component and compare different designs of turbine. When one want to characterize the whole engine, data about power transfer, pressure ratio or efficiency of the component are generally linked together to determine whole performance of the engine. For example when one want to assess the isotropic efficiency of a two-stage low pressure turbine $\eta_{is,2 \text{ stage}}$ with stage 1 at isotropic efficiency $\eta_{is,1}$ and stage 2 at isotropic efficiency $\eta_{is,2}$, the efficiency of the two-stage component is $\eta_{is,2 \text{ stage}} = \eta_{is,1} \times \eta_{is,2}$. The definitions given for performance quantities are related to uncooled turbine. When dealing with secondary flow influence that is a particular case for turbine cooling as in current study, some ambiguity can emerge especially in the definition of efficiency where actual power is compared against a hypothetical ideal process. The use of efficiency definition for uncooled turbine may lead to unproper conclusion. Indeed, additional energy is provided by purge flow to the flow between inlet and outlet of the domain that may increase actual work and as a consequence efficiency while some additional defficiency could have been induced by purge but not seen in the efficiency. An other difficulty in the defintition of efficiency with several streams is the choice of the hypothetical process for the mixing of these differents streams. Indeed, the possible mixing processes are non-unique and influence the resulting

efficiency. Among the first efficiency definitions for cooled turbine was proposed by Hartsel [211] for stationary cascade where efficiency is defined as the ratio of exit kinetic energy of actual mixed expansion to the total kinetic energy of separated unmixed isentropic expansion that can be written as

$$\eta_c = \frac{(\dot{m}_m + \dot{m}_c)(h_{tot,out} - h_{out})}{\dot{m}_m(h_{in,m} - h_{tot,m,is}) + \dot{m}_c(h_{in,c} - h_{tot,c,is})} \quad (\text{A.86})$$

Denominator is calculated by assuming that the main gas flow and coolant streams expand isentropically without mixing from their stagnation conditions to a common exit pressure. Additional efficiency definition have been developed especially by taking into account an isentropic or not mixing of the two flows before expansion. A detailed review of efficiency definition in cooled turbine is proposed in Young and Horlock [212].

Several authors studied the effect of the averaging procedure on pressure, temperature and subsequent performance quantities. The method to integrate pressure and temperature over the two-dimensional plane to obtain a one-dimensional pressure and temperature is non unique for mainly two reasons. Loss generation processes typically create a non-uniform flow, with subsequent mixing downstream. Measurement stations must often be placed at locations in which mixing is not complete, for example in multistage turbomachinery where the performance of one blade row is desired but the presence of downstream blading means the instrumentation is at a location with incomplete mixing. Thus, the first question that emerges is, should the remaining mixing downstream blade be taken into account in the averaging process. The second issue is relatively to the quantity that should be conserved according to the averaging process similarly to last subsection. As stated the mass averaging for total temperature is a proper averaging when one want to conserve enthalpy flux between the non-uniform flow on the measurement plane and the one-dimensional quantity. For total pressure, several averaging exist. The area average stagnation pressure but this quantity is not associated with application of any conservation law and there is no fundamental reason for its use. The mass average total pressure. For this type of averaging, for a uniform stagnation enthalpy on the plane and changes in stagnation pressure small compared to the (upstream) reference value, the mass average stagnation pressure at a given location represents the entropy flux at that station. These last two averaging are generally widely used but suffer from few theoretical basis. The mixed out average stagnation pressure is defined as the stagnation pressure that would exist after full mixing at constant area. To find this value we apply conservation of mass and momentum to the non-uniform profile, using the constant area control volume from measure plane to full mixed flow and neglecting frictional forces on the top and bottom walls of the channel. An other type of averaging is the averaging that conserves the entropy flux. In conjunction with mass averaging for total temperature this induces conservation of availability ($B = h - T_0 s$). The entropy flux and the mass average entropy are related by:

$$\int_A (s - s_{ref}) \rho u_x dA = \int_m (s - s_{ref}) d\dot{m} = (\bar{s}^M - s_{ref}) \dot{m} \quad (\text{A.87})$$

for a perfect gas with constant specific heats, the entropy change between any (stagnation) state and an initial reference state is according to eq.(2.14):

$$\frac{s - s_{ref}}{c_p} = \ln \left(\frac{T_t}{T_{ref}} \right) - \frac{\gamma - 1}{\gamma} \ln \left(\frac{p_t}{p_{ref}} \right). \quad (\text{A.88})$$

Last equation can be integrated over the mass flow to find the entropy flux. The requirement for the averaged flow to have the same stagnation enthalpy flux as the actual flow yields the condition for equality of entropy flux between the actual and the averaged flow as

$$\begin{aligned} \frac{\bar{s}^M - s_{ref}}{c_p} &= \left(\frac{1}{m} \right) \left\{ \int_m \ln \left[\left(\frac{T_{tot}}{T_{ref}} \right) \left(\frac{p_{ref}}{p_{tot}} \right)^{\frac{\gamma-1}{\gamma}} \right] d\dot{m} \right\} \\ &= \ln \left[\left(\frac{\bar{T}_{tot}^M}{T_{ref}} \right) \left(\frac{p_{ref}}{\bar{p}_{tot}^S} \right)^{\frac{\gamma-1}{\gamma}} \right]. \end{aligned} \quad (\text{A.89})$$

This equation defines an average stagnation pressure, \bar{p}_t^S , based on equality of entropy flux between actual and average flows, as

$$\frac{\bar{p}_{tot}^S}{p_{ref}} = \left\{ \frac{\bar{T}_{tot}^M}{T_{ref}} \right\}^{\frac{\gamma}{\gamma-1}} \left(\exp \left\{ \frac{\gamma}{(\gamma-1)m} \int_m \ln \left[\left(\frac{T_{rf}}{T_{tot}} \right) \left(\frac{p_{tot}}{p_{ref}} \right)^{\frac{\gamma-1}{\gamma}} \right] d\dot{m} \right\} \right). \quad (\text{A.90})$$

Tang [121] proposed a different averaging process compared to the work averaged procedure where the total temperature, velocity components are mass averaged and the static pressure is surface averaged. Onto a stator-rotor configuration, integrations were performed at vane leading edge, vane trailing edge and rotor trailing edge. At blade trailing edge the pressure based on entropy method was shown to be lower than the one proposed by the author since the entropy approach takes into account of losses that will be generated downstream. Low differences were observed between the entropy method and work average method. The author concluded that a small part of the expected mixing is taken into account by work averaging method. When the averaging process was led at rotor leading edge the differences between the different methods was very low since the mixing process could have been almost entirely made in the vane-rotor gap. However, the author pointed out that when efficiency is evaluated downstream vane based on the different pressure averaging method, discrepancy of unity in the efficiency could be observed.

When dealing with numerical simulation, the assessment of convergence is an important feature. Convergence can be evaluated as first step by looking at the convergence of one-dimensional data like mass flow and performance quantities. A more accurate evaluation can be led by studying the convergence of the frequency content of the different physical phenomena in the simulation domain as well as the convergence of higher order moments compared to mean quantities. Once converged, data can be extracted from the numerical simulation. For unsteady simulations, the time of extraction is

generally determined by low-frequency highly energetic phenomena in the domain. Temporal and spatial averaging are performed to be compliant with experiments when available or using quantities solution of a transport equation. The averaging process is generally not able to conserve all parameters of interest. The averaging can be then perform in the purpose to conserve the main quantities of interest. In this section, an averaging procedure was introduced to be compliant with the exergy analysis proposed at the beginning of this section.

This chapter introduced several flow model and approaches to deal with numerical simulation of turbulent flows in turbomachinery. Standard Navier-Stokes equations as well as lattice-Boltzmann are presented. DNS solves the whole turbulent spectrum but is still computationally expensive at current stage and, in the context of gas turbine, is mainly used on simplified low pressure turbine configurations where Reynolds number is relatively low. On the other side, (U)RANS simulation enables the use of affordable coarsened meshes but make the solution dependent on the turbulent model that have been tuned for simplified configurations which can be far from the flows in turbomachinery. Between these two approaches, LES solves high energetic structures while modeling small dissipative structures. This approach reduces model influence. The Reynolds number encountered in low pressure turbine makes possible (at an expensive cost) to perform wall resolved LES simulation with the take into account of technological effects particularly interesting in current study for the account of cavity and purge flow, using high order methods and eventual turbulence injection at inlet of the domain that may be an important factor in gas turbine. Analyzing losses in the flow field from numerical simulation requires assessments on the convergence, temporal and spatial averaging to properly analyse the data. Extraction time, snapshots, quantities on which averaging is performed are key parameters.

B

Derivation of energy-related transport equations

B.1	Energy-related transport equations	262
B.1.1	Transport equation for internal, kinetic and total energy .	262
B.1.2	Transport equation for total enthalpy	263
B.2	Exergy and useful work	264
B.2.1	Transport equation for exergy and useful work	264
B.2.2	Control volume analysis for exergy and useful work transport equations	265
B.3	The evaluation of viscosity in numerical simulation . .	271
B.3.1	The influence of turbulence modelling on actual viscosity	271
B.3.2	The influence of spatio-temporal discretization on actual viscosity	271

The purpose of this appendix is to give more details in the derivation of the different transport equations used along this thesis since only the final expression are given in the main chapters. Also, more details are given in the balance equations for exergy and useful work introduced in Chap. 2. The evaluation of viscosity in the numerical simulation is an important feature to be accounted for when loss generation want to be properly estimated, so the main sources contributing to total viscosity are presented with methods to be able to evaluate them.

B.1 Energy-related transport equations

The balance equations for the various forms of energy are first introduced in the emphasis to give their detailed derivation. These energy equations are then used in conjunction with first and second principle of thermodynamics to derive balance equations for exergy χ and useful work Ξ used in this thesis that are important quantities to track loss generation within the turbine component.

B.1.1 Transport equation for internal, kinetic and total energy

B.1.1.1 Transport equation for kinetic energy

Transport equation for kinetic energy E_k can be derived by multiplying momentum equation eq.(A.8b) introduced in section A.1.2 with u_i :

$$u_i \frac{\partial \rho u_i}{\partial t} + u_i \frac{\partial}{\partial x_j} (\rho u_i u_j + p \delta_{ij} - \tau_{ij}) = \rho u_i F_i \quad (\text{B.1})$$

For the temporal and convective term of last equation:

$$\begin{aligned} u_i \frac{\partial \rho u_i}{\partial t} + u_i \frac{\partial}{\partial x_j} (\rho u_i u_i) &= \frac{\partial \rho}{\partial t} u_i u_i - \rho \frac{\partial u_i u_i}{\partial t} + \frac{\partial \rho u_j}{\partial x_j} u_i u_i + \frac{\partial u_i u_i}{\partial x_j} \rho u_j \\ &= u_i u_i \left(\frac{\partial \rho}{\partial t} + \frac{\partial \rho u_j}{\partial x_j} \right) - \rho \frac{\partial u_i u_i}{\partial t} + \frac{\partial u_i u_i}{\partial x_j} \rho u_j \\ &= -\rho \frac{\partial u_i u_i}{\partial t} + \frac{\partial u_i u_i}{\partial x_j} \rho u_j \\ &= \frac{\partial \rho u_i u_i}{\partial t} - \frac{\partial \rho}{\partial t} u_i u_i + \frac{\partial \rho u_i u_i u_j}{\partial x_j} - \frac{\partial \rho u_j}{\partial x_j} u_i u_i \quad (\text{B.2}) \\ &= \frac{\partial \rho u_i u_i}{\partial t} + \frac{\partial \rho u_i u_i u_j}{\partial x_j} - u_i u_i \left(\frac{\partial \rho}{\partial t} u_i u_i + \frac{\partial \rho u_j}{\partial x_j} \right) \\ &= \frac{\partial \rho u_i u_i}{\partial t} + \frac{\partial \rho u_i u_i u_j}{\partial x_j} \\ &= \frac{\partial \rho E_k}{\partial t} + \frac{\partial \rho E_k u_j}{\partial x_j} \end{aligned}$$

For the pressure term:

$$u_i \frac{\partial (p \delta_{ij})}{\partial x_j} = \frac{\partial (p u_j)}{\partial x_j} - p \frac{\partial u_j}{\partial x_j} \quad (\text{B.3})$$

and the viscous term:

$$u_i \frac{\partial \tau_{ij}}{\partial x_j} = \frac{\partial (u_i \tau_{ij})}{\partial x_j} - \tau_{ij} \frac{\partial u_i}{\partial x_j} \quad (\text{B.4})$$

that finally lead to the kinetic energy transport equation:

$$\frac{\partial(\rho E_k)}{\partial t} + \frac{\partial}{\partial x_j} (\rho u_j E_k + p u_j - u_i \tau_{ij}) = \rho u_j F_j + p \frac{\partial u_j}{\partial x_j} - \tau_{ij} \frac{\partial u_i}{\partial x_j} \quad (\text{B.5})$$

B.1.1.2 Transport equation for total energy

Transport equation for total energy corresponds to the energy conservative equation from Navier-Stokes equation eq.(A.8c) introduced in section A.1.2:

$$\frac{\partial(\rho E_t)}{\partial t} + \frac{\partial}{\partial x_j} (\rho E_t u_j + p u_j - \tau_{ij} u_j + q_j) = \rho F_j u_j + \dot{Q} \quad (\text{B.6})$$

B.1.1.3 Transport equation for internal energy

Subtracting kinetic energy equation to total energy equation gives transport equation for internal energy:

$$\frac{\partial(\rho e)}{\partial t} + \frac{\partial}{\partial x_j} (\rho u_j e + q_j) = -p \frac{\partial u_j}{\partial x_j} + \tau_{ij} \frac{\partial u_i}{\partial x_j} \quad (\text{B.7})$$

B.1.2 Transport equation for total enthalpy

The total enthalpy is of special interest in turbomachinery since large transfers of energy occur requiring the use of the total energy balance equation in conjunction with the potential work of pressure. Transport equation for total enthalpy can be obtained by recalling the link between total energy and total enthalpy $\rho h_t = \rho E_{tot} + p/\rho$:

$$\begin{aligned} \frac{\partial(\rho h_{tot})}{\partial t} + \frac{\partial(\rho h_{tot})}{\partial x_j} &= \frac{\partial(\rho E_{tot})}{\partial t} + \frac{\partial(\rho E_{tot})}{\partial x_j} + \frac{\partial p}{\partial t} + \frac{\partial(p u_j)}{\partial x_j} \\ &= \frac{\partial}{\partial x_j} (-p u_j + \tau_{ij} u_j - q_j) + \frac{\partial p}{\partial t} - \frac{\partial p u_j}{\partial x_j} \\ &= \frac{\partial}{\partial x_j} (\tau_{ij} u_j - q_j) + \frac{\partial p}{\partial t} \end{aligned} \quad (\text{B.8})$$

B.2 Exergy and useful work

B.2.1 Transport equation for exergy and useful work

The exergy transport equation can be derived from the definition of exergy $\chi = h_t - h_0 - T_0(s - s_0)$:

$$\begin{aligned}
\frac{\partial(\rho\chi)}{\partial t} + \frac{\partial(\rho\chi u_j)}{\partial x_j} &= \frac{\partial(\rho((h_{tot} - h_0) - T_0(s - s_0)))}{\partial t} + \frac{\partial(\rho((h_t - h_0) - T_0(s - s_0))u_j)}{\partial x_j} \\
&= \frac{\partial(\rho h_{tot})}{\partial t} - T_0 \frac{\partial(\rho s)}{\partial t} + \frac{\partial(\rho h_{tot} u_j)}{\partial x_j} - T_0 \frac{\partial(\rho s u_j)}{\partial x_j} \\
&= \frac{\partial(\rho h_{tot})}{\partial t} + \frac{\partial(\rho h_{tot} u_j)}{\partial x_j} - T_0 \left(\frac{\partial(\rho s)}{\partial t} + \frac{\partial(\rho s u_j)}{\partial x_j} \right) \\
&= \frac{\partial}{\partial x_j} (\tau_{ij} u_j - q_j) + \frac{\partial p}{\partial t} - T_0 \left(-\frac{\partial(q_i/T)}{\partial x_i} + \frac{1}{T} \tau_{ij} \frac{\partial u_i}{\partial x_j} + \frac{\lambda}{T^2} \left(\frac{\partial T}{\partial x_i} \right)^2 \right) \\
&= \frac{\partial}{\partial x_j} (\tau_{ij} u_j - (1 - \frac{T_0}{T}) q_j) - \frac{T_0}{T} \tau_{ij} \frac{\partial u_i}{\partial x_j} - \frac{\lambda T_0}{T^2} \left(\frac{\partial T}{\partial x_i} \right)^2 + \frac{\partial p}{\partial t}
\end{aligned} \tag{B.9}$$

From exergy equation, the exit thermal work cannot be recovered and transformed into useful mechanical work in the context of gas turbine equipping aircraft¹ and the thermal work is lost leading to the notion of useful work that is the difference between exergy and thermal work lost. An energy conservation equation can be written between initial state and final state(p_0, T) where $T > T_0$, the environment temperature. The conservation equation can be written as:

$$\frac{d\rho\Xi}{dt} = \frac{\partial\rho\Xi}{\partial t} + \frac{\partial\rho\Xi u_j}{\partial x_j}. \tag{B.10}$$

Temporal derivative can be written as:

$$\begin{aligned}
\frac{\partial\rho\Xi}{\partial t} &= \frac{\partial((1 - T_{ex}/T)\rho e + (\rho p_0 u_i) + \rho u_i^2)}{\partial t} \\
&= (1 - \frac{T_{ex}}{T}) \frac{\partial(\rho e)}{\partial t} + \rho e \frac{\partial(1 - T_{ex}/T)}{\partial t} + p_0 \frac{\partial(\rho u_i)}{\partial t} + \frac{\partial(\rho u_i^2)}{\partial t} \\
&= (1 - \frac{T_{ex}}{T}) \frac{\partial(\rho e)}{\partial t} + \frac{\partial(\rho u_i^2)}{\partial t}
\end{aligned} \tag{B.11}$$

¹For electrical production, hot gas exit the gas turbine can go into a heat exchanger that heat the inflow of the gas turbine

For the convective part:

$$\begin{aligned}
\frac{\partial \rho \Xi u_i}{\partial x_i} &= \frac{\partial((1 - T_{ex}/T)\rho e + (\rho p_0 u_i) + \rho u_i^2)}{\partial t} \\
&= (1 - \frac{T_{ex}}{T}) \frac{\partial(\rho e) u_i}{\partial x_i} + \rho e \frac{\partial((1 - T_{ex}/T) u_i)}{\partial x_i} + p_0 \frac{\partial(\rho u_i) u_i}{\partial x_i} + \frac{\partial(\rho u_i^2) u_i}{\partial x_i} \quad (\text{B.12}) \\
&= (1 - \frac{T_{ex}}{T}) \frac{\partial(\rho e) u_i}{\partial x_i} + \frac{\partial(p_0 u_i)}{\partial x_i}
\end{aligned}$$

The expression for total derivative yield to:

$$\begin{aligned}
\frac{d\rho \Xi}{dt} &= (1 - \frac{T_{ex}}{T}) \left(\frac{\partial(\rho e)}{\partial t} + \frac{\partial(\rho e) u_i}{\partial x_i} \right) + (1 - T_{ex}/T) \left(\frac{\partial(\rho \frac{1}{2} u_i^2)}{\partial t} \right. \\
&\quad \left. + \frac{\partial(\rho u_i) \frac{1}{2} u_i^2}{\partial x_i} \right) + p_0 \frac{\partial(\rho u_i) u_i}{\partial x_i} - \frac{T_0}{T} p \frac{\partial u_i}{\partial x_i} \quad (\text{B.13})
\end{aligned}$$

Using internal energy and kinematic energy conservation proposed in eq.(2.42)(2.41):

$$\frac{d\rho \Xi}{dt} = (1 - \frac{T_{ex}}{T}) \left(-\frac{\partial q}{\partial x_i} + \frac{\partial \tau_{ij} u_j}{\partial x_i} - \left(\frac{T_{ex}}{T} \right) \tau_{ij} \frac{\partial u_i}{\partial x_j} - \frac{\partial(p - p_0)}{\partial x_j} \right) \quad (\text{B.14})$$

B.2.2 Control volume analysis for exergy and useful work transport equations

The study performed on control volumes requires the use mainly of two theorems that are the Green-Ostrograky and Reynolds theorem. A brief remind of these two theorems is proposed before to introduce control volume analysis for exergy and useful work transport equation.

B.2.2.1 Green-Ostrograky theorem

The Green-Ostrograky theorem also known as divergence or Gauss's theorem states that the outward flux of a tensor field through a closed surface is equal to the volume integral of the divergence over the region inside the surface. For a volume V which is compact and has a piecewise smooth boundary S. If F is a continuously differentiable vector field defined on a neighbourhood of V, then we have:

$$\iiint_V \frac{\partial F}{\partial x_i} dV = \oiint_S \mathbf{F} dS \quad (\text{B.15})$$

the left-hand side being a volume integral over the volume V, the right-hand side a surface integral over the boundary of the volume V.

B.2.2.2 Reynolds theorem

Reynolds transport theorem for a material volume $V(t)$ i.e. a control volume that travels and deforms in a fluid flow such that it always occupied by the same specific collection of fluid particles, states that

$$\frac{d}{dt} \int_{V(t)} F dV = \int_{V(t)} \frac{\partial F}{\partial t} dV + \int_{A(t)} [F(\mathbf{u} \cdot \mathbf{n})] dA \quad (\text{B.16})$$

where $A(t)$ is the material surface, a surface that encloses the material volume $V(t)$. From the definition of material volume as mentioned before, no fluid particles are allowed to leave or enter $V(t)$, and therefore $A(t)$ must travel at local velocity of the fluid \mathbf{u} . \mathbf{n} is the unit normal of $A(t)$ such that $A(t)$ is locally advancing along \mathbf{n} when $(\mathbf{u} \cdot \mathbf{n}) > 0$, and vice versa. F is an arbitrary scalar variable. Similarly, Reynolds transport theorem for an arbitrary moving control volume $V(t)$ states that:

$$\frac{d}{dt} \int_{V^*(t)} F dV = \int_{V^*(t)} \frac{\partial F}{\partial t} dV + \int_{A^*(t)} [F(\mathbf{b} \cdot \mathbf{n})] dA \quad (\text{B.17})$$

where \mathbf{b} is the velocity of the arbitrary moving control surface $A^*(t)$ that encloses $V^*(t)$, and it is observed in the same frame of reference as that of \mathbf{u} . In general, $\mathbf{b} \neq \mathbf{u}$. At a special moment of interest when $V^*(t)$ is instantaneously coincide with $V(t)$, we have $V(t) = V^*(t)$ and $A(t) = A^*(t)$. It is worth noting that at this particular coincidence moment, the total time derivative for both type of control volumes is different, i.e. $d/dt \int_{V^*(t)} (F) dV \neq d/dt \int_{V(t)} (F) dV$ because $V^*(t)$ and $V(t)$ enclose different fluid particles. However, the volume integral of $\partial F / \partial t$ (i.e. the temporal local rate of change of F) and the surface integral terms are similar for both type of control volumes at the coincidence moment. Subtracting eq.(B.17) from eq.(B.16) and re-arrange:

$$\frac{d}{dt} \int_{V(t)} F dV = \int_{V^*(t)} \frac{\partial F}{\partial t} dV + \int_{A^*(t)} [F(\mathbf{u} - \mathbf{b}) \cdot \mathbf{n}] dA \quad (\text{B.18})$$

This is the general Reynolds transport theorem for an arbitrary moving control volume $V^*(t)$.

B.2.2.3 Integration of exergy transport equation over control volumes

Exergy transport equation proposed in eq.(B.9) was written in differential form as:

$$\frac{\partial(\rho\chi)}{\partial t} + \frac{\partial(\rho\chi u_j)}{\partial x_j} = \frac{\partial}{\partial x_j} (\tau_{ij} u_j - (1 - \frac{T_0}{T}) q_j) - \frac{T_0}{T} \tau_{ij} \frac{\partial u_i}{\partial x_j} - \frac{\lambda T_0}{T^2} \left(\frac{\partial T}{\partial x_i} \right)^2 + \frac{\partial p}{\partial t}. \quad (\text{B.19})$$

By integrating over a control volume V and using the Reynolds transport theorem eq.(B.18) for the first term and divergence theorem eq.(B.15) for the second term gives for the left-hand side of the equation:

$$\iiint \frac{\partial(\rho\chi)}{\partial t} dV + \iiint \frac{\partial(\rho\chi u_j)}{\partial x_j} dV = \frac{d}{dt} \iiint (\rho\chi) dV - \oint (\rho\chi) u_{j,w} n_j dA + \oint (\rho\chi) u_j n_j dA. \quad (\text{B.20})$$

The control volume surface $\partial V(t)$ can be split into three types of disjointed sub-surfaces. Fixed walls $A_{FW}(t)$ where $u_j n_j = 0$, moving walls $A_{MV}(t)$ where $u_j n_j = u_{w,j} n_j$ (where w stands for velocity at the wall) and input/output boundaries A_{IO} (see Fig. 2.4 for control surfaces). This splitting approach is particularly convenient for turbine components since composed of static (stator) and rotating parts (rotors). Splitting the second and third terms in eq.(B.19) into subsurface integrals, the exergy balance in integral form can be written as:

$$\begin{aligned}
\frac{d}{dt} \iiint (\rho \chi) dV - \oint (\rho \chi) u_{j,w} n_j dA + \oint (\rho \chi) u_j n_j dA &= \frac{d}{dt} \iiint (\rho \chi) dV \\
&- \oint (\rho \chi) u_{j,w} n_j dA_{FW} - \oint (\rho \chi) u_{j,w} n_j dA_{MW} - \oint (\rho \chi) u_{j,w} n_j dA_{IO} \\
&+ \oint (\rho \chi) u_j n_j dA_{FW} + \oint (\rho \chi) u_j n_j dA_{MW} + \oint (\rho \chi) u_j n_j dA_{IO} \\
&= \frac{d}{dt} \iiint (\rho \chi) dV + \oint (\rho \chi) u_j n_j dA_{IO}.
\end{aligned} \tag{B.21}$$

The pressure difference being non-zero since exergy reduces to pressure term at the wall. The right-hand term can be developed by using the divergence theorem: For the right-hand side of eq.(B.9), we first develop pressure contribution using the Reynolds theorem:

$$\begin{aligned}
\iiint \frac{\partial(p)}{\partial t} dV &= \frac{d}{dt} \iiint p dV - \oint p u_{j,w} n_j dA \\
&= \frac{d}{dt} \iiint p dV - \oint (p - p_0) u_{j,w} n_j dA_{MV}
\end{aligned} \tag{B.22}$$

For the remaining contributions, the divergence theorem is used when it applies:

$$\begin{aligned}
&\iiint \frac{\partial}{\partial x_j} (\tau_{ij} u_i) dV - \iiint \frac{\partial}{\partial x_j} \left(\left(1 - \frac{T_0}{T}\right) q_j \right) dV - \iiint \frac{T_0}{T} \tau_{ij} \frac{\partial u_i}{\partial x_j} dV - \iiint \frac{\lambda T_0}{T^2} \left(\frac{\partial T}{\partial x_i} \right)^2 dV \\
&= \oint (\tau_{ij} u_i) n_j dA - \iiint \frac{\partial}{\partial x_j} \left(\left(1 - \frac{T_0}{T}\right) q_j \right) dV - \iiint \frac{T_0}{T} \tau_{ij} \frac{\partial u_i}{\partial x_j} dV - \iiint \frac{\lambda T_0}{T^2} \left(\frac{\partial T}{\partial x_i} \right)^2 dV
\end{aligned} \tag{B.23}$$

The surfacic integral for $\oint (\tau_{ij} u_j) n_j dA$ is limited to moving wall boundaries that lead to:

$$\oint (\tau_{ij} u_j) n_j dA = \oint (\tau_{ij} u_{w,j}) n_j dA_{MW} \tag{B.24}$$

The exergy transport equation integrated over the control volume expressed by gathering right and left-hand terms:

$$\begin{aligned} \frac{d}{dt} \iiint (\rho\chi) dV + \oint (\rho\chi) u_j n_j dA_{IO} = & \oint (p - p_0) u_{j,w} n_j dA_{MW} + \oint (\tau_{ij} u_{w,i}) n_j dA_{MW} \\ & - \iiint \frac{\partial}{\partial x_j} \left((1 - \frac{T_0}{T}) q_j \right) dV - \iiint \frac{T_0}{T} \tau_{ij} \frac{\partial u_i}{\partial x_j} dV - \iiint \frac{kT_0}{T^2} \left(\frac{\partial T}{\partial x_i} \right)^2 dV + \frac{d}{dt} \iiint p dV. \end{aligned} \quad (\text{B.25})$$

Alternatively, this equation can be written as

$$\frac{d}{dt} \iiint (\rho\chi) dV + \oint (\rho\chi) u_j n_j dA_{IO} = P_{shaft} + \chi_q + \Phi_{\nabla u} + \Phi_{\nabla T} + \frac{d}{dt} \iiint p dV \quad (\text{B.26})$$

where:

- $d/dt \iiint (\rho\chi) dV$, $d/dt \iiint p dV$: net unsteady effect within the system due to flow exergy accumulation and unsteady pressure (which can be positive or negative instantaneously)
- $P_{shaft} = - \oint ((p - p_0) u_{w,j} n_j - (\tau_{ij} u_{w,i}) n_j) dA_{MW}$: the shaft work extracted from the system (positive for turbine)
- $\chi_q = \iiint \partial/\partial x_j (1 - (T_0/T)) q_j dV$: the exergy gain/lost via heat transfer (positive for the case of heat loss, i.e. $(q_j \cdot n_j) > 0$ such that $(1 - T_0/T) > 0$)
- $\Phi_{\nabla u} = - \iiint (T_0/T) \tau_{ij} (\partial u_i / \partial x_j) dV$: the flow exergy destroyed by irreversibilities due to velocity gradients
- $\Phi_{\nabla T} = - \iiint \lambda (T_0/T^2) (\partial T / \partial x_i)^2 dV$: the flow exergy destroyed by irreversibilities due to temperature gradients.

Simple analysis of one dimensional shock waves show that the quantity varies deeply but continuously along the thickness of the shocks. It can be shown that the entropy production in the shock wave is related to the viscous term $\Phi_{\nabla u}$ and heat transfer $\Phi_{\nabla T}$ (see Fig. B.1). From a numerical point of view when one want to properly evaluate the loss related to the shock based on viscous and thermal dissipation, the shock thickness must be discretized by several grid points that is generally impracticable in real configuration since shock thickness is in the order of the mean free path ($\simeq 6 \times 10^{-8}$ for air at ambient conditions). The entropy increase is then generally made with a jump condition all along the shock, the shock being considered as a discontinuity where an increase of entropy takes place on an infinitely thin layer:

$$\Phi_{s.w.} = -T_0 \oint_{A_w} [\rho \delta s (v_j - u_j)] \cdot n_j dA_{s.w.} \quad (\text{B.27})$$

Therefore, when the shock wave can be resolved by numerical simulation, eq.(B.26) is sufficient since the contribution is contained in $\Phi_{\nabla u}$ and $\Phi_{\nabla T}$ but when one has

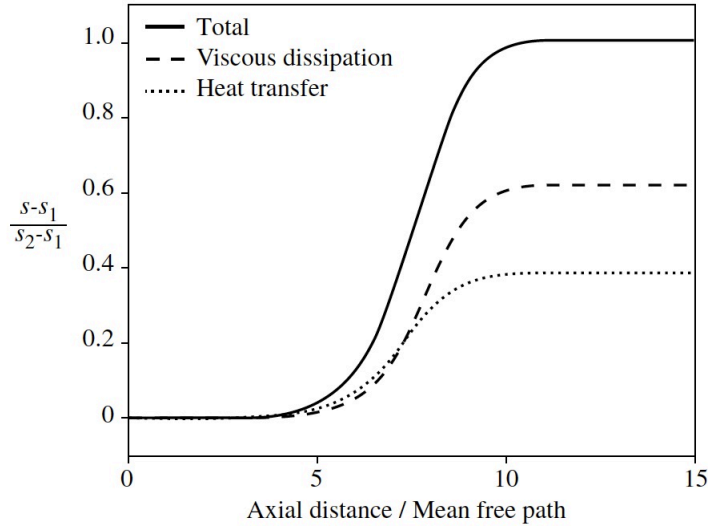


Figure B.1: Normalized entropy distribution across a shock; $M = 1.5$, upstream entropy taken as 0, downstream value = 1.0

insufficiently refined mesh, a jump condition has to be set at the location of the shock leading to a new expression for exergy transport equation:

$$\frac{d}{dt} \iiint (\rho\chi) dV + \oint (\rho\chi) u_j n_j dA_{IO} = P_{shaft} + \chi_q + \Phi_{\nabla u} + \Phi_{\nabla T} + \Phi_{s.w.} + \frac{d}{dt} \iiint p dV \quad (\text{B.28})$$

A shock sensor that can be used to determine the surface of the shock and whether a given cell should be considered as being enclosed by the surface is the sensor proposed by Lovely and Haimes [213]:

$$\Lambda_{s.w.} = \frac{\mathbf{u} \cdot \nabla \mathbf{p}}{c \|\nabla \mathbf{p}\|} \quad (\text{B.29})$$

where c is the local speed of sound. If $\Lambda_{s.w.} > 0.95$ the cell under consideration is tagged as being enclosed by the shock wave volume. The addition of a number of supplementary cells to this initial guess is known to enhance numerical accuracy. In practise, the addition of a number of supplementary cells (around 6-8) to this initial guess is known to enhance numerical accuracy. The expression of exergy can alternatively be developed to obtain a decomposition similar to the one proposed by Drela [214] recalling that $\chi = \delta h_t - T_0 \delta s = \delta e + (1/2)(u_1^2 + u_2^2 + u_3^2) + p/\rho - T_0 \delta s$ and under steady conditions meaning $d/dt \iiint (\rho\chi) dV$, $d/dt \iiint p dV = 0$. For left-hand term (convective contribution):

$$\begin{aligned} \oint (\rho\chi) u_j n_j dA_{IO} &= \oint (\rho \delta e) u_j n_j dA_{IO} + \oint \left(\frac{1}{2} \rho u_1^2\right) u_j n_j dA_{IO} \\ &+ \oint \left(\frac{1}{2} \rho (u_2^2 + u_3^2)\right) u_j n_j dA_{IO} + \oint p u_j n_j dA_{IO} - T_0 \oint (\rho \delta s) u_j n_j dA_{IO}. \end{aligned} \quad (\text{B.30})$$

Looking first at the contribution at inlet of the domain, the exergy supplied $\chi_{supplied}$ is:

$$\chi_{supplied} = \oint (\rho \delta e) u_j n_j dA_I + \oint \left(\frac{1}{2} \rho u_1^2 \right) u_j n_j dA_I - T_0 \oint (\rho \delta s) n_j dA_I. \quad (B.31)$$

For the contribution at outlet of the domain:

$$E_{mechanical}^{out} = \oint \left(\frac{1}{2} \rho u_1^2 \right) u_j n_j dA_O + \oint \left(\frac{1}{2} \rho (u_2^2 + u_3^2) \right) u_j n_j dA_O + \oint (p - p_0) u_j n_j dA_O \quad (B.32)$$

is the rate of mechanical exergy outflow and

$$E_{thermal}^{out} = \oint (\rho \delta e) u_j n_j dA_O + \oint (p_0) u_j n_j dA_O - \oint (\rho \delta s) n_j dA_O \quad (B.33)$$

is the rate of thermal exergy outflow. An alternative expression can be then obtained from the exergy balance equation by:

$$\chi_{supplied} + \chi q = P_{shaft} + E_{mechanical}^{out} + E_{thermal}^{out} + \Phi_{\nabla u} + \Phi_{\nabla T} + \Phi_{s.w.} \quad (B.34)$$

This last equation indicates that the exergy at inlet of the domain $\chi_{supplied}$ and the heat supplied at the border of the domain to the fluid χq is equal to the work given or extracted to the fluid P_{shaft} , the anergy generated in the volume due to mechanical, thermal gradients, shocks $(\Phi_{\nabla u} + \Phi_{\nabla T} + \Phi_{s.w.})$ and the mechanical and thermal energy available at the outlet of the domain $(E_{mechanical}^{out} + E_{thermal}^{out})$.

B.2.2.4 Integration of useful work transport equation over control volumes

Based on useful work transport equation in differential form eq.(B.14) and applying same procedure based on divergence and Reynold's theorem applied earlier for exergy, the integral form can be written as:

$$\begin{aligned} \iiint \frac{\partial(\rho \Xi)}{\partial t} dV + \oint (\rho \Xi) u_j n_j dA_{IO} &= - \oint ((p - p_0) u_{w,j} n_j - (\tau_{ij} u_{w,j}) n_j) dA_{MW} \\ &- \iiint \frac{\partial}{\partial x_j} \left(\left(1 - \frac{T_{ex}}{T} \right) q_j \right) dV \\ &+ \iiint \left(\left(\frac{\gamma - 1}{\gamma} \right) \frac{1}{p} q_j - \frac{T_{ex}}{T} \tau_{ij} \frac{\partial u_i}{\partial x_j} \right) dV \\ &- \iiint \left(\left(1 - \frac{T_{ex}}{T} \right) \left(\frac{\gamma - 1}{\gamma} \right) \frac{1}{p} q_j - \frac{T_{ex}}{T} \tau_{ij} \frac{\partial u_i}{\partial x_j} \right) dV \\ &= P_{shaft} + \chi_{q, T_{ex}} + \Phi_{\nabla u} + \Psi_{therm} + \Psi_{reheat} + \Psi_{recool} \end{aligned} \quad (B.35)$$

B.3 The evaluation of viscosity in numerical simulation

When assessing the loss generation in a component of gas turbine, a main quantity of interest as stated previously is the viscous dissipation that transfer useful kinetic energy to internal energy that cannot be extracted by the gas turbine to generate work. The viscous dissipation is expressed as $\tau_{ij}(\partial u_i/\partial x_j)$ with $\tau_{ij} = \mu(\partial u_i/\partial x_j + \partial u_j/\partial x_i)$. Similarly when considering the thermal contribution, effective conductivity needs to be properly evaluated. The following analysis is focused on the viscosity but same conclusions apply to conductivity. When exactly solving the Navier-Stokes equations, the viscosity is simply the viscosity of the fluid. In numerical simulation, this quantity can be different to the viscosity of the fluid especially due to the account for turbulence and spatio-temporal discretization. Indeed, in current study dealing with turbulent flows at large Reynolds numbers, simulating these flows requires modeling contributions of unresolved scales by the various turbulence modeling procedures, leading to Reynolds-averaged Navier-Stokes (RANS) simulations or large-eddy simulations (LES) that will incur a modification of actual viscosity.

B.3.1 The influence of turbulence modelling on actual viscosity

In DNS approaches, the mesh is adapted to resolve all turbulent scales. No additional turbulent viscosity is to be added since the lowest dissipative scales are accounted by the mesh. For RANS approaches, the mesh is not refined enough to solve the turbulence spectrum and a model has to be added to account for the turbulent cascade and the dissipation process at small scales. As stated in subsection 2.1.4, when applying the RANS formalism to entropy transport equation containing the viscous dissipation, under some assumption detailed in the section, the natural viscosity is turned into an equivalent viscosity that is the sum of viscosity of the fluid and a turbulent viscosity to account for same scale turbulence dissipation. Similarly to RANS approaches, due to subgrid scale model in LES approaches to account for the unresolved small scales by the mesh, an equivalent turbulent viscosity is introduced that depends on local mesh grid size.

B.3.2 The influence of spatio-temporal discretization on actual viscosity

The purpose of this subsection is to look at the influence of spatio-temporal discretization on the effective viscosity. To do that, we consider a simple one dimensional convection-diffusion equation with a constant of convection and μ the viscosity:

$$a \frac{du}{dx} = \mu \frac{d^2u}{dx^2} \quad (\text{B.36})$$

We consider here a simple discretization using upstream-differencing approximation on a uniform grid:

$$a \left(\frac{u(x_i) - u(x - \Delta x)}{\Delta x} \right) = \mu \left(\frac{u(x_i - \Delta x) - 2u(x_i) + u(x + \Delta x)}{\Delta x^2} \right) \quad (\text{B.37})$$

When expanding u in a Taylor series about x_i one can obtain:

$$u(x) = u(x_i) - \frac{du}{dx}(x - x_i) + \frac{1}{2} \frac{d^2u}{dx^2}(x - x_i)^2 + o(\Delta x^2) \quad (\text{B.38})$$

Substituting eq.(B.38) in (B.37) yields to:

$$a \frac{du}{dx} = \left(\mu + a \frac{\Delta x}{2} \right) \frac{d^2u}{dx^2} + o(\Delta x^2). \quad (\text{B.39})$$

If Δx , the space step is not negligible, a convection-diffusion equation is solved but with the convection-diffusion equation but with greater viscosity: $\mu_{total} = \mu + \mu_{numerical}$, $\mu_{numerical} = a * \Delta x / 2$. This example shows that the discretization of equations induce additional viscosity for the fluid simulated numerically. A von Neumann analysis of numerical schemes (frequency analysis) shows that discretization generally induce additional viscosity due to even partial differential terms and dispersion due to odd partial differential terms. This observation is also true for other approaches than finite differences like finite elements or finite volume approaches. The main sources of additional numerical viscosity are convective, diffusive and temporal schemes: a higher order scheme decreases the truncation error. Implication of temporal scheme also induce additional numerical viscosity depending on the time step chose. As stated on the simple case of a space discretization equation, results of numerical simulations of fluid flow are always contaminated by truncation errors introduced by the discretization of governing differential equations. This induces numerical dissipation and dispersion. For dissipation, the spatio-temporal discretization can be seen as additional viscosity added to the viscosity of the fluid. Truncation errors are only negligible if all physical scales are well resolved by the given mesh and time-step size. This is the case for DNS approaches where no viscosity is added for accounting turbulence since all scales are resolved and low or no numerical dissipation added since spatial and temporal step are low enough so that the additional terms appearing in the truncation of equations are negligible. For lower temporal or spatial resolution, however, truncation errors affect the simulation results. The consequence of turbulence modelling and spatio-temporal discretization is that the actual viscosity obtained from the numerical simulation is:

$$\mu_{effective} = \mu + \mu_t + \mu_{num}. \quad (\text{B.40})$$

The natural viscosity μ can be obtained from the Sutherland law, the turbulent viscosity μ_t from the turbulent model for a RANS approach or from the subgrid scale model in the case of a LES simulation. The main difficulty relies on the numerical viscosity μ_{num} . Some methods exist based on an a priori analysis of the numerical

scheme. However, these methods are dependant in the numerical scheme and no general rule exists. The purpose of this section is to present a method to evaluate the numerical viscosity incurred by spatio-temporal discretization in the general framework of LES simulation based on the result of the simulation (a posteriori method). We consider first for the sake of simplicity the Navier-Stokes momentum equation written for incompressible flow of density ρ . This equation can be written as:

$$\frac{\partial u_i}{\partial t} + u_j \frac{\partial u_i}{\partial x_j} = -\frac{\partial p}{\partial x_i} + \nu \frac{\partial^2 u_i}{\partial x_j^2}. \quad (\text{B.41})$$

This equation can be written in flux-vector formalism:

$$\frac{\partial \bar{u}}{\partial t} + (NS)\bar{u} = 0 \quad (\text{B.42})$$

where the operator NS contains all spatial derivative terms and \bar{u} denotes the analytical, and generally unknown velocity solution for the particular fluid flow problem. The numerical discretization according to the selected flow solver yields to:

$$\frac{\partial u}{\partial t_d} + (NS)_d u = 0 \quad (\text{B.43})$$

that provides the numerical velocity field $u_{i,j,k}(t_n)$ at all mesh points $0 \leq i < N_i$, $0 \leq j < N_j$, $0 \leq k < N_k$ and time step t_n . An important thing is that the numerical solution u is not identical to the analytical solution \bar{u} . The truncation error \mathbf{E} of the scheme giving velocity output u can be written as:

$$\left(\frac{\partial \mathbf{u}}{\partial t} \right)_d + (NS)_{d\mathbf{u}} = \frac{\partial \mathbf{u}}{\partial t} + (NS)\mathbf{u} + \mathbf{E} = 0 \quad (\text{B.44})$$

$$-\mathbf{E} = \frac{\partial \mathbf{u}}{\partial t} + (NS)\mathbf{u}. \quad (\text{B.45})$$

This expression is only formal because it requires the knowledge of the numerical solution as an analytical function for which the time derivative and spatial derivatives in the operator can be calculated. Assuming that the velocity field $u_{i,j,k}(t)$ has been determined with an arbitrary Navier-Stokes solver at several consecutive time steps that is to say $t_{n-1} = t_n - \Delta t$, $t_{n+1} = t_n + \Delta t$, the time derivative in last equation can be approximated at time t_n using central differences scheme:

$$\frac{\partial \mathbf{u}_{i,j,k}}{\partial t} \Big|_{CD} \approx \frac{\mathbf{u}_{i,j,k}(t_n + \Delta t) - \mathbf{u}_{i,j,k}(t_n - \Delta t)}{2\Delta t} \quad (\text{B.46})$$

this time derivative being affected by the discretization errors of the original Navier-Stokes solver. If no analytical expression for u as a function of x , y , z exists the spatial derivatives must be computed numerically, and to minimize the numerical

errors the highest order numerical formulas should be employed, leading to the approximate numerical formula for the truncation error

$$- \mathbf{E}_{i,j,k}(t_n \approx \frac{\partial \mathbf{u}_{i,j,k}}{\partial t})|_{CD} + (NS)_{ho} \mathbf{u}_{i,j,k} t_n) \quad (\text{B.47})$$

where $(NS)_{ho}$ is the discretized Navier-Stokes operator using arbitrary high order numerical differentiation formulas. From eq.(B.43) we see that the second term on the right-hand side of eq.(B.47) is the rate of change of the velocity field computed using a high order scheme, allowing to rewrite eq.(B.47) as

$$- \mathbf{E}_{i,j,k} \approx \frac{\partial \mathbf{u}_{i,j,k}}{\partial t} |_{CD} - \frac{\partial \mathbf{u}_{i,j,k}}{\partial t} |_{ho} . \quad (\text{B.48})$$

The above formula involves computation of time derivatives for the same velocity field $u_{i,j,k}$ but computed with two different discretizations of the same Navier-Stokes operator. Multiplying each time derivative by the velocity $u_{i,j,k}$ and using a product rule will formally lead to time derivatives for the energy $e_{i,j,k} = u_{i,j,k} u_{i,j,k} / 2$. While the same velocity is used in the computations, the resulting derivatives will be different because of different discretizations of the momentum equation. One can think of the given velocity field as an initial condition which is advanced forward in time with two differently discretized Navier-Stokes operators, leading to different rates of change of the energy. This results in the error estimate for the kinetic energy equation

$$- \mathcal{E}_{n,ho}^{i,j,k} = \frac{\partial e_{i,j,k}}{\partial t} |_{CD} - \frac{\partial e_{i,j,k}}{\partial t} |_{ho} \quad (\text{B.49})$$

i.e., we define the error as the difference between how the energy did evolved using a given finite difference/finite volume code and how it would have evolved if the discretization could be neglected. The equation (B.49) can thus be viewed as the residual of computing the energy decay rate in two different ways. In applying this concept in practice the first term on the right-hand side of eq.(B.49) is computed directly as a discretized time derivative of the energy data obtained in the numerical simulation, i.e., the energy $e_{i,j,k} = u_{i,j,k} u_{i,j,k} / 2$ is obtained from the velocity field at several time steps and the time derivative at time t_n is approximated, e.g., using central differences involving time levels t_{n+1} and t_{n-1} . The second term on the right-hand side of eq.(B.49) is computed indirectly, using terms in the energy equation originating from the spatial terms of the Navier-Stokes equation, i.e., from the representation symbolically given by the second term on the right-hand side of eq.(B.47). In this representation only the velocity field at time t_n and its spatial derivatives are used. In current method, the resolution requires a high order method. Originally, the first usage of this method was based on spectral difference method ensuring a high order integration but was limited to periodic domains. Schraner [215] was able to show that this method for the analysis of the energy equation does not necessarily needs to make reference to spectral schemes. When considering the residual

$$- \mathcal{E}_n^{i,j,k} = \frac{\partial e_{i,j,k}}{\partial t} |_{CD} - \frac{\partial e_{i,j,k}}{\partial t} |_{FD/FV} \quad (\text{B.50})$$

where the first term on the right-hand side is computed directly from the energy data and the second term is computed using finite difference or finite volume discretized spatial terms in the energy balance equation, the estimate may provide a robust, satisfying results and largely independent of the finite difference / finite volume discretizations used. The author attributed this to the fact that the kinetic energy is a derived quantity, obtained from the primitive variables, and the discretized kinetic energy balance eq.(B.50) is not subject directly to the constraints for the momentum equation eq.(B.47) that requires the application of a high order discretization. For numerical simulations performed with an arbitrary, grid-based, compressible Navier-Stokes solver the symbolic eq.(B.50) is replaced by the discretization:

$$-\mathcal{E}_n^{i,j,k} = \frac{\Delta(\rho e_{kin})}{\Delta t} + \frac{\Delta(\rho e_{kin} u_\alpha)}{\Delta x_\alpha} + u_\alpha \frac{\Delta(p)}{\Delta x_\alpha} - \mu u_\beta \frac{\Delta(\tau^{ij})}{\Delta x_i} \quad (\text{B.51})$$

where the time derivative on the right-hand side is approximated using the kinetic energy data from the simulations at time steps t_n and t_{n+1} . The remaining terms are discretized spatial terms in the energy equation at time step t_n . The residual $E_{i,j,k}(n)$ may be designated as the numerical dissipation due to discretization errors of the Navier-Stokes solver. In general, the residual contains effects of all terms in the truncation error of a numerical scheme, including dissipative as well as dispersive errors. Yet, for sufficiently large subdomains the dissipative contributions dominate in a sense that the subdomain integrated $E_{i,j,k}(n)$ is positive.



Boundary layer thickness

C.1	Methods for boundary layer thickness estimation	277
C.2	Implementation in the boundary layer module	280
C.3	Comparison of boundary layer thickness against elsA solver output	281

C.1 Methods for boundary layer thickness estimation

Similarly to the nature of boundary layer (laminar, transitional or turbulent) is an important feature in fluid mechanics, the boundary layer thickness is also an important quantity. From a general sight, the boundary layer thickness hypothetically splits the flow field in a rotational region where viscous effects are predominant close to the wall and a region out of boundary layer where the flow is generally considered as irrotational and perfect flow described by Euler equation can apply. For numerical simulations, the knowledge of boundary layer thickness can give a better estimate of the grid points height that have to be set to accurately resolved boundary layer. For RANS simulation, different eddy viscosity can be applied depending on the position in or out of the boundary layer requiring the knowledge of boundary layer as for the algebraic eddy viscosity model of Cebeci-Smith.

Most techniques for determining the outer edge of the viscous layer start in the inviscid flow field and approach the viscous layer using a suitable criterion. This practice is generally suitable for external flows where regions out of boundary layer are generally undisturbed. For turbomachine flows, the notion of undisturbed flow out of boundary layer is generally not fulfilled since velocity profile inversion can be observed when moving away from the wall and boundary layer. In contrast, the length scales in the present Appendix are calculated by investigating the viscous

layer starting at the wall. Thus, the detection criterion is found inside the viscous layer.

C.1.0.1 Stock-Haase method

The boundary layer thickness can be evaluated from Navier-Stokes data using the diagnostic function F :

$$F = y^a \left[\frac{\partial u}{\partial y} \right]^b \quad (\text{C.1})$$

and the boundary layer thickness is obtained for:

$$\delta = \epsilon F_{max} \quad (\text{C.2})$$

where Y_{max} is the wall distance, for which $F = F_{max}$. The value of a , b and ϵ depends on the nature of the boundary layer. For laminar boundary layer, these coefficients can be obtained by considering the quasi-similar solutions functions (f , G , G_1 , G_2) for compressible, laminar boundary layers including heat transfer effects:

$$f''' + f f'' + \beta \left((1 - f^2) + EG \right) = 0 \quad (\text{C.3})$$

$$G_1'' + \text{Pr} f G_1' - 2 \text{Pr} \beta (1 - E) f' G_1 - 2(1 - \text{Pr}) (f' f'')' = 0 \quad (\text{C.4})$$

$$G_2'' + \text{Pr} f G_2' = 0 \quad (\text{C.5})$$

$$G(\eta) = EG_1(\eta) + G_2(\eta) \quad (\text{C.6})$$

with the boundary conditions at $\eta = 0$:

$$f = f' = 0, \quad G_1' = 0, \quad G_2 = G_{2w} \quad (\text{C.7})$$

and with the boundary conditions at $\eta \rightarrow \infty$:

$$f' \rightarrow 1, \quad G_1 \rightarrow 0, \quad G_2 \rightarrow 0 \quad (\text{C.8})$$

where η is the non dimensional wall-normal coordinate, β and E are pressure gradient and kinetic energy parameter and $\text{Pr} = 0.72$. Quasi-similar solutions are established for different Mach numbers and pressure gradients that cover the whole range from highly accelerated up to reversed flow situations, including adiabatic, cooling, and heating cases. Through numerical experimentation, the values of a and b are determined that produce a nearly unique value for all considered cases resulting in

$$F_{\text{lam}} = y^{3.9} \left[\frac{du}{dy} \right] \quad (a = 3.9 \text{ and } b = 1) \quad (\text{C.9})$$

$$\delta_{\text{lam}} = 1.294 y_{\text{max}} \quad (\varepsilon = 1.294). \quad (\text{C.10})$$

For turbulent boundary layers, The assumption that Coles velocity profiles describe the turbulent boundary layer flow sufficiently accurately allows one to compute the values for a; b, and ϵ such that:

$$F_{\text{turb}} = y \left[\frac{du}{dy} \right] \quad (a = b = 1) \quad (\text{C.11})$$

$$\delta_{\text{turb}} = 1.936 y_{\text{max}} \quad (\varepsilon = 1.936). \quad (\text{C.12})$$

C.1.0.2 Method based on low variation of wall-normal velocity profile

The boundary layer is characterized by area of strong variation of wall normal-velocity then the velocity becomes almost constant out of boundary layer. From this observation has been developed the method based on the low variation of the velocity profile. When the first derivative of the boundary layer profile velocity is smaller than a constant K_{v1} for the considered point N and the step between one derivative and the previous one N-1 closer to the wall is smaller than a constant K_{v2} :

$$\left| \frac{du}{dy} \right| < K_{v1} \text{ and } \left| \left[\frac{du}{dy} \right]_N - \left[\frac{du}{dy} \right]_{N-1} \right| < K_{v2} \quad (\text{C.13})$$

the current point is considered as the edge of the boundary layer.

C.1.0.3 Method based on relative difference between the isentropic velocity and the velocity

The boundary layer flow is characterized by a rotational flow region where main of the shear occurs while the region out of boundary layer is generally irrotational and can be considered as perfect fluid. The isentropic velocity being the velocity that would be obtained without any loss generation from pressure measurement:

$$M_{is} = \sqrt{\left(\left(\frac{p_0^{\text{freestream}}}{p} \right)^{\frac{\gamma-1}{\gamma}} - 1 \right) \cdot \frac{2}{\gamma-1}} \quad (\text{C.14})$$

Since the region out of boundary layer is considered as perfect fluid, the real velocity profile should tend to the isentropic one when reaching boundary layer edge (see Fig. C.1). Based on this observation has been proposed the third criterion to estimate the edge of boundary layer. The boundary layer edge is reached when isentropic and actual velocity u are above a threshold K_{vis} :

$$\frac{|u_{is} - u|}{u_{is}} < K_{vis} \quad (\text{C.15})$$

or alternatively based on isentropic M_{is} and actual Mach number M:

$$\frac{|M_{is} - M|}{M_{is}} < K_{Mis}. \quad (\text{C.16})$$

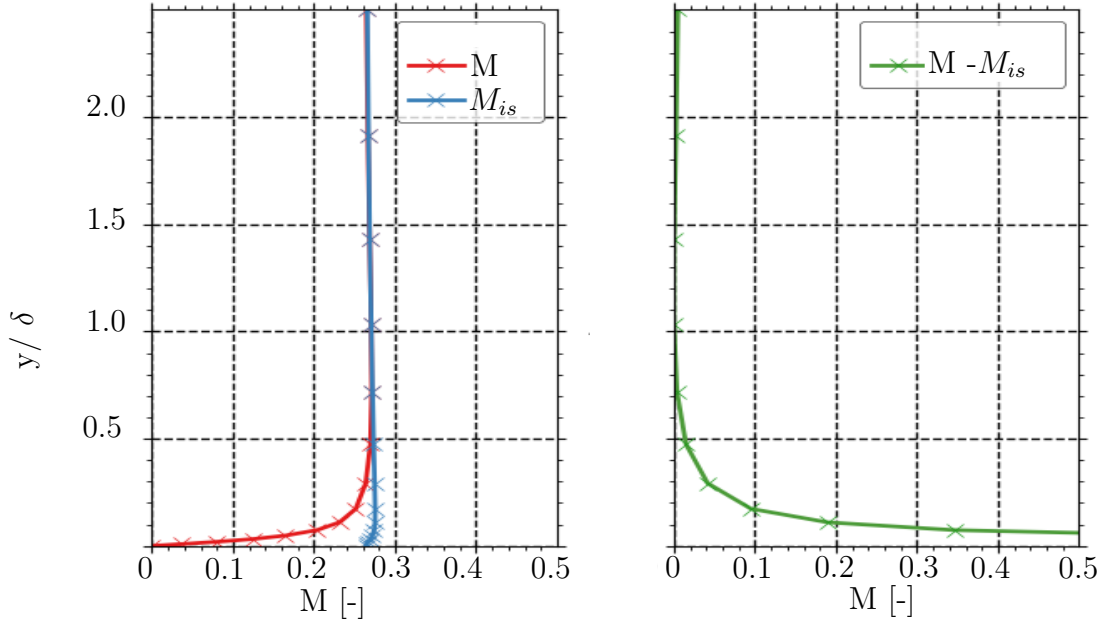


Figure C.1: Mach and isentropic Mach number to estimate boundary layer thickness

C.1.0.4 Method based on vorticity

This method is based on the definition of boundary layer where the flow is influence by viscous effects close to the wall and can be considered as inviscid flow elsewhere. Vorticity is mainly produced in near wall region, decaying exponentially when moving away to the wall and approaching zero when being out of the boundary layer. From this statement, the boundary layer thickness can be considered as the region where the vorticity has decayed to a small fraction of the maximum value that is closer to the wall. Michelassi et al. [216] proposed a criterion based on vorticity to estimate boundary layer thickness. This criterion is based on an arbitrary threshold ($\omega_{threshold}$) as

$$\omega_{threshold} = \omega_{min} + 0.01 (\omega_{max} - \omega_{min}). \quad (C.17)$$

beyond which the boundary layer is supposed to be for a considered point above the surface of interest. The maximum value ω_{max} is the one obtained generally close to the wall of the considered point. ω_{min} is the one obtained generally far from the wall in the inviscid flow region out of boundary layer. Alternatively, the vorticity can be integrated along the wall normal direction and when the integral reaches a constant or vary slowly, it can be said to be the edge of boundary layer.

C.2 Implementation in the boundary layer module

For any point of the considered surface on which the boundary layer thickness is to be estimated, a wall normal line to the considered point is drawn. The values of the flow field given to the boundary layer module are used to be interpolated onto this

line. For the Stock-Haase method, the value of the coefficients for the diagnostic function are implemented for turbulent boundary layer meaning $a = b = 1$ and $\varepsilon = 1.936$. The diagnostic function F being calculated in each point of the line from wall normal velocity gradients. These quantities can be computed since the three-dimensional flow field on the surface is given to the boundary layer module. For the condition on low variation of velocity gradients, the values are set to $K_{v1} = 0.01$ and $K_{v2} = 0.0001$. For the condition based on the difference of actual velocity compared to isentropic one, the value of the constant is set to $K_{vis} = K_{Mis} = 0.01$.

From the boundary layer thickness obtained from one of these methods or a mix of these methods, the different characteristic quantities of the boundary layer: the momentum boundary layer thickness θ and shape factor H . From these values is used the correlation of Green that makes possible to obtain a new value of the boundary layer thickness:

$$\delta = \delta^I * \left(\frac{\theta_s^I}{\delta_s^*} H_1 + 1 \right) \quad (C.18)$$

The final value of boundary layer thickness is mean value between the one obtained from one of the three methods and the correlation from Green:

$$\delta = \frac{\delta_{sf} + \delta_{num}}{2} \quad (C.19)$$

C.3 Comparison of boundary layer thickness against elsA solver output

In the ONERA solver elsA, the boundary layer can also be calculated. Three methods are used to estimate boundary layer thickness. A first method based on vorticity criterion, a second based on pressure criterion and a third one based on shear criterion. Starting from a node point at the wall, these different quantities are calculated by following the mesh line in the direction normal to the wall. In structured hexagonal meshes, using the mesh in near wall region to be approximated as the line normal to the wall is generally good approximation of real wall-normal line at least for the first points close to the wall. At each point of the mesh line are calculated pressure, shear and vorticity. The minimum value of such quantities (far from the wall) and maximum values (close to the wall) are calculated for each mesh line. Similarly to the former methods introduced previously, the boundary layer thickness is defined when some fraction of the difference between minimum and maximum value of the considered quantity is reached:

$$\frac{|p_{max} - p|}{p_{max} - p_{min}} < K_p \quad \frac{|\omega_{max} - \omega|}{\omega_{max} - \omega_{min}} < K_\omega \quad \frac{|(du/dy)_{max} - (du/dy)|}{(du/dy)_{max} - (du/dy)_{min}} < K_{shear} \quad (C.20)$$

The minimum boundary layer thickness of all three method is used as final value of thickness for the considered point on the surface. More theoretical and implementation details are given in Cliquet et al. [217]. Figure C.2 shows boundary layer

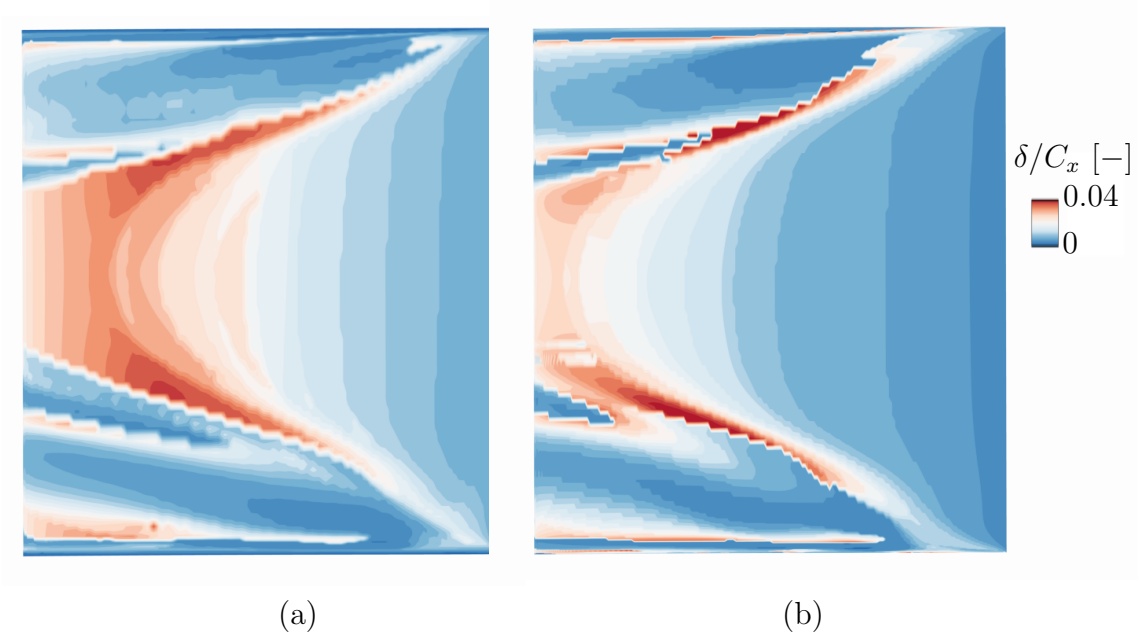


Figure C.2: Boundary layer thickness around blade suction side for linear cascade configuration without purge flow obtained from elsA (a) and boundary layer module (b)

thickness obtained from elsA solver and boundary layer module obtained around the blade of the linear cascade at no purge flow rate: The boundary layer thickness obtained from boundary layer module is thinner than the one obtained from elsA. However, the topology of boundary layer increase is similar and the regions where secondary flow structures interacts with blade suction side (thick regions are relatively well predicted). This comparison shows that even using different criteria and wall-normal line definition, the boundary layer estimation is relatively robust between the different methods.

List of Figures

1	Ideal and real (denoted ') Brayton cycle in T-S (a) and P-V diagrams (b)	xvi
2	Thermal efficiency for the ideal and real processes at different inlet combustion chamber temperature for compressor and turbine efficiency set to 0.9 (a) and propulsive efficiency for the jet engine based on the ratio between outlet and inlet velocity (b)	xvii
3	Jet engine (a) and turbofan (b) architectures Adapted from <i>Wikipedia: The jet engine</i>	xviii
4	Sketch of a gas turbine secondary air system. Courtesy of Rolls-Royce, <i>The Jet Engine</i> [3]	xix
5	Secondary air system in a turbine component (a) and at the rim seal interface (b). Courtesy of Rolls-Royce, <i>The Jet Engine</i> [3]	xxi
1.1	Sketch of a one stage turbine including the cavity between the nozzle guide vane and the rotor	3
1.2	Flow behaviour of a fluid initially at rest put in motion by a rotating disc (a) and a rotating fluid over a stationary disc (b). From Schlichting [8]	3
1.3	Auto-similar velocity profiles of the laminar flow between a rotor and a stator for different inter-disc Reynolds numbers Re_h . Top: axial velocity, middle: azimuthal velocity, bottom: radial velocity. The analytical derivation and computation of the velocity profiles is proposed in Bridel-Bertomeu [12]	5
1.4	Categories of flow encountered in enclosed rotor-stator cavity. Adapted from Owen and Rogers [18]	6
1.5	Sketch of turbine cavity and main annulus with main central core and pressure increase with radius	7
1.6	Observed flow patterns in the wheel space for simple rim seal at various non-dimensionalized purge flow rate C_w supplied in the cavity. From Phadke and Owen [19]	8
1.7	The different rim seal geometries (a) and the corresponding variation of $C_{w,min}$ with Re_θ with $G_c = 0.01$. Adapted from Phadke and Owen [19]	9
1.8	The effect of Re_θ on the variation of $C_{w,min}$ with mainflow Reynolds Re_u for axial rim seal at two gap ratio $G_c = 0.01$ (a) and $G_c = 0.02$ (b). Adapted from Phadke and Owen [22]	10

1.9	Sealing effectiveness for simple (a) and axial overlapping (b) rim seal $s/r_0 = 0.0048$, at various mainstream swirl flow fraction. Adapted from Phadke and Owen [22]	11
1.10	Ingress/egress process at the rim seal interface due to wake and potential effects. From Sangan et al. [27] (a). Streamlines of mainstream gas (red) and rim seal gas (blue) indicating a toroidal recirculation in the rim seal. From Savov et al. [28] (b)	12
1.11	The effect of C_w on the observed flow patterns in the wheel space for $Gc = 0.01$, $Re_\theta = 0$, $Re_u = 0.2 \times 10^6$	13
1.12	Instantaneous radial velocities (left: -70 to 50 m.s ⁻¹) and pressure (right: -15 to 15 kPa), $Re_\theta = 6 \times 10^6$. From Cao et al. [33]	16
2.1	Exergy fluxes in a turbomachine	29
2.2	Example of work output and exergy losses in a gas turbine as a fraction of the fuel exergy	30
2.3	Control volume located around a turbine stage. Example of viscous and thermal irreversibility creation from exergy approach. Adapted from Miller [51]	35
2.4	Control volume located around a turbine stage. Example of viscous and thermal irreversibility creation from exergy approach. Adapted from Miller [51]	36
2.5	The split of exergy χ in the flow mechanical work potential Ξ and flow thermal work potential, marked on a h-s diagram (a) and a control volume located around a turbine stage exhibiting the thermal creation from the flow mechanical work potential approach (b). Adapted from Miller [51]	38
2.6	Accumulated entropy in a rotor configuration, based on entropy flux through axial cut from volume integral of direct entropy generation S_{direct} from eq.(2.48) and volume integral of indirect entropy $S_{indirect}$ from eq.(2.69) (a). Comparison of direct and indirect methods for entropy using two different meshes (b). Adapted From Zlatinov [54]	46
2.7	Unsteady flow structures with corresponding characteristic length scale and frequency. From Lagraff et al. [66]	50
2.8	Blasius boundary layer profile for various pressure gradients (a) and start ($Re_{\theta_{start}}$)/end ($Re_{\theta_{end}}$) of transition based on momentum thickness Reynolds number over a flat plate without pressure gradient depending on the free stream turbulence (b). From Abu-Ghannam and Shaw [71]	53
2.9	Sketch of natural and bypass transition processes (a). From White [72]. Sketch of the different layers composing a turbulent boundary layer (b)	54
2.10	Sketch of possible transition process on aft part of low pressure turbine suction side depending on external disturbances (FST: Free Stream Turbulence, WNJ: Wake Negative Jet). Adapted from Cui et al. [76]	57

2.11	Variation of the shear stress with velocity in the boundary layer with $Re_\theta = 1000$ (a) and evolution of the dissipation coefficient for laminar and turbulent boundary layers based on the momentum thickness Reynolds number (b)	60
2.12	Mixing of two streams in a constant area duct corresponding to a simplified configuration of mixing process downstream a blade trailing edge. From Greitzer et al. [65]	63
2.13	Secondary flow structures in the passage proposed by Wang et al. [93]	65
2.14	Side (a) and downstream view (b) of simplified secondary flow structures in the passage proposed by Cui et al. [76]	66
2.15	Sketch of the tip leakage process over a rotor blade. From P. Lampart [105]	71
2.16	Evolution of an upstream wake in the passage of a downstream row, contours of entropy (a) and negative jet phenomenon (b). Adapted from Pullan [106]	73
2.17	Entropy contour at exit of the stator (left) and rotor (right). From Denton and Pullan [87]	74
2.18	Generation of entropy due to shear layer in an axisymmetric (1)/3D configuration (2) (a). From Zlatinov [54]. Sketch of the mixing of two streams (b). From Greitzer et al. [65]	77
2.19	Regions of entropy generation in an axial plane with vortex center (a). Radial velocity across the blade due to crossflow (1), blockage (2) contributions (b)	78
2.20	Decomposition of entropy production according to the velocity gradients (see eq.(3.12) p.146 for more details). From Zlatinov et al. [54]	79
3.1	View of the experimental set up. Adapted from Schuler [114]	83
3.2	Rim seal geometry	83
3.3	Inlet profiles at one axial chord length upstream of the blade leading edge: (a): azimuthal angle, (b): radial angle, (c): inlet total pressure (d): inlet total temperature. The height has been normalized by the height of the main annulus. $(P_{ref}, T_{ref})=(101\ 325\ \text{Pa}, 300\ \text{K})$	84
3.4	Turbulence intensity decay in the axial direction downstream the turbulence grid (a) and five-holes probe measurement positions (b)	85
3.5	Simulation domain	86
3.6	Structured multi-block 0-6H topology	88
3.7	y^+ distribution around the wetted surfaces: unwrapped blade (top), hub and shroud (bottom) for the RANS simulation. LE and TE stand respectively for leading and trailing edge	89
3.8	Leading edge discretization (a) : RANS elsA, (b) : LES elsA, (c) : LES AVBP, (d) : LES-LBM Pro-LB	90
3.9	y^+ distribution around the wetted surfaces: unwrapped blade (top), hub and shroud (bottom) for the LES elsA simulation (temporal average). LE and TE stand respectively for leading and trailing edge	91
3.10	Averaged grid dimension at the wall for the LES elsA simulation, s^+ : streamwise, n^+ : normal, r^+ : spanwise	92

3.11	Evolution of the mass flow rate at the inlet, cavity inlet and outlet based on the number of iterations performed (RANS)	95
3.12	Convergence of continuum, first momentum, energy and turbulent residuals (logarithm scale) for the RANS simulation	95
3.13	Evolution of the mass flow rate at the inlet, outlet (a) and cavity inlet (b) in time for the LES elsA simulation	96
3.14	Evolution of the mass flow rate at the inlet, outlet (a) and cavity inlet (b) in time for the LES AVBP simulation	96
3.15	Comparison of the pressure coefficient distribution around the blade (a): 4%, (b): 6%, (c): 50% and pressure coefficient downstream of the blade (d) for the A05 configuration for the standard and refined mesh grid (RANS simulation)	98
3.16	Comparison of the pressure loss coefficient downstream of the blade for the A05 configuration for coarse and fine grids, (a) : LES elsA, (b) : LES AVBP, (c) : LES-LBM Pro-LB	99
3.17	Comparison of the pressure coefficient distribution around the blade at (a): 4%, (b): 6%, (c): 50% span and pressure coefficient downstream of the blade for the A05 configuration for k- ω and Spalart-Allmaras turbulence model (RANS)	100
3.18	Suction side boundary layer thickness from k- ω turbulence model used in the study (a) and Spalart-Allmaras model (b)	101
3.19	Pressure coefficient around the blade at (a): 4%, (b): 6%, (c): 50% span for the A05 configuration using RANS approach and experimental results at the different blade height (d)	102
3.20	Pressure coefficient around the blade at 4, 6 and 50% span for the A05 configuration using the LES elsA approach	103
3.21	Pressure coefficient around the blade at (a): 4%, (b): 6%, (c): 50% span for the A05 configuration using the LES AVBP approach	104
3.22	Pressure coefficient around the blade at (a): 4%, (b): 6%, (c): 50% span the A05 configuration using the LES Pro-LB approach	105
3.23	Pressure loss coefficient downstream the blade for the A05 configuration for the different solvers (a): RANS, (b): LES elsA, (c): LES AVBP, (d): Pro-LB	106
3.24	Hub (a) and shroud (b) boundary layer thickness from the RANS simulation	107
3.25	Streak lines (a) and skin friction (b) at the shroud wall exhibiting rolling process of the horse shoe vortices from the LES simulation	108
3.26	Streak lines on the suction (left) and pressure side (right) for the A05 configuration from the RANS simulation (unwrapped blade)	109
3.27	Velocity vector close to the rim seal: face to leading edge (a)(c) and at the center of the channel (b)(d) for the A05 and S05 configuration	110
3.28	Total temperature distribution at the hub (a) and horseshoe vortex interaction with the cavity flow based on a iso q -criterion $q = 10^6$ colored by the streamwise vorticity from an instantaneous LES solution (b)	111
3.29	Isentropic Mach number at mid span for LES simulation	112

3.30	Streak lines at the hub from the temporally averaged LES (a) and sight from downstream to upstream of the secondary flows in the passage obtained using iso q -criterion $q = 10^6$ colored by vorticity from instantaneous LES solution (b)	113
3.31	Pressure coefficient and vorticity downstream the blade from instantaneous LES solution where experimental measurements have been performed	114
3.32	Spectrum and corresponding summed modes (1, 2, 3 and 4) related to the horse shoe vortex process at the shroud obtained from Dynamical Mode Decomposition (LES simulation)	115
3.33	Pressure standard deviation $\sigma(p)$ around the blade suction side (a), at hub and shroud (b)	116
3.34	Three-dimensional (a) and two-dimensional modes related to Kelvin-Helmholtz instability based on fully three-dimensional and two-dimensional meridional plane face to the blade leading edge (FB) and at the center of the passage (CP) (b)	117
3.35	Pressure coefficient and domain of fluctuation at 4% blade height (a) and downstream blade (b) where the characteristic time T corresponds to the time for a particle to be convected of one axial chord .	118
3.36	Density frequency spectrum in x, z cuts and around the blade with the A05 configuration and corresponding to the fundamental Kelvin-Helmholtz density mode	119
3.37	Positions in the linear cascade where the boundary layer profiles have been extracted for the RANS and LES simulations	120
3.38	Inlet hub boundary layer profiles for RANS (a) and LES simulations (b), see Fig. 3.37 for the corresponding extraction positions	120
3.39	Boundary layer profiles for the RANS (a) and LES simulation (b) upstream of the blade leading edge, see 5 in Fig. 3.37 for the corresponding extraction position	121
3.40	Streak lines on the suction and pressure side for the A05 configuration from the LES simulation (unwrapped blade)	121
3.41	Oil-painting visualization on the blade suction (a) and pressure side (b)	122
3.42	Boundary layer profiles on the blade suction side in the favourable pressure gradient portion for the RANS (a) and the LES simulations (b), see position 6, 7 and 8 in Fig. 3.37	123
3.43	Boundary layer profiles on the blade suction side in the adverse pressure gradient portion for the RANS (a) and LES simulations (b), see 9, 10, 11 in Fig. 3.37 for the corresponding extraction positions	124
3.44	Iso q -criterion $q = 10^7$ colored by the vorticity showing the turbulence injection at the inlet of the domain in the first time steps of the AVBP simulation (a) and the turbulent kinetic energy decay from the inlet of the domain to the blade leading edge based on a theoretical HIT decay and obtained in AVBP simulation (b)	126

3.45	Boundary layer profiles on the hub endwall (a) and around the blade (b) for the LES simulation AVBP with turbulence injection. The boundary layer profile extraction location is provided in Fig. 3.37 . . .	127
3.46	Lateral sight of blade suction side with iso q -criterion $q = 10^6$ colored by streamwise vorticity for the LES simulation AVBP with turbulence injection at the inlet	128
3.47	Pressure coefficient around the blade at mid-span (a) and pressure loss coefficient downstream of the blade for the axial rim seal at an intermediate purge flow rate for the LES simulation AVBP with turbulence injection at the inlet (b)	128
3.48	Evolution of the flow exergy from the inlet to outlet of the domain (a). Evolution of anergy along the simulation domain including viscous $\Phi_{\nabla u}$, thermal contribution $\Phi_{\nabla T}$ (b) and anergy production along the axial evolution $d\Phi_{\nabla u}/dx$ $d\Phi_{\nabla T}/dx$ (c). The right axis refers to thermal contribution and left axis to viscous contribution	132
3.49	Evolution of the anergy production along the simulation domain for viscous $d\Phi_{\nabla u}/dx$ (a) and thermal contributions $d\Phi_{\nabla T}/dx$ (b) including the mean and turbulent contributions	134
3.50	Example of a simulation domain discretized in axial subvolumes V_i (green). For a simple configuration where only the hub boundary layer is considered, V_i can be split in a subvolume associated to the hub boundary layer (red) and a remaining domain that is simply the subvolume V_i minus the subvolume associated to the hub boundary layer (blue)	136
3.51	Mean, turbulent and total entropy production for the different subdomains	138
3.52	Entropy production associated to mean and turbulent contributions for the hub and shroud	138
3.53	Mean and turbulent contribution to the blade boundary layer entropy production	139
3.54	Pressure and suction side contribution to the viscous entropy production	140
3.55	Mean and turbulent contribution to the viscous entropy production for the remaining term	141
3.56	Mean and turbulent entropy production related to the hub and shroud in the boundary layer at a constant distance from the wall ($y^+ = 30$)	142
3.57	Mean and turbulent viscous entropy production related to the suction side blade in the boundary layer at a constant distance from the wall ($y^+ = 30$)	143
3.58	Mean, turbulent and total entropy production in the boundary layer at mid-span, mid-height of blade suction side (a) and accumulated entropy production relatively to the wall-normal coordinate (b) . . .	143
3.59	Total thermal entropy production and contributions of the subdomains (hub, shroud, blade) and remaining domain	145

3.60	Iso-contour of the thermal entropy colored by temperature (a) and iso-contour of viscous entropy colored by temperature (b) exhibiting the secondary vortices downstream of the blade trailing edge (trailing shed and passage vortices)	146
3.61	Hub and shroud boundary layer viscous entropy production with wall-normal contributions (du_s/dr and du_c/dr)	147
3.62	Blade boundary layer entropy production with wall-normal contribution (du_s/dc)	148
3.63	Entropy production at the rim seal interface between the left corner at $x/C_x = -0.26$ and right corner at $x/C_x = -0.04$ including the terms with high contribution to entropy: shear layer for axial and tangential velocity gap (du_c/dr and du_s/dr) (a) and variation of radial velocity u_r close to rim seal right corner (b)	148
3.64	Viscous entropy production in the passage from the blade leading edge to trailing edge ($x/C_x = 0$ to $x/C_x = 1$) including the terms with high contribution to entropy: variation of radial velocity u_r in the passage (a) and u_c close to the trailing edge (b)	149
3.65	Axial cuts in the passage colored by viscous entropy production related to du_r/dc gradients	150
3.66	Viscous entropy production from upstream of the trailing edge $x/C_x = 0.9$ to the end of the domain $x/C_x = 3$ including the terms with high contribution to entropy: trailing shed vortex process (du_c/ds) (a) and radial velocity gradients (b)	151
3.67	Thermal entropy production along the domain with the large contribution of the radial variation of temperature (dT/dr)	151
3.68	Pressure coefficient around the blade at (a)-(b): 4, (c)-(d): 6 and (e)-(f): 50% span for the axial rim seal at the different purge flow rates based on the RANS approach (left figures) and experiments (right figures)	153
3.69	Pressure loss coefficient downstream of the blade for the axial rim seal at the different purge flow rates obtained from RANS simulations (a) and experiments (b)	154
3.70	Influence of the purge flow rate on entropy production for the total (a), blade (b), hub (c), shroud (d) and remaining term (e) contributions	155
3.71	Pressure coefficient around blade at 4, 6 and 50% span for the different rim seal geometries at high purge flow rate (1%) based on the RANS approach and experiments	157
3.72	Pressure loss coefficient downstream of the blade at high purge flow rate (1%) for the different rim seal geometries obtained from RANS simulations (a) and experiments (b)	158
3.73	Influence of the rim seal geometry (axial and simple overlapping) on entropy production for total (a), blade (b), hub (c) contributions . . .	158
3.74	Radial cut close to the hub colored by the radial velocity for axial (a) and single overlapping geometry (b)	159
3.75	Radial cut close to the hub colored by temperature for axial (a) and single overlapping geometry (b)	159

3.76	Mean and turbulent contribution to the viscous entropy from the RANS simulation (top). Resolved and subgrid contributions to the viscous entropy production based on the LES simulation without turbulence injection (bottom)	160
3.77	Total entropy production for the different subdomains in the LES simulation without turbulence injection	161
3.78	Total entropy production for the different subdomains in the LES simulation with turbulence injection	162
4.1	Low pressure turbine experimental test rig	166
4.2	Sketch of the two-stage linear cascade including the pressure taps, thermocouples and total pressure experimental measurement planes (MP0I)	167
4.3	Simulation domain representing 1/24 of the full test rig	170
4.4	Iso-contour of quantity "LIKE"	172
4.5	Grid refinement for rotor 1 including wake refinement of stator 1 and refinement in the cavities	173
4.6	y^+ resolution around the different blade suction sides S1, R1, S2, R2 (top) and at the hub surface (bottom)	174
4.7	y^+ resolution at the cavity walls	174
4.8	Temporal evolution of the mass flow rate at the inlet, outlet (a) and at the inlet of the cavities (b)	175
4.9	Pressure coefficient around the blade at (a): 5, (b): 20 and (c): 50% span of the stator 2 row and experimental measurements at the different nozzle guide vane height (d)	176
4.10	Evolution of the total and static pressure in the simulation domain compared to the experiments non-dimensionalized by the pressure at the outlet of the domain	177
4.11	Pressure loss coefficient downstream of stator 1 (a), rotor 1 (b) and stator 2 (c) obtained numerically compared to experimental data . . .	178
4.12	Evolution of the dimensionless volume-averaged kinetic energy for the entire cavity 1 (a) and evolution of the dimensionless kinetic energy of the rotor boundary layer (b) and stator boundary layer at the cavity mid-height (c)	180
4.13	Radial and tangential velocities in the cavity 1 in a meridional plane .	181
4.14	Radial and tangential velocities into the cavities 2 and 3 in a meridional plane	181
4.15	Three-dimensional streamlines in the cavities 1, 2 and 3	182
4.16	Azimuthally-averaged radial (a) and azimuthal (b) velocity profiles at cavity 1 mid-height	183
4.17	Azimuthally-averaged radial (a) and azimuthal (b) velocity profiles at cavity 2 mid-height	183
4.18	Azimuthally-averaged radial (a) and azimuthal (b) velocity profiles at cavity 3 mid-height	184
4.19	Axial velocity in the labyrinth (a) and pressure evolution normalized by pressure cavity 2 (b)	185

4.20	Repartition of cooling flow in cavity 1 and 2 on the three rim seal . .	185
4.21	Wall friction on the surfaces of stator 1 and on an axial plane downstream of the blade with pressure coefficient. The shroud and cavities are omitted	186
4.22	Boundary layer profile on the blade suction side at mid-span for stator row 1 (a) and 2 (b)	187
4.23	Suction side boundary layer thickness for stator 1 (a) and 2 (b) . . .	187
4.24	Total pressure, whirl and radial angle downstream of the first rotor row (compared to the nominal turning of the blade 64.6° and no radial angle) from simulation (top) and experiments (bottom) (MP02 plane)	188
4.25	Wall friction on the surfaces of stator 2 and axial plane downstream of the blade with pressure coefficient. The casing, rotor shrouding and cavities are omitted	189
4.26	Wall friction on the surfaces of stator 1, rotor 1 and axial plane downstream of the blade with total pressure showing wakes and secondary flow influence on the pressure coefficient downstream of the blade. The casing, rotor shrouding and cavities are omitted	190
4.27	Wall friction on the surfaces of rotor 1 and axial plane downstream of the blade with total pressure showing wakes, secondary and bypassed flow influence on the pressure coefficient downstream of the blade. The casing and cavities are omitted	191
4.28	Radial velocity at the rim seal interface in a radial and axial plane (a). Streamlines showing the recirculation zone at rim seal interface S1-R1. A: wake region, B: passage vortex. Rotor blade 1 and 2 have been omitted	192
4.29	Pressure distribution at the rim seal interface 1 (S1-R1) and 3 (S2-R2)	192
4.30	Radial evolution at the rim seal interface at the beginning ($x/C_x = 6.3$), middle ($x/C_x = 6.4$) and end of the cavity ($x/C_x = 6.5$) for axial (a), azimuthal (b), total pressure (c) and static temperature (d) . . .	193
4.31	Extracted power on first rotor along blade (a) and cumulated power (b), the first rotor blade extends from $x/C_x = 6.9$ to 7.6	195
4.32	Extracted power on second rotor along blade (a) and cumulated power (b), the second rotor blade extends from $x/C_x = 10.35$ to 11.1	196
4.33	Evolution of total viscous anergy production (resolved+subgrid) along the domain including subgrid scale model contribution	197
4.34	Evolution of total anergy production (resolved+subgrid) along the domain including the artificial contribution	198
4.35	Evolution of total thermal anergy production (resolved+subgrid) along the domain including subgrid scale model contribution	199
4.36	Temperature at the rim seal interface, along the hub and rotor 1 blade with migrating cavity flow on blade suction side	199
4.37	Total entropy production at the inlet (a) and outlet (b) of the domain one axial chord downstream of rotor 2 blade trailing edge including wall normal contributions	200
4.38	Evolution of the total viscous entropy production along the simulation and restricted to the hub/shroud wall normal contribution (du_s/dr) .	201

4.39	Iso-contour of entropy production along first stator row for the contribution du_s/dr (left) and du_c/dr (right)	201
4.40	Wall friction on the surfaces of stator one rotor one and axial plane downstream blade with total pressure showing wakes and secondary flow influence on pressure coefficient downstream blade. The shroud is omitted	202
4.41	Evolution of the total viscous entropy production along the simulation and restricted to the hub/shroud wall normal contribution (du_c/dr)	203
4.42	Total entropy production along the domain and blade wall normal contribution (du_s/dc)	203
4.43	Axial cuts at the trailing edge colored by viscous entropy production related to du_s/dc gradient for stator 1 and 2	204
4.44	Total entropy production along the domain and entropy production related to du_r/dc gradients	205
4.45	Axial cuts along the passage domain colored by viscous entropy production related to du_r/dc gradient for stator one and two	205
4.46	Iso-surface of q-criterion colored by streamwise vorticity showing upstream secondary vortices from stator 1 impacting rotor 1 in an upstream (a) and side view (b)	206
4.47	Pressure coefficient downstream of the rotor 1	206
4.48	Contribution of viscous and thermal anergy to the decrease of exergy or the flow	207
4.49	Contribution of the work extracted on the shaft to the decrease of exergy of the flow	207
A.1	Illustration of different scales to describe a flow. From left to right, macroscopic, mesoscopic and microscopic scales	223
A.2	One-dimensional continuous distribution function and discretization (D1Q3) to recover the exact integral value (a). Velocity distribution in three dimension (D3Q19) to recover the weakly compressible isothermal Navier-Stokes equations (b)	228
A.3	Link between velocity, space and time discretization in a Cartesian grid	229
A.4	Schematic view of steps 2 to 4 required to perform one iteration in LBM approach from a D1Q3 lattice. Courtesy of Coreixas [157]	230
A.5	Turbulent spectrum with degrees of modeling: DNS, LES and RANS. From Gravemeier et al. [159]	232
A.6	Reynolds number variation in a medium-sized gas turbine engine (a) and engine flight envelope Reynolds number for a medium-sized low pressure turbine (b). Adapted from Hourmouziadis [166]	234
A.7	Sketch of the scale splitting principle in LES due to the mesh. From Sagaut [178]	237
A.8	Computational domain with incoming and outgoing waves at the inlet and outlet of the domain	242
A.9	Hybrid (a) and structured meshes (b) around a low pressure turbine blade at mid-span	246

A.10	Grid requirements for LES and hybrid RANS-LES following Piomelli and Balaras [195] and adapted from Tucker [158] (a). Sketch of the influence of the grid resolution on the theoretical turbulence cascade (b)	247
A.11	Decomposition of the sources of pressure loss downstream of a blade in a simplified configuration	252
B.1	Normalized entropy distribution across a shock; $M = 1.5$, upstream entropy taken as 0, downstream value =1.0	269
C.1	Mach and isentropic Mach number to estimate boundary layer thickness	280
C.2	Boundary layer thickness around blade suction side for linear cascade configuration without purge flow obtained from elsA (a) and boundary layer module (b)	282

List of Tables

3.1	Characteristics of the cascade rig	84
3.2	Numerical setup for the Navier-Stokes numerical approaches	94
3.3	Numerical setup for the LBM numerical approach	94
3.4	Evalation of computational cost	97
3.5	Exergy balance at two different reference conditions	133
4.1	Characteristics of the stator and rotor rows	168
4.2	Characteristics of the annular test rig	169
4.3	Purge mass flow rate (kg.s^{-1}) for the different cases studied	169
A.1	Velocity particle and weight of Gauss-Hermite quadrature of the D3Q19 lattice	227

Bibliography

- [1] D. C. Wisler. Loss Reduction in Axial-Flow Compressors Through Low-Speed Model Testing. *Journal of Engineering for Gas Turbines and Power*, 107(2):354, 1985. (Cited p. xiv)
- [2] N. Gourdain, L. Y. M. Gicquel, and E. Collado. Comparison of RANS and LES for prediction of wall heat transfer in a highly loaded turbine guide vane. *Journal of Propulsion and Power*, 28(2):423–433, 2012. (Cited p. xv and 244.)
- [3] Rolls Royce. Rolls Royce - The Jet Engine. In *The Jet Engine*, pages 1–45. 1996. (Cited p. xix, xxi and 283.)
- [4] B.V. Johnson, G J Mack, R E Paolillo, and W A Daniels. Turbine Rim Seal Gas Path Flow Ingestion Mechanisms. In *30th AIAA/ASME/SAE/ASEE Joint Propulsion Conference*, 1994. (Cited p. 1)
- [5] V. W. Ekman. On the influence of the earth’s rotation on ocean-currents. 1905. (Cited p. 2)
- [6] Th. V. Kármán. Über laminare und turbulente Reibung. *ZAMM - Journal of Applied Mathematics and Mechanics / Zeitschrift für Angewandte Mathematik und Mechanik*, 1(4):233–252, 1921. (Cited p. 2)
- [7] W. G. Cochran and S. Goldstein. The flow due to a rotating disc. *Mathematical Proceedings of the Cambridge Philosophical Society*, 30(03):365, 1934. (Cited p. 2)
- [8] H. Schlichting and K. Gersten. *Boundary Layer Theory*, volume 9. 2001. (Cited p. 3, 55, 61 and 283.)
- [9] U. T. Bödewadt. Die Drehströmung über festem Grunde. *ZAMM - Journal of Applied Mathematics and Mechanics / Zeitschrift für Angewandte Mathematik und Mechanik*, 1940. (Cited p. 4)
- [10] G. K. Batchelor. Note on a class of solutions of the Navier-Stokes equations representing steady rotationally-symmetric flow. *Quarterly Journal of Mechanics and Applied Mathematics*, 4(1):29–41, 1951. (Cited p. 4 and 5.)
- [11] Alan J. Faller. Instability and transition of disturbed flow over a rotating disk. *Journal of Fluid Mechanics*, 230:245–269, 1991. (Cited p. 4)

- [12] T. Bridel-bertomeu. *Investigation of unsteady phenomena in rotor/stator cavities using Large Eddy Simulation*. PhD thesis, INP, 2016. (Cited p. 5, 179, 180 and 283.)
- [13] K. Stewartson. On the flow between two rotating coaxial disks. *Mathematical Proceedings of the Cambridge Philosophical Society*, 49(2):333–341, 1953. (Cited p. 5)
- [14] L.A. Maroti, G.G. Deak, and Kreith F.F. Flow Phenomena of Partially Enclosed Rotating Disks. *Journal of Basic Engineering*, pages 539–549, 1960. (Cited p. 5)
- [15] M. H. Rogers and G. N. Lance. The rotationally symmetric flow of a viscous fluid in the presence of an infinite rotating disk. *Journal of Fluid Mechanics*, 7(4):617–631, 1960. (Cited p. 5)
- [16] A. Sirivat. Stability experiment of flow between a stationary and a rotating disk. *Physics of Fluids A*, 3(11):2664–2671, 1991. (Cited p. 5)
- [17] J. W. Daily and R. E. Nece. Chamber Dimension Effects on Induced Flow and Frictional Resistance of Enclosed Rotating Disks. *Journal of Basic Engineering*, 82(1):217, 1960. (Cited p. 6 and 183.)
- [18] J. M. Owen and R. H. Roger. Flow and heat transfer in rotating-disc systems. Volume I - Rotor-stator systems. *NASA STI/Recon Technical Report A*, 90:45759, 1989. (Cited p. 6 and 283.)
- [19] U. P. Phadke and J. M. Owen. Aerodynamic aspects of the sealing of gas-turbine rotor-stator systems. Part 3: The effect of nonaxisymmetric external flow on seal performance. *International Journal of Heat and Fluid Flow*, 9(2):113–117, 1988. (Cited p. 8, 9 and 283.)
- [20] F. J. Bayley and J. M. Owen. Flow between a Rotating and a Stationary Disc. *Aeronautical Quarterly*, 20(04):333–354, 1969. (Cited p. 8)
- [21] F. J. Bayley and J. M. Owen. The Fluid Dynamics of a Shrouded Disk System With a Radial Outflow of Coolant. *Journal of Engineering for Gas Turbines and Power*, 92(3):335–341, 1970. (Cited p. 8)
- [22] U. P. Phadke and J. M. Owen. Aerodynamic aspects of the sealing of gas-turbine rotor-stator systems. Part 2: The performance of simple seals in a quasi-axisymmetric external flow. *International Journal of Heat and Fluid Flow*, 9(2):106–112, 1988. (Cited p. 10, 11, 13, 283 and 284.)
- [23] W. A. Daniels, B. V. Johnson, D. J. Graber, and R. J. Martin. Rim Seal Experiments and Analysis for Turbine Applications. 1992. (Cited p. 11)
- [24] D. Bohn, E. Johann, and U. Krüger. Experimental and Numerical Investigations of Aerodynamic Aspects of Hot Gas Ingestion in Rotor-Stator Systems With Superimposed Cooling Mass Flow. In *ASME 1995 International Gas*

- Turbine and Aeroengine Congress and Exposition*, volume 1, pages 1–12, 1995. (Cited p. 11 and 12.)
- [25] R. Teuber, Y. S. Li, J. Maltson, M. Wilson, G. D. Lock, and J. M. Owen. Computational extrapolation of turbine sealing effectiveness from test rig to engine conditions. *Proceedings of the Institution of Mechanical Engineers, Part A: Journal of Power and Energy*, 227(2):167–178, 2013. (Cited p. 11 and 12.)
 - [26] S. Dadkhah, A. B. Turner, and J. W. Chew. Performance of Radial Clearance Rim Seals in Upstream and Downstream Rotor-Stator Wheelspaces. *Journal of Turbomachinery*, 114(2):439–445, 1992. (Cited p. 12)
 - [27] C. M. Sangan, O. J. Pountney, J.A. Scobie, M. Wilson, J. M. Owen, and G. D. Lock. Experimental Measurements of Ingestion Through Turbine Rim Seals-Part III: Single and Double Seals. *Journal of Turbomachinery*, 135(5):051011, 2013. (Cited p. 12 and 284.)
 - [28] S. S. Savov, N. R. Atkins, and S. Uchida. A comparison of single and double lip seal geometries. In *Proceedings of ASME Turbo Expo 2016: Turbomachinery Technical Conference and Exposition*, number GT2016-56317, 2016. (Cited p. 12, 14, 16 and 284.)
 - [29] D. Bohn, B. Rudzinski, N. Surken, and W. Gartner. Experimental and Numerical Investigation of the Influence of Rotor Blades on Hot Gas Ingestion Into the Upstream Cavity of an Axial Turbine Stage. *Proceedings of ASME Turbo Expo 2000, May 8-11, 2000, Munich, Germany*, (C):1–8, 2000. (Cited p. 12 and 15.)
 - [30] A B Turner. Ingestion Into the Upstream Wheelspace of an Axial Turbine Stage. *Journal of Turbomachinery*, 116(2):327–332, 1994. (Cited p. 12 and 13.)
 - [31] S. S. Savov and N. R. Atkins. A Rim Seal Ingress Model Based on Turbulent Transport. In *Proceedings of ASME Turbo Expo 2017: Turbomachinery Technical Conference and Exposition*, volume 5B, page V05BT15A009, 2017. (Cited p. 12)
 - [32] H. T. Abe, J. K., and Takeuchi. An investigation of turbine disk cooling (experimental investigation and observation of hot gas flow into a wheel space). 1979. (Cited p. 13)
 - [33] C. Cao, J. W. Chew, P. R. Millington, and S. I. Hogg. Interaction of Rim Seal and Annulus Flows in an Axial Flow Turbine. In *Volume 5: Turbo Expo 2003, Parts A and B*, pages 1011–1019, 2003. (Cited p. 13, 15, 16 and 284.)
 - [34] E. De La Rosa Blanco, H. P. Hodson, and R. Vazquez. Effect of the leakage flows and the upstream platform geometry on the endwall flows of a turbine cascade. *Journal of Turb*, 6 Part A(January 2009):733–744, 2009. (Cited p. 14, 16, 77 and 78.)

- [35] M Rabs, F.-K Benra, H J Dohmen, and O Schneider. Investigation of Flow Instabilities Near the Rim Cavity of a 1.5 Stage Gas Turbine. In *Proceedings of ASME Turbo Expo: Power for Land, Sea and Air*, 2009. (Cited p. 14 and 16.)
- [36] R. Schädler, A. I. Kalfas, R. S. Abhari, G. Schmid, and S. Voelker. Modulation and Radial Migration of Turbine Hub Cavity Modes by the Rim Seal Purge Flow. *Journal of Turbomachinery*, 139(1):011011, 2016. (Cited p. 14 and 16.)
- [37] S. H. Ko and D. L. Rhode. Thermal Details in a Rotor-Stator Cavity at Engine Conditions With a Mainstream. *Journal of Turbomachinery*, 114(2):446, 1992. (Cited p. 14)
- [38] S H Ko, D L Rhode, and Z Guo. Computed Effects of Rim Seal Clearance and Cavity Width on Thermal Distributions. In *International Gas Turbine and Aeroengine Congress and Exposition*, 1993. (Cited p. 14)
- [39] T. S.D. O’Mahoney, N. J. Hills, J. W. Chew, and T. Scanlon. Large-Eddy simulation of rim seal ingestion. *Proceedings of the Institution of Mechanical Engineers, Part C: Journal of Mechanical Engineering Science*, 225(12):2881–2891, 2011. (Cited p. 15 and 17.)
- [40] R. Jakoby, T. Zierer, L. DeVito, K. Lindblad, J. Larsson, D. E. Bohn, J. Funcke, and A. Decker. Numerical Simulation of the Unsteady Flow Field in an Axial Gas Turbine Rim Seal Configuration. In *Proceedings of the ASME Turbo Expo 2004*, volume 4, pages GT2004–53829, 2004. (Cited p. 16 and 17.)
- [41] P. F. Beard, J. Chew, F. Gao, and K. S. Chana. Unsteady Flow Phenomena in Turbine Rim Seals. In *Volume 5A: Heat Transfer*, page V05AT15A001, 2016. (Cited p. 16)
- [42] J. Boudet, V. N. D. Autef, J. W. Chew, N. J. Hills, and O. Gentilhomme. Numerical simulation of rim seal flows in axial turbines. *Aeronautical Journal*, 109(1098):373–384, 2005. (Cited p. 16)
- [43] J. Boudet, N. J. Hills, and J. W. Chew. Numerical Simulation of the Flow Interaction Between Turbine Main Annulus and Disc Cavities. In *Volume 6: Turbomachinery, Parts A and B*, volume 2006, pages 553–562, 2006. (Cited p. 16)
- [44] S. Julien, J. Lefrancois, G. Dumas, G. Boutet-blais, S. Lapointe, J-F. Caron, R. Marini, and W. Canada. Simulation of flow ingestion and related structures in a turbine disk cavity. *Proceedings of ASME Turbo Expo 2010: Power for Land, Sea and Air GT2010*, (43994):1071–1080, 2010. (Cited p. 16)
- [45] C. Wang, S. Mathiyalagan, B. Johnson, J. Glahn, and D. Cloud. Rim Seal Ingestion in a Turbine Stage From 360 Degree Time-Dependent Numerical Simulations. *Journal of Turbomachinery*, 136(3):031007, 2013. (Cited p. 16)
- [46] F. Wlassow. *Analyse instationnaire aérothermique d’un étage de turbine avec transport de points chauds*. PhD thesis, Ecole Centrale de Lyon, 2012. (Cited p. 17, 87 and 88.)

- [47] F. Gao, J. W. Chew, P. F. Beard, D. Amirante, and N. J. Hills. Large-eddy simulation of unsteady turbine rim sealing flows. *International Journal of Heat and Fluid Flow*, 70:160–170, 2018. (Cited p. 17)
- [48] J. D. Denton. Loss Mechanisms in Turbomachines. *Journal of Turbomachinery*, 115(4):621, 1993. (Cited p. 20, 46, 59, 60, 64, 87, 99, 136, 137 and 144.)
- [49] S. Carnot. *Reflections on the Motive Power of Fire*. Dover, 1960. (Cited p. 22)
- [50] J. H. Horlock and William W. Bathie. Advanced Gas Turbine Cycles. *Journal of Engineering for Gas Turbines and Power*, 126(4):924, 2004. (Cited p. 26 and 30.)
- [51] R. J. Miller. Mechanical Work Potential. In *ASME Turbo Expo 2013*, volume 95488, pages 1–13, 2013. (Cited p. 35, 36, 38, 40 and 284.)
- [52] S. M. Lim, A. Dahlkild, and M. Mihaescu. Aerothermodynamics and Exergy Analysis in Radial Turbine With Heat Transfer. *Journal of Turbomachinery*, 140(9):091007, 2018. (Cited p. 37 and 38.)
- [53] A. Bejan. The Method of Entropy Generation Minimization, 1999. (Cited p. 37 and 46.)
- [54] M. B. Zlatinov, C. Sooi Tan, M. Montgomery, T. Islam, and M. Harris. Turbine Hub and Shroud Sealing Flow Loss Mechanisms. *Journal of Turbomachinery*, 134(6):061027, 2012. (Cited p. 40, 44, 46, 76, 77, 78, 79, 149, 284 and 285.)
- [55] G. Hauke and T. J. R. Hughes. A unified approach to compressible and incompressible flows. *Computer Methods in Applied Mechanics and Engineering*, 113(3-4):389–395, 1994. (Cited p. 41)
- [56] A.P. S. Wheeler, R.D. Sandberg, N. D. Sandham, R. Pichler, V. Michelassi, and G. Laskowski. Direct Numerical Simulations of a High-Pressure Turbine Vane. *Journal of Turbomachinery*, 138(7):071003, 2016. (Cited p. 42)
- [57] O. B. Adeyinka and G. F. Naterer. Modeling of Entropy Production in Turbulent Flows. *Journal of Fluids Engineering*, 126(6):893, 2004. (Cited p. 42)
- [58] J. S. Kramer-Bevan. A Tool for Analysing Fluid Flow Losses. Technical report, M.Sc. Thesis, University of Waterloo, Canada., 1992. (Cited p. 43)
- [59] F. Kock and H. Herwig. Local entropy production in turbulent shear flows: A high-Reynolds number model with wall functions. *International Journal of Heat and Mass Transfer*, 47(10-11):2205–2215, 2004. (Cited p. 43 and 47.)
- [60] J. Moore and J. G. Moore. Entropy Production Rates From Viscous Flow Calculations: Part I - A Turbulent Boundary Layer Flow. In *Volume 1: Turbomachinery*, page V001T01A032, 1983. (Cited p. 43 and 44.)

- [61] C. Tailliez and A. Arntz. CFD assesement of the use of exergy analysis for losses indentification in turbomachinery flows. In *53rd 3AF International Conference on Applied Aerodynamics*, Salon de Provence, France, 2018. (Cited p. 44)
- [62] V Lengani, D. Simoni, D. Pichler, R. Sandberg, R. Michelassi. On the identification and decomposition of the unsteady losses in a turbine cascade. In *Proceedings of ASME Turbo Expo 2018*, 2018. (Cited p. 45, 74 and 253.)
- [63] H Herwig and F Kock. Direct and indirect methods of calculating entropy generation rates in turbulent convective heat transfer problems. *Heat and Mass Transfer*, 43(3):207–215, 2007. (Cited p. 46)
- [64] M. Mansour, N. Chokani, A. I. Kalfas, and R. S. Abhari. Impact of Time-Resolved Entropy Measurement on a One-and-One-Half-Stage Axial Turbine Performance. *Journal of Turbomachinery*, 134(2):021008, 2012. (Cited p. 48)
- [65] M. B. Greitzer, E. M., Tan, C. S., Graf. *Internal flow: concepts and applications (Vol. 3)*. Cambridge edition, 2007. (Cited p. 48, 63, 77 and 285.)
- [66] J. E. Lagraff, D. E. Ashpis, M. L.G. Oldfield, and J. P. Gostelow. Unsteady flows in turbomachinery. Technical report, NASA, 2006. (Cited p. 50 and 284.)
- [67] R.Parker J.F. Watson. Interaction Effects between Blade Rows in Turbomachines. In *Institution of Mechanical Engineers*, pages 331–340, 1972. (Cited p. 51)
- [68] F. Leboeuf. Ecoulements 3D dans les turbomachines. Technical report, 2001. (Cited p. 51)
- [69] V. Penin, P. Kulisa, and F. Bario. Boundary layer transition on a low pressure turbine blade due to downstream potential interaction. *Proceedings of ASME Turbo Expo 2012*, 2012. (Cited p. 51)
- [70] H. P. Hodson and R. J. Howell. Blade row interaction, transition, and high-lift airfoils in low-pressure turbine. *Annual Review of Fluid Mechanics*, 37(1):71–98, 2005. (Cited p. 51)
- [71] B. J. Abu-Ghannam and R. Shaw. Natural Transition of Boundary Layers. *Journal Mechanical Engineering Science*, 22(5):213–228, 1980. (Cited p. 53, 56, 120, 127, 186 and 284.)
- [72] F. M. White and I. Corfield. *Viscous fluid flow*. 1991. (Cited p. 54 and 284.)
- [73] Robert Edward Mayle. The Role of Laminar-Turbulent Transition in Gas Turbine Engines. In *Volume 5: Manufacturing Materials and Metallurgy; Ceramics; Structures and Dynamics; Controls, Diagnostics and Instrumentation; Education; IGTI Scholar Award; General*, 1991. (Cited p. 55)

- [74] G. J. Walker. The Role of Laminar-Turbulent Transition in Gas Turbine Engines: A Discussion. *Journal of Turbomachinery*, 115(2):207, 1993. (Cited p. 55)
- [75] G. J. Walker and J. P. Gostelow. Effects of Adverse Pressure Gradients on the Nature and Length of Boundary Layer Transition. *Journal of Turbomachinery*, 112(April):196–205, 1990. (Cited p. 55)
- [76] J. Cui, V. Nagabhushana Rao, and P. Tucker. Numerical Investigation of Contrasting Flow Physics in Different Zones of a High-Lift Low-Pressure Turbine Blade. *Journal of Turbomachinery*, 138(1):011003, 2015. (Cited p. 57, 58, 66, 70, 91, 115, 120, 122, 246, 284 and 285.)
- [77] W. Saric. *Gortler Vortices*, volume 26. 1994. (Cited p. 58)
- [78] H. P. Wang, S. J. Olson, and R. J. Goldstein. Development of Taylor-Gortler Vortices Over the Pressure Surface of a Turbine Blade. *Journal of Heat Transfer*, 127(5):540, 2005. (Cited p. 58)
- [79] X. Wu and P. A. Durbin. Evidence of longitudinal vortices evolved from distorted wakes in a turbine passage. *Journal of Fluid Mechanics*, 446:199–228, 2001. (Cited p. 58 and 233.)
- [80] J. G. Wissink. DNS of separating, low Reynolds number flow in a turbine cascade with incoming wakes. *International Journal of Heat and Fluid Flow*, 24(4):626–635, 2003. (Cited p. 58)
- [81] W. P. Jones and B. E. Launder. The prediction of laminarization with a two-equation model of turbulence. *International Journal of Heat and Mass Transfer*, 1972. (Cited p. 58)
- [82] R. B. Langtry and F. R. Menter. Correlation-Based Transition Modeling for Unstructured Parallelized Computational Fluid Dynamics Codes. *AIAA Journal*, 47(12):2894–2906, 2009. (Cited p. 58)
- [83] D. Keith Walters and Davor Cokljat. A Three-Equation Eddy-Viscosity Model for Reynolds-Averaged Navier-Stokes Simulations of Transitional Flow. *Journal of Fluids Engineering*, 130(12):121401, 2008. (Cited p. 58)
- [84] Michele Marconcini, Roberto Pacciani, Andrea Arnone, Vittorio Michelassi, Richard Pichler, Yaomin Zhao, and Richard Sandberg. Large Eddy Simulation and RANS Analysis of the End-Wall Flow in a Linear Low-Pressure-Turbine Cascade—Part II: Loss Generation. *Journal of Turbomachinery*, 2018. (Cited p. 64)
- [85] V. Michelassi, L.-W. Chen, R. Pichler, and R. D. Sandberg. Compressible Direct Numerical Simulation of Low-Pressure Turbines-Part II: Effect of Inflow Disturbances. *Journal of Turbomachinery*, 137(7):071005, 2015. (Cited p. 64, 72 and 234.)

- [86] R. Pichler, V. Michelassi, R. Sandberg, and J. Ong. Highly Resolved Large Eddy Simulation Study of Gap Size Effect on Low-Pressure Turbine Stage. *Journal of Turbomachinery*, 2017. (Cited p. 64 and 73.)
- [87] J. Denton and G. Pullan. A Numerical Investigation Into the Sources of Endwall Loss in Axial Flow Turbines. In *Volume 8: Turbomachinery, Parts A, B, and C*, page 1417, 2012. (Cited p. 64, 69, 70, 74, 141 and 285.)
- [88] C. H. Sieverding. Recent Progress in the Understanding of Basic Aspects of Secondary Flows in Turbine Blade Passages. *Journal of Engineering for Gas Turbines and Power*, 107(2):248, 1985. (Cited p. 65 and 106.)
- [89] L.S. Langston. Secondary Flows in Axial Turbines-A Review. *Annals of the New York Academy of Sciences*, 934(1):11–26, 2006. (Cited p. 65)
- [90] L. S. Langston, M. L. Nice, and R. M. Hooper. Three-Dimensional Flow Within a Turbine Cascade Passage. *Journal of Engineering for Power*, 99(1):21, 1977. (Cited p. 65)
- [91] A. A. Yamamoto. Production and Development of Secondary Flows and Losses in Two Types of Straight Turbine Cascades: Part 1-A Stator Case. *J. Turbomach.*, 109(2):186–193, 1987. (Cited p. 65 and 67.)
- [92] R. J. Goldstein, H. P. Wang, and M. Y. Jabbari. The Influence of Secondary Flows Near the Endwall and Boundary Layer Disturbance on Convective Transport From a Turbine Blade. In *Volume 4: Heat Transfer; Electric Power; Industrial and Cogeneration*, page V004T09A020, 1994. (Cited p. 65)
- [93] H. P. Wang, S. J. Olson, R. J. Goldstein, and E. R. G. Eckert. Flow Visualization in a Linear Turbine Cascade of High Performance Turbine Blades. *Journal of Turbomachinery*, 119(1):1, 1997. (Cited p. 65, 108 and 285.)
- [94] C J Baker. The Oscillation of Horseshoe Vortex Systems. *Journal of Fluids Engineering-Transactions of the Asme*, 113(3):489–495, 1991. (Cited p. 65)
- [95] R. L. Simpson. Aspects of turbulent boundary-layer separation. *Progress in Aerospace Sciences*, 32(5):457–521, 1996. (Cited p. 65)
- [96] A.S.W. Thomas. The unsteady characteristics of laminar juncture flow. *Physics of Fluids*, 30(2):283–285, 1987. (Cited p. 65)
- [97] M. R. Visbal. Structure of laminar juncture flows. *AIAA Journal*, 29(8):1273–1282, 1991. (Cited p. 65)
- [98] S. Harrison. Secondary Loss Generation in a Linear Cascade of High-Turning Turbine Blades. In *Volume 1: Turbomachinery*, page V001T01A021, 1989. (Cited p. 66 and 108.)
- [99] B. M. Holley, S. Becz, and L. S. Langston. Measurement and Calculation of Turbine Cascade Endwall Pressure and Shear Stress. *Journal of Turbomachinery*, 128(2):232, 2006. (Cited p. 66)

- [100] L. S. Langston. Crossflows in a Turbine Cascade Passage. *Journal of Engineering for Power*, 102(4):866, 1980. (Cited p. 67)
- [101] J. A. Walsh and D. G. Gregory-Smith. Inlet Skew and the Growth of Secondary Losses and Vorticity in a Turbine Cascade. *Journal of Turbomachinery*, 112(4):633, 1990. (Cited p. 68)
- [102] S Harrison. The Influence of Blade Lean on Turbine Losses. *ASME Journal of Turbomachinery : Gas Turbine and Aeroengine Congress and Exposition*, 114(January 1992):7, 1992. (Cited p. 68)
- [103] J Dunham. A Review of Cascade Data on Secondary Losses in Turbines. *Journal of Mechanical Engineering Science*, 12(1):48–59, 1970. (Cited p. 69)
- [104] D. G. Gregory-Smith, C. P. Graves, and J. a. Walsh. Growth of Secondary Losses and Vorticity in an Axial Turbine Cascade. *Journal of Turbomachinery*, 110(1):1, 1988. (Cited p. 70)
- [105] P. Lampart. Tip Leakage Flows in Turbines. *Task Quarterly*, 10(2):139–175, 2007. (Cited p. 71 and 285.)
- [106] G. Pullan. Secondary Flows and Loss Caused by Blade Row Interaction in a Turbine Stage. In *Volume 5: Turbo Expo 2004, Parts A and B*, pages 1247–1257, 2004. (Cited p. 73 and 285.)
- [107] Denis Koschichow, Jochen Fröhlich, Ilker Kirik, and Reinhard Niehuis. DNS of the Flow Near the Endwall in a Linear Low Pressure Turbine Cascade With Periodically Passing Wakes. 2014. (Cited p. 75)
- [108] M. Pau, G. Paniagua, D. Delhayé, A. De la Loma, and P. Ginibre. Aerothermal Impact of Stator-Rim Purge Flow and Rotor-Platform Film Cooling on a Transonic Turbine Stage. *Journal of Turbomachinery*, 132(2):021006, 2010. (Cited p. 75)
- [109] J. B. Young and R. C. Wilcock. Modeling the Air-Cooled Gas Turbine: Part 1-General Thermodynamics. *Journal of Turbomachinery*, 124(2):207, 2002. (Cited p. 76)
- [110] K. Reid, J. Denton, G. Pullan, E. Curtis, and J. Longley. The Effect of Stator-Rotor Hub Sealing Flow on the Mainstream Aerodynamics of a Turbine. *ASME Conference Proceedings*, 2006(4241X):789–798, 2006. (Cited p. 76)
- [111] F. Kost and M. Nicklas. Film-cooled turbine endwall in a transonic flow field: Part I - Aerodynamic measurements. *Journal of Turbomachinery*, 123(4):709–719, 2001. (Cited p. 77 and 106.)
- [112] G. Paniagua, R. Denos, and S. Almeida. Effect of the Hub Endwall Cavity Flow on the Flow-Field of a Transonic High-Pressure Turbine. In *Volume 5: Turbo Expo 2004, Parts A and B*, pages 1153–1163, 2004. (Cited p. 77 and 78.)

- [113] J. H. P. Ong, R. J. Miller, and S. Uchida. The Effect of Coolant Injection on the Endwall Flow of a High Pressure Turbine. In *Volume 6: Turbomachinery, Parts A and B*, volume 2006, pages 915–924, 2006. (Cited p. 77)
- [114] P. Schuler, K. Dullenkopf, and H.-J. Bauer. Investigation of the Influence of Different Rim Seal Geometries in a Low-Pressure Turbine. *Volume 7: Turbomachinery, Parts A, B, and C*, pages 715–729, 2011. (Cited p. 77, 78, 83, 151 and 285.)
- [115] H. M. Abo El Ella, S. A. Sjolander, and T. J. Praisner. Effects of an Upstream Cavity on the Secondary Flow in a Transonic Turbine Cascade. *Journal of Turbomachinery*, 134(5):051009, 2012. (Cited p. 77)
- [116] I. Popović and H. P. Hodson. Aerothermal Impact of the Interaction Between Hub Leakage and Mainstream Flows in Highly-Loaded High Pressure Turbine Blades. *Journal of Turbomachinery*, 135(6):061014, 2013. (Cited p. 77)
- [117] K. D. Gallier, P. B. Lawless, and S. Fleeter. Development of the Unsteady Flow on a Turbine Rotor Platform Downstream of a Rim Seal. *ASME Conference Proceedings*, 2004(41707):939–947, 2004. (Cited p. 77)
- [118] P. E. Roach. The generation of nearly isotropic turbulence by means of grids. *International Journal of Heat and Fluid Flow*, 8(2):82–92, 1987. (Cited p. 83)
- [119] T. J. Poinsot and S. K. Lelef. Boundary conditions for direct simulations of compressible viscous flows. *Journal of Computational Physics*, 101(1):104–129, 1992. (Cited p. 88, 242 and 243.)
- [120] L. Cambier and J.P. Veulliot. Status of the elsa software for flow simulation and multi-disciplinary applications. page 664, 2008. (Cited p. 88 and 248.)
- [121] E. Tang. *Modélisation et analyse de l’interaction turbine HP-Anneau de roue*. PhD thesis, Ecole Centrale de Lyon, 2016. (Cited p. 88, 172, 179 and 258.)
- [122] P. Tucker, S. Eastwood, C. Klostermeier, R. Jefferson-Loveday, J. Tyacke, and Y. Liu. Hybrid LES Approach for Practical Turbomachinery Flows: Part 2—Further Applications. *ASME Turbo Expo 2010: Power for Land, Sea and Air*, 134(March):2, 2010. (Cited p. 88 and 246.)
- [123] M. Pau, G. Paniagua, D. Delhayé, A. de la Loma, and P. Ginibre. Aerothermal Impact of Stator-Rim Purge Flow and Rotor-Platform Film Cooling on a Transonic Turbine Stage. In *Volume 6: Turbomachinery, Parts A, B, and C*, pages 1391–1404, 2008. (Cited p. 89)
- [124] M. Marconcini R. Pichler, Y. Zhao and R. D. Sandberg, V. Michelassi, R. Paciani and A. Arnone. LES and RANS analysis of the end-wall flow in a linear LPT cascade with variable inlet conditions, Part I: Flow and secondary vorticity fields. In *ASME Turbo Expo 2018: Turbomachinery Technical Conference and Exposition*, Oslo, Norway, 2018. (Cited p. 90, 91 and 196.)

- [125] U. Piomelli. Wall-layer models for large-eddy simulations, 2008. (Cited p. 91 and 246.)
- [126] N. Gourdain, F. Sicot, F. Duchaine, and L. Gicquel. Large eddy simulation of flows in industrial compressors: a path from 2015 to 2035. *Phil. Trans. R. Soc. A*, 372(2022):20130323, 2014. (Cited p. 91)
- [127] N. Afzal. Power law and log law velocity profiles in fully developed turbulent pipe flow: Equivalent relations at large Reynolds numbers. *Acta Mechanica*, 2001. (Cited p. 92)
- [128] H. Nishikawa, M. Rad, and P. Roe. A third-order fluctuation splitting scheme that preserves potential flow. 2013. (Cited p. 92)
- [129] M. Daroukh. *Effects of distortion on modern turbofan tonal noise*. PhD thesis, INP, 2017. (Cited p. 93)
- [130] N. Gourdain. Prediction of the unsteady turbulent flow in an axial compressor stage. Part 1: Comparison of unsteady RANS and LES with experiments. *Computers and Fluids*, 2015. (Cited p. 93)
- [131] N. Gourdain. Prediction of the unsteady turbulent flow in an axial compressor stage. Part 2: Analysis of unsteady RANS and LES data. *Computers and Fluids*, 2015. (Cited p. 93)
- [132] F. R. Menter. Performance of popular turbulence model for attached and separated adverse pressure gradient flows. *AIAA Journal*, 1992. (Cited p. 93)
- [133] A. Fosso P., H. Deniau, F. Sicot, and P. Sagaut. Curvilinear finite-volume schemes using high-order compact interpolation. *Journal of Computational Physics*, 2010. (Cited p. 93)
- [134] A. Jameson, W. Schmidt, and E. Turkel. Numerical solutions of the Euler equations by finite volume methods using Runge-Kutta time-stepping schemes. *AIAA paper*, 1981. (Cited p. 93)
- [135] F. Nicoud and F. Ducros. Subgrid-scale stress modelling based on the square of the velocity gradient tensor Subgrid-scale stress modelling based on the square of the velocity gradient tensor. *Flow, Turbulence and Combustion*, 62(3):183–200, 1999. (Cited p. 93, 240 and 248.)
- [136] O. Colin and M. Rudgyard. Development of High-Order Taylor-Galerkin Schemes for LES. *Journal of Computational Physics*, 162(2):338–371, 2000. (Cited p. 93 and 248.)
- [137] O. Malaspinas and P. Sagaut. Advanced large-eddy simulation for lattice Boltzmann methods: The approximate deconvolution model. *Physics of Fluids*, 23(10), 2011. (Cited p. 93)

- [138] S. Stolz, N. A. Adams, and L. Kleiser. An approximate deconvolution model for large-eddy simulation with application to incompressible wall-bounded flows. *Physics of Fluids*, 13(4):997–1015, 2001. (Cited p. 93 and 249.)
- [139] O. P. Sharma and T. L. Butler. Predictions of Endwall Losses and Secondary Flows in Axial Flow Turbine Cascades. *Journal of Turbomachinery*, 109(86):229, 1987. (Cited p. 106)
- [140] G. I. Mahmood and S. Acharya. Experimental Investigation of Secondary Flow Structure in a Blade Passage With and Without Leading Edge Fillets. *Journal of Fluids Engineering*, 2007. (Cited p. 108)
- [141] Advisory Group for Aerospace Research and Development (AGARD). *Secondary Flows in Turbomachines*. 1990. (Cited p. 108)
- [142] H. P. Hodson and R. G. Dominy. Three-Dimensional Flow in a Low-Pressure Turbine Cascade at Its Design Condition. *Journal of Turbomachinery*, 109(2):177, 1987. (Cited p. 123)
- [143] A Smirnov, S Shi, and I Celik. Random Flow Simulations with Bubble Dynamics Model. In *Proceedings of FEDSM00 ASME 2000 Fluids Engineering Division Summer Meeting*, volume FEDSM2000-, 2000. (Cited p. 125)
- [144] L. Segui Troth. *Multi-physics coupled simulation of gas turbine*. PhD thesis, 2017. (Cited p. 125, 126, 244 and 245.)
- [145] F. Fontaneto. *aero-thermal performance of a film-cooled high pressure turbine blade/vane: a test case for numerical codes validation*. PhD thesis, 2014. (Cited p. 125)
- [146] P. Sagaut and C. Cambon. *Homogeneous turbulence dynamics*. 2018. (Cited p. 125 and 126.)
- [147] D. Lengani, D. Simoni, M. Ubaldi, P. Zunino, F. Bertini, and V. Michelassi. Accurate Estimation of Profile Losses and Analysis of Loss Generation Mechanisms in a Turbine Cascade. *Journal of Turbomachinery*, 139(12):121007, 2017. (Cited p. 134)
- [148] C. Dapogny, C. Dobrzynski, and P. Frey. Three-dimensional adaptive domain remeshing, implicit domain meshing, and applications to free and moving boundary problems. *Journal of Computational Physics*, 262:358–378, 2014. (Cited p. 172)
- [149] A. Pogorelov, M. Meinke, and W. Schroder. Large-Eddy Simulation of the Unsteady Full 3D Rim Seal Flow in a One-Stage Axial-Flow Turbine. *Flow, Turbulence and Combustion*, 2018. (Cited p. 179)
- [150] Yazan Taamneh. Thermal analysis of gas turbine disk integrated with rotating heat pipes. *Case Studies in Thermal Engineering*, 2017. (Cited p. 179)

- [151] Sébastien Poncet, Éric Serre, and Patrice Le Gal. Revisiting the two first instabilities of the flow in an annular rotor-stator cavity. *Physics of Fluids*, 2009. (Cited p. 180)
- [152] Jens Nørkær Sørensen, Igor Naumov, and Robert Mikkelsen. Experimental investigation of three-dimensional flow instabilities in a rotating lid-driven cavity. *Experiments in Fluids*, 2006. (Cited p. 180)
- [153] O. Colin. *Simulation aux Grandes Echelles de la Combustion Turbulente et Prémélangée dans les Statoréacteurs*. PhD thesis, INP, 2000. (Cited p. 197)
- [154] O. Reynolds. An Experimental Investigation of the Circumstances Which Determine Whether the Motion of Water Shall Be Direct or Sinuous, and of the Law of Resistance in Parallel Channels. *Philosophical Transactions of the Royal Society of London*, 1883. (Cited p. 221 and 231.)
- [155] Q. Li, Y. L. He, Y. Wang, and W. Q. Tao. Coupled double-distribution-function lattice Boltzmann method for the compressible Navier-Stokes equations. *Physical Review E - Statistical, Nonlinear, and Soft Matter Physics*, 2007. (Cited p. 228)
- [156] A. Mezrhab, M'h. Bouzidi, and P. Lallemand. Hybrid lattice-Boltzmann finite-difference simulation of convective flows. *Computers and Fluids*, 2004. (Cited p. 228)
- [157] C. Coreixas, G. Wissocq, G. Puigt, J-F. Boussuge, and P. Sagaut. Recursive regularization step for high-order lattice Boltzmann methods. *Physical Review E*, 2017. (Cited p. 230 and 292.)
- [158] P. G. Tucker. Computation of unsteady turbomachinery flows: Part 2-LES and hybrids. *Progress in Aerospace Sciences*, 47(7):546–569, 2011. (Cited p. 231, 247 and 293.)
- [159] V. Gravemeier. Current methods for the numerical simulation of turbulent flows. *CAFDEM Infoplaner*, pages 42–43, 2007. (Cited p. 232 and 292.)
- [160] S. Jamshed. Introduction to CFD. In *Using HPC for Computational Fluid Dynamics*. 2015. (Cited p. 231)
- [161] Lewis F. Richardson. *Weather prediction by numerical process, second edition*. 2007. (Cited p. 232)
- [162] A. N. Kolmogorov. The Local Structure of Turbulence in Incompressible Viscous Fluid for Very Large Reynolds Numbers. *Proceedings of the Royal Society A: Mathematical, Physical and Engineering Sciences*, 1991. (Cited p. 233)
- [163] G. N. Coleman and R. D. Sandberg. A primer on direct numerical simulation of turbulence-methods, procedures and guidelines. Technical report, 2010. (Cited p. 233)

- [164] J. Kim, P. Moin, and R. Moser. Turbulence statistics in fully developed channel flow at low reynolds number. *Journal of Fluid Mechanics*, 177:133–166, 1987. (Cited p. 233 and 237.)
- [165] L. Krishnan and N. D. Sandham. Effect of Mach number on the structure of turbulent spots. *Journal of Fluid Mechanics*, 566:225–234, 2006. (Cited p. 233)
- [166] J. Hourmouziadis. Aerodynamic design of low pressure turbines. *AGARD Lecture Series*, 167(167), 1989. (Cited p. 234 and 292.)
- [167] Michelassi V., Wissink J., and Rodi W. Analysis of DNS and LES of Flow in a Low Pressure Turbine Cascade with Incoming Wakes and Comparison with Experiments. *Flow, Turbulence and Combustion*, 69(3-4):295–330, 2002. (Cited p. 233)
- [168] J. G. Wissink and W. Rodi. Direct numerical simulation of flow and heat transfer in a turbine cascade with incoming wakes. *Journal of Fluid Mechanics*, 569:209–247, 2006. (Cited p. 233)
- [169] G. Kalitzin, X. Wu, and P. A. Durbin. DNS of fully turbulent flow in a LPT passage. *International Journal of Heat and Fluid Flow*, 24(4):636–644, 2003. (Cited p. 233)
- [170] R. Ranjan, S. M. Deshpande, and R. Narasimha. New insights from high-resolution compressible DNS studies on an LPT blade boundary layer. *Computers and Fluids*, 153:49–60, 2017. (Cited p. 234)
- [171] A. Garai, L. Diosady, S. Murman, and N. Madavan. DNS of Flow In a Low-Pressure Turbine Cascade Using a Discontinuous-Galerkin Spectral-Element Method. In *ASME Turbo Expo*, pages 1–10, 2015. (Cited p. 234)
- [172] L. W. Chen, R. Pichler, and R. D. Sandberg. Compressible DNS of a low pressure turbine subjected to inlet disturbances. In *ERCOFTAC Series*, volume 20, pages 383–388, 2015. (Cited p. 234)
- [173] P. Cardamone, P. Stadtmuller, and L. Fottner. Numerical Investigation of the Wake-Boundary Layer Interaction on a Highly Loaded LP Turbine Cascade Blade. In *Volume 5: Turbo Expo 2002, Parts A and B*, pages 401–409, 2002. (Cited p. 234)
- [174] A Favre. Equations des gaz turbulents compressibles. *Journal de mécanique*, 4(3):361–421, 1965. (Cited p. 235)
- [175] B. Aupoix. Introduction to turbulence modelling for compressible flow. chapter Introducti. 2002. (Cited p. 235)
- [176] S. B. Pope. *Turbulent Flows*, volume 1. 2000. (Cited p. 237 and 240.)
- [177] P. R. Spalart. Direct Simulation of a Turbulent Boundary Layer up to $Re = 1410$. *Journal of Fluid Mechanics*, 187:61–98, 1988. (Cited p. 237)

- [178] P. Sagaut. *Large Eddy Simulation for Incompressible Flows: An Introduction*. 2006. (Cited p. 237, 248 and 292.)
- [179] J. Smagorinsky. General circulation experiments with primitive equation I. The basic experiment. *Monthly Weather Review*, 91(3):99–164, 1963. (Cited p. 239)
- [180] H. Fujiwara, P. R. Voke, and C. Arakawa. Large-Eddy Simulation of TL10 LP Turbine Blade Row. In *Engineering Turbulence Modelling and Experiments 5*, pages 751–758. 2002. (Cited p. 239)
- [181] T. Léonard, L.Y. M. Gicquel, N. Gourdain, and F. Duchaine. Steady/Unsteady Reynolds-Averaged Navier-Stokes and Large Eddy Simulations of a Turbine Blade at High Subsonic Outlet Mach Number. *Journal of Turbomachinery*, 137(4):041001, 2014. (Cited p. 239)
- [182] W. A. McMullan and G. J. Page. Towards Large Eddy Simulation of gas turbine compressors. *Progress in Aerospace Sciences*, 52:30–47, 2012. (Cited p. 239 and 244.)
- [183] M. Germano, U. Piomelli, P. Moin, and W. H. Cabot. A dynamic subgrid-scale eddy viscosity model. *Physics of Fluids A*, 3(7):1760–1765, 1991. (Cited p. 239)
- [184] S. J. Eastwood, P. G. Tucker, H. Xia, and C. Klostermeier. Developing large eddy simulation for turbomachinery applications. *Philosophical Transactions of the Royal Society A: Mathematical, Physical and Engineering Sciences*, 367(1899):2999–3013, 2009. (Cited p. 240 and 245.)
- [185] K. Matsuura and C. Kato. Large-Eddy Simulation of Compressible Transitional Cascade Flows with and without Incoming Free-Stream Turbulence. *JSME International Journal Series B*, 49(3):660–669, 2006. (Cited p. 240 and 244.)
- [186] K.W. Thompson. Time dependent boundary conditions for hyperbolic systems. *Journal of Computational Physics*, 68(1):1–24, 1987. (Cited p. 242)
- [187] N. Odier, M. Sanjosé, L. Gicquel, T. Poinso, S. Moreau, and F. Duchaine. A characteristic inlet boundary condition for compressible, turbulent, multi-species turbomachinery flows, 2018. (Cited p. 243)
- [188] A. Colombo and A. Crivellini. Assessment of a sponge layer non-reflecting boundary treatment for high-order CAA/CFD computations. *Computers and Fluids*, 2016. (Cited p. 244)
- [189] R. H. Kraichnan. Diffusion by a random velocity field. *Physics of Fluids*, 13(1):22–31, 1970. (Cited p. 244)
- [190] F. Xiao, M. Dianat, and J. J. McGuirk. An LES Turbulent Inflow Generator using A Recycling and Rescaling Method. *Flow, Turbulence and Combustion*, 2017. (Cited p. 244)

- [191] N. Dhamankar, G. Blaisdell, and A. Lyrantzis. An overview of turbulent inflow boundary conditions for large eddy simulations. In *AIAA-Aviation*, Dallas, 2015. (Cited p. 245)
- [192] A. Gomar, N. Gourdain, and G Dufour. High fidelity simulation of the turbulent flow in a transonic axial compressor. *European Turbomachinery Conference*, 37(1998):1–11, 2011. (Cited p. 245)
- [193] P. R. Spalart, S. Deck, M. L. Shur, K. D. Squires, M. Kh Strelets, and A. Travin. A new version of detached-eddy simulation, resistant to ambiguous grid densities. *Theoretical and Computational Fluid Dynamics*, 20(3):181–195, 2006. (Cited p. 246)
- [194] G. A. Gerolymos, G. J. Michon, and J. Neubauer. Analysis and Application of Chorochronic Periodicity in Turbomachinery Rotor/Stator Interaction Computations. *Journal of Propulsion and Power*, 18(6):1139–1152, 2002. (Cited p. 246)
- [195] U. Piomelli and E. Balaras. Wall-Layer Models for Large Eddy Simulations. *Annual Review of Fluid Mechanics*, 34:349–374, 2002. (Cited p. 247 and 293.)
- [196] G. Comte-Bellot and S. Corrsin. Simple Eulerian time correlation of full-and narrow-band velocity signals in grid-generated, 'isotropic' turbulence. *Journal of Fluid Mechanics*, 48(2):273–337, 1971. (Cited p. 246)
- [197] D. K. Bisset, R. A. Antonia, and D. Britz. Structure of large-scale vorticity in a turbulent far wake. *Journal of Fluid Mechanics*, 218:463–482, 1990. (Cited p. 247)
- [198] N. D. Sandham and R. D. Sandberg. Direct numerical simulation of the early development of a turbulent mixing layer downstream of a splitter plate. *Journal of Turbulence*, 10:1–17, 2009. (Cited p. 247)
- [199] P. Beaumier and J. M. Bousquet. Applied CFD for analysing aerodynamic flows around helicopters. *Icas 2004*, 2004. (Cited p. 248)
- [200] G. Mouret, N. Gourdain, and L. Castillon. Adaptation of Phase-Lagged Boundary Conditions to Large Eddy Simulation in Turbomachinery Configurations. *Journal of Turbomachinery*, 2015. (Cited p. 248)
- [201] L. Y. M. Gicquel, N. Gourdain, J.-F. Boussuge, H. Deniau, G. Staffelbach, P. Wolf, and T. Poinso. High performance parallel computing of flows in complex geometries. *Comptes Rendus Mécanique*, 339(2-3):104–124, 2011. (Cited p. 248)
- [202] N. Lamarque. *Schémas numériques et conditions limites pour la simulation aux grandes échelles de la combustion diphasique dans les foyers d'hélicoptère*. PhD thesis, INP Toulouse, 2007. (Cited p. 248)

- [203] G. Wang, F. Duchaine, D. Papadogiannis, I. Duran, S. Moreau, and L.Y.M. Gicquel. An overset grid method for large eddy simulation of turbomachinery stages. *Journal of Computational Physics*, 2014. (Cited p. 248)
- [204] K. Xu. A Gas-Kinetic BGK Scheme for the Navier-Stokes Equations and Its Connection with Artificial Dissipation and Godunov Method. *Journal of Computational Physics*, 171(1):289–335, 2001. (Cited p. 248)
- [205] H. Touil, D. Ricot, and E. L  v  que. Direct and large-eddy simulation of turbulent flows on composite multi-resolution grids by the lattice Boltzmann method. *Journal of Computational Physics*, 256:220–233, 2014. (Cited p. 248)
- [206] E. L  v  que, F. Toschi, L. Shao, and J. P. Bertoglio. Shear-improved Smagorinsky model for large-eddy simulation of wall-bounded turbulent flows. *Journal of Fluid Mechanics*, 570:491–502, 2007. (Cited p. 248)
- [207] M. Casey and T. Wintergerste. ERCOFTAC - Special interest group on "quality and trust in industrial CFD" - Best practice guidelines. Technical Report January, 2000. (Cited p. 249)
- [208] M. H. Barber and T. Ahmed. Fast Fourier Transform Convergence Criterion for Numerical Simulations of Periodic Fluid Flows. *AIAA Journal*, 2005. (Cited p. 250)
- [209] J. P. Clark and E. A. Grover. Assessing Convergence in Predictions of Periodic-Unsteady Flowfields. In *Volume 6: Turbomachinery, Parts A and B*, volume 2006, pages 1831–1841, 2006. (Cited p. 250)
- [210] N. A. Cumpsty and J. H. Horlock. Averaging Non-Uniform Flow for a Purpose. In *Volume 6: Turbo Expo 2005, Parts A and B*, pages 1–14, 2005. (Cited p. 254 and 255.)
- [211] J. E. Hartsel. Prediction of Effects of Mass-Transfer Cooling on the Blade-Row Efficiency of Turbine Airfoils. In *AIAA*, San Diego, 1972. (Cited p. 257)
- [212] J. B. Young and J. H. Horlock. Defining the Efficiency of a Cooled Turbine. *Journal of Turbomachinery*, 128(4):658, 2006. (Cited p. 257)
- [213] D. Lovely and R. Haimes. Shock detection from computational fluid dynamics results. In *14th Computational Fluid Dynamics Conference*, 1999. (Cited p. 269)
- [214] M. Drela. Power Balance in Aerodynamic Flows. *AIAA Journal*, 47(7):1761–1771, 2009. (Cited p. 269)
- [215] F. S. Schraner, J. A. Domaradzki, S. Hickel, and Nikolaus A. Adams. Assessing the numerical dissipation rate and viscosity in numerical simulations of fluid flows. *Computers and Fluids*, 114:84–97, 2015. (Cited p. 274)

- [216] V. Michelassi, F. Martelli, R. Dénos, T. Arts, and C. H. Sieverding. Unsteady heat transfer in stator-rotor interaction by two equation turbulence model. *ASME 1998 International Gas Turbine and Aeroengine Congress and Exhibition*, 1998. (Cited p. 280)
- [217] J. Cliquet, R. Houdeville, and D. Arnal. Application of Laminar-Turbulent Transition Criteria in Navier-Stokes Computations. *AIAA Journal*, 46(5):1182–1190, 2008. (Cited p. 281)

Influence des écoulements de cavité inter-disque sur l'aérodynamique d'une turbine

Résumé: Afin de faire face aux fortes températures rencontrées par les composants en aval de la chambre de combustion, des prélèvements d'air plus frais sont réalisés au niveau du compresseur. Cet air alimente les cavités en pied de turbine et refroidi les disques rotor permettant d'assurer le bon fonctionnement de la turbine. Ce manuscrit présente une étude numérique de l'effet de ces écoulements de cavité au pied de la turbine sur ses performances aérodynamiques. Les phénomènes d'interaction entre l'air de cavité en pied de turbine et l'air de veine principal est un phénomène encore difficilement compris. L'étude de ces phénomènes est réalisée au travers de différentes approches numériques (RANS, LES et LES-LBM) appliquées à deux configurations pour lesquelles des résultats expérimentaux sont disponibles. Une première configuration en grille d'aube linéaire en amont de laquelle différentes géométries d'entrefer (interface entre plateforme rotor et stator) et débits de cavité pouvaient être variés. Une seconde configuration annulaire composée de deux étages de turbine comprenant les cavités en pied et plus proche d'une configuration industrielle. Les pertes additionnelles associées à l'écoulement de cavité sont mesurées et étudiées à l'aide d'une méthode basée sur l'exergie (bilans d'énergie dans l'objectif de générer du travail).

Mots-clés: aérodynamique turbine, écoulements de purge en pied d'aube, espace inter-disque, entrefer, processus de mélange; pertes, simulations numériques.

Influence of inter-disc cavity flow on turbine aerodynamics

Abstract: In order to deal with high temperatures faced by the components downstream of the combustion chamber, some relatively cold air is bled at the compressor. This air feeds the cavities under the turbine main annulus and cool down the rotor disks ensuring a proper and safe operation of the turbine. This thesis manuscript introduces a numerical study of the effect of the cavity flow close to the turbine hub on its aerodynamic performance. The interaction phenomena between the cavity and main annulus flow are not currently fully understood. The study of these phenomena is performed based on different numerical approaches (RANS, LES and LES-LBM) applied to two configurations for which experimental results are available. A linear cascade configuration with an upstream cavity and various rim seal geometries (interface between rotor and stator platform) and cavity flow rate available. A rotating configuration that is a two stage turbine including cavities close to realistic industrial configurations. Additional losses incurred by the cavity flow are measured and studied using a method based on exergy (energy balance in the purpose to generate work).

Keywords: axial turbine aerodynamic, cavity purge flow, wheel-space, rim seal, mixing processes, loss accounting, exergy analysis, numerical simulation.